Modélisation de l'amortissement dans les analyses dynamiques non-linéaires de structures en béton armé : modèles matériaux et identification expérimentale

Clotilde Chambreuil

université
PARIS-SACLAY

Modelling of damping in nonlinear dynamic analyses of reinforced concrete structures : constitutive formulations and experimental identification

Modélisation de l'amortissement dans les analyses dynamiques non-linéaires de structures en béton armé : modèles matériaux et identification expérimentale

Thèse de doctorat de l'université Paris-Saclay

École doctorale n°579 : sciences mécaniques et énergétiques, matériaux et géosciences (SMEMaG)
Spécialité de doctorat : Génie Civil
Graduate School : Sciences de l'ingénierie et des systèmes,
Référent : ENS Paris-Saclay

Thèse préparée dans l'unité de recherche LMT - Laboratoire de Mécanique et Technologie (Université Paris-Saclay, ENS Paris-Saclay, CNRS), sous la direction de **Frédéric RAGUENEAU**, Professeur des Universités, le co-encadrement de **Cédric GIRY**, Maître de Conférence, et le co-encadrement de **Pierre LÉGER**, Professeur des Universités

Thèse soutenue à Paris-Saclay, le 21 Mars 2022, par

Clotilde CHAMBREUIL

Composition du jury

Jean-François Semblat	Président & Examinateur
Professeur des Universités, ENSTA / Institut Polytechnique de Paris	
Stéphane Grange	Rapporteur & Examinateur
Professeur des Universités, INSA Lyon	
Maria Paola Santisi d'Avila	Rapporteure & Examinatrice
Maîtresse de Conférence - HDR, Université Côte d'Azur	
François Voldoire	Examinateur
Ingénieur de recherche, EDF R&D Division	
Frédéric Ragueneau	Directeur de thèse
Professeur des Universités, ENS Paris-Saclay	

Titre : Modélisation de l'amortissement dans les analyses dynamiques non-linéaires de structures en béton armé : modèles matériaux et identification expérimentale

Mots clés : Amortissement, Béton armé, Dynamique, Modèle non-linéaire, Bilan énergétique, Identification et actualisation de l'amortissement

Résumé : En plus de la nouvelle réglementation sismique mise en place en 2011 sur le territoire français, l'accident nucléaire de Fukushima la même année a poussé le gouvernement français à investir pour la sécurité des bâtiments nucléaires. Pour assurer la viabilité de telles structures, des modèles performants sont nécessaires et doivent intégrer une description fine des phénomènes physiques. Dans le cas de structures en béton armé, la plus grande difficulté vient du manque de connaissances sur l'évolution de l'endommagement et la capacité du béton à dissiper de l'énergie.

Depuis les années 1970, l'amortissement est considéré comme un élément prédominant pour l'analyse de structures sous chargements dynamiques. Dans le cas des structures en béton armé, de nombreuses sources d'amortissement agissent en parallèle. Lorsqu'une structure est soumise à un séisme, elle dissipe de l'énergie par hystérésis à l'échelle du matériau et par d'autres phénomènes modélisés par un amortissement visqueux (échelle globale). La revue bibliographique en début de thèse vise à traiter la notion d'amortissement dans la littérature avec des modèles proposés plus ou moins complexes, et l'identification de cette grandeur dans le but d'améliorer les modèles.

Différentes questions relatives à la notion d'amortissement se sont posées dans le cadre de ces travaux : Dans le cadre d'analyses dynamiques non-linéaires, quelles sont les formulations d'amortissement visqueux les plus représentatives des réponses structurales ? Comment évolue l'amortissement au cours d'analyses non-linéaires ? Comment peut-on améliorer les modèles d'amortissement à l'échelle locale pour réduire l'amortissement visqueux nécessaire à l'échelle globale ?

Pour répondre à ces questions, un modèle multi-fibre est développé, sous le logiciel Cast3M, à partir de données expérimentales sur des poutres en béton armé. Des modèles de comportement non-linéaires pour le béton sont utilisés. Expérimentalement, les armatures en acier n'ont pas plastifié donc les travaux se concentrent sur la fissuration du béton lorsque les aciers d'armature restent dans le domaine linéaire. Le modèle numérique est calibré sur des essais quasi-statiques. Seize formulations de matrices d'amortissement classiques sont ensuite étudiées, sur des essais dynamiques, avec des taux d'amortissement variant de 0.5% à 5%. Les réponses des différents modèles sont comparées grâce aux réponses expérimentales et à des analyses énergétiques. Il apparaît donc nécessaire de modéliser suffisamment de phénomènes physiques à l'échelle locale (fissuration, friction, effet unilatéral) afin d'obtenir des résultats cohérents avec les réponses expérimentales.

Dans le dernier chapitre, une méthode d'identification de l'amortissement est développée sur un modèle à un degré-de-liberté équivalent au modèle multi-fibre de la poutre en béton armé. L'objectif est d'identifier l'évolution temporelle du taux d'amortissement visqueux en parallèle de l'endommagement de la poutre. La principale conclusion est que le taux d'amortissement visqueux évolue exponentiellement par rapport à un indice d'endommagement, défini à partir de la dégradation de la rigidité de la poutre. Cependant, si la valeur d'endommagement est inférieure à 0.6, considérer un taux d'amortissement constant égal à 4% semble adéquat. Finalement, un modèle d'amortissement actualisé à l'échelle locale est proposé en se basant sur le développement des non-linéarités dans le béton. L'avantage de ces modèles, en plus d'être représentatifs des résultats expérimentaux, est alors leur base physique à l'échelle locale du matériau. Les phénomènes principalement influents sont le développement des fissures (endommagement) et le frottement dans les fissures.

Title : Modelling of damping in nonlinear dynamic analyses of reinforced concrete structures : constitutive formulations and experimental identification

Keywords : Damping, Reinforced Concrete, Dynamic, Nonlinear Model, Energy Balances, Damping Identification and updating

Abstract : In addition to the new seismic zoning of the French territory in 2011, the Fukushima nuclear accident the same year prompted the French government to focus on the safety of nuclear buildings. To ensure the viability of such structures, performative models are required, so they must integrate fine physical phenomena descriptions. In the case of reinforced concrete structures, the significant difficulty comes from the lack of knowledge about the damage evolution and the ability of concrete to dissipate energy.

Since the 1970s, damping has been considered a predominant element in analysing structures under dynamic loading. For reinforced concrete structures, many sources of damping act in parallel. When a structure is subjected to an earthquake, it dissipates energy by hysteresis at the material scale and other phenomena modelled by viscous damping (global scale). The bibliographical review at the beginning of the thesis aims to treat the notion of damping in the literature with more or less complex proposed models and the identification of this quantity to improve the models.

Various problematic relating to the concept of damping are of interest in this PhD work : In the framework of nonlinear dynamic computations, which local and global viscous damping formulations best represent the experimental structural response ? How are local and global damping energy dissipation mechanisms evolving during nonlinear dynamic computations ? How could we improve the damping modelling at the local scale, on a physical basis, to reduce the requirement of arbitrary equivalent viscous damping at the global scale ?

A multi-fibre model is developed in Cast3M software from experimental data on reinforced concrete beams to answer these research questions. Nonlinear behaviour models for concrete are used. Experimentally, the steel reinforcement is not plasticised, so the work focuses on concrete cracking when the steel reinforcement remains in the linear domain. The numerical model is calibrated on quasi-static tests. Sixteen formulations of classical damping matrices are then studied, on dynamic tests, with damping rates varying from 0.5% to 5%. The responses of the different models are compared with the experimental responses and energy analyses. Therefore, it appears necessary to model sufficient physical phenomena at the local scale (cracking, friction, unilateral effect) to obtain results consistent with the experimental responses.

In the last chapter, a damping identification method is developed on a one degree-of-freedom model equivalent to the multi-fibre model of the reinforced concrete beam. The objective is to identify the transient evolution of the viscous damping rate in parallel with the beam damage. The main conclusion is that the viscous damping rate evolves exponentially with respect to a damage index defined from the degradation of the beam stiffness. However, if the damage value is less than 0.6, considering a constant damping rate equal to 4% seems adequate. Finally, a locally updated damping model is proposed based on the development of nonlinearities in concrete. The advantage of these models is their physical basis at the local scale of the material, in addition to their representation of the experimental results. The main influencing phenomena are crack development (damage) and friction in cracks.

Résumé substantiel

Contexte

La mise en place en 2005 de l'Eurocode 8 (NF EN 1998-1, 2005) ainsi que l'évolution de la connaissance scientifique sur le risque sismique ont conduit, en 2011, à la décomposition du territoire français en cinq zone de sismicité. Seules les structures classiques dans la zone de sismicité 1 ne sont pas soumises à des règles sismiques. Entre l'ancien et le nouveau découpage, le nombre de municipalités françaises soumises aux règles sismiques est passé de 5 000 à 20 000. De plus, l'accident nucléaire de Fukushima en 2011 a poussé le gouvernement français à investir pour la sécurité des bâtiments nucléaires, motivé en particulier par la présence de cinq centrales nucléaires sur des zones de sismicité 3 ou 4. Pour assurer la viabilité ou augmenter la durée de vie de ces structures, des calculs numériques doivent être réalisés prenant en compte la nouvelle réglementation sismique et l'état actuel de vieillissement des structures. Les modèles doivent donc intégrer finement les phénomènes physiques tout en restant robustes, efficaces et précis.

La difficulté avec les structures en béton armé provient du manque de connaissance sur l'évolution de leur endommagement, telle que la fissuration, lorsqu'elles sont soumises à des séismes, ainsi que la capacité du béton à dissiper de l'énergie sismique. Ces dissipations sont classiquement modélisées à deux échelles : locale et globale. À l'échelle locale, les dissipations sont décrites par des lois de comportement non-linéaires considérant plus ou moins de phénomènes physiques. L'identification des modèles se fait grâce à des essais en laboratoire. La considération de ces dissipations à l'échelle de la structure est obtenue par intégration des données locales. À l'échelle globale, en revanche, les dissipations caractérisent les interactions de la structure avec son environnement. Elles sont classiquement modélisées par un amortissement visqueux, c'est-à-dire proportionnel à la vitesse. Cette stratégie permet de prendre en compte les phénomènes physiques non modélisés ou encore mal compris.

Enjeux scientifiques, problématique et objectifs

Depuis les années 1970, l'amortissement est considéré comme un élément prédominant pour l'analyse de structures sous chargements dynamiques. Dans le cas des structures en béton armé, de nombreuses sources d'amortissement agissent en parallèle. Smyrou, Priestley, and Carr (2011) ont proposé une classification de ces sources d'amortissement entre les sources internes et externes. Les sources externes correspondent aux interactions de la structure avec son environnement. Pour les sources internes, les dissipations dépendent des phénomènes activés par le séisme et modifient les caractéristiques des matériaux (béton, acier et interface acier-béton). La difficulté pour considérer ces phénomènes est la méconnaissance de certains d'entre eux et l'existence de couplages. C'est pourquoi différentes stratégies existent dans la littérature pour pallier ces problèmes.

Lorsqu'une structure est soumise à un séisme, elle dissipe de l'énergie par hystérésis à l'échelle du matériau (locale) et par d'autres phénomènes modélisés par un amortissement visqueux. En ingénierie,

des modèles d'amortissement visqueux sont souvent utilisés avec des modèles matériaux linéaires afin de gagner en temps de calculs. Les modèles d'amortissement visqueux classiques sont soit de type Rayleigh, c'est-à-dire proportionnels aux matrices de masse et/ou de rigidité du problème, soit de type modal, c'est-à-dire calculés à partir des propriétés modales de la structure. La matrice de Rayleigh, déduite des travaux de Rayleigh (1877) and Rayleigh (1896), est toujours la plus utilisée de par sa simplicité d'utilisation. Des difficultés apparaissent cependant lorsque des analyses non-linéaires sont réalisées. En effet, considérer la matrice de rigidité initiale ne permet pas de prendre en compte l'évolution du matériau au cours du temps. De nombreux articles scientifiques se sont intéressés à la matrice de Rayleigh, en particulier Hall (2006), aux problèmes découlant de son utilisation, ainsi qu'à des solutions pour améliorer les résultats. Les principales adaptations de la matrice de Rayleigh sont : (i) éliminer la matrice de masse qui induit des forces non réelles (F. Charney et al., 2017), (ii) utiliser la matrice de rigidité tangente pour prendre en compte le développement des non-linéarités (Hall, 2006; Petrini et al., 2008), ou encore (iii) mettre à jour les paramètres de proportionnalité grâce à des analyses modales sur la structure endommagée, … D'autres formulations classiques de matrices d'amortissement, c'est-à-dire construites à partir de matrices de masse et rigidité, ont également été proposées par T. K. Caughey (1960), T. K. Caughey and O'Kelly (1965a), and Bernal (1994). Les matrices modales sont, quant-à-elles, construites à partir des modes propres de la structure. Wilson and Penzien (1972) and Chopra and McKenna (2016) ont, par exemple, proposé des formulations de ce type. De nombreux autres modèles d'amortissement ont également été proposés dans la littérature mais sont rarement utilisés en ingénierie en raison de leur complexité. Dans les logiciels d'éléments finis, les matrices de type Rayleigh et modales sont toujours majoritairement mises en œuvre. C'est pourquoi de nombreux articles scientifiques s'intéressent également à comparer ces formulations classiques sur des exemples précis. Cependant, très peu de ces analyses sont basées sur des résultats expérimentaux et accompagnées d'analyses énergétiques pour compléter la comparaison des formulations.

L'identification de l'amortissement sur des structures réelles représente également un défi scientifique d'actualité. Tout d'abord, elle est nécessaire afin de déterminer les paramètres des modèles d'amortissement discutés précédemment. Elle est également un moyen de faire de la détection d'endommagement puisque les propriétés modales d'une structure sont intimement liées à ses propriétés physiques. La recherche s'intéresse à cette notion d'identification de l'amortissement que ce soit sur des éléments structuraux ou sur des structures complètes au travers de stratégies expérimentales ou numériques. Une majorité des taux d'amortissement visqueux équivalents identifiés est comprise entre 1% et 5% (Carneiro et al., 2006; Heitz, Giry, et al., 2017), ce qui est cohérent avec les 5% souvent considérés dans les codes de calculs. Cependant, lorsque des éléments endommagés sont étudiés, des taux d'amortissement pouvant atteindre 20% (Tinawi et al., 2000) peuvent être identifiés, ce qui démontre la nécessité de devoir actualiser cette grandeur lorsque des analyses non-linéaires sont réalisées. Crambuer (2013) montre même qu'actualiser correctement un taux d'amortissement pendant des analyses non-linéaires permet de s'affranchir de modèles matériaux complexes, conduisant à un gain de temps de calcul.

À la suite d'une analyse bibliographique présentée dans le premier chapitre de ce manuscrit, différentes problématiques sont considérées et servent de fil directeur pour les travaux réalisés :

> **Dans le cadre d'analyses dynamiques non-linéaires, quelles sont les formulations d'amortissement visqueux les plus représentatives des réponses structurales ?**
>
> **Comment évolue l'amortissement au cours d'analyses non-linéaires ?**
>
> **Comment peut-on améliorer les modèles d'amortissement à l'échelle locale pour réduire l'amortissement visqueux nécessaire à l'échelle globale ?**

Il est important de noter que la portée du travail se limite à la fissuration du béton lorsque les aciers d'armature restent dans le domaine linéaire.

Structure de la thèse

Pour répondre aux différentes problématiques, le manuscrit est décomposé en trois chapitres. Il synthétise les travaux réalisés pendant les trois années de thèse. Le premier chapitre est une synthèse bibliographique et une revue critique des travaux existants dans la littérature, tandis que le deuxième chapitre s'intéresse au modèle multi-fibre ainsi qu'à l'analyse numérique des différents modèles d'amortissement. Enfin, le troisième chapitre présente les différents travaux réalisés autour de la notion d'amortissement (identification et modèle local). Finalement, un conclusion générale vient clôturer le travail et ouvrir des perspectives à plus ou moins long terme.

Analyse des modèles d'amortissement classiques (chapitre 2)

Au cours de ses travaux de thèse, Heitz (2017) a réalisé une campagne expérimentale importante sur des poutres en béton armé au CEA (Commissariat à l'énergie atomique et aux énergies alternatives) sur la table sismique AZALÉE. L'objectif de la campagne était de réaliser des essais quasi-statiques et dynamiques afin d'obtenir des données pour évaluer les dissipations d'énergie sismique en fonction de la structure, des matériaux et des signaux sismiques. À partir de la connaissance du banc d'essai, des matériaux et des résultats expérimentaux, un modèle numérique multi-fibre a été développé, dans le contexte de la présente thèse, sur le logiciel Cast3M. Un modèle multi-fibre a été choisi car il présente de nombreux avantages : (i) gain de temps de calcul et de mémoire nécessaire (faible nombre de degrés-de-liberté par rapport à un modèle solide 3D), (ii) facilité d'utilisation, (iii) prise en compte de modèles locaux non-linéaires simples car 1D et (iv) une analyse des résultats simple car similaire à un problème poutre. Une poutre en béton armé de six mètres de long est modélisée, avec une section de $20 \times 40 \, \text{cm}^2$. Différents types d'armatures sont utilisés mais la poutre principalement utilisée dans les analyses réalisées est une poutre constituée de huit armatures à haute adhérence. Lors des essais expérimentaux, les aciers sont restés dans leur comportement linéaire donc un modèle simple est utilisé pour les armatures. Pour le béton, deux modèles non-linéaires, implémentés dans Cast3M, sont considérés ici afin d'étudier l'influence de leur complexité. En effet, le premier modèle, BARFRA, utilisé par exemple par Dufour (1998) and Crambuer, Richard, et al. (2013), est plus simple car il ne considère qu'un modèle d'endommagement dissymétrique traction/compression. Le second, RICBET, développé par Richard and Ragueneau (2013), est plus complexe puisqu'il considère de la plasticité en compression et de l'endommagement et du frottement en traction, en plus de prendre en compte l'effet unilatéral du béton. Les modèles matériaux ont été calibrés grâce aux essais quasi-statiques. Pour les conditions aux limites, des appuis élastiques (rigidités en translation et rotation) ont été considérés afin de représenter le comportement modal non endommagé des poutres. La calibration des rigidités a été réalisée grâce aux fréquences propres expérimentales non endommagées des deux premiers modes de la poutre. Enfin, afin de correspondre aux poutres testées expérimentalement, des masses additionnelles ont été ajoutées aux quart et trois-quart de la poutre multi-fibre. Ces masses permettaient, expérimentalement, d'avoir des propriétés modales correspondant aux propriétés du banc d'essai.

Seize formulations de matrices d'amortissement différentes ont été implémentées dans Cast3M, avec ou sans actualisation au cours du temps. Afin de comparer les réponses de chacune d'elles, des calculs énergétiques ont été réalisés, ainsi que des analyses des réponses dynamiques (accélérations, déplacements, forces, fréquences propres endommagées) de la poutre. En particulier, il a été démontré qu'il est nécessaire de modéliser suffisamment de phénomènes physiques à l'échelle locale (fissuration, friction, effet unilatéral) afin d'obtenir des résultats cohérents avec les réponses expérimentales. Parmi les formulations d'amortissement étudiées, les matrices de type Rayleigh ont mis en évidence de meilleurs corrélations avec les résultats expérimentaux dynamiques et énergétiques. En particulier, la matrice de rigidité seule ou accompagnée de la matrice de masse, présente de bonnes capacités à caractériser la réponse ex-

périmentale, surtout lorsque la matrice tangente est utilisée. Cependant, il est également démontré que les conclusions dépendent fortement des choix de paramètres utilisés (taux d'amortissement visqueux, choix des modes à amortissement imposé, actualisation des paramètres de proportionnalité, actualisation de la matrice de rigidité, amplitude du signal d'entrée, ...). En particulier, le taux d'amortissement visqueux utilisé pour la détermination des paramètres de proportionnalité doit être choisi attentivement et aucune valeur fonctionnant dans tous les cas ne peut être fournie. On peut tout de même dire que, dans le cas de l'utilisation de modèles dissipant de l'énergie par hystérésis, un taux d'amortissement inférieur à 2% semble suffire, même si celui-ci dépend encore fortement du signal d'entrée. Au niveau énergétique, l'énergie dissipée par amortissement visqueux représente généralement la majeure partie de l'énergie dissipée démontrant qu'une part importante de phénomènes dissipatifs n'est toujours pas connue et ne peut pas être modélisée physiquement. En ce qui concerne les phénomènes dissipatifs à l'échelle du béton, le frottement est le plus important et nécessite d'être correctement modélisé.

Identification de l'amortissement (chapitre 3 - sections 3.1 à 3.4)

Pour répondre à la deuxième problématique, une méthode d'identification de l'amortissement est développée sur un modèle à un degré de liberté (DDL) équivalent au modèle multi-fibre de la poutre en béton armé. Pour réaliser l'équivalence, une projection sur le premier mode de la poutre est utilisée. Il est tout d'abord démontré que le développement de non-linéarités n'entraîne pas de couplage supplémentaire entre les modes de la poutre. La projection sur base modale est donc acceptable. Puisque le modèle de la poutre, avec les masses additionnelles et les appuis élastiques, ne permet pas de définir les modes propres analytiquement, une méthode pour approximer les données modales à partir de sous-systèmes est proposée. Que ce soit sur les fréquences propres ou les premiers modes propres, les réponses approchées obtenues sont proches des modèles expérimentaux et numériques validant la méthode d'approximation. La méthode d'identification de l'amortissement est inspirée des travaux de Demarie and Sabia (2011). L'objectif est d'identifier l'évolution temporelle du taux d'amortissement visqueux en parallèle de l'endommagement de la poutre. Premièrement, la méthode est développée avec un modèle de comportement linéaire avec identification du taux d'amortissement et de la fréquence propre permettant de déterminer un indicateur d'endommagement. Ensuite, l'algorithme est adapté afin de prendre en compte un modèle matériau dissipant de l'énergie par hystérésis. Le modèle IDEFIX proposé par Heitz, Giry, et al. (2019) est utilisé et le taux d'amortissement visqueux équivalent est identifié et étudié en parallèle du développement des non-linéarités dans le modèle IDEFIX.

Avec l'identification linéaire, différents essais expérimentaux sont analysés. La principale conclusion est que le taux d'amortissement visqueux évolue exponentiellement par rapport à un indice d'endommagement, défini à partir de la dégradation de la rigidité de la poutre. Cependant, si la valeur d'endommagement est inférieure à 0.6, considérer un taux d'amortissement constant égal à 4% semble adéquat. Au-delà de cette limite, il est en revanche nécessaire d'actualiser le taux d'amortissement en fonction du niveau d'endommagement de la poutre. La difficulté observée avec cette méthode d'identification linéaire est une mauvaise représentation des dissipations d'énergie. C'est pourquoi un modèle non-linéaire a été développé afin d'améliorer la représentation des dissipations physiques.

Modèle d'actualisation de l'amortissement (chapitre 3 - sections 3.5 à 3.6)

Grâce à la méthode d'identification présentée précédemment et des résultats obtenus, on en déduit que le taux d'amortissement est fortement dépendant de l'endommagement. C'est pourquoi un travail, sur le modèle équivalent à un DDL, a été réalisé pour déterminer des modèles d'amortissement actualisés

à partir des variables internes des modèles non-linéaires. Tout d'abord, une analyse paramétrique de modèles d'amortissement et de modèles de comportement a été réalisée. On démontre ainsi que les modèles d'amortissement visqueux, c'est-à-dire proportionnels à la vitesse, sont les plus performants et que le phénomène de frottement doit être pris en compte dans le modèle de comportement afin de représenter la réponse expérimentale des poutres. Différents modèles, liant directement les variables des phénomènes non-linéaires à une valeur d'amortissement, sont choisis et leur capacité à représenter le comportement réel des poutres est étudiée. Des réponses dynamiques représentatives des réponses expérimentales ont été obtenues. L'avantage des modèles proposés est alors leur base physique à l'échelle locale du matériau.

Le dernier objectif présenté dans ce manuscrit est l'adaptation des modèles locaux d'actualisation de l'amortissement du problème à un DDL au problème multi-fibre. Pour cela, le calcul de deux types de matrices a été implémenté dans Cast3M : un modèle de matrice d'amortissement diagonale et un modèle avec couplages. De plus, différentes variables ont été analysées telles que l'endommagement, la variable représentative du frottement, ainsi que la contrainte dans l'acier qui est représentative de l'endommagement dans la poutre. La difficulté principale de la méthode proposée est l'identification de la fonction d'évolution de l'amortissement. Une fois ce travail réalisé, on obtient des résultats dynamiques représentatifs des résultats expérimentaux, validant la méthodologie. Une fois de plus, la décomposition des dissipations est, quant-à-elle, fortement modifiée.

Contributions originales et conclusions

Les contributions originales de cette thèse sont :
- ✓ La mise en relation de données expérimentales et numériques,
- ✓ La comparaison de modèles de matrices d'amortissement à partir de données énergétiques dans le cadre d'analyses non-linéaires,
- ✓ Le développement d'une méthode d'identification de l'évolution temporelle de l'amortissement en parallèle de l'endommagement des éléments structuraux,
- ✓ L'évaluation des modes de vibration analytiques approximés pour un système complexe,
- ✓ Le développement d'un nouveau modèle d'amortissement actualisé à l'échelle locale à partir des variables internes de modèles de comportement non-linéaires.

Les principales conclusions de cette thèse sont développées dans le chapitre 3.7.2. Tout d'abord, l'étude de la littérature scientifique relative à l'amortissement de structures en béton armé a montré que :
- ✓ Les principaux modèles d'amortissement à l'échelle de la structure sont de type "visqueux" et sont classés entre les modèles "classiques" et "modaux". La matrice d'amortissement de Rayleigh est toujours la plus utilisée dans les codes de calculs malgré les difficultés qu'elle entraîne. La difficulté principale rencontrée par les modèles généralement utilisés est leur manque de représentativité physique.
- ✓ Des modèles locaux sont proposés pour mieux représenter les phénomènes physiques. Dans le cas du béton armé, les phénomènes dissipatifs sont complexes, nombreux et souvent couplés, rendant leur modélisation difficile.
- ✓ L'identification de l'amortissement est un dernier point largement développé dans la littérature. Les objectifs étant de déterminer les valeurs d'amortissement à utiliser dans les analyses numériques ou d'évaluer l'évolution de l'amortissement en fonction de l'endommagement des structures. La difficulté avec les méthodes proposées est qu'elles peuvent conduire à de fortes variations de valeurs d'amortissement pour des données similaires.

Le chapitre 2 s'intéresse au modèle multi-fibre et à la comparaison des modèles d'amortissement. Les principales conclusions sont :

✓ Le choix du modèle multi-fibre s'est avéré pertinent pour les objectifs de l'étude. Les propriétés des poutres testées expérimentalement et non-endommagées ont pu être retrouvées numériquement et les modèles non-linéaires ont pu être calibrés sur les essais quasi-statiques.

✓ À partir des réponses dynamiques, on remarque que le modèle de comportement RICBET (modélisant le plus de phénomènes dissipatifs) est à privilégier pour caractériser les réponses expérimentales. En terme de matrice d'amortissement, les matrices de type Rayleigh avec la matrice tangente sont celles caractérisant le mieux les réponses expérimentales. Le taux d'amortissement à utiliser avec ce type de matrice est de l'ordre de 2% lorsque des non-linéarités se développent dans la poutre.

✓ À partir des analyses énergétiques, il a été démontré que l'énergie d'amortissement visqueux est toujours celle qui dissipe le plus d'énergie. À l'échelle du matériau, le phénomène dissipant le plus d'énergie est le frottement entre les lèvres des fissures.

En comparant tous les résultats étudiés, on remarque tout de même que le choix de la formulation et des paramètres du modèle d'amortissement est fortement dépendant des grandeurs d'intérêt. C'est donc afin de mieux comprendre les phénomènes en lien avec l'amortissement que les travaux du chapitre 3 ont été réalisés. Les principales conclusions sont :

✓ Le développement des non-linéarités au cours du calcul n'entraîne pas de couplage entre les modes de la base modale du système, donc les analyses sur base modale peuvent être réalisées.

✓ Ainsi, il a été développé une méthode d'identification de l'amortissement à partir de la projection sur base modale des données expérimentales et/ou numériques. En identifiant avec un modèle linéaire, on obtient une évolution exponentielle de l'amortissement en fonction de la dégradation de la rigidité de la poutre. En-dessous d'un endommagement de l'ordre de 0.6, il a été démontré qu'un amortissement visqueux équivalent constant de 4% peut être utilisé. Mais, au-delà, l'actualisation de l'amortissement est nécessaire. Enfin, utiliser un modèle de comportement non-linéaire dans l'identification permet d'améliorer la représentativité des dissipations.

✓ Finalement, le modèle d'amortissement actualisé à l'échelle locale a démontré de bonnes performances pour représenter les résultats expérimentaux que ce soit sur le modèle équivalent à un degré-de-liberté ou sur le modèle multi-fibre. Les principales variables à considérer pour l'actualisation sont les variables d'endommagement et de frottement.

Valorisations scientifiques

Les travaux présentés dans ce manuscrit ont été valorisés par :

✓ la publication d'un article scientifique dans une revue avec révision par les pairs : "Seismic energy dissipation in reinforced concrete beam: investigating damping formulations" dans le journal *European Journal of Environmental and Civil Engineering.* 27 pages. (Chambreuil et al., 2021)

✓ la participation à des conférences nationales et internationales :

▶ 10$^{\text{ème}}$ Colloque National AFPS (2019) : rédaction d'un article de conférence "Analyse de la dissipation dans des éléments de structures en béton armé" - 10 pages - et présentation.

▶ 14$^{\text{th}}$ Virtual Congress WCCM & ECCOMAS 2020 (2021) : présentation "Damping in reinforced concrete beams".

▶ 8$^{\text{th}}$ ECCOMAS Thematic Conference on Computational Methods in Structural Dynamics and Earthquake Engineering (2021) : rédaction d'un article de conférence "Local scale damping model for reinforced concrete elements" - 12 pages - et présentation.

De plus, deux articles supplémentaires sont en cours de rédaction :

✓ "Identification method for equivalent viscous damping ratios of cracked concrete beams using linear and nonlinear concrete material models"

✓ "A nonlinear damping model for reinforced concrete seismic cracking response"

REMERCIEMENTS

Ce manuscrit représente l'accomplissement de trois années de travail. La réussite de ce projet n'aurait pas été possible sans la présence, autour de moi, d'un certain nombre de personnes que je souhaite remercier ici.

Tout d'abord, je souhaiterais remercier l'ensemble des membres du jury qui ont accepté d'évaluer mon travail et m'ont fait l'honneur d'assister à ma soutenance de thèse. Monsieur Stéphane Grange, Professeur des Universités à l'INSA Lyon, et Madame Maria Paola Santisi d'Avila, Maîtresse de Conférence HDR à l'Université Côte d'Azur, merci pour votre relecture attentive du manuscrit et vos rapports extrêmement intéressants et valorisants qui m'ont permis d'élaborer la version définitive de mon manuscrit ainsi que ma soutenance. Monsieur François Voldoire, Ingénieur de Recherche à EDF R&D Division, merci pour l'intérêt porté à mes travaux dès ma première année de thèse et jusqu'à la soutenance. Monsieur Jean-François Semblat, Professeur des Univesités à l'ENSTA, merci d'avoir accepté de présider ce jury. L'ensemble des discussions qui ont suivi la présentation m'ont apporté un grand nombre de pistes de réflexions pour la suite de ma carrière.

L'accomplissement de cette thèse n'aurait, bien entendu, pas été possible sans l'accompagnement permanent de mes encadrants de thèse. C'est pourquoi je remercie chaleureusement mon directeur de thèse Frédéric Ragueneau, Professeur des Universités à l'ENS Paris-Saclay, et mon co-encadrant Cédric Giry, Maître de Conférence à l'ENS Paris-Saclay. Merci pour la proposition de ce sujet de thèse qui m'a extrêmement intéressée et occupée pendant ces trois années. Merci pour les heures passées à discuter de mes multiples résultats et pour les relectures attentives de mes travaux. Tout ceci m'a permis d'avancer sur ce projet en acquérant de nouvelles compétences au cours des années. Merci pour votre soutien sans faille qui m'a permis de tenir pendant les moments de doute. Merci également à Cédric pour les heures passées à travailler ensemble sur le code. Enfin, je n'oublierai pas de remercier Pierre Léger, Professeur des Universités à l'École Polytechnique de Montréal, qui a accepté de se joindre au projet et de m'accueillir dans son laboratoire à deux reprises au cours de ma thèse. Merci pour les nombreuses discussions qui m'ont permis d'appréhender mes travaux sous un autre angle. Merci à mes encadrants de m'avoir permis de vivre cette expérience internationale grâce à la recherche de financement et à toute l'aide pour les démarches administratives. Et merci pour votre soutien et votre présence pendant les périodes de confinement qui ont marqué une grande partie de mes trois années de thèse impactant de manière non négligeable mon avancement et mon travail.

Comment rêver d'un meilleur environnement de travail que le LMT dans lequel j'ai réalisé ma thèse. Je souhaite remercier tous les membres du laboratoire que j'ai pu rencontrer et avec qui j'ai pu échanger pendant ces trois années. Tout d'abord, un grand merci à nos gestionnaires pour leur aide énorme et leur disponibilité à toute épreuve. Merci aux doctorants, chercheurs, enseignants-chercheurs, techniciens, membres des centres d'essais et de calcul avec qui j'ai pu échanger que ce soit au bar, lors de repas au Crous ou dans les couloirs. L'ambiance du laboratoire m'a permis de vivre sereinement mes trois années de thèse. Un merci particulier à Ronan d'avoir partagé ces trois années avec moi et d'avoir été là dans les bons moments comme ceux de doute.

Merci également à toutes les personnes rencontrées à l'École Polytechnique de Montréal pour les

CONTENTS

LIST OF FIGURES

LIST OF TABLES

Acronyms

1D	One-dimensional
2D	Two-dimensional
3D	Three-dimensional
CD	Caughey damping
CRD	Rayleigh damping with the commit stiffness matrix
dam	Damage material model
dam_fri	Coupling of damage and friction material model
dam_fri_uni	Coupling of damage, friction and unilateral effect material model
DOF	Degree-of-freedom
DOFs	Degrees-of-freedom
DSSij	Decreasing sinus sweep signal with frequencies evolving from i Hz to j Hz
ElVD	Elastic velocity damping
EVD	Equivalent viscous damping
EVDR	Equivalent viscous damping ratio
FE	Finite Element
FEM	Finite Element Method
FFT	Fast Fourier Transform
fri	Friction material model
HA	High-adherence
HB	Harmonic block of the input signal
HPBM	Half-power bandwidth method
IKPD	Initial stiffness proportional damping
IKPDL	Capped initial stiffness proportional damping
ITHA	Inelastic time history analysis
KPD	Stiffness proportional damping
linC	"Linear" material model with a constant stiffness
linNC	"Linear" material model with a non-constant stiffness
LVDT	Linear Variable Differential Transducer

MD	Modal damping
MDOF	Multi-degrees-of-freedom
MPD	Mass proportional damping
NLel	Nonlinear elasticity model
NLVD	Nonlinear viscous damping
NSS	Natural seismic signal
ODE	Ordinary Differential Equation
QBD	Quasi-brittle damping
QSC1	Quasi-static test exciting the first mode
QSC2	Quasi-static test exciting the second mode
RC	Reinforced concrete
RD	Rayleigh damping
RDtd	Rayleigh damping with time-dependent coefficients
SC1	Band-passed white-noise signal exciting the first mode
SC12	Band-passed white-noise signal exciting the first and second modes
SC2	Band-passed white-noise signal exciting the second mode
SDOF	Single-degree-of-freedom
SPS1	Quasi-static test exciting the first mode with various actuator velocities
SPS1	Quasi-static test exciting the second mode with various actuator velocities
TKPD	Tangent stiffness proportional damping
TMD	Tuned mass dampers
TRD	Rayleigh damping with the tangent stiffness matrix
TRDtd	Rayleigh damping with the tangent stiffness matrix and time-dependent coefficients
vcD	Viscous damping + constant damping
vD	Viscous damping
vdpcD	Damping proportional to displacement and velocity + constant damping
vdpD	Damping proportional to displacement and velocity
vKPD	Viscous damping (stiffness proportional type)
vMPD	Viscous damping (mass proportional type)
vRD	Viscous damping (Rayleigh type)
WN	White-noise part of the input signal
WN1	White-noise signal exciting the first mode
WN12	White-noise signal exciting the first and second modes
WN2	White-noise signal exciting the second mode
WPD	Wilson-Penzien damping

Main Symbols

1 - General mathematical symbols

a	Scalar
$sg(a)$	Sign of a
$|a|$	Absolute value of a
$a_\pm$	Index meaning that a is differentiated into traction and compression
$a_{\max}$	Maximal value of a
$a_{\min}$	Minimal value of a
$\bar{a}$	Normalized space value of a
$\vec{a}$	a-axis of space
n_a	Number of variables a_i
$\underline{v}$	Space-dependent vector
$\mathbf{v}$	Time-dependent vector
v_i	i^{th} vector element
$\mathrm{d}\underline{v}$ or $\mathrm{d}\mathbf{v}$	Vector increment
$\mathbb{A}$	Matrix
$\mathbb{A}^T$	Transpose of matrix $\mathbb{A}$
$\mathbb{A}^{-1}$	Inverse of matrix $\mathbb{A}$
$\mathrm{Tr}\,(\mathbb{A})$	Trace of the matrix $\mathbb{A}$
i	First sum or list index
j	Second sum or list index
$A, B, C, \ldots$	Coefficients
x	Space variable
$\mathrm{d}x$	Incremental displacement
t	Time variable
$\mathrm{d}t$ or Δt	Time increment
δ_{ij}	Kronecker's symbol
$\mathcal{R}$	Rayleigh's quotient
γ and β	Parameters of Newmark's algorithm
π	Archimedes' constant ~ 3.14

XXX

$f(a_i)$	Function of different variables a_i with $i \in [\![1, n_a]\!]$
$\dot{f}$	Time derivation of f
f'	Space derivation of function f
∂f	Partial derivation of function f
$X(x)$	Continuous space-dependent function
$T(t)$	Continuous time-dependent function
δ	Dirac distribution
$\mathcal{H}$	Transfert function
$a^{(i)}$ or a_i	Variable at iteration i
$a^{(t)}$ or a_t	Variable at time t
$a^{(e)}$ or a_e	Variable on element e
$a^{(n)}$	Variable on node n
$a^{(s)}$	Variable on section s
$a^{(\text{compo})}$	Variable for the component compo (u_y, θ_z)
i	Imaginary variable
$\Im(a)$	Imaginary part of complex variable a
$\Re(a)$	Real part of complex variable a
$\Delta_{\mathcal{L}^2}$	Euclidean norm error in percentage

2 - Geometrical data

r	Radius
θ	Rotation variable
H	Height
L or l	Beam length
h	Height of the beam section
b	Width of the beam section
S	Beam section
S_h	Beam homogenised section
I_h	Beam section homogenised quadratic momentum
S_y and S_z	Shear section in $\vec{y}$- and $\vec{z}$-direction
α_{s_y} and α_{s_z}	Parameter to compute the shear section in $\vec{y}$- and $\vec{z}$-direction
I_z	Inertia moment ($\vec{z}$-axis)
M_{add}	Additional mass
$x_{m_{add}}$	Position of an additional mass
K_T	Translational stiffness of beam supports
K_R	Rotational stiffness of beam supports
$\mathscr{L}$	Beam length for integration
$\mathscr{V}$	Beam volume for integration
$\mathbb{N}$	Matrix of integration functions
$\mathbb{B}$	Matrix of derived integration functions

3 - Material models

a_c	Variable a for concrete
a_s	Variable a for steel
a_T	Tangent value of variable a
a_S	Secant value of variable a
C_{ijkl}	$ijkl$th term of the elasticity tensor
E	Young's modulus
G	Shear modulus
ν	Poisson's ratio
ρ	Density
f_t	Concrete tensile strength
f_{cm}	Mean compressive strength of concrete
σ	Stress
σ^π	Friction stress
σ^p	Plasticity stress
$\mathbf{F_G}$	Generalized stresses
ε	Strain
ε_s	Sliding strain
ε^e	Elastic strain
ε^π	Friction strain
ε^p	Plasticity strain
$\mathbf{E_G}$	Generalized strains
F	Total force
F^π	Friction force
F^η	Force associated with the unilateral effect
F^e	Elastic force
F_c	Crack closure force
u	Total displacement
u^π	Friction displacement
M	Momentum
V	Shear force
Ψ	State potential
Ψ^e	Elastic state potential
Ψ^π	Friction state potential
w	Crack width
μ	Ductility
r_k	Post yield stiffness coefficient
γ	Curvature
$\mathrm{V_{int}}^{(i)}$	ith internal variable
d	Damage variable

z	Damage work hardening variable
η	Unilateral effect variable
p	Plasticity variable
α or α^{π}	Friction work hardening variable
Y	Restitution rate for damage
Z	Thermodynamic force related to an isotropic work hardening and associated with damage
ζ	Restitution rate for unilateral effect
R	Thermodynamic force related to an isotropic work hardening and associated with plasticity
X or X^{π}	Thermodynamic force related to a kinematic work hardening and associated with friction

4 - Dynamic equations

$\mathbf{u}$	Displacement of a SDOF system
$\dot{\mathbf{u}}$	Velocity of a SDOF system
$\ddot{\mathbf{u}}$	Acceleration of a SDOF system
$\ddot{\mathbf{u}}_s$	Seismic acceleration of a SDOF system
$\underline{\mathbf{U}}$	Relative displacement vector
$\underline{\dot{\mathbf{U}}}$	Relative velocity vector
$\underline{\ddot{\mathbf{U}}}$	Relative acceleration vector
$\underline{\mathbf{U}}_a$	Relative displacement vector
$\underline{\dot{\mathbf{U}}}_a$	Relative velocity vector
$\underline{\ddot{\mathbf{U}}}_a$	Relative acceleration vector
$\underline{\Gamma}$	Vector given the direction of seismic excitation
$\ddot{\mathbf{U}}_s$	Seismic ground acceleration
$\mathbf{U}_s$	Seismic ground displacement
$\bullet_i$ or $\bullet^{(i)}$	Modal projection on mode i
κ_i	Modal projection of seismic acceleration on mode i
$\boldsymbol{\alpha}_i$	Displacement in generalized coordinates
$\dot{\boldsymbol{\alpha}}_i$	Velocity in generalized coordinates
$\ddot{\boldsymbol{\alpha}}_i$	Acceleration in generalized coordinates
m	Mass
c_v	Viscous damping coefficient
c_c	Critical viscous damping coefficient
k	Stiffness
k_0	Initial stiffness
k_d	Damaged stiffness
$\mathbb{M}$	Mass matrix
$\mathbb{C}$	Damping matrix
$\mathbb{K}$	Linear stiffness matrix
$\mathbb{K}_0$	Initial stiffness matrix

$\mathbb{K}_T$	Tangent stiffness matrix
$\mathbb{K}_C$	Commit stiffness matrix
$\mathbb{K}_S$	Secant stiffness matrix
$\mathbf{f}_g$	Global internal force
$\mathbf{f}_d$	Damping force
$\mathbf{f}_{int}$	Internal force
$\underline{\mathbf{f}}_{\mathbf{int}}$	Internal force (MDOF)

5 - Modal properties

$\mathcal{B}$	Modal basis
$\underline{\phi}$	Eigenmode
$\overline{\lambda}$	Eigenvalue
f	Frequency
f_0	Fundamental mode frequency
f_r	Resonant frequency
f_n	Natural frequency
ω	Eigenfrequency
ω_0	Initial eigenfrequency
ω_d	Eigenfrequency at a damage level
$\widetilde{\omega}$	Complex eigenfrequency
T_{eq}	Equivalent eigenperiod
ξ	Viscous damping ratio
ξ_{eq}	Equivalent viscous damping ratio
ξ_{el}	Elastic damping ratio
ξ_{hyst}	Hysteretic damping ratio
ξ_d	Damage-dependent viscous damping ratio
ξ_r	Residual viscous damping ratio
ξ^*	Reduced viscous damping ratio
ξ^{mod}	Modal damping ratio
δ	Logarithmic decrement
$\mathbb{C}^{mod}$	Modal damping matrix
$\mathbb{M}^{mod}$	Modal mass matrix
$\varepsilon_{\text{coupling}}$	Criterion for mode couplings
$\bullet_{ssb}$	Associated with the simply supported beam
$\bullet_T$	Associated with the subsystem with translational elastic supports
$\bullet_R$	Associated with the subsystem with rotational elastic supports
$\bullet_{M_{add,j}}$	Associated with the subsystem with the jth additional mass

6 - Identification method

$\bullet_w$ or $\bullet^{(w)}$	Relative to the wth window
w	Index of the window of interest
t_w	Length of a window
$T_{w,c}$	Calibrated length of a "classical window"
$T_{w,m}$	Calibrated length of a "moving window"
$\delta_{T_{w,m}}$	Calibrated lag time between two windows for moving windows
ε_{id}	Error criterion for the identification method
$\varepsilon_{id,lim}$	Limit error criterion for the identification method
$\mathbf{f}_{id}$	Function to identify
$\mathbf{f}_c$	Computed function for the identification
$\omega_{1,w}$	First mode eigenfrequency identified on window w
$\xi_{1,w}$	First mode damping ratio identified on window w
$\xi_{1,expo}^{(exp)}(d)$	Damping ratio's exponential function, for the first mode, defined with experimental data
$\xi_{1,ratio}^{(exp)}(d)$	Damping ratio's polynomial function, for the first mode, defined with experimental data

7 - Proposed damping models

$\mathbf{f}_{\text{damping}}$	Damping force model
$\mathbf{f}_{\text{internal}}$	Material constitutive force model
F_{input}	Input force
VI	Internal variable (d, u^π/ε^π, η) or another variable (σ_s) for damping updates
fct	Evolution function for damping updates (lin, inv or exp)
$\alpha_{\text{VI,fct}}$, $\beta_{\text{VI,fct}}$ ($\gamma_{\text{VI,fct}}$, $\delta_{\text{VI,fct}}$)	Parameters of a damping model depending on VI variable and with a fct evolution function
$\alpha_{\text{VI,fct},f}$, $\beta_{\text{VI,fct},f}$ ($\gamma_{\text{VI,fct},f}$, $\delta_{\text{VI,fct},f}$)	Parameters of a damping model depending on VI variable and the input force, and with a fct evolution function
$\mathscr{P}_i$	ith parameter of the studied damping model depending on VI variable (with or without the input force), and with a fct evolution function
$\mathscr{P}_{i,0}$	Initial value of the ith parameter of the studied damping model depending on VI variable (with or without the input force), and with a fct evolution function
$c_{v,\text{fct}}(\text{VI})$	Proposed damping coefficient model depending on the variable VI and with the fct evolution function
$c_{v,\text{fct},f}(\text{VI})$	Proposed damping coefficient model depending on VI variable and the input force, and with a fct evolution function
$\mathbb{C}_{\text{elem}}$	Elemental updated damping matrix
$\mathbb{C}_{\text{updated}}$	Total updated damping matrix

8 - Energies

$E_{\bullet,r}$	Relative energy
$E_{\bullet,a}$	Absolute energy
$\mathrm{d}E_{\bullet}$	Energy increment
$\bullet_d$	Associated with damage dissipative phenomena
$\bullet_p$	Associated with plasticity dissipative phenomena
$\bullet_f$	Associated with friction dissipative phenomena
$\bullet_u$	Associated with unilateral effect dissipative phenomena
E_k	Kinetic energy
E_i	Imparted energy
E_t	Total energy
E_d	Damping energy
E_a	Absorbed energy
E_s	Strain energy
E_{diss}	Dissipated energy
$E_{diss,f}$	Dissipated energy at nominal failure
$E_{diss,y}$	Dissipated energy at first yield
$A_{half-loop}$	Dissipated energy through half a cycle (cyclic loading)
E_{el}	Stored elastic energy
$\mathcal{D}$	Dissipation variable deduced from Clausius-Duhem inequality
E_h	Hysteretic energy
W_h	Work hardening energy

INTRODUCTION

Societal, economic and industrial context

The establishment of a European seismic building code in 2005 - Eurocode 8 (NF EN 1998-1, 2005) - and the scientific knowledge evolution about seismic hazard resulted in developing new seismic zoning in France. So, since October 22, 2010, the French territory has been decomposed into five seismic zones, as presented in figure 1 in parallel to the old division. For seismic zone classified 1, no regulation is applied for typical risk structures. However, seismic building codes are required for all other zones following Eurocode 8 (BRGM, 2019). It increased from 5,000 to above 20,000 the number of French cities submitted to seismic regulations (Haquet, 2011; Enerzine.com, 2011).
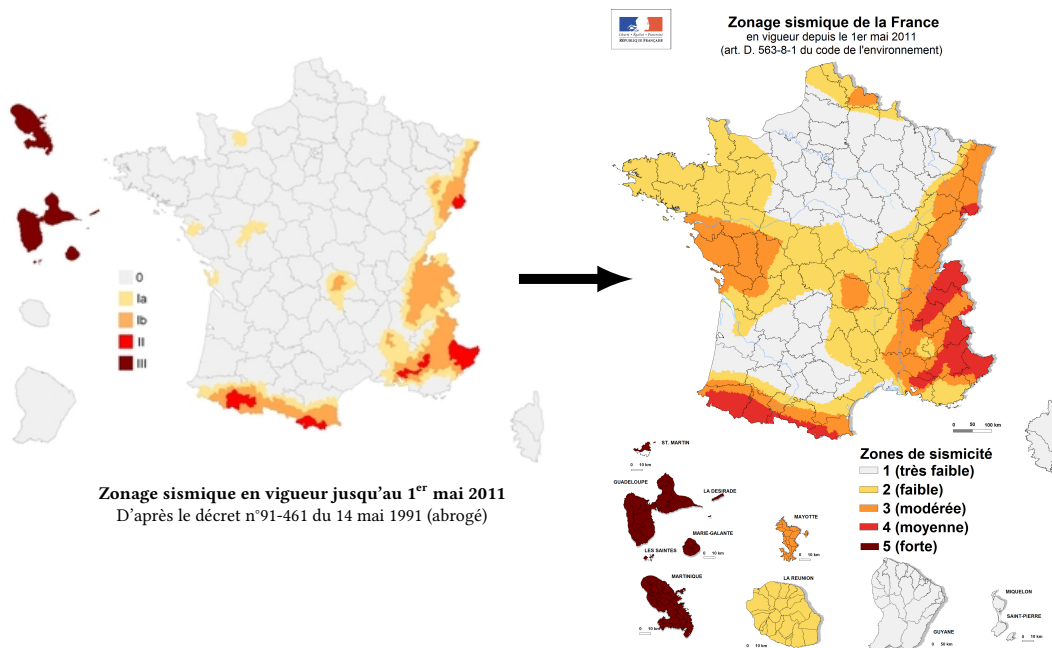
Figure 1: Evolution of the seismic zoning in France before and after 2011 (BRGM, 2019)

In parallel to the regulation evolution regarding "classical structures", the Fukushima nuclear accident in 2011 prompted the French government to focus on the safety of nuclear buildings. Before those events, the seismic risk was already considered for nuclear buildings, with specific methods and particular excitations. However, five nuclear power plants have been located in a "moderate" seismic zone

(3) since 2011, requiring particular attention from the French nuclear safety authority: ASN ("Autorité de Sûreté Nucléaire"). Funds were therefore raised for research on seismic risk. To ensure the viability of such critical structures or increase their lifespan, computations must be carried out, considering the new seismic regulations and the structure current states. The models to develop should integrate sophisticated physical phenomena description while respecting robustness, efficiency, and accuracy criteria. The research works performed during this PhD take place in this context because it focuses on improving numerical models for dynamic nonlinear structural analyses of reinforced concrete structures.

Scientific context

A significant difficulty with reinforced concrete structures comes from the lack of knowledge about its nonlinear phenomenon evolutions when submitted to seismic accelerations and the ability of concrete to dissipate energy through its hysteretic behaviour. Different scales can be considered in line with the described phenomena: the local scale or the global scale to model the energy dissipations observed in a structure.

In a continuous model framework, dissipative mechanisms are described at the local scale by constitutive laws including more or less complex phenomena and their couplings (concrete cracking, friction, steel/concrete sliding, …(Vassaux et al., 2015)). Figure 2 proposes a schematic representation of some phenomena at the steel/concrete interfaces (Jehel, 2009) or concrete level. The identification of the constitutive relationship parameters is classically obtained by laboratory tests or virtual testing on a representative material sample or the characterised interface. Dissipations are transcribed into the global structure responses through the nonlinear internal forces obtained by integrating elementary quantities in the finite element method framework.
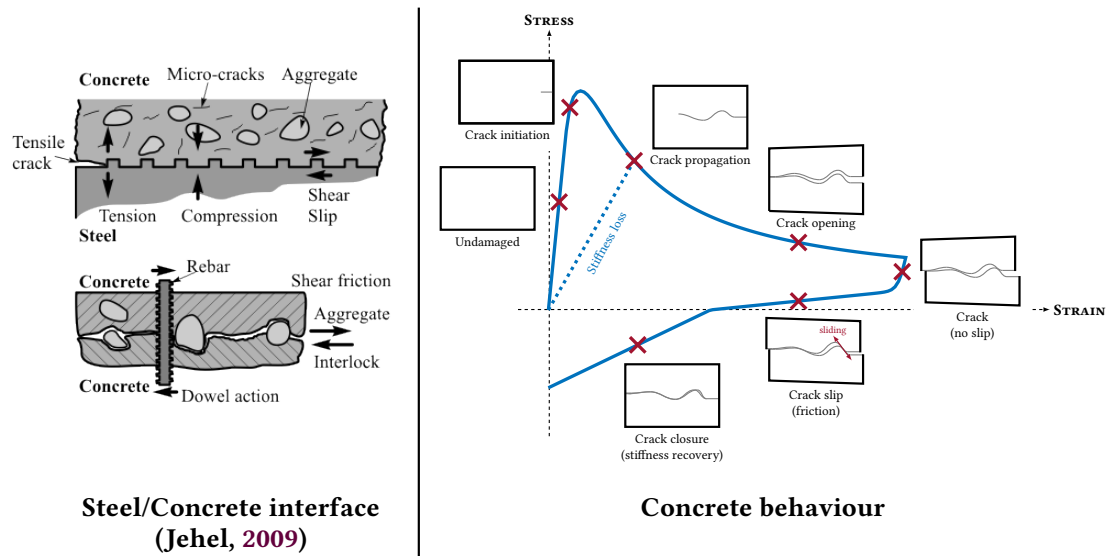
Figure 2: Dissipative phenomena mechanisms of reinforced concrete

On the global scale, dissipative phenomena resulting from the structure interaction with its environment, from the internal dissipations at the junctions between structural elements, are traditionally described by classical viscous damping, that is to say, a quantity proportional to the velocity. This term allows, in practice, to represent the dissipations, whose physics is poorly controlled or too complex. The damping rate orders of magnitude involved being relatively low, the dissipation identifications and

descriptions are generally made in the modal basis of the associated undamped vibratory problem. For example, this is the case with experimental modal analyses of structures or structural elements, leading to the notion of "viscous damping ratio". In this context, forms of damping matrices, which are functions of structural mass and stiffness matrices or defined on a modal basis, are commonly used. This description allows keeping the decoupled equations written in the modal basis for a linear regime (Chopra, 1995). Moreover, the damping identification and construction are performed from a limited number of coefficients because the first eigenmodes mainly drive the responses of civil engineering structures. For example, the Rayleigh damping matrix is a linear combination of the mass and stiffness matrices. This previous damping description has the significant drawback of not having a physical basis for its expression. In addition, because the damping representation is based on a quantity derived from the integration of local material properties (i.e. stiffness matrix), the nonlinear material evolution leads to an uncontrolled modification of the global damping matrix. Alternatives to this description propose, in particular, to consider an update of the stiffness matrix by considering the structural tangent stiffness (Jehel, Léger, and Ibrahimbegovic, 2014). Despite the response description improvement, this strategy has a slight physical basis and remains costly in computational time, especially when there is no analytical expression of the tangent modulus for the considered material constitutive law.

Recent work (Heitz, Le Maoult, et al., 2018) in the framework of T. Heitz's thesis (Heitz, 2017) proposes an experimental analysis and a dissipation identification of a reinforced concrete beam based on an equivalence between the local internal dissipations and a global viscous dissipation. This work allowed them to identify and discriminate the local quantities that strongly influence the equivalent viscous damping. This work, and the experimental database produced, represents a solid basis for analysing and understanding local dissipation evolutions and their influence on global damping to transcribe them in the framework of accurate numerical modelling in dynamics of nonlinear structures.

Research questions

Stevenson (1980) defined *damping* as the "means by which the response motion of a structural system is reduced as the result of energy losses". In the same idea, S. Crandall (1970) defined it as the "mechanism that removes energy from a system". So, they are both pointing to the link between energy dissipations and damping. Viscous damping models at the global scale aim at representing all unmodelled dissipative phenomena. However, they strongly lack a physical basis. Mainly, in engineering, linear constitutive models are considered with the use of global viscous damping models because of the gain in computational time. To improve the representativeness of structural models, nonlinear constitutive models must be considered in structural analyses. Nevertheless, their influence of damping on structural dynamic responses are still poorly understood, and few recommendations are proposed in the literature to combine viscous damping models with nonlinear constitutive laws. Therefore, the following research questions are of interest in this PhD work.

> **In the framework of nonlinear dynamic computations, which local and global viscous damping formulations best represent the experimental structural responses?**

> **How are local and global damping energy dissipation mechanisms evolving during nonlinear dynamic computations?**

> **How could we improve the damping modelling at the local scale, on a physical basis, to reduce the requirement of arbitrary equivalent viscous damping at the global scale?**

Methodology

Reinforced concrete beams are considered throughout this thesis work. The experimental campaign performed by Heitz, Le Maoult, et al. (2018) is considered as a reference. The beams have a length of 6 m for a section of $0.4 \times 0.2 \, \text{m}^2$. Different rebar patterns are studied, but the one especially used herein is eight high adherence rebars of diameter 8 mm. For concrete, two formulations classified in Eurocode 2 (NF EN 1992-1-1, 2005) were used, and, in this thesis, a focus is done on concrete C25/30. Normalised tests were experimentally performed, given the concrete and steel properties. Quasi-static

Figure 3: Dynamic experimental setup (Heitz, Le Maoult, et al., 2018)

and dynamic tests, applied to beam weak axis, were performed respectively on strong floor and shake table AZALÉE at CEA. Figure 3 shows, for example, the dynamic setup. Additional masses of 310 kg were added on the quarter and three-quarters of the beam to match the beam eigenfrequencies to available facilities. They were placed on air cushion devices to avoid the beam cracking under its weight and friction with the shake table. Effect of moderate earthquakes was of interest, so the maximal accelerations applied on the beams are around $3 \, \text{m/s}^2$. In quasi-static, imposed displacement until 100 mm were considered. In addition, the beam damage evolution was followed using the modal properties deduced from hammer shock tests.

To answer the proposed research questions, and based on the presented experimental campaign, work developed in that thesis is divided into three parts:

(1) The first part aims at evaluating the performances of classical viscous damping formulations to perform nonlinear dynamic analyses. The experimental campaign carried out by Heitz, Le Maoult, et al. (2018) provides an extensive database that can be used to compare the numerical responses to experimental data. Numerical models are developed in Cast3M software with a multi-fibre approach and nonlinear constitutive models. The analysis of energy dissipations and numerical computations characterises the links between global and local dissipations, depending on viscous damping model properties. Two existing nonlinear constitutive models in Cast3M (BARFRA and RICBET discussed in chapter 2) are studied to represent concrete behaviour under seismic excitations. They are considering some dissipative phenomena, given information about the most influential ones. Those analyses allow understanding the behaviour of nonlinear constitutive models in reinforced concrete structural computations. These models are seldom used in practical engineering applications, and linear models with viscous damping models are preferred to dissipate the energy. Indeed, the codes, generally, only ask linear computations. The nonlinear models are more challenging to use, and further expertise is required. In addition, they sometimes lack robustness because computations can diverge. The computation time is also increased, but the multi-fibre approach partially compensates for this increase compared to complete 3D solid finite element models. Finally, using nonlinear models is a way to reduce the safety margins by being more representative of reality. Thus, recommendations can be made for engineers performing nonlinear dynamic computations by studying such models.

(2) The second part presents an original damping identification method to evaluate its evolution parallel to damage development. A comparison of linear and nonlinear constitutive models characterising

the reinforced concrete behaviour is proposed to understand the influence of viscous damping all along with dynamic computations. The method is based on an equivalent single-degree-of-freedom (SDOF) model computed by the projection on the modal basis of the studied system.

(3) Finally, the third part is based on observations deduced from the identified viscous damping coefficients to propose new models to update damping for the equivalent SDOF system. These suggested models are then implemented to develop an updated damping matrix strategy at the element level for the multi-fibre computations. The defined damping matrices, updated considering local damage variables $(d, \varepsilon^{\pi}, \dots)$, are used to perform nonlinear dynamic computations for comparison with classical damping formulations studied in chapter 2.

An essential aspect of the performed works is that steel rebars remain in their elastic range, as experimentally designed. Indeed, the objective is to study the contribution of concrete cracking to damping and energy dissipation in the case of moderate earthquake excitations.

Original contributions

During the three parts of thesis works, different original contributions are developed and document the research questions:
- ✓ Correlations between measured and computed data,
- ✓ Comparison of damping models based on energy balance studies in nonlinear dynamic analyses,
- ✓ Development of a methodology to identify the transient evolution of damping concerning the structural element damage,
- ✓ Evaluation of an approximate analytical eigenbasis of a complex system,
- ✓ Development of a new local model of damping based on nonlinear internal variables of the concrete constitutive models $(d, \varepsilon^{\pi}, \dots)$.

Content of thesis

The thesis is split into three chapters. The first one provides a literature review focusing on damping phenomena at local and global scales. After defining the notion of damping, different damping models are studied. Then, methodologies to characterise that modal property is described, and some links between damping and damage indices are analysed. Finally, the shake table experimental campaign on reinforced concrete beams, which is the basis of herein developed works, is presented.

The second chapter is interested in modelling reinforced concrete beams with nonlinear behaviour. A multi-fibre model in Cast3M is proposed. General information on multi-fibre models is given before the beam model is presented. Then, the calibration of the model against quasi-static tests is explained, and the studied viscous damping formulations are presented. Finally, the dynamic computations performed with different modelling parameters (damping matrix formulation, viscous damping ratios, modes with imposed viscous damping ratios, matrix updates, …) are analysed by comparing the global response with experimental data, as well as energy calculations.

The third chapter presents the development of updated damping models. The influence of mode couplings in nonlinear dynamic computations and a theoretical eigenbasis are first studied for the beam of interest. Then, the damping identification method is developed and applied with a linear model. Improvements are then performed using a nonlinear constitutive model. Finally, damping models depending on nonlinear internal variables are proposed for the SDOF equivalent system. Then, they are implemented on the multi-fibre model by proposing newly updated damping matrix formulations based on elemental internal variables.

Chapter 1

ENERGY DISSIPATION MECHANISMS AND DAMPING MODELS

Contents

1.1   Energy dissipation in earthquake engineering

When an earthquake excites a structure, energy is imparted to the system (Crambuer, 2013). This energy is a function of the earthquake acceleration. Some of the energy returns to the ground while the rest is dissipated. These dissipations may be a consequence of the nonlinearities developing within the structure. Yet, to ensure the structural element safety and the structure ability to resist the earthquake excitation, the state of nonlinearity reached by the structure must be evaluated. A too strong degradation could lead to the structure collapse. That is why dissipative phenomena are studied to be adequately modelled and to dissipate the right amount of energy during seismic excitations. In section 1.1.1 physical dissipative phenomena are presented, and the global dynamic equations are then introduced in section 1.1.2 to discuss dissipated energies in section 1.1.3.

1.1.1   Introduction to dissipative phenomena

S. Crandall (1970) defined a "damping mechanism" as a "mechanism that removes energy from a system". So, it avoids the structural displacements to grow without any limit if the structure is excited to its resonant frequency. In the same idea, Stevenson (1980) defined "damping" as "the means by which the response motion of a structural system is reduced as the result of energy losses". In particular, for reinforced concrete (RC) structures, many coupled sources act together to dissipate the energy (Heitz, 2017). Kareem and Gurley (1996) said that "there are as many damping mechanisms as there are modes of converting mechanical energy into heat". Smyrou, Priestley, and Carr (2011) proposed a classification of the damping sources between the external (1.1.1.1) and internal (1.1.1.2) ones.

1.1.1.1   External sources

"External sources" represent all interactions between the structure and its environment, so they are not relative to the constitutive materials (Heitz, 2017). They do not influence the mechanical structure properties (Crambuer, 2013). Many external dissipative sources have to be considered.

(a)   Fluid-structure interaction   The fluid-structure interaction is defined when a structure is in contact with a fluid. It can be the interaction with water in the case of dams (Hall, 1988; Seghir, Tahakourt, and Bonnet, 2009) or off-shore structures and tanks (Livaoğlu and Doğangün, 2006; Seghir, Tahakourt, and Bonnet, 2009; Ozdemir, Souli, and Fahjan, 2010). The second fluid studied in seismic analyses is the air associated with the wind. The friction of the building in the air is seen as a dissipative phenomenon favourable for the structure but generally completely negligible.

(b)   Soil-structure interaction (fig. 1.1)   The second type of external source is the soil-structure interaction, acting mainly through the interaction between the structure, its foundations and the soil, which are interdependent (Dutta and Roy, 2002). Seismic waves propagate in the soil when an earthquake occurs and lead to structural movement. Then, the structure induces additional forces on the ground creating new seismic waves (Ele, 2017). The interaction is strongly dependent on the structural and soil properties. In earthquake engineering, the soil-structure inter-

Figure 1.1: Effect of the soil-structure interaction (Ele, 2017)

action consideration seems beneficial because of the energy dissipated in the soil (Institut-Seism, 2021). Part of the energy transmitted to the structure returns to the ground and is dissipated by two mechanisms: (i) radiation weakening when the waves are moving away from the structure, and (ii) internal damping of soil as it deforms (Ele, 2017).

Figure 1.2: "Pounding damage at Hotel De Carlo" (Arnold, 1985)

(c)   Structure-structure interaction   When structures are close to each other, interactions can occur when they are vibrating as there can be pounding between the structures (fig. 1.2). It is particularly damaging in dense urban areas (Polycarpou and Komodromos, 2012; Langlade et al., 2021). The dynamic properties of one structure are dependent on the other ones. It comes in the addition of the soil-structure interaction because the energy emitted by one structure to the ground will affect the second one (Lou et al., 2011).

(d)   Equipment and non-structural elements   All the previous damping sources are mainly in the exterior structure environment.   However, the equipment and non-structural elements inside the structure can also significantly dissipate energy. They are considered as external sources because they are not required for the structure lateral load resistance (Heitz, 2017). It is the case of functional parts like doors, windows or pipes, and non-structural elements like plasterboards or infill masonry (Elmenshawi, Sorour, et al., 2010). Energy dissipation can be a consequence of element degradation in the case of infilling masonry, for example (friction, interaction with the frames). Such elements can thus represent determining factors for the structure collapse during earthquake excitations (Samouh and Kotronis, 2011).

(e)   Added dampers   The last external damping source is added dampers. For Crouse and McGuire (2001), energy dissipation is a "means of reducing the seismic response of structures". So, when the natural phenomena previously presented are insufficient to ensure structural safety or the required comfort for building users, devices such as friction dampers, fluid dampers or isolators can be added to the structure. To reduce seismic and wind effects, Kareem, Kijewski, and Tamura (1999) proposed passive and active devices representing viscous dampers. Indeed, the structural dampers can be divided into passive (the most used), active, semi-active and hybrid dampers (Gutierrez Soto and Adeli, 2013). Gutierrez Soto and Adeli (2013) paper aimed at reviewing the tuned mass dampers (TMD), which were non-viscous dampers. The conventional TMD is used in high-rise buildings (fig. 1.3). The problem

Figure 1.3: "The tuned mass damper in Taipei 101" (Dolev, 2008)

with this damper is that it is damped only for one frequency that can change when an earthquake occurs. It is also an expensive technical solution. New devices, like the tuned liquid column dampers, seem more promising. Finally, hysteretic dampers can also be added to structures to protect them in the case of earthquakes. Skinner et al. (1980) studied the hysteretic dampers in steel (dissipation through

plastic deformation), lead or sliding devices (PTFE[1] sliding bearings). Kelly, Skinner, and Heine (1972) also focused on those hysteretic dampers. They studied devices functioning with plastic deformation. In the case of earthquake excitations, the structure mainly absorbs energy at the connection points. This absorption is required to ensure structural resistance, but it strongly damages the connections. That is why Kelly, Skinner, and Heine (1972) proposed to use devices with plastic deformations to absorb the energy and protect the connections.

1.1.1.2 Internal sources

For internal sources, the dissipations depend on the phenomena activated by the earthquake excitation and induce modifications of material properties. The material behaviour represents the primary source of internal damping. For RC elements, dissipations occur at concrete, steel and interface levels.

(a) Concrete In concrete, the energy dissipation is mainly due to cracks. The fracture energies G_f and G_F are material properties characterising the initiation and propagation of cracks. G_f mainly controls the maximal load, while G_F controls the post-peak behaviour (fig. 1.4) (Saouma, 2000).[2] Therefore, it is assumed that the energy only dissipates when the cracks open the first time. A small amount of energy is consumed when the cracks are created and propagate. Secondly, friction between the crack surfaces is another energy dissipating phenomenon in concrete.
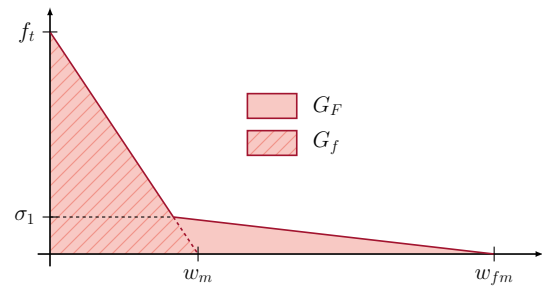
Figure 1.4: Definition of fracture energies

(b) Reinforcement The energy dissipated through steel rebars in RC elements is the consequence of steel yielding (hysteresis loops), which occurs in the case of high excitations.

(c) Steel-concrete bond Finally, energy is dissipated at the steel-concrete interface. Figure 1.5b well describes the phenomena that occur at the steel/concrete interface and dissipate energy (Jehel, 2009). Then, different parameters have shown some influence on the interface behaviour: the type of rebars, the level of concrete confinement (Eligehausen, Popov, and Bertero, 1982), the corrosion (Richard, 2010) or the crack level (Torre-Casanova, 2012) demonstrating the coupling between different dissipative phenomena. These effects influence the interface roughness or its capacity to be damaged and, consequently, the amount of energy dissipated at the interface.

1.1.1.3 Synthesis

The different presented dissipative phenomena are summarised in figure 1.5. They are more or less activated depending on the structure and its environment. In addition, some damping sources can be coupled. For example, more energy will be dissipated if cracks are close to the steel/concrete interface. In the following, approaches to model the most influential dissipative phenomena will be studied.

---

[1]Polytetrafluoroethylene

[2]For the definition of the two energies, a bilinear model is considered (fig. 1.4). The values defined in the figure are: (i) w_m is the crack width corresponding to the intersection of the first linear portion with the horizontal axis, (ii) w_{f_m} corresponds to the critical crack opening, (iii) f_t is the tensile strength, and (iv) σ_1 is the stress at the limit of the two linear models.

(a) External sources   (b) Internal sources
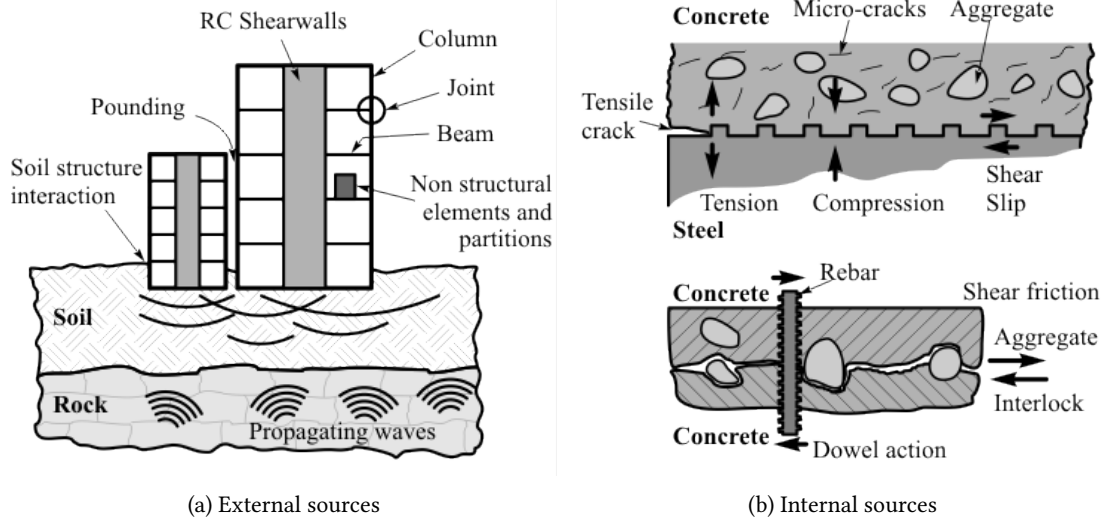
Figure 1.5: Schemes summarising the damping sources (Jehel, 2009)

The models could be at different scales (local or global) depending on the accuracy required for each phenomenon. The global scale will be chosen for the more complex damping sources. Finally, coupled models could be defined for linked phenomena.

1.1.2   Formulation of the seismic problem

In the presented thesis work, a reinforced concrete beam is studied. So, no interaction with other structures or the soil is considered. The dissipations will be partitioned between the local and the global scale depending on the dissipative phenomena. This section, therefore, focuses on the dynamic equilibrium of the studied case. The first dynamic equations are presented for a single-degree-of-freedom (SDOF) system (section 1.1.2.1) and then for a multi-degrees-of-freedom (MDOF) system (section 1.1.2.2).

1.1.2.1   A single-degree-of-freedom system

For a system with one degree-of-freedom (DOF), as presented in figure 1.6, submitted to earthquake excitation, the general time-dependent dynamic equation, in the relative frame, is given in equation (1.1):[3]

$$m.\ddot{\mathbf{u}} + \mathbf{f}_d\left(\dot{\mathbf{u}}, \mathbf{u}\right) + \mathbf{f}_{int}\left(\dot{\mathbf{u}}, \mathbf{u}\right) = -m.\ddot{\mathbf{u}}_s \tag{1.1}$$

where m is the system mass, $\mathbf{u}$, $\dot{\mathbf{u}}$ and $\ddot{\mathbf{u}}$ are respectively the system displacement, velocity and acceleration and $\ddot{\mathbf{u}}_s$ is the seismic acceleration. The global internal force is commonly decomposed between (i) a viscous damping force $\mathbf{f}_d\left(\dot{\mathbf{u}}, \mathbf{u}\right) = \mathbf{f}_d\left(\dot{\mathbf{u}}\right)$ depending on velocity because no solid damping is considered with the environment, and (ii) the internal force $\mathbf{f}_{int}\left(\dot{\mathbf{u}}, \mathbf{u}\right) = \mathbf{f}_{int}\left(\mathbf{u}\right)$ depending on displacement because the velocity dependency is negligible (Dubé, 1994). For a linear system, the damping force is proportional to a damping coefficient c_v, and the internal force is proportional to the stiffness k, leading to equation (1.2):

$$m.\ddot{\mathbf{u}} + c_v.\dot{\mathbf{u}} + k.\mathbf{u} = -m.\ddot{\mathbf{u}}_s \tag{1.2}$$

---

[3]A convention is chosen for the equations: the time-dependent variables are written in bold type and the time variable is not explicitly indicated. For example, the time-dependent displacement variable for a SDOF system is written $\mathbf{u}$ and not $u(t)$.

In equation (1.2), the mass and stiffness can be easily determined from the knowledge of the studied structure. However, the damping value determination turns out to be more complicated because it depends on the structure but also its environment, as discussed in section 1.1.1. The global dissipations are modelled through the damping coefficient c_v, while more sophisticated dissipative phenomena can be modelled through a nonlinear internal force $\mathbf{f}_{int}(\mathbf{u})$. Studying SDOF systems leads to analytical solutions to the problem. Notably, for an undamped system ($c_v =$
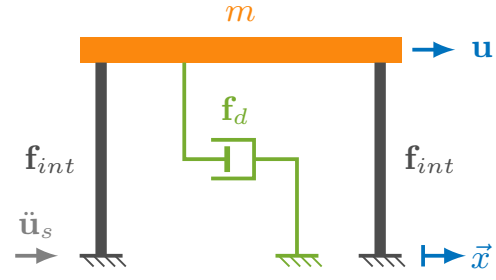
Figure 1.6: SDOF system

0), the solution is only depending on the natural eigenfrequency $\omega_0 = \sqrt{\frac{k}{m}}$, the initial conditions and the excitation. Then, when the system is damped, a third term influences its response: the viscous damping ratio ξ defined as the ratio between the viscous damping coefficient c_v and a critical damping c_c, for which no oscillatory motion is observed in free vibration: $\xi = \frac{c_v}{c_c}$.

1.1.2.2   A multi-degrees-of-freedom system

From the continuous problem, the application of the finite element method (FEM) leads to the matrix dynamic equation, in the relative frame, in equation (1.3):

$$\mathbb{M} \cdot \underline{\ddot{U}} + \mathbb{C} \cdot \underline{\dot{U}} + \underline{\mathbf{f}_{\mathbf{int}}}\left(\underline{U}, \ldots\right) = -\sum_k \mathbb{M} \cdot \underline{\Gamma}_k \cdot \ddot{U}_{s,k} \qquad (1.3)$$

with $\mathbb{M}$ and $\mathbb{C}$ the mass and damping matrices and $\underline{U}$, $\underline{\dot{U}}$ and $\underline{\ddot{U}}$ the relative displacement, velocity and acceleration space- and time-dependent vectors. $\underline{\mathbf{f}_{\mathbf{int}}}\left(\underline{U}, \ldots\right)$ is the internal force depending on the displacement field and numerous internal variable fields associated with nonlinear phenomena. $\underline{\Gamma}_k$ with $k \in \{x, y, z\}$ gives the direction of the seismic excitations where $\ddot{U}_{s,k}$ with $k \in \{x, y, z\}$ are the seismic accelerations in the three space-direction. This equation can be rewritten in an absolute formalism (eq. 1.4), where the absolute displacement field $\underline{U}_a$ is defined as the sum of relative $\underline{U}$ and seismic ground $\mathbf{U}_{s,k}$ with $k \in \{x, y, z\}$ displacement fields (eq. 1.5):

$$\mathbb{M} \cdot \underline{\ddot{U}}_a + \mathbb{C} \cdot \underline{\dot{U}} + \underline{\mathbf{f}_{\mathbf{int}}}\left(\underline{U}, \ldots\right) = \underline{\mathbf{0}} \qquad (1.4)$$

$$\underline{U}_a = \underline{U} + \sum_k \underline{\Gamma}_k \cdot \mathbf{U}_{s,k} \qquad (1.5)$$

In the relative frame, a damped linear MDOF system excited by an earthquake can be described by equation (1.6):

$$\mathbb{M} \cdot \underline{\ddot{U}} + \mathbb{C} \cdot \underline{\dot{U}} + \mathbb{K} \cdot \underline{U} = -\sum_k \mathbb{M} \cdot \underline{\Gamma}_k \cdot \ddot{U}_{s,k} \qquad (1.6)$$

with $\mathbb{K}$ the stiffness matrix. An efficient method to determine the response of such a system is to project the equation on the modal basis $\mathcal{B}^4$ established from the system eigenvalues $\{\lambda_i\}_{i\in[\![1;N]\!]}$ and eigenvectors $\left\{\underline{\phi}_i\right\}_{i\in[\![1;N]\!]}$ where N is the chosen number of modes to reduce the basis ($\mathbb{P}$ is the transfer matrix build from the eigenmodes). Indeed, such a basis is orthogonal as regards the mass and stiffness matrices given equation (1.7):

$$\underline{\phi}_i^T \cdot \mathbb{M} \cdot \underline{\phi}_j = m_i \times \delta_{ij} \quad \text{and} \quad \underline{\phi}_i^T \cdot \mathbb{K} \cdot \underline{\phi}_j = k_i \times \delta_{ij} \quad \forall\{i,j\}_{[\![1;N]\!]^2} \qquad (1.7)$$

---

[4]In the case of a damped system, the basis is complex.

with δ_{ij} the Kronecker's symbol associated with modes i and j. In addition, if the basis is orthonormal with respect to the mass matrix, $m_i = 1$ and $k_i = \lambda_i = \omega_i^2$. The problem eigencharacteristics are obtained by solving the undamped eigenvalue problem in equation (1.8):

$$(\mathbb{K} - \lambda_i.\mathbb{M}) \cdot \underline{\phi}_i = \underline{0} \tag{1.8}$$

The displacement can hence be decomposed on the modal basis by equation (1.9):

$$\underline{\mathbf{U}} = \sum_{i=1}^{N} \boldsymbol{\alpha}_i.\underline{\phi}_i \tag{1.9}$$

where $\{\boldsymbol{\alpha}_i\}_{i\in[\![1;N]\!]}$ represent the generalised coordinates depending on time. Projecting the undamped system equations on the modal basis leads to decoupled equations.

The orthogonality in basis $\mathcal{B}$ is no more verified for a damped system. Except that, in the case of low damping, it can be demonstrated that the imaginary parts of complex eigenmodes and eigenfrequencies are negligible (see proof below). Thus, the same basis can be considered for the low damped and undamped systems. The damping matrix is therefore built to be orthogonal on the modal basis: $\underline{\phi}_i^T \cdot \mathbb{C} \cdot \underline{\phi}_j = c_i \times \delta_{ij}$. That strategy is called "proportional damping matrix". Viscous damping ratios associated to each mode are determined with the equivalence $\xi_i = \dfrac{c_{v,i}}{2.\omega_i.m_i}$ and a decoupled system of equations is solved.

Proof. **"$\mathbb{C}$ is diagonal in the modal basis"** $\sim$ **"if $\mathbb{C}$ is low, $\mathbb{P}^T.\mathbb{C}.\mathbb{P}$ is diagonal":**

Let us consider ω_i, and $\underline{\phi}_i$ respectively the eigenfrequencies and eigenmodes of the undamped system. For low but non-null damping, λ_i and $\underline{z}_i$ are solutions of the equation (1.10):

$$\left(\lambda_i^2\mathbb{M} + \lambda_i\mathbb{C} + \mathbb{K}\right) \cdot \underline{z}_i = \underline{0} \tag{1.10}$$

with:
- ✓ $\lambda_i = \pm i.\omega_i + \Delta\lambda$
- ✓ $\underline{z}_i = \underline{\phi}_i + \Delta\underline{z}$

Defining the eigenfrequencies and eigenmodes from small variations (respectively $\Delta\lambda$ and $\Delta\underline{z}$) of the undamped system ones leads to equation (1.11):

$$\left[\left(-\omega_i^2 + 2i.\Delta\lambda.\omega_i + \Delta\lambda^2\right)\mathbb{M} + (i.\omega_i + \Delta\lambda)\,\mathbb{C} + \mathbb{K}\right] \cdot \left(\underline{\phi}_i + \Delta\underline{z}\right) = \underline{0} \tag{1.11}$$

By neglecting the second order terms, equation (1.12) is deduced:

$$\left(-\omega_i^2\mathbb{M} + \Delta\lambda \cdot \mathbb{C} + \mathbb{K}\right)\underline{\phi}_i + \left(-\omega_i^2\mathbb{M} + \mathbb{K}\right)\Delta\underline{z} + i\left(2.\Delta\lambda.\omega_i\mathbb{M} + \omega_i\mathbb{C}\right)\underline{\phi}_i + i\left(\omega_i\mathbb{C}\right)\Delta\underline{z} = \underline{0} \tag{1.12}$$

Then, because $\mathbb{C} << \mathbb{M}, \mathbb{K}$ and $\left(-\omega_i^2\mathbb{M} + \mathbb{K}\right)\underline{\phi}_i = \underline{0}$, equation (1.13) is obtained:

$$\left(-\omega_i^2\mathbb{M} + \mathbb{K}\right)\Delta\underline{z} + i\omega_i\left(2.\Delta\lambda \cdot \mathbb{M} + \mathbb{C}\right)\underline{\phi}_i = \underline{0} \tag{1.13}$$

Let us project the imaginary part on mode j (eq. 1.14):

$$2.\Delta\lambda\left(\underline{\phi}_j^T \cdot \mathbb{M} \cdot \underline{\phi}_i\right) + \underline{\phi}_j^T \cdot \mathbb{C} \cdot \underline{\phi}_i = 0 \tag{1.14}$$

With $\underline{\phi}_j^T \cdot \mathbb{M} \cdot \underline{\phi}_i = \delta_{ij}$ it can be deduced that:

✓ $c_{ij}^{mod} = 0$ $\forall\, j \neq i$

✓ $\Delta\lambda = -\frac{c_i^{mod}}{2.m_i^{mod}}$ $\forall\, j = i$ with $c_i^{mod} = \underline{\phi}_i^T \cdot \mathbb{C} \cdot \underline{\phi}_i$ and $m_i^{mod} = \underline{\phi}_i^T \cdot \mathbb{M} \cdot \underline{\phi}_i$

Finally, the damping matrix is well diagonal in the modal basis in low damping because the non-diagonal terms of the damping matrix are of second order. ∎

1.1.3   Description of energies

From the seismic equations presented in the previous section, energies at the structural level can be defined. Uang and Bertero (1990) proposed an approach for quantifying the energies associated with a SDOF system. Energies are defined from the derivation of the dynamic absolute or relative equations. Then, their quantification is applied for MDOF structures by Uang and Bertero (1990), Léger and Dussault (1992), and Ghavamian (1998). The proposed approaches quantify the energies developing in a structure from the works associated with the structure forces.

Let us define $\mathrm{d}t$ as an infinitesimal time interval and $\mathrm{d}\underline{\mathbf{U}}$ the structural relative displacement variation over this time interval. Thus, the energies developing in the structure are deduced from equation (1.4) and can be written as in equation (1.15):

$$\left(\mathbb{M} \cdot \ddot{\underline{\mathbf{U}}}_a\right) \cdot \mathrm{d}\underline{\mathbf{U}} + \left(\mathbb{C} \cdot \dot{\underline{\mathbf{U}}}\right) \cdot \mathrm{d}\underline{\mathbf{U}} + \underline{\mathbf{f}}_{\mathbf{int}}\left(\underline{\mathbf{U}}\right) \cdot \mathrm{d}\underline{\mathbf{U}} = \mathbf{0} \tag{1.15}$$

1.1.3.1   Absolute energy definition

By replacing $\mathrm{d}\underline{\mathbf{U}} = \mathrm{d}\underline{\mathbf{U}}_a - \mathrm{d}\underline{\mathbf{U}}_s$ with $\mathrm{d}\underline{\mathbf{U}}_s = \sum_k \underline{\Gamma}_k \cdot \mathrm{d}\mathbf{U}_{s,k}$, Uang and Bertero (1990) decomposed the energy associated with the inertial force given equation (1.16):

$$\left(\mathbb{M} \cdot \ddot{\underline{\mathbf{U}}}_a\right) \cdot \mathrm{d}\underline{\mathbf{U}}_a + \left(\mathbb{C} \cdot \dot{\underline{\mathbf{U}}}\right) \cdot \mathrm{d}\underline{\mathbf{U}} + \underline{\mathbf{f}}_{\mathbf{int}}\left(\underline{\mathbf{U}}\right) \cdot \mathrm{d}\underline{\mathbf{U}} = \left(\mathbb{M} \cdot \ddot{\underline{\mathbf{U}}}_a\right) \cdot \mathrm{d}\underline{\mathbf{U}}_s \tag{1.16}$$

So, equation (1.17) defines the energy balance during the time interval $\mathrm{d}t$.

$$\mathrm{d}E_{k,a} + \mathrm{d}E_d + \mathrm{d}E_a = \mathrm{d}E_{i,a} \tag{1.17}$$

where $\mathrm{d}E_{k,a}$, $\mathrm{d}E_d$, $\mathrm{d}E_a$ and $\mathrm{d}E_{i,a}$ are respectively the absolute kinematic, viscous damping, absorbed (or internal) and absolute imparted energy variations. Then, to obtain the energy at time t from the beginning of the excitation, energy variations are integrated on the interval of interest. Thus, the involved energies are given in equation (1.18):

$$\int \left(\mathbb{M} \cdot \ddot{\underline{\mathbf{U}}}_a\right) \cdot \mathrm{d}\underline{\mathbf{U}}_a + \int \left(\mathbb{C} \cdot \dot{\underline{\mathbf{U}}}\right) \cdot \mathrm{d}\underline{\mathbf{U}} + \int \underline{\mathbf{f}}_{\mathbf{int}}\left(\underline{\mathbf{U}}\right) \cdot \mathrm{d}\underline{\mathbf{U}} = \int \left(\mathbb{M} \cdot \ddot{\underline{\mathbf{U}}}_a\right) \cdot \mathrm{d}\underline{\mathbf{U}}_s \tag{1.18}$$

Some terms can be simplified, giving equation (1.19):

$$\frac{1}{2}\left(\mathbb{M} \cdot \dot{\underline{\mathbf{U}}}_a\right) \cdot \dot{\underline{\mathbf{U}}}_a + \int \left(\mathbb{C} \cdot \dot{\underline{\mathbf{U}}}\right) \cdot \dot{\underline{\mathbf{U}}}\,\mathrm{d}t + \int \underline{\mathbf{f}}_{\mathbf{int}}\left(\underline{\mathbf{U}}\right) \cdot \mathrm{d}\underline{\mathbf{U}} = \int \left(\mathbb{M} \cdot \ddot{\underline{\mathbf{U}}}_a\right) \cdot \mathrm{d}\underline{\mathbf{U}}_s \tag{1.19}$$

Finally, the energy balance is summarised in equation (1.20):

$$E_{k,a} + E_d + E_a = E_{i,a} \tag{1.20}$$

where $E_{k,a}$, E_d, E_a and $E_{i,a}$ are respectively the absolute kinematic energy, the viscous damping energy, the absorbed (or internal) energy and the absolute imparted energy.

This first energy analysis is performed using the decomposition of the displacement increment $\mathrm{d}\underline{\mathbf{U}}$ $(= \mathrm{d}\underline{\mathbf{U}}_a - \mathrm{d}\underline{\mathbf{U}}_s)$. It leads to a first definition of the imparted and kinematic energies. This approach is defined as the "absolute" energy balance.

1.1.3.2 Relative energy definition

In Uang and Bertero (1990) works, a second approach was proposed, where the decomposition (absolute and relative) was considered at the inertial force level.

Equation (1.21) defines the energies obtained by the dynamic equilibrium in the relative coordinate system, from equation (1.3):

$$\left(\mathbb{M} \cdot \ddot{\underline{U}}\right) \cdot d\underline{U} + \left(\mathbb{C} \cdot \dot{\underline{U}}\right) \cdot d\underline{U} + \underline{f_{int}}\left(\underline{U}\right) \cdot d\underline{U} = -\left(\mathbb{M} \cdot \underline{\Gamma} \cdot \ddot{U}_s\right) \cdot d\underline{U} \tag{1.21}$$

By integration, equation (1.22) gives the "relative" energy equation:

$$\frac{1}{2}\left(\mathbb{M} \cdot \dot{\underline{U}}\right) \cdot \dot{\underline{U}} + \int \left(\mathbb{C} \cdot \dot{\underline{U}}\right) \cdot \dot{\underline{U}}\, dt + \int \underline{f_{int}}\left(\underline{U}\right) \cdot d\underline{U} = -\int \left(\mathbb{M} \cdot \underline{\Gamma} \cdot \ddot{U}_s\right) \cdot d\underline{U} \tag{1.22}$$

Finally, the energy balance is summarised in equation (1.23):

$$E_{k,r} + E_d + E_a = E_{i,r} \tag{1.23}$$

where $E_{k,r}$, E_d, E_a and $E_{i,r}$ are respectively the relative kinematic, viscous damping, absorbed (or internal) and relative imparted energies.

1.2 Damping models in dynamic structural computations

When a structure is subjected to an earthquake, it dissipates energy by hysteretic actions and other phenomena. Those dissipative phenomena have to be modelled to get relevant results from dynamic computations. The choice of the mathematical damping model plays a major role in the accurate representation of the amplitude evolution of dissipated energies. Many papers in the literature focus on damping matrix formulations for MDOF numerical analyses. Viscous, hysteretic or numerical damping can be considered in computations (section 1.2.1). At the structural level, two major strategies are mainly considered to keep a diagonal damping matrix on the modal basis: Rayleigh-type damping and modal damping (section 1.2.2). To go further in consideration of physical phenomena, local models are also investigated (section 1.2.3). Then, comparisons of the proposed damping models are performed on different structural examples (section 1.2.4). Appendix A presents a nomenclature of damping matrices explored in literature and exposed in this section.

1.2.1 Various damping types

Let us consider three SDOF systems submitted to a seismic acceleration as presented in figure 1.6 with $m = 29440\,\text{kg}$ and $k = 1.32 \times 10^7\,\text{N/m}$. A multi-frequency sinusoidal acceleration is chosen, and the associated input force is plotted in figure 1.7 with $\mathbf{F}_{\text{input}} = -m.\ddot{\mathbf{u}}_s$. Different damping models can be considered depending on the forms of the internal $\mathbf{f}_{int}$ and damping $\mathbf{f}_d$ forces. Table 1.1 indicates the studied damping types and
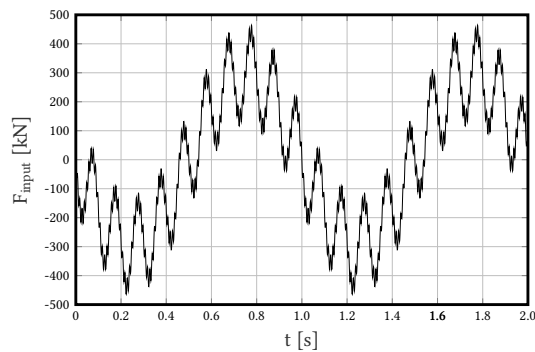
Figure 1.7: Input force (superposition of 1 Hz, 10 Hz, 100 Hz and 1000 Hz sine functions) for the study of the damping types

Table 1.1: Damping types

Damping type	Name	Formulation
Viscous	–	$\mathbf{f}_d = c_v \dot{\mathbf{u}}$
	Linearity	$\mathbf{f}_{int} = k.\mathbf{u}$
Hysteretic	Elastoplasticity[1]	$\mathbf{f}_{int} = k.(\mathbf{u} - \mathbf{u}_p)$
	Damage[2]	$\mathbf{f}_{int} = k(1-d).\mathbf{u}$
Numerical	–	–

[1] $\mathbf{u}_p$ is the plastic displacement   [2] d is the damage variable

(a) Linear   (b) Elastoplastic   (c) Damage
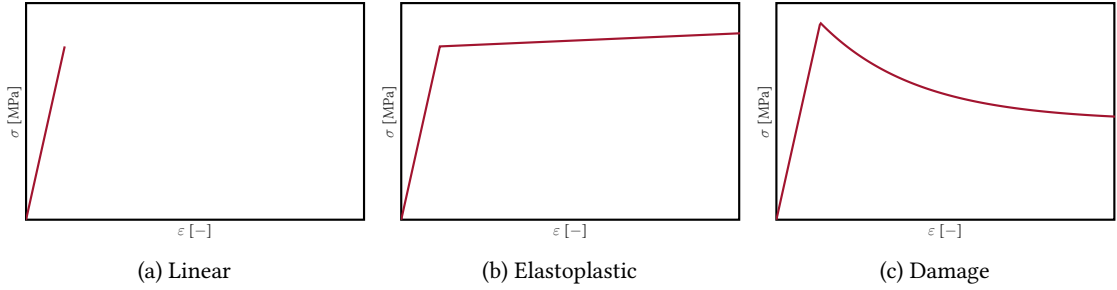
Figure 1.8: Studied constitutive models

figure 1.8 shows the constitutive laws of the hysteretic models in table 1.1. The three models are defined with Young's modulus of $E = 22\,\text{GPa}$. The tensile strength for the elastoplastic and damaged models is $f_y = 1\,\text{MPa}$. Then, the elastoplastic models considers a hardening modulus of $H = 5\,\text{GPa}$. The value d is defined by an exponential function, for the damage model. The Newmark's algorithm is used to solve equation (1.1) for the different proposed models. Then, energies are evaluated based on the formulations presented in section 1.1.3. All plotted energies are normalised with respect to their final values. For dissipative energies, it corresponds to their maximal values with respect to time.

The first analysis is performed with Newmark's algorithm parameters equal to $\gamma = 1/4$ and $\beta = 1/2$ to eliminate the numerical damping. Thus, a focus is made on hysteretic and viscous damping models. In figure 1.9, viscous damping is considered with the three constitutive models. For each model, the hysteretic (E_{hyst}) and viscous damping (E_{damp}) energies are plotted. No
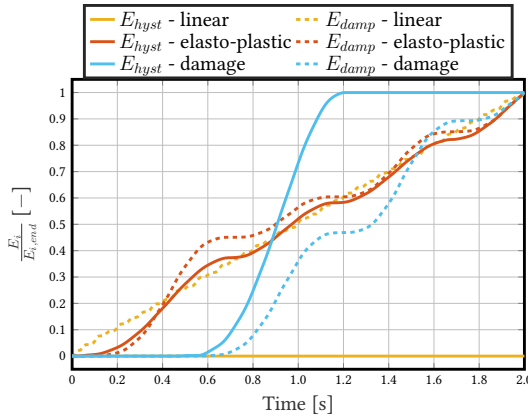
Figure 1.9: Different types of damping - one DOF system - dissipative energies

dissipation occurs at the material level for the linear model, so the hysteretic energy is always null. Between the damage and elastoplastic models, the evolution of the hysteretic energy is different. For the damage model, dissipation is only observed with an increase of the damage variable. On the contrary, a more continuous evolution is observed with the elastoplastic model. Then, for the viscous damping energy, even if the same parameter c_v is used with the three models, the energy evolution depends on the constitutive model. However, it also increases during the computation because it represents energy lost by the system.

In figure 1.10, only the hysteretic energy is plotted with the elastoplastic and damage models but in the cases of a null or non-null viscous damping coefficient. It appears that the influence of viscous damping is reversed for the two material models. Indeed, for the damage model, with viscous damping, the energy is dissipated more rapidly compared with the one without damping. For the elastoplastic model, the dissipation evolves more rapidly without damping. In any case, the introduction of viscous damping leads to a decrease in the total dissipation by the hysteretic model.

Figure 1.11 presents the influence of the input signal frequency content on the dissipated energies[5]. Both damage and elastoplastic models are
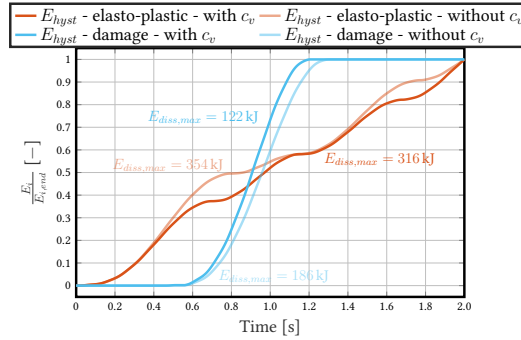
Figure 1.10: Different types of damping - one DOF system - dissipative energies - influence of viscous damping

studied here. It appears that the signal frequencies influence the hysteretic and viscous damping energies. For the elastoplastic model (fig. 1.11a), the lowest is the frequency, the fewer oscillations are obtained on energy evolutions. So, the energies are influenced by the first signal frequency. On the contrary, figure 1.11b exhibits a different behaviour for the damage model: energy increases by small steps are observed with $f = 0.2\,\mathrm{Hz}$ demonstrating the influence of the second signal frequency ($10\,\mathrm{Hz}$). However, the lowest is the first signal frequency, and the fastest are reached the final dissipated energies.

(a) Elasto-plastic model

(b) Damage model
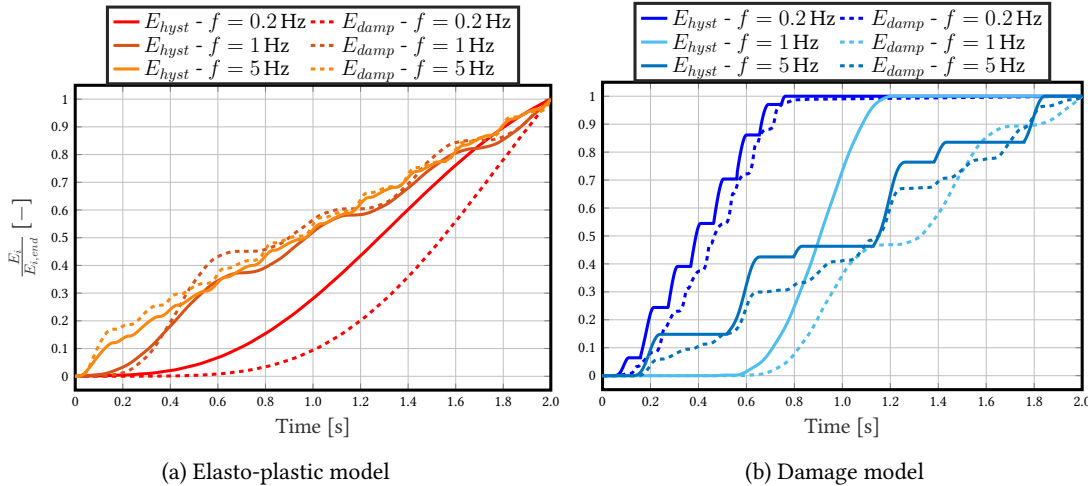
Figure 1.11: Different types of damping - one DOF system - influence of the input signal frequency

---

[5]It should be noticed that the results are also influenced by the problem properties like m or k.

Then, figure 1.12 shows the numerical damping. γ parameter of Newmark's algorithm varies between $1/10$, $1/2$ and $\sim 1/1.11$. Figures 1.12a and 1.12c present the responses with viscous damping, and figures 1.12b and 1.12d present the responses when no viscous damping is considered. The case $\gamma = 1/2$ and $\beta = 1/4$ does not induce numerical energy dissipations, while positive numerical damping appears with $\gamma > 1/2$ and negative one appears with $\gamma < 1/2$ (Alarcon, 2015). It is demonstrated here particularly with the displacement responses because with $\gamma = 0.1$ the highest displacements are reached. On the contrary, with $\gamma = 0.9$, the smallest ones are reached because of the numerical damping. However, all figures show that the numerical damping induces few differences with the signal considered. All analyses presented in this thesis will be performed with $\gamma = 1/2$ and $\beta = 1/4$ precisely to avoid the numerical damping.

(a) With viscous damping - energies

(b) Without viscous damping - energies

(c) With viscous damping - displacement

(d) Without viscous damping - displacement
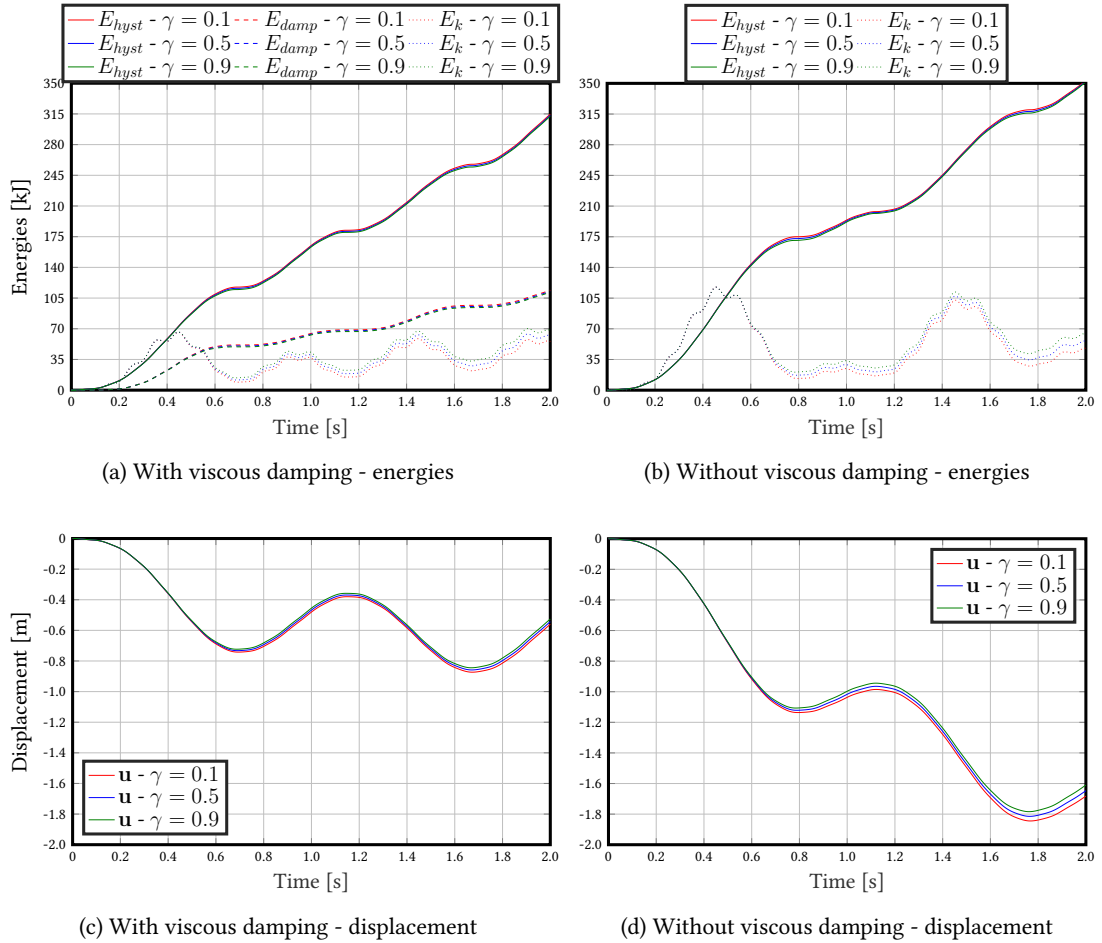
Figure 1.12: Different types of damping - one DOF system - numerical damping - elasto-plastic model

1.2.2   Damping models at the structural level - global description

For the study of MDOF structures, damping models at the global level are characterised by a viscous damping matrix $\mathbb{C}$ or by a hysteretic model. In the case of linear systems, the dynamic equation of the

viscously damped system is written in equation (1.24):

$$\mathbb{M} \cdot \underline{\ddot{\mathbf{U}}} + \mathbb{C} \cdot \underline{\dot{\mathbf{U}}} + \mathbb{K} \cdot \underline{\mathbf{U}} = \underline{\mathbf{F}}(t) \tag{1.24}$$

where the viscous damping matrix $\mathbb{C}$ can be built with the model properties like the stiffness and mass matrices ("classical" damping), or it can be described using the eigenmodes (modal damping). In addition to viscously damped systems, hysteretically, with a complex stiffness matrix, can also be defined as presented in equation (1.25):

$$\mathbb{M} \cdot \underline{\ddot{\mathbf{U}}} + \mathbb{K}\left(1 + j.\eta_k\right) \cdot \underline{\mathbf{U}} = \underline{\mathbf{F}}(\Omega) \tag{1.25}$$

for a harmonic loading of frequency Ω and where j is the complex variable given $j^2 = -1$, and η_k is a parameter given the level of complexity in the stiffness matrix. The complex formulation in equation (1.25) is particularly representative of visco-elastic material. Because no visco-elastic effects are obtained in the analyses performed in this thesis, that damping type will not be studied in the following.

Due to the lack of knowledge about the different damping phenomena (1.1.1), the aim of models presented in this section is generally to represent the global capacity of the structure to dissipate energy. So, proportional to the velocity, viscous damping is a non-physical but convenient way to describe the dissipation at the structural level.

By definition, a classical damping matrix is a diagonal matrix in the modal basis of the undamped system. Unless it lacks a physical basis, a classical damping formulation is often used to directly integrate the dynamic equation when the damping matrix must be completely defined. It is an easy-to-use mathematical tool. Therefore many of the upcoming damping formulations are classical matrices (F. A. Charney, 2008). In addition, damping ratios are associated with each eigenmode for modal damping. The global matrix must only be assembled if the problem is solved in the entire space.

1.2.2.1 Rayleigh damping (RD) and derivatives

(a) Generalities on Rayleigh damping   Rayleigh was the first to introduce the idea of viscous proportional damping (Rayleigh, 1877; Rayleigh, 1896). Even if he was not using matrix algebra, its results were close to those described here. What is commonly called the "Rayleigh damping matrix" (eq. 1.26) is composed of two terms: the first one is proportional to the mass matrix $\mathbb{M}$ and mainly represents the external dampers linked with the degrees-of-freedom (DOFs), and the second one is proportional to the initial stiffness matrix $\mathbb{K}_0$ and mainly represents the viscous damping between DOFs.

$$\mathbb{C} = a_0 \cdot \mathbb{M} + a_1 \cdot \mathbb{K}_0 \tag{1.26}$$

with constant parameters a_0 and a_1. Only two damping ratios for two selected frequencies are required to determine the Rayleigh damping matrix (fig. 1.13): ξ_i for ω_i and ξ_j for ω_j associated to modes i and j. According to equation (1.26), the equivalent damping associated with mode n is written as $\xi_n = \dfrac{a_0}{2.\omega_n} + \dfrac{a_1.\omega_n}{2}$. So, the solution of the following system (eq. 1.27) is enough to determine the two parameters.

$$\begin{cases} \xi_i = \dfrac{a_0}{2.\omega_i} + \dfrac{a_1.\omega_i}{2} \\[2mm] \xi_j = \dfrac{a_0}{2.\omega_j} + \dfrac{a_1.\omega_j}{2} \end{cases} \quad \Longleftrightarrow \quad \begin{cases} a_0 = \dfrac{2\omega_i\omega_j}{\omega_i^2 - \omega_j^2}\left(\xi_j\omega_i - \xi_i\omega_j\right) \\[2mm] a_1 = \dfrac{2}{\omega_i^2 - \omega_j^2}\left(\xi_i\omega_i - \xi_j\omega_j\right) \end{cases} \tag{1.27}$$

The Rayleigh damping matrix is still the most employed in engineering due to its simplicity. Indeed, for a FE model, the mass and stiffness matrices description can simply be done with the studied system knowledge.

The choice of modes i and j has to be carefully done. Most of the approaches proposed in the literature to determine the most appropriate modes are based on the least square method. The problem

is that the methods are often based on the first mode and the last one with a non-negligible contribution. However, the second mode chosen can be very high, particularly for large structures. So, significant errors on damping ratios for lower modes, playing a significant role, can appear. Song and C. Su (2017) discussed those difficulties and proposed another method based on the modal participating mass.

However, following Rayleigh (1896), many studies have been developed in the literature to show the problems encountered with this matrix and find so-

Figure 1.13: Rayleigh equivalent damping for $\xi_1 = \xi_2$

lutions to improve it. Notably, Hall (2006) enumerated some difficulties produced with the Rayleigh damping matrix. First, spurious damping forces develop, leading to overestimating the dissipated energy in structure and underestimating structural failure risk. Second, for nonlinear analyses, it is not easy to control damping. Mainly because with the initial stiffness $\mathbb{K}_0$, it is impossible to represent the cracking or any other energy dissipating phenomena. Nevertheless, in terms of deformations, the results are pretty accurate for low levels of nonlinearities.

(b) Mass-proportional damping (MPD) With the mass-proportional damping formulation $\mathbb{C} = a_0 \cdot \mathbb{M}$, some spurious damping forces are eliminated (Zareian and Medina, 2010). However, Zareian and Medina (2010) also indicated that the MPD matrix does not allow to characterise the experimental responses because the high-frequency content is not damped (fig. 1.13). Finally, because the mass-proportional part corresponds mainly to the environment of the structure, Zareian and Medina (2010) explained that its influence would be much more critical for underwater structures, which are not the case in the structures studied in this thesis.

(c) Stiffness-proportional damping (KPD) The mass-proportional part is one of the difficulties often discussed in the literature with the Rayleigh damping matrix. Hall (2006) explained that very high damping can develop in the case of rigid body movements (what happens during seismic analyses in the relative frame) or when a structural element reaches a high velocity (for example, when a dam slides on its base). It can be observed in figure 1.13 with the strong increase of ξ_n for low values of ω_n. So, lots of papers recommend eliminating the mass-proportional part in the Rayleigh damping matrix, like F. Charney et al. (2017) and Hall (2006), and considering the stiffness-proportional damping formulation $\mathbb{C} = a_1 \cdot \mathbb{K}$.

However, Petrini et al. (2008) demonstrated that using the initial stiffness matrix in the KPD formulation appeared inappropriate because a large amount of energy was dissipated, resulting in too small displacements. It was problematic primarily because this model was often used and is still used in inelastic dynamic analyses. In the same idea, Hall (2006) discussed the lack of modal damping ratio control with the KPD formulation. So, to reduce the damping forces and obtain the most accurate results, Hall (2006) proposed to bound and control the damping force. While Petrini et al. (2008) focused on using a tangent stiffness-proportional damping formulation (TKPD) because it allowed to reduce and contain the damping forces. The counterpart of the result improvements with the TKPD formulation was the substantial increase in computational time because the stiffness matrix had to be evaluated for each time step. If the structure exhibited significant stiffness variations, numerical instabilities were able to develop, for example, with numerical schemes such as Newton-Raphson (F. A. Charney, 2008).

(d) **Rayleigh damping updating** The papers presented herein aim to update the RD matrix, with the tangent stiffness matrix, for example, to keep its advantages and enhance numerical responses. Zareian and Medina (2010) interested in a new damping model based on RD formulation with the tangent stiffness matrix but keeping stiffness-proportional damping only in elements remaining in the elastic regime. The method showed good performances in estimating the seismic collapse capacity and was viable for cyclic deterioration cases. Then, F. Charney et al. (2017) proposed to update: (i) RD with the full tangent stiffness matrix, and (ii) RD with the partial initial stiffness matrix. In the partial formulation, the idea was to keep only the elastic terms in the stiffness-proportional part. It avoided the apparition of spurious damping forces when the system became inelastic. However, spurious energy could still develop due to hysteresis inside the element. Jehel, Léger, and Ibrahimbegovic (2014) also based their work on RD with the tangent stiffness matrix by developing analytical formulas to control damping ratios in inelastic time history analyses. Another idea was then proposed by Nakamura (2017) and Nakamura (2019) to improve the RD formulation with the complex stiffness in equation (1.28) built with a causal unit imaginary function, a significant component of the hysteretic damping:

$$\widetilde{\mathbb{K}}(\omega) = \mathbb{K}_0(1 + 2\xi \cdot i \cdot sg(\omega)) \tag{1.28}$$

where i is the imaginary variable, $\widetilde{\mathbb{K}}$ the complex stiffness matrix and $sg(\omega)$ the sigh of ω. This method improves the frequency range of a constant damping ratio. Finally, Salehi and Sideris (2018) developed a strategy of continuous evolution, at first order, of the tangent-stiffness matrix to improve the RD formulation.

In addition to mass and stiffness matrices, two parameters are considered for computing the RD matrix (a_0 and a_1) and can thus be updated during computations. First, Léger and Dussault (1992) proposed to update the parameters by computing the eigenfrequencies of the damaged structure at each time step. With the new eigenfrequencies, the system (1.27) was able to be solved with constant damping ratios ξ_1 and ξ_2. The use of the tangent-stiffness matrix accompanied the parameter updates. The proposed formulation better controlled the energy dissipated by viscous damping in nonlinear analyses. However, the computation of parameters for each time step was very time-consuming. In addition, if the structure exhibited high stiffness degradation level, the methodology became challenging to perform. Crambuer (2013) also discussed the advantages and disadvantages of this method: (i) no artificial damping occurred, (ii) the frequency dropped due to the structural stiffness degradation, and (iii) damage was not overestimated for low frequencies. However, (i) the damping was again overestimated for high frequencies, (ii) the computational time increased a lot, and (iii) the updating was still not based on particular dissipative phenomena. Then, based on the advantages and difficulties encountered with the classical RD formulation as well as the updates already discussed, F. A. Charney (2008) recommended making a mix of formulations (eq. 1.29), with $a_1(t)$ the coefficient updated during computation.

$$\mathbb{C} = a_0 \cdot \mathbb{M} + a_1 \cdot \mathbb{K}_0 + a_1(t) \cdot \mathbb{K}_T \tag{1.29}$$

Finally, instead of updating eigenfrequencies, the idea could have been to update damping ratios during the computation. By considering the fact that the concrete cracks influence the damping ratio, Crambuer (2013) proposed damping updating methodologies where the damping ratio depends on damage, loading level, and crack surface erosion (more detailed in section 1.3.3.2). Thus, Crambuer (2013) explained that by accurately updating damping, simplified models could be able to model the global damping evolution of structural elements.

1.2.2.2 Caughey damping matrix

Rayleigh damping-type matrices are not the only classical damping formulations. T. K. Caughey (1960) and T. K. Caughey and O'Kelly (1965b) proposed a "generalised Rayleigh damping formulation". The

idea came from the remark that undamped linear systems possess normal modes. T. K. Caughey (1960) and T. K. Caughey and O'Kelly (1965b) determined a sufficient and necessary condition for damped dynamic systems, continuous or discrete, to also possess normal classical modes. The developed "Caughey damping (CD) matrix" is expressed in equation (1.30):

$$\mathbb{C} = \mathbb{M} \cdot \sum_i a_i \left[\mathbb{M}^{-1} \cdot \mathbb{K} \right]^i \tag{1.30}$$

Because the damping matrix is decoupled in the modal basis, this matrix is also a "classical" one. However, F. Charney et al. (2017) explained that this kind of behaviour did not exist in real structures except for elastic systems under ambient vibrations. The proportional character of the model enabled a resolution on a modal basis. In addition, the sum in equation (1.30) expanded the number of modes for which damping ratios can be imposed. Several drawbacks are listed by Smyrou, Priestley, and Carr (2011) and F. Charney et al. (2017): (i) the increasing number of damping parameters to identify as regards the range of i in equation (1.30), (ii) specific numerical strategies to handle negative power of matrix $\mathbb{M}$ and (iii) the spurious damping values for high frequency.

Updates of this matrix were proposed: (i) Bernal (1994) who considered only the negative exponents of the matrix to limit the development of spurious forces. (ii) Luco (2008) focused on the Caughey series coefficient determinations based on experimental damping data to restore the system well-conditioning.

1.2.2.3   Modal damping formulations

"Modal damping" (MD) formulations consist in computing a damping matrix from eigenmodes. First, Wilson and Penzien (1972) proposed an adaptation of T. K. Caughey (1960) and T. K. Caughey and O'Kelly (1965b) works on the modal basis. Their purpose was to determine an orthogonal damping matrix based on modal damping ratios that could be evaluated from the structural physical properties. Two methods were developed: (i) a Caughey damping matrix using a numerical procedure for its construction, and (ii) a direct evaluation of a modal damping matrix, that is to say, a matrix composed by the sum of modal terms. The proposed matrix is expressed in equation (1.31):

$$\mathbb{C} = \mathbb{M} \cdot \left[\sum_{i=1}^{N-1} \frac{2\xi_i \omega_i}{m_i} \underline{\phi}_i \underline{\phi}_i^T \right] \cdot \mathbb{M} \tag{1.31}$$

where m_i is the modal mass associated with mode i ($m_i = \underline{\phi}_i^T \cdot \mathbb{M} \cdot \underline{\phi}_i$) and N is the total number of nodes. This formulation is more efficient in terms of computation time than the Caughey matrix because no power of the mass matrix has to be computed. Wilson and Penzien (1972) recommended determining the damping ratios required to build the matrix in equation (1.31), with structural physical properties.

Following the idea of Wilson and Penzien (1972) to use modal damping to form an orthogonal damping matrix, Chrisp (1980) developed two modal dampings: (i) a linear model (eq. 1.32) and (ii) a trilinear one (eq. 1.33). The viscous damping ratios are so evolving with the frequencies.

$$\xi_i = A \times f_i \tag{1.32}$$

$$\xi_i = \begin{cases} \xi_a & \forall\, f < f_a \\ \dfrac{\xi_b - \xi_a}{f_b - f_a} \times (f - f_a) + \xi_a & \forall\, f_a < f < f_b \\ \xi_b & \forall\, f_b < f \end{cases} \tag{1.33}$$

where f_a and f_b (associated with the damping ratios f_a and f_b) are two limited frequencies characterising the linear part of the model. The advantages of these models are: (i) the damping localisation, (ii) the

spurious damping force limitation and (iii) the distinction between damping dissipation and hysteretic one (Ni et al., 2019).

Chopra and McKenna (2016) and Chopra and McKenna (2017) rewrote the modal damping matrix in equation (1.34) to eliminate the spurious damping forces:

$$\mathbb{C} = \sum_{i=1}^{N} \frac{4\pi}{T_i} \xi_i \frac{\left(\mathbb{M}\underline{\phi}_i\right)\left(\mathbb{M}\underline{\phi}_i\right)^T}{\underline{\phi}_i^T \mathbb{M}\underline{\phi}_i} \tag{1.34}$$

where $T_i = \frac{1}{f_i} = \frac{2\pi}{\omega_i}$ is the eigenperiod associated with mode i.

As we discussed the possible updates of the Rayleigh damping matrix, nonlinear damping formulations could be defined for modal damping. It is the case when the damping matrix is actualised for each time-step using an eigenvalue analysis based on the tangent-stiffness matrix $\mathbb{K}_T$. The advantage is to increase the accuracy of the dynamic response, but this is firmly time-consuming. In addition, Smyrou, Priestley, and Carr (2011) proposed to use modal damping with 5% as damping ratio for all modes, except for the first mode where a reduced damping ratio was considered. Equation (1.35) presents the reduced damping ratio ξ^* depending on the ductility μ and the post-yield stiffness coefficient r_k:

$$\xi^* = \xi \frac{(1 - 0.1(\mu - 1)(1 - r_k))}{\sqrt{\mu/(1 + r_k\mu - r_k)}} \tag{1.35}$$

It allows eliminating the excessive damping in the post-yield phase for inelastic analyses.

1.2.2.4   Other damping models

To avoid limitations of classical proportional damping formulations, C.-L. Lee (2019) and C.-L. Lee (2020) papers proposed the damping matrix in equation (1.36):

$$\mathbb{C} = \sum_{i=1}^{N} \left[\mathbb{M}_{C_i} - \left(\mathbb{M}_{C_i} \cdot (\mathbb{M}_{C_i} + \mathbb{K}_{C_i})^{-1} \cdot \mathbb{M}_{C_i} \right) \right] \tag{1.36}$$

where $\mathbb{M}_{C_i} = 4\xi_i\omega_i \cdot \mathbb{M}$ and $\mathbb{K}_{C_i} = \frac{4\xi_i}{\omega_i} \cdot \mathbb{K}$ for $i \in [\![1; N]\!]$. This smooth function was developed to match the desired damping ratios ξ_i for as many frequencies ω_i as requested. The construction of this matrix is based on the basis function (eq. 1.37):

$$\xi(\omega) = \sum_{i=1}^{N} \frac{2\omega_i\omega}{\omega_i^2 + \omega^2} \xi_i \tag{1.37}$$

The advantages of this model are its capacity to fit easily damping curves, especially for constant damping in a broad frequency range, the spurious damping force elimination and the computation time efficiency. In C.-L. Lee (2022), they went even further by defining a four bell-shaped proportional damping model to improve the performances of their models.

Then, the idea proposed by Luco and Lanzi (2017) was to reduce the loss of energy in nonlinear components because it was already taken into account in hysteretic energy dissipation. It presented two advantages: (i) the decrease in damping forces and (ii) the separation between the hysteretic and viscous damping. In Lanzi and Luco (2018), the formulation of the damping matrix $\widetilde{\mathbb{C}}$ in equation (1.38) was considered to keep the dissipations proportional to elastic components of velocity and applied the idea previously discussed in Luco and Lanzi (2017):

$$\widetilde{\mathbb{C}} = \mathbb{K}_T \cdot \mathbb{K}^{-1} \cdot \mathbb{C} \cdot \mathbb{K}^{-1} \cdot \mathbb{K}_T \tag{1.38}$$

where $\mathbb{C}$ could be the Rayleigh, Caughey or modal damping.

Another idea was developed in Adhikari (2000), Adhikari and Woodhouse (2000), Adhikari and Woodhouse (2001a), and Adhikari and Woodhouse (2001b) works corresponding to the identification of viscous and non-viscous damping models using complex modes. The considered dynamic equation of motion is presented in equation (1.39)

$$\mathbb{M} \cdot \underline{\ddot{U}} + \int_{-\infty}^{t} \mathcal{G}\left(t - \tau\right) \cdot \underline{\dot{U}}\, dt + \mathbb{K} \cdot \underline{U} = \underline{0} \tag{1.39}$$

where $\mathcal{G}\left(\tau\right)$ is the kernel function to identify. The method can reasonably predict the spatial damping location. However, accurate $\mathcal{G}\left(\tau\right)$ models are required to describe the physical phenomena associated with damping adequately. Adhikari (2006) went further by proposing a new generalised proportional damping still based on smooth continuous functions of the mass and stiffness matrices.

1.2.3   Damping models at the local level

Energy dissipations are due to physical phenomena at the material level. In section 1.2.2, they have been described at the global scale through the definition of a damping matrix $\mathbb{C}$. Some models describing the dissipations at the local level are considered in this section.

1.2.3.1   Material models

(a)   Hysteretic damping   Hysteretic damping (also called structural damping) differs from viscous damping because it is related to displacements and not to velocities. For nonlinear behaviour materials, the hysteretic damping is determined experimentally using harmonic cyclic loadings. It is related to the positive work of external forces, representing the energy dissipated through the structure (Boyere, 2011).

First analytical studies of hysteretic damping were performed by T. Caughey and Vijayaraghavan (1970), following the Kimball and Lovell (1927) works on aircraft fields. T. Caughey and Vijayaraghavan (1970) focused on a "linear hysteretic" damping and demonstrated that the energy loss associated with Reid model Reid (1956) was proportional to the square of the displacement amplitude. Then, S. H. Crandall (1991) explained that "structures exhibit a variety of damping mechanisms with energy losses that vary in many ways with amplitude and frequency". That is why he compared analytic responses of an ideal damper and a band-limited hysteretic one.

Analytical studies were also performed on SDOF systems based on vibrations theory. Muravskii (2004) proposed an analysis of three frequency-independent damping models, representing an alternative for equivalent viscous damping and complex stiffness model. First, the hysteretic model in equation (1.40) was based on the formulation of (Reid, 1956):

$$F_{el-d} = k \left(u + c_d . |u| \frac{\dot{u}}{|\dot{u}|} \right) \tag{1.40}$$

where F_{el-d} is the force corresponding to the sum of the elastic and damping forces and k and c_d respectively the stiffness and damping coefficients. The damping ratio associated, and determined from the hysteretic cycles, is given in equation (1.41) and appears to be linear with the damping coefficient.

$$\xi_{hyst} = \frac{c_d}{\pi} \tag{1.41}$$

Then, for the modified hysteretic model (fig. 1.14), an elastic spring was added to the previous model, and the damping ratio became (eq. 1.42):

$$\xi_{hyst} = \frac{c_d}{\pi} \frac{r_s - 1 - c_d}{r_s - 1 + c_d} \tag{1.42}$$

where $r_s = \frac{k_s}{k}$ and k_s is the stiffness of the SDOF spring. Finally, the quasi-hysteretic nonlinear model was based on the displacement mean value, and the associated damping ratio was given in equation (1.43):

$$\xi_{hyst} = \frac{c_d}{2} \qquad (1.43)$$

The quasi-hysteretic model was recommended to arbitrary input signals.

Finally, Val and Segal (2005) works also focused on SDOF systems submitted to earthquake ground motions. They used a hysteretic damping model (elasto-slip model of Masing type (Segal and Val, 2006)) to avoid the development of an unrealistic damage level for structures submitted to earthquakes.

(b)   Damage, smeared crack, plasticity   Studying energy dissipations occurring at the concrete level is a means to develop cracks prediction models. First, Hillerborg, Modéer, and Petersson (1976) proposed an approach based on the fact that when cracks occurred, a certain amount of energy G_C was absorbed, and when the cracks propagated, stored energy was released. The defined G_C value was, so, equivalent to the fracture energy G_f in figure 1.4.

Then, to limit the amount of required viscous damping energy, research focused on models describing the physical phenomena. For example, Dubé, Pijaudier-Cabot, and Borderie (1996) proposed a rate dependent damage model well characterising the loading rate effect on concrete responses. Another example developed by Ragueneau, La Borderie, and Mazars (2000) aimed at coupling damage and hys-

Figure 1.14: Modified hysteretic model (Muravskii, 2004)

teretic dissipations. They developed a constitutive equation model that dissipated the energy due to two dissipative phenomena: (i) the cracking and (ii) the frictional sliding between crack surfaces. The thermodynamic state potential (1D) is presented in equation (1.44):

$$\rho.\Psi = \frac{1}{2}\left(1-d\right).\varepsilon.E.\varepsilon + \frac{1}{2}\left(\varepsilon - \varepsilon_s\right).d.E.\left(\varepsilon - \varepsilon_s\right) \qquad (1.44)$$

where ρ is the material density, Ψ the state potential, E the material Young's modulus, d the damage index, ε the total strain and ε_s the sliding strain. It is more physical to model internal dissipations at the elementary level than global ones. It is recognised that a link exists between the state of failure and the global damping in RC structures. However, the lack of knowledge appears in the residual hysteresis loop, corresponding to the energy dissipation at a stabilised damage level. That is why a new constitutive concrete model was developed, including the residual hysteretic loop. The model did not require more global damping for seismic calculations because everything was dissipated at the elemental level in the coupling between cracking and sliding. The idea would be taken up by Richard, Ragueneau, et al. (2010) to improve the hysteretic representation of concrete behaviour. The thermodynamic framework of such models will be discussed in chapter 2.

1.2.3.2   Structural element models

The concept of absorbed energy, discussed in section b for concrete, is also considered to predict concrete resistance in structural elements. Ohno and Nishioka (1984) performed experiments on five RC columns to evaluate their energy absorption capacity. Indeed, they considered that value being a "well-suited index for seismic safety". Then, Amara (1996) started from the Griffith energy balance model to

predict the crack growth in RC. Remarkably, the thermodynamic potential was defined by integrating the strain energy. The proposed local model showed a good ability to predict the formation and propagation of the cracks. Then, by comparing the strain energy absorbed by RC columns with their strain energy absorption capacity, Watson, Zahn, and Park (1994) proposed an index for the column rupture definition. Mander, Priestley, and Park (1988) developed, for their part, a stress-strain model to predict the longitudinal compressive strain in concrete. For this aim, equality between the strain energy capacity of the transverse reinforcement and the strain energy stored in the concrete due to confinement was estimated. Tanaka (1990) used the Mander, Priestley, and Park (1988) model to determine concrete ultimate longitudinal compressive strain at the beginning of cracking. Finally, those kinds of analyses were developed at the structural level as proposed by S. S. Bhattacharjee and Léger (1993). They were interested in a FEM for seismic fracture analyses of concrete gravity dams, assuming a nonlinear fracture behaviour for concrete. The smeared fracture model aimed to predict dams seismic cracking and energy response. The dissipated energy definition E_{diss} due to fracture is given in the equation (1.45):

$$E_{diss} = E_R - (E_{el} - E_{el,0}) \tag{1.45}$$

where E_R is the internal work done by nonlinear restoring forces, E_{el} the stored elastic energy and $E_{el,0}$ the pre-seismic elastic strain energy. The model led to an evaluation of the earthquake capacity of dams without performing experimental tests and showed that the fracture energy parameter G_f was necessary for such analyses.

More recently, Grammatikou, Fardis, and Biskinis (2019) discussed the assumption that hysteretic energy dissipation was linked with post-yield inelastic behaviour in damping models. By quantifying this hysteretic energy dissipation in RC elements, Grammatikou, Fardis, and Biskinis (2019) showed that some dissipations also appeared in pre-yield cycles. Those dissipations were a function of the features (ductility, shear-span-to-depth ratio, transverse reinforcement ratio, ...) and deformation histories. That is why a new hysteretic model was proposed based on modified Takeda and modified Clough models by adding dissipations in pre-yield cycles. Thus, energy dissipations before and after yielding could be decomposed. The new model presented the advantage of not requiring viscous damping except if some non-modelled elements were dissipating energy.

Finally, dissipative phenomena have also been coupled in material models to represent the behaviour of RC elements, such as Heitz, Giry, et al. (2019) in the case of damage, friction and plasticity couplings, following the same objective as Ragueneau, La Borderie, and Mazars (2000) in equation (1.44). The thermodynamic framework of such models will be developed in chapter 3.

1.2.3.3   Local viscous damping

Another strategy to model damping at the elemental level is to adapt structural viscous or hysteretic damping models at the local level. First, Puthanpurayil, Lavan, et al. (2016) adapted the Rayleigh and Wilson-Penzien damping at the elemental level, respectively presented in equations (1.46) and (1.47):

$$\mathbb{C}_e = a_{0,e} \cdot \mathbb{M}_e + a_{1,e} \cdot \mathbb{K}_e \tag{1.46}$$

$$\mathbb{C}_e = \mathbf{\Theta}_e \mathbf{\Psi}_e \mathbf{\Theta}_e^T \tag{1.47}$$

where $\mathbb{C}_e$, $\mathbb{M}_e$ and $\mathbb{K}_e$ are the elemental dampings, mass and stiffness matrices associated with the element e. For the Rayleigh damping adaptation, $a_{0,e} = 2.\xi_{RD,e,1}.\dfrac{\omega_{e,i}\omega_{e,j}}{\omega_{e,i} + \omega_{e,j}}$ and $a_{1,e} = 2.\xi_{RD,e,2}.\dfrac{1}{\omega_{e,i} + \omega_{e,j}}$ are elemental damping proportional parameters and could be constant or varying with tangent stiffness elemental matrix. Parameters $\omega_{e,i}$ and $\omega_{e,j}$ are the ith and jth elemental undamped frequencies. $\xi_{RD,e,1}$ and $\xi_{RD,e,2}$ are the viscous damping ratios associated with the elementary Rayleigh damping model for

the mass and stiffness proportional parts. For Wilson-Penzien adaptation, $\boldsymbol{\Psi}_e$ is a diagonal matrix composed of $\psi_{e,i} = \dfrac{2.\xi_{WPD,e,i}.\omega_{e,i}}{\phi_{e,i}^T \cdot \mathbb{M}_e \cdot \phi_{e,i}}$ and $\boldsymbol{\Theta}_e$ is the mass normalised elemental mode shape matrix. $\xi_{WPD,e,i}$ is the ith viscous damping ratio associated with the elementary Wilson-Penzien model. The elemental formulations appeared to be more reliable than global ones, but the elemental frequencies were not representative of structural properties. The computational time was comparable to an updating of Rayleigh damping with the tangent stiffness. Then, Carr et al. (2017) upgraded Puthanpurayil, Lavan, et al. (2016) elemental Wilson-Penzien formulation by considering the nonlinearities with a tangent matrix. Indeed, considering elemental nonlinearities in elemental damping was a way to consider the global system nonlinearities. Structural analyses showed the model conservative effect, which was interesting from an engineering point of view. Later, Puthanpurayil, Carr, and Dhakal (2018) repeated the same idea but to adapt two nonlocal continuum elasticity based damping models for nonlinear dynamic analyses: (i) the Russel spatial hysteresis model and (ii) the extended Sorrentino model. Again, local models appeared to better behave than global ones. The advantages were: (i) eliminating spurious forces and the representativeness of dissipations. However, there is no explicit experimental evidence about the supposed better representation of elemental models (Puthanpurayil, Carr, and Dhakal, 2018).

All damping models at the elemental level aimed to be more representative of physical dissipative phenomena than the viscous damping model at the structural level. Mainly, the RD matrix is strongly used, but no physics is associated with it. That is why Semblat (1997) proposed a rheological interpretation of RD. The rheological model aimed to involve the same attenuation-frequency dependence as RD, based on the link between internal friction and frequency. The chosen model was the generalised Maxwell model (fig. 1.15), given the viscous damping ratio in equation (1.48):

$$\xi \approx \frac{1}{2 \times \left[\dfrac{E.\,(\xi_1 + \xi_2)}{\xi_1^2} \cdot \dfrac{1}{\omega} + \dfrac{\xi_2}{E}.\omega \right]} \tag{1.48}$$

It consisted of three parameters (ξ_1 and ξ_2 were viscous parameters, and E was an elastic parameter). It was analytically demonstrated that if $\xi < 25\%$, the proposed model perfectly coincided with the RD of a SDOF system.

Then, Voldoire (2019) also developed an idea to include damping in the material behaviour model. A nonlinear behaviour was established with viscous dissipations linked to damage states. Indeed, the damage variable described the memory of material stiffness and strength degradations. It allowed modelling "residual" damping, giving a result close to the global RD model but with a spatial and temporal description of energy dissipations. The evaluation of the proposed model was

Figure 1.15: Generalised Maxwell model

done on a one-dimensional rheological study. The dissipation occurred when damage increased and during transitory phases due to $a_0(d)$ and $a_1(d)$ parameters. Experimentally, those parameters appeared to increase. But because the damage was not an observable state variable, parameter evolutions through the elastic stiffness degradation was preferred: $a_0\left(k(d)\right)$ and $a_1\left(k(d)\right)$. For example, in the case of constant damage, the residual damping ratio $\xi_r(d)$ evolution at fundamental frequency f_0 was given by equation (1.49):

$$\xi_r(d) = \xi_{f_0} \cdot \left[1 + 2.5 \left(1 - \frac{k(d)}{k} \right) \right] \tag{1.49}$$

1.2.4   Synthesis - comparison of damping models

There is no consensus about the best formulation to use in seismic analyses in literature. In addition, a large number of models are proposed. That is why numerous papers are interested in comparing different damping formulations on particular examples. Table 1.2 synthesises the damping formulations compared in all papers presented in the preceding paragraphs (alphabetical classification). The nomenclature of the damping formulations is presented in Appendix A. Rayleigh, mass-proportional, stiffness-proportional and modal dampings are the most used formulations in the literature because of their implementation simplicity. Generally, the comparisons allow authors to study each damping formulation behaviour and propose damping model recommendations for studied structures. For example, Hall (2006) demonstrated that the TKPD advantage was its capacity to reduce and contain the damping forces compared to IKPD and MPD. In addition, CSI (2011) presented the characteristics of the Perform3D program for nonlinear structural analyses of building structures and recommended adding a small amount of RD when a MD was used to damp a little the higher modes. Indeed, the number of modes used in MD was always inferior to the number of structural DOFs.

1.2.4.1   Reinforced concrete (RC) structures

(a)   Structural elements   Experimental campaigns were performed on RC elements given data to study performances of numerical models. For example, Correia, Almeida, and Pinho (2013) focused on cantilevered RC columns with masses on their tops. By comparing experimental and numerical responses, they showed the following conclusions: (i) with a KPD, excessive damping appeared for higher modes, and numerical problems occurred with softening models. Especially, using the IKPD gave the worst results. (ii) The difficulty with MPD appeared when a strong inelastic behaviour occurred because of the lack of rational energy dissipation reduction. (iii) With RD, the same problems as MPD developed if the first mode controlled the response. Otherwise, the difficulties of KPD appeared but to a lesser extent. Finally, the recommendation was to use the MPD or even the TKPD or RD with the tangent stiffness. Nevertheless, chosen viscous damping ratios must stay under 3%, and if phenomena dissipate a large amount of energy, they must be explicitly modelled.

Then, H. Q. Luu et al. (2011) and Karaton, Osmanlı, and Gülşan (2021a) and Karaton, Osmanlı, and Gülşan (2021b) were interested in shear walls tested experimentally. H. Luu et al. (2013) studied different modelling assumptions, including damping based on large-scale table tests of slender eight-story RC shear wall specimens. Two models were considered: (i) a multi-fibre model with nonlinear constitutive models for concrete and steel, and (ii) a finite element model with 2D plane stress elements with slightly different hysteretic models. In comparison with experimental data, it appeared that both models gave similar results. RD with the tangent or commit matrices gave close results. However, using the tangent stiffness matrix was more time consuming because updates were made at each iteration and not only at the end of each time step. As for recommendations, RD with a damping ratio of 2% for modes 1 and 2 should be chosen with the multi-fibre model. For the second model, it should be preferable to use RD with 1.5% of damping ratio for modes 1 and 3. More hysteretic energy was dissipated with that model explaining the smaller damping ratio. Mode 1 should always be considered because it dominates the dynamic response, but the second or third mode choice does not affect the conclusions. In Karaton, Osmanlı, and Gülşan (2021a), two experimentally tested RC shear wall structures were studied with displacement-based fibre elements considering different damping formulations and damping ratios. Numerous dynamical responses were observed, and the best damping formulation evolved depending on the responses. However, in global, as H. Luu et al. (2013), RD gave an error inferior to 11% with experimental data. It was shown that the damping ratio choice for one damping formulation depended on the structure. In Karaton, Osmanlı, and Gülşan (2021b), the more significant conclusions are that KPD and RD are the best damping formulations with viscous damping ratios between 2% and 3%.

Table 1.2: Synthesis of technical papers comparing different damping formulations

Damping[*]	Abbasi[1]	Anajafi[2]	Baba-Hamed[4]	Bhattacharjee[6]	Correia[7]	Dao[8]	Hall[9]	Karaton[12]	Kumar[13,14]	Léger[15]	Luco[16]	Luu[17]	Martinez[18]	Pant[19]	Perform3D[21]	Qian[22]	Ryan[23]	Sousa[24]
RD	x	x	x[5]		x	x	x[10]	x	x		x	x	x	x	x	x	x	x
MPD			x		x			x	x					x[20]				x
IKPD	x	x[3]	x	x	x	x		x	x				x	x[20]			x	
TKPD	x		x	x	x					x			x	x[20]				x
TRD			x[5]				x[11]			x	x	x	x	x				x
CRD												x						
RDtd														x				
TRDtd														x				
QBD										x								
IKPDL							x											
MD						x			x		x		x	x	x	x		
CD							x											
WPD							x											
NLVD																x		
EIVD							x						x					
No damping				x									x					

[*] The complete names are expressed in appendix A

[1] Abbasi and Moustafa (2019) [2] Anajafi, Medina, and Santini-Bell (2019) [4] **Baba-Hamed2020** [6] S. S. Bhattacharjee and Ghrib (1995) [7] Correia, Almeida, and Pinho (2013) [8] Dao and Ryan (2013) [9] Hall (2018) [12] Karaton, Osmanlı, and Gülşan (2021a) and Karaton, Osmanlı, and Gülşan (2021b) [15] Léger and S. Bhattacharjee (1994) [16] Luco and Lanzi (2019) [17] H. Luu et al. (2013) [13,14] M. Kumar and Whittaker (2019) and S. Kumar and M. Kumar (2021) [18] Martinez and Kowalsky (2020) [19] Pant, Wijeyewickrema, and ElGawady (2013) [21] CSI (2011) [22] Qian, Chopra, and McKenna (2020b) and Qian, Chopra, and McKenna (2020a) [23] Ryan and Polanco (2008) [24] **Sousa2018**

[3] With β based on the first or second modal period
[5] Classical and reduced Rayleigh damping
[10] Classical and condensed Rayleigh damping
[11] Study of two versions of TRD: an incremental version and a total version
[14] Damping formulation combinations are also studied
[20] With constant or updated coefficients

(b)   Buildings   For the study of complete RC buildings, Sousa et al. (2020) performed their analyses based on the experimentation of three distinct RC structures and the conclusions of an international benchmark. Indeed, the large dispersion of results in the benchmark, even for teams using the same simulation software, showed that the modelling principles are not generalised. So, Sousa et al. (2020) realised sensitivity analyses of modelling options that were critical in the structure response, including equivalent viscous damping (EVD). A structural fibre model was considered. First, it was recommended to use a low damping ratio, between 0.5% to 2%. Then, for a mass distributed system, TKPD was better because of the lack of damping of the higher modes with MPD. Nevertheless, MPD was better to characterise the acceleration amplitudes. So, the choice of the formulation is dependent on the response of interest.

The conclusions of Baba-Hamed and Davenne (2020) were different. A low-rise RC three-story building was studied with seven earthquake ground motions. It was thus observed that neither the mass nor stiffness proportional damping was appropriate for nonlinear time history analyses of RC buildings. Indeed, the ratio of the damping force over the based shear force increase could not be adequately represented with both formulations. So, it was recommended to prefer the reduced TRD formulation F. A. Charney (2005) with $0.707 \times \omega_1$ and $0.707 \times \omega_2$ to reduce the studied ratio.

(c)   Bridges   Buildings were not the only RC structures studied in the literature. Abbasi and Moustafa (2019) mainly focused on the damping model influence on the nonlinear response of RC bridges subjected to an earthquake. In addition, uncertainties were applied on excitation, geometry and material properties. It was observed that, depending on the damping model, the structure fragility curve was more or less influenced by the uncertainties applied to a particular parameter. Then, the sensitivity on damping parameters varied from a bridge element to another. However, what appeared, was that the damping ratio played a significant role compared to the choice of the used stiffness matrix (initial or tangent). If high degradations are reached, more hysteretic damping develop, so less viscous damping is required, and the choice of damping formulation becomes less decisive. It was recommended to prefer the TKPD with 5% of damping ratio and consider ten modes in linear analyses because the higher modes had a non-negligible influence on bridge responses under seismic excitations. No recommendations are proposed for inelastic analyses. For such analyses, Martinez and Kowalsky (2020) show, indeed, the considerable influence of the damping model thanks to sensitivity analyses on modelling parameters for performance-based design of bridges. Only the damping formulation was evolving for the damping parameters, resulting in up to 100% differences in displacement ductility. Here, TKPD and Zero damping led to the largest displacements. In contrast, MD led to the minimum seismic demands.

1.2.4.2   Other types of structures

(a)   Analytical structures   More analytical studies are performed to evaluate the influence of damping models in dynamic structural analyses. For example, Luco and Lanzi (2019) focused on the analytical and numerical analyses of a simple elastic frame to debate the common literature conclusions about damping models. They showed that TRD presented no spurious damping forces but that some numerical artefacts existed, contradicting the Chopra and McKenna (2016) conclusions. In addition, MD eliminated the spurious forces, but it introduced significant oscillations in the velocity response, which was also a numerical artefact due to time discretization.

(b)   Gravity dams   Damping analyses were associated with fracture propagation models for gravity dams to evaluate the dam ability under seismic excitations. For example, Léger and S. Bhattacharjee (1994) studied cracking profiles and energy dissipated in gravity dams. Fracture dissipations appeared negligible compared to damping energy, so a careful choice of damping formulation had to be done. Mainly, the elasto-brittle damping model (only the elements staying elastic are considered for computing

the damping matrix) was the most conservative and was recommended here, in contrast to IKPD that restrained the crack propagations. By studying a continuum fracture propagation model with different damping formulations, S. S. Bhattacharjee and Ghrib (1995) even went so far as to recommend using no viscous damping at all to improve the representability of crack opening.

1.2.4.3   The particularity of base-isolated structures

Before 2008, damping model recommendations in the literature for base-isolated buildings were to combine the superstructure damping with the isolation system one, which were completely independent. Generally, RD with a damping ratio inferior to 5% for the superstructure and a combination of viscous and hysteretic damping for the isolation system were used. Nevertheless, there is still no consensus about the choice of damping models, and numerous papers are dealing with this difficulty. Ryan and Polanco (2008) focused on different buildings of various story numbers and demonstrated that even when the hereafter recommendations on base-isolated buildings were correctly followed, RD appeared not to be relevant because of the undesirable suppression of the first mode response. So, it was recommended to prefer a KPD based on the first mode of the superstructure because it negligibly affected the first mode. A correct amount of energy was also dissipated for higher modes.

Then, Pant, Wijeyewickrema, and ElGawady (2013) studied the behaviour of three-story reduced scale buildings tested on a shake table. Again, it was observed that the choice of damping formulation and damping ratio played a significant role in dynamic responses. In the case of direct nonlinear integration time-history analyses with RD-type formulations, it was recommended to compute coefficients with a modal analysis of the entire base-isolated building with the post elastic stiffness of the isolated system. For nonlinear time-history analyses with MD, choosing the damping ratio was strongly dependent on the formulation. So, a fixed value could not be defined for all cases. For Dao and Ryan (2014), based on experimental data on fixed-base and isolated systems, RD was adequate in the case of fixed-base structures. However, more modes had to be considered for isolated systems, so MD should be preferred to increase the frequency range participating in the structural response.

More recently, Anajafi, Medina, and Santini-Bell (2019) suggested using KPD only based on the superstructure with a coefficient based on the second mode of the isolated building. Conclusions were based on the analyses of base-isolated buildings with linear and nonlinear isolation systems. It was shown that RD induced unrealistic high damping in the first mode and that this "damping leakage" (artificial viscous damping to the isolated first mode) was able to induce a significant underestimation of modal responses. In the same idea, M. Kumar and Whittaker (2019) and S. Kumar and M. Kumar (2021) recommended using damping formulations that did not induce damping leakage. Studies focused on base-isolated nuclear power plants. Three models using two different software (OpenSees and LS-DYNA) were compared. MPD led to damping leakage. TRD and updated parameters did not improve the results compared to a simple RD, while the computational time enormously increased. MD had to be used with caution because it could induce damping leakage. Finally, the conclusion was that damping formulations should be chosen depending on the quantities of interest and model types.

1.3   Damping identification and related damage indices

Damping models presented in section 1.2 are strategies to represent damping effects in structural computations. The proposed model difficulties are their calibration and the choice of required parameters. That is why that section focuses on damping identification methods (1.3.1) applied to experimental data (1.3.2) to propose damping models (1.3.3).

A second objective of identifying dynamic structural properties (i.e. eigenfrequencies, mode shapes, damping) is to perform damage detection. Indeed, these properties evolve with respect to the damage state of the structure. In contrast with many studies regarding eigenfrequency and mode shape identification, the evaluation of damping is still a matter of debate. This section proposes a synthesis of methodologies used in the literature to evaluate damping.

1.3.1　Synthesis of methodologies to evaluate the damping

1.3.1.1　Methodologies

(a)　Method descriptions　M. S. Cao et al. (2017) presented a state-of-the-art of diverse methods to extract damping ratios from experimental data. Evaluating a damping ratio for the structure is a part of global investigation methods. Damping is obtained thanks to quantities associated with the structure global response (e.g. discrete displacement field). Methods are separated into three families: (i) the time domain, (ii) the frequency domain, and (iii) the time-frequency domain.

For the time domain, (i) the Ibrahim time method, (ii) the random decrement method and (iii) the Hilbert transform method were cited, but the most often used is the logarithmic decrement method. The idea of the logarithmic decrement method is to use the peaks of the structure free vibration response. So, in the assumption of viscous damping as the only source of dissipation, the logarithmic decrement δ is defined in equation (1.50):

$$\delta = \ln\left(\frac{x_i}{x_{i+1}}\right) = \frac{2\pi\xi}{\sqrt{1-\xi^2}} \tag{1.50}$$

where x_i and x_{i+1} are two successive peaks of the temporal response. The damping ratio is thus given in equation (1.51):

$$\xi \approx \frac{1}{2\pi}\ln\left(\frac{x_i}{x_{i+1}}\right) \tag{1.51}$$

In order to improve accuracy, more cycles (m_c) can be taken into account, as proposed in equation (1.52):

$$\xi \approx \frac{1}{2\pi.m_c}\ln\left(\frac{x_i}{x_{i+m_c}}\right) \tag{1.52}$$

Using more cycles to improve accuracy must be carefully considered because Daneshjoo and Gharighoran (2006) explained that the chosen number of cycles significantly influenced on the damping ratio evaluation. If too few cycles are considered, the damping ratio evaluated is higher than the reality, which is not safe in structural design. In RC structures, especially when cracks occur, the damping is not only viscous (that is to say, proportional to velocity) but also proportional to displacement. So, the exponential decrease considered is not accurately characterising the natural behaviour.

Another idea was proposed by Demarie and Sabia (2011): it consisted of a nonlinear and non-parametric method to identify nonlinear damping and frequencies of damaged RC elements. The method is based on a time-varying polynomial approximation of the system dynamics. The advantage of such a non-parametric identification is that no assumption is required about the nonlinearity types or localisations. However, the identified quantities could not be correlated to the system equations of motion. The first step is to determine the optimal polynomial time-varying system from decomposition on time windows. It is based on the assumption that equations can approximate the system response for each time window with two polynomials depending on the velocity and the displacement. These polynomials represent the unknown nonlinear viscous force and the elastoplastic internal force. Then, a minimisation is performed to obtain the best polynomial parameters representing the functions to identify. The second step consists of the damping identification performed with the analysis of the dissipated energies associated with the system identified in the first step.

For the frequency domain, (i) the frequency-curve-fitting method, (ii) the peak picking method or (iii) the half-power bandwidth method (HPBM) are efficient ones. The last one is the most used for damping identification because of its easy-to-use. It is an acceptable method for MDOF structures if the modes are decoupled. Let f_r be the resonant frequency of the system and f_{r1} and f_{r2} the frequencies for which the amplitude at resonance is divided by $\sqrt{2}$. The damping ratio is defined in equation (1.53):

$$\xi = \frac{f_{r2} - f_{r1}}{2.f_r} \tag{1.53}$$

The HPBM will be used in the following chapters of the manuscript. That is why paragraph 1.3.1.1(b) proposes a more in-depth analysis of the method. Other frequency-domain methods are proposed in the literature like, for example, Adhikari and Woodhouse (2000), Adhikari and Woodhouse (2001a), and Adhikari and Woodhouse (2001b) works already discussed in section 1.2.2.4. Also, Papagiannopoulos and Beskos (2009) proposed a simple identification model based on classical damped linear building frames and extended to non-classical damped structures. The roof-to-basement transfer function was used in the frequency domain. The model assumption was the equivalence, discretely, between the modulus of the frequency response transfer function on the non-classical damped system and the one of the classically damped system. The damping ratio for a mode n was defined in equation (1.54):

$$\xi_n = \frac{-\Re(\widetilde{\omega}_n)}{|\widetilde{\omega}_n|} \tag{1.54}$$

where $\widetilde{\omega}_n$ is the structure complex eigenfrequency associated to mode n coming from the quadratic eigenproblem of equation (1.55):

$$\left(-\widetilde{\omega}^2.\mathbb{M} + i\widetilde{\omega}.\mathbb{C} + \mathbb{K}\right) \cdot \underline{\phi} = 0 \tag{1.55}$$

The model gives high accurate damping for regular frames with uniform damping distribution.

Finally, for the time-frequency domain, M. S. Cao et al. (2017) discussed the following methods: (i) the Wigner-Ville distribution, (ii) the short-time Fourier transform, (iii) the Choi-Williams distribution, and (iv) the continuous wavelet transforms, which is the most used.

The study developed in M. S. Cao et al. (2017) paper led to a few recommendations and remarks. Remarkably, the damping is much more sensitive, in some damage cases, than the structure frequencies or mode shapes. However, to improve the results, the mechanisms related to damping needs to be better understood, and reliable damping models are required.

(b)   Focus on the half-power bandwidth method

Bias error evaluation Seybert (1981) based his investigation on a paradox: the resonant response of a structure is dependent on damping, and the structure peak response determines damping. That is why he focused on bias error for the HPBM compared to the peak response method. The damping ratio was estimated from the density ratio of the output response spectra over the input one. A second-order model with the transfer function $\mathcal{H}(r)$ in equation (1.56) was characterised with a white noise input:

$$\mathcal{H}(r) = \frac{1}{1 - r_f^2 + 2.i.\xi.r_f} \tag{1.56}$$

where $r_f = {}^f\!/_{f_n}$ is the frequency ratio. Numerical analyses were performed to validate the normalised bias error formulation, and a random error was also presented. In conclusion, it was observed that the bias obtained in the response spectra determination led to errors in the damping estimation with the HPBM. Indeed, the bias error with that method was three times higher than with the peak response method. However, better results could be obtained if the 80% of peak response was used because zero

bias was developed at that response value. Finally, the random error could decrease if the coherence was large, but conflicts could appear between random and bias errors.

Method accuracy and recommendations Olmos and Roesset (2009) assessed the accuracy of this method to estimate the damping in various modes. Three damping formulations were compared: (i) equal damping in all modes, (ii) MPD, and (iii) KPD. In addition, two structures were studied: (i) a simply supported flexural beam under free vibrations and (ii) a column undergoing axial vibrations. The damping type mostly influenced damping estimation with the HPBM. MPD gave better damping estimations for a large number of modes. In contrast, KPD led to wildly inaccurate results for the higher modes.

Then, the HPBM uses the structural frequency response from forced vibrations, ambient vibrations or earthquake excitations. J.-T. Wang, Jin, and Zhang (2012) focused on the method accuracy to estimate the damping ratio of MDOF systems. A two-DOFs linear system was studied from its displacement response. A parametric analysis was performed by varying many parameters influencing the response curve. The first conclusion was that the HPBM could significantly overestimate system damping ratios, which was unsafe. Then, parameters influencing the damping estimation error were (i) the ratio ω_2/ω_1, (ii) the amplitude ratio of the two modes, and (iii) the damping ratios themselves (if they were higher, the error in the estimation would be higher).

Finally, both papers demonstrate that the HPBM should be carefully used depending on the damping model used in the numerical analyses.

Improvements Again, HPBM validity is studied here but with some improvements. First, Papagiannopoulos and Hatzigeorgiou (2011) assessed the HPBM accuracy to estimate damping ratios in SDOF and MDOF structures with linear viscous damping, even if non-classical modes were considered. Numerical analyses were performed with different damping formulations in equations (1.57), (1.58) and (1.59):

$$\frac{f_{n2} - f_{n1}}{f_n} \approx 2\xi \tag{1.57}$$

where f_n is the natural structure frequency,

$$\frac{f_{r2} - f_{r1}}{f_r} \approx 2\xi \tag{1.58}$$

where f_r is the structure resonant frequency (if $\xi \ll 1$, $f_r \approx f_n$),

$$\frac{f_{ra2} - f_{ra1}}{f_{ra}} \approx 2\xi + 8\xi^3 \tag{1.59}$$

where f_{ra} is the acceleration resonant frequency, $(f_{n1}, f_{n2}, f_{r1}, f_{r2}, f_{ra1}, f_{ra2})$ frequencies for which the amplitudes were divided by $\sqrt{2}$ compared with the associated peak amplitude. The HPBM classical form led to significant errors, so it had to be abandoned. On the contrary, the third-order correction provided conservative and more reliable results for SDOF and MDOF structures. Finally, it was recommended to apply the HPBM on the acceleration frequency response transfer function and consider damping ratios estimated for higher modes with caution.

In the same idea, I. Wang (2011) compared (i) the use of displacement response and acceleration one, and (ii) the third-order approximation with the first-order one and the exact solution. Because the HPBM is often applied on the displacement response and with a simplification to the first order considering a small damping ratio. Acceleration FRF derivation was equal to equation (1.59). A similar equation was used with the displacement resonant frequency and a coefficient equal to 4 in front of the third damping ratio order. It was shown that the first order gave accurate results if $\xi < 10\%$. However, the

third-order approximation should be considered for higher damping ratios to decrease the truncation error. Furthermore, again higher approximations should be used to improve results.

Finally, as I. Wang (2011) paper explained, the third-order was still not sufficient to accurately decrease errors for high damping ratios. So, Wu (2015) proposed new approximate formulas with displacement and acceleration frequency response functions. The new formulas were brief and led to excellent accuracy for low and high damping ratios. The maximal error obtained was 1.6% with proposed models, against 45% for the third-order approximation.

1.3.1.2 Evaluated damping reliability

A question could be asked on all identification methods: what is the reliability of the damping value obtained? To answer this question, an evaluation example strategy was proposed by Cruz and Miranda (2019). They proposed different metrics to evaluate the reliability of damping values obtained using the modal minimisation parametric system identification technique, a time-domain method. Their study assumed that modal damping with linear viscous damping was the most often applied in dynamic structural applications. However, with the same data, different people find different damping values. It is problematic if damping choices are required for numerical analyses based on experimental data.

The three metrics were (i) the dynamic amplification factors, (ii) the Arias modal contribution and (iii) the enhanced reliability intervals. The role of the dynamic amplification factor was to determine, for one mode, if the excitation provided by the earthquake was significant enough to give reliable damping associated with this mode. If one were not enough amplified by the excitation, its response would be too small to be relevant. Thus, the damping ratio associated would have to be excluded from the reliable ones. Then, the Arias modal contribution gave information on the relative contribution of each mode. Finally, enhanced reliability intervals informed the objective function sensitivity (function to minimise in the identification technique) to the damping ratio variations. Those metrics performances were studied on a 32-story building. Using them allowed them to identify the determined damping ratios which were reliable or not.

1.3.2 Experimental identification

This section illustrates the use of damping identification methods on RC elements (1.3.2.1) or entire structures (1.3.2.2). Furthermore, the link between damping values and structural damage is illustrated.

1.3.2.1 Experiments on structural elements

Equivalent viscous damping (EVD) models are associated with SDOF systems or modal values associated with MDOF. Damping ratios identified in this section are deduced from experimental campaigns on RC structural elements. Different identification methods give damping ratio values for various element types. The results are synthesised in table 1.3 for viscous damping and table 1.4 for hysteretic damping.

(a) Identification methods Franchetti, Modena, and M. Feng (2009) performed experimental and theoretical studies to propose a damping detection method with a quadratic damping model (eq. 1.60).

$$F_d = -c_q.\dot{u}|\dot{u}| \tag{1.60}$$

where F_d is the damping force and c_q a coefficient. The experimental campaign applied impulsive loading on three precast prestressed RC beams with different prestressed levels and used free vibrations to determine the coefficient c_q. The choice of a quadratic damping model appeared to represent the dissipated energies well and to be more sensitive to the damage level than viscous damping. The proposed

Table 1.3: Experimental viscous damping determination on structural elements

Author	Method	Experiment	Damping value
Carneiro et al. (2006)	Logarithmic decrement	Pseudo-dynamic tests on RC beams (free and forced harmonic vibrations)	$2.5\% \rightarrow 5.5\%$
Casas and Aparicio (1994)	Logarithmic decrement	Hammer-tests on RC beams (free vibrations)	$0.8\% \rightarrow 3.7\%$
Chowdhury, Loo, and Fragomeni (2000)	Logarithmic decrement	26 reinforced or partially prestressed beams under free-vibration tests	$0.04 < \delta < 0.16^{*}$
Daneshjoo and Gharighoran (2006)	Logarithmic decrement	Free-vibration response of cracked and uncracked beams	$0.08 < \delta < 0.18^{*}$
Daneshjoo and Gharighoran (2008)	Logarithmic decrement	Steady-state vibrations on RC beams and static loading at mid-span	$1.0\% \rightarrow 3.0\%$
Franchetti, Modena, and M. Feng (2009)	Multi-input multi-output curve fitting + Hilbert transform technique	3 precast prestressed RC beams under free vibrations	$0.1\% \rightarrow 1.6\%$
Heitz, Richard, et al. (2017)	Identification of an updated SDOF model for each mode	Quasi-static and dynamic tests (shake table) on RC beams	$0.0\% \rightarrow 5.0\%$
Sakamoto et al. (2006)	Logarithmic decrement	Pillar-shaped unreinforced low-strength concrete specimens tested on a shake table	$2.0\% \rightarrow 5.5\%$
L. Su et al. (2019)	Identification of an exponential damping	Three groups (depending on reinforcement) of RC cantilever beams under dynamic loadings	$0.5\% \rightarrow 8.0\%$

[*] The logarithmic decrement is related to the damping ratio by $\delta = \dfrac{2\pi\xi}{\sqrt{1-\xi^2}}$. So, Chowdhury, Loo, and Fragomeni (2000) identification is equivalent to a damping ratio between 0.02% and 0.4%. For Daneshjoo and Gharighoran (2006) identification, the equivalence gives a damping ratio between 0.01% and 0.52%.

method could be used for quality control of precast beams by performing free vibration tests. However, it is still required to apply the method to existing structures by considering ambient vibrations because it is impossible to produce free vibrations on such structures.

Table 1.4: Experimental hysteretic damping determination on structural elements

Author	Method	Example	Damping value
Carneiro et al. (2006)	Ratio of energies	Pseudo-dynamic tests on RC beams (free and forced harmonic vibrations)	$2.5\% \rightarrow 5.5\%$
Crambuer, Richard, et al. (2012)	Ratio of energies (half-cycle)	Quasi-static three-point bending tests on RC uncracked or pre-cracked beams	$1.0\% \rightarrow 3.0\%$ for $F < 40kN$ and $> 7\%$ otherwise
Elmenshawi and Brown (2010)	Ratio of energies	RC beams with high concrete strength	$2.0\% \rightarrow 20\%$
Heitz, Giry, et al. (2017)	Jacobsen's area	Quasi-static and dynamic tests (shake table) on RC beams	$0.0\% \rightarrow 5.0\%$
Vintzileou, T. Tassios, and Chronopoulos (2007)	Ratio of energies	37 full-scale confined columns submitted to cyclic shear and bending under constant axial load	$\sim 20\%$

Another idea was developed by L. Su et al. (2019), based on Biot works about convolution damping models. They studied a particular case of such models: the exponential one, characterised by the kernel matrix function $\mathbb{G}(t)$ in equation (1.61):

$$\mathbb{G}(t) = \sum_{i=1}^{n_m} \mathbb{C}_i \cdot \tau_i \exp\left(-\tau_i t\right) \tag{1.61}$$

where $\mathbb{C}_i$ is the damping coefficient matrix and τ_i a relaxation factor, associated with dissipative mechanism i, and n_m the number of different damping mechanisms. Dynamic tests on RC cantilever beams with various reinforcement ratios were realised to obtain frequency response functions. The beams were grouped according to steel bar diameters and reinforcement ratios. Obtained damping ratios with hammer tests were close to theoretical values, whatever reinforcement ratios. So, an important conclusion was that the reinforcement ratio had no impact on the damping properties of undamaged structures. Then, numerical analyses were performed with the proposed exponential damping model and RD. Despite some errors compared to experimental data, the proposed damping model appeared to better represent the energy dissipation capacity of RC structures than RD, especially for high order modes. So this model better characterises the damping property of RC structures.

Earthquake engineering requires to characterise properly dynamic structural properties. In particular, the damping, which characterises the dissipated energy during earthquakes. Carneiro et al. (2006) carried out an experimental campaign on RC beams under mechanical vibrations, using a pseudo-dynamic method. One of these test advantages was the lower cost compared with dynamic tests. Also, all intermediate structure states could be controlled. The dynamic model considered was a SDOF system. Two different excitations were applied: free and forced harmonic vibrations (more damageable if the harmonic frequency was close to the beam resonance). Thus, the damping effect on steady-state was evaluated. Measured results led to the drawing of hysteresis loops, which were considered the consequence of

dynamic hysteresis.   Even if pseudo-dynamic
tests do not give a dynamic response, translat-
ing cyclic dissipation into viscous damping is a
classical approach. So, the damping ratio is evalu-
ated by equation (1.62) first proposed by Jacobsen
(1960):

$$\xi_{eq} = \frac{1}{4\pi}\frac{E_{diss}}{E_s} = \frac{1}{4\pi}\frac{E_{diss}}{^1/2.k_0.u_{cm}^2} \qquad (1.62)$$

as presented in figure 1.16, where E_{diss} is the dis-
sipated energy, E_s the strain energy, k_0 the initial
stiffness and F_m and u_{cm} respectively the maxi-
mal force and displacement of the studied cycle.
As a conclusion, Carneiro et al. (2006) observed
that the damping ratio decreased when the con-
crete strength increased and when the reinforce-
ment ratio increased.

(b)   Link between damping and damage
To further study dynamic structural properties,
some papers focus on the link between damage

Figure 1.16: Determination of the equivalent
viscous damping for a half-cycle (Jacobsen, 1960)

and damping because damage influences those dynamic properties. The first parameter, linked to damp-
ing, studied was the dissipated energy. The energy dissipation capacity is an essential property in the
seismic performances of structures. The dissipation of input energy is required to avoid structural fail-
ure under earthquakes. Spencer (1969) focused on prestressed structures: nine prestressed concrete
members were tested under cyclic loadings by applying end rotations to the beams. The two parame-
ters evaluated from the experimental data were the stiffness and the energy dissipated during one cycle
of steady-state loading. In conclusion, both studied properties depended on the loading but not on the
frequency or number of cycles applied. For the damping energy, values between 0 and 1.25 kip.in were
obtained, corresponding approximately to 0 to 140 J. In addition, the damping was low for uncracked
members. So, the first earthquake that would occur to a prestressed structure would significantly impact
its properties.
Nmai and Darwin (1984) studied the performances of RC beams using an energy dissipation index.
Structural parameters considered were (i) the reinforcement ratio, (ii) the nominal stirrup capacity, (iii)
the stirrup spacing and (iv) the bottom over top reinforcement ratio. The analyses of experimental
results and a comparison with four other studies led to the following conclusions. The dissipated energy
could be increased by (i) reducing the stirrup spacing, (ii) increasing the bottom over top reinforcement
ratio, or (iii) decreasing the displacement-ductility. Similarly, Dhakal and Maekawa (2001) explained
that the seismic response of RC columns varied a lot with the reinforcement scheme and the axial load.
That is why it was not easy to define and predict the post-peak response of such columns.
    Then, experiments were performed on RC elements to discuss structure safety. For example, Casas
and Aparicio (1994) paper focused on methods allowing the inspection and monitoring of RC struc-
tures as bridges by using damping properties. The proposed methodology was based on acceleration
measurements because they were easier to record than displacements. Experiments on beams were per-
formed with different cracking patterns. Impact hammers were applied on beams, and free vibrations
were recorded. The method is well-performed in identifying beam damage state in terms of extension,
number of cracks, and damage localisation. Damping varied from 0.8% to 3.7%. However, most im-
portantly, it was shown that damping was not dependent on initial stiffness, and no direct relation was
found between damping ratio and damage.
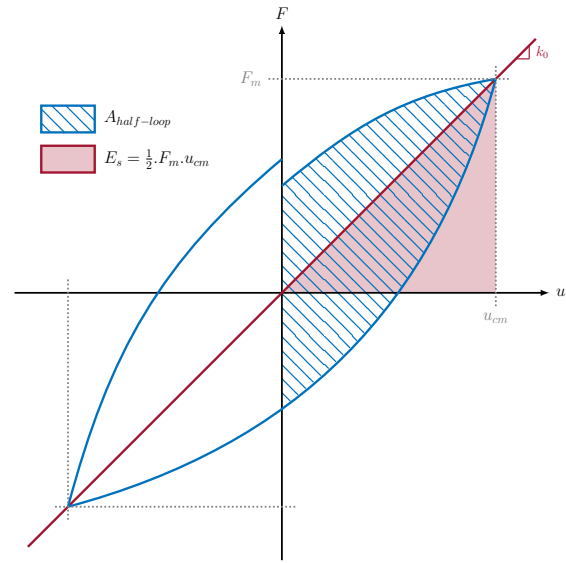
Following the same objective, Sakamoto et al. (2006) focused on evaluating dam safety after strong earthquakes. Tests on a shake table were performed on pillar-shaped unreinforced low-strength concrete specimens. Effects of cracks on the dynamic behaviour of concrete structure elements were determined. In conclusion, the first resonant frequency and damping ratio were well influenced by the tensile cracks. The damping ratio varied from 2% for a tensile fracture under 10% to 5.5% for 90% of tensile fracture. On the contrary to Casas and Aparicio (1994) analysis, Sakamoto et al. (2006) work observed that the damping ratio could be used as a damage index.

More recently, other papers focused on the correction between damage and damping. Daneshjoo and Gharighoran (2008) worked on beams experimentally submitted to dynamic cyclic loadings with a vibrating motor and eccentric masses. A concentrated load was added at mid-span, increasing the severity of cracks. The damping ratio was determined using the logarithmic decrement method applied to free vibration responses. In terms of damping, it was observed that the damping was viscous and frictional in the cracked zone and that the frictional part increased with damage. The linear decrease of the dynamic response, corresponding to frictional damping, implied that damping due to micro-cracks was more important than the viscous one. Finally, the damping ratio appeared to increase with the degree of cracks and the dynamic load, which was also demonstrated by Franchetti, Modena, and M. Feng (2009). Damping ratio and damage state were so well correlated.

In the same idea, Crambuer, Richard, et al. (2012) work consisted in studying three-point bending tests on eight beams with different longitudinal reinforcement ratios. To consider loading history, some beams were tested without any damaged loading ("uncracked" characteristics), and the other ones were pre-loaded to study the characteristics of "precracked" beams. Particular attention was given to crack evolution and prior damage effects on damping ratio evolution. The image correlation technique was used to observe beam deformations. Then, for each loading cycle, an equivalent damping ratio and damage indices were computed to propose a correlation between the energy dissipation and the nonlinear material behaviour. The selected method to define the damping ratio was presented in figure 1.16. For a load under $40\,kN$ corresponding to 60% of the beam capacity, damping ratio values were mostly located between 1% and 3%. They also highlighted the influence of loading history and damage state on damping.

The same conclusion was obtained by Vintzileou, T. Tassios, and Chronopoulos (2007), whose aim was to validate Eurocode 8 (NF EN 1998-1, 2005) recommendations for confining reinforcement of columns. Thirty-seven full-scale columns subjected to large cyclic displacements under constant axial loads were studied and showed the link between hysteretic damping and the force response degradation. For a force response degradation under 20%, damping ratios deduced stayed around 20%.

(c)   Remarks on other concrete materials   Analyses are performed on plain concrete to understand the damping behaviour of RC material. Jones and Welch (1967) focused on the evolution of the damping ratio concerning the plain concrete formulation. The damping ratio appeared to be higher in sand-cement mortars than in concrete and lean concrete than concrete with more significant cement content. It was also observed that the damping ratio depended on the quantity of liquid water in the concrete and on the boundaries between paste and aggregate. The paper aim was also to evaluate the dynamic Young's modulus of the elements, but no unique relationship between that value and the damping ratio was found. Non-structural materials have also been studied like the polymer concrete in Orak (2000) paper. With free vibration experiments, it was shown that the same damping ratios were obtained for different filler ratios.

1.3.2.2   Experiments on entire structure models

Studying damping in structural elements is a way to understand phenomena and propose recommendations. However, focusing on the entire structure damping behaviour is also a way to evaluate the

accuracy of design models and improve those models. Table 1.5 synthesises analyses presented in this section about the evaluation of damping ratios on global RC structures.

Table 1.5: Experimental damping determination on structure models

Author	Method	Example	Damping value
Z. Cao et al. (2020)	Logarithmic decrement	Concrete gravity dam with 15 earthquake records (free vibrations)	$2.0\% \rightarrow 6.0\%$
Celebi et al. (2020)	Subspace state-space system identification	73-story Wilshire Grand in downtown Los Angeles under Mw7.1 July 5, 2019, earthquake	$0.49\% \rightarrow 3.55\%$ (3 modes and 3 directions)
M. Q. Feng (2007)	Random decrement signature technique	Bridge model under white-noise signal (shake table)	$0.5\% \rightarrow 6.5\%$
Frizzarin et al. (2008)	Random decrement signature technique	Large-scale concrete bridge model under seismic excitations (shake table)	$1.0\% \rightarrow 8.0\%$
Miranda and Cruz (2020)	Veletsos and Meek (MDOF system)	150 instrumented buildings in California	$1.0\% \rightarrow 20\%$
Petrini et al. (2008)	Ratio of energies	Cyclic and dynamic tests on scaled bridge piers	$3.0\% \rightarrow 30\%$
Salane and Baldwin (1990)	Modal damping ratio based on mode shapes	Single-span laboratory bridge model and full-scale three-span highway bridge	$0.8\% \rightarrow 3.0\%$
Tinawi et al. (2000)	Logarithmic decrement	4 3.4m-high plain concrete gravity dam models (shake table)	1% (uncracked) $\rightarrow 23\%$ (cracked)

(a)   Damping identification methods   M. Q. Feng (2007) studied a time-domain method using non-linear damping as a structural damage index. The significant advantage of the proposed method was that it did not require knowledge about the undamaged structure. The idea was to decouple damping between a viscous part and a friction one. In particular, free vibration tests were well suited to evaluate the friction damping because the linear decay obtained was linked with structural damage. However, free vibrations were not easy to apply on in-situ structures. So, the proposed methodology was instead based on the random decrement technique because it gave a free vibration signal from ambient vibrations.

Then, Z. Cao et al. (2020) proposed a method to assess damping ratios with earthquake records. The idea was to consider data at the structure top and decompose them between a free vibration part and

a forced vibration one. Then the damping ratio was computed with the logarithmic decrement method on identified free vibrations.

Finally, damping ratios could be identified from instrumented buildings what was studied by Celebi et al. (2020) and Miranda and Cruz (2020). Celebi et al. (2020) proposed to use an input-output system identification method to identify the modal properties of the 73-story Wilshire Grand in downtown Los Angeles during the July 5, 2019, earthquake. The building was not damaged, and damping ratios for three modes and three directions were computed. The analysis difficulty was that the damping ratios obtained with the proposed methods differed from those obtained from ambient vibrations. So, it was not easy to evaluate the performances from one or another method. Then, Miranda and Cruz (2020) studied the dependence of damping ratio on fundamental periods because, in design codes, that effect was not considered. Damping ratios of 150 instrumented buildings were evaluated with the Veletsos and Meek method.

(b)   Identified damping   M. Q. Feng (2007) experimentally tested a bridge model on a shake table. Computed damping ratios ranged between 0.5% and 6.5%. It was observed that, when damage grew, friction damping also increased to the detriment of viscous one. Petrini et al. (2008) also studied scaled bridge piers under (i) a cyclic test allowing the hysteretic damping model calibration and (ii) a dynamic test to compare with the numerical analyses. The aim of Petrini et al. (2008) was to determine the most appropriate damping model for inelastic time history analyses (ITHA). Larger damping ratios were obtained (between 3% and 30%). Then, Z. Cao et al. (2020) studied a concrete gravity dam with fifteen earthquake records. Similar damping ratios than M. Q. Feng (2007) were obtained (between 2% and 6%). The reservoir water influence was also evaluated. When the water level increased from $60\,\mathrm{m}$ to $100\,\mathrm{m}$, the damping ratio increased 1% more. In Miranda and Cruz (2020), damping ratios varying between 1% and 20% were again obtained. An interesting conclusion deduced was that the soil-structure interaction induced the dependency of damping ratios on fundamental periods and, so, on building height. An empirical relationship in equation (1.63) was thus obtained between the effective damping ratio and the building height H:

$$\xi = 0.21 \times H^{-0.47} \tag{1.63}$$

Table 1.5 shows that for the undamaged structure under dynamic vibrations, damping ratios approximately between 0.5% and 8% are globally obtained. So the value of 5% generally used in dynamic analyses seems to be a mean of identified damping ratios. However, when nonlinearities occur, the damping ratio can increase. Also, for higher modes, larger damping ratios can be reached. Moreover, cyclic tests seem to overestimate damping ratios.

(c)   Link between damage and dissipations in structures   As studied for structural elements, the link between damage and dissipations is of interest in studying structures. However, damage identification often requires the knowledge of undamaged structure properties, what is a constraining condition for existing structures (Franchetti, Modena, and M. Feng, 2009) and strategies to overcome this are required.

Turner and Pretlove (1988), Salane and Baldwin (1990) and Frizzarin et al. (2008) studied bridges. First, Turner and Pretlove (1988) performed an experimental campaign to evaluate the capacity of the random traffic loading to sufficiently excite natural structural frequencies. It was shown that the natural frequencies were, in this case, better than mode shapes to estimate bridge degradations. The experimental study was performed on a beam model with moving loads representing the random traffic. The effect of damping was mainly investigated. Natural frequencies were more identifiable when damping decreased, and higher-order natural frequencies could be determined.

Then, Salane and Baldwin (1990) also carried out an experimental study on two structures: (i) a single-span laboratory bridge model and (ii) a full-scale three-span highway bridge. They were submitted to (i)

transient excitations, (ii) steady-state vibrations, and (iii) acoustic emission. Remarkably, they focused on steady-state vibrations to evaluate modal stiffness and damping. A correlation was found between the evolution of modal stiffness, mode shapes and damping with the deterioration of the structure. However, contrary to Turner and Pretlove (1988), the mode shapes were, here, the best deterioration indicators. Because when changes in modal damping or resonant frequencies occurred, it indicated that structure characteristics were submitted to modifications. However, it was impossible to differentiate which part of the structure evolved with these last two modal properties.

Finally, sensor-based structural health monitoring can be performed to detect the damage state of in-situ structures quickly. Frizzarin et al. (2008) proposed a time-domain damage detection method with nonlinear damping. Damping was used as a damage index and was determined with dynamic vibration responses. The method did not require knowledge of undamaged structural properties. Seismic damage was applied on a large-scale concrete bridge model with a shake table. Then, the random decrement signature technique on ambient vibrations evaluated damping. In conclusion, a strong correlation was found between the damage state of the beam, equivalent to the structural stiffness evolution, and the nonlinear damping. So, damping appeared to be a suitable damage index.

Then, dams are also structures of interest. Because few dams around the world were already submitted to strong earthquakes, little data exists about dams resistance under strong seismic excitations. Therefore, Tinawi et al. (2000) aim was to evaluate dam dynamic characteristics from the perspective of dam safety improvement. Four 3.4m-high plain concrete gravity dam models were tested on a shake table. The free vibration decay technique led to viscous damping values ranging from 1% for uncracked structures to 23% for cracked ones. The high values obtained for cracked dams were not an intrinsic property of the material but were mainly a result of crack evolution. That is why a parametric study should be performed to evaluate the viscous damping influence on crack propagation.

Finally, these papers show that the damping can be linked with the damage state. However, they disagree on the best modal properties to identify damage depending on the loading or the type of structure.

1.3.3 Identified damping models

Finally, in addition to identifying damping ratios, several works further identify damping models as functions of different structural parameters. Identifications are based either on experimental data (1.3.3.1) or on numerical strategies (1.3.3.2).

1.3.3.1 Identification based on experimental data

Because damping mechanisms are challenging to define and are not well understood, no generalised mathematical formulae of damping can be developed (Daneshjoo and Gharighoran, 2006). So, experimental analyses lead to identifying damping models. The identified damping ratio results of studied papers are synthesised in tables 1.3 and 1.4.

(a) Damping as a function of ductility An introduction of equivalent viscous damping (EVD) was discussed in section 1.2.1. It is a concept first proposed by Jacobsen (1960) that can be synthesised in equation (1.64) and related to figure 1.16:

$$\xi_{eq} = \xi_{el} + \frac{E_{diss}}{4\pi.E_s} = \xi_{el} + \frac{1}{\pi}\frac{A_{half-loop}}{F_m.u_{cm}} \qquad (1.64)$$

where ξ_{eq} is the equivalent viscous damping ratio (EVDR), ξ_{el} the elastic damping ratio and $A_{half-loop}$ the dissipated energy for one half-cycle. Numerous empirical models have been proposed in the literature. Table 1.6 summarises those models performed in Rodrigues et al. (2012) paper. Rodrigues et

al. (2012) studied uniaxial and biaxial loading on columns and evaluated damping ratios with equation (1.64). Then, a comparison was performed with the different models in table 1.6 depending on the ductility μ, defined in equation (1.65):

$$\mu = \frac{\kappa}{\kappa_y} \tag{1.65}$$

where κ_y is the displacement in tension rebar first yield, and sometimes on the post-yield stiffness coefficient r_k. Results should be carefully compared because each model appeared to be calibrated for one particular type of structural element. Rosenblueth and Herrera (1964) focused on purely hysteretic damping to characterise slightly nonlinear materials and structures. Then, Gulkan and Sozen (1974) explained that the inelastic response could be interpreted as the elastic response of a fictitious linear structure with the stiffness and the dissipated energy modelled by functions of the maximal displacement. Iwan and Gates (1979) studied six hysteretic systems under twelve earthquakes to deduce an effective linear period and an effective damping ratio. Later, Kowalsky, Priestley, and MacRae (1995) proposed a procedure for displacement-based seismic design for SDOF systems based on the analyses of cantilever bridge columns. Stojadinovic and Thewalt (1996) proposed two hysteretic models to represent the experimental behaviour of RC structures. They used the least-square method to obtain the EVD model presented. They assumed that the EVDR stayed around 5% during pre-yield load cycles, and it grew to 25% for the displacement equivalent to the ultimate structure capacity. Priestley and Grant (2005) compared different damping formulations and deduced a relationship between the elastic viscous damping value to use in time-history analyses and the constant value applied in direct displacement-based design. Then, Priestley, Calvi, and Kowalsky (2007) focused on different research projects to propose a viscous damping formulation as presented in equation (1.66):

$$\xi_{eq} = 0.05 + D\left[\frac{\mu - 1}{\mu . \pi}\right] \tag{1.66}$$

where $D \in [0.1, 0.7]$ depending on hysteresis rules and that Rodrigues et al. (2012) considered equal to 0.565 in their paper. The same form of the model was proposed by Dwairi, Kowalsky, and Nau (2007) without elastic viscous damping. They demonstrated that the proposed model led to lower displacement prediction error based on multi-span bridges. Finally, H. Q. Luu et al. (2011) and H. Luu et al. (2013) works had been discussed in paragraph 1.3.2.1(a).

Similar studies were performed to evaluate the characteristics of particular concrete, like high strength concrete in Elmenshawi and Brown (2010). An experimental campaign was carried out on beams with concrete strengths of 30, 70 and 150 MPa. The influence on damping characteristics of (i) the bottom over top reinforcement ratio, (ii) the transverse reinforcement ratio, and (iii) the shear span to depth ratio was also studied. Manufactured specimens represented an exterior beam-column connection in a ductile moment-resisting frame. Cyclic displacements leading to significant elastic damage were applied to the specimens. Dissipated energy and equivalent viscous damping ratios (eq. 1.62) were connected with displacement ductility. Three cycles of the same amplitude were always performed to stabilise the damage state, but the damping ratio through the first cycle appeared higher than the other ones because more cracks opened during the first cycle. From experimental data, formulae were proposed to define the link between dissipated energy (eq. 1.67) and the equivalent viscous damping ratio (eq. 1.68 for longitudinal reinforcement symmetric beams and eq. 1.69 for asymmetric beams) with the ductility:

$$\frac{E_{diss,f}}{E_{diss,y}} = \mu\left(3.43 . \mu - 4.1\right) \tag{1.67}$$

where $E_{diss,y}$ and $E_{diss,f}$ are the energies dissipated respectively at first yield and nominal failure.

$$\xi_{eq} = 7.23 + 6.1 \ln\left(\mu\right) \tag{1.68}$$

Table 1.6: Equivalent viscous damping models (Rodrigues et al., 2012)

Model developed by	Equation	Application field
Rosenblueth and Herrera (1964)	$\xi_{eq} = \xi_{el} + \dfrac{2}{\pi}\left[\dfrac{(1-r_k)(\mu-1)}{\mu - r_k\cdot\mu + r_k\cdot\mu^2}\right]$	Bilinear elastoplastic system
Gulkan and Sozen (1974)	$\xi_{eq} = \xi_{el} + 0.2\left[1 - \dfrac{1}{\sqrt{\mu}}\right]$	Takeda model
Iwan and Gates (1979)	$\begin{cases} T_{eq} = T_{el}\left[1 + 0.12(\mu-1)^{0.939}\right] \\ \xi_{eq} = \xi_{el} + 5.87(\mu-1)^{0.371} \end{cases}$	Numerical study of 6 hysteretic systems under 12 different earthquakes
Kowalsky, Priestley, and MacRae (1995)	$\xi_{eq} = \xi_{el} + \dfrac{1}{\pi}\left[1 - \dfrac{1-r_k}{\sqrt{\mu}} - r_k\cdot\sqrt{\mu}\right]$	Takeda model
Stojadinovic and Thewalt (1996)	$\xi_{eq} = \begin{cases} 4.7 & \text{if } \mu < 1.0 \\ -0.4\mu^2 + 7.1\mu - 2 & \text{else} \end{cases}$	Cyclic quasi-static tests on columns
Priestley and Grant (2005)	$\xi_{eq} = 5 + \dfrac{5}{\pi}\left[1 - \dfrac{1}{\sqrt{\mu}}\right]$	Concrete walls and columns
Priestley, Calvi, and Kowalsky (2007)	$\xi_{eq} = 0.05 + 0.565\left[\dfrac{\mu-1}{\mu\pi}\right]$	Comparison of many research projects
Dwairi, Kowalsky, and Nau (2007)	$\xi_{eq} = C\left[\dfrac{\mu-1}{\mu\pi}\right]$	Study of a large number of real earthquake accelerograms on hysteretic multi-span bridges
H. Q. Luu et al. (2011) and H. Luu et al. (2013)	$\xi_{eq} = \sqrt{100 - 6.5(\mu-5)^2} \quad \text{if } \mu < 5.0$	Tests on a shake table for RC elements

$$\xi_{eq} = 1.38 + \mu \left(3.33 - 0.43 \, . \, \mu \right) \tag{1.69}$$

It was thus demonstrated that (i) if the concrete strength increased, the hysteretic energy capacity of the beam could be improved. However, that conclusion had to be carefully considered because of all other parameters that had a non-negligible influence. (ii) The hysteretic energy capacity was improved by reducing shear demand and increasing the bottom over top reinforcement ratio. (iii) The bottom reinforcements managed the crack opening, strongly impacting them. (iv) The dissipated energy decreased when the damage level increased. (v) The EVDR appeared to be constant before reinforcement yielding, and the identified values were 7.23% for symmetric beams and 4.27% for asymmetric beams. Finally, (vi) damping ratio values obtained ranged from 2% to 20%, a broad variation compared to other papers.

(b)   Damping as a function of residual deflection   Based on the lack of methods and codes given an evaluation of the damping capacity for concrete members at the design stage, Salzmann (2003) used an experimental campaign to propose a damping capacity formula for reinforced and prestressed concrete beams. Previously, Penzien (1964) had already demonstrated that the damping ratio was dependent on (i) the loading history, (ii) the displacement demand and (iii) the cracking state. It was correlated with the prestressed properties. Salzmann (2003) focused on forty-one full- and half-scale beams divided into two groups to study the loading history influence on structural damping properties. Static load tests were performed along with hammer tests to evaluate damping properties. The logarithmic decrement was chosen to evaluate damping ratios. However, the classical method presented bias due to its assumptions: the viscous damping and the exponentially decreased amplitude response. So, an enhanced logarithmic decrement method was proposed to ensure consistency and accuracy: the "decay curve method". Using the experimental data, the logarithmic decrement proposed for "untested" reinforced beams $\delta_{\text{undamaged,RC}}$ is presented in equation (1.70):

$$\delta_{\text{undamaged,RC}} = 0.223 \times \left(\frac{\rho_t}{s_t} + \frac{\rho_c}{s_c} \right)^{0.19} \tag{1.70}$$

$$\delta_{\text{undamaged,pres}} = 1.4 \times 10^{-10} \times P.e_P^2 - 9.4 \times 10^{-6} \times P.e_P + 0.2 \tag{1.71}$$

where P is the amount of prestressed force and e_P its eccentricity. Finally, the total logarithmic decrement δ is given by equation (1.72):

$$\delta = \beta_{fl}.\Delta_r + \delta_{undamaged} \tag{1.72}$$

where Δ_r is the residual deflection and $\beta_{fl} = 0.0007 \times e^{0.018 . f_{cm}}$. Equations for the residual deflection were also proposed. All those formulae were validated with the experimental database but also with Chowdhury, Loo, and Fragomeni (2000) tests.

Furthermore, Daneshjoo and Gharighoran (2006) interested in damping parameters for bridge beam-slabs. The influence of residual deflection and damage state on damping was investigated. The beam crack development led to higher damping ratios, which meant more energy was dissipated when more cracks were present. Damping equations were finally proposed. The cracked logarithmic decrement δ_{cr} is given in equation (1.73):

$$\delta_{cr} = 12.193 \times \left(\alpha_{\Delta_r} \right)^{0.1496} \tag{1.73}$$

where α_{Δ_r} is the ratio of the residual deflection, for the unloaded beam at any stage of the experiment, over the elastic deflection. A comparison of damping ratios obtained with the above formulae was made with the formulae of Salzmann (2003) in equations (1.70) and (1.72). The conclusion deduced was that the two formulae gave close results for uncracked beams. However, the difference exceeded 15% for cracked beams, which was not negligible.

(c)   Damping as a function of crack opening   The dynamic response of a structure is particularly a function of damping. So, the aim of Chowdhury, Loo, and Fragomeni (2000) was to evaluate the link between cracking behaviour and damping characteristics of reinforced and partially prestressed beams from full-size tests on 26 beams. Free vibration tests were performed, and the logarithmic decrement method was used to compute damping ratios. Empirical formulae to predict the damping logarithmic decrement δ were proposed for reinforced (eq. 1.74) and partially prestressed (eq. 1.75) beams, based on the residual crack width w_r, a function of the instantaneous average crack width:

$$\delta = 0.075 \times 10^{0.205.w_r} \tag{1.74}$$

$$\delta = 0.070 \times 10^{0.220.w_r} \tag{1.75}$$

Logarithmic decrement values obtained experimentally and from the above formulae ranged from 0.04 to 0.16. The differences between experimental data and numerical prediction were inferior to 30%.

(d)   Damping as a function of damage indices   Energy dissipations should be accurately quantified to predict the response of RC structures under earthquake excitation. Following this objective, Heitz, Richard, et al. (2017) proposed a damping modelling strategy using physical-motivated evolution laws of damping ratios. Quasi-static and dynamic tests were performed on RC beams (more details in section 1.4). A constitutive model was first calibrated on experimental data. In addition, dynamic structural properties were evolving with damage state d, in the idea of equation (1.76) for the damping ratio:

$$\xi_{eq}(d) = \xi_{el} + \xi_{hyst}.d \tag{1.76}$$

Then, Heitz, Giry, et al. (2017) work focused on uncoupling viscous and hysteretic damping ξ_{hyst}. The same experimental campaign was used to develop a numerical model whose parameters, representing physical phenomena, were identified from experimental data. This model was then used to perform a numerical study, whose goal was to evaluate the influence of parameters on damping ratios and energy dissipations. It appeared that quasi-static and dynamic tests gave close damping ratios, whose values were comprised between 0% and 5%. To go further, a damping ratio model depending on a damage index and the displacement demand was proposed in Heitz, Giry, et al. (2019) and calibrated with a numerical parametric study. The aim was to propose a model that dissipated the right amount of energy. The evolution of two parameters was characterised: (i) a degradation index defined as $\Gamma = \dfrac{\gamma_m}{\gamma_y}$ with γ_m the maximal historic curvature measured at mid-span and γ_y the theoretical first steel yielding curvature, and (ii) the displacement demand defined as the mid-span curvature γ. A correlation was deduced between the damping ratio and the two parameters in equation (1.77):

$$\xi_{eq} = \bar{C} \times f(\Gamma)g(\gamma) \tag{1.77}$$

where $\bar{C}$ is a normalised coefficient. The main conclusion was that the obtained damping ratio surface could be used as a chart for a predictive choice of damping ratio. Thus, considering damping ratio evolution in nonlinear time-history analyses could be possible.

1.3.3.2   Identification with numerical strategies

The last paper discussed in the previous section Heitz, Giry, et al. (2019) linked with this final section where damping models are identified with numerical strategies. Indeed, Heitz, Giry, et al. (2019) realised a numerical parametric study to obtain the relation in equation (1.77). Nevertheless, numerical analyses were associated with an experimental-based calibration of a complex RC constitutive model.

Crambuer (2013) strategy was reversed. The aim was to propose an updated damping model to dissipate the right amount of energy without requiring a complex constitutive model. The initial hypothesis

was the damping ratio decomposition between an elastic part and a hysteretic one. It was demonstrated that the damping ratio due to concrete cracking depended on damage index, loading intensity and crack surface erosion. That is why three damping models were studied: (i) $\xi_{hyst} = \xi_d$ depending only on the damage, (ii) $\xi_{hyst} = \xi_d.\Gamma_U$ depending on the damage and crack surface erosion, and (iii) $\xi_{hyst} = \xi_D.\Gamma_I$ depending on the damage and loading intensity. A simple constitutive model (only damage phenomenon) was considered. The damping evolutions were identified by comparing dissipated energy with a more complex constitutive model considering different dissipative phenomena (damage, friction, unilateral effect). For the first model, an evaluation of dissipated energy was performed for each cycle, and the damping ratio was identified with equation (1.78):

$$\xi_d = \arg\min \left(\left| E_{diss}^{\text{Richard 2}} - 2\pi \sqrt{k_d.m} \times \xi.\omega_d.\sqrt{1-\xi^2} \times u_c^2 \right| \right) \tag{1.78}$$

where $E_{diss}^{\text{Richard 2}}$ is the dissipated energy with the complex constitutive model, k_d the damaged stiffness, ω_d the eigenfrequency at considered damage level and u_c the cycle amplitude. Then, for the second damping model, an erosion criterion was defined in equation (1.79) because the more cracks opened, the less they were dissipating energy. Γ_U evolved from 1 for a new crack to 0 for a crack completely eroded.

$$\Gamma_U = 1 - \frac{m_{c,d}}{m_{c,m}} \tag{1.79}$$

where $m_{c,d}$ is the number of cycles since the last damageable one and $m_{c,m}$ a maximal number of cycles depending on the structure. As a remark, it was indicated that the notion of "cycle" was challenging to define for seismic loading. So, it was considered that a cycle was beginning when displacements went from positive to negative values. Finally, for the third model, an identification similar to the first one was used given a parameter Γ_I varying from 0 for a cycle of null intensity to 1 for a cycle with an intensity equal to the cracking cycle. The RC columns and error computations study showed that the third model was the best. In conclusion, if the damping ratio could be accurately updated, it was possible to develop simplified models. Those models represented the global behaviour of structural elements subjected to bending without considering intrinsically local dissipative phenomena.

1.4   Experimental campaign and data

Damping identification (section 1.3) is generally based on experimental data (tables 1.3, 1.4 1.5 and 1.6). However, damping models proposed in section 1.2 are more often studied numerically. Most comparisons in table 1.2 evaluate damping matrix formulations without relying on experimental data. Works developed in the following chapters will focus on those two research topics. The experimental campaign presented here will be a guideline: numerical models will be validated through the experimental data, and a higher understanding of physical phenomena will be possible.

In his work Heitz (2017), Heitz, Richard, et al. (2017), and Heitz, Giry, et al. (2019), T. Heitz performed an experimental campaign on RC beams at the French Alternative Energies and Atomic Energy Commission (CEA) on the AZALÉE shaking table. The campaign aimed to perform dynamic and quasi-static tests to propose data for evaluating seismic energy dissipations depending on structural, material and input excitation characteristics. In the literature, papers studying dissipation assessment in RC elements with quasi-static or dynamic tests exist. Nevertheless, comparisons of both tests on the same elements and setup facilities are lacking. It was what motivated the experimental campaign. The other study objective was the coupling between modes to characterise the fundamental mode damage effect on other modes and the combination of modes excited at the same time for dissipation analyses.[6]

1.4.1   Reinforced concrete specimens and setup

1.4.1.1   Geometry

Studied elements were RC beams of length $6\,\mathrm{m}$ and section $0.2 \times 0.4\,\mathrm{m}^2$. The length was chosen to match the shaking table dimensions. To avoid the beam cracking under its weight and to be able to excite the beam first modes with the facilities, the beam was tested horizontally to its weak axis.

Four different geometries were studied for the rebars: (i) 4 high-adherence (HA) rebars of diameter $20\,\mathrm{mm}$ given a reinforcement ratio of 1.57% and a bond surface of $25.1\,\mathrm{cm}^2/\mathrm{m}$, (ii) 8 HA rebars of diameter $16\,\mathrm{mm}$ given a reinforcement ratio of 2.01% and a bond surface of $40.2\,\mathrm{cm}^2/\mathrm{m}$, (iii) 4 HA rebars of diameter $12\,\mathrm{mm}$ given a reinforcement ratio of 1.41% and a bond surface of $37.7\,\mathrm{cm}^2/\mathrm{m}$ and (iv) 4 round bars of diameter $12\,\mathrm{mm}$ given a reinforcement ratio of 1.41% and a bond surface of $37.7\,\mathrm{cm}^2/\mathrm{m}$. The different types of reinforcement allowed the investigation of three parameters: the reinforcement ratio, the steel-concrete bond surface and the influence of friction between steel and concrete on dissipated energy.

1.4.1.2   Materials

(a)   Concrete   Two concrete formulations, classified in Eurocode 2 (NF EN 1992-1-1, 2005), were considered: C25/30 for twenty-one beams and C45/55 for two beams. Because of the large number of beams with the first formulation, concrete production was divided into A and B groups. Different normalised tests were performed to characterise concrete: (i) compressive tests on cylinders of diameter $16\,\mathrm{cm}$ and height $32\,\mathrm{cm}$ at 28 days of drying and six months of cure, (ii) cyclic compressive tests on the same specimen types after six months of cure to evaluate dissipated energy and (iii) monotonic three-point bending tests on $84 \times 10 \times 10\,\mathrm{cm}^3$ prisms to measure the concrete fracture energy G_f (corresponding to the energy dissipated through initiation and propagation of cracks) and the tensile strength. Values were over-estimated for the last property because the breaking zone was imposed during the test (weakest link theory). The synthesis of mechanical properties for the different concrete sets is presented in table 1.7.

---

[6]All data presented in section 1.4 are extracted from (Heitz, 2017).

Table 1.7: Concretes mechanical properties (Heitz, 2017)

| Mechanical properties | | Concrete | | |
Name	Unit	C1A[*]	C1B[*]	C2[**]
$f_{c,28d}{}^{(1)}$	[MPa]	35.0	29.7	45.4
$f_{c,6m}{}^{(2)}$	[MPa]	36.9	33.0	47.4
$E_{c,28d}{}^{(1)}$	[GPa]	26.4	28.7	29.2
$E_{c,6m}{}^{(2)}$	[GPa]	26.2	28.1	28.2
$E_{diss,6m}{}^{(2)}$	[J]	4192	3467	4322
$G_{f,6m}{}^{(2)}$	[J/m^2]	84.9	80.0	81.0
$f_{t,G_f,6m}{}^{(2)}$	[GPa]	2.09	2.22	2.47

[*] C25/30   [**] C45/55
[1] At 28 days, $f_{c,28d}$ is the concrete strength and $E_{c,28d}$ the Young's modulus.
[2] At 6 months, $f_{c,6m}$ is the concrete strength, $E_{c,6m}$ the Young's modulus, $E_{diss,6m}$ the energy dissipated for the loading/unloading cycle at maximal stress, $G_{f,6m}$ the concrete fracture energy and $f_{t,G_f,6m}$ the concrete tensile strength deduced after $G_{f,6m}$ measurement tests.

(b)   Steel   The steel rebars were classically characterised with traction tests. The material properties determined are presented in table 1.8.

Table 1.8: Steel mechanical properties (Heitz, 2017)

| Mechanical properties | | Reinforcement type | | | |
Name	Unit	HA12	HA16	HA20	RL12
Elastic limit	[MPa]	528	568	$> 560^{(1)}$	468
Young's modulus	[GPa]	206	217	$210^{(1)}$	218

[1] Clamping claws are not available, so values are chosen from manufacturer data.

(c)   Steel-concrete bound   Pull-out tests were finally performed to characterise the steel-concrete interface strength. Various failure modes were observed due to the different concrete strengths and the rebar diameters. Maximal adherence stress with a round rebar was around 0.2×10^4 MPa for a bond-slip of 1 mm, while maximal adherence stresses between 1.5×10^4 MPa and 2.3×10^4 MPa were obtained for ribbed rebars with bond slips at maximal stresses between 2.2 mm and 4.5 mm. Result variations were significant, and no general conclusions were deduced regarding concrete or steel characteristic influences.

1.4.2   Experimental setup

Figure 1.17 presents a 3D view of the experimental setup in the case of dynamic tests.

1.4.2.1   Beam supports

(a)   End supports For the boundary conditions, the objective was to resist only horizontal loading, to avoid the appearance of resisting moments at beams ends, and stay elastic. The support was inspired by La Borderie (1991) and was composed of two clamping frames and two steel blades. The two blades were designed with a numerical study to resist a design force of 45 kN and a design rotation around the z-axis of $6°$. The supports (fig. 1.17) were clamped on the beam and fixed on the black components positioned next to the beam because of shaking table dimensions ($6\,\mathrm{m} \times 6\,\mathrm{m}$ for a beam length of $6\,\mathrm{m}$). So, the effective beam length became $5.90\,\mathrm{m}$.
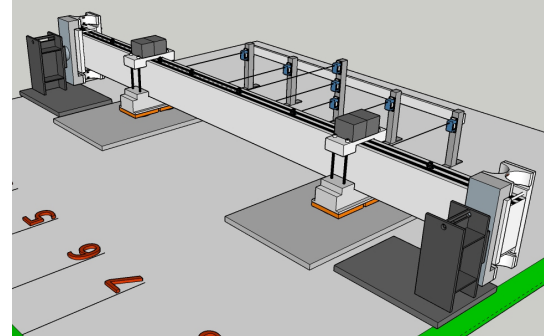
Figure 1.17: 3D view of the dynamic experimental setup (Heitz, 2017) - beam length $L = 6\,\mathrm{m}$ and beam section $S = 0.2 \times 0.4\,\mathrm{m}^2$

(b)   Additional masses Additional masses of $310\,\mathrm{kg}$ were added at beam quarter-spans to adapt the beam modal properties to available facilities. In addition, to avoid cracks to opening due to self-weight loading, intermediate supports were placed under the additional masses. Those supports were resting on air cushion devices, which cancelled friction with the table. The additional masses were clamped on the beam and relied on the intermediate supports (orange pieces in figure 1.17).

1.4.2.2   Sensors

Numerous sensors were positioned all along the beam, as presented in figure 1.18 with their references displayed next to each sensor.
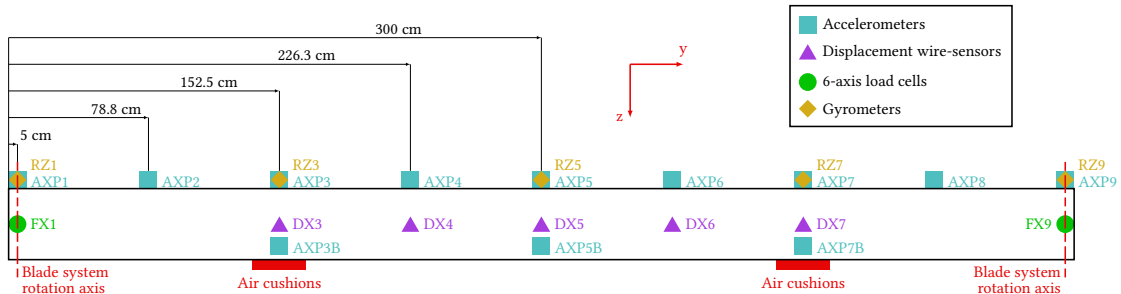
Figure 1.18: Sensor positions (Heitz, 2017)

Displacement For the displacement measurements, three systems were used. Only in the case of quasi-static tests, LVDT (Linear Variable Differential Transformer) sensors were associated with both actuators (DXV3 and DXV7 but not represented in figure 1.18). Then, five wire's sensors (DX3 to DX7) were used for dynamic tests. For all tests, a Videometric® system allowed image correlation and to deduce the beam fibre mean displacements.

Acceleration Accelerometers (AXP1 to AXP9) were fixed above the beam for the acceleration measurements. Some of them were mounted alone, given accelerations in one direction only. The other ones were mounted by a group of three to measure accelerations in the three directions.

Rotational velocity   Gyrometers (RZ1 to RZ9) were used to measure the vertical rotational velocities around the bending direction.

Force   Two 6-axis load cells (FX1 to FX9) were positioned at beam ends. They were fixed between the beam and support columns. They allowed the measurement of x-axis loads and the experimental setup validation (no vertical load had to be developed). Finally, they could be used to quantify unintended forces through supports, if required. Then, only for quasi-static tests, two one-axial load cells (not represented in figure 1.18) were added to actuators to evaluate the loading forces.

Strain   Strain gauges were used to validate the elastic behaviour of steel blades.

1.4.3   Tests and experimental results

Three types of tests were performed on the beams: hammer shock tests (section 1.4.3.1), quasi-static tests (section 1.4.3.2) and dynamic tests (section 1.4.3.3). Beams under quasi-static tests reached damage level that is why they were not used again for dynamic experiments. Two identical beams were constructed to compare quasi-static and dynamic tests.

1.4.3.1   Hammer shock tests

(a)   Test description   Hammer shock tests were performed on all beams to evaluate the eigenfrequency evolutions according to different damage states. The first three modes were characterised. Four shocks were applied at mid-span for the first and third modes, symmetrical ones. For the second mode, anti-symmetric, four shocks were applied at quarter-span. By plotting the acceleration response Fast Fourier Transform (FFT) with the nine accelerometers and taking the four-shock average, eigenfrequencies and mode shapes of the three modes were deduced. The average led to a reduction of noise influence on the FFT.

(b)   Results   The imaginary parts of acceleration FFT responses are plotted in figure 1.19 for the beam HA16-C1A-1 in the initial stage. Figure 1.19a shows the response when shocks are applied at mid-span, and the shapes of modes 1 and 3 are observable. In figure 1.19b, shock responses at quarter-span are plotted. Mode 1 is again excited in addition to mode 2. The three first eigenfrequencies can be evaluated for each beam by studying all shock test recordings, as presented in table 1.9, still in the initial state. The undamaged frequencies will be used to calibrate the numerical model in the following. Then, after the first damageable test, a frequency decrease is particularly notable by studying shock test responses after quasi-static tests of increasing amplitudes.

(a) Shocks at mid-span   (b) Shocks at quarter-span
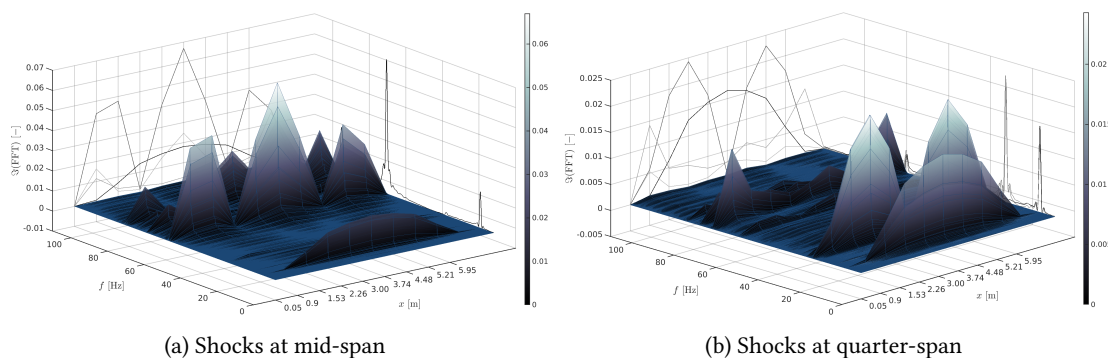
Figure 1.19: Imaginary part of acceleration FFT response - beam HA16-C1A-1

Table 1.9: Eigen-frequencies obtained with hammer shock tests for undamaged beams (extracted from Heitz (2017))

Beam type	Mode 1	Mode 2	Mode 3
RL12-C1B	7.13 Hz	22.5 Hz	58.9 Hz
HA12-C1B	6.81 Hz	21.5 Hz	57.2 Hz
RL12-C2	6.84 Hz	22.0 Hz	57.7 Hz
HA12-C1A	7.14 Hz	22.5 Hz	57.8 Hz
HA16-C1A	7.11 Hz	23.1 Hz	58.2 Hz
HA20-C1A	7.16 Hz	22.6 Hz	57.6 Hz

1.4.3.2   Quasi-static tests

(a)   Test description   Quasi-static tests were performed on a strong floor with two actuators (fig. 1.20). The aim was to assess hysteretic energy for the first two bending vibration modes. When actuators were acting in phase, a four-point bending test exciting the first beam mode was done (QSC1). The second mode was activated when they were in opposition (QSC2). Both tests were reverse cyclic quasi-static tests. Cycle amplitudes were increasing during loading, and for each amplitude, three cycles were performed to stabilise energy dissipations. The tests were carried out with a constant velocity of 0.4 mm/s and displacement control (fig. 1.21a). Thanks to additional tests, the strain rate influence was finally explored (SPS1 and SPS2).

(b)   Results   Figure 1.21b presents the load-displace- ment curve obtained with the beam HA16-C1A-1. Displacements were measured at beam mid-span and loads at supports with load cells. The beam capacity curves were deduced from the load-displacement responses. Then, the concrete strength and rebar pattern influences could be studied by comparing those capacity curves (fig. 1.22 (Heitz, 2017)). The study conclusions were: (i) the concrete strength did not significantly impact the capacity curve, maybe because both materials were not distinct enough, (ii) the increase of rebar specific surface increased the post-yield stiffness, and (iii) using round re-bars or HA steel reinforcements gave similar responses because of the lack of confinement. Then, the beams submitted to QSC2 tests exhibited an apparent stiffness eight times larger than with QSC1 tests.

Figure 1.20: Quasi-static experimental setup (Heitz, 2017)

Energetic analyses were also performed on load-displacement curves. First, three phenomena were observed (fig. 1.21b): (i) the stiffness loss characterising essentially the crack openings, (ii) the hysteresis cycles due especially to crack surface friction and bond-slip, and (iii) the pinching effect, which has been

(a) Input signal

(b) Load-displacement curve
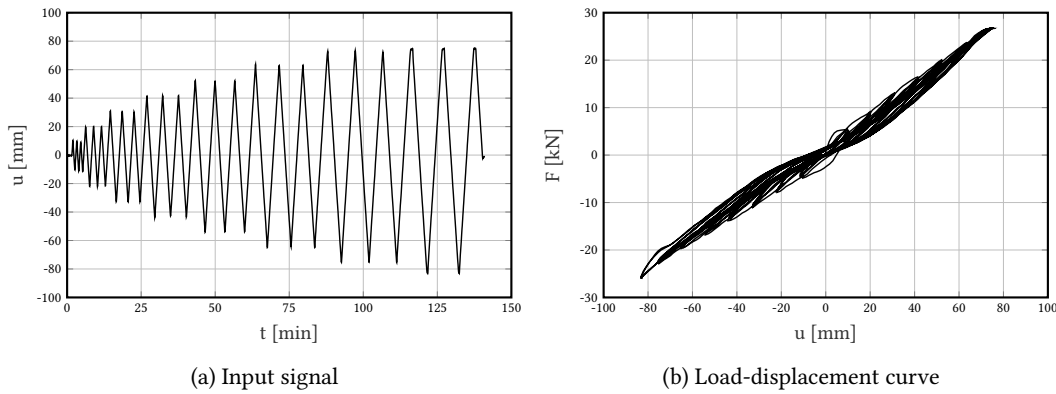
Figure 1.21: QSC1 test on the beam HA16-C1A-1
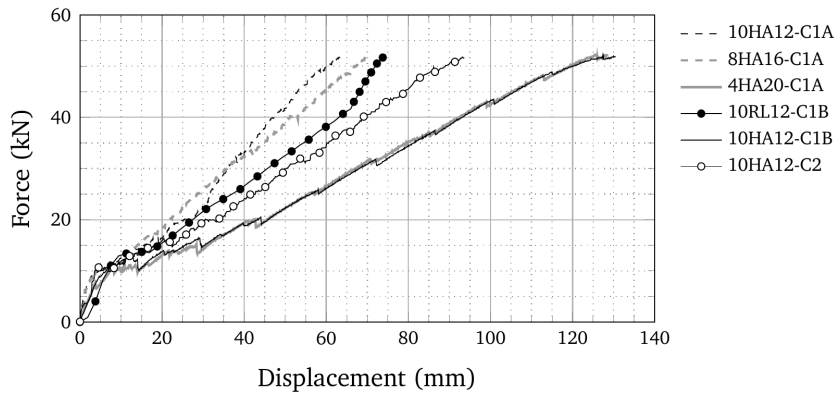
Figure 1.22: Capacity curves for different beams (Heitz, 2017)

a phenomenon still poorly understood. An updated Jacobsen's area method was applied to evaluate dissipated and stored energies in addition to the damping ratio for each cycle amplitude. The evolution of those three properties was thus obtained as functions of the cyclic amplitude u_c. Equation (1.80), for example, give the equivalent viscous damping ratio ξ_{eq} evolution:

$$\xi_{eq} = 9.43 \times 10^{-3} + 0.136 \times u_c^{-1} \tag{1.80}$$

Hence, it was demonstrated that the EVDR was dependent not only on ductility but also on cyclic amplitude. In the SPS1 and SPS2 tests, the EVDR evolution through actuator velocity v_a was assessed. A linear trend was obtained: $\xi_{eq} = A \times v_a$ where A is a constant. The slope A appeared to increase when the displacement amplitude u decreased, following equation $A = 28.2 \times u^{-1.20}$.

1.4.3.3   Dynamic tests

(a)   Test description   The dynamic tests were performed on a shaking table. Four different types of signals were applied on the beams: (i) a white-noise signal (WN), (ii) a band-passed white noise (SC), (iii) a decreasing sinus sweep (DSS), and (iv) a natural seismic signal (SS1). First, white-noise signals could be applied with low amplitudes (example in figure 1.23a) to study beam modal properties or with

(a) WN1 test

(b) DSS85 test
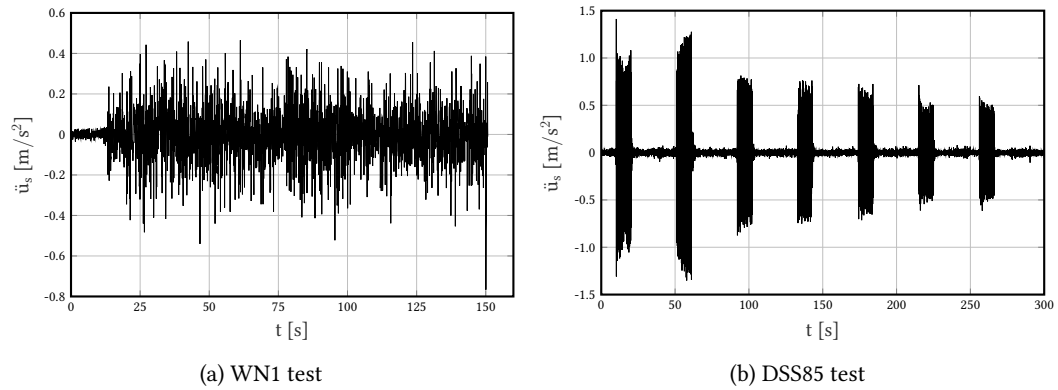
Figure 1.23: Input signals of the two first dynamic tests carried out on HA16-C1A-2 beam

higher-level to excite mode shapes for various damage levels. The modes one and two could be studied independently or together using the shake table six DOFs. Then, the band-passed white noise signals were characterised by the sum of mono-harmonic accelerations with increasing frequencies. The mode shapes associated with modes 1 and/or 2 could again be activated depending on the acceleration direction. The decreasing sinus sweeps signals (example in figure 1.23b) corresponded to successive mono-harmonic acceleration signals with decreasing frequencies. Between two successive mono-harmonic accelerations, white noise was added. A denomination DSS85 signified that the frequencies were evolving from $8\,\text{Hz}$ to $5\,\text{Hz}$. Finally, the studied natural seismic signal was characterised by a peak ground acceleration of $0.47\,\text{g}$ recorded on the third floor of the Kashiwazaki-Kariwa nuclear power plant (Japan). For the beams submitted to dynamic loadings, various input signals were successfully applied to consider the beam damage state.

(b)   Results   Different analyses could be performed with all dynamic experimental data deduced from the tests. The acceleration and displacement responses could be studied in the time and frequency domain (fig. 1.24). For example, the frequency-domain response enabled beam eigenfrequencies with the white-noise signals. In addition, by applying the HPBM (half-power bandwidth method) on frequency-domain responses, EVDR could be defined. Then, Heitz (2017) proposed a non-parametric identification

(a) Time-domain

(b) Frequency-domain
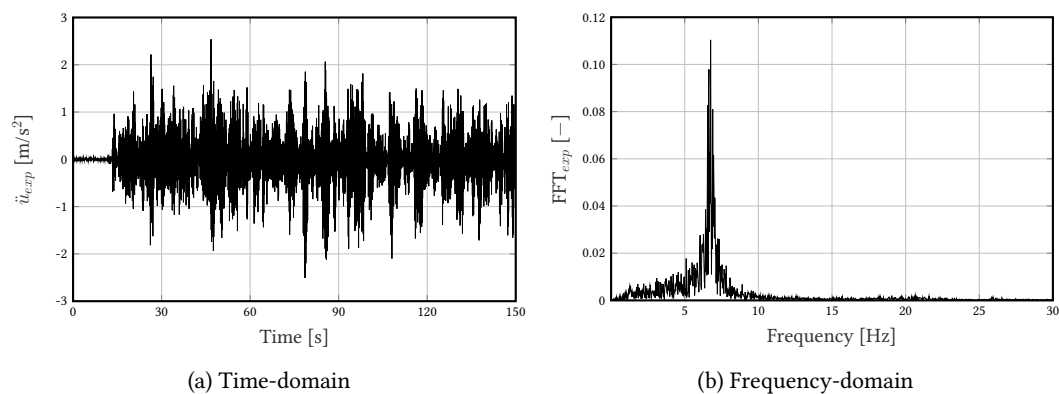
Figure 1.24: Mid-span acceleration response of the beam HA16-C1A-2 submitted to the WN1 input signal in figure 1.23a

method on sliding windows to propose EVDR and eigenfrequency evolutions during white-noise or decreasing sinus sweep signals. The method implies errors (bias), so the results should be carefully questioned. Conclusions were: (i) high variations could be obtained for the EVDR, and (ii) identified parameters were strongly dependent on chosen windows (the more extensive the maximal displacement in the window was, the lower was the damping ratio).

1.4.3.4   Identified damping ratios

In conclusion, table 1.10 was proposed in Heitz (2017) to synthesise the EVDR identified on the experimental data using different analyses. Similar values were obtained with the QSC1 test and the numerical studies under free vibrations. With the non-parametric method, the ductility and displacement amplitudes considered varied from the first analyses (QSC1 test and numerical analysis under free vibrations), but closer values were considered. With this method, fast damping ratio variations were observed, so it was not easy to give a unique value. The presented interval was still consistent with the two first values. Finally, it was impossible to evaluate EVDR for large displacement amplitudes with the hammer shock tests. The consequence was that the hammer shock tests were inadequate to evaluate damping values for computations leading to large displacements.

Table 1.10: EVDR values identified with different methods (Heitz, 2017)

Test	Method	Equivalent viscous damping ratio
QSC1[1]	Jacobsen's area	2.7%
Virtual free vibrations[2]	Numerical analysis	3.1%
Hammer shocks[3]	$\Im$(FFT) analysis	$9 - 12\%$
DSS52[4]	Non-parametric identification	$1 - 3\%$

[1] At $\nu = 14.6$ and displacement amplitude of $35\,\mathrm{mm}$ (beam HA20-C1A-1)
[2] At $\nu = 14.6$ and displacement amplitude of $35\,\mathrm{mm}$ (beam HA20-C1A-1)
[3] On a damaged beam (HA12-C1B for 9% and HA20-C1A for 12%)
[4] At $\nu = 18.6$ and displacement amplitude of $35\,\mathrm{mm}$ (beam HA16-C1A-2)

1.5   Synthesis and scientific gap

Evaluating reinforced concrete structure safety under earthquake excitations requires proper modelling of energy dissipations. Because of RC material nonlinear and complex behaviour, the seismic equation derivation leads to different damping types: viscous, hysteretic and numerical (1.1). In earthquake engineering, viscous damping is intensely studied because it conveniently represents unknown dissipative phenomena. Indeed, the challenging link with the notion of damping is the large number of phenomena to consider. To overcome this challenge, numerous research studies focus either on damping model propositions (1.2) or damping identification methods (1.3).

1.5.1   Damping models at the structural level

The damping models presented in section 1.2.2 are classified between classical and modal damping models. Classical ones are based on the stiffness and mass characteristics of the studied system. On the contrary, modal damping models are developed from eigenmodes. Damping characteristics with both model categories are linked with the structural velocity response given the "viscous damping". In earthquake engineering, those strategies are generally used because of their simplicity. Simple elastic constitutive models are generally considered by modelling energy dissipations through viscous damping. Notably, the Rayleigh damping (RD) formulation, a classical one, remains the most used. Mathematically, it is an efficient tool because the damping matrix is diagonal in the modal basis, allowing to decouple equations in MDOF system analyses. However, a linear combination of mass and stiffness matrices exhibits unexpected phenomena in the initial RD model when used for nonlinear analyses. That is why many papers focus on this model to improve structural numerical responses. Adaptations are: (i) removing the mass proportional part to eliminate spurious forces, (ii) updating the stiffness matrix part to consider the structure degradation or (iii) updating the two proportionality parameters, …

Instead of proposing damping models, many papers evaluate various existing models based on particular examples. Table 1.2 synthesises the damping formulations compared in those papers. It appears that the RD-type formulations are the most studied and modal damping (MD) models to a slightly lesser extent. Using the tangent-stiffness proportional damping (TKPD) model is the most recommended, mainly because it is a way to reduce and contain the damping forces. Classical RD should be avoided because it leads to the strongest damping most of the time. So, it is not a conservative model for earthquake engineering. However, conclusions have to be carefully considered. Indeed, various papers agree that the choice of damping formulation should be made depending on the response quantities of interest and the numerical model (FE, fibre, …). In addition, parameters to compute damping matrices, like viscous damping ratios, choice of modes, … are also dependent on the structure and the damping formulation considered. However, it is shown that the initial viscous damping ratio choice, in particular, plays a significant role in the structural dynamic responses. It exhibits the impossibility of proposing one damping model universally accepted for dynamic structural analyses. Lots of choices stay at the discretion of the users. Engineers, for example, must seek a compromise between the computational time, which can enormously increase when updates are performed during computations, and result accuracy. It is, finally, the reason explaining the still extensive use of RD.

More complex damping models are also proposed in the literature. However, they are rarely used because they do not enhance the physical representation of energy dissipations despite their implementation complexity, unavailability in commercial FE programs, and high time-consuming.

Scientific gap
Few papers in the literature are performing damping formulation comparisons based on experimental campaigns. They instead concentrate on damping model influences on numerical responses. In addition, dissipation energies are bare of interest in damping model studies. That is why a numerical investigation will be performed in chapter 2 to compare frequently used damping formulations based on the data obtained with the experimental campaign presented in section 1.4. Experimental data will be used to evaluate the damping model potentials to represent dynamic responses. Energy studies at the structural and material levels will lead to a better understanding of physical dissipative phenomena. Indeed, most models are not based on physical phenomena and are only mathematical tools. So, at the end of chapter 3, a new damping matrix formulation updated at the element level will be proposed considering some of the main concrete dissipative phenomena.

1.5.2   Damping models at the local level

Research studies aim to characterise hysteretic damping to better represent physical phenomena at the local level. For RC material, complex constitutive models are proposed. However, modelling all dissipative phenomena is impossible because of their couplings and large numbers. So, a small amount of viscous damping is generally required with dissipative constitutive models.

In addition, some papers propose to adapt structural viscous damping models at the elementary level. Indeed, it allows considering nonlinear local behaviours, representative of nonlinear structural phenomena. Advantages advocated for those methodologies, discussed by the scientists, are their higher reliability than the global formulations and the better representation of dissipations. However, it still lacks experimental evidence of those conclusions.

Scientific gap
Hysteretic behaviour models are little used in engineering due to the lack of knowledge about their dissipative phenomena. Studying two different hysteretic models for concrete, in the numerical analysis of chapter 2, will enable us to characterise some dissipative phenomena at the concrete level and to better understand what physically occurs during dynamic excitations on RC elements. Then, the damping matrix formulation proposed in chapter 3 will be updated at the element level, and comparisons will still be performed with experimental data, in addition to energetic analyses. Hence, it will be the first step in experimental and energetic evaluations of elemental damping models.

1.5.3   Damping identification

Finally, section 1.3 reviews damping identification methods in the literature. Several objectives are followed in the papers: (i) identifying damping values to be applied in numerical models, (ii) identifying damping evolution models as functions of different variables to allow damping updates in numerical analyses, or (iii) using damping as a damage index for the safety evaluation of existing structures.

The equivalent viscous damping ratio generally considered in engineering is 5% for all earthquake excitations, when performing linear analyses, and based on code guidelines. However, it is demonstrated that when the structural damage increases, hysteretic damping also grows, decreasing viscous damping. Therefore, using a unique EVDR all along computation represents a strong hypothesis. Experimental EVDR identifications are performed either on structural elements or entire structures. A synthesis of identified values for different structures is presented in tables 1.3, 1.4 and 1.5. Many analyses lead to EVDR between 1% and 6%, consistent with the 5% commonly used. However, all identified values must be carefully analysed because of the identification methodology bias. Moreover, significant variations are observed, mainly when history loadings are considered. For cracked structural RC ele-

ments, EVDR determined can reach 20%. So, considering a constant EVDR for damaged structures is not representative of the behaviour of real RC structures under damageable loadings.

Then, as modal properties are linked to structural damage states, they are often used to perform damage identification on existing structures. Eigenfrequencies and mode shapes were first intensely studied, but damping is also of interest today. However, there is no consensus about its capacity to permit damage detection. Mainly, if the damping is an adequate tool to characterise structural damage, it does not localise it. In in-situ experiments, free vibrations are not applied to the structure, so the simple logarithmic decrement method can not be used to identify damping. So, other methodologies are considered, but they must be carefully used. That is why some papers propose improved methodologies to evaluate damping characteristics with ambient vibrations, or at least without requiring free vibrations.

Finally, the last research subject is the damping model identifications as functions of various parameters. Most of them are based on ductility. Nevertheless, proposed model variations in table 1.6 show the difficulty to propose a global model, succeeding for all types of elements. Though, it is shown that using adequately updated damping models during computation could be a way to improve dynamic responses without requiring complex constitutive models.

Scientific gap

Performative identification methods are still required to improve confidence in the identified damping values and to be able to develop models. In chapter 3, an identification method will be of interest to evaluate the evolution of EVDR and eigenfrequencies during dynamic damageable signals. The identification method will be applied to experimental and numerical data with various dynamic signals. Thus, it will be possible to characterise the numerical model ability to represent experimental damping characteristics. EVDR evolutions as functions of damage indices could, then, be proposed and compared with the ones in the literature.

Modelling of dissipations in reinforced concrete beams

Contents

2.1   Description of the multi-fibre model

Based on the experimental campaign performed by Heitz (2017) and presented in section 1.4, a multi-fibre model of experimentally tested beams is built on a finite element (FE) software: Cast3M, which is developed by the French Alternative Energies and Atomic Energy Commission (CEA). A theoretical presentation of multi-fibre models is proposed in section 2.1.1. Then, the geometry and boundary conditions (2.1.2), constitutive material models (2.1.3) and input signals (2.1.4) are detailed to characterise experiments best.

2.1.1   Multi-fibre model relevancy

Studying reinforced concrete (RC) elements under earthquake excitations requires dynamic analyses with nonlinear material behaviours. The three-dimensional (3D) finite elements are efficient tools, especially for structure complex parts like joints or assemblies. However, it becomes less practical when applied to the whole structure because of the computational time and memory required. That is why other numerical strategies developed as fibre models. Spacone and El-Tawil (2004) presented a state-of-the-art of nonlinear analysis of steel-concrete composite structures, and the multi-fibre approach was presented with some of its assumptions taken over later. Microscopic approaches based on solid mechanics were used to consider nonlinearities due to material behaviour, and fibre models were part of it. The idea of such models was to consider a beam problem where sections are divided into fibres. So, each fibre is independent of the other in terms of constitutive law. For example, in the case of RC, a few fibres represent reinforcements, and the other ones represent concrete (fig. 2.1). Several materials can be assigned to a single FEM, which is interesting for composite materials (Moulin, 2010). The principal advantages, developed in the literature, of the fibre models are: (i) their ease of use, (ii) the consideration of local behaviour, (iii) the reduced computational time, (iv) the low amount of DOFs required, and (v) the result analysis interpretations made more accessible by the similarity with beam problems (Moulin, 2010; Capdevielle, 2017; Grange, Mazars, and Kotronis, 2007; Kotronis, 2008; Mazars, X. H. Nguyen, et al., 2005; Spacone, Filippou, and Taucer, 1996a; Adelaide, Richard, and Cremona, 2011). Capdevielle (2017) even proposed the approach validity field and limits. Mainly, normal stresses should prevail (slender beams, for example). However, limits appear when shear deformations become large, so many papers focus on overcoming this difficulty.

2.1.1.1   Multi-fibre models in the literature

Papers dealing with fibre models are divided into two groups in the literature: (i) the ones using fibre models structural analyses and (ii) the ones proposing fibre element enhancements.

The fibre models were developing in the last fifteenth years. First, Mazars, X. H. Nguyen, et al. (2005) used multi-fibre beam elements with the Bernoulli kinematic to perform a modal analysis on a third-scale model of a braced RC structure tested on a shake table in Lisbon. The multi-fibre approach was chosen for spatial discretisation because of the computation flexibility. It accurately represented the experimental structure eigenmodes. In the same idea, Grange, Mazars, and Kotronis (2007) focused on a 7-story RC structure tested for a benchmark. Timoshenko multi-fibre beam elements were used to perform a nonlinear dynamic analysis. The study conclusions were a good approximation of global structural responses and a decrease in computational time. Thus, this type of model could be used to study various structures and parametric analyses, an idea also shared by Kotronis (2008). Then, F. Wang et al. (2007) developed a multi-fibre model in Cast3M to simulate RC columns, previously tested under static loading. A bond-slip relationship was considered, and the numerical results match experimental ones up to failure. It was also suggested that such analyses could be considered in existing building

evaluations. Finally, Souid et al. (2009) went further by using a multi-fibre model to propose an efficient model for pseudo-dynamic tests. The paper aim was to capture the studied structure dynamic failure using an advanced damage model for concrete.

A few older papers could be found in multi-fibre model improvements. Notably, Taucer, Spacone, and Filippou (1991), Spacone, Filippou, and Taucer (1996a), and Spacone, Filippou, and Taucer (1996b) focused on fibre beam-column elements for nonlinear static and dynamic analyses of RC frames. The proposed beam-column FE was discretised into longitudinal steel and concrete fibres. Each fibre had a nonlinear constitutive law, leading to the structure hysteretic behaviour. The proposed element was applied to three different examples for which experimental data existed. It appeared to be reliable, numerically robust and computationally efficient. Indeed, good agreements with experimental data were obtained for pseudo-static tests, mainly when small damage occurred. However, refinements were still required for high inelastic deformations.

Initial fibre elements were based on Bernoulli hypotheses: plane sections stayed planes and perpendicular to the beam axis. This model first enhancement was to develop a fibre element based on Timoshenko hypotheses to avoid considering the section perpendicularity. By staying in the small strain hypothesis, Kotronis (2000) and Kotronis, Davenne, and Mazars (2004) proposed a 3D Timoshenko multi-fibre FE to be free of shear locking. The implemented method was based on high order integration functions. The shearing energy consideration allowed the use of the elements with any section. Element validation was performed on a column under cyclic loading with nonlinear behaviour and demonstrated its performance. In the same idea, Mazars, Kotronis, et al. (2006) focused on an enhanced multi-fibre beam element, taking into account shear and torsion, also with high order integration functions. Nonlinear behaviour using an advanced constitutive law was applied to the fibre. Its combination with the warping kinematic gave accurate results for different section forms, as demonstrated on RC columns. Then, to resume existing multi-fibre elements, Kotronis (2008) compared three models: (i) an Euler-Bernoulli multi-fibre element, (ii) a Timoshenko element with first-order integration functions and (iii) a Timoshenko element with higher-order integration functions. The last model mainly required fewer DOFs to represent analytical or experimental results. However, considered functions were dependent on beam elastic properties. Thus, homogenised sections were required, which was the case for RC structures. Kotronis (2008) finally proposed a new Timoshenko element where integration functions were independent of material properties. It was also studied in Le Corvec (2012) paper with constraint warping and shear-lag effect description. It appeared that using multi-fibre beam elements in addition to damage and plasticity constitutive laws led to a good representation of structural behaviour. Kotronis (2008) even concluded by explaining that damage and plasticity distributions could be qualitatively determined, predicting critical failure areas. Finally, Caillerie, Kotronis, and Cybulski (2015) also worked on a new Timoshenko element, as well as Capdevielle et al. (2016) where the warping profile was updated based on the damage state.

Not only the shear behaviour has been considered in multi-fibre enhancements. For example, the corrosion consideration was studied by Adelaide, Richard, and Cremona (2011) (model for steel-concrete interface) or by Ragueneau, Q. T. Nguyen, and Berthaud (2006).

2.1.1.2   Formulation in Cast3M (Guedes, Pegon, and Pinto, 1994)

In Cast3M, multi-fibre models are proposed with Timoshenko hypotheses. The general principle is to consider the kinematic hypotheses allowing to pass from global structural displacements (beam scale) to node-local deformations (section scale) (Adelaide, Richard, and Cremona, 2011). The multi-fibre beam element is a FE based on beam theory. Each section is divided into fibres (fig.2.1), and each fibre local constitutive law is applied. The element advantage is that the stress-strain relationship for each fibre is uni-

dimensional. For example, both materials are characterised by a law linking normal and shearing stresses to axial and transverse strains for RC. For the interface, a perfect condition is considered.

Figure 2.1: One section of the multi-fibre model with one fibre of concrete and one of steel

Let us consider a 3D beam of length L and section S (fig.2.2). Figure 2.3 presents the multi-fibre approach developed in Cast3m. It starts with the beam discretisation into beam elements, with two nodes of length l_e. The beam is oriented in the $\vec{x}$-axis, and the sections are discretised on the $\vec{y}$- and $\vec{z}$-axes. For a time step, with the knowledge of beam nodal displacements, the multi-fibre approach gives the associated node forces, following the next steps through three different scales:

1. At the beam scale, nodal displacements $\mathbf{U}_e$ and rotations $\boldsymbol{\theta}_e$ are known for each beam element. Each beam element is composed of twelve DOFs (six per node). Then, generalised strains $\mathbf{E}_{\mathbf{G}}^{(e)}$ are computed with nodal displacements (eq. 2.1) at beam element Gauss points.

$$\mathbf{E}_{\mathbf{G}}^{(e)} = \mathbb{B}.\mathbf{U}_e \tag{2.1}$$

with $\mathbb{B}$ the matrix of derived integration functions.

2. At the section scale, using Timoshenko hypotheses, the strains of all fibres (corresponding to the section integration points) can be deduced given $\boldsymbol{\varepsilon}_e$.

3. At the fibre scale, the constitutive material laws applied on strains leads to the stresses $\boldsymbol{\sigma}_e$ in fibres.

4. Back to the section scale, by integrating stresses on section, generalised stresses $\mathbf{F}_{\mathbf{G}}^{(e)}$ are deduced at section centre, given values at beam element Gauss points.

5. At the beam scale, nodal forces are finally computed by integrating generalised stresses with the beam element (eq. 2.2).

$$\mathbf{F}_e = \int_0^{l_e} \mathbb{B}^T.\mathbf{F}_{\mathbf{G}}^{(e)}.\mathrm{d}x \tag{2.2}$$
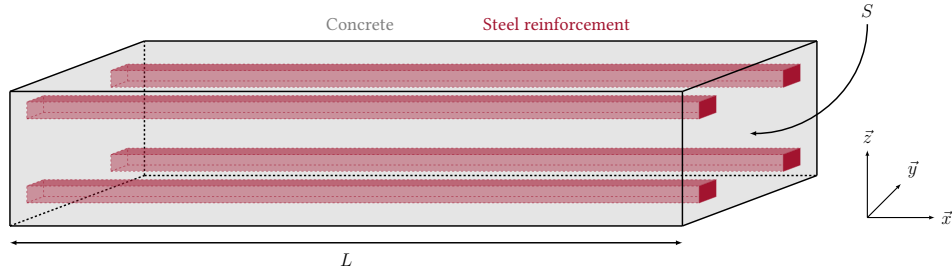
Figure 2.2: Model of a RC beam

Considered integration functions are of first-order : $N_1 = 1 - {x}/{l_e}$ and $N_2 = {x}/{l_e}$. Selecting such functions had an influence on the element numerical performances. Generalised strain linear terms should be eliminated to avoid difficulties linked with shear locking. In addition, Kotronis (2008) recommended a minimum of two Gauss points for each beam element to correctly integrate nodal forces when a nonlinear material behaviour was considered.
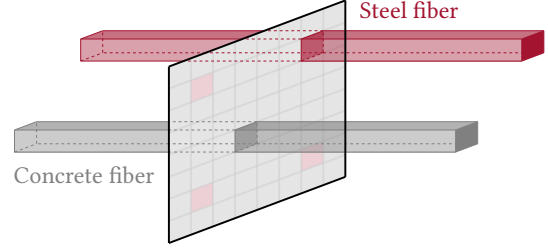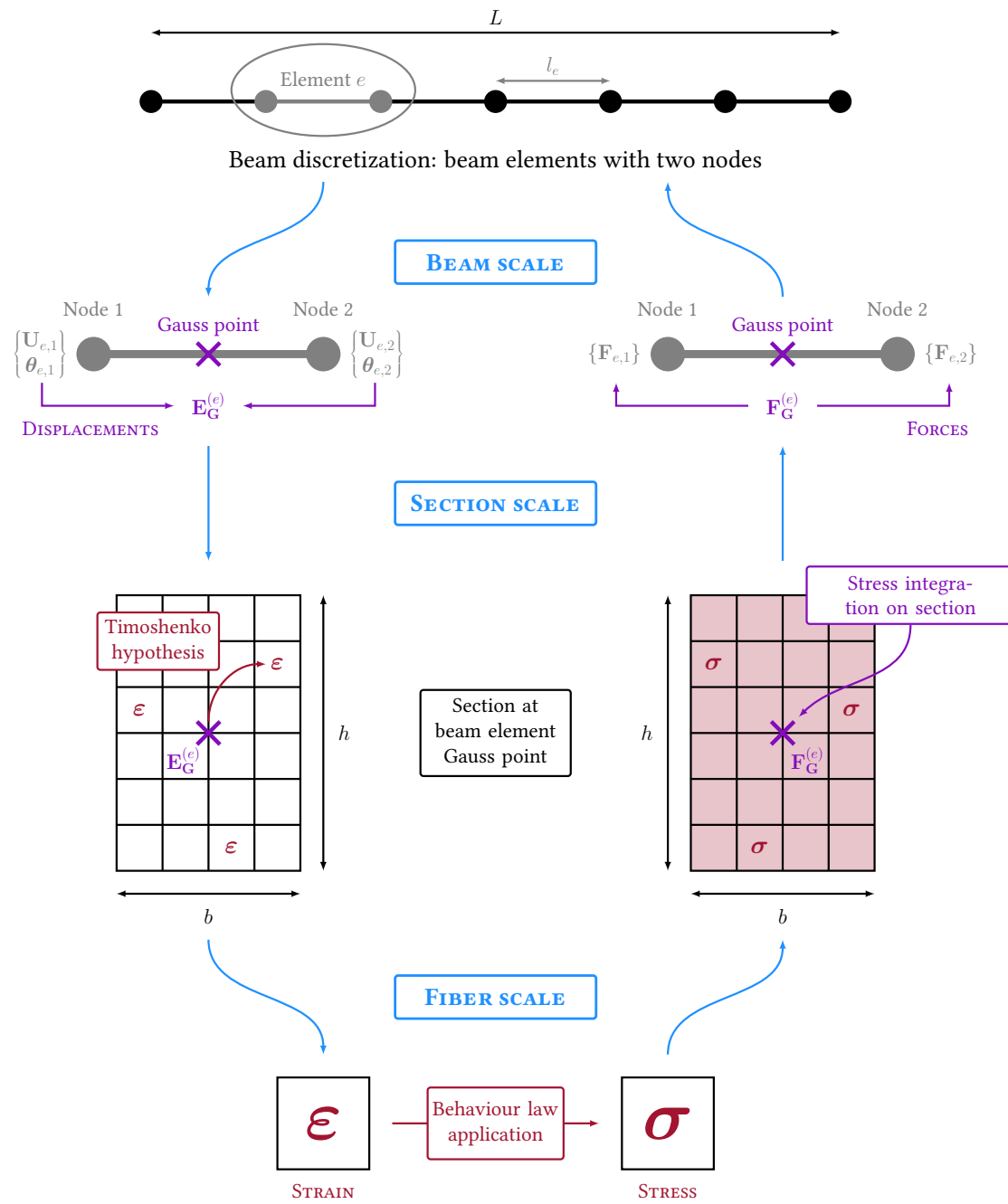
Figure 2.3: Multi-fibre approach algorithm

2.1.2   Beam geometry and boundary conditions

The developed multi-fibre model aims to be as representative as possible of the experimental setup to compare numerical and experimental results. One particular experimentally tested beam is considered for the numerical analysis: the beam referred to as HA16-C1A since they provide analysable experimental results. Two beams of this kind have been constructed: the beam HA16-C1A-1 for quasi-static tests and the beam HA16-C1A-2 for dynamic experiments.

2.1.2.1   Geometry

The beam length is $6\,\mathrm{m}$, and its section $0.2 \times 0.4\,\mathrm{m}^2$, to match the experimental setup. In addition, eight high-adherence (HA) steel rebars of diameter $16\,\mathrm{mm}$ are considered. Figure 2.4 presents the beam discretisation into sections (fig. 2.4c) and the section discretisation into fibres (fig. 2.4b). In figure 2.4c, the sections are positioned at the Gauss points of beam elements. Beam elements are linear segments, so only one Gauss point is considered for each element. Beam and section discretisations are chosen to compromise computational time and the accuracy of results. Mainly, an energetic convergence analysis was performed to validate the section discretisation. Each rebar is modelled with four fibres to take into account rebar sections. Because, experimentally, rebars stayed linear, their discretisation does not significantly influence numerical results. However, concrete discretisation plays a significant role in response accuracy. The beam is excited through its weak axis, so more elements have to be considered along with the section basis, as observed in figure 2.4b. Two-dimensional (2D) linear quadrangle elements are used for concrete (fig. 2.4e), as well as steel rebars (fig. 2.4d). So, four Gauss points are considered in 2D chosen elements. Eight elements on beam width provide an appropriate representation of the evolution of concrete nonlinearities inside the beam.

(a) System scheme

(b) Complete section discretisation

(c) Beam discretisation

(d) Steel rebar discretisation

(e) One element of the concrete section
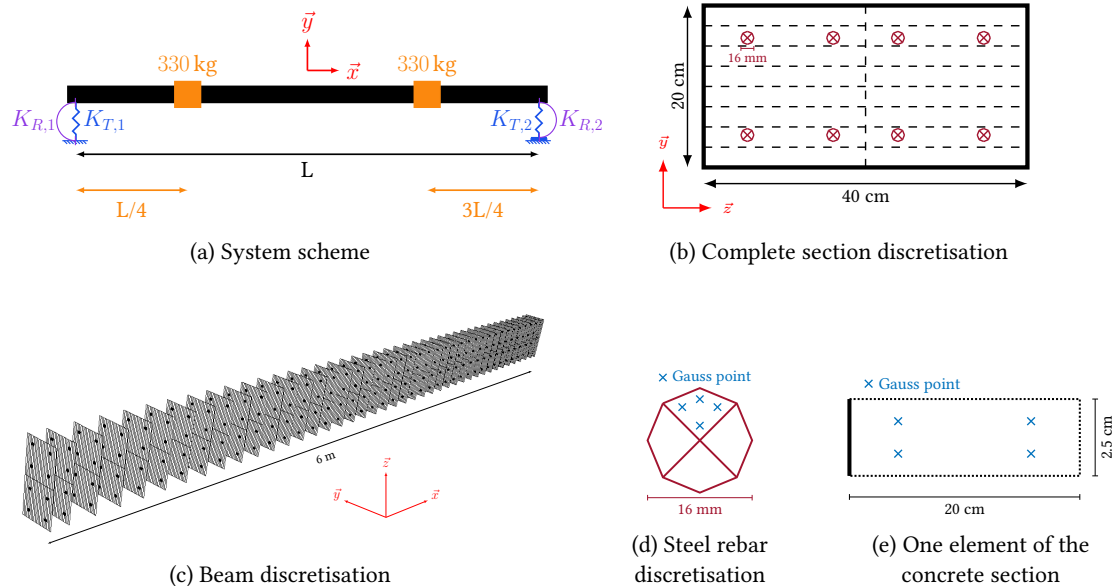
Figure 2.4: Model scheme and discretisation

2.1.2.2   Boundary conditions

Experimental supports were designed to obtain an isostatic system. So, the first numerical model also checked this hypothesis. However, the study of numerical modal properties demonstrated an incompatibility with experimental characteristics of the undamaged beam. Considering simple supports did not allow to match the undamaged beam eigenfrequencies. That is why spring supports are finally preferred (fig. 2.4a). Their calibration is presented in section 2.2.1.

Then, additional masses (fig. 2.4a) are positioned at beam quarter-spans, as done experimentally. Vertical displacements at beam quarter-spans are blocked to model intermediate supports under both masses. Because of the air-cushions under intermediate supports, the friction on the shake table is reduced as much as possible, so horizontal displacements are not numerically constrained.

2.1.3   Material models

2.1.3.1   Concrete model

Concrete is a quasi-brittle material. Nonlinear models are so required to characterise it. Different concrete constitutive laws are implemented in Cast3M. The numerical study aims to evaluate the influence of modelled dissipative phenomena. So, two different models are considered. The simplest model (2.1.3.1(a)), called "BARFRA", was used, for example, by Dufour (1998) or Crambuer (2013). The second one (2.1.3.1(b)), more complex and named "RICBET", was developed by Richard and Ragueneau (2013). The model equations presented in this section will be used to evaluate peculiar dissipative energies.

(a)   BARFRA model   BARFRA is a simple unilateral damage model with damage decoupling between traction and compression. Crack opening in traction is considered by a damage variable, as well as the compressive behaviour. Two different damage variables are considered to consider the concrete asymmetric behaviour.

Table 2.1 presents the variables associated with the BARFRA model, and equation (2.3) expresses the state potential associated with this material model.

<p align="center">Table 2.1: BARFRA constitutive model variables</p>

Observable	Internal	Associated forces	Phenomena
ε	$\longrightarrow$	σ	Elasticity
	$d_+ \longrightarrow$	Y_+	Damage ($\varepsilon > 0$) - stiffness degradation
	$d_- \longrightarrow$	Y_-	Damage ($\varepsilon < 0$) - stiffness degradation
	$z_+ \longrightarrow$	Z_+	Isotropic hardening ($\varepsilon > 0$)
	$z_- \longrightarrow$	Z_-	Isotropic hardening ($\varepsilon < 0$)

$$\rho\Psi = \frac{1}{2}(1 - d_+)\langle\varepsilon_{ij}\rangle_+ C_{ijkl} \langle\varepsilon_{kl}\rangle_+ + H_+(z_+) + \frac{1}{2}(1 - d_-)\langle\varepsilon_{ij}\rangle_- C_{ijkl} \langle\varepsilon_{kl}\rangle_- + H_-(z_-) \quad (2.3)$$

with Ψ the state potential, ρ the density, d_+ and d_- the damage variables respectively associated with positive and negative strains, $\langle\varepsilon_{ij}\rangle_+$ and $\langle\varepsilon_{ij}\rangle_-$ respectively the positive and negative strain parts, z_+ and z_+ the work hardening variables associated with d_+ and d_-, H_+ and H_- functions, and C_{ijkl} the

$ijkl$th term of the elasticity tensor. Then, state laws, expressed in equation (2.4), can be deduced from equation (2.3):

$$
\begin{cases}
\sigma_{ij} = \dfrac{\partial \rho \Psi}{\partial \varepsilon_{ij}} = (1 - d_+)\, C_{ijkl} \left\langle \varepsilon_{kl} \right\rangle_+ + (1 - d_-)\, C_{ijkl} \left\langle \varepsilon_{kl} \right\rangle_- \\[2ex]
Y_+ = -\dfrac{\partial \rho \Psi}{\partial d_+} = \dfrac{1}{2} C_{ijkl} \left\langle \varepsilon_{kl} \right\rangle_+^2 \\[2ex]
Y_- = -\dfrac{\partial \rho \Psi}{\partial d_-} = \dfrac{1}{2} C_{ijkl} \left\langle \varepsilon_{kl} \right\rangle_-^2 \\[2ex]
Z_+ = \dfrac{\partial \rho \Psi}{\partial z_+} = \dfrac{\mathrm{d} H_+(z_+)}{\mathrm{d} z_+} \\[2ex]
Z_- = \dfrac{\partial \rho \Psi}{\partial z_-} = \dfrac{\mathrm{d} H_-(z_-)}{\mathrm{d} z_-}
\end{cases}
\tag{2.4}
$$

with Y_+ and Y_- the restitution rates for damage and Z_+ and Z_- the thermodynamic forces related to a kinematic work hardening. Finally, by applying Clausius-Duhem inequality, the dissipation law of the BARFRA model is given in equation (2.5):

$$
\mathcal{D} = \begin{pmatrix} Y_+ \\ Y_- \\ -Z_+ \\ -Z_- \end{pmatrix}^T \cdot \begin{pmatrix} \dot{d}_+ \\ \dot{d}_- \\ \dot{z}_+ \\ \dot{z}_- \end{pmatrix} \geqslant 0
\tag{2.5}
$$

(b)   RICBET model   RICBET is a more complex model well adapted for cyclic and seismic loadings, including more complex phenomena. It considers damage in tension, plasticity in compression, the unilateral concrete effect associated with inelastic crack closure, and friction phenomena between crack surfaces. It is characterised by twelve parameters: two for the elasticity range, two for the damage modelling, two for friction, one for the unilateral effect and five for plasticity.

Table 2.2 presents the RICBET model variables. Equation (2.6) expresses the state potential associated with this material model:

$$
\rho \Psi = \frac{1}{2} \left(1 - d\right) . \left(\varepsilon_{ij} - \varepsilon_{ij}^p\right) C_{ijkl} \left(\varepsilon_{kl} - \varepsilon_{kl}^p\right) + \frac{1}{2} d . \left(\varepsilon_{ij} - \eta . \varepsilon_{ij}^{\pi} - \varepsilon_{ij}^p\right) C_{ijkl} \left(\varepsilon_{kl} - \eta . \varepsilon_{ij}^{\pi} - \varepsilon_{kl}^p\right)
$$
$$
+ \frac{1}{2} \gamma . \alpha_{ij}\, \alpha_{ij} + H(z) + G(p) \quad \text{(2.6)}
$$

with d the damage variable, ε_{ij}, ε_{ij}^p and ε_{ij}^{π} respectively the total, plastic and friction strains, η the unilateral effect internal variable, C_{ijkl} the $ijkl$th term of elasticity tensor, γ a coefficient relative to friction, α_{ij} the friction work hardening internal variable, H and G some functions respectively of damage work hardening z and of plasticity internal variable p. Then, state laws can be deduced as expressed in equation (2.7):

Table 2.2: RICBET constitutive model variables

Observable	Internal	Associated forces	Phenomena
ε	$\longrightarrow$	σ	Elasticity
	$\varepsilon^{\pi} \longrightarrow$	σ^{π}	Friction
	$\varepsilon^{p} \longrightarrow$	σ	Plasticity
	$\alpha \longrightarrow$	X	Kinematic hardening associated to friction
	$d \longrightarrow$	Y	Damage - stiffness degradation
	$z \longrightarrow$	Z	Isotropic hardening associated to damage
	$\eta \longrightarrow$	ξ	Unilateral effect
	$p \longrightarrow$	R	Isotropic hardening associated to plasticity

$$
\begin{cases}
\sigma_{ij} = \dfrac{\partial \rho \Psi}{\partial \varepsilon_{ij}} = -\dfrac{\partial \rho \Psi}{\partial \varepsilon_{ij}^{p}} = (1-d).C_{ijkl}\left(\varepsilon_{kl} - \varepsilon_{kl}^{p}\right) + d.C_{ijkl}\left(\varepsilon_{kl} - \eta.\varepsilon_{kl}^{\pi} - \varepsilon_{kl}^{p}\right) \\[2ex]
\sigma_{ij}^{\pi} = -\dfrac{\partial \rho \Psi}{\partial \varepsilon_{ij}^{\pi}} = \eta.d.C_{ijkl}\left(\varepsilon_{kl} - \eta\varepsilon_{kl}^{\pi} - \varepsilon_{kl}^{p}\right) \\[2ex]
Y = -\dfrac{\partial \rho \Psi}{\partial d} = \dfrac{1}{2}\left(\varepsilon_{ij} - \varepsilon_{ij}^{p}\right)C_{ijkl}\left(\varepsilon_{kl} - \varepsilon_{kl}^{p}\right) - \dfrac{1}{2}\,d.\left(\varepsilon_{ij} - \eta.\varepsilon_{ij}^{\pi} - \varepsilon_{ij}^{p}\right)C_{ijkl}\left(\varepsilon_{kl} - \eta\varepsilon_{ij}^{\pi}\right) \\[2ex]
\zeta = -\dfrac{\partial \rho \Psi}{\partial \eta} = d.\varepsilon_{ij}^{\pi}C_{ijkl}(\varepsilon_{kl} - \varepsilon_{kl}^{\pi} - \varepsilon_{kl}^{p}) \\[2ex]
R = \dfrac{\partial \rho \Psi}{\partial p} = \dfrac{dG(p)}{dp} \\[2ex]
X_{ij} = \dfrac{\partial \rho \Psi}{\partial \alpha_{ij}} = \gamma.\alpha_{ij} \\[2ex]
Z = \dfrac{\partial \rho \Psi}{\partial z} = \dfrac{dH(z)}{dz}
\end{cases}
\tag{2.7}
$$

with σ_{ij} and σ_{ij}^{π} the total and friction stresses, Y and ζ the restitution rates for damage and unilateral effect, R and Z the thermodynamic forces related to an isotropic work hardening and X_{ij} the thermodynamic force related to a kinematic work hardening. Finally, by applying Clausius-Duhem inequality, we get the RICBET model dissipation law in equation (2.8):

$$
\mathcal{D} =
\begin{pmatrix}
\sigma_{ij} \\
\sigma_{ij}^{\pi} \\
Y \\
\zeta \\
-R \\
-X_{ij} \\
-Z
\end{pmatrix}^{T}
\cdot
\begin{pmatrix}
\dot{\varepsilon}_{ij}^{p} \\
\dot{\varepsilon}_{ij}^{\pi} \\
\dot{d} \\
\dot{\eta} \\
\dot{p} \\
\dot{\alpha}_{ij} \\
\dot{z}
\end{pmatrix}
\geqslant 0
\tag{2.8}
$$

(c)   Comparison of cyclic responses   Figure 2.5 presents the constitutive law of both models for one concrete element submitted to traction and compression excitations. Figures 2.5a and 2.5b show one cycle of traction and compression. The compressive plasticity behaviour of RICBET leads to lower maximal compressive stresses, compared to the BARFRA model considering a linear behaviour in the studied strain range. For RICBET, the development of nonlinearities in compression occurs at $15.8\,\mathrm{MPa}$ corresponding to $45\% \times f_c$ with f_c the concrete compressive strength. Experiments carried out do not reach nonlinearities in compression. That is why the model traction behaviours are more of interest and are presented in figures 2.5c and 2.5d. Six traction cycles are applied on the element with increasing cycle amplitudes. Both models are linear until the tensile strength of $1\,\mathrm{MPa}$. Then, damage appears for BARFRA, as soon as the tensile strength is reached. So, the stiffness is deteriorating, and lower stresses are obtained. An exponential decrease in strength is considered, converging towards $0.5\,\mathrm{MPa}$, the residual tensile strength. Figure 2.5a shows a sudden change in stiffness between traction and compression behaviours of the BARFRA model, compared to the RICBET one. The behaviour of the RICBET model is more complex. After reaching the tensile strength, the stress rises slightly, but nonlinearities begin to occur. Then, as for BARFRA, an exponential decrease of the stress limit is observed. During unloadings, hysteresis cycles are obtained corresponding to the energy dissipated by friction. When a null strain is reached, the stiffness is slightly recovered. This unilateral effect gives an intermediate stiffness between traction and compression cycles, leading to a smoother transition.

(a) BARFRA - traction/compression

(b) RICBET - traction/compression

(c) BARFRA - traction cycles

(d) RICBET - traction cycles
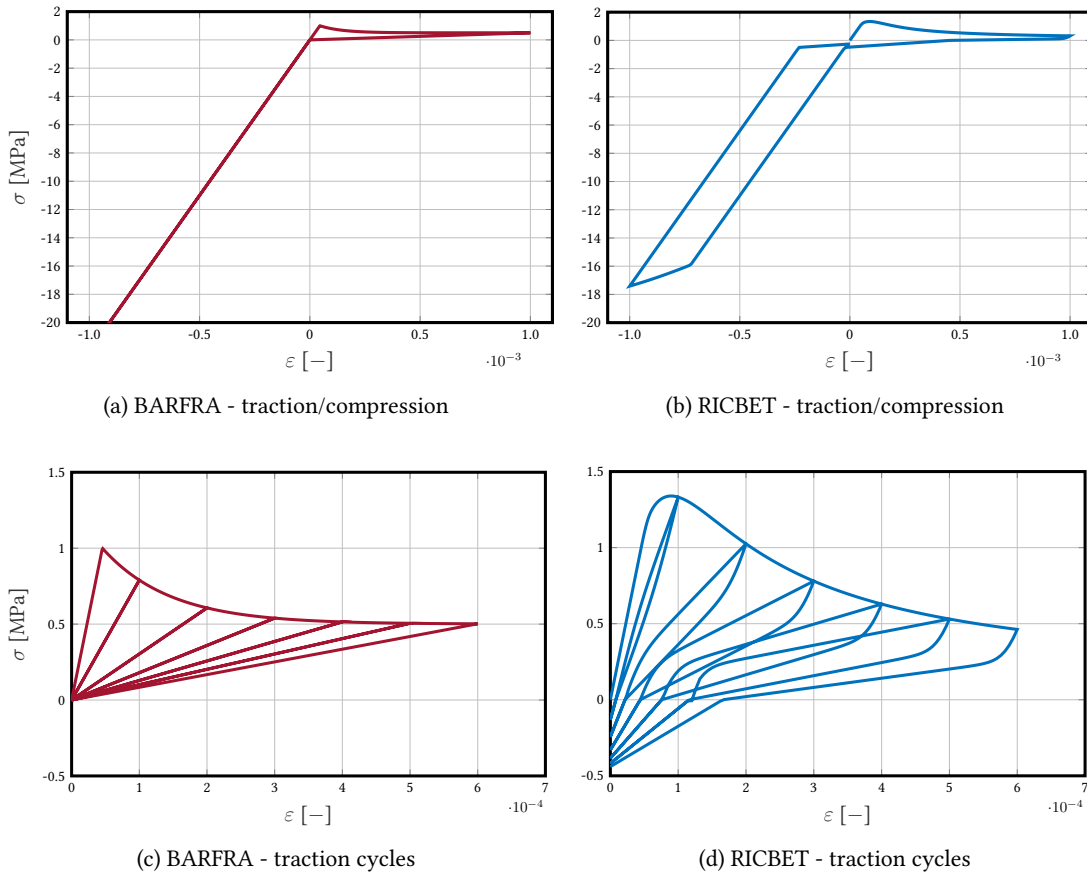
Figure 2.5: Constitutive laws for one concrete element

(d)   Concrete dissipative phenomena   Desmorat, Ragueneau, and Pham (2007) gave a signification of dissipative phenomena: (i) damage is characterising crack opening leading to a decrease of Young's modulus, (ii) the unilateral effect is the opposite because it corresponds to the crack closure and stiffness recovery, and (iii) the friction is a consequence of crack surface roughness and aggregate interlock, leading to inelastic strains and dilatancy. Crack surfaces and aggregate contacts are submitted to friction sliding due to roughness. The macroscopic consequence is the appearance of hysteresis loops. All these phenomena have been studied in different papers like (T. P. Tassios and Vintzēleou, 1987; Riggs and Powell, 1986; Basista and Gross, 1998) for crack evolution, (Halm and Dragon, 1998; Zhu, Kondo, and Shao, 2008) for damage and friction or (Dragon, Halm, and Désoyer, 1998) considering the unilateral effect. The scheme in figure 2.6 proposes a synthesise of all presented works to understand the microscopic representation of modelled dissipative phenomena. The traction response of the RICBET model is considered as a basis. In the elastic part, no damage occurs in concrete. After the tensile strength, cracks begin to initiate and propagate, leading to a loss of stiffness. In parallel with crack propagations, cracks are opening up more and more while loading is still increasing. Then, during unloading, cracks are closing, and contacts appear and induce locking because of rough lips. Nevertheless, sliding occurs if the unloading continues, and some energy is dissipated through friction. Finally, a part of the stiffness is recovered when the cracks are closed again.
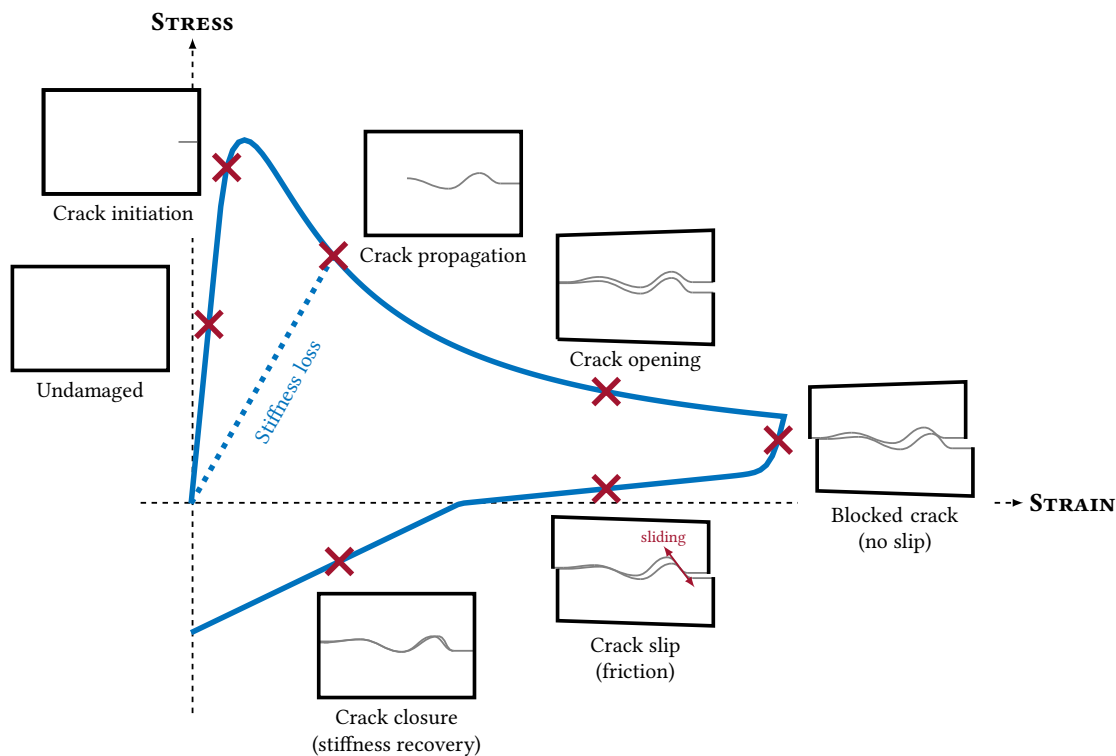
Figure 2.6: Scheme of concrete dissipative phenomena

2.1.3.2   Steel model

The experimental campaign aim was to keep steel reinforcements in their linear range. That is why the model choice for steel is not as fundamental as concrete.

An elastoplastic behaviour law, already implemented in Cast3M, is considered. Its name is "ACIER_UNI", and an elastoplastic law characterises it with linear hardening and the parameters in table 2.3. The behaviour law is expressed in equations (2.9) and (2.10):

$$\sigma^* = (1 - b)\frac{\varepsilon^*}{\left(1 + \varepsilon^{*R}\right)^{1/R}} + b.\varepsilon^* \tag{2.9}$$

$$R(\xi) = R_0 - \frac{a_1.\xi}{a_2 + \xi} \tag{2.10}$$

with $\sigma^* = \frac{\sigma}{\sigma_0}$, $\varepsilon^* = \frac{\varepsilon}{\varepsilon_0}$, $b = \frac{E_h}{E_s}$ and $R(\xi)$ representing the Bauschinger effect. Classical recommended values of the parameters are also expressed in table 2.3, while appendix B.2 presents the parameter significations. No dissipation will occur at the steel level, so the model equations are not developed herein.

Table 2.3: ACIER_UNI behaviour model parameters (appendix. B.2)

Name	Value	Unit	Name	Value	Unit
YOUN	208	GPa	NU	0.3	—
RHO	7850	kg/m^3	STSY	560	MPa
EPSU	0.05	—	STSU	656	MPa
EPSH	0.0025715	—	FALD	12.5	—
A6FA	620	—	CFAC	0.50	—
AFAC	0.006	—	R0FA	20	—
BFAC	0.000877	—	A1FA	18.5	—
A2FA	0.15	—			

2.1.4   Loading

Experimental input signals were presented in section 1.4.3. Numerically, the same input data have been considered to excite the beams.

Quasi-static experiments were carried out with actuators. Numerically, imposed displacements are applied at beam quarter-spans corresponding to the actuator positions. The signal in figure 1.21a is symmetrically applied at both input points, exciting the first mode of the beam. The numerical response will be used in section 2.2.2 to calibrate the concrete constitutive model parameters.

Dynamic tests were performed with a shake table. So, the acceleration received by the beam is transformed into a load equivalent loading. This load is applied under each node of the model. The succession of dynamic signals in table 2.4 was tested experimentally. So, the same succession is considered numerically to study the loading history influence. The signals in figure 1.23 are mainly the first and second studied signals.

2.2   Model calibration

To better represent the observed behaviour, the multi-fibre model must be calibrated. Notably, the undamaged modal properties (2.2.1) and the concrete model parameters (2.2.2) significantly influence the numerical responses and have to be carefully identified.

Table 2.4: The succession of dynamic signals

	Name	Maximal acceleration		Name	Maximal acceleration
1	WN1	$0.65\,\mathrm{m/s^2}$	**2**	DSS85b	$1.33\,\mathrm{m/s^2}$
3	DSS52b	$1.84\,\mathrm{m/s^2}$	**4**	DSS52a	$0.93\,\mathrm{m/s^2}$
5	DSS52a	$1.40\,\mathrm{m/s^2}$	**6**	DSS52a	$2.05\,\mathrm{m/s^2}$
7	DSS52a	$2.91\,\mathrm{m/s^2}$	**8**	WN1	$2.09\,\mathrm{m/s^2}$
9	WN1	$2.66\,\mathrm{m/s^2}$	**10**	WN1	$2.88\,\mathrm{m/s^2}$
11	DSS138b	$0.45\,\mathrm{m/s^2}$	**12**	DSS138b	$0.44\,\mathrm{m/s^2}$
13	DSS138b	$0.48\,\mathrm{m/s^2}$	**14**	DSS138b	$0.50\,\mathrm{m/s^2}$

Experimentally, the beam three first eigenfrequencies are studied because they are in the available facility range. However, being at the instrumentation and shake table range limits, the third value must be considered with caution. Numerically, the VIBR operator in Cast3M is a tool to study generalised masses $\left(\underline{\phi}_i^T \cdot \mathbb{M} \cdot \underline{\phi}_i\right)$ and so the effective modal ones $m_{i,d}$ defined in equation (2.11):

$$m_{i,d} = \frac{\left(\underline{\phi}_i^T \cdot \mathbb{M} \cdot \mathbf{I}_d\right)^2}{\left(\underline{\phi}_i^T \cdot \mathbb{M} \cdot \underline{\phi}_i\right)} \qquad (2.11)$$

with $m_{i,d}$ the effective modal mass in direction d and associated with mode i and $\mathbf{I}_d$ a vector composed of "1" values for components in the d-direction and "0" values for other components. In the y-direction, corresponding to the beam excitation one, the sum of thirty modal masses gives a total mass of $1792.2\,\mathrm{kg}$ for the beam. Then, considering only the three first modes leads to $1776.4\,\mathrm{kg}$ corresponding to 99.1% of the total mass. So, using the three first modes of the beam for its analysis is representative of the global beam behaviour.

2.2.1 Stiffness support calibration

Hammer shock tests on the undamaged beams gave their three first eigenfrequencies (tab. 2.5). Numerical modal analyses did not match the experimental eigenfrequencies with the isostatic boundary conditions. So, spring supports are preferred with translational and rotational stiffnesses. Due to the setup symmetry, identical stiffnesses of each type are considered for both supports. Their calibrations were performed with a methodology equivalent to meta-models. Four parameters were examined: (i) the concrete Young's modulus, (ii) the steel Young's modulus, (iii) the translational support stiffness, and (iv) the rotational support stiffness. Numerous computations with evolving values of these parameters led to a response surface evaluation. Then, the surface extrapolation gave the best four parameters to characterise the two first beam eigenfrequencies. The third one was not considered because the confidence in experimental measurements was low. Finally, few iterations were performed on smaller grids until the convergence of parameters. Three beams were experimentally studied, and the parameters in table 2.6 were identified.

Stiffnesses in table 2.6 are identical for the three beams because the same supports were used for the experimental tests. Higher differences are obtained on Young's modulus values. For concrete, differences can be a consequence of material variability. However, steel rebars have been manufactured, so less variability is usually observed. What can explain the variations between the beams is the rebar

Table 2.5: Eigenfrequencies of the three tested beams

Beam	f_1 [Hz]	f_2 [Hz]	f_3 [Hz]
HA12	7.05	23.2	59.1
HA16	7.24	23.5	58.8
HA20	7.16	22.6	57.9

Table 2.6: Support calibrations of three beams

Beam	Concrete Young's modulus	Steel Young's modulus	Translational stiffness	Rotational stiffness
HA12	19 GPa	184 GPa	1.10×10^7 N/m	1.00×10^4 N.m/rad
HA16	22 GPa	208 GPa	1.10×10^7 N/m	1.00×10^4 N.m/rad
HA20	22 GPa	196 GPa	1.10×10^7 N/m	1.00×10^4 N.m/rad

positions. Experimentally, the rebars could be slightly shifted from one beam to another. In addition, a parametric numerical study demonstrated the significant influence of rebar positions on the modal properties of the undamaged beams. The three numerical models consider perfect rebar positions. So, the exact experimental placings can be reflected numerically in steel Young's modulus.

2.2.2   Model parameters identification

BARFRA and RICBET concrete models presented in section 2.1.3.1 comprise nine and fifteen parameters. To determine the parameter values, a parametric study is performed to match the experimental responses of the quasi-static test QSC1. Identified parameters are indicated in table 2.7 for the BARFRA model and in table 2.8 for RICBET, respectively associated with appendices B.1.1 and B.1.2 for parameter descriptions.

Table 2.7: BARFRA behaviour model values (appendix. B.1.1)

Name	Symbol	Value	Unit	Name	Symbol	Value	Unit
YOUN	E_c	22	GPa	NU	ν	0.2	—
RHO	ρ_c	2300	kg/m^3	FC	f_c	25	MPa
FC_R	$f_{r,c}$	0.05	MPa	STRC	$\varepsilon_{s,c}$	1.0×10^{-5}	—
FT	f_t	1.0	MPa	FT_R	$f_{r,t}$	0.5	MPa
STRT	$\varepsilon_{s,t}$	1.0×10^{-5}	—				

Figure 2.7 exhibits the numerical responses of both constitutive models for the QSC1 test. Experimental global stiffness degradation is adequately represented with both concrete models. However, differences are observed following the phenomena described with each model. With RICBET (fig. 2.7b), hysteretic cycles are developing, and the pinching effect is observable due to crack closure. A better match with experimental data is thus obtained with the more complex model because it better characterises dissipative phenomena.

Table 2.8: RICBET behaviour model values (appendix. B.1.2)

Name	Symbol	Value	Unit	Name	Symbol	Value	Unit
YOUN	E_c	22	GPa	NU	ν_c	0.2	−
RHO	ρ_c	2300	kg/m^3	FT	f_t	1.0	MPa
ALDI	$a_{b,t}$	9.0×10^{-3}	−	GAM1	γ_1	9.0	−
A1	a_1	10×10^{-6}	−	SIGF	σ_{cc}	−0.5	MPa
FC	f_c	35	MPa	AF	a_f	7.5	−
AG	a_g	1.0	−	AC	a_c	4.0×10^{10}	−
BC	b_c	600	−	SIGU	σ_u	−10	MPa
HYST	a_h	1	−				

(a) BARFRA

(b) RICBET
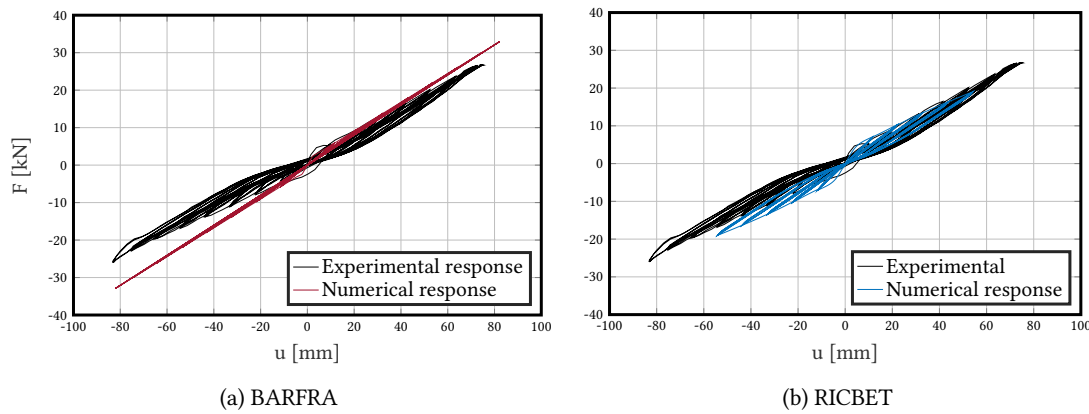
Figure 2.7: Responses of the calibrated concrete models in comparison with the experimental quasi-static data

2.2.3   Global stiffness correction - dynamic loading

Two HA16-C1A beams were constructed to perform the experimental campaign. The beam HA16-C1A-1 was tested under quasi-static excitations, and its properties were used in previous analyses to calibrate the multi-fibre model. Then, the HA16-C1A-2 beam was used to carry out dynamic experiments. Despite the identical properties desired, few differences are obtained between the two beams: particularly on undamaged beam eigenfrequencies, as indicated in table 2.9.

Theoretical values are deduced from equation (2.12) for the mode i using a homogenised RC section:

$$f_i = \frac{\omega_i}{2.\pi} = \frac{(i \times \pi)^2}{2.\pi} \sqrt{\frac{E_c.I_h}{\rho_c.S_h.L^4}} \tag{2.12}$$

with E_c the concrete Young's modulus, I_h the homogenised quadratic inertia of the section, ρ_c the concrete density, S_h the homogenised area of the section, and L the beam length. Comparing mean experimental data and numerical ones shows perfect adequacy for the first mode and an acceptable one for the second mode. However, a more significant error is obtained for the third mode, which could result from instrumentation limits. Less confidence is associated with the third eigenfrequency, so it is not calibrated.

Table 2.9: Eigenfrequencies of the undamaged tested beams HA16-C1A in comparison with theoretical data

	Theory	**Beam HA16-C1A-1**[1]	**Beam HA16-C1A-2**[1]	**Mean of both beams**[2]
Mode 1	$7.04\,\mathrm{Hz}$	$7.24\,\mathrm{Hz}^{(0.41\%)}$	$6.99\,\mathrm{Hz}^{(0.68\%)}$	$7.11\,\mathrm{Hz}^{(+0.99\%)}$
Mode 2	$23.9\,\mathrm{Hz}$	$23.5\,\mathrm{Hz}^{(0.35\%)}$	$22.6\,\mathrm{Hz}^{(0.00\%)}$	$23.1\,\mathrm{Hz}^{(-3.35\%)}$
Mode 3	$68.9\,\mathrm{Hz}$	$58.8\,\mathrm{Hz}^{(0.10\%)}$	$57.6\,\mathrm{Hz}^{(0.17\%)}$	$58.2\,\mathrm{Hz}^{(-15.5\%)}$

[1] Indicated frequency corresponds to the mean value of four hammer shock tests, and the exponent is the standard deviation of the four tests.
[2] The exponent corresponds to the error with the theoretical value in the first column.

Then, experimental values for the beams HA16-C1A-1 and HA16-C1A-2 are deduced from hammer shock tests before any excitation to obtain undamaged properties. For each value determination, a mean of four test responses is computed and standard deviations, always inferior to 1%, demonstrate good repeatability of experiments. However, between the beams, non-negligible eigenfrequency differences are deduced. So, the model calibration on the HA16-C1A-1 beam could present difficulties in representing experimental dynamic test responses. That is why few corrections are applied on the numerical model and particularly on the concrete Young's modulus, based on the beam HA16-C1A-2 properties. Identified Young's modulus from the quasi-static test is 22 GPa, while experimental characterisation of this material property was 26.2 GPa. Using the experimental Young's modulus gives $f_1 = 6.89\,\mathrm{Hz}$ and $f_2 = 20.7\,\mathrm{Hz}$ corresponding respectively to 3.09% and 10.3% of error compared to the mean values in table 2.9. Recalibrating Young's modulus on the first mode leads to 28.5 GPa and an error of 8.35% on the second mode eigenfrequency. While a recalibration on the second mode provides Young's modulus of 40.4 GPa and an error of 13.8% on the first mode eigenfrequency. In conclusion, increasing Young's modulus of 8% to match the first mode eigenfrequency is acceptable, mainly because the induced error on the second mode eigenfrequency is still admissible. However, the second mode's calibration requires a 54% increase of Young's modulus and a too large error on the first mode.

Finally, table 2.10 synthesises the numerical eigenfrequencies with the three concrete Young's modulus. Numerical dynamic analyses are performed on the undamaged white-noise signal called WN1 to validate the carried out corrections. With the BARFRA model, the three concrete Young's modulus values do not affect the numerical response global stiffness. However, with RICBET constitutive model, few differences are observed. So, a compromise is performed between the different analyses, and a concrete Young's modulus of 26.2 GPa (corresponding to the value obtained with the compressive tests) is finally chosen for the dynamic computations. It represents a ratio of 1.2 compared to the 22 GPa identified with the undamaged modal analyses. So, the ratio is close to the 1.25 multiplier generally considered between quasi-static and dynamic Young's modulus.

2.3   Viscous damping formulations

***Reminder:** The nomenclature of the classical damping formulation acronyms used in the following can be found in appendix A (table A.1).*

As discussed in the literature, numerical model parameters significantly influence dynamic responses.

Table 2.10: Influence of concrete Young's modulus in undamaged numerical eigenfrequencies

	Experimental	**Numerical**[1]		
		$E_c = 22\,\text{GPa}$	$E_c = 26.2\,\text{GPa}$	$E_c = 28.5\,\text{GPa}$
Mode 1	$7.11\,\text{Hz}$	$6.45\,\text{Hz}^{(-9.3\%)}$	$6.89\,\text{Hz}^{(-3.1\%)}$	$7.11\,\text{Hz}^{(0.0\%)}$
Mode 2	$23.1\,\text{Hz}$	$19.7\,\text{Hz}^{(-14.7\%)}$	$20.7\,\text{Hz}^{(-10.5\%)}$	$21.2\,\text{Hz}^{(-8.4\%)}$
Mode 3	$58.2\,\text{Hz}$	$44.7\,\text{Hz}^{(-23.2\%)}$	$46.0\,\text{Hz}^{(-21.0\%)}$	$46.6\,\text{Hz}^{(-20.0\%)}$

[1] Exponents correspond to the error with the experimental value in the first column.

By using the experimental data, a numerical parametric study is performed with: (i) two concrete constitutive models to evaluate the required accuracy of dissipation representation, (ii) sixteen classical viscous damping formulations with or without parameter updates, and (iii) various damping ratios varying from 0.5% to 5% for different modes. Thus, the analysis aims to discuss the ability of different structural viscous damping models to represent the observed behaviour of the modelled RC beam.

2.3.1   Classification

Table 2.11 synthesises studied viscous damping formulations, which have been implemented based on the mass and stiffness matrices or with modal analyses. The first column indicates the nomenclature already used in chapter 1 and links to the names in the second column. Damping ratios (third column) are imposed for different modes indicated in the fourth column for all damping formulations. Finally, in the last one, a ✗ indicates that the considered parameters are constant during computations, while a ✓ implies parameter updates corresponding to the multiplicative parameters in front of the matrices. More implementation details are presented in section 2.3.2.

2.3.2   Implementation details

2.3.2.1   Damping matrix computations

(a)   Rayleigh damping and derivatives   Rayleigh damping (RD) type formulations, discussed in section 1.2.2.1 and derived from equation (1.26), are the first ten (RD p% to SKPD p%) in table 2.11. For RD, MPD and KPD formulations, for which only initial beam properties are required, the mass (MASS operator) and/or the initial stiffness (RIGI operator) matrices are computed from the structural properties, particularly considering the additional masses (MASS operator) for the mass matrix and the boundary conditions (BLOQ operator) for the stiffness matrix. Then, to solve the system in equation (1.27) and determine a_0 and/or a_1 parameters, modal analysis (VIBR operator) is performed on the undamaged beam, and two damping ratios are chosen for some modes. When two modes are required (RD, for example), modes 1 and 2 are considered because they are used for modal calibration. However, if only one mode is required, the first one is chosen because the beam response depends on it. Finally, the damping matrix is assembled. Then, when the secant or tangent stiffness matrix is used (CRD, SRD, CKPD and SKPD), the stiffness matrix is re-evaluated at the end of each time step using the tangent or secant Young's modulus, whose computation is explained in section 2.3.2.2. In these cases, parameters a_0 and a_1 are constant during all computations. On the contrary, the initial stiffness is kept all   along   with computation   when   the   parameters   are   updated (RD_ACT, MPD_ACT   and   KPD_ACT).

Table 2.11: Damping classification

Classification	Formulation	Damping ratio	Mode	Parameter updating[1]
RD p%	Classical Rayleigh damping	p %	1 and 2	✗
RD_ACT p%	Classical Rayleigh damping	p %	1 and 2	✓
CRD p%	Commit-stiffness Rayleigh damping[2,3]	p %	1 and 2	✗
SRD p%	Secant-stiffness Rayleigh damping[2]	p %	1 and 2	✗
MPD p%	Mass proportional damping	p %	1	✗
MPD_ACT p%	Mass proportional damping	p %	1	✓
KPD p%	Initial-stiffness proportional damping	p %	1	✗
KPD_ACT p%	Initial-stiffness proportional damping	p %	1	✓
CKPD p%	Commit-stiffness proportional damping[2,3]	p %	1	✗
SKPD p%	Secant-stiffness proportional damping[2]	p %	1	✗
MD p%	Modal damping	p %	1 to 6	✗
MD_ACT p%	Modal damping	p %	1 to 6	✓
WPD p%	Wilson-Penzien damping	p %	1 to 6	✗
WPD_ACT p%	Wilson-Penzien damping	p %	1 to 6	✓
CWPD p%	Commit-stiffness Wilson-Penzien damping[2,3]	p %	1 to 6	✗
SWPD p%	Secant-stiffness Wilson-Penzien damping[2]	p %	1 to 6	✗

[1] ✗ means that the parameters stay constant during the computation while ✓ indicates parameter updates. For the last case, modal analysis is performed, and the updated eigenfrequencies are used to compute the new parameters. The damping ratio stays constant.

[2] The stiffness matrix is updated for each time step.

[3] The commit-stiffness is equivalent to the tangent-stiffness except that the "commit" term is used when the matrix is updated only after each time step (and not after each iteration).

However, the frequencies used for the parameter computations are determined at each time step with a modal analysis. Viscous damping ratios ξ_1 and ξ_2 are, for their part, constants.

(b) Modal damping Modal damping formulations (MD and MD_ACT) are expressed in equation (1.34). To compute the damping matrix, a modal analysis on the undamaged beam is required (`VIBR` operator) to determine the eigenfrequencies or eigenperiods and the eigenmodes. The number of considered modes is at the user appreciation. A compromise between time computation and accuracy must be judged. The significant influence of the three first modes has already been discussed using effective modal mass determination. In addition, slightly increasing the number of modes does not influence the computational time. Choosing an even number of modes avoids reaching negative damping ratios for higher modes. So, a choice of six modes is made for modal damping formulations. With Cast3M, `XXT` and `XTMX` operators are used to compute the numerator $\left(\left(\mathbb{M}\underline{\phi}_i \right) \left(\mathbb{M}\underline{\phi}_i \right)^T \right)$ and denominator $\left(\underline{\phi}_i^T \mathbb{M}\underline{\phi}_i \right)$ for each term of the sum. For MD, the damping matrix computation is performed only at the beginning. However, for MD_ACT, an updated modal analysis is performed at each time step given new eigenperiods and eigenmodes, and the matrix is re-composed with the updated modal properties.

(c) Wilson-Penzien damping Wilson-Penzien damping (WPD) formulation and derivatives (WPD, WPD_ACT, CWPD and SWPD) correspond to equation (1.31). The damping matrix computation is strongly similar to MD formulations. A modal analysis is performed to determine the eigenmodes and eigenfrequencies. Then, `XXT` $\left(\underline{\phi}_i \underline{\phi}_i^T \right)$ and `XTMX` $\left(\mathbb{M} \cdot \left[\sum_{i=1}^{N-1} \frac{2\xi_i \omega_i}{m_i} \underline{\phi}_i \underline{\phi}_i^T \right] \cdot \mathbb{M} \right)$ operators are applied for each mode to evaluate the terms of the sum associated with the considered modes. Finally, considering six modes, for the same reasons as MD, leads to the computation of equation (1.31) second part. A proportional stiffness term is, then, added. So, for WPD, the initial stiffness matrix is considered, and no updating is performed during computation. For WPD_ACT, the initial stiffness matrix is still considered during all computation, but the a_1 parameter and eigenproperties are updated using modal analyses for each time step. For CWPD and SWPD, respectively, the tangent and secant matrices are computed at each time step to update the proportional stiffness part of the matrix, in the same way as for RD-type formulations presented in section 2.3.2.2.

2.3.2.2 Evaluation of the secant and tangent Young's modulus

`RIGI` operator (evaluation of a stiffness matrix) is applied on an updated concrete constitutive model for each beam element to compute the tangent or secant stiffness matrix. Depending on the constitutive model choice, all parameters in tables 2.7 or 2.8 are identical to the initial values except for the concrete Young's modulus.

To determine the tangent $E_T^{(t_i)}$ (eq. 2.13) or secant $E_S^{(t_i)}$ (eq. 2.14) Young's modulus at time step t_i, additional internal variables are defined in the model files.

$$E_T^{(t_i)} = \frac{\sigma^{(t_i)} - \sigma^{(t_{i-1})}}{\varepsilon^{(t_i)} - \varepsilon^{(t_{i-1})}} \tag{2.13}$$

$$E_S^{(t_i)} = \frac{\sigma^{(t_i)}}{\varepsilon^{(t_i)}} \tag{2.14}$$

with $\sigma^{(t_i)}$ and $\varepsilon^{(t_i)}$ respectively the stress and strain in the fibre direction at time step t_i. A strain limit is considered to avoid numerical modulus divergences with low strains: for $\varepsilon^{(t_i)} < \varepsilon_{\text{limit}}$ the modulus is not updated. For both models, a parametric study was performed to determine the limit value, given equation (2.15):

$$\varepsilon_{\text{limit}} = \frac{f_t}{E_c} = 3.5 \cdot 10^{-5} \tag{2.15}$$

with f_t the concrete tensile strength and E_c the initial concrete Young's modulus. Another difficulty was observed with the BARFRA model corresponding to the considerable modulus variation between

traction and compression behaviours. So, a hyperbolic tangent function has been defined to smooth the transition for strain absolute values inferior to $\varepsilon_{\text{limit}}$. The function calibration led to the equation (2.16):

$$E_T^{(t_i)}\left(\varepsilon^{(t_i)}\right) = E_S^{(t_i)}\left(\varepsilon^{(t_i)}\right) = \frac{1}{2} \cdot \left[1 + \tanh\left(-5.0 \cdot 10^5 \times \varepsilon^{(t_i)}\right)\right] \tag{2.16}$$

For each beam element, the tangent or secant Young's modulus of concrete fibres is integrated on the section to obtain one value for the element. This value is then considered for the determination of the element constitutive model. Thus, combining all elemental models leads to a constitutive model for the entire beam. Finally, the `RIGI` operator determines the updated tangent or secant stiffness matrix.

2.4   Dynamic simulations and comparison with experimental data

A sizeable numerical campaign is performed with variable model parameters, as presented in section 2.3. Analyses discussed herein aim at comparing the numerical responses with experimental data. The used sensors were defined in the experimental campaign description (section 1.4). So, acceleration-, displacement- and force-history responses are available. In section 2.4.1, analysis methods are introduced to understand the developed results in sections 2.4.2 and 2.4.3. All dynamic computations are performed using a Newmark-beta algorithm (implicit Newmark with $\gamma = 1/2$ and $\beta = 1/4$), and no numerical damping is developed because the experimental time increments are small enough.

2.4.1   Dynamic data analyses

Error computations are performed between experimental and numerical data (2.4.1.2) to evaluate the damping model ability to characterise RC beam behaviours. Comparisons are performed in the time domain and in frequency one (2.4.1.1) to characterise the evolution of modal properties due to the increase in damage level.

2.4.1.1   Signal processing

(a)   Experimental data   Because experimental dynamic signals are considered input ones for numerical computations, they are processed to smooth data using convolution methods. If $\mathbf{v} = \{v_i\}_{i \in [\![1;n_T]\!]}$ is the vector of experimental data, then the vector $\mathbf{v}_s = \{v_{s,i}\}_{i \in [\![1;n_T+n_{\text{smooth}}-1]\!]}$ with smooth values is composed of elements $v_{s,k}$ in equation (2.17):

$$v_{s,k} = \sum_{i=1}^{n_{\text{smooth}}} \frac{1}{n_{\text{smooth}}} \times v_{k-i+1} \tag{2.17}$$

with n_{smooth} a number to calibrate. The aim is to limit the noise influence while keeping the global variations of experimental data. So, a parametric study on this number gave $n_{\text{smooth}} = 10$ for all studied experimental data: input signals and beam responses.

(b)   From time domain to frequency domain   The Fast Fourier Transform (FFT) is applied on computed or measured data from the time to the frequency domain. In the case of white-noise signals, an extensive frequency range is obtained. So, filters can be considered to focus on values around the first eigenfrequencies of the beam. The dynamic beam response is mostly characterised by its first and second

modes. So, frequencies above 30 Hz can be eliminated. At the end of the dynamic experiments, the beam was not completely damaged. Thus, we can consider that the beam frequency will not converge towards zero. A small frequency range around zero can also be filtered to avoid strong peak amplitudes to develop around zero. However, due to the initial smoothing of experimental data, filtering low frequencies does not significantly influence the frequency responses.

(c)   Eigenfrequency evaluation   A focus on the first beam eigenfrequency is conducted to compare experimental and numerical data. For white-noise signals, frequency responses of displacements or accelerations lead to a principal peak characterising the beam response. The major peak frequency is, so, considered as the beam eigenfrequency at the studied damage state. It is convenient to compare two computations or one computation with experimental data. The peak amplitude is also interesting, particularly in damping ratio influences. Indeed, the stronger is the damping ratio, the lower is the peak amplitude. So, by comparing numerical peak amplitudes with the experimental ones, it is possible to define the most appropriate damping ratio. An

Figure 2.8: Eigenfrequency and peak amplitude determination on a white-noise response

example of eigenfrequency f_{id} and peak amplitude $a_{p,\text{id}}$ identification is presented in figure 2.8 for the white-noise WN1 test.
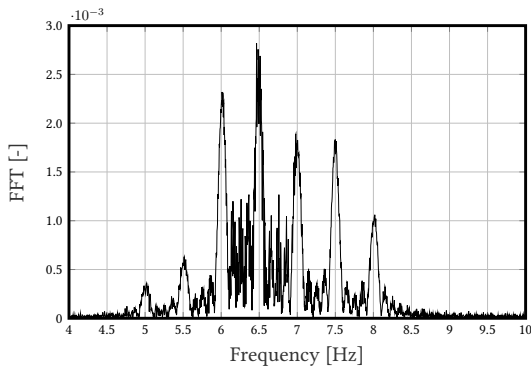
Figure 2.9: Frequency response between $4\,\text{Hz}$ and $10\,\text{Hz}$ of a complete DSS2 test

(d)   White-noise and harmonic signal decomposition for DSS tests   A zoom between $4\,\text{Hz}$ and $10\,\text{Hz}$ of the frequency response to the DSS2 entire test is shown in figure 2.9. Seven peaks are observable, with the corresponding frequencies varying from $5\,\text{Hz}$ to $8\,\text{Hz}$ with an increment of $0.5\,\text{Hz}$. Alternatively, these values are precisely the imposed frequencies of harmonic signal blocks (fig. 1.23b). Practically, these values are precisely the imposed frequencies of harmonic signal blocks (fig. 1.23b). So, beam properties are not deductible from this plot. A decomposition of responses is performed between harmonic and white-noise blocks. Then, studying each white-noise signal part response, independently from harmonic parts, allows evaluating the beam modal properties at different damage states. For signals DSS2 and DSS3, corresponding respectively to numbers 2 and 3 in table 2.4, the signal decomposition is plotted in figure 2.10.

2.4.1.2   Errors between experimental and numerical data

Errors are computed to evaluate differences between experimental data and numerical results. In the case of a simple value, the Euclidean norm is considered given the error $\Delta_{\mathcal{L}^2}$ in percentage, in equa-

(a) DSS2   (b) DSS3
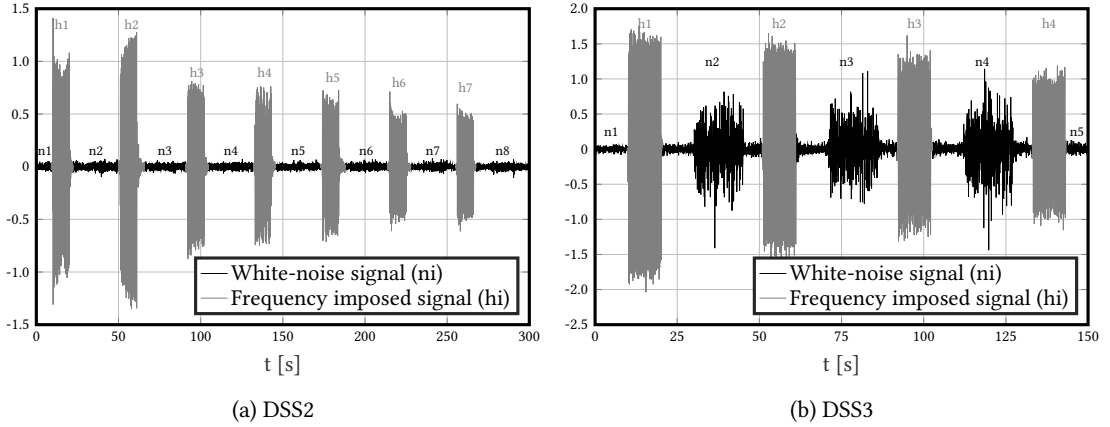
Figure 2.10: Decomposed input signals between harmonic and white-noise parts

tion (2.18):

$$\Delta_{\mathcal{L}^2} = 100 \times \sqrt{\frac{(v_{comp} - v_{ref})^2}{v_{ref}^2}} \tag{2.18}$$

with v_{comp} the value to be compared to the reference one v_{ref}.

A time-dependent error can be computed to characterise the signal parts more or less well represented numerically for time-dependent responses. For each element of a vector, equation (2.18) is applied. However, the error can strongly increase when the reference value is close to zero. So, a limit is chosen under which the error is not considered: a first criterion is thus defined from a given percentage of the maximal amplitude of the experimental response. From a parametric study, a criterion of 3% was determined. Finally, if a global error is required, the mean value of the error vector is considered. In addition to the first criterion, a second one is chosen to eliminate the highest and lowest errors of the mean value. Because the error computation aim is mainly to compare one damping formulation to another, it is not only the exact error value that is of interest, but mainly the variation from one to another. Such comparisons are, indeed, possible with the proposed error computation method.

2.4.2   Calibration on an elastic test

The first dynamic test applied on the HA16-C1A-2 RC beam is a white-noise signal with low amplitude (tab. 2.4). The input signal is presented in figure 1.23a. Experimentally, no damage was observed on the beam after this test: the beam stayed in its linear behaviour. According to this assumption, only five damping formulations are compared: RD, MPD, KPD, MD and WPD (table 2.11), because if nonlinearities do not develop, updated matrices are equal to the initial one. In addition, damping ratios from 0.5% to 5% have been tested and compared with experimental data. In the following, the presented results focus on damping ratios of 0.5% and 1%. Beyond 1%, the dynamic response is too damped to match the experimental behaviour.

2.4.2.1   Concrete constitutive model comparisons

Figure 2.11 presents the numerical acceleration responses for RD formulation with BARFRA and RICBET constitutive models and with damping ratios of 0.5% and 1%. Displacements could also be plotted, but the excessively noisy experimental data do not allow pertinent comparisons with numerical data. In
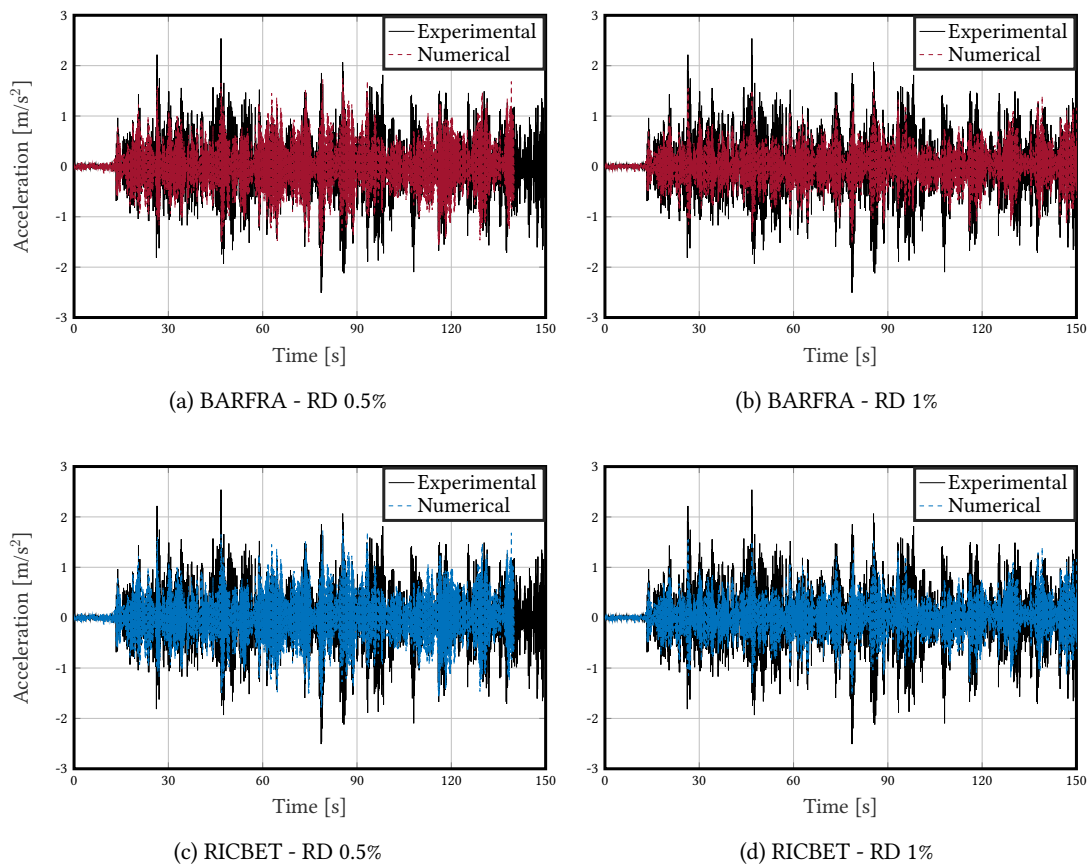
Figure 2.11: WN1 test - Acceleration responses

any case, the numerical acceleration fits appropriately. As expected, increasing the damping ratio leads to lower accelerations. In addition, in figure 2.12, a zoom between 12 s and 20 s leads to a more detailed comparison: BARFRA and RICBET responses are exactly superposed, as expected due to the linearity of the test, demonstrating the good performances of both constitutive models. When higher acceleration amplitudes are reached experimentally, 0.5% of damping ratio is better representative, while 1% damps the response too much. However, when smaller accelerations are observed, even 1% of damping ratio is insufficient to match the experimental data. It highlights a limitation of considering the constant viscous damping model in dynamic analyses.

2.4.2.2   Damping model comparisons

Applying the beam eigenfrequency identification method detailed in paragraph 2.4.1.1(c) on experimental data leads to an eigenfrequency of 6.74 Hz, corresponding to 3.5% under the value determined with hammer shock tests (6.99 Hz) for the HA16-C1A-2 beam. The gap could be due to experimental measurement uncertainties and identification method biases. Numerically, identified eigenfrequencies are around 6.9 Hz (tab. 2.12) closer from shock hammer test values and always with an error lower than 3% with the experimental dynamic response. So, the errors between experimental and numerical responses remain in the uncertainty range. Table 2.12 shows no difference between BARFRA and RICBET
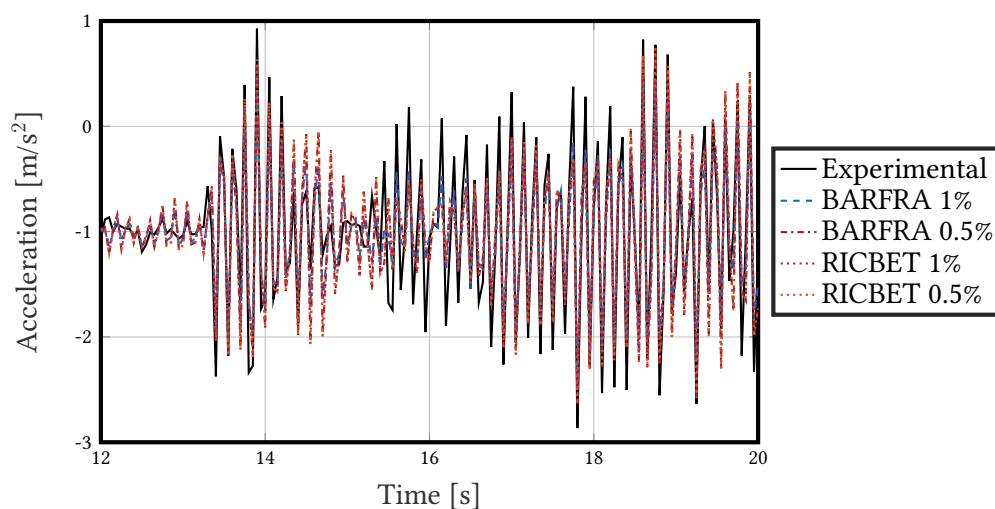
Figure 2.12: WN1 test - Damping formulation comparisons

Table 2.12: Frequency analyses of WN1 test - linear elastic response

Damping formulation	BARFRA			RICBET		
	Damping ratio	Frequency	Error	Damping ratio	Frequency	Error
RD	0.5%	6.9 Hz	+2.3%	0.5%	6.9 Hz	+2.3%
	1%	6.9 Hz	+2.3%	1%	6.9 Hz	+2.3%
KPD	0.5%	6.9 Hz	+2.3%	0.5%	6.9 Hz	+2.3%
	1%	6.9 Hz	+2.3%	1%	6.9 Hz	+2.3%
MPD	0.5%	6.9 Hz	+2.3%	0.5%	6.9 Hz	+2.3%
	1%	6.9 Hz	+2.3%	1%	6.9 Hz	+2.3%
MD	0.5%	-	-	0.5%	6.9 Hz	+2.3%
	1%	-	-	1%	6.9 Hz	+2.3%
WPD	0.5%	6.6 Hz	-2.1%	0.5%	6.7 Hz	-0.6%
	1%	6.6 Hz	-2.1%	1%	6.5 Hz	-3.6%

models for RD, KPD and MPD formulations. It demonstrates the linear behaviour of the studied RC beam submitted to the WN1 test. The same eigenfrequencies are also obtained with 0.5% and 1% of damping ratios. So, this modal property does not seem to be influenced by the viscous damping ratio, at least for linear computations.

For MD and WPD formulations, conclusions are slightly different. No eigenfrequency is identified with the MD formulation and BARFRA model because of the incompatibility observed between these two models. With RICBET, however, the MD gives the same response as other damping formulations, validating the matrix implementation. Then, with WPD formulation, the identified eigenfrequencies

are lower and closer to the experimental dynamic response. Also, values are dependent on constitutive models and damping ratios.

In addition to eigenfrequencies, the same analysis can be performed to compare peak amplitudes. It is, particularly, a way to outline the damping ratio influence. Mainly, it can be deduced that the 1% damping ratio is too high, while 0.5% is a little too small. So, the appropriate damping ratio for this test would be around 0.6% for RD, MPD and KPD formulations. In contrast, WPD formulation has a more substantial damping effect. So even with 0.1% of damping ratio, it still appears to be too large.

In conclusion, the two constitutive models also characterise, numerically, the linear behaviour observed experimentally. Then, it appears that other model parameters, other than RD-type formulations, more influence the linear dynamic responses obtained with modal damping matrices.

2.4.3 Numerical simulation of a damageable test (DSS2)

The numerical analyses on the WN1 test validated the implemented damping matrices and the constitutive model abilities to perform dynamic computations. Now, the DSS2 test (second test in table 2.4), whose input signal is plotted in figure 1.23b, is of interest because it is the first damageable test. The sixteen damping formulations of table 2.11 are tested again with BARFRA and RICBET constitutive models and with damping ratios varying from 0.5% to 5%. The first computations, performed with a damping ratio of 0.5%, showed a lack of viscous damping to match the experimental responses. That is why larger values have been studied, and results obtained with 1%, 2%, 3% and 5% are mainly studied.

For the WN1 test, the time computations were similar from one formulation to another because no update was performed. Now, huge variations are observable. In the case of the RD-type formulations with RICBET model and a damping ratio of 2%, updating the stiffness matrix increases the computational time by 17% (CRD and SRD), and updating a_0 and a_1 parameters raises the required time by 33% due to the modal analysis to perform at each time step. In addition, the difference between RICBET and BARFRA is higher than for the WN1 test due to the more complexity of the RICBET model when nonlinearities develop.

Table 2.13 presents converged computations with both constitutive models, the four damping ratios of interest and the sixteen studied damping formulations. The DSS2 input signal comprises seven harmonic blocks with white-noise signals between blocks. So, the numerical computations are decomposed in seven increments equivalent to the harmonic blocks. When dynamic response divergences are observed, symbol ✗ is indicated in table 2.13 with a number corresponding to the increment during which the divergence occurred. The experimental time step was 0.005 s, and the equal value is generally used for the numerical computations. However, this value was too high for some of them to allow the material model convergence, and a time step two times smaller was considered. However, even by decreasing even more the time step, some damping models still led to instabilities in material responses.

Before comparing the modelling parameters, some beam deformations are presented in figure 2.13. One modelling is chosen herein, but more comparisons are proposed in appendix D.1 (fig. D.1 and D.2). The time steps chosen correspond to the most significant displacement amplitudes of the dynamic response. It appears that, in all cases, the beam movement is completely defined by its first mode.

2.4.3.1 Concrete constitutive model comparisons

First, the constitutive models (BARFRA and RICBET) are compared for some results. Table 2.13 shows divergences for the same damping formulations between RICBET and BARFRA, but, in general, BARFRA diverges for lower increments than RICBET. That is to say, that with BARFRA, instabilities occur at higher signal frequencies than with the RICBET model.

Table 2.13: Completed computations of the DSS2 test

Damping formulation	BARFRA				RICBET			
	1%	2%	3%	5%	1%	2%	3%	5%
RD	✓	✓	✓	✓	✓	✓	✓	✓
RD_ACT	✓	✓	✓	✓	✓	✓	✓	✓
CRD	✓	✓	✓	✓	✓	✓	✓	✓
SRD	✓	✓	✓	✓	✓	✓	✓	✓
KPD	✓	✓	✓	✓	✓	✓	✓	✓
KPD_ACT	✓	✓	✓	✓	✓	✓	✓	✓
CKPD	✓	✓	✓	✓	✓	✓	✓	✓
SKPD	✓	✓	✓	✓	✓	✓	✓	✓
MPD	✓	✓	✓	✓	✓	✓	✓	✗(7)
MPD_ACT	✓	✓	✓	✓	✓	✓	✓	✓
MD	✗(2)	✗(2)	✗(2)	✗(2)	✗(6)	✗(6)	✗(6)	✗(6)
MD_ACT	✗(2)	✗(2)	✗(2)	✗(2)	✗(6)	✓	✗(5)	✗(7)
WPD	✗(7)	✗(7)	✗(7)	✗(7)	✓	✓	✓	✓
WPD_ACT	✓	✓	✓	✓	✓	✓	✓	✓
CWPD	✗(1)	✗(1)	✗(1)	✗(1)	✗(7)	✗(7)	✗(7)	✗(7)
SWPD	✗(1)	✗(1)	✗(1)	✗(1)	✗(7)	✗(7)	✗(7)	✗(7)

[*] ✓   signifies that the computation went until the end.
[*] ✗(i) signifies that the computation diverged during the increment i with $i \leqslant 7$.

(a) Time step $t^{(i-1)}$ (b) Time step $t^{(i)}$ (c) Time step $t^{(i+1)}$
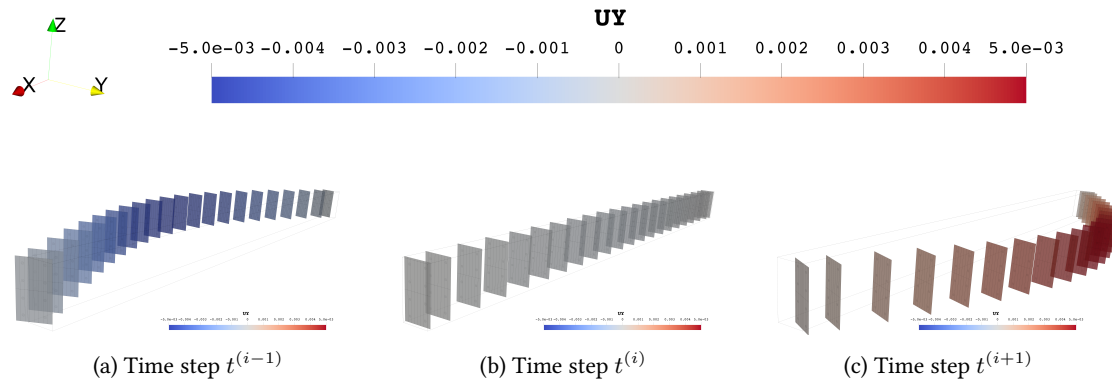
Figure 2.13: DSS2 test - Beam displacement $[m]$ - damping formulation comparisons
RICBET - RD 2%

Figure 2.14 presents the numerical responses of BARFRA and RICBET models with KPD_ACT damping formulation and a damping ratio of 2%. The time acceleration response is similar for both constitutive models (fig. 2.14a and 2.14d), except at the fifth block. With BARFRA, a lower acceleration than
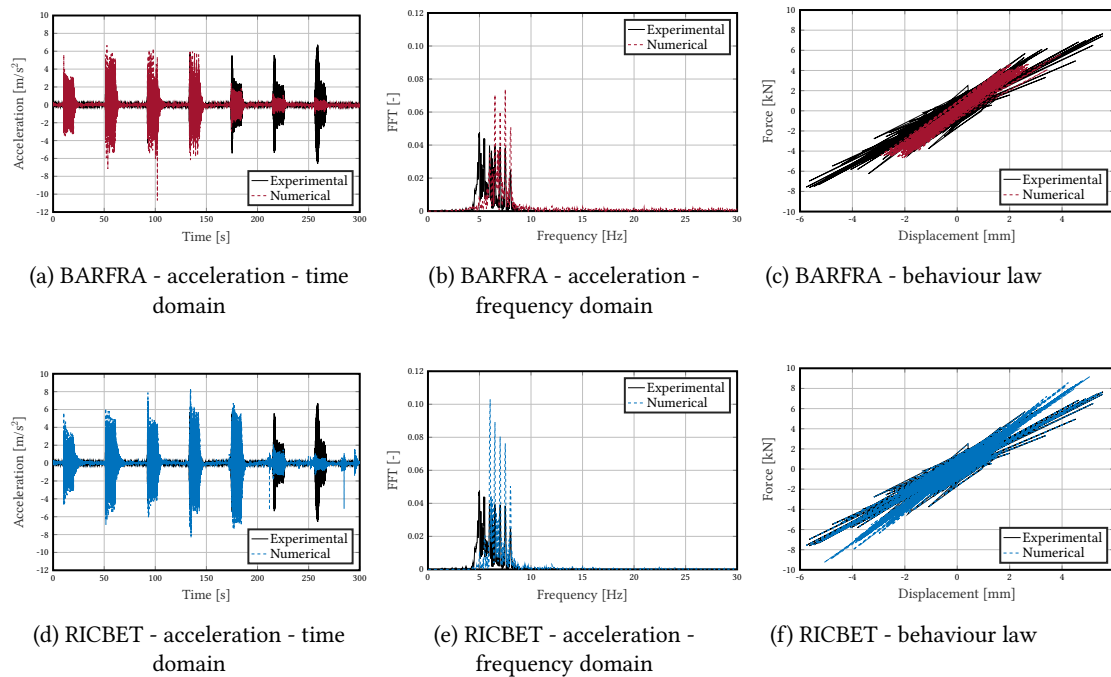
Figure 2.14: DSS2 test - Dynamic responses - KPD_ACT 2%

the experimental response is observed, meaning that, numerically, the beam is no more in resonance for a frequency signal of $6\,$Hz. With RICBET, the beam appears to be still damaged during this block, while the beam acceleration is only reduced in the following block. With BARFRA, the damaged beam eigenfrequency reaches around $6.5\,$Hz, while it instead reaches $6.0\,$Hz with RICBET. So, the final damage level is lower with BARFRA constitutive model. By comparing with the experimental response, it appears that both models do not damage the beam enough. This conclusion is also observable in the constitutive relation laws (fig. 2.14c and 2.14f) because the global numerical stiffness is higher than the experimental one. The differences between the model behaviours can be discussed from these two figures. The pinching effect observed on quasi-static tests also appears here with RICBET. With BARFRA, on the contrary, no null forces are obtained for zero displacements, which is more representative of experimental data. However, experimental displacements around zero values are very noisy, so that no conclusion can be deduced about a better representation of the BARFRA model. Then, in terms of maximal forces, it appears that RICBET induces too large values, making it conservative. On the contrary, BARFRA gives extreme values very close to the experimental ones but only at one instant and, most of the time, forces are smaller than the experimental data. Finally, acceleration responses in the frequency domain (fig. 2.14b and 2.14e) show that the higher frequencies are less damped with the BARFRA model. However, the peak amplitudes are more representative of experiments.

The results presented in figure 2.14 demonstrate that the two constitutive models can more or less characterise the experimental behaviour depending on the data of interest. While BARFRA reduces the computational time and better evaluates extreme force, displacement or acceleration responses, RICBET presents a more conservative behaviour and is closer to the experimental damage state. However, by comparing other damping formulations, different conclusions can be deduced (see BARFRA results in figures 2.17 and 2.18). Notably, for the MPD-type formulations, BARFRA leads to maximal displacement and force values, respectively five and ten times larger than the experimental values. In these cases, the high frequencies strongly influence responses. Indeed, it was already seen in figure 2.14b that the high

frequencies were less damped with the BARFRA model, and the MPD-type formulations do not damp the high frequencies, meaning that the model is not dissipating energy through nonlinearities. So, the use of BARFRA accentuates the difficulties observed with MPD-type formulations. It is also observable on RD-type formulations to a lesser extent because of the significant influence of the mass proportional part in RD. Because of BARFRA problems, comparing damping models in the following part will be performed with the RICBET model.

2.4.3.2   Damping model comparisons

First, table 2.13 shows that the damping ratio choice does not influence the computational convergence. So, this is not the lack of viscous damping that can explain a computational convergence but rather the combination of a damping formulation and a material model. Then, in terms of damping formulations, modal and Wilson-Penzien types exhibit difficulties in performing nonlinear analyses with studied input signals.

(a)   Formulations   Figure 2.15 synthesises the load-displacement curve envelops obtained with the RICBET constitutive model and all damping formulations associated with a damping ratio of 2%. These curves are plotted based on the displacements at the beam centre and the forces at supports. The first line exhibits the envelop monotonic skeletons (also called "capacity curves"), demonstrating the good performance of all damping models to characterise the experimental linear behaviour. But the nonlinearities are developing too late, so larger maximal forces are reached numerically for the same displacements as experimentally. Figures 2.15e to 2.15h show the entire load-displacement curve envelops allowing to study the hysteresis loops. First, MD, CWPD and SWPD exhibit behaviours that are not representative of the experimental data because, based on table 2.13, these formulations diverge with RICBET and 2% of damping ratio. Then, despite its convergence, RD_ACT cannot match the experimental data because too large forces and displacements are reached. For other formulations, different load-displacement curves are obtained. (i) WPD and WPD_ACT (fig. 2.15h) are almost linear, so very few nonlinearities occur, and no energy is dissipated. (ii) For MPD-type formulations (fig. 2.15g), a low damage level is again reached because the unloading stiffnesses are close to the initial ones. So, the beam is not damaged enough compared to the experimental response. However, compared to WPD-type, a small amount of energy is dissipated, demonstrating the development of few nonlinearities. (iii) For MD formulation (fig. 2.15g), an adequate amount of damage (deduced from the stiffness degradation) is developed, but too large displacements and forces are reached. (iv) Then, with KPD-type formulations (fig. 2.15f), the stiffness loss is higher than MPD-type formulations for the same maximal displacements, so the experimental behaviour is better represented. However, it seems again to lack of dissipations. (v) Finally, small cycles are obtained for RD-type formulations (except RD_ACT) in figure 2.15e, leading to a lack of damage compared to experiments. The numerical responses are close to MPD-type formulation ones except that more energy is dissipated (as observed with the hysteretic cycles). So, one more time, it appears here that the mass proportional part strongly influences RD, but the stiffness one has a correcting effect. It can be concluded that the KPD-type formulations are the best to represent experimental hysteretic loops.

Indications on final damaged states can be deduced from figure 2.15. Figure 2.16 can be analysed to further study the development of damage through computations. The decomposition between harmonic blocks and white-noise signal parts presented in figure 2.10a is applied to numerical and experimental acceleration responses. The duration of all blocks is sufficient to reach steady-state responses so that frequency identifications can be performed. The first line focuses on harmonic blocks. A linear evolution of frequencies is observed experimentally and numerically because it corresponds to the signal properties: from one block to another, the frequencies are decreasing from $0.5\,\text{Hz}$, so an evolution between $8\,\text{Hz}$ and $5\,\text{Hz}$ is obtained. Four formulations cannot correctly characterise this decrease: three
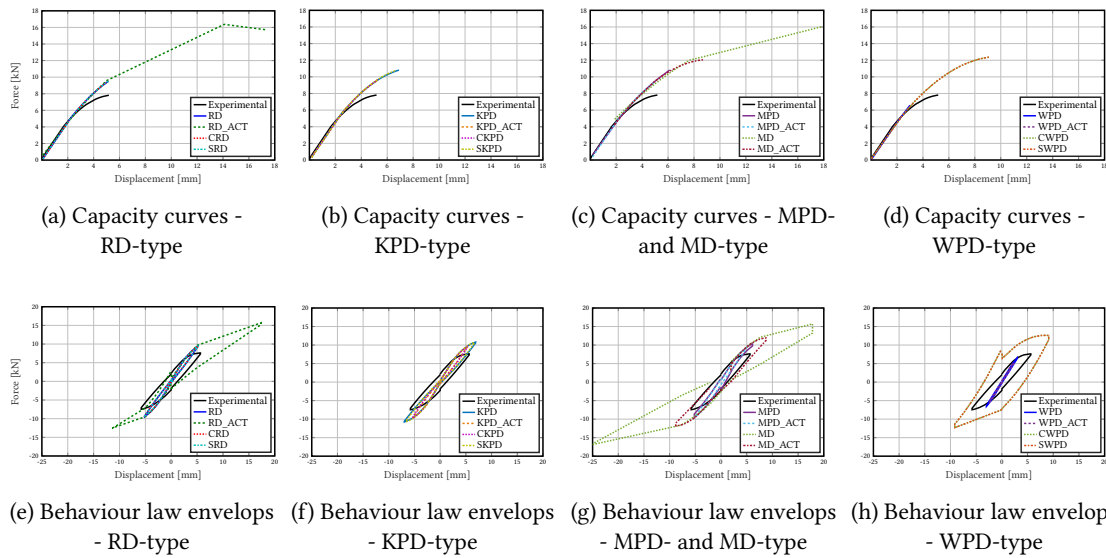
Figure 2.15: DSS2 test - Envelops of the behaviour responses - (RICBET 2%)

are the damping models leading to divergent computations. They mainly show difficulties characterising the first block as MD_ACT, which converges only with a damping ratio of 2%. So, it appears that some inadequate damping formulations can be identified at the computation beginning.

Then, the white-noise signal parts must be of interest to study the beam modal properties. Figures 2.16e to 2.16h present the evolution of the beam eigenfrequencies for white-noise blocks, that is to say, after different damage levels imposed by the harmonic blocks with large amplitudes. The white-noise blocks 1 and 8 are very shorts, so stronger errors can be obtained on these blocks. Experimentally, the first eigenfrequency is $8\,\text{Hz}$. However, using the hammer shock and WN1 tests, an undamaged beam eigenfrequency around $7\,\text{Hz}$ was identified. So, the initial eigenfrequency can not be above the undamaged value, which explains that numerically the initial values are around 7 Hz. WPD and WPD-type formulations are the only formulations given the same eigenfrequencies that experimental data for the three first blocks. Despite the possible errors in eigenfrequency identification at the beginning, the global tendency during computations is a decrease in frequencies, meaning that the beam damages along with the DSS2 test. From block 6, the frequency stabilises, so the harmonic block at $6\,\text{Hz}$ is the last one damaging the beam. After this block, the input signal frequency must be lower than the beam eigenfrequency, and the beam does no more enter in resonance, leading to beam movements of lower amplitudes. Numerically, the general tendency also presents a decrease but is much less significant than the experimental one. It means that the beam is numerically not damaged enough, consistent with the conclusions performed in load-displacement curve envelops (fig. 2.15e to 2.15h). It is the case of RD, CRD, SRD, KPD, KPD_ACT, CKPD, MPD and MPD_ACT formulations. For RD_ACT and MD_ACT, better matching with the experimental data is obtained, corresponding to the larger damage observed in the previous analysis. RD_ACT formulation is, therefore, an example showing that the damping model performance depends on the variable of interest: the damage state is better characterised with RD_ACT formulation. At the same time, too large displacements and forces are reached. Unlike RD_ACT, SKPD demonstrates that even if the constitutive law correctly represents the experimental data, it is not the case for the damage state. Finally, some blocks frequency identifications were not possible for some formulations due to unrealistic dynamic responses, explaining that some data are missing.

(a) HB - RD-type   (b) HB - KPD-type   (c) HB - MD- / MPD-type   (d) HB - WPD-type

(e) WN - RD-type   (f) WN - KPD-type   (g) WN - MD-/MPD-type   (h) WN - WPD-type
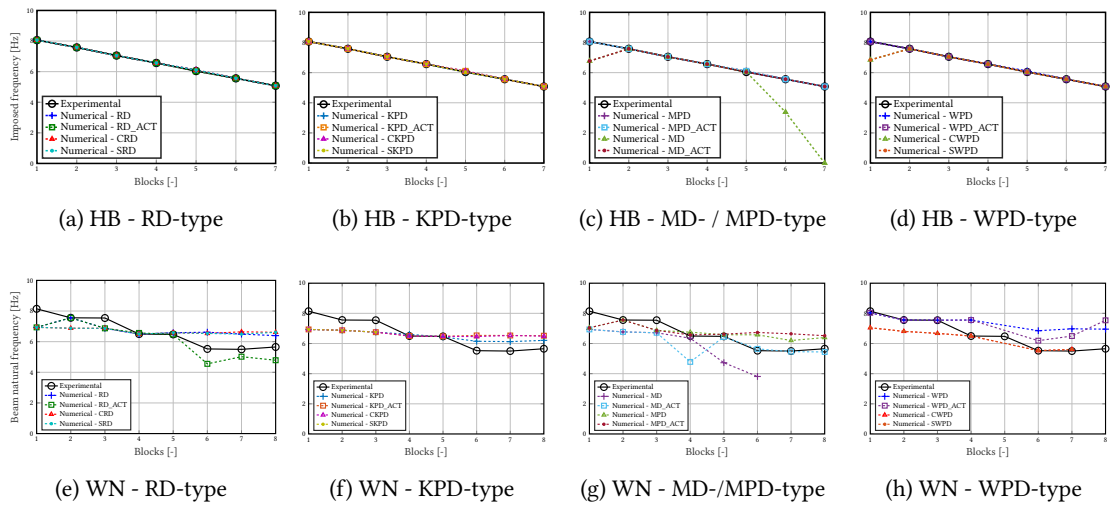
Figure 2.16: DSS2 test - Frequency responses (white-noise signals - WN - and harmonic block signals - HB -) - RICBET 2%

(b)   Damping ratios   Figures 2.17 and 2.18 present the damping ratio choice influence. First, from figure 2.17, it appears that the more significant is the damping ratio, the smaller is the hysteresis loop, as expected. If more viscous damping is applied in the model, the beam movements are strongly damped, and lower damage is developed in the beam. As discussed with the different formulations, increased energy dissipation leads to significant errors in extreme forces and displacements. So a compromise is required to choose the adequate damping ratio. Then, the four formulations in figure 2.17 are attentively studied, and some observable differences. For WPD formulation (fig. 2.17d), because of its strong damping effect, whatever the damping ratio is, the response is always linear. Then, for RD (fig. 2.17a), 1% of damping ratio is not strong enough, but the load-displacement curves are equal with 2%, 3% and 5% of damping ratios. In the same idea, with KPD, no influence of damping ratio is obtained. On the contrary, with CRD (fig 2.17b) and CKPD (fig. 2.17c), a more linear evolution is observed on responses from one damping ratio value to another, more representative of the expected behaviour. First, with 1%, using the tangent stiffness seems to stabilise the numerical response, maybe because the energy dissipations are better balanced and physically modelled. All these remarks demonstrate the better performance of the damping models with the tangent stiffness matrix.

The same damping ratio comparisons are performed with BARFRA constitutive model. Figures 2.17e to 2.17h demonstrate the strong difficulties of BARFRA to characterise the experimental behaviour, whatever the damping formulation or the damping ratio. Extreme values numerically attained with RD (fig. 2.17e) and CRD (fig. 2.17f) are ten times too large. With CKPD (fig. 2.17g) and WPD (fig. 2.17h) the hysteresis loops are not developed, and even the beam global stiffness is not matching. So, BARFRA constitutive model should be carefully used because results matching the experimental behaviours are only obtained with some viscous damping models.

In terms of damage state evolutions, figure 2.18 presents the beam eigenfrequency evolutions for white-noise input signal parts. With RD (fig. 2.18a), because of the large loops with 1% of damping ratio, lower eigenfrequencies are obtained than with the other damping ratios. All studied damping ratios, except 1%, gave equal constitutive laws, and similar modal properties are deduced. So there is no damping ratio influence with this formulation. Then, with CRD (fig. 2.18b), the lower is the damping ratio, the lower is the final beam eigenfrequency. It is in adequacy with load-displacement curves because the more damage develops, the more the eigenfrequency decreases. For CKPD (fig. 2.18c),

(a) RICBET - RD   (b) RICBET - CRD   (c) RICBET - CKPD   (d) RICBET - WPD

(e) BARFRA - RD   (f) BARFRA - CRD   (g) BARFRA - CKPD   (h) BARFRA - WPD
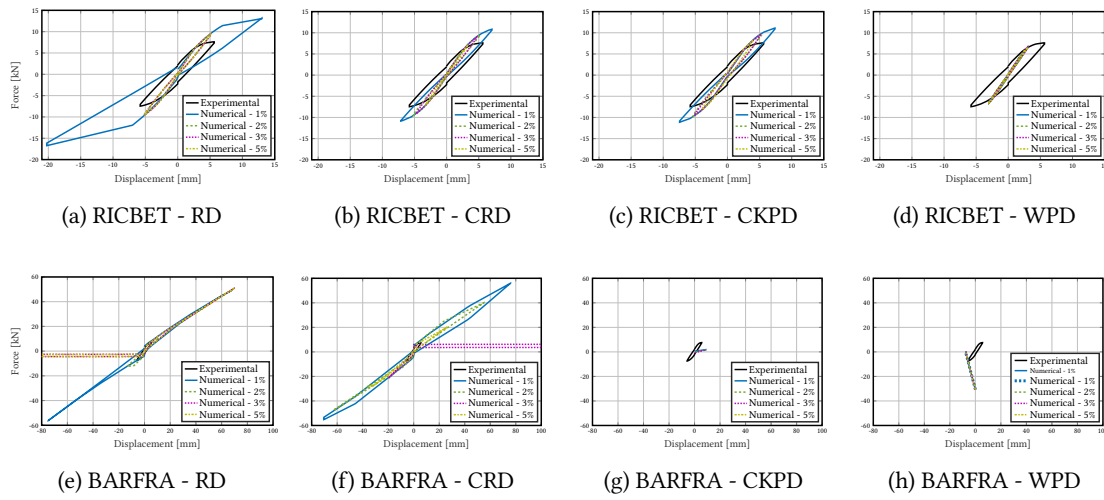
Figure 2.17: DSS2 test - Behaviour law envelops - damping ratio comparisons

(a) RICBET - RD   (b) RICBET - CRD   (c) RICBET - CKPD   (d) RICBET - WPD

(e) BARFRA - RD   (f) BARFRA - CRD   (g) BARFRA - CKPD   (h) BARFRA - WPD
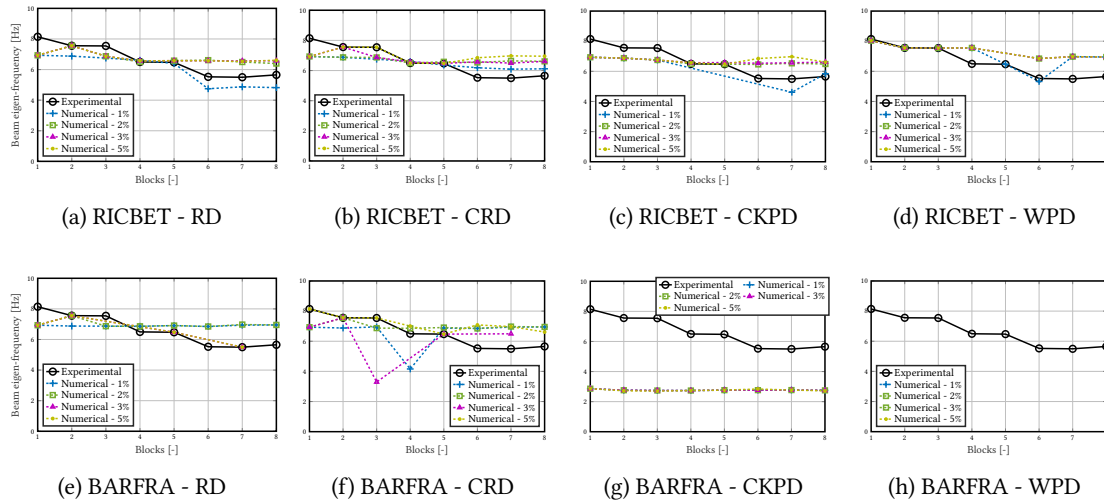
Figure 2.18: DSS2 test - Frequency responses of the white-noise signals - damping ratio comparisons

while a similar influence was observed on the behaviour laws than CRD, here the damping ratio does not impact the eigenfrequencies, except for 1%, which exhibits divergences. Finally, for WPD (fig. 2.18d), as observed in figure 2.16h, it appears that a linear behaviour consideration does not allow to represent the response modal frequency content.

The description of frequencies with the BARFRA constitutive model (fig. 2.18e to 2.18h) again exhibits this model difficulty in performing nonlinear dynamic computations. Inconsistent results are obtained, and they do not allow physical conclusions about this material model.

2.4.4   Numerical responses of complementary tests

Based on the analyses performed with the DSS2 test, a smaller number of damping formulations are compared on the following tests (number 3 to 5 in table 2.4) and only RICBET constitutive model is considered. Notably, modal and Wilson-Penzien formulations are not considered because of their convergence difficulties or their incapacity to represent experimental responses. Three tests are presented with two damping formulations (RD and KPD_ACT). Different damping ratios were tested and the ones presented give the best results for each test: 1% for DSS3, 0.5% for DSS4 and 1% for DSS5. As DSS2, the three studied tests are decreasing sinus sweep signals with different frequencies and amplitudes, and the numbers correspond to the order of experiments.

First, figure 2.19 presents the acceleration responses in the time domain. For the DSS3 test (fig. 2.19a and 2.19d) numerical data are well matching the experimental ones with maximal accelerations slightly too large. On the contrary, the two other tests maximal experimental accelerations are not reached numerically. This effect could be due to a lack of damage leading to a too rigid beam model. Numerically, the resonance is attained one block too early compared to the experimental data. What is interesting with the time acceleration responses is to observe the end of each harmonic block. The beam behaves in free vibrations because the input signal becomes almost null. An exponential decrease is obtained, and the selected damping ratio can be discussed. For DSS3 and DSS5 tests, RD and KPD_ACT both match the experimental data, so 1% of damping ratio is pertinent. However, for the DSS4 test, RD and KPD_ACT give different results, and KPD_ACT is not damped enough. It again demonstrates that the damping ratio does not follow a general tendency and needs to be selected carefully depending on the computation and damping formulation.

(a) DSS3 - RD 1%	(b) DSS4 - RD 0.5%	(c) DSS5 - RD 1%
(d) DSS3 - KPD_ACT 1%	(e) DSS4 - KPD_ACT 0.5%	(f) DSS5 - KPD_ACT 1%
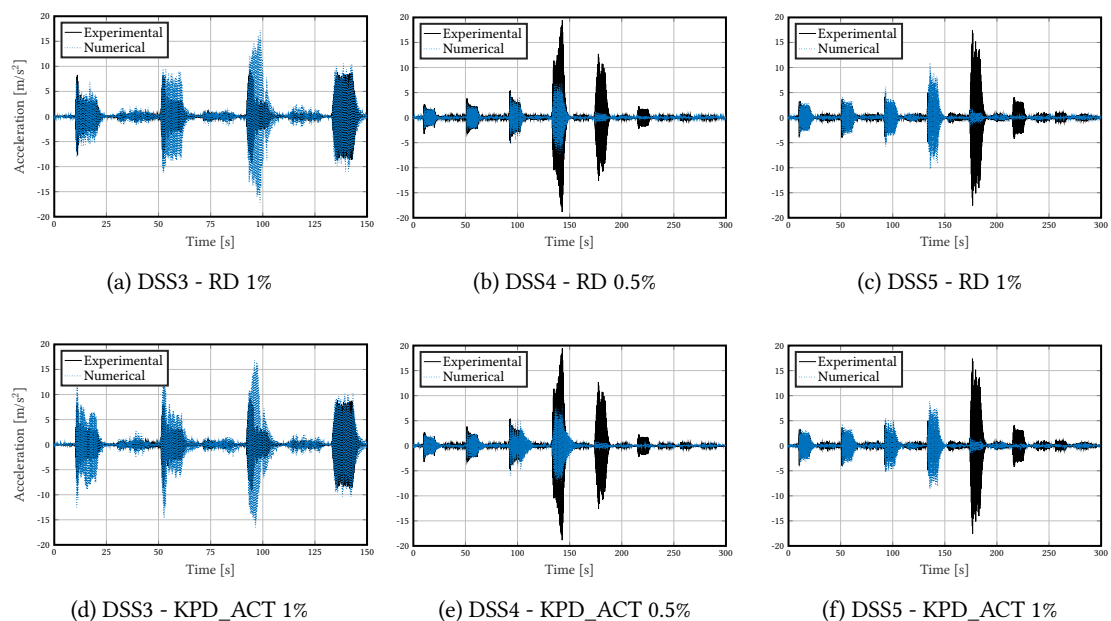
Figure 2.19: DSS3 to DSS5 tests - Acceleration responses - RICBET

Then, figure 2.20 shows that all computations correctly match the global beam stiffness. However, a considerable difficulty appears in hysteresis modellings. While for the DSS3 test, the hysteresis loops are too large, not enough energy is dissipated numerically for DSS4 and DSS5 tests. So, despite a good matching in dynamic responses, the models have shortcomings in energy dissipation. At the structural

(a) DSS3 - 1%   (b) DSS4 - 0.5%   (c) DSS5 - 1%
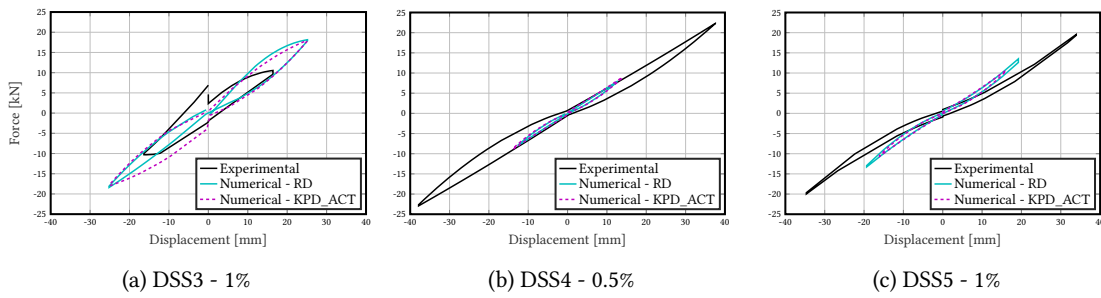
Figure 2.20: DSS3 to DSS5 tests - Behaviour law envelops - RICBET

level, these shortcomings are solved with viscous damping. Nevertheless, if hysteresis phenomena were better modelled, the viscous damping requirement could be significantly reduced. As for the accelerations in figure 2.19, it appears that neither the maximal beam displacements nor the extreme forces are characterised. So, these computation results should not be considered to validate the structure safety.

Finally, the eigenfrequencies of the three tests are displayed in figure 2.21. As for the DSS2 test, the harmonic responses present a linear amplitude decreasing trend corresponding to the imposed harmonic signals and are correctly modelled numerically (fig. 2.21a to 2.21c). Nevertheless, the last block of DSS4 and DSS5 tests is poorly characterised numerically. It is due to the low amplitude of the input signal leading to a numerical characterisation of the beam properties and not the signal ones. Now, if the extreme block values are removed because of their few data, experimentally, a continuous decrease can be noticed until the end of the DSS4 test in figures 2.21d to 2.21f. Then the eigenfrequency stabilises during the DSS5 test. Thus, the beam is damaged, particularly during the DSS3 test and a little during the DSS4 one. The undamaged beam frequency was around 7 Hz, and a decrease until 3 Hz was observed about damage phenomena. Numerically, the decrease matches the experimental data except for the

(a) DSS3 - harmonic - $\xi = 1\%$ (b) DSS4 - harmonic - $\xi = 0.5\%$ (c) DSS5 - harmonic - $\xi = 1\%$

(d) DSS3 - white-noise - $\xi = 1\%$ (e) DSS4 - white-noise - $\xi = 0.5\%$ (f) DSS5 - white-noise - $\xi = 1\%$
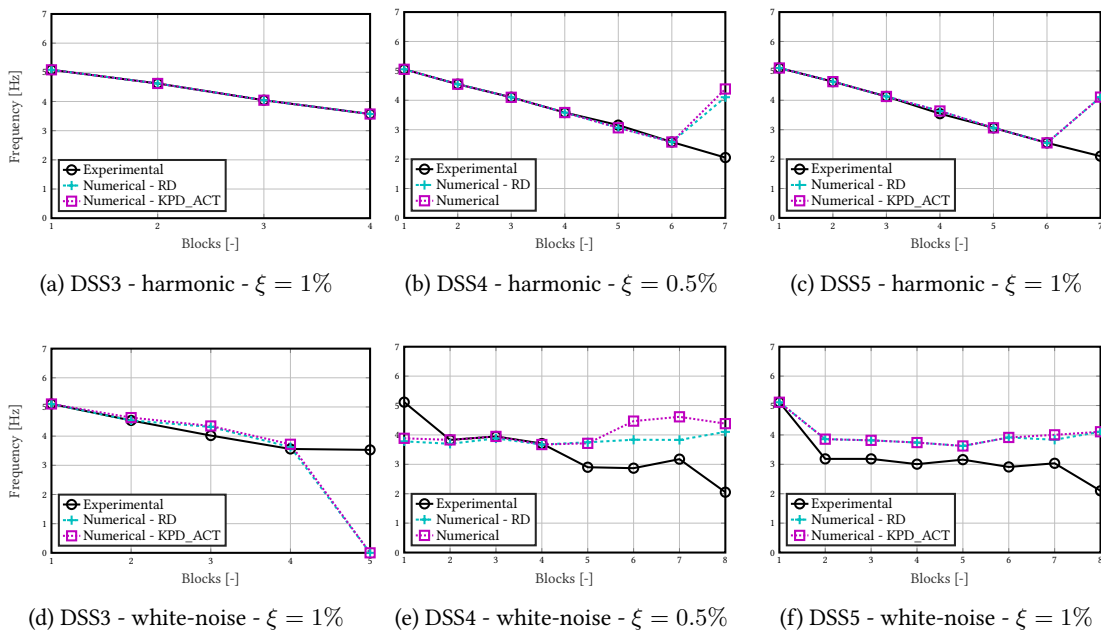
Figure 2.21: DSS3 to DSS5 tests - Frequency evolutions - RICBET

last block. Then, at the beginning of the DSS4 test, the experimental frequency is more significant than at the end of the third computation, which is not physically acceptable because the beam damage can not decrease. The experimental error can be due to an intense noise on measured accelerations with low amplitudes. It explains, thus, the difference between the numerical and experimental responses for the first block. For blocks 2 to 4, the numerical frequencies match the experimental ones. However, from block 5, the numerical frequency does not decrease as expected. It is linked with figure 2.19 because the beam is not damaged enough during the fourth harmonic block, so the frequency decrease is not observable. The lack of damage leads to the constant frequency during the end of DSS4 and all DSS5 tests. The frequency is not evolving as well as experimentally. Stabilisation of the eigenfrequency is obtained numerically and experimentally but with a higher numerical value. An explanation for this observation could be a lack of representativeness of the material model (the damage value is converging towards a too low value) or the lack of mechanism descriptions (steel-concrete interface, for example). The damage function presents an asymptote (fig. 2.5d) not allowing to reach the observed experimental damage.

2.5   Energy balance analyses

Previously, the performances of studied model parameters were evaluated through some comparisons with experimental data. This section analyses energy distributions at the structural (or global) and material (or local) levels. First, the implementation of energy computations in Cast3M is explained in section 2.5.1. Then, a study of constitutive models is proposed with one DOF system submitted to quasi-static cycles in traction and compression (section 2.5.2). Finally, sections 2.5.3 and 2.5.4 focus on dissipations respectively at the structural and concrete levels during the carried out numerical computations.

2.5.1   Description and implementation of energies

2.5.1.1   Energy classification

Absolute and relative energy balance computations are defined in section 1.1.3. Table 2.14 synthesises the equations of energies at the structural level. Imparted, kinetic and damping energies can be computed with the matrices of the problem, so only an integration along the beam is required to compute these values. However, for the absorbed energy, in the case of a nonlinear constitutive material model, the stiffness matrix can not be used to compute the energy, so the behaviour law integration on beam volume is required.

The absorbed energy is linked with the dissipative phenomena. That is why an energy classification at the material level is also proposed in table 2.15. The terms defined in this table will be used during the energy analyses, particularly in section 2.5.4. The hysteretic and associated work hardening energies are defined with sums because they deal with the constitutive models dissipative phenomena.

2.5.1.2   Hysteretic energies of constitutive models

Both studied concrete models derive from a thermodynamic approach. So, the hysteretic and associated work hardening energies can be deduced from the state potential, considering the Clausius-Duhem inequality. For the BARFRA model (eq. 2.5), only a damage dissipative phenomenon $E_{h,d}$ is considered with an isotropic work hardening $W_{h,d}$ (tab. 2.16). For the RICBET model (eq. 2.8), four dissipative phenomena are considered: (i) the plasticity in compression $E_{h,p}$ associated with an isotropic work

Table 2.14: Energies classification - structural level

Name	Symbol	Equation[b]
Imparted energy	$\boldsymbol{E_i}$[a]	$\begin{aligned} E_{i,r} &= -\int_{\mathscr{L}} \left(\mathbb{M}.\ddot{\mathbf{U}}_s.\mathrm{d}\mathbf{U} \right) \mathrm{d}x \\ E_{i,a} &= \int_{\mathscr{L}} \left(\mathbb{M}.\ddot{\mathbf{U}}_a.\mathrm{d}\mathbf{U}_s \right) \mathrm{d}x \end{aligned}$
Kinetic energy	$\boldsymbol{E_k}$[a]	$\begin{aligned} E_{k,r} &= \int_{\mathscr{L}} \left(\mathbb{M}.\ddot{\mathbf{U}}.\mathrm{d}\mathbf{U} \right) \mathrm{d}x \\ E_{k,a} &= \int_{\mathscr{L}} \left(\mathbb{M}.\ddot{\mathbf{U}}_a.\mathrm{d}\mathbf{U}_a \right) \mathrm{d}x \end{aligned}$
Damping energy	$\boldsymbol{E_d}$	$E_d = \int_{\mathscr{L}} \left(\mathbb{C}.\dot{\mathbf{U}}.\mathrm{d}\mathbf{U} \right) \mathrm{d}x$
Absorbed energy	$\boldsymbol{E_a}$	$E_a = \int_{\mathscr{V}} \left(\sigma_c.\dot{\varepsilon}_c + \sigma_s.\dot{\varepsilon}_s \right) \mathrm{d}\mathscr{V}$ [c]
Total energy	$\boldsymbol{E_t}$[a]	$\begin{aligned} E_{t,r} &= E_{k,r} + E_d + E_a \\ E_{t,a} &= E_{k,a} + E_d + E_a \end{aligned}$

[a] Relative / absolute decomposition
[b] $\int_{\mathscr{L}} (.)\,\mathrm{d}x$ is the integral on beam length $\mathscr{L}$ and $\int_{\mathscr{V}} (.)\,\mathrm{d}\mathscr{V}$ is the integral on beam volume $\mathscr{V}$
[c] $._c$ and $._s$ subscripts are respectively for "concrete" ans "steel"

Table 2.15: Absorbed energy decomposition

Name	Symbol	Equation[a],[b],[c]
Hysteretic energy	$\boldsymbol{E_h}$	$E_h = \sum_{i=1}^{n_{E_h}} E_{h,i}$
Concrete strain energy (elastic recoverable)	$\boldsymbol{E_{s,c}}$	$E_{s,c} = \int_{\mathscr{V}} \left(\sigma_c.\dot{\varepsilon}_c^e \right) \mathrm{d}\mathscr{V}$
Steel strain energy (elastic recoverable)	$\boldsymbol{E_{s,s}}$	$E_{s,s} = \int_{\mathscr{V}} \left(\sigma_s.\dot{\varepsilon}_s^e \right) \mathrm{d}\mathscr{V}$
Work hardening	$\boldsymbol{W_h}$	$W_h = \sum_{i=1}^{n_{W_h}} W_{h,i}$
Dissipated energy	$\boldsymbol{E_{diss}}$	$E_{diss} = E_h - W_h$

[a] $n_{E_h} = 1$ and $n_{W_h} = 1$ for BARFRA model and $n_{E_h} = 4$ and $n_{W_h} = 3$ for RICBET model
[b] $\int_{\mathscr{V}} (.)\,\mathrm{d}\mathscr{V}$ is the integral on beam volume $\mathscr{V}$
[c] $._c$ and $._s$ subscripts are respectively for "concrete" ans "steel"

Table 2.16: Classification of energies - BARFRA

Phenomenon	Hysteretic energy $E_{h,i}$	Work hardening $W_{h,i}$
Damage	$E_{h,d} = \int_{\mathscr{V}} \left(Y.\dot{d} \right) \, \mathrm{d}\mathscr{V}$	$W_{h,d} = \int_{\mathscr{V}} \left(Z.\dot{z} \right) \, \mathrm{d}\mathscr{V}^{*}$

[*] Isotropic work hardening

* Isotropic work hardening

hardening $W_{h,p}$, (ii) the friction $E_{h,f}$ with a kinematic work hardening $W_{h,f}$, (iii) the damage $E_{h,d}$ with an isotropic work hardening, and (iv) the unilateral effect $E_{u,h}$. Expressions of these energies are written in table 2.17.

Table 2.17: Classification of energies - RICBET

Phenomenon	Hysteretic energy $E_{h,i}$	Work hardening $W_{h,i}$
Plasticity	$E_{h,p} = \int_{\mathscr{V}} \left(\sigma_c.\dot{\varepsilon}_c^p \right) \, \mathrm{d}\mathscr{V}$	$W_{h,p} = \int_{\mathscr{V}} \left(R.\dot{p} \right) \, \mathrm{d}\mathscr{V}^{*}$
Friction	$E_{h,f} = \int_{\mathscr{V}} \left(\sigma^{\pi}.\dot{\varepsilon}^{\pi} \right) \, \mathrm{d}\mathscr{V}$	$W_{h,f} = \int_{\mathscr{V}} \left(X.\dot{\alpha} \right) \, \mathrm{d}\mathscr{V}^{**}$
Damage	$E_{h,d} = \int_{\mathscr{V}} \left(Y.\dot{d} \right) \, \mathrm{d}\mathscr{V}$	$W_{h,d} = \int_{\mathscr{V}} \left(Z.\dot{z} \right) \, \mathrm{d}\mathscr{V}^{*}$
Unilateral effect	$E_{h,u} \int_{\mathscr{V}} \left(\zeta.\dot{\eta} \right) \, \mathrm{d}\mathscr{V}$	-

[*] Isotropic work hardening
^{**} Kinematic work hardening

2.5.1.3   Implementation of energy computations

The kinetic E_k, imparted E_i and damping E_d energies are directly computed with the knowledge of mass (kinematic and imparted energies) or damping (damping energy) matrices. At each time step, displacement, velocity and acceleration increments are known for each beam node. Products between matrices and vectors are thus computed, and the incremental values are summed along time given the energy evolutions over time.

The last term of the energy balance equation, the absorbed energy, could be computed similarly in the case of a linear material behaviour using the stiffness matrix. However, the stress-strain curve must be integrated into beam volume because nonlinear constitutive models are considered here. Because of the inhomogeneous section, the sum of concrete and steel absorbed energies gives the interest value. The integrations on sections are already performed, considering both materials, given the forces and displacements at beam nodes (multi-fibre methodology algorithm in figure 2.3). So, only the integration along the beam is required with the INTG operator applied on an "evolution"[1].

The hysteretic and work hardening energy computations are also implemented to study the different dissipative phenomena. First, all internal variables and associated forces (tab. 2.1 and 2.2) are defined in the constitutive model files, as well as the dissipative terms defined by equations (2.5) and (2.8). All computed values are incremental. Thus, during computations, at each time step, dissipative terms are

---

[1]The "evolution" is an object of Cast3M to characterise the evolution of a value $f(x)$ as a function of another value x. The evolution is composed of two (or more) vectors corresponding to x and $f(x)$.

integrated on sections (INTG operator applied on an "element field"[2]) and is expressed at beam nodes. Finally, integrations are performed for the total absorbed energy, and the incremental energy values are obtained. Then, the time-dependent energies are computed by accumulating the incremental data.

Different parametric analyses were performed to validate the energy computations. Mainly, it was observed that the energies are strongly dependent on the structure discretisation. So, the equality between the load-displacement curve integration on beam length and the stress-strain integration on beam volume was investigated to choose an adequate section discretisation on the weak axis without increasing too much computational time. For BARFRA, five elements were sufficient, while at least eight were required for the RICBET model (fig. 2.4b). These numbers, allowing the representation of stress and strain gradients, have been chosen for the numerical computations.

Finally, despite the fixed beam geometrical data, the influence of beam slenderness was studied to characterise the shear effects on energy computations. Timoshenko hypotheses considered in Cast3M are, indeed, including them. The absorbed energy in the tangent direction appeared to be at most 1% of the value. So, the shear locking is well avoided.

2.5.2   Dissipative energies of constitutive models

One fibre element of concrete is considered and submitted to quasi-static traction and compression cycles. Two traction/compression cycles are studied.

2.5.2.1   Energy distribution at the material level

First, figure 2.22 presents the absorbed energy decomposition proposed in table 2.15 for both concrete models, with the associated constitutive laws. The steel strain energy $E_{s,s}$ is not plotted here because only concrete is studied.

For the BARFRA model, the constitutive law (fig. 2.22a) shows that the first cycle completely damaged the element in traction because the second cycle begins with the slope of the first cycle ends. In compression, no-nonlinearity develops, and the behaviour stays linear in the studied strain range. Then, for the energy distribution in figure 2.22b, it appears that hysteretic, work hardening and dissipated energies are only evolving during the first traction cycle. Indeed, this is the only one inducing nonlinearities, as discussed in the behaviour law. Then, absorbed and strain energies are equal because a damage model is considered, so the total strain is equal to the elastic one and $\int_{\mathscr{V}} (\sigma_c.\dot{\varepsilon}_c^e)\,\mathrm{d}\mathscr{V} = \int_{\mathscr{V}} (\sigma_c.\dot{\varepsilon}_c)\,\mathrm{d}\mathscr{V}$ given $E_{s,c} = E_a$. This energy increases during compression loading and decreases symmetrically during compression unloading. So, recoverable energy is well developed during compression. The defined strain energy does not return to zero for a zero strain in the traction parts.

RICBET constitutive law (fig. 2.22c) shows that the second cycle begins with the damaged stiffness obtained after the first cycle until the stress reaches the final value of the first traction loading. Then, damage continues to develop while traction loading increases. Because of the more considerable damage value, the traction unloading part follows a more "gentle" slope than during the first cycle. The null strain value, corresponding to the limit of stiffness recovery, is reached later. In compression, a stiffness recovery is observed with a less steep slope than in the first cycle because this slope depends on damage level. Then, the elastic stiffness is reached at the limit of $-0.5\,\mathrm{MPa}$, and the unloading response follows the same curve as the loading. Indeed, the same maximal strain is considered for both cycles, so no more plasticity develops during the second cycle. Let us take a look at the energy distribution in figure 2.23d. First, the elastic strain energy, computed with $\varepsilon^e = \varepsilon - \varepsilon^p - \eta.\varepsilon^\pi$, slightly increases during the first cycle beginning because of the small linear behaviour in traction. Then, it decreases when the nonlinearities develop to reach a null value at the null strain. During compression, the elastic

---

[2]The "element field" is an object defined in Cast3M for data considered at model elements. So, knowledge of the element formulation is generally required to process data.

(a) BARFRA - constitutive law

(b) BARFRA - absorbed energy decomposition

(c) RICBET - constitutive law

(d) RICBET - absorbed energy decomposition
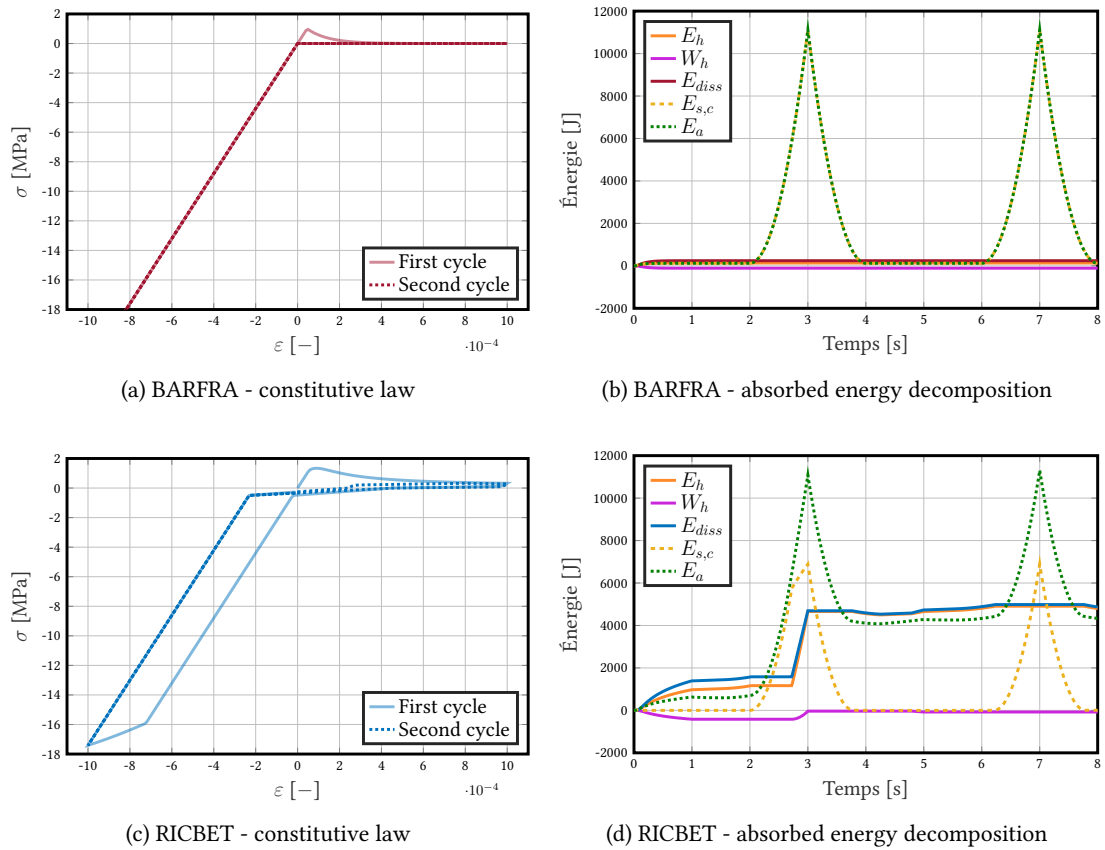
Figure 2.22: Energy analysis of one fibre element of concrete - two traction/compression cycles

energy increases during the linear behaviour and stabilises when plasticity occurs. Then, it is recovered during the unloading. At the beginning of the second cycle, the damage stiffness is again followed, so no linear behaviour develops, and the strain energy stays null. Finally, the strain energy appears again in compression. The effect of hysteretic, work hardening and dissipated energies are reversed because they correspond to nonlinear behaviours. They stay constant when the elastic strain energy evolves and inversely. Hysteretic and dissipated energies are not monotonous because of the unilateral effect, which develops recoverable energy, as seen in figures 2.23d to 2.23f. Finally, the absorbed energy evolution is more complex due to the combination of nonlinear and elastic energies.

2.5.2.2   Dissipative phenomena

Then, figure 2.23 focuses on the decomposition of hysteretic and work hardening energies as presented in tables 2.16 and 2.17, respectively, for the BARFRA and RICBET models. Figures 2.23a and 2.23d exhibit the responses of two traction and compression cycles. In contrast, only traction cycles are considered in figures 2.23b and 2.23e, and in figures 2.23c and 2.23f only compression cycles are of interest.

With the BARFRA model (fig. 2.23a to 2.23c), the hysteretic energy is only associated with damage. Nonlinearity develops during the first traction cycle (0 to 1 s in figures 2.23a and 2.23b). The work hardening associated energy is negative for damage. Clausius-Duhem inequality (eq. 2.5) is checked because the dissipative energy stays positive, validating the thermodynamical approach of the BARFRA

(a) BARFRA - traction/compression   (b) BARFRA - only traction   (c) BARFRA - only compression

(d) RICBET - traction/compression   (e) RICBET - only traction   (f) RICBET - only compression
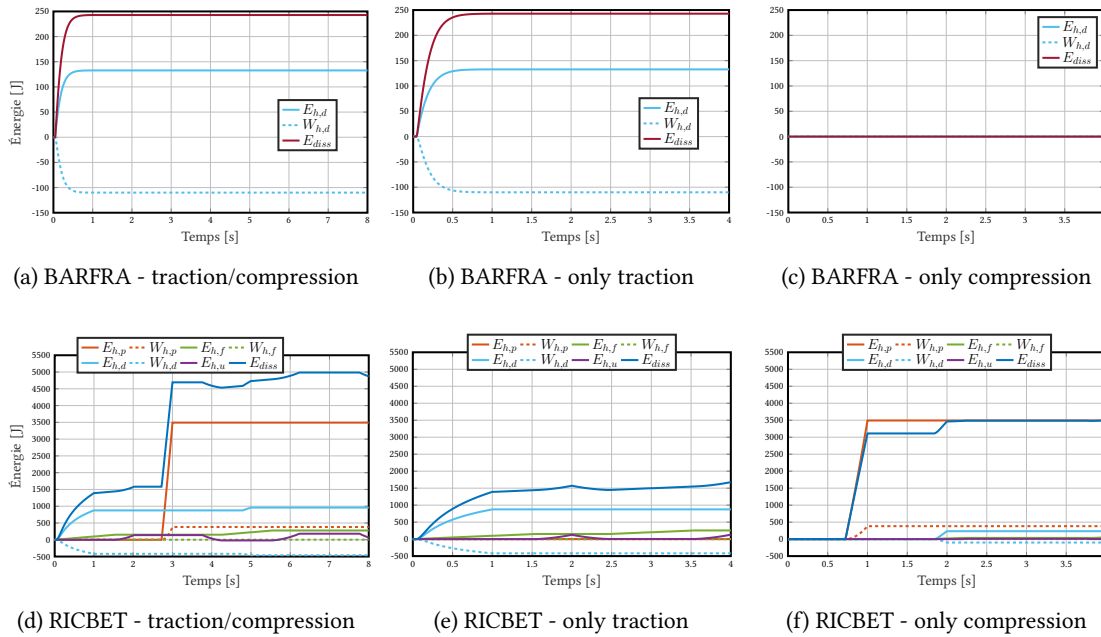
Figure 2.23: Energy distribution of dissipative phenomena for one fibre element - two cycles

model.

RICBET model (fig. 2.23d to 2.23f) is characterised by four dissipative phenomena. For traction cycles (fig. 2.23e), the plasticity energy is null because the plasticity model is defined for compression. The damage energy only evolves during the first second corresponding to the first loading, meaning that during the second cycle, no more damage develops. On the contrary, the friction energy increases during both cycles because when cracks are opening, they dissipate energy. Here, the damage energy represents the major part of the dissipated one because of the few considered cycles. Then, for the unilateral effect, this is recoverable energy developing only during stiffness recovery. Contrary to crack openings, crack surface friction, which involves heat transfers, the unilateral effect is not responsible for any energy transfer and does not eliminate energy from the system. Finally, in terms of work hardening energies, the one associated with damage is also negative, as for the BARFRA model. For friction phenomena, the work hardening energy is negligible in this case. In compression (fig. 2.23f), the most dissipative phenomenon is plasticity with a positive associated work hardening energy.[3] Because the stress becomes positive at the first cycle end, the element is submitted to traction. So, damage energy, followed by friction and unilateral effect, also appears. The same loading is applied during the second cycle, so no additional plasticity develops, and only friction induces few energy dissipations. Due to the positive plasticity work hardening, the dissipated energy is lower than the plastic hysteretic energy. Finally, dissipated energies during traction and compression cycles in figure 2.23d are a combination of dissipations in figures 2.23e and 2.23f. The plasticity is the most dissipative phenomenon here because of the strong nonlinearities reached in compression. It will not be the case in the RC beam analysis. The Clausius-Duhem inequality (eq. 2.8) is again checked in the three figures because the dissipated energy is always positive, validating the thermodynamical approach of the RICBET model.

---

[3]Here, only a concrete fibre is studied. That is why no discussion is done in terms of steel yielding. It would be required in a RC element analysis if nonlinearities were to develop in compression.

2.5.3   Energy balances at the structural level

The dynamic computations are now studied in terms of energy dissipations at the structural level, based on the decomposition in table 2.14. First, figure 2.24 presents the absorbed energy decomposition between steel reinforcements and concrete to validate the experimental objective. Steel absorbed energy is recoverable, corresponding only to the elastic strain energy. No nonlinearity develops at the steel material level. The rebars are well staying in their elastic range. On the contrary, the nonlinearity developments at the concrete level induce an un-recoverable total absorbed energy.
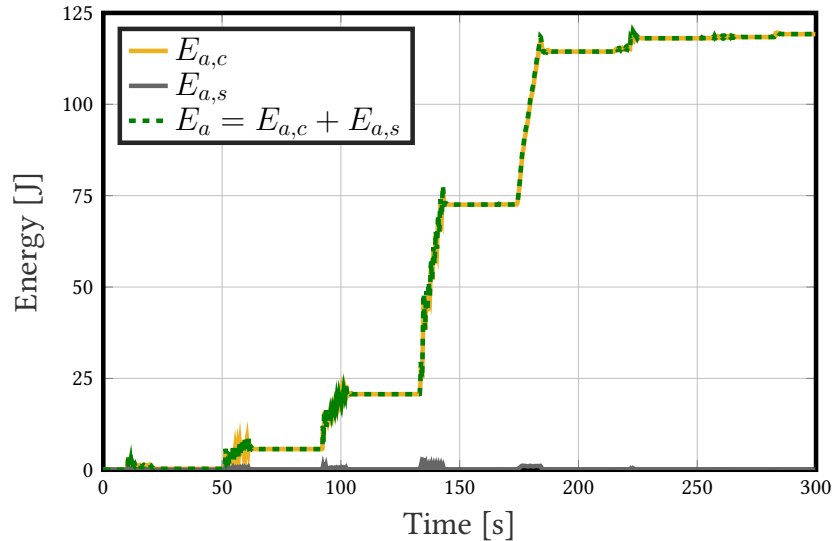
Figure 2.24: DSS2 test - Total absorbed energy decomposition between steel and concrete

2.5.3.1   WN1 test

Figure 2.25 displays the absolute and relative energy decompositions at the structural level (tab. 2.14), as well as the associated errors between total and imparted energies. The total energy is decomposed between damping, absorbed and kinetic energies. The absorbed energy is recoverable for both formulations because of the computation linearity: the only non-null energy being the strain energy at the material level. Then, the relative and absolute energy balances appear to behave similarly and are validated. The errors in figures 2.25c and 2.25d are converging towards values inferior to 5%, so it can be considered that the energy implementations are accurate. In the beginning, more significant errors are due to the weak values of imparted energy. Finally, the global errors written represent the mean of time-domain errors and again demonstrate a good accuracy or results for both formulations.

Because the absolute energy balance (section 1.1.3.1) exhibits an equal distribution and because it is commonly used in earthquake engineering, figures 2.26 and 2.27 focus on this formulation. The three model parameters are studied herein: (i) the choice of material behaviour (BARFRA and RICBET), (ii) the choice of damping formulation (RD, MPD, KPD, MD and WPD) and (iii) the choice of damping ratio (0.5% and 1%).

In figure 2.26, the final values of total and imparted energies are plotted to evaluate the ability of each damping formulation to characterise the energies accurately. Remarkably, the modal damping formulation leads to considerable differences between total and imparted final energies. In addition, BARFRA and RICBET do not give the same responses with this formulation (MD) despite the com-

(a) Absolute energy balance

(b) Relative energy balance

(c) Absolute energy balance error

(d) Relative energy balance error
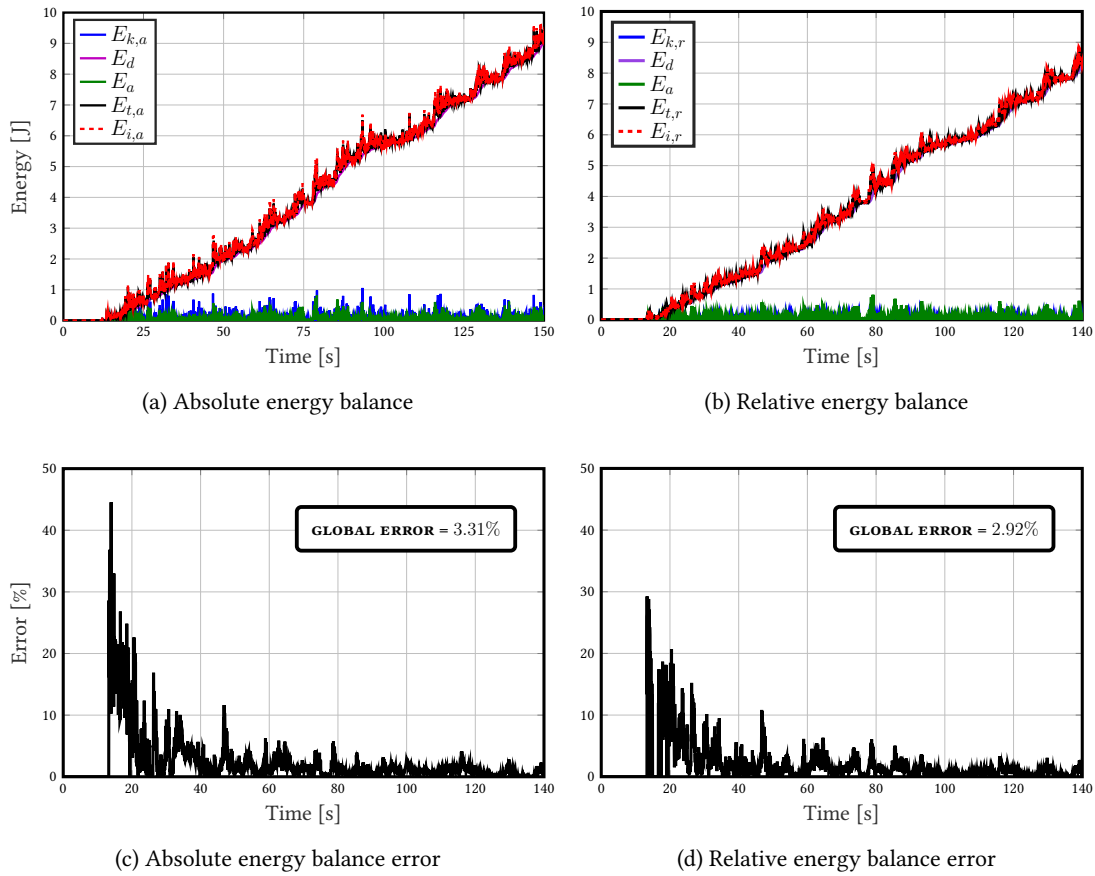
Figure 2.25: WN1 test - Structural energy balances - RICBET - RD 0.5%

putation linearity, again demonstrating the incompatibility between BARFRA and MD formulation as already discussed. So, this formulation is not adequate for this kind of input signal. Minor differences are observable between the four other formulations between BARFRA and RICBET responses, particularly for KPD formulation. It demonstrates that microscopic cracks may open during this test despite the expected computation linearity, leading to very few energy dissipations. It is not observable in the global responses because the maximal displacement depends neither on the constitutive model nor the damping model. Only the increase in viscous damping ratio leads to lower maximal displacements. In comparison with the experimental data, all computations minimise the maximal displacements, particularly WPD with its more substantial damping effect. Finally, the relative energy values are also plotted and follow the same tendencies as the absolute ones. So, the errors seem to result from damping and absorbed energies. Indeed, the kinetic energy is the only one varying between both formulations, and its consequence is observed in the lower amplitudes in the case of relative energy balances. Then, when the damping ratio increases, the damping energy also rises, followed by the imparted and total ones.

Figure 2.27 presents the total energy decomposition at the computation end between damping, absorbed and kinetic energies. Despite the almost linearity of this test, the MD formulation exhibits a non-negligible value of final absorbed energy, which is not physical because the beam was not damaged. This value can explain the substantial gap between total and imparted energies (fig. 2.26a and 2.26c): the non-null absorbed energy improves the total one, while the imparted energy is not changed. On the

(a) BARFRA - $\xi = 0.5\%$

(b) RICBET - $\xi = 0.5\%$

(c) BARFRA - $\xi = 1\%$

(d) RICBET - $\xi = 1\%$
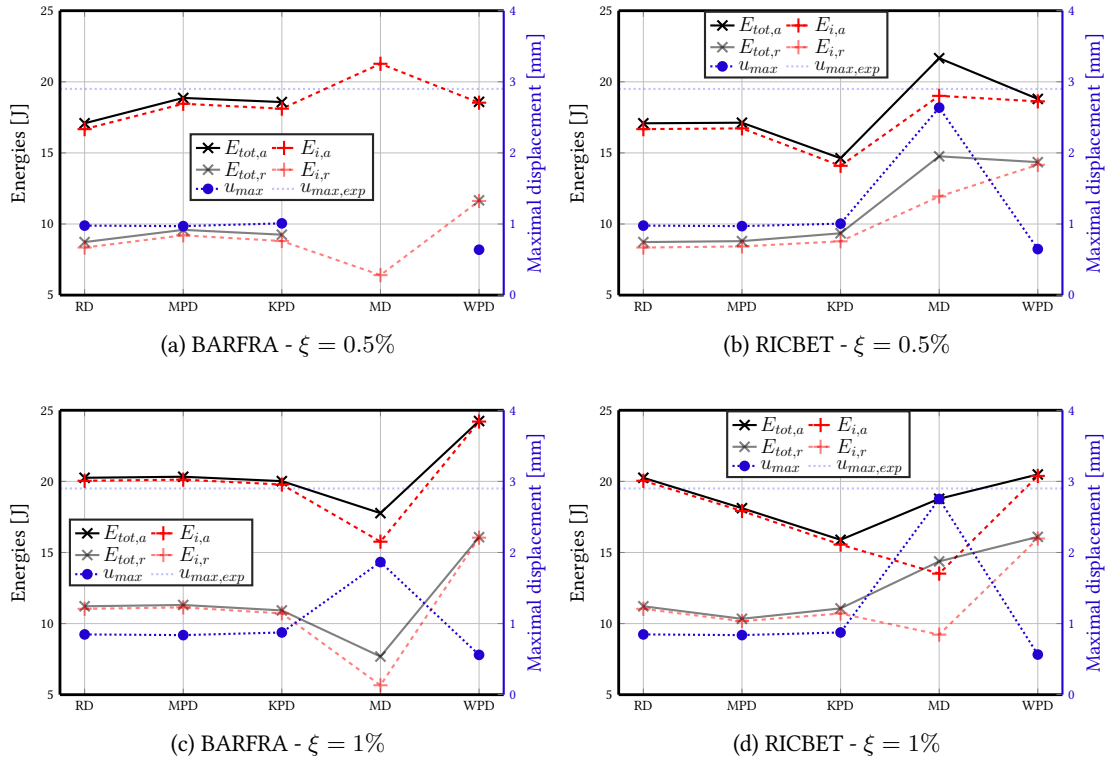
Figure 2.26: WN1 test - Imparted and total energies in parallel to the maximal displacement - absolute energy balance

contrary, the absorbed energy is negligible for all other formulations, as expected. Some variations are observable between BARFRA and RICBET constitutive models, particularly for KPD and WPD formulations. With RICBET, the kinetic energy is smaller than with the BARFRA model. It demonstrates that BARFRA and RICBET are not given exactly the same responses. So, low nonlinearities are developed. In addition, the damping formulation choice influences the numerical response. Finally, as expected, it appears that increasing the damping ratio leads to an increase of the damping energy proportion and a reduction of the kinetic one.

2.5.3.2   DSS2 test

DSS2 test is the first test leading to visible damage on the tested beam. Figure 2.28 again presents the absolute and relative energy balances accompanied with their errors along time. The kinetic energy is negligible in both cases because of values reached by other energies. In addition, relative and absolute energy balances are similar because both decompositions' damping and absorbed energies are equal. The absorbed energy is no more recoverable because of nonlinearities. All energies increase by increments corresponding to the harmonic signal parts with large amplitudes. So, with the absorbed energy study, it can be deduced that damage begins to develop during the second block and continues during the third to fifth blocks, which are the ones with frequencies between 7.5 Hz and 6 Hz, close to the beam eigenfrequency. It is also well observable in figure 2.29, where the proportions between damping, absorbed and kinetic energies are plotted after each harmonic block. A substantial variation of absorbed energy proportion is notable between $n2$ (white-noise after the first block) and $n3$ (white-noise after

(a) BARFRA - $\xi = 0.5\%$

(b) RICBET - $\xi = 0.5\%$

(c) BARFRA - $\xi = 1\%$

(d) RICBET - $\xi = 1\%$
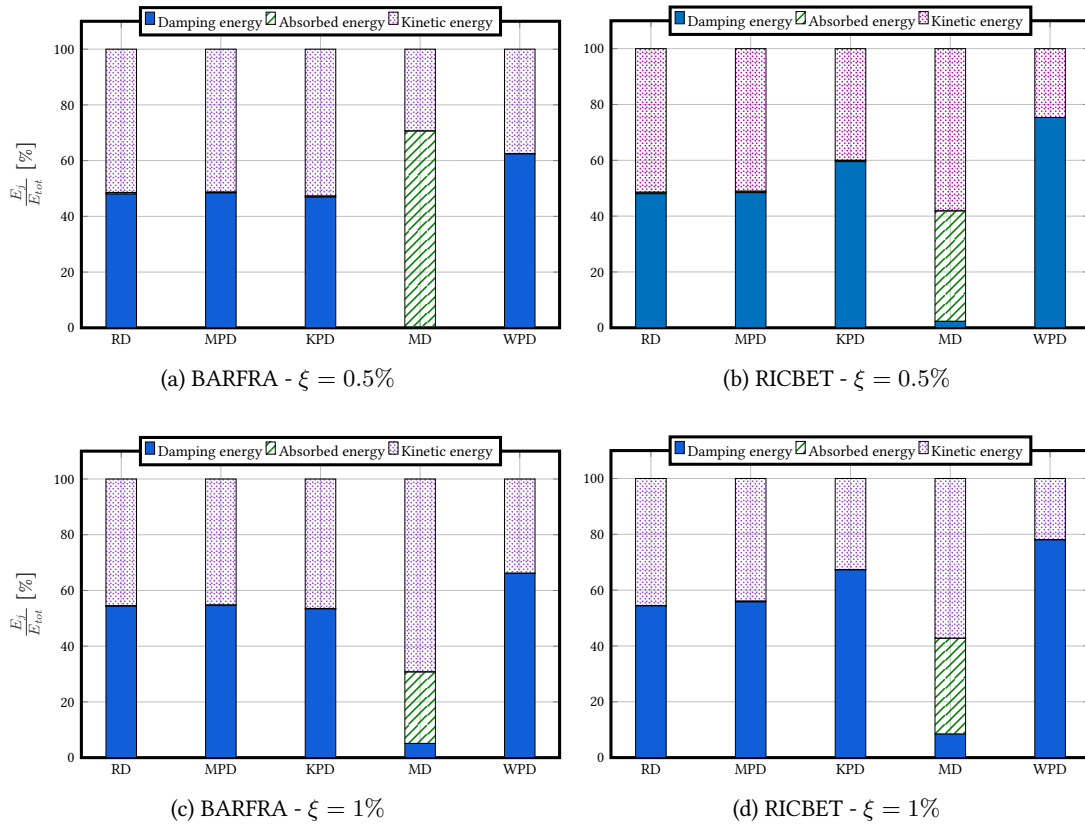
Figure 2.27: WN1 test - Distribution of dissipative energies at the structural level - absolute energy balance

the second block) blocks. Then, it continues to increase until a stabilisation after the fifth block.

Back to figure 2.28, in terms of errors[4], an exact equivalence is obtained between total and imparted energies because the global error is around 1.5%. In the beginning, the errors are localised during damageable blocks, undoubtedly due to the nonlinearity development as discussed with the WN1 test. In the end, a more stable error is due to the damping energy because the gap between total and imparted energies is equal to the increase of damping energy. So, this error is removed with other damping formulations.

Then, the aim of figures 2.29 and 2.30 is to compare BARFRA and RICBET constitutive models with two damping formulations for which the dynamic responses with the BARFRA model were satisfactory: RD and KD_ACT. These figures show that both models behave differently in terms of energies. The proportion of absorbed energy (fig. 2.29) is much more prominent with the BARFRA model, linked with the larger displacements computed (fig. 2.30). So, even if BARFRA considers less dissipative phenomena, the model can dissipate a significant amount of energy. The absorbed energy evolution discussed above is more regular with the RICBET model and RD formulation between the second and fifth blocks. With the BARFRA model, the second harmonic block much more damages the beam. It can be deduced that

---

[4]The error evaluates the gap between the total and imparted energies $\int_t \dfrac{|E_{tot}(t) - E_i(t)|}{|E_i(t)|}\,\mathrm{d}t$.

(a) Absolute energy balance

(b) Relative energy balance

(c) Absolute energy balance error

(d) Relative energy balance error
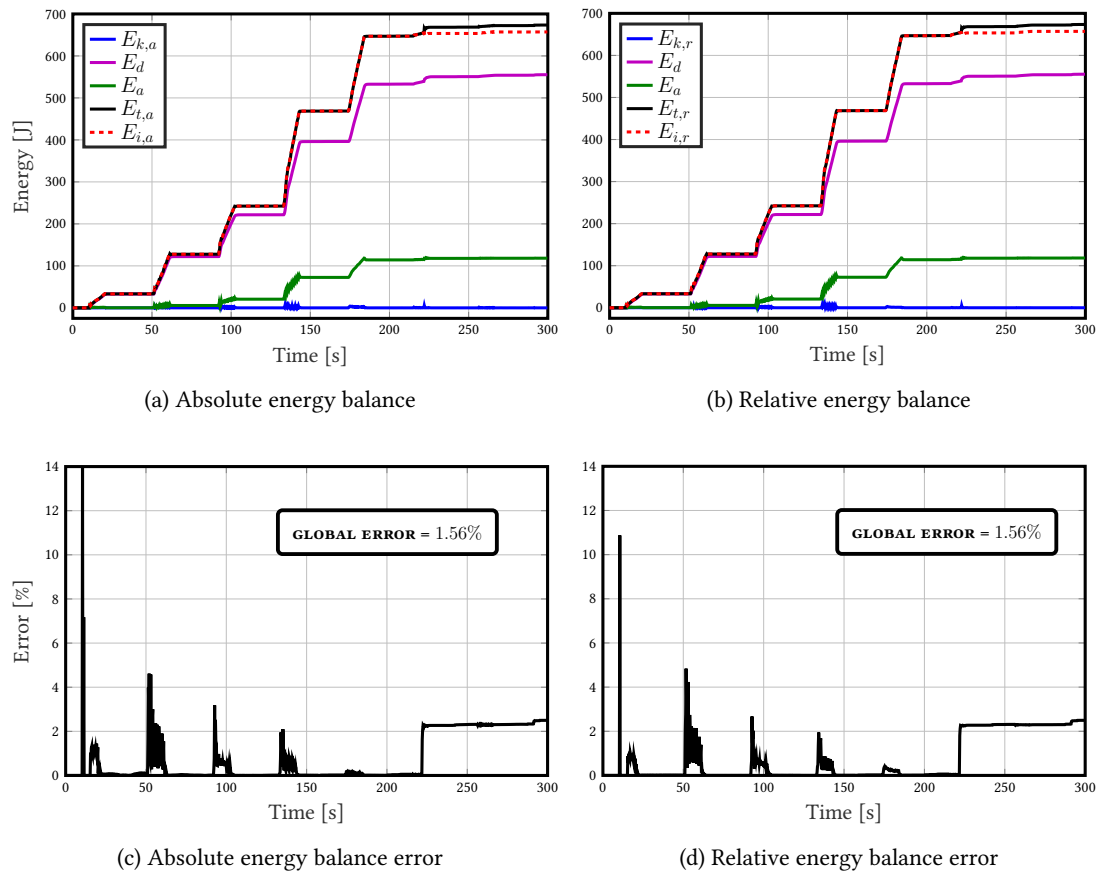
Figure 2.28: DSS2 test - Structural energy balances - RICBET - RD 2%
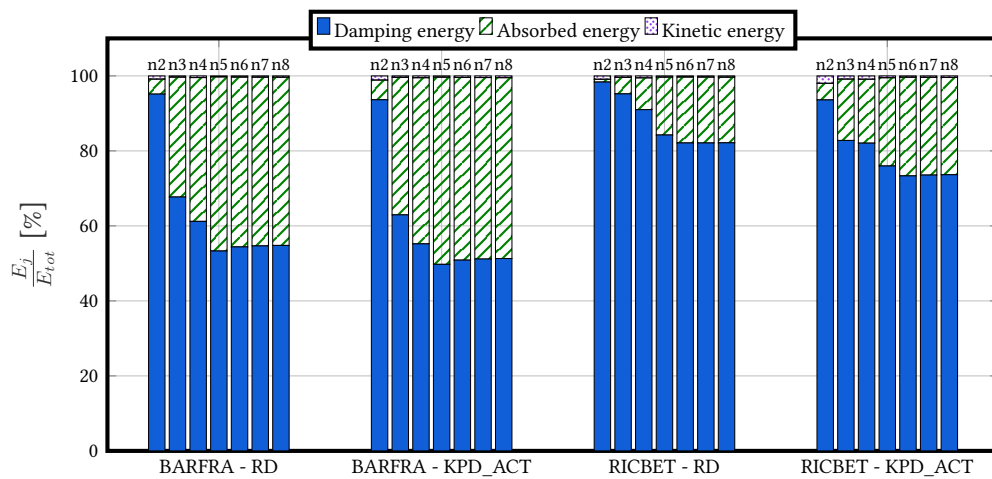
Figure 2.29: DSS2 test - Distribution of dissipative energies at the structural level along the computation - 2%
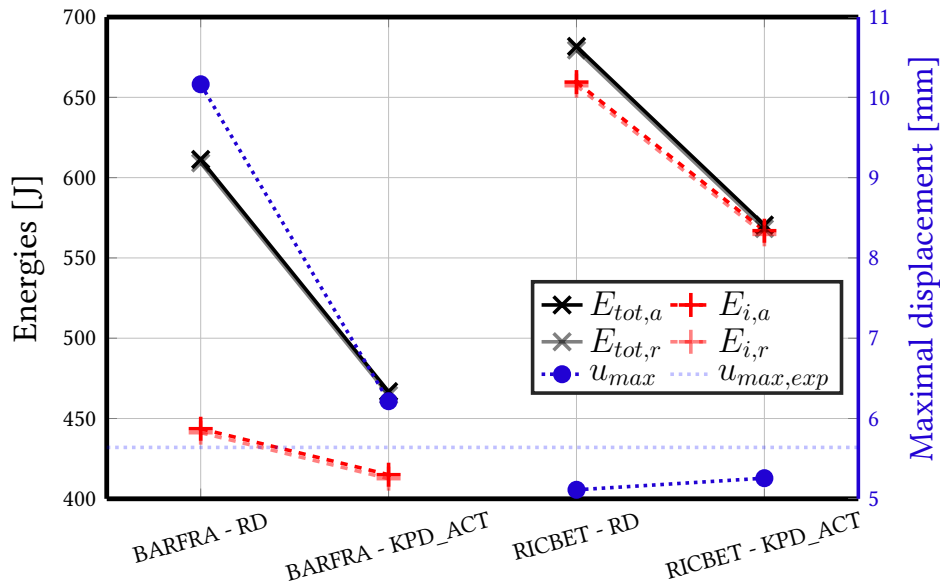
Figure 2.30: DSS2 test - Imparted and total energies in parallel to the maximal displacement - 2%

the second block leads to a crack opening. Because this is the only dissipative phenomenon with BAR-FRA, a large amount of energy is dissipated at this moment. On the contrary, with the RICBET model, the dissipations are more balanced between the different phenomena than with the BARFRA modal, and this model can accurately represent the evolution of dissipations. Finally, figure 2.30 shows that the absolute and relative balances are similar with smaller relative values because of the kinetic energy. The errors between final imparted and total energies are much larger with BARFRA. The total energy is larger than the imparted one, so unrealistic energy is dissipated with the BARFRA model. Finally, between the damping formulations, KPD_ACT appears to be better than RD, particularly in terms of maximal displacements compared with the experimental value, BARFRA giving a too large value and RICBET a too-small one.

RICBET is now considered to compare the damping formulations because of the better dynamic responses obtained with this constitutive model and its best ability to characterise energies. Again, figure 2.31 focuses on comparing imparted and total energies and maximal displacements. Figure 2.32 is particularly interested in the dissipation decomposition between damping and absorbed energies at the computation ends. Because the beam movement stops at the end, the kinetic energy must be null at this moment, so it is not plotted.

Figure 2.31 first shows that the final energies are inversely proportional to the maximal displacements and are depending on damping formulations because of the integration through displacement increments. Indeed, more damage occurs if larger displacements are reached and a more considerable amount of absorbed energy is developed. However, this induces a reduction of the damping energy to a more substantial extent, explaining the decrease of energy. In addition, the relative and absolute energy balances are similar because equality between the relative and absolute energies is observed here. Some formulations are inducing accurate energy balances corresponding to equality of total and imparted energies: (i) for RD-type formulations only RD_ACT must be removed, (ii) on the contrary, for MPD-types, the parameter update is improving the energy characterisation, (iii) all of the KPD-type formulations are accurately representing the energetic structural behaviour, (iv) while neither MD nor MD_ACT are adequate, (v) finally, the use of the tangent or secant stiffness matrices in WPD-type formulations must be avoided.
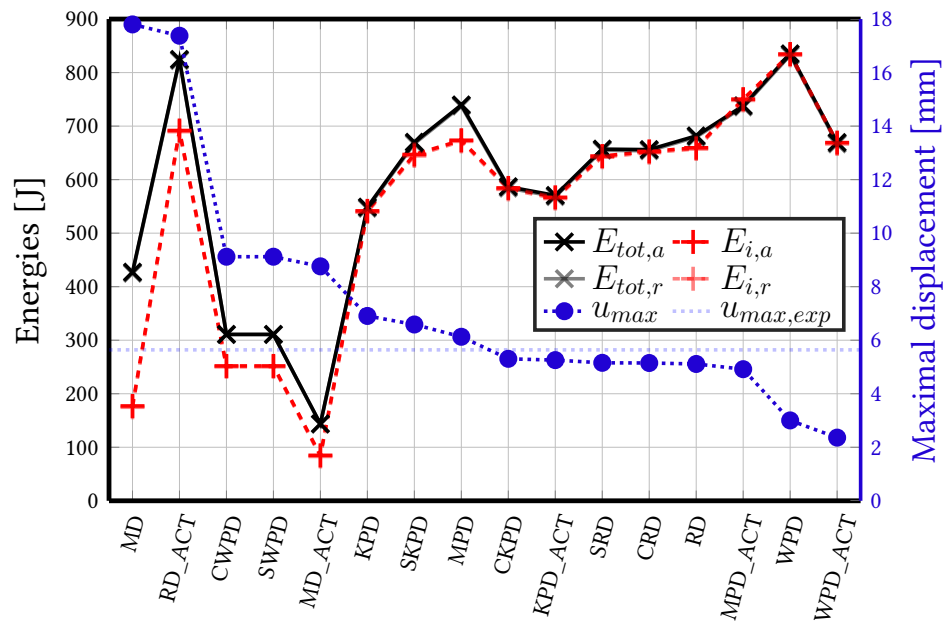
Figure 2.31: DSS2 test - Imparted and total energies in parallel to the maximal displacement - RICBET - 2%
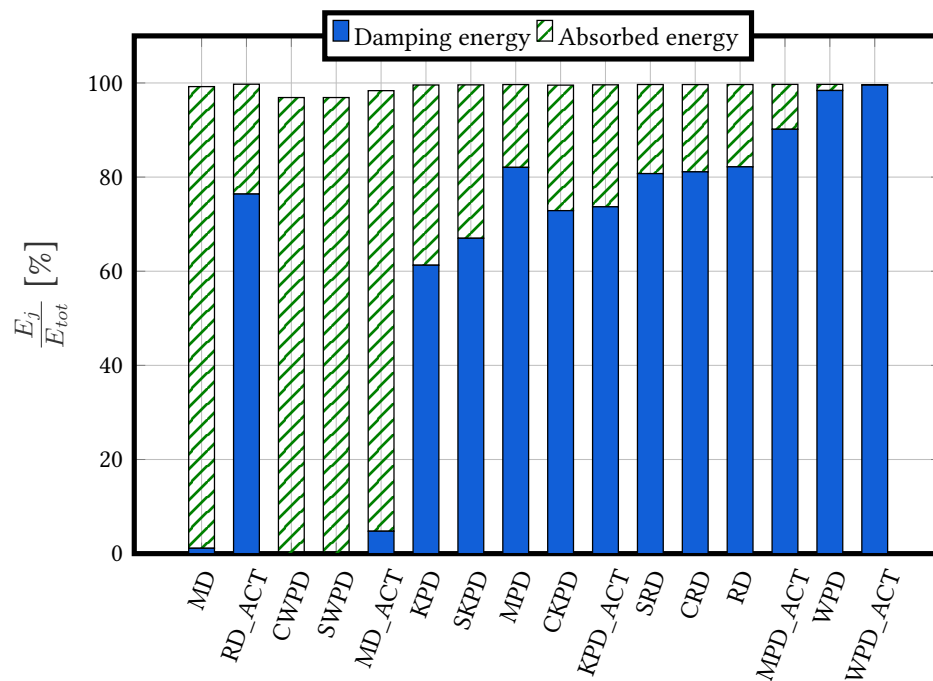
Figure 2.32: DSS2 test - Distribution of dissipative energies at the structural level - RICBET - 2%

Again, figure 2.32 demonstrates that each damping formulation impacts energy computations differently. For WPD and WPD_ACT, almost no absorbed energy develops because the computations stay linear. On the contrary, with MD, MD_ACT or CWPD and SWPD, the damping energy is negligible, demonstrating the considerable impact of material dissipations. However, because it was previously observed that these formulations were not leading to numerical responses matching the experimental ones, it can be deduced that this behaviour is not representative of the physical one. Now, the RD-, MPD- and KPD-type formulations can be compared. KPD-type ones induce lower damping energy values, while MPD-types leads to the most considerable damping energy proportions. RD-type formulations are in the middle because of the impact of both mass and stiffness proportional parts. This observation is in adequacy with the literature, where it was demonstrated that the mass proportional part in RD is responsible for developing spurious damping forces. RD_ACT leads to stronger hysteresis loops, as discussed in part 2.4.3. That is why the proportion of absorbed energy is superior to other RD-type formulations. If RD_ACT is eliminated from the analyses, it appears that updating the parameters or the stiffness matrix during computations induces the most substantial influence of the damping energy compared to the absorbed one.

The final model parameter to study is the damping ratio. Figures 2.33 and 2.34 focus on four damping formulations (RD, CRD, CKPD and WPD) with four damping ratios (1%, 2%, 3% and 5%). Figure 2.33 shows that the damping ratio influence on final energies strongly depends on the damping formulation. It is not very important for RD and WPD formulations (fig. 2.33a and 2.33b). While increasing the damping ratio induces an increase of final energies, accompanied by a decrease of the maximal displacements for CRD and CKPD (fig. 2.33c and 2.33d). When the damping ratio increases, a decrease of the beam
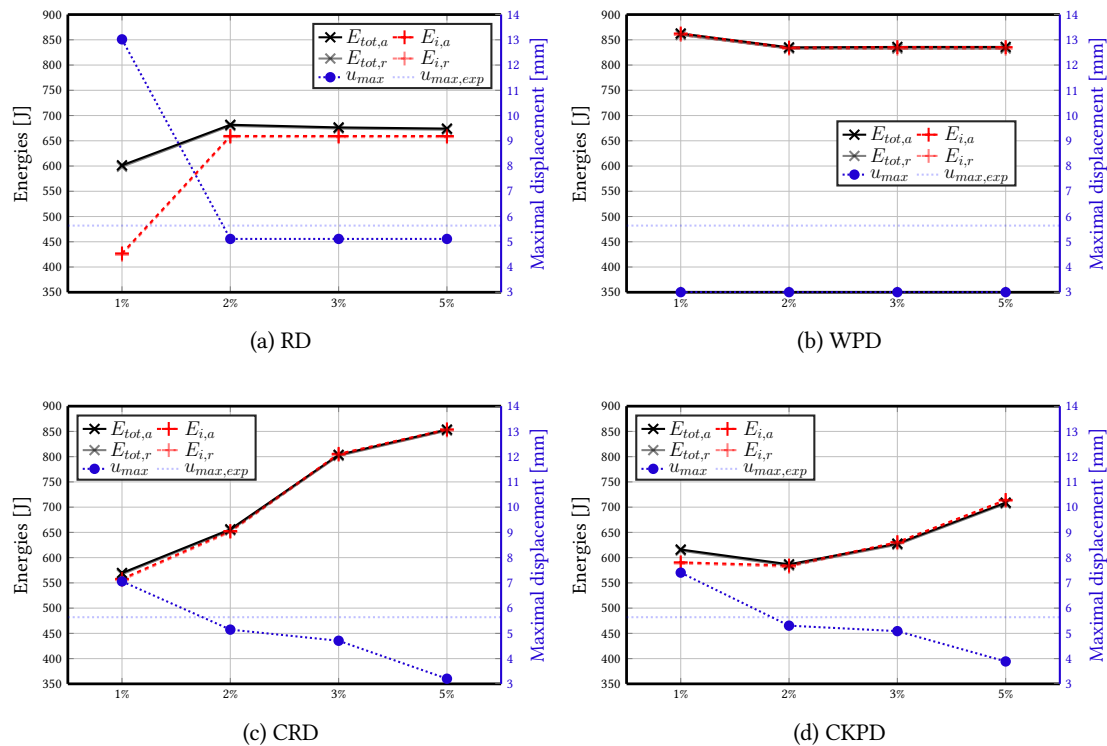
Figure 2.33: DSS2 test - Imparted and total energies in parallel to the maximal displacement - RICBET - ξ influence

(a) RD

(b) WPD

(c) CRD

(d) CKPD
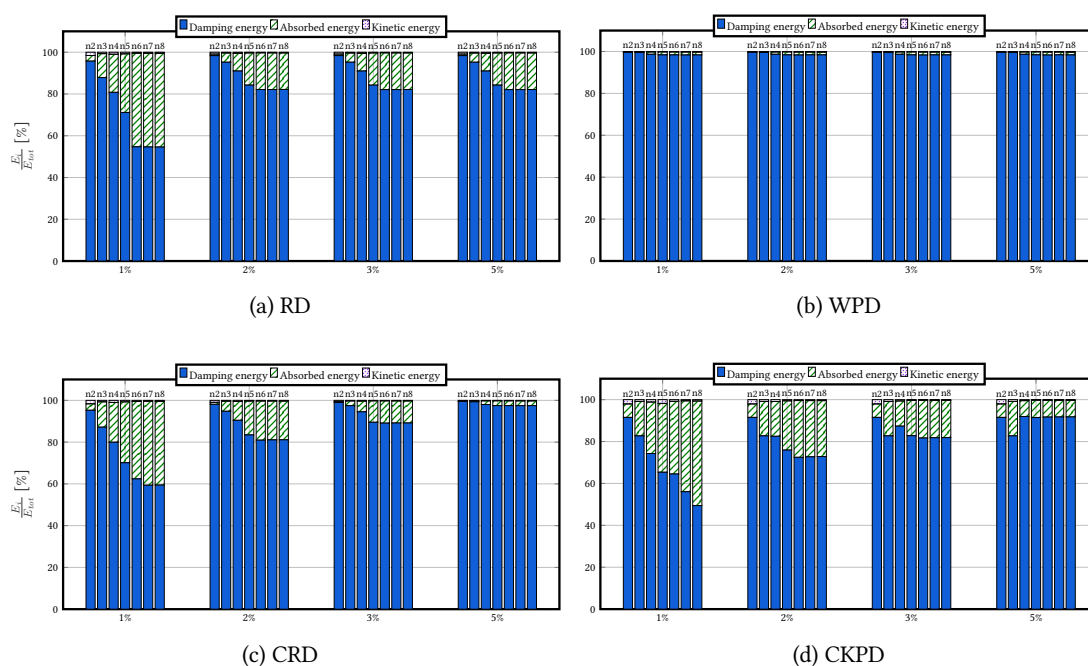
Figure 2.34: DSS2 test - Distribution of dissipative energies at the structural level along the computation - RICBET - ξ influence

movement amplitudes is expected, and particularly of the maximal displacement. So, using the tangent stiffness matrix seems to be more representative of the experimental behaviour. If no update is performed during the computation, the response is merely influenced by the damping formulation choice than by the damping ratio. Then, a larger error is obtained between the final total and imparted energies for a damping ratio of 1% for all formulations. The total energy is larger than the imparted one, so it can be supposed that the absorbed energy is too strong in this case. 1% of damping ratio is insufficient to obtain an equitable energy balance compared to stronger viscous damping ratios.

In terms of total energy decomposition at the computation end, figure 2.34 presents the proportion evolutions for each white-noise signal part, again with the same four damping formulations and four damping ratios. As observed in figure 2.33, CRD and CKPD exhibit a behaviour strongly dependent on the damping ratio. At the same time, there is no more influence for RD, above 2%, and WPD shows the same decomposition for all damping ratios. Let us now focus on each damping formulation. With WPD, the (fig. 2.34b) the absorbed energy is negligible along with computation because of its strong damping effect leading to a linear behaviour during the DSS2 test. With RD (fig. 2.34a), the absorbed energy proportion linearly increases until $n6$ white-noise block and stabilises then with all damping ratios. So, it signifies that the damage develops in the beam until the fifth harmonic block but no more later. Then, other nonlinearity developments are observed from one damping ratio to another with CRD (fig. 2.34c). When the damping increases, nonlinearities appear during a smaller number of harmonic blocks, and the proportions of both energies stabilise later in the computation. Indeed, if the viscous damping applied on the beam increases, the beam movement amplitudes are reduced, and minor damage occurs. It, thus, leads to a lower decrease of the beam eigenfrequency, and harmonic blocks with lower eigenfrequencies are no more inducing resonance in the beam. It explains the sooner stabilisation and the reduction of absorbed energy proportion. This conclusion is also applicable to CKPD formulation (fig. 2.34d). Finally, an important conclusion from figures 2.27, 2.32 and 2.34 is that the damping energy always represents the major part of the total energy (in the case of adequate damping formulations),

demonstrating the significant impact of the viscous damping in structural nonlinear dynamic analyses.

2.5.3.3   Complementary tests

Section 2.4.4 was interested in three complementary dynamic tests. Figures 2.35 and 2.36 characterise the structural energy representations of these tests. Different energy amplitudes are reached during the three tests. Substantial errors are obtained for the DSS3 test between the imparted and total energies, with total energy inferior to the imparted one. It can be due to the lack of damage occurring during the first two harmonic blocks because it appears in figure 2.36a that no damage develops during these blocks. From figure 2.19, it was deduced that the DSS3 test was the best dynamically characterised. Now, it appears that energetically this is the contrary. Again, it demonstrates that an accurate description of energies does not always accompany an accurate representation of beam movements. It can also explain the lack of damage discussed for the DSS4 test. If the beam is not damped enough during the DSS3 test, the eigenfrequency does not decrease enough, and the beam resonance is reduced, leading to smaller
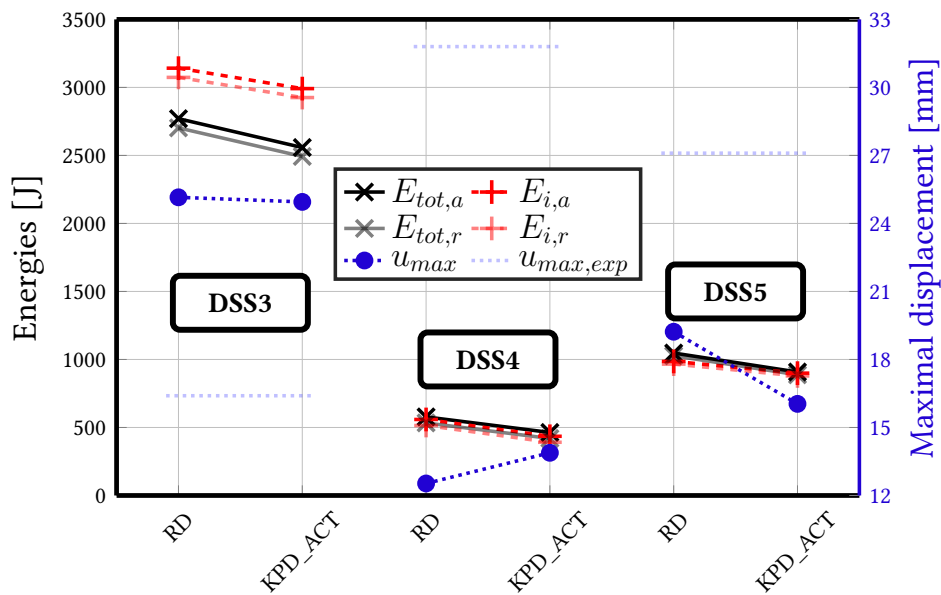
Figure 2.35: DSS3 to DSS5 tests - Imparted and total energies in parallel to the maximal displacement - RICBET

(a) DSS3 - 1%   (b) DSS4 - 0.5%   (c) DSS5 - 1%
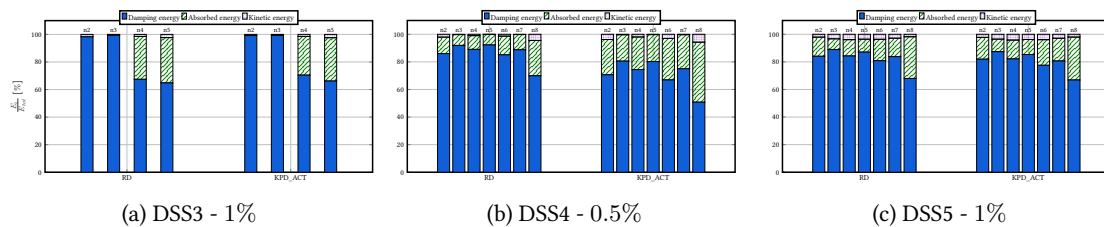
Figure 2.36: DSS3 to DSS5 tests - Distribution of dissipative energies at the structural level along the computation - RICBET

beam movements. Finally, for DSS4 and DSS5 tests, energy balances are validated in figure 2.35. However, the evolutions of energy proportions in figures 2.36b and 2.36c are not smooth: oscillations are observed from one block to another what will have to be explained using the analyses of dissipative phenomena in concrete (section 2.5.4).

2.5.4   Dissipative phenomena at the concrete level

This section aims to study the absorbed energy decomposition proposed in table 2.15 from the different dissipative phenomena described in table 2.16 for the BARFRA model and table 2.17 for the RICBET model. Dissipations occur when the concrete reaches a nonlinear behaviour. It was previously demonstrated that the WN1 test conserves the beam in its elastic behaviour. In figure 2.37, it is thus shown that the absorbed energy is equal to the elastic strain one, and the hysteretic or dissipated energies are null. It validates the beam elastic behaviour again during this test. So, the analyses will be focused on the DSS2 and the following tests.
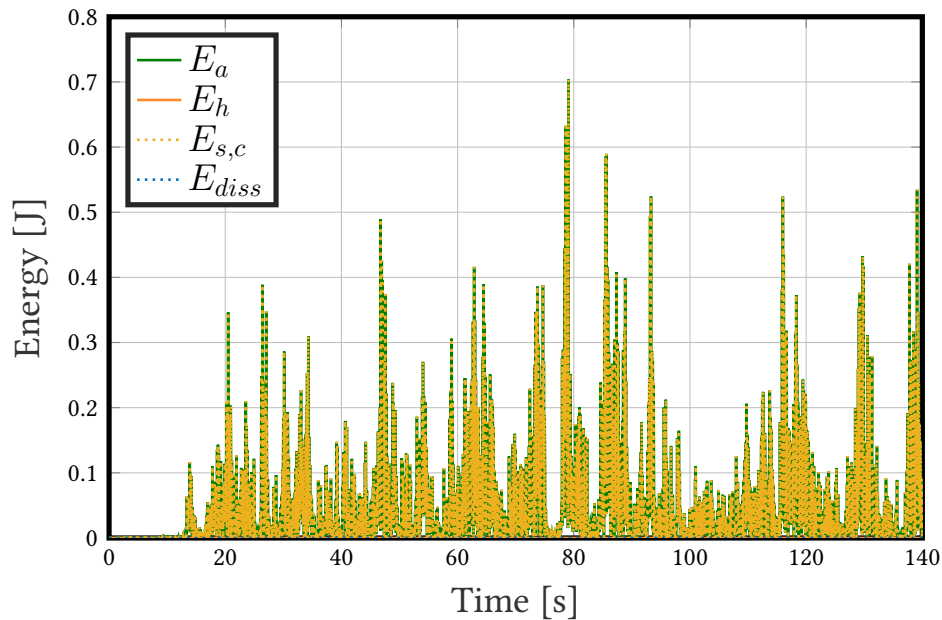
Figure 2.37: WN1 test - Concrete energy balance - RICBET - RD 0.5%

First, the classical RD formulation with a damping ratio of 2% and the RICBET constitutive model is considered in figure 2.38. Figure 2.38a displays the energies defined in table 2.15. The strain energy is negligible compared to the other ones because it is the elastic part of the behaviour. Then, differences between absorbed, hysteretic and dissipated energies come from considering the work hardening energies and the strain one. It appears that they are very close from one to another, meaning that the work hardening energy is, as the strain one, negligible. The three non-negligible energies are cumulative what explains the stepwise increase during the computation, corresponding to the harmonic signal parts. These conclusions are similar to all damping models and constitutive models. Then, the hysteretic and work hardening energies are decomposed between the dissipative phenomena in figure 2.38b. It appears that friction is the most substantial dissipative phenomenon, and the stepwise increase observed in figure 2.38a is mainly due to the friction phenomenon. No work hardening associated with friction

(a) Concrete energy balance   (b) Dissipative phenomena   (c) Dissipative phenomena [%]
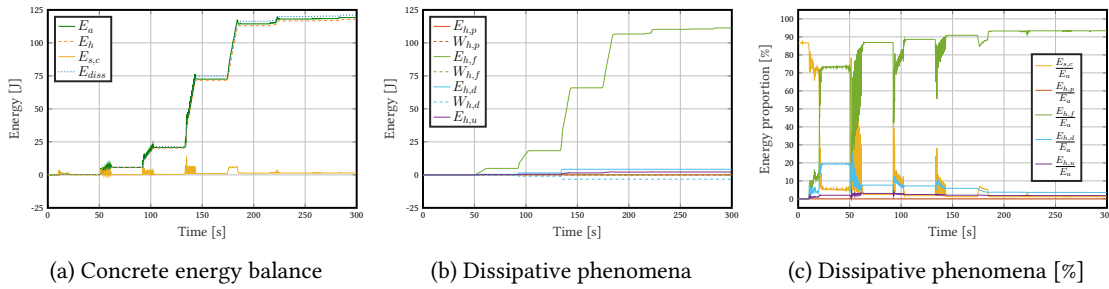
Figure 2.38: DSS2 test - Concrete energy analysis - RICBET - RD 2%

develops for the considered signal. On the contrary, the amount of energy dissipated through the damage phenomenon is much smaller, but a negative work hardening energy accompanies it. Finally, the unilateral effect dissipates also a tiny amount of energy. On the contrary, no energy is dissipated through plasticity, so no nonlinearity is reached in compression for concrete. Finally, figure 2.38c presents the time history energy evolutions along computation. In the beginning, the beam behaves elastically, so only the strain energy exists. Nevertheless, as soon as cracks open, the damage is activated and dissipates energy. Because dynamic tests are performed, cyclic loadings are applied on the beam, and the consequence is the development of friction at crack surfaces directly after the crack openings. That is why friction and unilateral effect energies appear directly after the damage one. Then, no more cracks open if the input signal is reduced, so the damage energy stabilises, but the crack surface friction still exists. The substantial increase of friction proportion characterises this. Finally, for each harmonic block, if it is more damaging the beam, new cracks are opening, and the proportion of damage energy increases to the detriment of friction one, which explains the curve forms. No dissipative energy is decreasing; these are the proportions that are evolving. Finally, because the friction and damage energies control the dissipations, a focus will be performed on themselves to compare the damping models.

Figure 2.39 shows the friction and damage energies normalised to their final values and the ratio of friction energy on the sum of damping and friction energies. Two damping formulations (RD and CRD) are presented herein with the two extreme damping ratios (1% and 5%).[5] With these figures, it appears that both friction and damage energies are only increasing during computation, as expected because they are unrecoverable energies. However, their evolutions are different: the damage energy increases are discontinuous contrary to friction ones. Because the damage energy is only dissipated once when cracks are opening. In contrast, the friction energy is dissipated continuously when cracks exist, on the condition that the crack opening is smaller than the aggregate sizes. In addition, the ratio evolution again demonstrates that at the beginning of each damageable harmonic block, damage occurs just before the friction phenomenon because the cracks must be opened before dissipating energy through friction.

A different damage behaviour develops between RD and CKPD, with a damping ratio of 1% (fig. 2.39a and 2.39c). The most severe damage occurs during the fifth block with RD formulation, while the evolution is more regular with CKPD, even if more severe damage also occurs during the fifth block. Experimentally, the monitoring of crack openings would be a way to improve the study of different damping formulations using dissipated energy tendencies. Now, the observation is different with 5% of damping ratio. First of all, the final damage is reached during the fourth block and not the fifth. With RD, a regular evolution appears similar to CKPD and 1%. However, with CKPD and 5%, only three damage steps are observed. So, the development of nonlinearities in dynamic nonlinear computations strongly depends on the selected damping formulation and damping ratio (fig. C.1 and C.2).

---

[5]All damping formulations with a damping ratio of 2% are plotted in figure C.1 (appendix C.1) to go further in the analysis. In addition, the four studied damping ratios are compared in figures C.2 (appendix C.2) for RD, CRD, CKPD and WPD damping formulations.

(a) RD 1%

(b) RD 5%

(c) CKPD 1%

(d) CKPD 5%
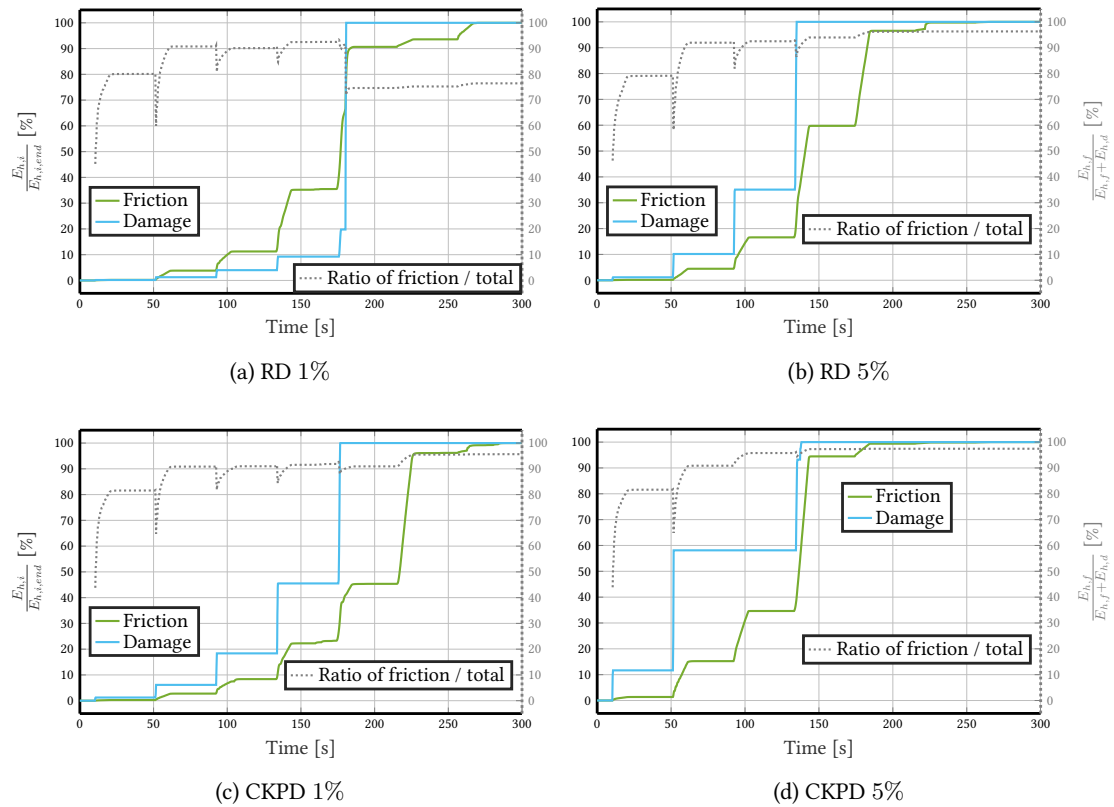
Figure 2.39: DSS2 test - Dissipation proportions at the material level - RICBET - some results

Concrete constitutive models are, now, compared in figure 2.40 for three damping formulations and a damping ratio of 2%. In the BARFRA model, the only dissipative phenomenon is the damage. The figure shows that the evolution of the damage energy in the BARFRA model is a mix of damage and friction with RICBET. Indeed, discontinuous increases are observable, followed by continuous ones. The damage model implemented in BARFRA represents a global model of concrete dissipative behaviour. Again, stepwise increases are obtained with BARFRA, but the proportions differ from RICBET. It demonstrates that the development of nonlinearities in nonlinear dynamic computations is also dependent on the constitutive model.

(a) RD

(b) CRD

(c) KPD_ACT
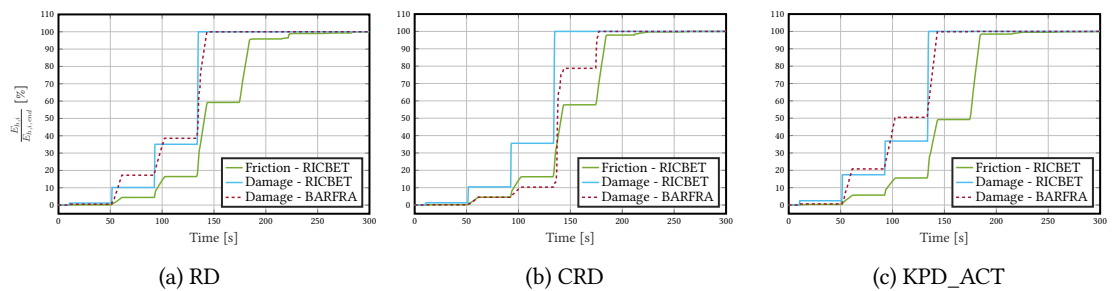
Figure 2.40: DSS2 test - Dissipation proportions at the material level - RICBET and BARFRA - 2%

Finally, the following tests are studied in figure 2.41. As discussed in previous analyses, a last level of damage occurs during the DSS3 test. During DSS4 and DSS5 tests, no more cracks opened. However, the friction is still dissipating energy during the three tests due to cracks. From one formulation to another, only the proportion amplitudes are evolving. Finally, the oscillatory evolution of the absorbed energy in figure 2.36 is necessarily a consequence of the friction between crack surfaces. It can be assumed that the friction energy is strongly influenced by the input signal contrary to the damage one because the friction variable is oscillating with the cyclic signals while the damage one is monotonously increasing. That is why the oscillations only appear during the DSS4 and DSS5 tests.

(a) DSS3 - RD 1%   (b) DSS4 - RD 0.5%   (c) DSS5 - RD 1%

(d) DSS3 - KPD_ACT 1%   (e) DSS4 - KPD_ACTD 0.5%   (f) DSS5 - KPD_ACT 1%
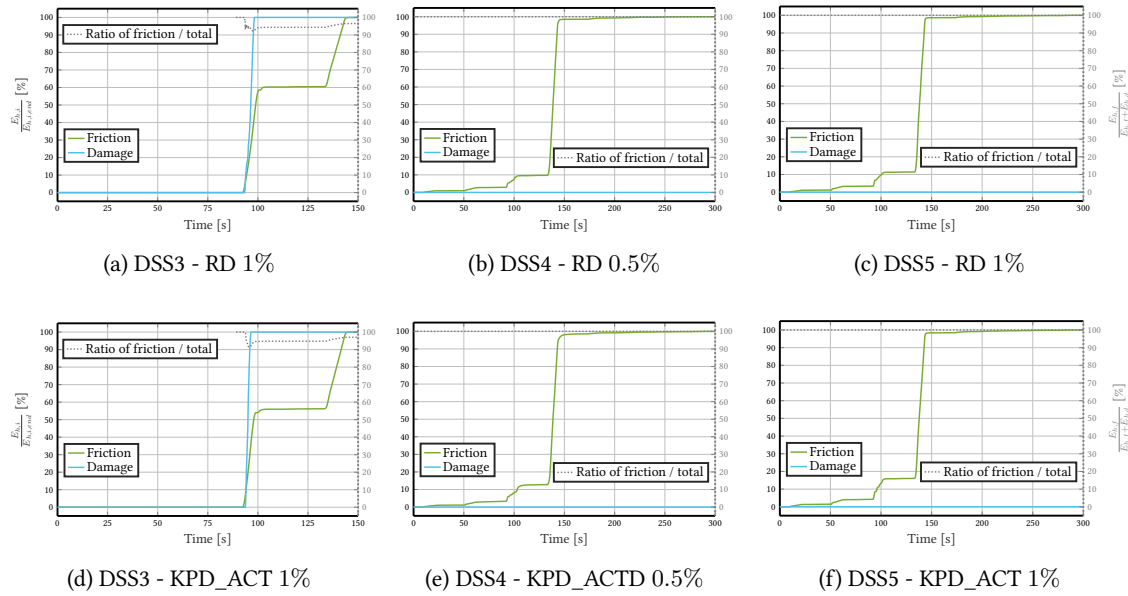
Figure 2.41: DSS3 to DSS5 tests - Dissipation proportions at the material level - RICBET

To go further, the evolutions of both variables of interest can be followed during the computation using a 3D representation of the multi-fibre beam. The damage variable is plotted at the end of each increment because it is a monotonous value. In contrast, the friction variable is plotted in the middle of increments to have an envelope value. An example of obtained results is plotted in figures 2.42 and 2.43 for the RD formulation, a damping ratio of 2% and the RICBET constitutive model. The evolutions along all increments with these modelling parameters are then plotted in appendices D.2.1 (fig. D.3) and D.2.2 (fig. D.5). In addition, in appendices D.2.1 (fig. D.4) and D.2.2 (fig. D.6), a comparison of five damping formulations is proposed. It appears in figure D.3 that the damage variable stabilises between the fourth and fifth increments, as already discussed in previous analyses. Then, between the different damping formulations in figure D.4, more severe damage is obtained with KPD and CKPD formulations. For the friction variable, the evolution along time in figure D.5 is more complex to study because it is constantly evolving with the beam excitation. Between the formulations in figure D.6, it also appears different variations. So, the nonlinearities are evolving differently from one model to another, with the largest nonlinearities observed with the KPD-type damping formulations.

(a) d - increment $t^{(i-1)}$ (b) d - increment $t^{(i)}$ (c) d - increment $t^{(i+1)}$
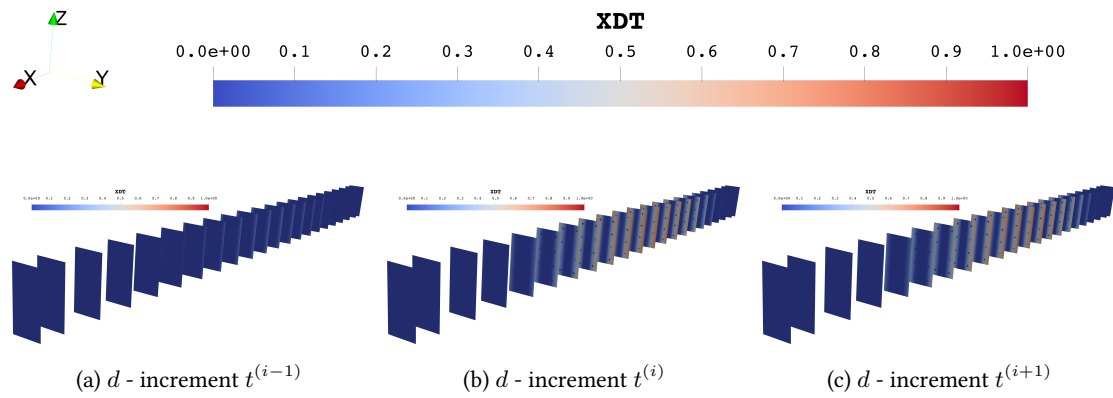
Figure 2.42: DSS2 test - Damage variable evolution along the beam - RICBET - RD 2%

(a) ε^{π} - increment $t^{(i-1)}$ (b) ε^{π} - increment $t^{(i)}$ (c) ε^{π} - increment $t^{(i+1)}$
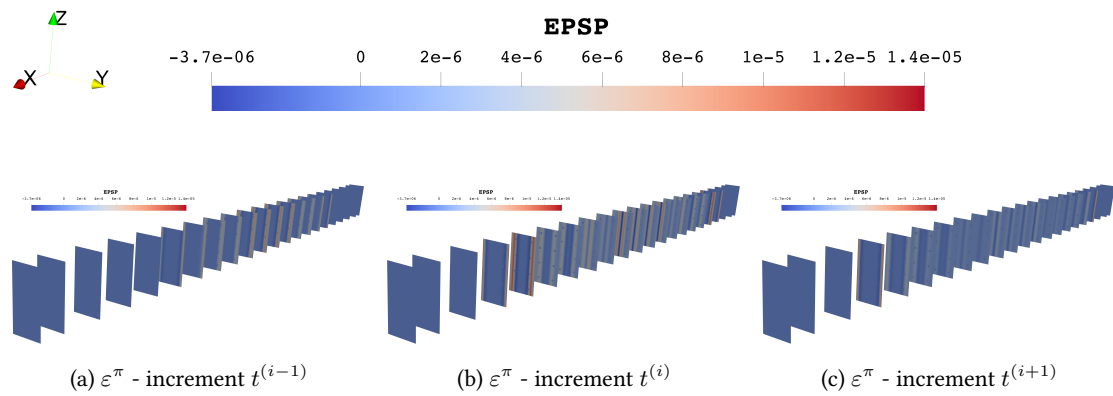
Figure 2.43: DSS2 test - Friction deformation variable evolution along the beam - RICBET - RD 2%

2.6 Synthesis

2.6.1 Performed analyses

An exhaustive numerical analysis was performed on RC beams and based on experimental data. The model has been developed in Cast3M with a multi-fibre approach. It has been calibrated on quasi-static tests before performing nonlinear dynamic analyses. Different modelling parameters have been studied: the concrete constitutive model, the viscous damping matrix and the damping ratio considered to evaluate damping formulation parameters. For the DSS2 test, sixteen damping formulations have mainly been studied with five damping ratios (0.5%, 1%, 2%, 3%, 5%) and two constitutive models. Thus, it corresponded to 160 computations with seven increments of mean duration one hour and forty-five minutes, leading to an approximative computational time of $1,680$ hours only for the DSS2 test. This number explains why some comparison choices have been made. But, the numerical analysis could have been even more enriched by studying: (i) the use of different damping ratios for the considered modes (for example, in the case of RD-type damping formulations or the modal damping matrices), (ii) the choice of the modes to use (for example, considering the modes 1 and 3 for the RD-type formulations), (iii) the use of a non-constant damping ratio for the parameter updates, or (iv) the combination of stiffness matrix and parameters updates, …

Two studies have been performed to compare the studied damping parameters. First, the comparison of numerical dynamic responses with the experimental data. The accelerations, displacements, forces and eigenfrequencies at different damage states have been interesting. Then, an exhaustive energetic analysis has been performed to evaluate the distribution of dissipative energies at the structural level and the dissipative phenomenon evolutions at the material level. A synthesis of performed analyses is proposed in figures 2.44 and 2.45. Some dynamic and energetic indicators are considered on the presented "spider" diagrams[6]: (i) the global acceleration error, (ii) the global displacement error, (iii) the global force error, (iv) the mean error on the harmonic signal part frequencies, (v) the mean error on the white-noise signal part frequencies, (vi) the global error of absolute energy balance and (vii) the ratio of damping energy on the total one. So, the best performative models are the ones given the largest area on these representations.

As a remark, some results were compared with engineering software: (i) ARTEMIS is software to identify damping values on time-dependent data (A/S, 1999), and (ii) NONLIN can evaluate structural energy balances (Advanced Structural Concepts, 2004). With ARTEMIS, identifying damping values with the considered input signals has proved complicated because of the signal definitions and the noisy experimental data. Then, NONLIN was an excellent tool to validate the energy implementations on a SDOF system at the beginning. Indeed, the comparison was performed with an elastoplastic model because no constitutive model equivalent to BARFRA or RICBET is proposed in this software. However, performing such analyses was interesting to understand how the engineering software functions and think about what is missing.

2.6.2 Important conclusions

Based on the results discussed in section 2.4, the BARFRA constitutive model (fig. 2.45c and 2.45d) is inadequate to perform nonlinear dynamic analyses. Indeed, this model lacks dissipative phenomenon modelling, despite its ability to dissipate a substantial amount of energy. It can thus be concluded that the dissipated energy is unrealistic. In addition, the brutal variation of stiffness between compression and traction can be problematic in the case of seismic excitations. However, the more complex model, RICBET (fig. 2.45a and 2.45b), can validly represent the experimental behaviour. However, based on the

---

[6]The considered error is defined in section 2.4.1.2.

(a) RD-type

(b) KPD-type

(c) MP- and MD-type

(d) WPD-type
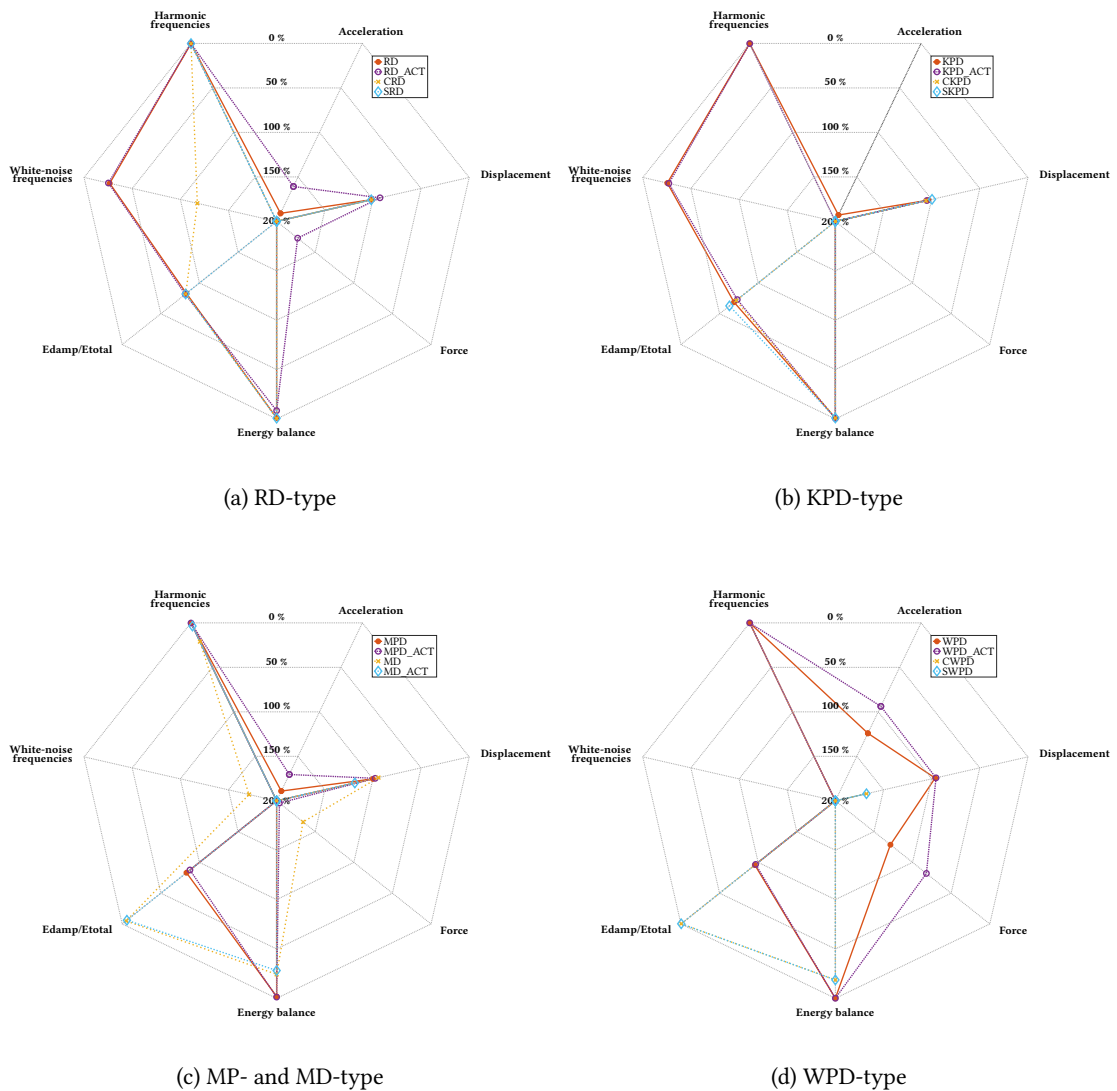
Figure 2.44: DSS2 test - Synthesis of damping formulation comparisons - RICBET - 2%

DSS4 and DSS5 test analyses, it seems that the model limits are reached. Indeed, the difficulty to match the experimental data for these two tests seems to be a consequence of the available maximal numerical damage, defined by the brittleness parameter $a_{b,t}$ in table 2.8.

Between the damping formulations (fig. 2.44), it was demonstrated that the WPD-type formulations (fig. 2.44d) have a too strong damping effect avoiding nonlinearities to develop. So it should not be used with the studied signals. Likewise, the MD-type formulations (fig. 2.44c) often exhibit unrealistic forces. MD is not able to characterise the energies even for a linear computation. In addition, both formulation types are generally inducing negligible damping energy, which is not representative of reality. So, RD-type formulations are the most appropriate. Nevertheless, the choice of these formulations must be careful. With only MPD (fig. 2.44c), few levels of damage are developed, and unrealistic forces appear. Due to the proportional stiffness part, these issues are reduced in RD-type formulations (fig. 2.44a).

(a) RICBET - RD

(b) RICBET - CRD

(c) BARFRA - RD

(d) BARFRA - CRD
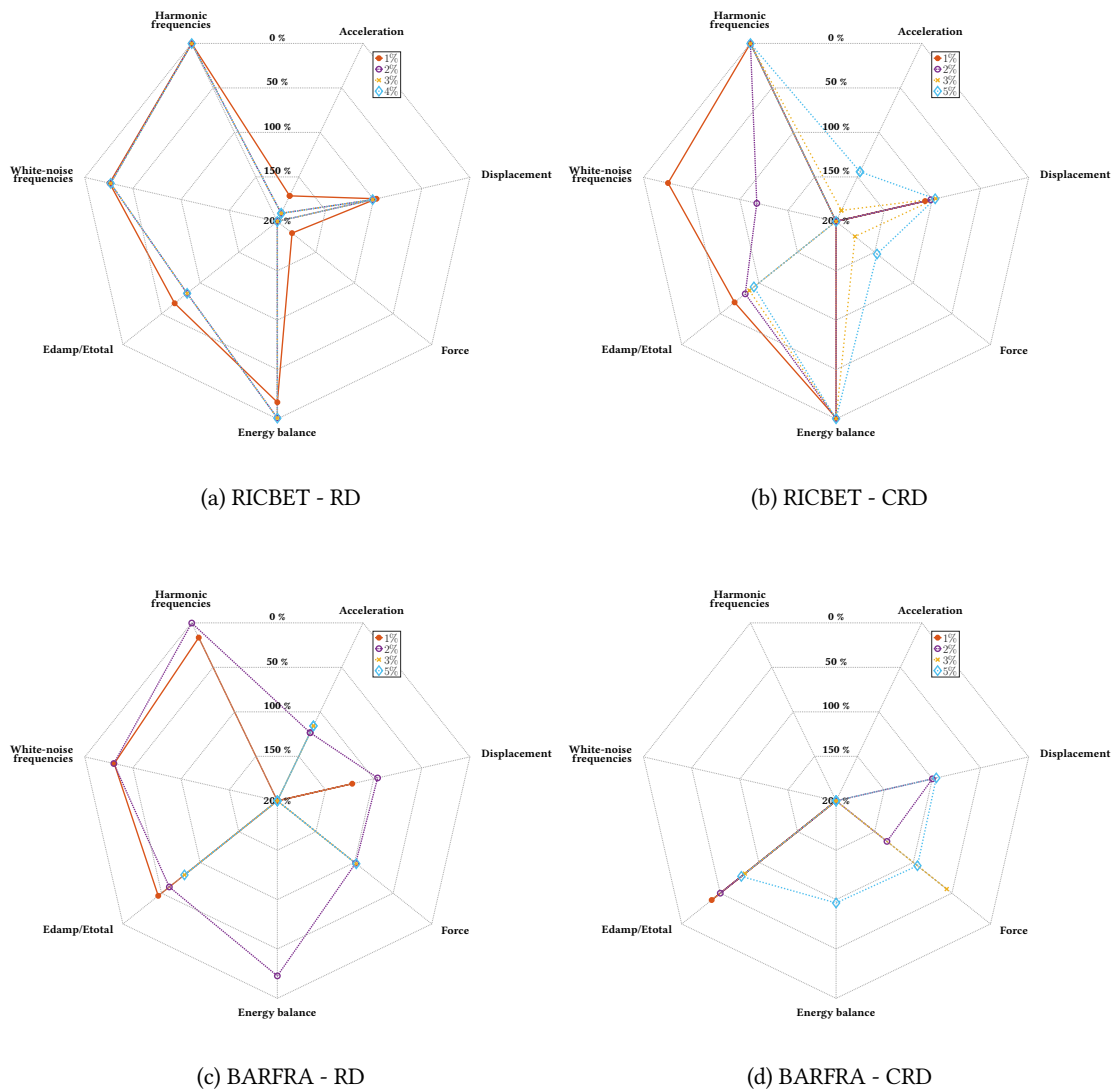
Figure 2.45: DSS2 test - Synthesis of damping ratio and constitutive model comparisons

However, the mass proportional part still plays a significant role in RD. So, RD- and KPD-type formulations (fig. 2.44a and 2.44b) are the best performative in representing experimental data with an adequately calibrated damping ratio. The accuracy is even improved by using the tangent stiffness matrix because the energy dissipations seem to be more distributed. This conclusion was obtained by considering a compromise of accuracy between all studied results. Indeed, particularly for RD-type formulations in figure 2.44a, RD_ACT gives the largest area demonstrating its better general performance. For the KPD-type formulations in figure 2.44b, KPD appears to be the best closely followed by KPD_ACT. All these results are synthesised in table 2.18. The formulations are classified based on the areas in "spider" diagrams of figure 2.44, from the largest to the lowest. An important conclusion of all performed analyses is that the most appropriate damping formulation strongly depends on the variable of interest (serviceability displacements, internal design forces, maximal accelerations, damage development,

Table 2.18: Classification of damping formulations based on "spider" diagram area - RICBET 2%

	Formulation	Area [% of total area]		Formulation	Area [% of total area]
1	RD_ACT	35.2%	9	CWPD − SWPD	12.9%
2	WPD_ACT	31.7%	10	MD_ACT	11.9%
3	KPD	30.7%	11	MPD_ACT	11.5%
4	KPD_ACT	29.2%	12	SKPD	9.76%
5	RD	28.9%	13	MPD	9.43%
6	WPD	23.4%	14	CKPD	9.14%
7	MD	19.5%	15	SRD	8.39%
8	CRD	17.7%			

energy dissipation, …). Particularly, the choice of the damping formulation appears even to influence the distribution of energies in elastic computations. For example, the stiffness matrix or parameters updates increase the damping energy proportion in dissipations.

From the analyses on damping ratio choices, similar conclusions can be discussed. This value must be carefully chosen depending on the damping formulation, the input signal, … Few recommendations can, regardless, be proposed: (i) the choice of the damping ratio does not play a significant role if the initial stiffness is considered in RD- or KPD-type formulations, (ii) on the contrary, the damping ratio strongly influences the response in the case of the tangent stiffness matrix use and (iii) when a nonlinear constitutive model is considered a low level of damping ratio must be considered (table 2.19). For the elastic WN1 test, only 0.5% is required, and for the most damageable tests, 1% to 2% are given the best results. Notably, it is observed energetically that 1% of damping ratio is insufficient for the DSS2 test. A last important conclusion is that the damping formulation choice influences the beam response more than the damping ratio choice without any damping update.

The last study on the dissipative phenomena particularly shows that the friction phenomenon is the most dissipative one. As expected experimentally, the plasticity energy does not develop, so any non-

Table 2.19: Classification of viscous damping ratios based on "spider" diagram area - RICBET and BARFRA - RD and CRD

	RD			CRD	
	Formulation	Area [% of total area]		Formulation	Area [% of total area]
1	BARFRA 2%	48.0%	1	RICBET 1%	30.0%
2	RICBET 1%	34.5%	2	RICBET 5%	19.4%
3	RICBET 2%	28.9%	3	RICBET 2%	17.7%
4	RICBET 3%	28.9%	4	BARFRA 5%	12.3%
5	RICBET 5%	28.8%	5	RICBET 3%	12.0%
6	BARFRA 1%	20.4%	6	BARFRA 2%	2.35%
7	BARFRA 3%-5%	0.00%	7	BARFRA 1%-3%	0.00%

linearity is reached in compression. Then, the analyses focus on the damage, representing the concrete cracking and friction energy evolutions: the damage evolves discontinuously and always precedes the friction energy because the cracks must be open to dissipate energy by crack surface friction.

2.6.3 Scientific problems highlighted

Finally, some problematics are deduced from the performed numerical computations concerning the use of a viscous damping matrix in nonlinear dynamic computations. First, no damping model can be proposed as a universal solution for all dynamic nonlinear computations. All analyses demonstrate that compromises must always be made in the damping model choices, mainly depending on the interest data. For example, it was shown that for the DSS3 test, accurate acceleration responses were obtained compared to the experimental data. However, the energies were inaccurately characterised (a consequence of the lack of accuracy on hysteresis loops). Then, with all damping formulations studied, the damping energy always represents more than 50% of the dissipated energies. It demonstrates the strong influence of viscous damping in nonlinear dynamic computations and the necessity of improving its modelling. It also appears that the nonlinearity evolutions are strongly dependent on the chosen damping formulations and damping ratios. So, there is a difficulty in using nonlinear models in dynamic analyses. Their advantage would be to characterise the material dissipations better. Nevertheless, they are insufficient, so viscous damping is required, strongly influencing the nonlinearities. So, it is impossible to validate the accuracy of the dissipation representations, while the choice of the damping formulation is complex and no perfect solution exists.

Chapter 3

DAMPING IDENTIFICATION AND NEW DAMPING MODEL BASED ON LOCAL NONLINEAR PHENOMENA

Contents

3.1   Damping projection on the modal basis

The numerical resolution of undamped dynamic problems can be performed easily because the system is uncoupled on the modal basis. This hypothesis is still valid for lightly damped systems, as demonstrated in section 1.1.2.2. That is why damping matrices of the Rayleigh type are considered. A simple form of damping matrix diagonal in the modal basis and easily constructed is, for example, the Rayleigh damping matrix. However, suppose updates are performed to consider the development of nonlinearities through the tangent stiffness matrix, for example. In that case, the system has no more reason to stay decoupled in the undamaged eigenbasis. Thus, in this section, some analyses are performed to evaluate the development of couplings between modes when nonlinearities develop in computations.

3.1.1   Theory

A nonlinear MDOF system excited by an earthquake can be described by equation (3.1) already presented in section 1.1.2.2:

$$\mathbb{M} \cdot \underline{\ddot{U}} + \mathbb{C} \cdot \underline{\dot{U}} + \underline{\mathbf{f}}_{\mathbf{int}}\left(\underline{U}\right) = -\sum_{k} \mathbb{M} \cdot \underline{\Gamma}_k \cdot \ddot{U}_{s,k} \tag{3.1}$$

with $k \in \{x, y, z\}$. On the undamped system modal basis $\mathcal{B} = \left\{\underline{\phi}_i\right\}_{i \in [\![1,N]\!]}$, the displacement can be re-written as in equation (3.2):

$$\underline{U} = \sum_{i=1}^{N} \boldsymbol{\alpha}_i \cdot \underline{\phi}_i \tag{3.2}$$

where $\left\{\boldsymbol{\alpha}_i\right\}_{i \in [\![1,N]\!]}$ are the generalised coordinates. By replacing the displacement expression in equation (3.1), equation (3.3) is obtained:

$$\mathbb{M} \cdot \left(\sum_{i=1}^{N} \ddot{\boldsymbol{\alpha}}_i \cdot \underline{\phi}_i\right) + \mathbb{C} \cdot \left(\sum_{i=1}^{N} \dot{\boldsymbol{\alpha}}_i \cdot \underline{\phi}_i\right) + \underline{\mathbf{f}}_{\mathbf{int}}\left[\sum_{i=1}^{N} \boldsymbol{\alpha}_i \cdot \underline{\phi}_i\right] = -\sum_{k} \mathbb{M} \cdot \underline{\Gamma}_k \cdot \ddot{U}_{s,k} \tag{3.3}$$

The basis is orthogonal, so the modes verify $\underline{\phi}_i^T \cdot \mathbb{M} \cdot \underline{\phi}_j = m_i \times \delta_{ij}$ and $\underline{\phi}_i^T \cdot \mathbb{K} \cdot \underline{\phi}_j = k_i \times \delta_{ij}$ for all $\{i, j\} \in [\![1; N]\!]^2$. However, for a damped system, the damping matrix is not necessarily diagonal in the modal basis. So, a modal damping matrix $\mathbb{C}^{mod}$ can be defined by considering the terms C_{ij}^{mod} (eq. 3.4) for all $\{i, j\} \in [\![1; N]\!]^2$ with N the number of considered modes.

$$C_{ij}^{mod} = \underline{\phi}_i^T \cdot \mathbb{C} \cdot \underline{\phi}_j \qquad , \qquad \forall \{i, j\} \in [\![1; N]\!]^2 \tag{3.4}$$

Two ideas can be developed: (i) considering the initial damping matrix and performing modal analyses to compute the updated eigenmodes at different damage levels, or (ii) considering the updated damping matrix at different damage levels and keeping the undamaged eigenmodes. The second will be of interest in the following.

Then in the case of a classical damping matrix, that is to say, that $\mathbb{C}^{mod}$ is initially diagonal, the projection on mode j of equation (3.3) leads to equation (3.5):

$$\left(\underline{\phi}_j^T \cdot \mathbb{M} \cdot \underline{\phi}_j\right) \ddot{\boldsymbol{\alpha}}_j + \left(\underline{\phi}_j^T \cdot \mathbb{C} \cdot \underline{\phi}_j\right) \dot{\boldsymbol{\alpha}}_j + \underline{\phi}_j^T \cdot \underline{\mathbf{f}}_{\mathbf{int}}\left[\sum_{i=1}^{N} \boldsymbol{\alpha}_i \cdot \underline{\phi}_i\right] = -\sum_{k} \left(\underline{\phi}_j^T \cdot \mathbb{M} \cdot \underline{\Gamma}_k\right) \cdot \ddot{U}_{s,k} \tag{3.5}$$

And, because the basis is generally normalised to the mass matrix, given $\underline{\phi}_i^T \cdot \mathbb{M} \cdot \underline{\phi}_i = m_i = 1$ for all $i \in [\![1; N]\!]$, equation (3.5) can be simplified in equation (3.6), where the only direction considered is the one with the higher effective modal mass for the fundamental mode ($k = y$):

$$\ddot{\boldsymbol{\alpha}}_j + 2.\xi_j.\omega_j \times \dot{\boldsymbol{\alpha}}_j + \mathbf{f}_{\mathbf{int}\,j} = -L_j \ddot{\mathbf{U}}_s \tag{3.6}$$

where $\mathbf{f}_{\mathbf{int}\,j} = \underline{\phi}_j^T \cdot \mathbf{f}_{\mathbf{int}} \left[\displaystyle\sum_{i=1}^{N} \boldsymbol{\alpha}_i.\underline{\phi}_i \right]$ is the internal force projected on mode j, $L_{j,k} = \left(\underline{\phi}_j^T \cdot \mathbb{M} \cdot \underline{\Gamma}_k \right)$ is a generalised displacement projected on mode j, $L_j = \left(\underline{\phi}_j^T \cdot \mathbb{M} \cdot \underline{\Gamma}_y \right)$ and $2.\xi_j.\omega_j = \left(\underline{\phi}_j^T \cdot \mathbb{C} \cdot \underline{\phi}_j \right) = C_{jj}^{mod}$ is the diagonal term of the modal damping matrix $\mathbb{C}^{mod}$ associated with mode j. So, equivalent viscous damping can be identified from the last relation as presented in equation (3.7):

$$\xi_j = \frac{C_{jj}^{mod}}{2.\omega_j} \tag{3.7}$$

where ω_j is the initial eigenfrequency associated with mode j. As a remark, equation (3.7) becomes equation (3.8) if the basis is not normalised to the mass matrix.

$$\xi_j = \frac{C_{jj}^{mod}}{2.\omega_j.m_j} \tag{3.8}$$

3.1.2 Results

Some analyses are performed from the results of the DSS2 test computations performed in the numerical analysis of chapter 2. First, figure 3.1 focuses on the identified viscous damping ratios associated with ten modes at different time steps. The Rayleigh damping matrix, computed with a viscous damping ratio of 2% for modes 1 and 2 and with the tangent stiffness matrix (CRD), is studied along with the DSS2 test. So, the identified viscous damping ratios evolve over time and can be correlated with the damage level. The identified viscous damping ratios of the ten studied modes decrease along with computation. The beam damage level so influences those values. However, the influence is less significant for the first modes than for the higher ones. Then, for all time steps, the viscous damping ratios follow the same tendency with a decrease between the first and second modes and an increase after. It is well representative of the evolution of the viscous damping ratio for RD, as discussed in figure 1.13 of section 1.2.2.1.

Figure 3.2 focuses on the identified viscous damping ratios for the beam with different damping formulations. The evolutions are plotted with the initial matrices. As expected, it appears that KPD follows almost a linear evolution with the frequency, while MPD follows an inverse decrease, and RD is a combination of the two others. Finally, WPD behaves similarly to MPD (zoom in figure 3.2b), so the lowest modes are strongly damped compared with the highest, which are not damped at all.

Finally, figure 3.3 presents the modal damping matrices $\mathbb{C}^{mod}$ for two damping formulations considering the tangent stiffness matrix (Rayleigh - RD - and Wilson-Penzien - WPD - damping) before any damage and after two damage levels. RD with the tangent stiffness was computed with a viscous damping ratio of 2% for modes 1 and 2. WPD was computed with 2% of viscous damping ratio on modes 1 to 6 and with updates based on re-computation of the modal basis after each time step (choices based on the most performative formulations discussed in chapter 2). Only three modes are plotted here because they characterise more than 99% of the beam modal mass. The matrices are almost diagonal for both formulations even after the stronger damage level applied on the beam during the DSS2 test. Only a small coupling is observed between the first and third modes because they are symmetrical. Then, amplitude differences are observed from one damage level to another with a decrease of the modal damping values, demonstrating the effect of the damping matrix update. Finally, with CRD (fig. 3.3a to 3.3c), the
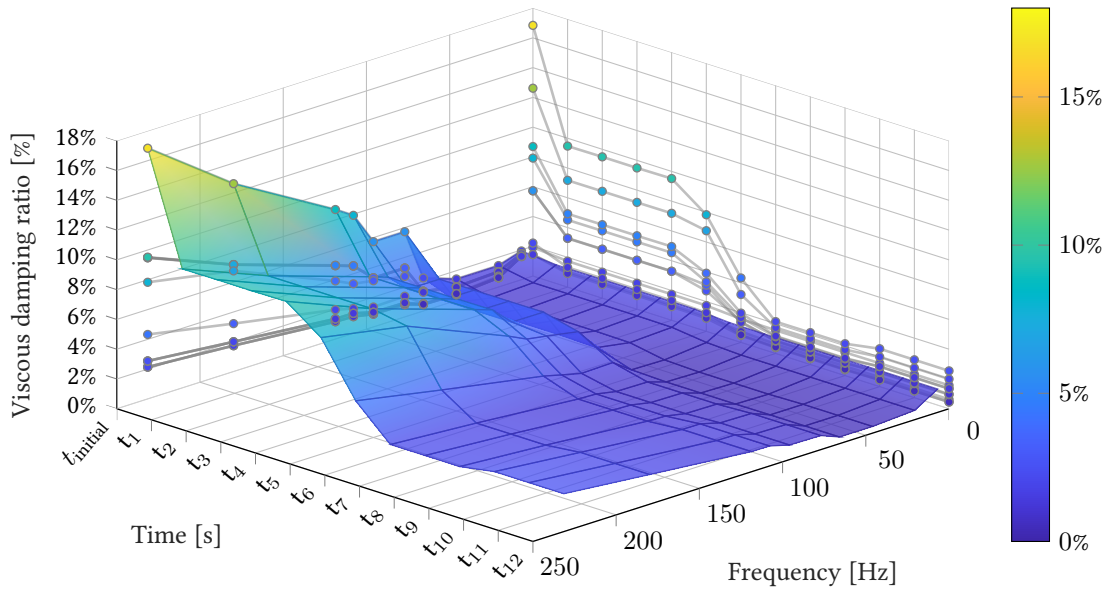
Figure 3.1: Equivalent viscous damping ratios (eq. 3.8) for ten modes over time

(a) Entire response

(b) Zoom for $\xi < 6\%$
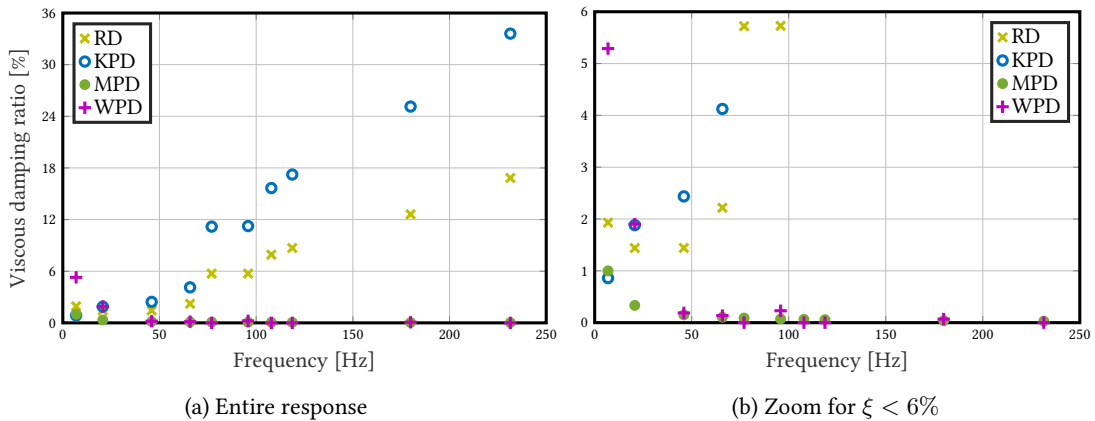
Figure 3.2: Equivalent viscous damping ratio for ten modes - initial matrices

first mode is the less damped, while an inverse evolution is observed with CWPD (fig. 3.3d to 3.3f). These remarks can be explained with figure 3.2: (i) for RD, the three first modes are similarly damped, and (ii) for WPD, the two first modes are much more damped than the third one.

In conclusion, figure 3.3 illustrates that the damping matrix is nearly uncoupled in the modal basis when nonlinearities develop, so resolutions on the modal basis are still accurate even for the nonlinear computations studied herein with the tangent stiffness matrix.

(a) CRD - undamaged   (b) CRD - damage level 1   (c) CRD - damage level 2

(d) CWPD - undamaged   (e) CWPD - damage level 1   (f) CWPD - damage level 2
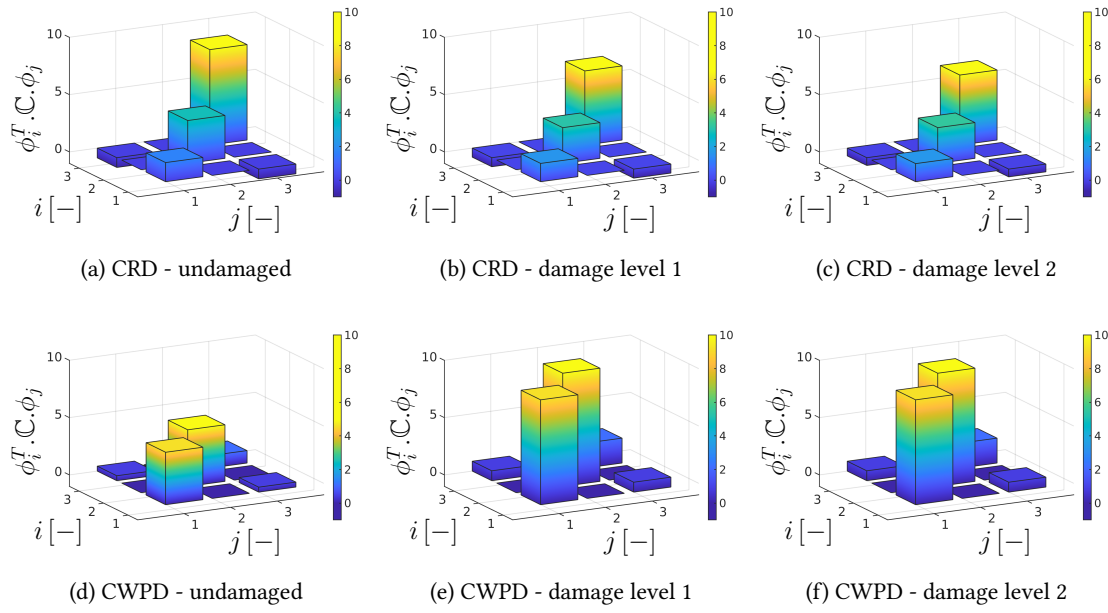
Figure 3.3: Projection of the damping matrix on the undamaged eigenbasis - DSS2 test - RICBET - 2%

3.2 Modal basis of the studied beam

A numerical model of the reinforced concrete (RC) beam is proposed in chapter 2. It is a complex system composed of a simple beam with elastic supports and additional masses. No analytical model of the studied complex system can be defined. That is why strategies that combine the subsystem modal bases (section 3.2.2) and the modal basis of the simply supported beam (section 3.2.1) are used. Finally, a comparison between experimental, numerical and approximate analytical modal properties is proposed in section 3.2.3.

3.2.1 Modal analysis of a simple beam

3.2.1.1 Analytical continuous eigenbasis for an elastic behaviour

In the case of an elastic framework, the vibration equation of an Euler-Bernoulli beam in flexion (fig. 3.4) is expressed in equation (3.9):

$$E_c.I_h\frac{\partial^4 u_y}{\partial x^4}(x,t) + \rho_c.S_h\frac{\partial^2 u_y}{\partial t^2}(x,t) = 0 \tag{3.9}$$

with ρ_c the concrete density, S_h the homogenised section, E_c the concrete Young's modulus and I_h the homogenised inertia.

The general form of the stationary wave is given in equation (3.10):

$$u_y(x,t) = X(x).T(t) \tag{3.10}$$

where $T(t) = A_1\cos(\omega t) + A_2\sin(\omega t)$ is the time-dependent function and $X(x) = B_1\cos(\lambda.x) + B_2\sin(\lambda.x) + B_3\cosh(\lambda.x) + B_4\sinh(\lambda.x)$ is the space-dependent function linked by $\omega^2 = \lambda^4\dfrac{E_c.I_h}{\rho_c.S_h}$.
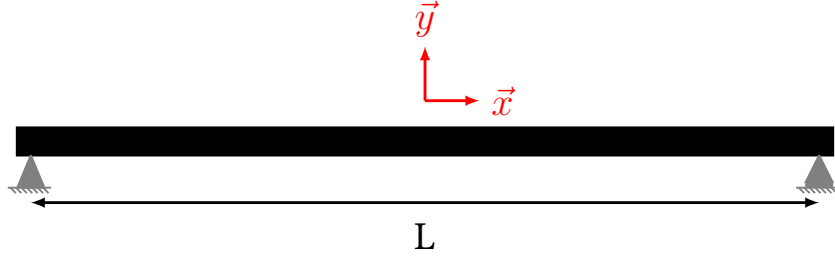
Figure 3.4: Simply supported beam scheme

Then, the boundary conditions are null vertical displacements and moments at the beam extremities corresponding to $X(x=0) = X(x=L) = 0$ and $\left.\dfrac{\mathrm{d}^2 X}{\mathrm{d}x^2}\right|_{x=0} = \left.\dfrac{\mathrm{d}^2 X}{\mathrm{d}x^2}\right|_{x=L} = 0$. The system can thus define the displacement space function in equation (3.11):

$$
\left\{
\begin{array}{rcl}
\varphi_i(x) & = & \sin\left(\dfrac{i\pi x}{L}\right) \\[2mm]
\lambda_i & = & \dfrac{i\pi}{L} \\[2mm]
\omega_i & = & \left(\dfrac{i\pi}{L}\right)^2 \sqrt{\dfrac{E_c.I_h}{\rho_c.S_h}}
\end{array}
\right.
\quad , \qquad \forall\, i \in \mathbb{N}
\tag{3.11}
$$

where $\{\varphi_i(x)\}_{i\in\mathbb{N}}$ and $\{\omega_i\}_{i\in\mathbb{N}}$ are respectively the mode shapes and eigenfrequencies.

3.2.1.2   Finite element model

In the case of finite element models, the beam is discretised in space elements, so the eigenmodes are decomposed on these elements $\underline{\phi}_{ssb,i}$ given the simply supported beam (*ssb*) total eigenbasis $\mathcal{B}_{tot,ssb} = \left\{\underline{\phi}_{ssb,i}\right\}_{i\in\mathbb{N}}$. The eigenmodes are still associated with the eigenfrequencies $\{\omega_{ssb,i}\}_{i\in\mathbb{N}}$ given in equation (3.11). Finally, the eigenbasis can be reduced on the N-most influential eigenmodes given $\mathcal{B}_{ssb}$ in equation (3.12):

$$
\mathcal{B}_{ssb} = \left\{\underline{\phi}_{ssb,i}\right\}_{i\in[\![1;N]\!]}
\tag{3.12}
$$

Practically, the modal properties are obtained thanks to numerical modal analysis.

3.2.2   Analytical modal analysis of a complex model

The methodology to evaluate the analytical eigenbasis of a complex system is to study each subsystem independently and combine them.

3.2.2.1   Decomposed subsystems

(a)   Simply supported beam with elastic supports   The multi-fibre beam is composed of rotational and translational elastic supports. Figure 3.5 presents the scheme of the subsystem considered herein. The complete demonstration of the equations (3.13) and (3.14) are presented in appendix E. The new stiffness parameters to consider are indicated in table 3.1.
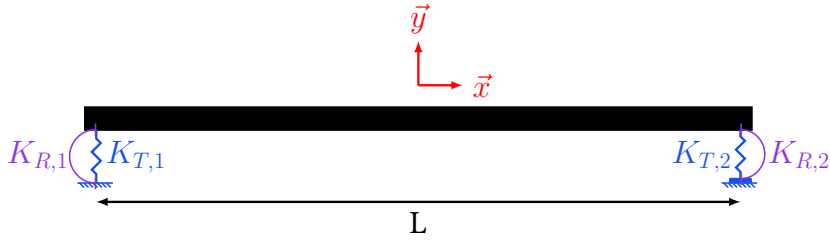
Figure 3.5: Scheme of the beam on elastic supports

Table 3.1: Boundary conditions with elastic supports

Position	Forces	Momentum
$x = 0$	$V(0, t) = -K_{T,1} \times u_y(0, t)$	$M(0, t) = K_{R,1} \times \theta_z(0, t)$
$x = L$	$V(L, t) = K_{T,2} \times u_y(L, t)$	$M(L, t) = -K_{R,2} \times \theta_z(L, t)$

A system with four equations and four unknowns (eq. E.22 in appendix E.2) is obtained by transforming the terms in table 3.1. Some abacus can be used to obtain analytical solutions to such problems. For example, Karnovsky and Lebed (2000) proposed the analytical eigenproperties for one beam with two translational elastic supports (eq. 3.13) - the demonstration is proposed in appendix E.3 - or for one beam with two rotational elastic supports (eq. 3.14) - the demonstration is proposed in appendix E.4. The presented equations are simplified because $K_{T,1} = K_{T,2} = K_T$ as $K_{R,1} = K_{R,2} = K_R$ and the terms $\bar{\lambda} = L.\lambda$ and $\bar{x} = {}^x/_L$ are considered.

$$\begin{cases} K_T^{*\,2} + K_T^*.\dfrac{2\bar{\lambda}^3\left[-\sinh(\bar{\lambda})\cos(\bar{\lambda}) + \cosh(\bar{\lambda})\sin(\bar{\lambda})\right]}{2\sin(\bar{\lambda})\sinh(\bar{\lambda})} + \dfrac{\bar{\lambda}^6\left[1 - \cos(\bar{\lambda})\cosh(\bar{\lambda})\right]}{2\sin(\bar{\lambda})\sinh(\bar{\lambda})} = 0 \\[3mm] X_T(\bar{x}) = \sin(\bar{\lambda}\bar{x}) + \dfrac{\sin(\bar{\lambda})}{\sinh(\bar{\lambda})}\sinh(\bar{\lambda}\bar{x}) + \gamma_T\left[\cos(\bar{\lambda}\bar{x}) + \cosh(\bar{\lambda}\bar{x}) + \gamma_{T1}\sinh(\bar{\lambda}\bar{x})\right] \end{cases} \quad (3.13)$$

where $K_T^* = \dfrac{K_T.L^3}{E_c.I_h}$, $\gamma_{T1} = \dfrac{\cos(\bar{\lambda}) - \cosh(\bar{\lambda})}{\sinh(\bar{\lambda})}$ and $\gamma_T = \dfrac{\sinh(\bar{\lambda}) - \sin(\bar{\lambda})}{2\frac{K_T^*}{\bar{\lambda}^3}\sinh(\bar{\lambda}) + \cos(\bar{\lambda}) - \cosh(\bar{\lambda})}$.

$$\begin{cases} K_R^{*\,2} + K_R^*.\dfrac{2\bar{\lambda}\left[\sin(\bar{\lambda})\cosh(\bar{\lambda}) - \cos(\bar{\lambda})\sinh(\bar{\lambda})\right]}{1 - \cos(\bar{\lambda})\cosh(\bar{\lambda})} + \dfrac{2\bar{\lambda}^2\sin(\bar{\lambda})\sinh(\bar{\lambda})}{1 - \cos(\bar{\lambda})\cosh(\bar{\lambda})} = 0 \\[3mm] X_R(\bar{x}) = \sin(\bar{\lambda}\bar{x}) - \sinh(\bar{\lambda}\bar{x}) + \gamma_R\left[\cos(\bar{\lambda}\bar{x}) - \cosh(\bar{\lambda}\bar{x}) - \dfrac{2\bar{\lambda}}{K_R^*}\sinh(\bar{\lambda}\bar{x})\right] \end{cases} \quad (3.14)$$

where $K_R^* = \dfrac{K_R.L}{E_c.I_h}$ and $\gamma_R = \dfrac{\sinh(\bar{\lambda}) - \sin(\bar{\lambda})}{\cos(\bar{\lambda}) - \cosh(\bar{\lambda}) - 2\frac{\bar{\lambda}}{K_R^*}\sinh(\bar{\lambda})}$.

The functions $X_T(\bar{x})$ and $X_R(\bar{x})$ correspond to the mode shapes associated respectively with the translational and rotational elastic supports. The values $\{\bar{\lambda}_{T,i}\}_{i\in\mathbb{N}}$ and $\{\bar{\lambda}_{R,i}\}_{i\in\mathbb{N}}$ can be deduced from

the equations (3.13) and (3.14). The associated eigenfrequencies are equal to $\omega_{T,i} = \dfrac{\bar{\lambda}_{T,i}^2}{L^2}\sqrt{\dfrac{E_c.I_h}{\rho_c.S_h}}$ and

$\omega_{R,i} = \dfrac{\bar{\lambda}_{R,i}}{L^2}\sqrt{\dfrac{E_c.I_h}{\rho_c.S_h}}$ for all $i \in \mathbb{N}$.

(b)   Simply supported beam with additional masses   Figure 3.6 presents the beam with one additional mass positioned at $x_{m_{add}}$. As for the elastic supports, Karnovsky and Lebed (2000) gave an abacus to solve this problem. The complete demonstration is presented in appendix E.5. First, the eigenfrequencies are deduced from equation (3.15), with $\bar{x}_1 = {x_1}/{L}$, $\bar{x}_2 = 1 - \bar{x}_1$ and $\alpha_M = {M_{add}}/{\rho_c.S_h.L}$.

$$2\sin(\bar{\lambda})\sinh(\bar{\lambda}) - \alpha_M\bar{\lambda}\left[\sin(\bar{\lambda}\bar{x}_1)\sin(\bar{\lambda}\bar{x}_2)\sinh(\bar{\lambda}) - \sinh(\bar{\lambda}\bar{x}_1)\sinh(\bar{\lambda}\bar{x}_2)\sin(\bar{\lambda})\right] = 0 \qquad (3.15)$$
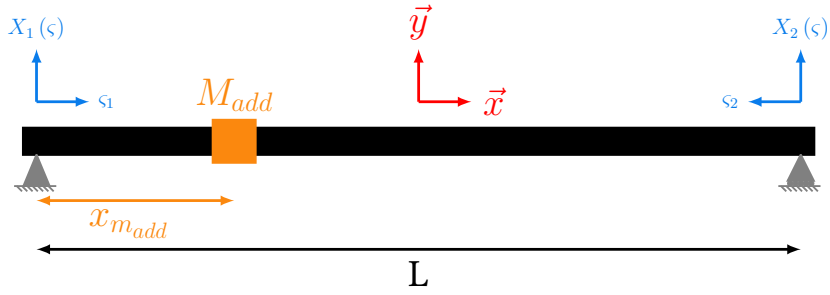
Figure 3.6: Scheme of the beam with one additional mass

The eigenfrequencies are then given by $\omega_{M_{add},i} = \dfrac{\bar{\lambda}_{M_{add},i}^2}{L^2}\sqrt{\dfrac{E_c.I_h}{\rho_c.S_h}}$ for all $i \in \mathbb{N}$.

Then, to evaluate the mode shapes, figure 3.6 decomposition is considered, given two parts for the mode shapes and four unknowns as expressed in equation (3.16).

$$\begin{cases} X_1(\bar{x}) & = & A\sin(\bar{\lambda}\bar{x}) + B\sinh(\bar{\lambda}\bar{x}) \\ X_2(\bar{x}) & = & C\sin(\bar{\lambda}\bar{x}) + D\sinh(\bar{\lambda}\bar{x}) \end{cases} \qquad (3.16)$$

Four compatibility equations (eq. 3.17) are thus used to determine the four unknowns of equation (3.16): (i) the displacement compatibility, (ii) the slope compatibility, (iii) the bending moment compatibility, and (iv) the shear force compatibility corresponding to the dynamic equilibrium of the moving lumped mass.

$$\begin{cases} X_1(\bar{x} = \zeta_1) & = & X_2(\bar{x} = \zeta_2) \\[2mm] \left.\dfrac{\mathrm{d}X_1}{\mathrm{d}\bar{x}}\right|_{\bar{x}=\zeta_1} & = & -\left.\dfrac{\mathrm{d}X_2}{\mathrm{d}\bar{x}}\right|_{\bar{x}=\zeta_2} \\[2mm] \left.\dfrac{\mathrm{d}^2X_1}{\mathrm{d}\bar{x}^2}\right|_{\bar{x}=\zeta_1} & = & \left.\dfrac{\mathrm{d}^2X_2}{\mathrm{d}\bar{x}^2}\right|_{\bar{x}=\zeta_2} \\[2mm] \left.\dfrac{\mathrm{d}^3X_1}{\mathrm{d}\bar{x}^3}\right|_{\bar{x}=\zeta_1} + \left.\dfrac{\mathrm{d}^3X_2}{\mathrm{d}\bar{x}^3}\right|_{\bar{x}=\zeta_2} & = & -\lambda^4\dfrac{M_{add}}{\rho_c.S_h} \times X_1(\bar{x} = \zeta_1) \end{cases} \qquad (3.17)$$

with $\zeta_1 = {}^{x_{m_{add}}}/L$ and $\zeta_2 = 1 - \zeta_1$. Rewritten in a matrix form with $A = 1$ gives equation (3.18):

$$\begin{bmatrix} \sinh(\bar\lambda\zeta_1) & -\sin(\bar\lambda\zeta_2) & -\sinh(\bar\lambda\zeta_2) \\ \cosh(\bar\lambda\zeta_1) & \cos(\bar\lambda\zeta_2) & \cosh(\bar\lambda\zeta_2) \\ \sinh(\bar\lambda\zeta_1) & \sin(\bar\lambda\zeta_2) & -\sinh(\bar\lambda\zeta_2) \end{bmatrix} \begin{Bmatrix} B \\ C \\ D \end{Bmatrix} = \begin{Bmatrix} -\sin(\bar\lambda\zeta_1) \\ -\cos(\bar\lambda\zeta_1) \\ \sin(\bar\lambda\zeta_1) \end{Bmatrix} \tag{3.18}$$

Remark: The additional mass introduces an extra inertial force on the beam. So, another method to solve that subsystem would be to add that force (eq. 3.19) on the right part of the wave equation (3.9).

$$- M_{add} \times \delta\left(x - x_{m_{add}}\right) \times \ddot{u}_y\left(x_1, t\right) \tag{3.19}$$

where δ is the Dirac distribution and $\ddot{u}_y\left(x_1, t\right)$ the acceleration at the mass position.

3.2.2.2   Combination of the subsystems

The complete beam can be decomposed into four subsystems: (i) a simple beam on translational elastic supports, (ii) a simple beam with elastic supports, (iii) a simply supported beam with one additional mass at $x_{m_{add,1}} = L/4$, and (iv) a simply supported beam with one additional mass at $x_{m_{add,2}} = 3.L/4$. Table 3.2 summarizes the eigenproperties deduced for each subsystem with the eigenmodes discretised along the beam. The aim is so, now, to combine those responses to evaluate the complete system eigenproperties.

Table 3.2: Synthesis of the subsystem eigenproperties

	Simply supported beam	Translational elastic supports	Rotational elastic supports	First additional mass	Second additional mass
Frequency	$\omega_{ssb,i}$ (eq. 3.11)	$\omega_{T,i}$ (eq. 3.13)	$\omega_{R,i}$ (eq. 3.14)	$\omega_{M_{add,1},i}$ (eq. 3.15)	$\omega_{M_{add,2},i}$ (eq. 3.15)
Mode	$\underline{\phi}_{ssb,i}$ (eq. 3.11)	$\underline{\phi}_{T,i}$ (eq. 3.13)	$\underline{\phi}_{R,i}$ (eq. 3.14)	$\underline{\phi}_{M_{add,1},i}$ (eq. 3.18)	$\underline{\phi}_{M_{add,2},i}$ (eq. 3.18)

(a)   Combination of frequencies   Some methods are proposed in the literature to evaluate the analytical eigenfrequencies of complex systems. First, Dunkerley (1893) developed "a method to estimate the lowest natural frequency of a dynamic system, which is composed of substructures (components) of which the lowest natural frequencies are known". He demonstrated that the first eigenfrequency of a global system is given by the combination of the subsystem eigenfrequencies considered in parallel (eq. 3.20):

$$\frac{1}{\omega_1^2} \leqslant \sum_{k=1}^{n_{ss}} \frac{1}{\omega_k^2} \tag{3.20}$$

where ω_k is the kth SDOF subsystem eigenfrequency and n_{ss} is the total number of subsystems. Levy (1991) proposed to extend the evaluation to higher modes by using an iterative procedure to determine all the eigenfrequencies of the global system.

In addition, Low (2000) focused on the study of beams carrying concentrated masses to evaluate the ability of Dunkerley's formula to approximate the system eigenfrequencies. The formulation proposed

for a beam carrying $n_{m_{add}}$ concentrated masses is given in equation (3.21):

$$\frac{1}{\omega_i^2} \approx \sum_{k=1}^{n_{m_{add}}} \left(\frac{1}{\omega_{M_{add,k}}^2} \right) - (n_{m_{add}} - 1)\frac{1}{\omega_{ssb,i}^2} \tag{3.21}$$

where $\omega_{ssb,i}$ is the eigenfrequency of the beam without mass. The eigenfrequency of each subsystem considers the simply supported beam without additional masses. So the terms $\left[-(n_{m_{add}} - 1) \times \dfrac{1}{\omega_{ssb,i}^2} \right]$ removes the multiple consideration of the simply supported beam effect on the global system eigenfrequency.

Based on Low (2000)'s proposition, the formulae in equation (3.22) is proposed to evaluate the beam eigenfrequencies:

$$\frac{1}{\omega_i^2} = \frac{1}{\omega_{T,i}^2} + \frac{1}{\omega_{R,i}^2} + \frac{1}{\omega_{M_{add,1},i}^2} + \frac{1}{\omega_{M_{add,2},i}^2} - 3 \times \frac{1}{\omega_{ssb,i}^2} \quad , \qquad \forall\, i \in [\![1; N]\!] \tag{3.22}$$

where ω_i is the complete beam eigenfrequency associated with mode i.

To validate equation (3.22), modal analyses are performed in Cast3M software with each subsystem and the complete beam to obtain the associated ten first eigenfrequencies. Figure 3.7 exhibits the complete numerical system eigenfrequencies compared to the ones deduced from the subsystem eigenfrequencies combinations in equation (3.22). The computed eigenfrequencies match the ones extracted from the complete model. So, Low (2000)'s formula seems to be adequate for more extensive applications than only additional masses.
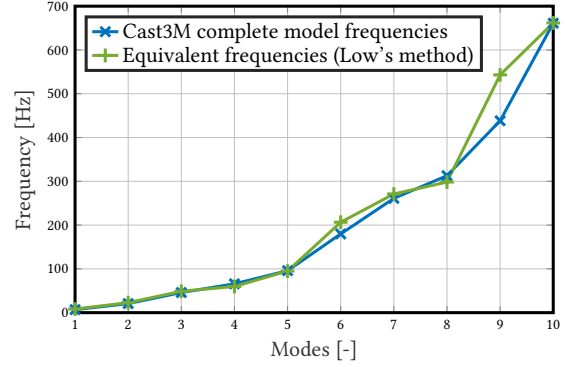
Figure 3.7: Validation of eigenfrequency combinations

(b)   Combination of mode shapes   The idea for mode shape combinations is to use Rayleigh's quotient defined in equation (3.23) for a FE model:

$$\mathcal{R}\left(\underline{\phi}_i \right) = \frac{\underline{\phi}_i^T \cdot \mathbb{K} \cdot \underline{\phi}_i}{\underline{\phi}_i^T \cdot \mathbb{M} \cdot \underline{\phi}_i} \tag{3.23}$$

The starting hypothesis is that the global system mode shape $\underline{\phi}_i$ can be written as a linear combination of the subsystem ones (eq. 3.24).

$$\underline{\phi}_i = \alpha_{T,i} \times \underline{\phi}_{T,i} + \alpha_{R,i} \times \underline{\phi}_{R,i} + \alpha_{M_{add,1},i} \times \underline{\phi}_{M_{add,1},i} + \alpha_{M_{add,2},i} \times \underline{\phi}_{M_{add,2},i} \quad , \quad \forall\, i \in [\![1; N]\!] \tag{3.24}$$

Then, to determine the proportionality parameters, Rayleigh's quotient minimisation is considered, meaning that the system in equation (3.25) is solved.

$$\frac{\partial \mathcal{R}\left(\underline{\phi}_i \right)}{\partial \alpha_{T,i}} = 0 \quad , \quad \frac{\partial \mathcal{R}\left(\underline{\phi}_i \right)}{\partial \alpha_{R,i}} = 0 \quad , \quad \frac{\partial \mathcal{R}\left(\underline{\phi}_i \right)}{\partial \alpha_{M_{add,1},i}} = 0 \quad , \quad \frac{\partial \mathcal{R}\left(\underline{\phi}_i \right)}{\partial \alpha_{M_{add,2},i}} = 0 \tag{3.25}$$

where the Rayleigh's quotient expression is given in equation (3.26) for a continuous model, adapted to the studied beam and deduced from equation (3.23):

$$
\mathcal{R}\left(\phi\right) = \frac{\dfrac{1}{2}\displaystyle\int_0^L E_c.S_h\left(\dfrac{\mathrm{d}\phi}{\mathrm{d}x}\right)^2 \mathrm{d}x + \dfrac{1}{2}K_T\left[\phi(0)^2 + \phi(L)^2\right] + \dfrac{1}{2}K_R\left[\left.\dfrac{\mathrm{d}\phi}{\mathrm{d}x}\right|_{x=0}^2 + \left.\dfrac{\mathrm{d}\phi}{\mathrm{d}x}\right|_{x=L}^2\right]}{\dfrac{1}{2}\displaystyle\int_0^L \rho_c.S_h\phi^2\,\mathrm{d}x + M_{add,1}\times\phi\left(\dfrac{L}{4}\right)^2 + M_{add,2}\times\phi\left(\dfrac{3.L}{4}\right)^2} \tag{3.26}
$$

As for the eigenfrequencies, a validation is performed using the numerical model of independent subsystems and the complete beam model. To improve the determined eigenbasis, Gram-Schmidt's algorithm (theorem 1) is applied to define an orthonormal basis.

Theorem 1. *If $(\mathbf{v}_n)_{n\in N}$ is a pre-Hilbertine space free family, then there is one and only one orthonormal family $(\mathbf{e}_n)_{n\in N}$, such as:*
  ✓ *$\mathrm{Vect}(\mathbf{e}_0,\ldots,\mathbf{e}_n) = \mathrm{Vect}(\mathbf{v}_0,\ldots,\mathbf{v}_n)$, $\forall n$,*
  ✓ *Scalar products $(\mathbf{e}_n|\mathbf{v}_n)$ are strictly positive for all n.*

Gram-Schmidt's orthonormalisation procedure is, then, defined by the iterations in equation (3.27):

$$
\begin{cases}
\mathbf{u}_1 &=& \mathbf{v}_1\,, & \mathbf{e}_1 &=& \frac{\mathbf{u}_1}{\|\mathbf{u}_1\|} \\[4pt]
\mathbf{u}_2 &=& \mathbf{v}_2 - \mathrm{proj}_{\mathbf{u}_1}\left(\mathbf{v}_2\right)\,, & \mathbf{e}_2 &=& \frac{\mathbf{u}_2}{\|\mathbf{u}_2\|} \\[4pt]
\mathbf{u}_3 &=& \mathbf{v}_3 - \mathrm{proj}_{\mathbf{u}_1}\left(\mathbf{v}_3\right) - \mathrm{proj}_{\mathbf{u}_2}\left(\mathbf{v}_3\right)\,, & \mathbf{e}_3 &=& \frac{\mathbf{u}_3}{\|\mathbf{u}_3\|} \\[4pt]
&\vdots& & &\vdots& \\[4pt]
\mathbf{u}_k &=& \mathbf{v}_k - \sum_{j=1}^{k-1}\mathrm{proj}_{\mathbf{u}_j}\left(\mathbf{v}_k\right)\,, & \mathbf{e}_k &=& \frac{\mathbf{u}_k}{\|\mathbf{u}_k\|}
\end{cases} \tag{3.27}
$$

where the orthogonal projection operator on a vector line and directed by the vector $\mathbf{u}$ is given by $\mathrm{proj}_{\mathbf{u}}\left(\mathbf{v}\right) = \frac{\langle\mathbf{u},\mathbf{v}\rangle}{\langle\mathbf{u},\mathbf{u}\rangle}\mathbf{u}$, $\langle.,.\rangle$ is the scalar product on considered space, $[\mathbf{v}_1,\ldots,\mathbf{v}_k]$ is an unrelated vector set, $[\mathbf{u}_1,\ldots,\mathbf{u}_k]$ is a set of two-by-two orthogonal vectors and $[\mathbf{e}_1,\ldots,\mathbf{e}_k]$ is a set of two-by-two orthonormal vectors. The normalisation has to be performed based on the mass or stiffness matrix. So, the vector-based products are also made with respect to the mass, respectively stiffness, matrix. The mass matrix will be considered for the normalisation in the performed analyses.

3.2.3 Adequacy between analytical, numerical and experimental models

The analytical eigenfrequencies of subsystems are evaluated from the equations presented in sections 3.2.1 and 3.2.2. The computed values are indicated in table 3.3 for the beam three first modes. The last column of table 3.3 gives the complete system eigenfrequencies computed with equation (3.22). The subsystem frequencies are higher than the complete system ones. Mainly, the rotational elasticity of supports exhibits a negligible impact because the three frequencies $f_{R,i}$ are close to the simply supported beam ones $f_{ssb,i}$. On the contrary, the addition of translational elastic supports $f_{T,i}$ or additional masses $f_{M_{add,1},i}$ and $f_{M_{add,2},i}$ induces a reduction of eigenfrequencies. The equality observed between the two masses is a consequence of the studied system symmetry. Then, in figure 3.8, the computed analytical eigenfrequencies are compared with the experimental and numerical ones. The first eigenfrequency is equal for the three models. A small error is observed for the second mode between the numerical frequency and the two others. Indeed, a compromise was performed for the numerical model calibration, leading to a small error on the second eigenfrequency. Finally, for the third mode, the analytical frequency is

Table 3.3: Analytical eigenfrequencies of subsystems and the complete beam

| | Frequencies [Hz] | | | | | |
| | $f_{ssb,i}$ | $f_{T,i}$ | $f_{R,i}$ | $f_{M_{add,1},i}$ | $f_{M_{add,2},i}$ | f_i |
	Simply supported	Trans. springs	Rot. springs	Add. mass 1	Add. mass 2	Complete beam
Mode 1	9.28	8.61	9.29	8.28	8.28	**7.18**
Mode 2	37.1	27.6	37.1	31.3	31.3	**22.9**
Mode 3	83.5	47.2	83.5	78.3	78.3	**45.3**

closer to the numerical one, but the confidence in the experimental one is too low to conclude on that value. In conclusion, the applied methods to determine the analytical eigenfrequencies accurately work for the modes of interest.

Then, the method described in paragraph 3.2.2.2(b) to combine mode shapes is also applied to the three first modes. A comparison is performed with the experimental mode shapes, deduced from the hammer-shock tests, as discussed in paragraph 1.4.3.1(b), and the numerical ones deduced from a modal analysis on the complete beam model. Figures 3.9a to 3.9c exhibit the results without applying Gram-Schmidt's algorithm, on the contrary to figures 3.9d to 3.9f. The analytical first mode matches the two other ones.

Figure 3.8: Comparison of the three first eigenfrequencies

The non-null values at supports are due to the translational elastic supports. The analytical response is closer to the numerical ones without applying Gram-Schmidt's algorithm, while the orthonormalisation application leads to a better analytical representation of experimental data. That effect is observed for the three modes demonstrating the importance of considering an orthonormal eigenbasis. Then, the second mode is also accurately characterised, but it is more difficult for the third one as observed on eigenfrequencies. For the third mode, the fact that the experimental shape is not symmetric also shows low confidence. So, again, the proposed combination method is adequate for the eigenproperties of interest.

3.3   Proposition of a damping identification method

One of the scientific gaps discussed in chapter 1 from the literature analysis is the development of a performative damping identification method. This section aims to propose a damping identification method to identify the transient evolution of equivalent viscous damping ratios and eigenfrequencies based on experimental or numerical data. The proposed method is based on a SDOF system equivalent to the beam multi-fibre model. The system is projected in the modal basis evaluated in section 3.2 to perform this equivalence. This projection is possible because it was demonstrated, in section 3.1, that such projection is still possible for nonlinear computations using the tangent stiffness matrix.

The method proposed by Demarie and Sabia (2011) and presented in paragraph 1.3.1.1(a) is used in this section. The SDOF system considered is the projected beam response. The projection is performed on the first mode of the beam eigenbasis because this mode mainly characterises the beam movement.

(a) Mode 1   (b) Mode 2   (c) Mode 3

(d) Mode 1 - Gram-Schmidt   (e) Mode 2 - Gram-Schmidt   (f) Mode 3 - Gram-Schmidt
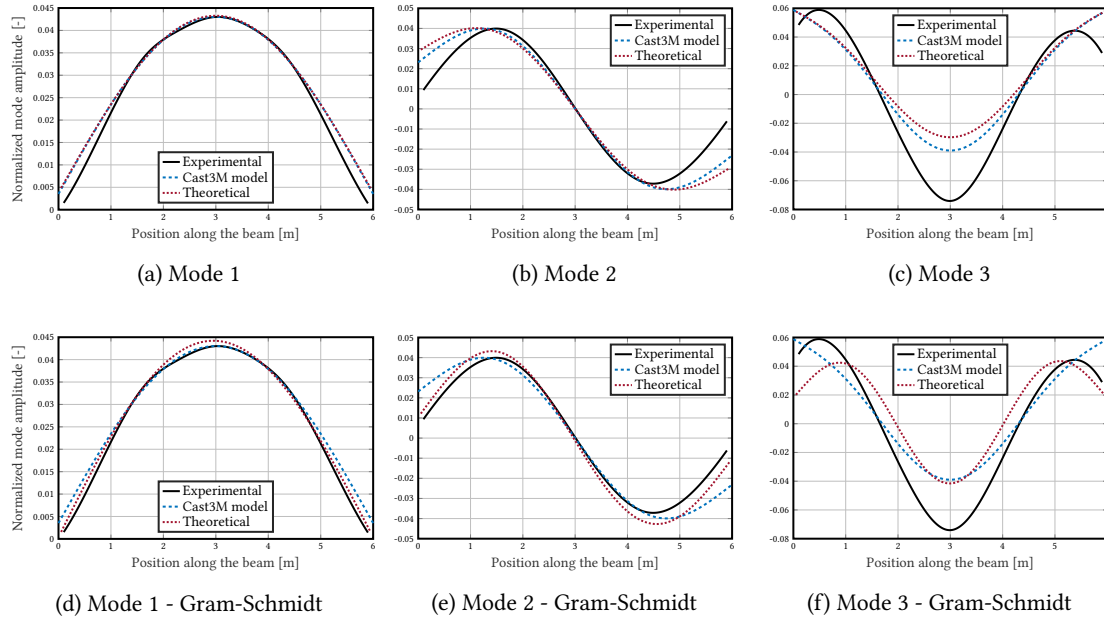
Figure 3.9: Combination of mode shapes - Rayleigh's quotient method

3.3.1 Method algorithm

The proposed method is based on the idea that the global response of the RC beam can be decomposed into a set of equivalent SDOF systems. In addition, the total studied signal is decomposed into time windows. First, the method algorithm is presented in the hypothesis of linear behaviour in section 3.3.1.1, and then, required modifications are discussed in the case of a nonlinear behaviour (section 3.3.1.2).

3.3.1.1 Algorithm for a by-pieces linear constitutive model

Figure 3.10 presents the algorithm in the case of linear behaviour. First, the modal eigenbasis is computed following the methodology discussed in section 3.2. Then, because it was demonstrated in chapter 2 that the beam movement is mostly characterised by its first mode and because the first mode represents 89.6% of the total modal mass, a projection of the global system is performed on the first eigenmode. Equation (3.5) projected on the first eigenmode for a linear behaviour model becomes equation (3.28):

$$\left(\underline{\phi}_1^T \cdot \mathbb{M} \cdot \underline{\phi}_1 \right) \times \ddot{\boldsymbol{\alpha}}_1 + \left(\underline{\phi}_1^T \cdot \mathbb{C} \cdot \underline{\phi}_1 \right) \times \dot{\boldsymbol{\alpha}}_1 + \left(\underline{\phi}_1^T \cdot \mathbb{K} \cdot \underline{\phi}_1 \right) \times \boldsymbol{\alpha}_1 = - \left(\underline{\phi}_1^T \cdot \mathbb{M} \cdot \underline{\Gamma} \right) \times \ddot{\mathbf{U}}_s \quad (3.28)$$

where $\mathbb{K}$ is the linear stiffness matrix. The following modal properties are thus defined from equation (3.28) and computed from the eigenbasis knowledge:

✓ the modal mass of the first eigenmode: $m_1 = \underline{\phi}_1^T \cdot \mathbb{M} \cdot \underline{\phi}_1$,

✓ the modal damping of the first eigenmode: $c_1 = \underline{\phi}_1^T \cdot \mathbb{C} \cdot \underline{\phi}_1$,

✓ the modal stiffness of the first eigenmode: $k_1 = \underline{\phi}_1^T \cdot \mathbb{K} \cdot \underline{\phi}_1$,

✓ the modal projection of the seismic acceleration on the first mode: $\kappa_1 = \dfrac{\underline{\phi}_1^T \cdot \mathbb{M} \cdot \underline{\Gamma}}{\underline{\phi}_1^T \cdot \mathbb{M} \cdot \underline{\phi}_1}$, called the modal participation factor.
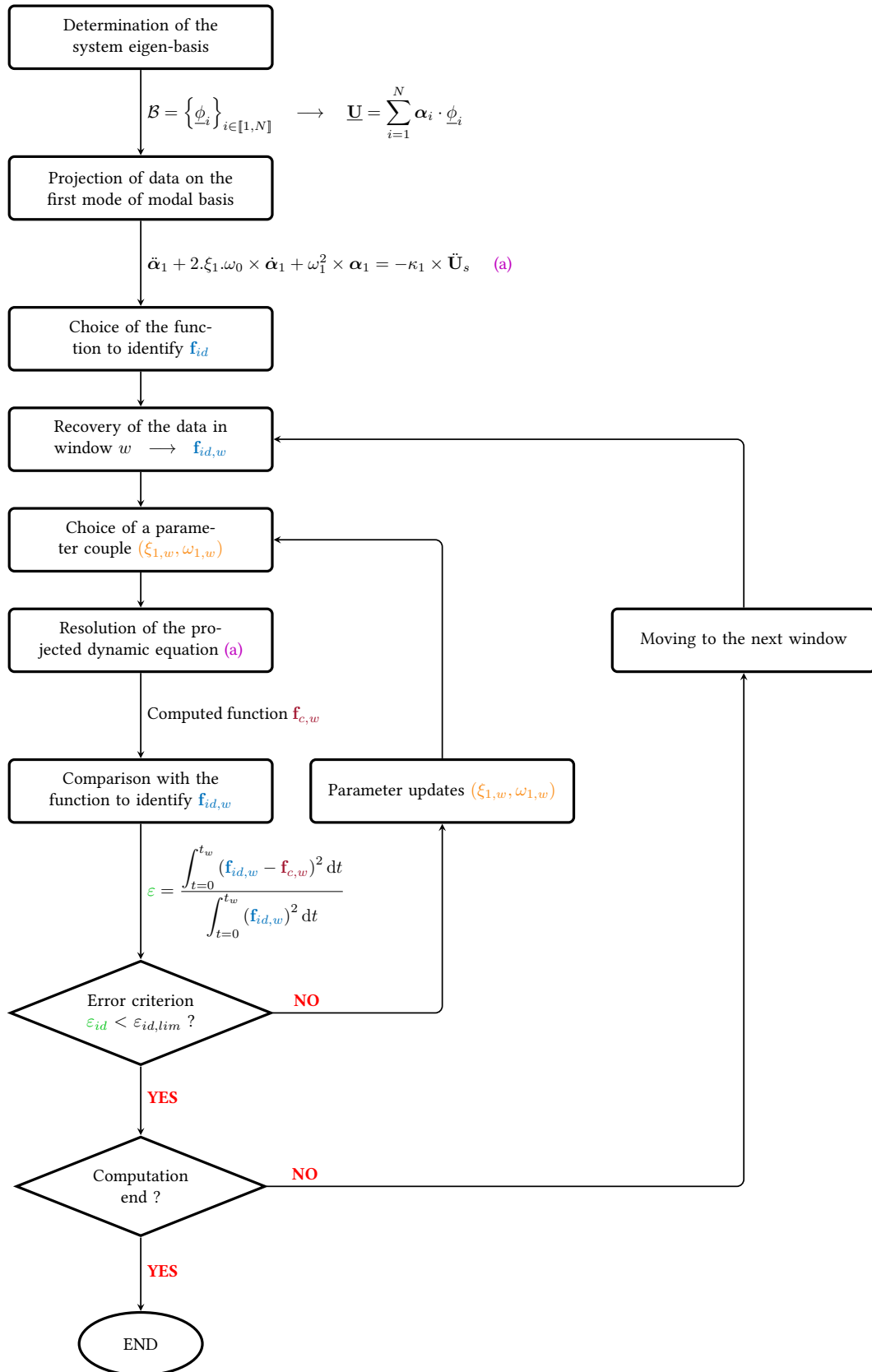
Figure 3.10: Algorithm of the damping identification method

Then, by dividing equation (3.28) by the modal mass m_1, equation (3.29), corresponding to (a) in figure 3.10, is obtained:

$$\ddot{\boldsymbol{\alpha}}_1 + 2.\xi_1.\omega_0 \times \dot{\boldsymbol{\alpha}}_1 + \omega_1^2 \times \boldsymbol{\alpha}_1 = -\kappa_1 \times \ddot{\mathbf{U}}_s \qquad (3.29)$$

where $2.\xi_1.\omega_0 = {}^{c_1}/_{m_1}$ and $\omega_1^2 = {}^{k_1}/_{m_1}$.

Then, a function to identify $\mathbf{f}_{id}$ (the target function for the identification) must be defined from experimental data or responses of the numerical computations. It can be the acceleration, velocity or displacement responses, or a combination of these functions. Windows are defined to decompose the input signal in n_w time segments for which the response can be modelled with a linear behaviour. These windows have to verify two properties: (i) long enough to have sufficient data for the identification, and (ii) short enough to validate the linear tangent behaviour hypothesis.

So, in each time window of length t_w, the performed steps are presented in the algorithm 1.[1] At the beginning, the data of $\mathbf{f}_{id}$ are extracted in the studied window w given $\mathbf{f}_{id,w}$ as well as the projected seismic acceleration $\ddot{\mathbf{U}}_{s,w}$. The Newmark's algorithm (3 in appendix F.1) is applied with the parameters $\gamma = {}^1/_2$ and $\beta = {}^1/_4$ because these parameters give an unconditionally stable system while conserving system energy. For updating the parameters, the "interior-point method" is used. The stopping criterion is a variation inferior to 10^{-10} of identified parameters: if $\underline{x}_w$ has to be identified, the optimization algorithm stops when $\left\| \underline{x}_w^{(k+1)} - \underline{x}_w^{(k)} \right\| < 10^{-10}$. The "interior-point method" is described in appendix F.2. Finally, when $\xi_{1,w}$ and $\omega_{1,w}$ are deduced on the window w, algorithm 1 is applied again on the next window up to the last one.

Algorithm 1: Algorithm of the identification method for the window w

input : $\mathbf{f}_{id,w}$, $\ddot{\mathbf{U}}_s^{(1,w)}$

output: $\xi_{1,w}$, $\omega_{1,w}$

begin

$\quad \xi_{1,w}^{(0)} = \xi_{1,w-1}$, $\omega_{1,w}^{(0)} = \omega_{1,w-1}$

$\quad$ **while** $\varepsilon_{id}^{(k)} > \varepsilon_{id,lim}$ **do**

$\quad\quad$ Computation of the response at step k solved with the Newmark's algorithm:

$$\ddot{\boldsymbol{\alpha}}_{1,w}^{(k)} + 2.\xi_{1,w}^{(k)}.\omega_0 \times \dot{\boldsymbol{\alpha}}_{1,w}^{(k)} + \left(\omega_{1,w}^{(k)} \right)^2 \times \boldsymbol{\alpha}_{1,w}^{(k)} = -\kappa_1 \times \ddot{\mathbf{U}}_s, w$$

$\quad\quad$ Computation of $\mathbf{f}_{c,w}^{(k)}$

$\quad\quad$ Computation of the error $\varepsilon_{id}^{(k)}$: $\varepsilon_{id}^{(k)} = \dfrac{\displaystyle\int_{t=0}^{t_w} \left(\mathbf{f}_{id,w} - \mathbf{f}_{c,w}^{(k)} \right)^2 \mathrm{d}t}{\displaystyle\int_{t=0}^{t_w} \left(\mathbf{f}_{id,w} \right)^2 \mathrm{d}t}$

$\quad\quad$ Updating of the parameters $\left(\xi_{1,w}^{(k+1)}, \omega_{1,w}^{(k+1)} \right)$ using the interior-point method

$\quad$ **end**

$\quad \xi_{1,w} = \xi_{1,w}^{(k_c)}$, $\omega_{1,w} = \omega_{1,w}^{(k_c)}$

end

---

[1] The index 1 corresponds to the projection in the first mode.
The index w corresponds to the window of interest.
The index k corresponds to the iteration step, and k_c is the convergence iteration.

3.3.1.2   Modifications for nonlinear constitutive models

In the case of a nonlinear constitutive model, with a displacement field $\underline{\mathbf{U}} = \boldsymbol{\alpha}_1 \cdot \underline{\phi}_1$, equation (3.28) is replaced by equation (3.30):

$$\left(\underline{\phi}_1^T \cdot \mathbb{M} \cdot \underline{\phi}_1 \right) \times \ddot{\boldsymbol{\alpha}}_1 + \left(\underline{\phi}_1^T \cdot \mathbb{C} \cdot \underline{\phi}_1 \right) \times \dot{\boldsymbol{\alpha}}_1 + \underline{\phi}_1^T \cdot \mathbf{f_{int}} \left(\boldsymbol{\alpha}_1 . \underline{\phi}_1 \right) = - \left(\underline{\phi}_1^T \cdot \mathbb{M} \cdot \underline{\Gamma} \right) \times \ddot{\mathbf{U}}_s \quad (3.30)$$

Simplifying by m_1, this equation can be rewritten in equation (3.31):

$$\ddot{\boldsymbol{\alpha}}_1 + 2.\xi_1.\omega_0 \times \dot{\boldsymbol{\alpha}}_1 + \mathbf{f_{int\,1}} = -\kappa_1 \times \ddot{\mathbf{U}}_s \quad (3.31)$$

where $\mathbf{f_{int\,1}} = \dfrac{\phi_1^T \cdot \mathbf{f_{int}} \left(\boldsymbol{\alpha}_1 . \underline{\phi}_1 \right)}{m_1}$ and the parameter to identify is ξ_1. The parameters of the nonlinear model $\mathbf{f_{int\,1}}$ are identified on a cyclic test. So the variations of dynamic dissipations are only carried by the viscous damping ξ_1. The equation to solve for a nonlinear constitutive model is expressed in equation (3.32):

$$\ddot{\boldsymbol{\alpha}}_{1,w}^{(k)} + 2.\xi_{1,w}^{(k)}.\omega_0 \times \dot{\boldsymbol{\alpha}}_{1,w}^{(k)} + \mathbf{f_{int}}_{1,w}^{(k)} = -\kappa_1 \times \ddot{\mathbf{U}}_{s,w} \quad (3.32)$$

where $\mathbf{f_{int}}_{1,w}^{(k)}$ is the nonlinear internal force associated with the computed displacement on the modal basis $\boldsymbol{\alpha}_{1,w}^{(k)}$. A Modified Newmark's algorithm (algorithm 2 from the knowledge of time step $t-1$ data) is thus used to solve the nonlinear equation, with $k_t^{(t)}$ the tangent stiffness at time step t.

3.3.2   Calibration of the method parameters

3.3.2.1   Simplify problem presentation

The identification method performances strongly depend on numerous choices the user has to make. The study of a three DOFs system (fig. 3.11) is so considered to discuss the possible method characteristics. In addition, a simple seismic signal presented in figure 3.12 is used as seismic acceleration. Integration with the Newmark's scheme and a linear constitutive model are used to define the "reference solution" (fig. 3.13). A mass proportional damping is considered $c_i = a_0.m_i$ (as schematised in figure 3.13) with $m_i = 500\,\text{kg}$ for all $i \in [\![1;3]\!]$, given $\xi_i = \frac{a_0}{2.\omega_i}$ as damping ratio for node i in figure 3.11. A modal analysis gives the mass-normalised mode shapes in figure 3.13a. Table 3.4 presents the modal properties of the studied three DOFs system, corresponding
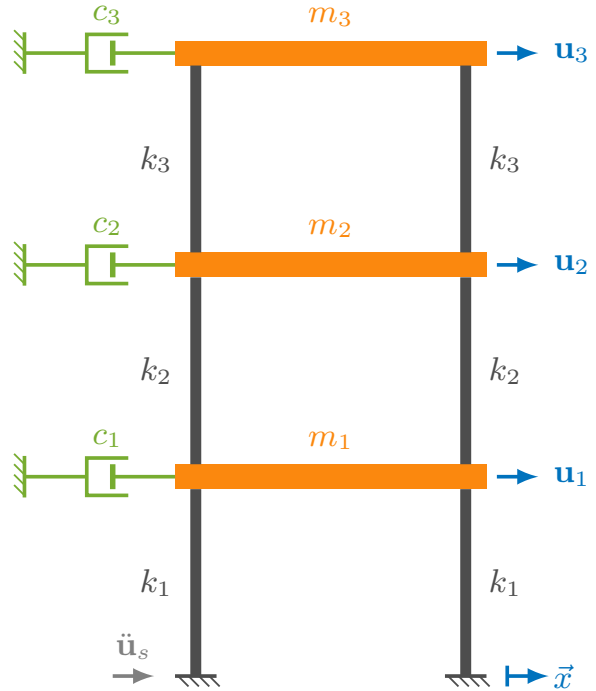
Figure 3.11: Three DOFs discrete system

Algorithm 2: Modified Newmark's algorithm

input : $\boldsymbol{\alpha}_{1,w}(t-1)$, $\dot{\boldsymbol{\alpha}}_{1,w}(t-1)$, $\ddot{\boldsymbol{\alpha}}_{1,w}(t-1)$, $\mathbf{f}_{\text{int}1,w}(t-1)$, $\ddot{\mathbf{U}}_{s,w}(t)$, Δt, γ, β, $k_t^{(t-1)}$, m_1, c_1, κ_1, $R_n^{(t-1)}$

output: $\boldsymbol{\alpha}_{1,w}(t)$, $\dot{\boldsymbol{\alpha}}_{1,w}(t)$, $\ddot{\boldsymbol{\alpha}}_{1,w}(t)$, $\mathbf{f}_{\text{int}1,w}(t)$, $k_t^{(t)}$, $R_n^{(t)}$

begin

$\quad u = \boldsymbol{\alpha}_{1,w}(t-1)$, $R_n = R_n^{(t-1)}$, $f_{ext} = \kappa_1 \times \ddot{\mathbf{U}}_{s,w}(t)$

$\quad \Delta u^{(0)} = 0$, $\varepsilon^{(0)} = 1$

$\quad A_m = \dfrac{m_1}{\beta.\Delta t^2} + c_1.\dfrac{\gamma}{\beta.\Delta t} + k_t^{(t-1)}$

$\quad a^* = -\dfrac{1}{\beta.\Delta t} \times \dot{\boldsymbol{\alpha}}_{1,w}(t-1) - \left(\dfrac{1}{2.\beta} - 1\right) \times \ddot{\boldsymbol{\alpha}}_{1,w}(t-1)$

$\quad v^* = \left(1 - \dfrac{\gamma}{\beta}\right) \times \dot{\boldsymbol{\alpha}}_{1,w}(t-1) + \left(1 - \dfrac{\gamma}{2.\beta}\right) \times \Delta t \times \ddot{\boldsymbol{\alpha}}_{1,w}(t-1)$

$\quad b^* = f_{ext} - (m_1 \times a^* + c_1 \times v^*)$

$\quad b = b^* - R_n$

$\quad$ **while** $\varepsilon^{(k)} > \varepsilon_{lim}$ **do**

$\qquad \delta u^{(k)} = \dfrac{b^{(k)}}{A_m}$

$\qquad \Delta u^{(k)} = \Delta u^{(k-1)} + \delta u^{(k)}$

$\qquad u^{(k)} = u^{(k-1)} + \delta u^{(k)}$

$\qquad$ Application of the behaviour law to deduce $f_{mod}^{(k)}\left[u^{(k)}\right]$

$\qquad f_{int}^{(k)} = m_1 \times \left(a^* + \dfrac{\Delta u^{(k)}}{\beta.\Delta t^2}\right) + c_1 \times \left(v^* + \gamma.\dfrac{\Delta u^{(k)}}{\beta.\Delta t}\right) + f_{mod}^{(k)}\left[u^{(k)}\right]$

$\qquad \varepsilon^{(k)} = \left|\dfrac{f_{ext} - f_{int}^{(k)}}{f_{ext}}\right|$

$\qquad R_n^{(k)} = \left(\dfrac{m_1}{\beta.\Delta t^2} + c_1.\dfrac{\gamma}{\beta.\Delta t}\right) \times \Delta u^{(k)} + f_{mod}^{(k)}\left[u^{(k)}\right]$

$\qquad b^{(k)} = b^* - R_n^{(k)}$

$\quad$ **end**

$\quad \boldsymbol{\alpha}_{1,w}(t) = u^{(k_c)}$, $\dot{\boldsymbol{\alpha}}_{1,w}(t) = v^* + \gamma.\dfrac{\Delta u^{(k_c)}}{\beta.\Delta t}$, $\ddot{\boldsymbol{\alpha}}_{1,w}(t) = a^* + \dfrac{\Delta u^{(k_c)}}{\beta.\Delta t^2}$

$\quad k_t^{(t)} = \dfrac{f_{mod}^{(k_c)}\left[u^{(k_c)}\right]}{u^{(k_c)}}$

$\quad \mathbf{f}_{\text{int}1,w}(t) = f_{mod}^{(k_c)}\left[u^{(k_c)}\right]$

$\quad R_n^{(t)} = R_n^{(k_c)}$

end

---

to the exact values of the parameters to identify with the proposed method. Finally, the acceleration responses for the three nodes are plotted in figure 3.13b.

The method parameters to evaluate are:
- ✓ the number of modes n_m for the projection on the modal basis,
- ✓ the global response used to define $\mathbf{f}_{id}$,
- ✓ the window properties (t_w),

✓ the modal parameters (ξ_i and ω_i) to identify. In addition, few remarks are discussed concerning the influence of the initial and extreme parameter values. In some cases, some evolution constraints for the parameters are also applied from one window to another.
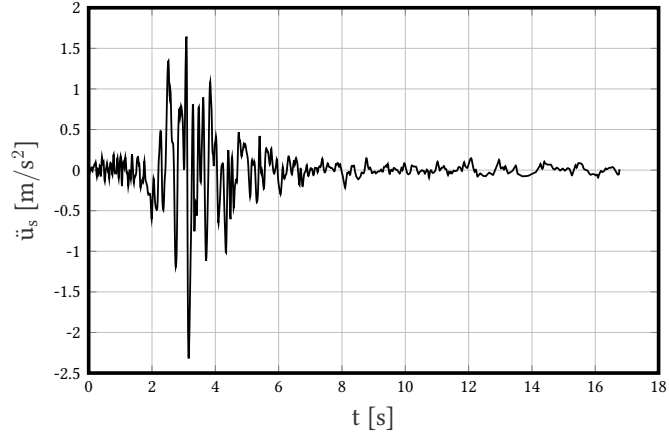
Figure 3.12: Seismic acceleration

(a) Mass-normalised mode shapes

(b) Acceleration response
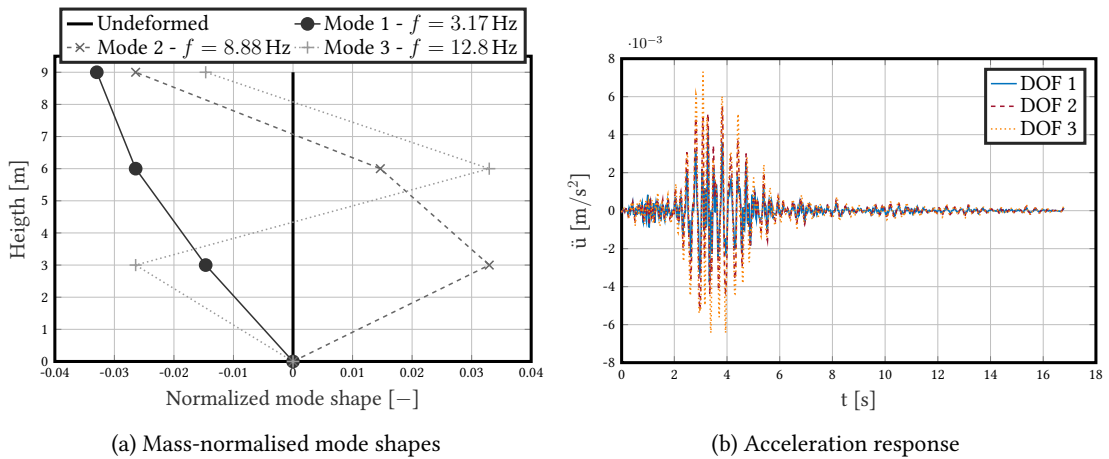
Figure 3.13: "Reference solution" of the three DOFs system

Table 3.4: "Reference modal properties" to identify

| Mode | Eigenfrequency | | Damping ratio |
	[rad/s]	[Hz]	[%]
n°1	19.90	3.17	10.1
n°2	55.77	8.88	3.59
n°3	80.59	12.8	2.48

3.3.2.2   Parameter calibrations

In the analyses presented in this section, the following parameters are considered:
- ✓ projection on the first mode of the eigenbasis ($n_m = 1$),
- ✓ the acceleration response of node 3 is considered as objective function $\mathbf{f}_{id}$,
- ✓ classical windows are considered with a length $t_w = T_{w,c} = 0.2\,\text{s}$,
- ✓ ξ_1 and ω_1 are the parameters to identify.

In each paragraph, a parameter is studied and evolves. The objective of those analyses is to test the method implementation by discussing some choice influences.

(a)   Number of modes for the projection on the modal basis   The system is composed of three DOFs. The three mode shapes associated are plotted in figure 3.13a. The modal masses associated are: $\tilde{m}_1 = 1371.1\,\text{kg}$, $\tilde{m}_2 = 112.3\,\text{kg}$ and $\tilde{m}_3 = 16.6\,\text{kg}$. Using the projections respectively on the first mode, on the two first modes and the three modes, identification errors are 6.1%, 2.8% and 0.96%. The three identification errors illustrate the intuitive result that increasing the number of modes allows a better representation of the function to identify. However, it significantly increases the computational time. Furthermore, the identified parameters associated with the third mode are not converging towards the target values because they do not influence the system response enough.

(b)   Objective function   The DOF of interest must first be chosen to define the objective function. Figure 3.13b shows the acceleration responses for the three DOFs. The first DOF is the closest to the fixed support, so its acceleration amplitude is the lowest, contrary to DOF number 3. As expected, the global identification errors are the strongest for DOF 1. Then, different global responses (displacement, velocity, acceleration, force) can be considered objective functions. A combination of different functions could also be considered. For the studied example, the identifications of respectively displacement, velocity and acceleration lead to global errors equal to 26%, 1.6% and 6.1%. The more significant error with the displacement is due to the transitory phase during which the method tries to stabilise around the target parameters. This phase is longer with the displacement response than with the two others. An idea to improve the response could be to add relaxation.

(c)   Window properties   On each window, it is considered that the system response behaves as a linear SDOF system. So, the window length must be short enough to check this hypothesis. However, enough data have to be used for the identification, so the window length also has to be long enough to have a sufficient number of data. In addition, two strategies can be studied: (i) windows ones after the others with the initial conditions for the window (w) corresponding to the end of the previous window ($w - 1$), or (ii) partially superpose the windows to obtain smoother responses at window interfaces. These strategies are respectively called "classical windows" and "moving windows". For the studied system, the lengths given the minimal errors for both window types are respectively $T_{w,c} = 0.2\,\text{s}$ for classical windows, corresponding to twenty-time increments, and $T_{w,m} = 0.4\,\text{s}$, corresponding to 40 time increments, with a lag time of $\delta_{T_{w,m}} = T_{w,m}/3$ for moving windows. The "moving windows" do not improve the identification responses, but the associated computational time is higher that is why they will not be used.

(d)   Initial values and variations of parameters to identify   Equation (3.29) is considered, and parameters ξ_1 and ω_1 are identified with a global identification error of 6.1%. As expected, the initial values and limits of the parameters to identify play a significant role in the identification performances. Coherent initial values must be considered to reduce the initial transient phase and ensure the method convergence towards expected parameters. Furthermore, because the beam properties are physically not

able to vary too much from one window to another, a constraint minimisation is introduced through a definition of a maximal variation for both parameters.

3.3.2.3   Simple system identified response

Considering the best identification characteristics from all influential parameters leads to the identification response in figure 3.14. Figure 3.14a shows that the identified acceleration is very well matching the "reference solution", which is linked with errors in figure 3.14b. A global error under 10% demonstrates the good performance of the developed method. Figure 3.14b also exhibits a transient phase corresponding to the convergence of identified parameters towards the target values, mainly observed in figure 3.14d with the eigenfrequency. For the damping ratio, more substantial variations are observed. A hypothesis could be that the viscous damping energy is low compared to the other during the computation. So strong errors of viscous damping ratio do not influence the global response, and the algorithm can not correct these errors. It could be the consequence of a lack of sensitivity to the damping, which is the interest value.

In conclusion, the method seems to be performative to identify an objective function, but the interpretation of parameters has to be carefully discussed.

(a) Acceleration

(b) Errors on windows

(c) Identified damping ratio

(d) Identified eigenfrequency
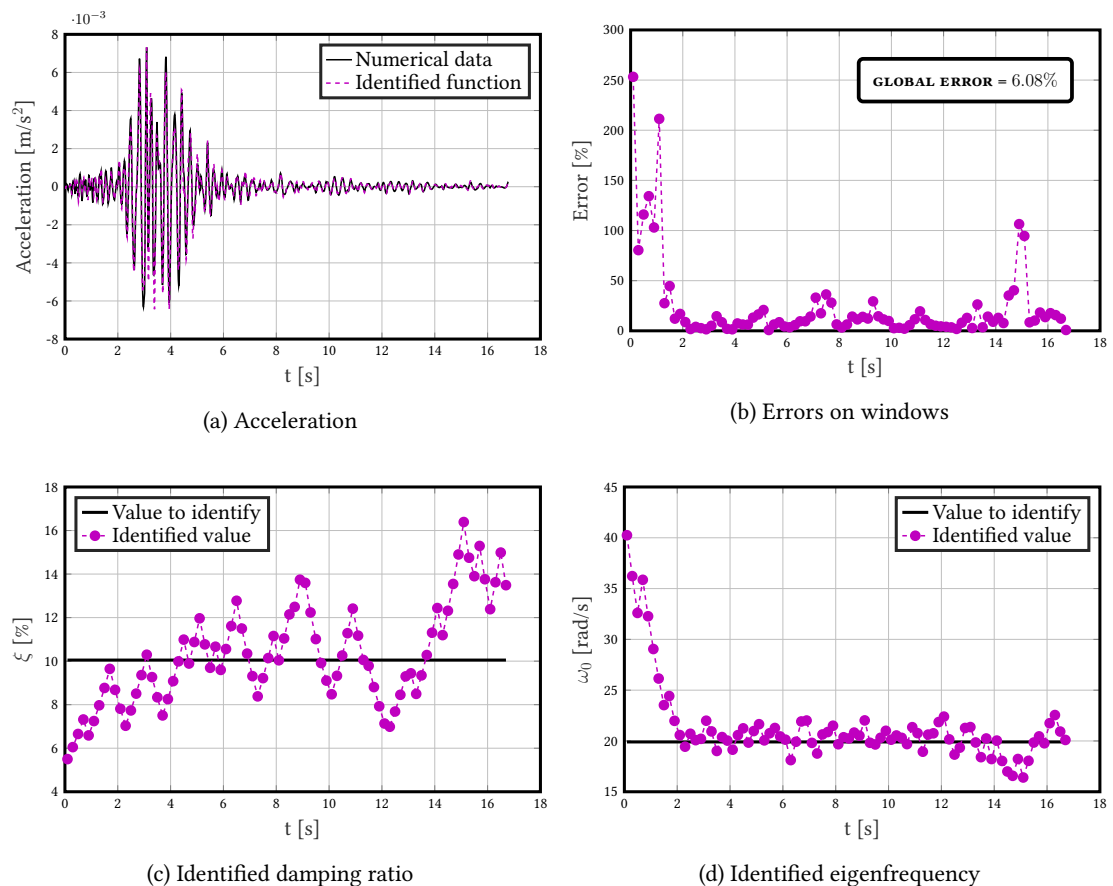
Figure 3.14: Validation of the damping identification method on a three simple DOFs system

3.3.3   Method validation

After performing a parametric study with a simple discrete system, the damping identification method is applied to the experimental and numerical (Cast3M) beam responses analysed in chapter 2. WN1 test is chosen to validate the proposed method because concrete and steel materials stay elastic. The experimental response is identified, as well as the numerical one with RICBET constitutive model and Rayleigh damping formulation computed with a viscous damping ratio of 1%.

The following choices are made for the beam system based on a parametric study. (i) The first beam effective modal mass represents 89.6% of the total mass based on the experimental data. So, the projection on beam first mode is considered sufficient. This result is confirmed by the study performed by Heitz, Giry, et al. (2019). The first mode shape considered is the one identified analytically. (ii) For the objective function, the node at the centre of the beam is considered (i.e. the node with the most significant displacement in the fundamental mode shape). The experimental data considered is the acceleration as it shows the best signal-to-noise ratio with respect to displacement measurements. (iii) According to the preliminary test performed, no significant improvements are observed with moving windows, so classical ones are considered. A new parametric study is performed with the data to identify to validate these windows length ($T_{w,c} = 1.0\,\text{s}$). (iv) Finally, parameters ξ_1 and ω_1 are considered for the identification. Their initial values are respectively 5%, a classical viscous damping ratio, and $44\,\text{rad/s}$ ($7.0\,\text{Hz}$) the undamaged beam eigenfrequency. 10% of the maximal variation is applied as a constraint from one window to another.

Figures 3.15 and 3.16 present the results of the damping identification method applied on WN1 numerical and experimental data. First, the global responses are plotted in figure 3.15 with the "exact values" corresponding to the numerical or experimental data and the "identified values" corresponding to the data deduced from the identification method. Experimentally, the velocity is not measured. That is why no "exact value" is presented in figure 3.15b. So, if figures 3.15a and 3.15d are considered, a good

| (a) Experimental acceleration | (b) Experimental velocity | (c) Experimental displacement |

| (d) Cast3M acceleration | (e) Cast3M velocity | (f) Cast3M displacement |
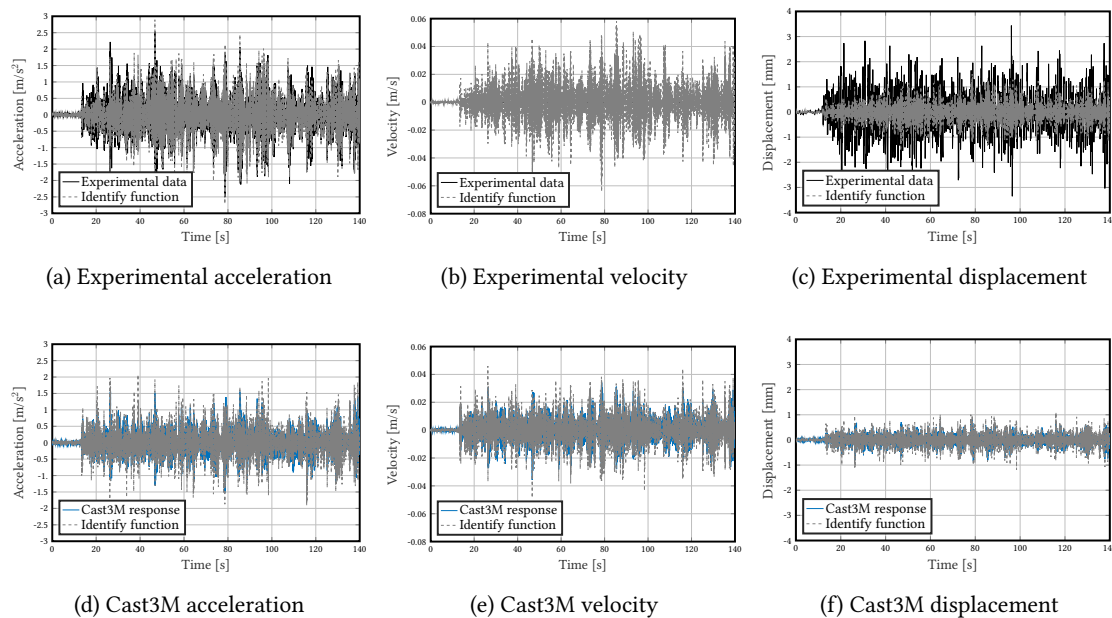
Figure 3.15: WN1 test - Application of the damping identification method on beam responses - global responses

(a) Viscous damping ratios

(b) Frequencies
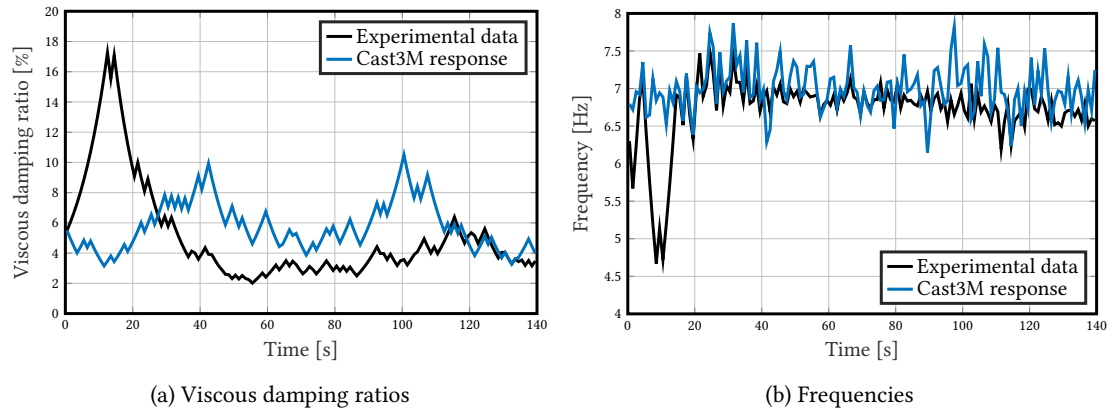
Figure 3.16: WN1 test - Application of the damping identification method on beam responses - identified parameters

match is observed between exact and identified responses. By studying the identification errors, higher values are obtained with the experimental data because the initial experimental values are very noisy. Experimentally, a global error of 363% is obtained, while it is only 73.1% for the numerical data. The apparent significant errors result from the comparison of data oscillating around null values. So, what is more interesting than the values themselves is their comparison, in parallel of the time evolution of exact and identified responses. An explanation for the more significant experimental error could be the noise on low amplitude measurements. It could also explain the amplitude differences in figure 3.15c between exact and identified displacements. Indeed, the three plotted global responses demonstrate good method performances to identify dynamic data with the numerical data.

Then, identified parameters are presented in figure 3.16. Experimentally, figures 3.16a and 3.16b again show the transitory phase during which the system tries to stabilise. It corresponds to the very low accelerations at the computation beginning. After this phase, the parameters stabilise and oscillate around constant values. This oscillation could be a numerical bias. Numerically, oscillations are also observable but with more considerable variations. In addition, while both computations lead to eigen-frequencies around $7\,\mathrm{Hz}$ corresponding to the undamaged beam eigenfrequency (fig. 3.16b and 3.16b), the viscous damping ratios exhibit bigger differences. Experimentally (fig. 3.16a), a stabilisation around 4% is obtained while it is mainly around 6% for the numerical data (fig. 3.16a). Experimentally, the identified viscous damping ratio corresponds to the recommended value in earthquake engineering using a linear constitutive model, with modification factors for the anticipated nonlinear behaviour. It demonstrates that 5% seems to be a good value for remaining elastic RC structures.

3.4   Viscous damping identification of a SDOF model

The previous section presented and validated the damping identification algorithm with a linear system. Let us use it to evaluate the viscous damping ratios and eigenfrequencies in the case of nonlinear structural behaviour. DSS2 and DSS3 tests, whose input signals are presented in figures 2.10a and 2.10b, are of interest. A by-pieces linear constitutive model will first be considered in section 3.4.1 to propose evolutions of the damping ratio as a function of a damage variable. Then, a nonlinear constitutive model will be used in section 3.4.2 to discuss how the consideration of hysteretic dissipations influences the identified viscous damping.

The same method characteristics considered in the validation are used herein, except that the win-

dow length is adapted to the time increments given $T_{w,c} = 0.2\,\mathrm{s}$ and corresponding to forty increments in each window.

3.4.1   Linear constitutive model

Equation (3.29) is used to identify the viscous damping ratio ξ_1 and the damaged beam eigenfrequency ω_1. A damage index is defined by equation (3.33):

$$d = 1 - \left[\frac{k(t)}{k_0}\right] = 1 - \left[\frac{\omega(t)}{\omega_0}\right]^2 \tag{3.33}$$

3.4.1.1   Experimental data

DSS2 and DSS3 tests are the most damaging dynamic tests applied on the HA16-C1A-2 RC beam. The signal harmonic parts are the ones damaging the beam. The white-noise parts have very low amplitudes and are strongly noisy. So they lead to diffuse clouds of data and limit the result interpretations. Consequently, the identification is made only with the signal harmonic parts. The acceleration responses measured experimentally at the beam centre are considered herein for identification purposes. The viscous damping ratios and eigenfrequencies are identified, and the damage index is deduced from equation (3.33). Finally, the global identified responses are presented in figure 3.17 associated with identification errors in figure 3.18. The viscous damping ratio evolution is plotted in figure 3.19 as a function of the damage index for both tests. There are no constraints on the damage evolution, so this is not damaged in the thermodynamic sense.

Figure 3.17 shows a good accuracy between the experimental and identified responses, particularly for the accelerations (fig. 3.17a and 3.17c) because the identification is performed on this response. Acceleration equivalences can be characterised by figure 3.18, where global errors are much more minor than for the WN1 test previously analysed. Indeed, by removing white-noise parts for the identification, the noisiest parts are eliminated, reducing the error. It appears that the peaks at the block beginnings are challenging to characterise, as it was observed with the numerical computations using the multi-fibre model. It could be a consequence of the limitation of the viscous damping evolution ($\pm 10\%$). For the displacements (fig. 3.17b and 3.17d), the DSS2 test exhibits a long transient phase before stabilising around the exact values. So, divergences at the beginning are only due to numerical bias. It can be supposed that a too-small eigenfrequency is unexpectedly evaluated at the beginning leading to a displacement response with long periods. Then, from around $30\,\mathrm{s}$, the identification response stabilises and no more bias is observed even during the DSS3 test.

Identified parameters induce the viscous damping ratio evolution defined in figure 3.19 as a function of the damage index d defined in equation (3.33). The damage evolution from one test to another is well observable. Identified damage indices for the DSS3 test are superior to those of the DSS2 test. By considering all data, two experimental viscous damping ratio functions can be identify: $\xi_{1,expo}^{(exp)}(d)$ and $\xi_{1,ratio}^{(exp)}(d)$ respectively in equations (3.34) and (3.35).

$$\xi_{1,expo}^{(exp)}(d) = 2.96 \times 10^{-3} \times \exp\left(4.75 \times d\right) \tag{3.34}$$

$$\xi_{1,ratio}^{(exp)}(d) = \frac{-62.1 \times d - 385}{d^2 - 1.36 \times 10^4 \times d + 1.41 \times 10^4} \tag{3.35}$$

Furthermore, two different behaviours seem to exist before and after $d = 0.6$. For damage indices inferior to 0.6, the viscous damping ratio is almost constant and equal to 4%, while above $d = 0.6$, the viscous damping ratio can not be considered constant anymore. The value of 4% for null damage is in
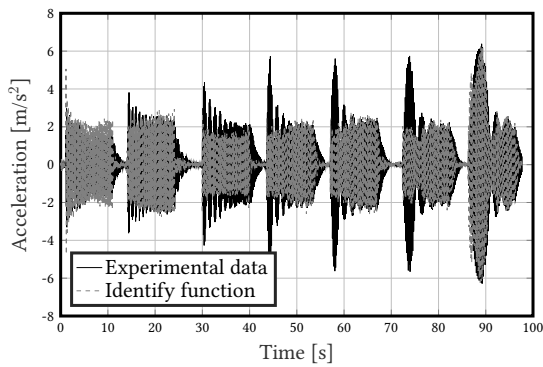
(a) DSS2 test - acceleration
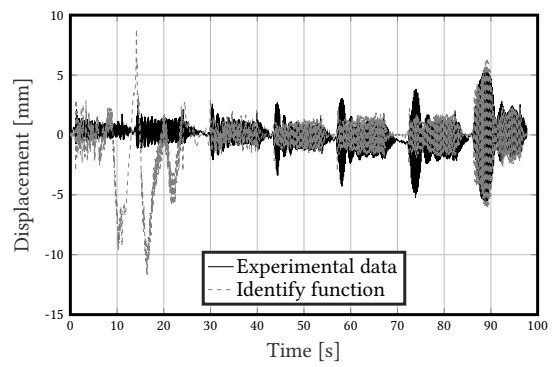
(b) DSS2 test - displacement
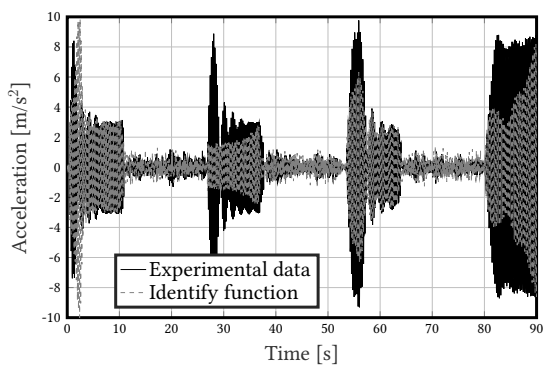
(c) DSS3 test - acceleration
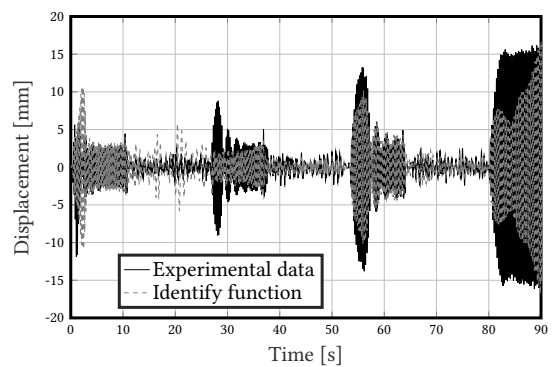
(d) DSS3 test - displacement

Figure 3.17: DSS2 and DSS3 tests - Global responses of identified experimental data - harmonic signal parts
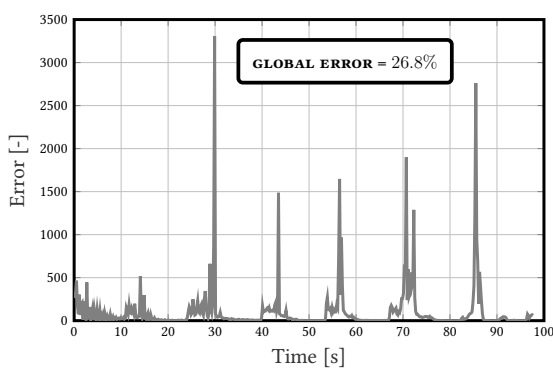
(a) DSS2 test
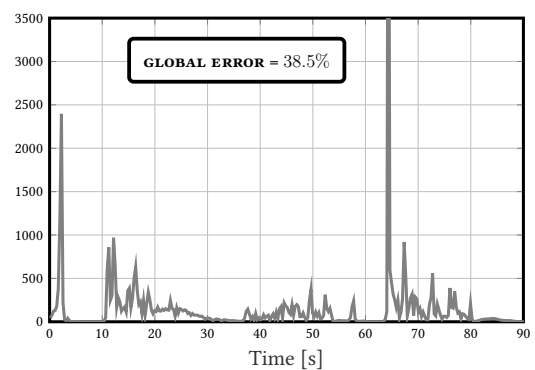
(b) DSS3 test

Figure 3.18: DSS2 and DSS3 tests - Identification errors - harmonic signal parts
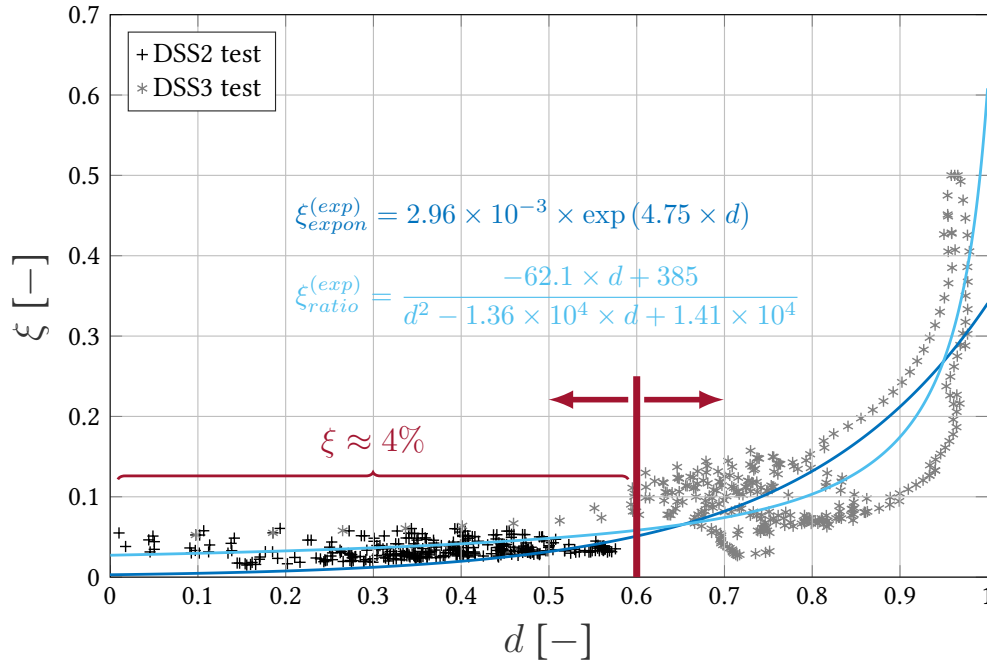
Figure 3.19: DSS2 and DSS3 tests - $\xi_1(d)$ identified on experimental data - harmonic signal parts

adequacy with the results of the WN1 test and the identification of experimental data where a value around 5% was deduced. The function best representing the two distinct behaviours is the ratio in equation (3.35). So, it can be recommended, to engineers, that using a constant viscous damping ratio is acceptable if the damage is low enough. However, updates should be performed in dynamic numerical analyses above a specific range of damage.

Remark : This limit $d_{crit} = 0.6$ was also defined by Roth, Léger, and Soulaïmani (2015) as a threshold to switch from continuum to XFEM concrete cracking models. The limit represents a transition between diffuse damage and macrocracks. The dissipations seem to increase with the development of macrocracks.

3.4.1.2   Numerical data (Cast3M)

As for the experimental data, the damping identification method can be applied to the numerical responses obtained with the multi-fibre model in Cast3M and presented in chapter 2. Then the evolution $\xi_1(d)$ could be compared from one damping formulation to another or between the two studied constitutive models.

Figure 3.20 presents some identified accelerations. Different comparisons are exposed: (i) the RD-type formulations (fig. 3.20a to 3.20c), (ii) the KPD-type formulations (fig. 3.20g to 3.20i), (iii) the viscous damping ratios (fig. 3.20c and 3.20d to 3.20f), and (iv) the BARFRA constitutive model (fig. 3.20j to 3.20l) compared to the associated RICBET responses (fig. 3.20a, 3.20c and 3.20h). Globally, the identified functions are well matching the numerical data. The responses with the most significant global errors (CKPD and RD_ACT for RICBET and RD, CRD and KPD_ACT for BARFRA) present the most significant maximal accelerations. These high values were not observed experimentally, so they are not due to physical phenomena. They should be a consequence of the multi-fibre numerical model because it is impossible

(a) RICBET - RD 2%
global error = 46.3%

(b) RICBET - RD_ACT 2%
global error = 63.0%

(c) RICBET - CRD 2%
global error = 54.0%

(d) RICBET - CRD 1%
global error = 51.4%

(e) RICBET - CRD 3%
global error = 47.8%

(f) RICBET - CRD 5%
global error = 45.4%

(g) RICBET - KPD 2%
global error = 52.9%

(h) RICBET - KPD_ACT 2%
global error = 51.9%

(i) RICBET - CKPD 2%
global error = 65.0%

(j) BARFRA - RD 2%
global error = 57.2%

(k) BARFRA - CRD 2%
global error = 82.8%

(l) BARFRA - KPD_ACT 2%
global error = 60.3%

Figure 3.20: DSS2 test (harmonic parts) - Identified accelerations

to reproduce themselves with the SDOF equivalent system used for the identification. As soon as the damping formulations lead to smooth acceleration responses, it is possible to obtain an accurate identi-

fied response with or without damping matrix updates. Then, for the damping ratio influence, it appears that the error is decreasing with the increase of the viscous damping ratio. A by-pieces linear model is considered for identification, and the developed nonlinearities are reduced when the viscous damping ratio increases. It could explain the better identification of these data. Finally, identifications performed with BARFRA results give more significant errors than with RICBET because the data are not smooth enough. Nevertheless, as for RICBET, the last blocks with RD and KPD_ACT are very well-identified because no damage evolution and a more stable response are observed. As discussed in section 3.3.3, the apparent large errors result from the comparison of data oscillating around null values.

The identified parameters can also be studied as presented in figures 3.21, 3.22 and 3.23, respectively to compare the damping formulations, the viscous damping ratios and the constitutive models. In figure 3.21, it can be concluded that all RD-type formulations give similar responses, as well as all KPD-type ones. However, the evolution differs between both groups because the identified damping ratios are smaller above $d = 0.6$ for KPD-type formulations than RD-type ones. For the viscous damping influence, figure 3.22 shows, as expected, that the larger it is, the higher are the identified damping ratios for one damage value. Finally, between BARFRA and RICBET (fig. 3.20), the identified damping ratios with BARFRA are generally stronger than with RICBET.

(a) RD-type formulations

(b) KPD-type formulations
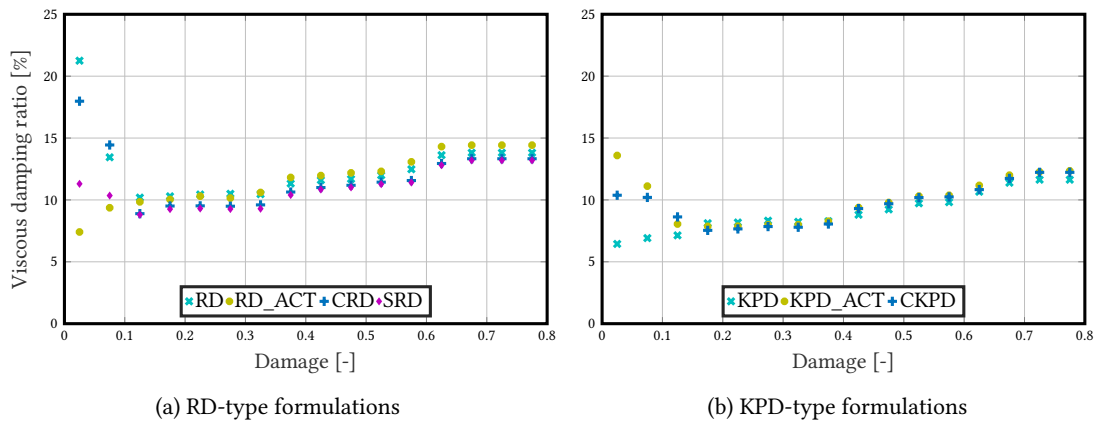
Figure 3.21: DSS2 test (harmonic parts) - Numerical identified evolutions $\xi_1(d)$ - RICBET 2%
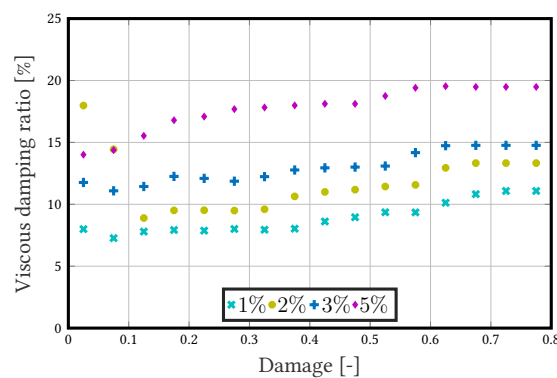
Figure 3.22: DSS2 test (harmonic parts) - Numerical identified evolutions $\xi_1(d)$ - RICBET CRD - viscous damping ratio influence

(a) RD   (b) CRD   (c) KPD_ACT
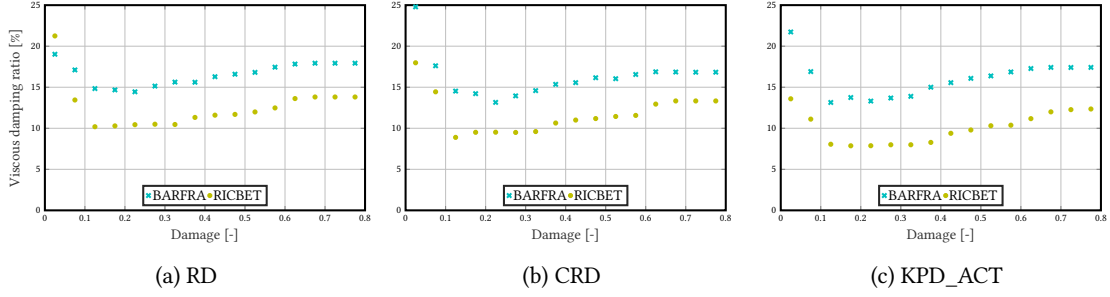
Figure 3.23: DSS2 test (harmonic parts) - Numerical identified evolutions $\xi_1(d)$ - constitutive model influence - 2%

In conclusion, it is possible to identify the numerical data by considering a linear equivalent SDOF system. However, the identified parameters are not giving a different evolution contrary to the experimental data. In addition, the identified damping ratios are more significant than the ones identified on experimental data. So, the numerical models cannot represent the damping content of experimental data. To improve these results, a nonlinear constitutive model could thus be used in the identification method to dissipate energy at the local scale and limit the dissipations at the global scale.

3.4.2   Nonlinear constitutive model

A SDOF nonlinear model representing the RC behaviour was proposed by Heitz, Giry, et al. (2019), and it is named IDEFIX in the present study. It was calibrated based on the experimental campaign presented in section 1.4 and used in the presented work. The model was then used to perform a numerical study of equivalent viscous damping ratio dependences on two engineering demand parameters: the mid-span curvature γ and a degradation index Γ corresponding to the maximum historic curvature at mid-span γ_m over the first steel yielding curvature γ_y. It led to an equivalent viscous damping ratio surface response (eq. 3.36):

$$\xi_{eq} = \bar{C} \times f(\Gamma)g(\gamma) \tag{3.36}$$

where $\bar{C}$ is a coefficient of normalisation, and the identified functions are expressed in equations (3.37) and (3.38):

$$f(\Gamma) = \frac{3.679 \times \Gamma}{\Gamma + 0.2806} \tag{3.37}$$

$$g(\gamma) = \frac{0.03759 \times \gamma}{\gamma^2 - 0.004994 \times \gamma + 8.397 \times 10^{-5}} \tag{3.38}$$

It can be noticed that $g(\gamma)$ corresponds to the form obtained in equation (3.35) from the experimental data identification.

The thermodynamic framework of the IDEFIX model, and the corresponding dissipative phenomena, will be presented in section 3.4.2.1. Then, the proposed damping identification method will be used in section 3.4.2.2 to identify equivalent viscous damping ratios using algorithm 2.

3.4.2.1   Nonlinear model presentation

(a)   Thermodynamic framework   Based on the internal and observable global variables in table 3.5, Helmholtz's free energy Ψ is used to define the state potential. Considered phenomena are the damage with the unilateral effect, the friction and the pinching effect. In the following, the index $\cdot_\pm$ means that the variable takes different values in tension $(+)$ and compression $(-)$.

Table 3.5: IDEFIX model variables

Observable	Internal	Associated forces	Phenomena
u $\longrightarrow$		F	Elasticity
	$u^\pi \longrightarrow$	F^π	Friction
	$\alpha^\pi \longrightarrow$	X^π	Kinematic hardening associated to friction
	$d_\pm \longrightarrow$	$Y_\pm$	Damage (stiffness degradation)
	$z_\pm \longrightarrow$	$Z_\pm$	Isotropic hardening associated to damage
	$\eta \longrightarrow$	F^η	Unilateral effect

The state potential $\Psi\left(u, d_\pm, u^\pi, \alpha^\pi, \eta\right)$ is expressed in equation (3.39) by the decomposition between an elastic (eq. 3.40) part $\Psi^e\left(u, d_\pm, \eta\right)$ and friction (eq. 3.41) one $\Psi^\pi\left(u^\pi, \alpha^\pi, \eta, d_\pm\right)$. Especially, $d_\pm$, η and $K_p(\eta)$ expressions are defined in equation (3.42).

$$\Psi\left(u, d_\pm, u^\pi, \alpha^\pi, \eta\right) = \Psi^e\left(u, d_\pm, \eta\right) + \Psi^\pi\left(u^\pi, \alpha^\pi, \eta, d_\pm\right) \tag{3.39}$$

where u is the displacement variable, $d_\pm$ the damage variable (two variables for two crack families on each side of the beam), u^π the friction displacement variable, α^π the variable associated with friction work hardening and η the crack closure variable evolving from 0 (crack completely closed) to 1 (crack opened) to take into account the pinching effect.

$$\Psi^e\left(u, d_\pm, \eta\right) = \frac{1}{2}.K_p(\eta).\left(1 - d_\pm\right).u^2 \tag{3.40}$$

where $K_p(\eta)$ is the altered stiffness meaning that the pinching effect appears progressively with the damage evolution.

$$\Psi^\pi\left(u^\pi, \alpha^\pi, \eta, d_\pm\right) = \frac{1}{2}.K_p(\eta).d_\pm.(u - u^\pi)^2 + \frac{1}{2}.b^\pi.(\alpha^\pi)^2 \tag{3.41}$$

where b^π is a parameter for the model of friction work hardening.

$$\begin{cases} d_\pm = d_\infty.\left(1 - \left(\dfrac{Y_0}{Y_\pm^d}\right)^q\right) \\[3mm] \eta = d_\pm.\exp\left(-\left|\dfrac{u}{U_c}\right|\right) \\[3mm] K_p(\eta) = K.(1 - \eta) \end{cases} \tag{3.42}$$

where d_∞ is the maximum potential damage given a secant stiffness $K_0.\left(1 - d_\infty\right)$ for an infinite displacement, Y_0 the initial energy threshold for damage, $Y_\pm^d = \dfrac{1}{2}.K_p(\eta).(u)_\pm^2$ the energy rate driving damage, q a coefficient driving the slope right after the damage initiation in the force-displacement curve and U_c characterising the crack closure displacement. Then, the state laws are deduced from the

state potential derivation towards model variables. They are given in equation (3.43):

$$
\begin{cases}
F = \dfrac{\partial \Psi}{\partial u} = K_p(\eta).\left(1 - d_\pm\right).u + K_p(\eta).d_\pm.\left(u - u^\pi\right) \\[2mm]
F^\pi = -\dfrac{\partial \Psi}{\partial u^\pi} = K_p(\eta).d_\pm.\left(u - u^\pi\right) \\[2mm]
X^\pi = \dfrac{\partial \Psi}{\partial \alpha^\pi} = b^\pi.\alpha^\pi \\[2mm]
Y_\pm = -\dfrac{\partial \Psi}{\partial d_\pm} = \dfrac{1}{2}.K_p(\eta).u^2 - \dfrac{1}{2}.K_p(\eta).(u - u^\pi)^2 \\[2mm]
Z_\pm = \dfrac{\partial \Psi}{\partial z_\pm} = \dfrac{dH}{dz_\pm} = \dfrac{Y_0}{\left(1 + \dfrac{z_\pm}{d_\infty}\right)^{1/q}} - Y_0 \\[4mm]
F^\eta = -\dfrac{\partial \Psi}{\partial \eta} = \dfrac{1}{2}.K.\left(1 - d_\pm\right).u^2 + \dfrac{1}{2}.K.d_\pm.(u - u^\pi)^2
\end{cases}
\tag{3.43}
$$

where F is the total force, F^π the friction force, X^π the thermodynamic force related to a kinematic work hardening, $Y_\pm$ the energy restitution rate associated to damage, $Z_\pm$ the thermodynamic force related to an isotropic work hardening and F^η the force associated with the pinching effect. Finally, by applying the Clausius-Duhem inequality, IDEFIX model dissipation law in equation (3.44) can be deduced:

$$
\mathcal{D} = \begin{pmatrix} F^\pi \\ -X^\pi \\ Y_\pm \\ -Z_\pm \\ F^\eta \end{pmatrix}^T \cdot \begin{pmatrix} \dot{u}^\pi \\ \dot{\alpha}^\pi \\ \dot{d}_\pm \\ \dot{z}_\pm \\ \dot{\eta} \end{pmatrix} \geqslant 0
\tag{3.44}
$$

(b)   Model calibration   IDEFIX model comprises eight parameters presented in table 3.6. The parameter calibrations are performed on quasi-static experimental data. First, the capacity curve is used to identify δ_y, k_0, p_{idefix} and q. Then, a^π, b^π, U_c and l_p are deduced from the complete response identification because hysteresis loops are required to determine these parameters. The identified parameter

Table 3.6: Calibrated parameters of Heitz, Giry, et al. (2019) model

Parameter	Description	Value	Unit
δ_y	Yield displacement	2.61	mm
k_0	Initial stiffness	3.262	N.mm^{-1}
p_{idefix}	Stiffness loss coefficient	0.20	—
q	Fragility coefficient	0.35	—
a^π	Hysteresis loops width	1249	N
b^π	Initial stiffness of the hysteresis loops	82.3	N.mm^{-1}
U_c	Crack closure displacement	57.1	mm
l_p	Pinching coefficient	1.14×10^{-11}	—

values are given in table 3.6. In addition, figure 3.24 presents the capacity curve and complete response with experimental and numerical (IDEFIX model) data. A good match is observed. The experimental one is not entirely symmetrical for global responses, so more significant errors are observed for negative displacements.

(a) Capacity curve

(b) Global response
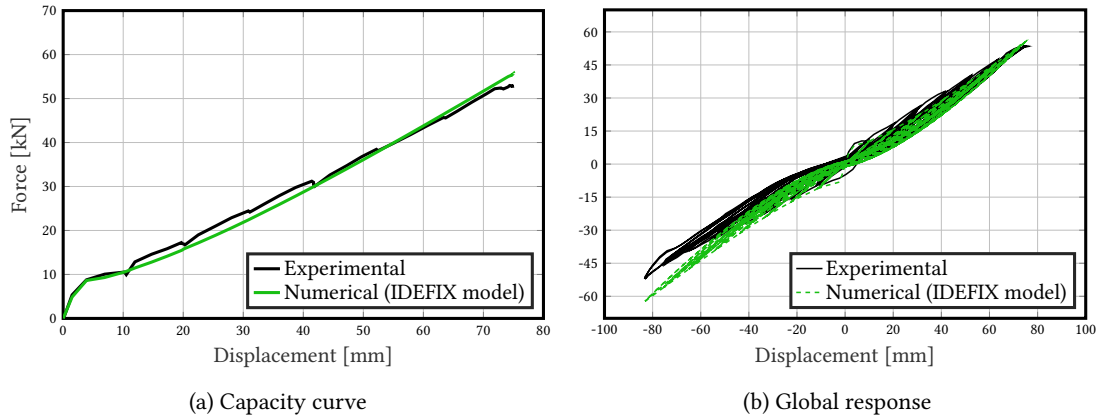
Figure 3.24: Quasi-static responses of calibrated IDEFIX numerical model

(c) Dissipative phenomena For a quasi-static test, the total energy is only composed of the absorbed one. Figure 3.25 presents the energies associated with the quasi-static response in figure 3.24b. First, figure 3.25a validates the energy balance because the hysteretic energy represents the total numerical energy recoverable part. It can be easily compared with the experimental energy by computing the integration of hysteresis loops. The conclusion is that the numerical model dissipates a lower amount of energy than the physical beam. Then, figure 3.25b presents the decomposition between the different dissipative phenomena of the numerical absorbed energy. As for the RICBET model, IDEFIX is particularly dissipating energy through friction. Finally, figure 3.25c shows the evolution of experimental and numerical total energy envelops as functions of the damage variable. It appears that the experimental and numerical energies begin to increase around $d = 0.5$, and the most substantial variations occur after $d = 0.6$, demonstrating that something occurs at that threshold, as observed in identified viscous damping ratios (fig. 3.19). While the RC structure develops low nonlinearities, a small amount of hysteretic energy is dissipated, and a constant small equivalent viscous damping ratio adequately represents physical dissipations. However, after a certain amount of nonlinearities, the hysteretic energy increases strongly. So, if a linear model is considered with an equivalent viscous damping ratio to model the dissipations, the energy must be dissipated through the equivalent viscous damping. The amount of energy is thus dependent on the damage level to represent the substantial hysteretic energy variations best.

3.4.2.2 Viscous damping ratio identification

In section 3.3.1.2 was presented the algorithm modifications to take into consideration a nonlinear constitutive model. Equation (3.31) is used to identify the parameter ξ_1, which is the only one playing an additional role in dynamic. The experimental response and a numerical one (RICBET constitutive model with CRD formulation and 2% of viscous damping ratio), computed with Cast3M, are studied. Figure 3.26 presents the identified accelerations compared to the experimental and numerical solutions. Identifying only the viscous damping ratio with the linear behaviour (i.e., a fixed value for ω_1) is insufficient to obtain accurate identifications because nonlinearities develop during this test. On the contrary,

(a) Energy balance analysis   (b) Decomposition of the dissipated   (c) Total energies as functions of
                                          energy   damage
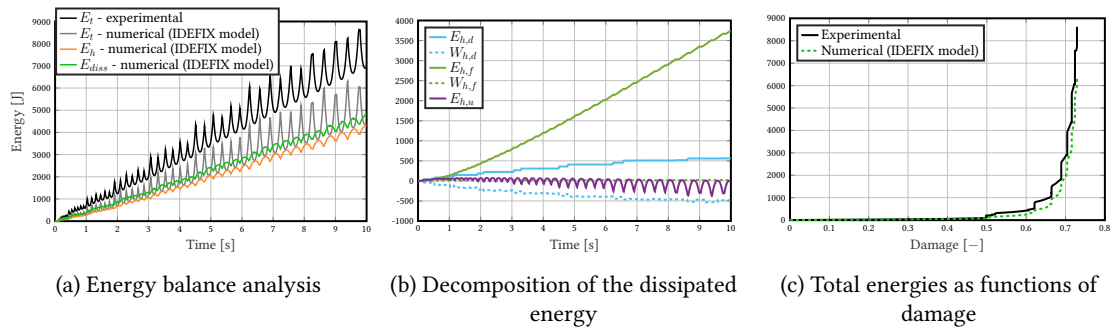
Figure 3.25: Quasi-static energy balance with IDEFIX model

(a) Experimental - elastic model

(b) Experimental - IDEFIX model

(c) Numerical - elastic model

(d) Numerical - IDEFIX model
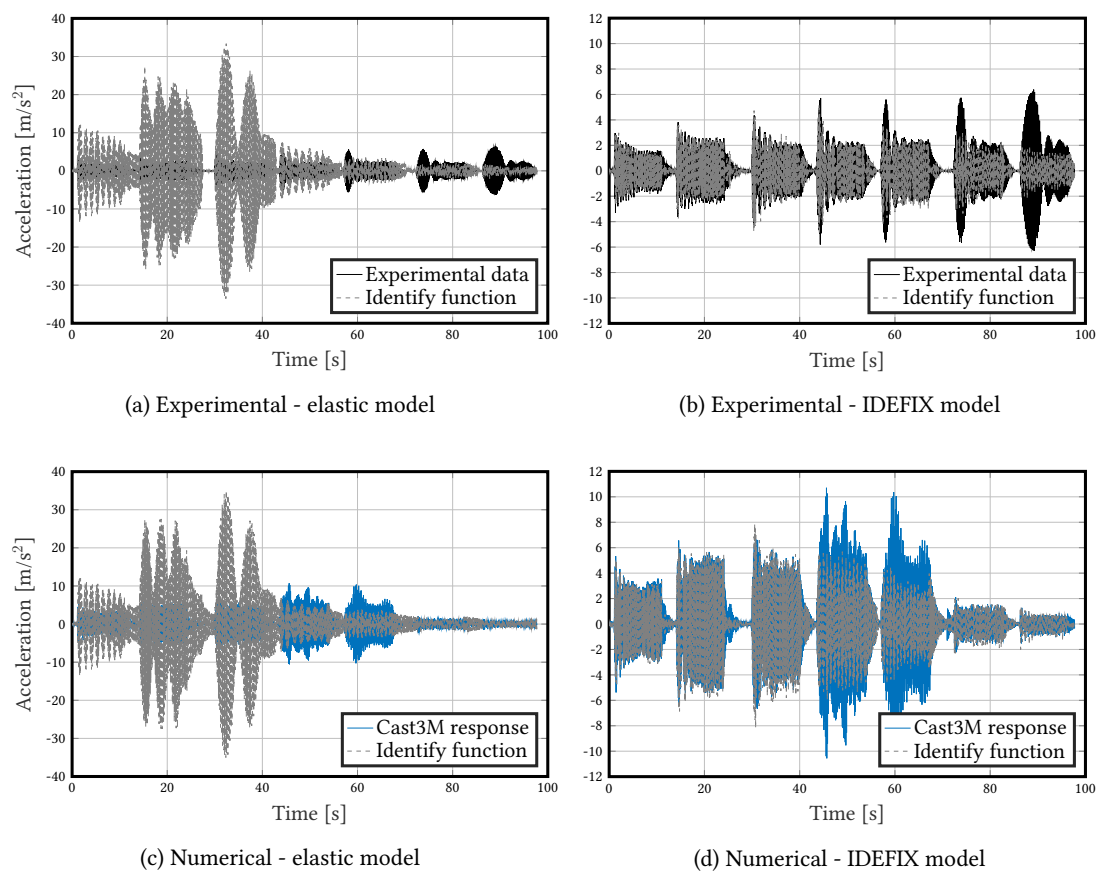
Figure 3.26: DSS2 test (harmonic parts) - Identified accelerations with IDEFIX model

for the numerical and experimental data, using a nonlinear constitutive model allows to model nonlinearities, and so to better identify the experimental and numerical data.

Then, in figure 3.27 are plotted the identified viscous damping ratios. First, figures 3.27a and 3.27b give their values for each window, along with computation. Few variations are observed for the linear behaviour (fig. 3.27a), and small values are identified. That is why the identified accelerations are

(a) $\xi_1(t)$ - elastic model

(b) $\xi_1(t)$ - IDEFIX model

(c) Experimental data - $\xi_1(\gamma, \Gamma)$ - IDEFIX model

(d) Cast3M response - $\xi_1(\gamma, \Gamma)$ - IDEFIX model
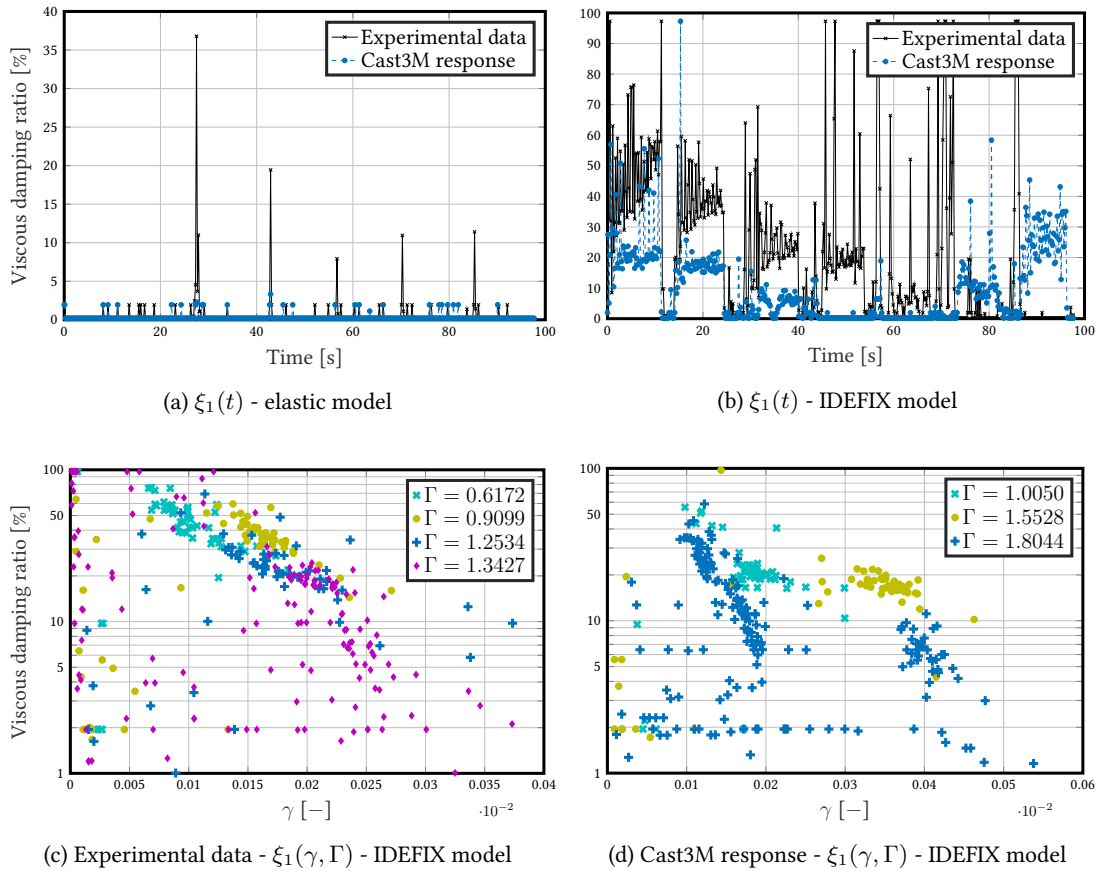
Figure 3.27: DSS2 test (harmonic parts) - Identified viscous damping ratios with IDEFIX model - dependence on the damage indices γ and Γ

not damped enough during the first blocks. On the contrary, substantial variations of identified viscous damping ratios are obtained with the IDEFIX model (fig. 3.27b). The most significant values are obtained with the largest amplitudes in the signal parts. From one block to another, identified viscous damping ratios are decreasing. In the beginning, no energy is dissipated through nonlinearities, and more significant viscous damping is obtained. Then, the nonlinearities develop, and the identified viscous damping ratios become more negligible. So, considering physical dissipations through the nonlinearities induces a reduction of required viscous damping representing the unmodelled dissipations.

Between numerical and experimental data, on the contrary of linear identification in section 3.4.1, lower identified equivalent viscous damping ratios are deduced from the numerical data. Thus, considering the local dissipations allows characterising only the unmodelled phenomena with the viscous part characterised by ξ.

As the damage variable (fig. 3.28a) for the complete RC behaviour is not the best damage index, the viscous damping ratio evolution is preferred using the damage index and the indicator of cycle amplitudes proposed by Heitz, Giry, et al. (2019) in equation (3.36). Figures 3.27c and 3.27d respectively present the experimental and numerical evolutions of $\xi_1(\gamma)$ for the different values of Γ^2 with a logarithmic scale. For both data, at a fixed value of Γ, $\xi_1(\gamma)$ follows, globally, a linear decrease in the logarithmic

---

[2]Γ is a degradation index "defined as the maximum historic curvature measured at mid-span over the theoretical first steel yielding curvature" (Heitz, Giry, et al., 2019).

(a) Damage

(b) Friction
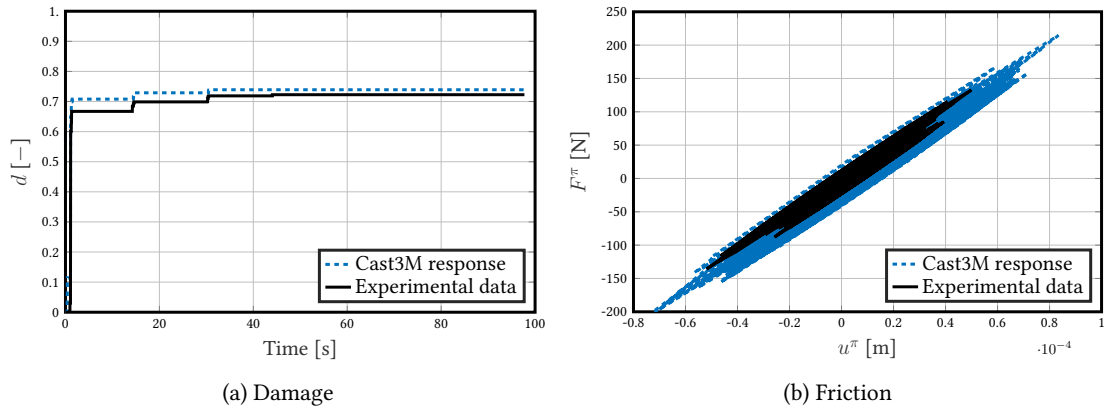
Figure 3.28: DSS2 test (harmonic parts) - Nonlinear parameter evolutions - IDEFIX model

space, so an exponential evolution in the initial space. In addition, if Γ increases, ξ_1 decreases. For the damage index Γ, the stronger it is, the more energy is dissipated through nonlinearities, and the lower is the required viscous damping ratio.

Then, nonlinear dissipative phenomena computed with the IDEFIX model are plotted in figure 3.28. They are characterising the RC behaviour. For the damage evolution (fig. 3.28a), a substantial variation is observed at the beginning corresponding to crack opening in concrete. So, after reaching $d = 0.6$, the steel reinforcements mainly take up the forces. Experimental and Cast3M response evolutions are similar, increasing at the same instants. The only difference is the slightly higher value with the numerical data computed with Cast3M. For the friction behaviour (fig. 3.28b), the same conclusions can be made: the evolutions are similar, but the experimental dissipations are lower than the numerical (Cast3M) ones.

Finally, larger values for damage indices are obtained for Cast3M results with respect to experimental ones. Furthermore, the identified values for viscous damping ratio are smaller for Cast3M. From the comparison of the damage and viscous damping ratio evolutions between Cast3M and experimental data, one can conclude that there is: (i) a lack of dissipation in the model (too large damage values are reached numerically), and (ii) a need to improve the link between the damage and additional viscous damping at the local scale to compensate for the lack of dissipation in the model.

3.4.3   Synthesis

To conclude, it appears that the proposed damping identification method is accurately working with linear and nonlinear constitutive models in the condition that proper method parameters are considered. In the case of a linear behaviour used to identify a damaging test, the nonlinearities can be considered by identifying the damaged beam eigenfrequency. It is a first way to define a damage index and propose an evolution of the equivalent viscous damping ratios as a function of a damage index (eq. 3.33). However, the difficulty observed with the linear behaviour strategy is the unrealistic characterisation of dissipations. The second proposed strategy was to consider a RC nonlinear constitutive model to improve the latter. Other damage indices, more representative of the global RC behaviour, can be used to propose evolutions of equivalent viscous damping ratios. Finally, by comparing experimental and numerical (Cast3M) data, it is possible to evaluate the performances of the numerical (Cast3M) models to accurately model the dissipative phenomena.

Enhancements could be developed to define the error function and improve the identification per-

formance. Indeed, it was observed that, in some cases, a slight phase shift between the reference and identified responses could induce huge errors and lead to wrong identified responses.

3.5 A new damping model as a function of internal variables - SDOF system

It was demonstrated in the previous section that the equivalent viscous damping ratio is strongly dependent on damage indices. That is why the objective herein is to propose an equivalent viscous damping ratio formulation depending on different internal variables $V_{\text{int}}{}^{(i)}$ of the considered nonlinear constitutive model. The projection of the experimental response over the fundamental mode is considered for the analysis. In order to focus on the nonlinear terms linked to velocity and displacement, the relative and seismic accelerations are input data coming from experiments.

3.5.1 Initial analysis

The advanced identification method is again used in presented analyses to identify different model parameters. The dynamic equation projected on the first mode is re-written in equation (3.45):

$$\mathbf{f}_{\text{d}}\left(\dot{\boldsymbol{\alpha}}_1, V_{\text{int}}{}^{(i)}\right) + \mathbf{f}_{\text{int}}\left(\boldsymbol{\alpha}_1, V_{\text{int}}{}^{(i)}\right) = -\kappa_1 \times \ddot{\mathbf{U}}_s - m_1 \times \ddot{\boldsymbol{\alpha}}_1 \qquad (3.45)$$

where κ_1 is the modal participation factor, $\mathbf{f}_{\text{d}}$ is the damping model depending on velocity $\dot{\boldsymbol{\alpha}}_1$ and n_{fd} internal variables $\left\{V_{\text{int}}{}^{(i)}\right\}_{i \in [\![1, n_{fd}]\!]}$ and $\mathbf{f}_{\text{int}}$ is the constitutive model depending on displacement $\boldsymbol{\alpha}_1$ and n_{fi} internal variables $\left\{V_{\text{int}}{}^{(i)}\right\}_{i \in [\![1, n_{fi}]\!]}$.

The right part of equation (3.45) depends on seismic $\ddot{\mathbf{U}}_s$ and system $\ddot{\boldsymbol{\alpha}}_1$ accelerations. To focus on the nonlinear part, the experimental data are considered for these accelerations. The fourth-order Runge-Kutta solver is used to solve the first-order ODE (Ordinary Differential Equation) (eq. 3.46). The solver is changed compared with the previous analyses due to the variable change. The recurrence expression is given in equation (3.47) with $y(t_n) = y_n$ and $\Delta t = t_{n+1} - t_n$:

$$y' = f(t, y) \qquad (3.46)$$

$$y_{n+1} = y_n + \frac{\Delta t}{6}\left(A + 2B + 2C + D\right) \qquad (3.47)$$

where the initial condition is $y(t_0) = y_0$, $A = f(t_n, y_n)$, $B = f\left(t_n + \frac{\Delta t}{2}, y_n + \frac{\Delta t}{2}.A\right)$, $C = f\left(t_n + \frac{\Delta t}{2}, y_n + \frac{\Delta t}{2}.B\right)$ and $D = f(t_n + \Delta t, y_n + \Delta t.C)$.

Combinations of constitutive models, presented in table 3.7, and damping models in table 3.8 are studied. The proposed damping models are mainly based on viscous damping. The constitutive models are based on dissipative phenomena discussed in previous analyses. The identification method is applied to determine the parameters presented in tables 3.7 and 3.8. For those identifications, windows are considered, so parameter variations are obtained. However, constant values of the parameters are required to consider explicit models. So, the mean values of the identified parameters are finally chosen.

The identification errors are presented in table 3.9. The global conclusion is that the damping models are much less influential on the dynamic responses than the constitutive models. Mainly, considering a tangent stiffness (**linNC**) is a way to model all dissipations, giving minor errors. Even if the errors are

Table 3.7: Proposed constitutive models - $\mathbf{f}_{\text{int}}$

Name	Expression	Parameters to identify
"Linear" with a constant stiffness - **linC**	$\mathbf{f}_{\text{int}} = k_1.\boldsymbol{\alpha}_1$	−
"Linear" with a non constant stiffness - **linNC**	$\mathbf{f}_{\text{int}} = k_d.\boldsymbol{\alpha}_1$	k_d
Damage - **dam**	$\mathbf{f}_{\text{int}} = k_1.(1-d).\boldsymbol{\alpha}_1$	d
Proposed nonlinear elasticity model[a] - **NLel**	$\mathbf{f}_{\text{int}} = k_1.\left(\boldsymbol{\alpha}_1 - \boldsymbol{\alpha}_1^{\pi}\right)$	a_f^{π} and b_f^{π}
Coupling of damage with the proposed nonlinear elasticity model[b] - **dam_NLel**	$\mathbf{f}_{\text{int}} = k_1.\left(\boldsymbol{\alpha}_1 - d.\boldsymbol{\alpha}_1^{\pi}\right)$	d, a_f^{π} and b_f^{π}
Coupling of damage, with the proposed nonlinear elasticity model and unilateral effect[b,c] - **dam_NLel_uni**	$\mathbf{f}_{\text{int}} = k_1.(1-d).\boldsymbol{\alpha}_1 + d.k_1.\left(\boldsymbol{\alpha}_1 - \eta.\boldsymbol{\alpha}_1^{\pi}\right)$	d, a_f^{π}, b_f^{π} and F_c
IDEFIX 1[d,e]	$\mathbf{f}_{\text{int}} = K_p(\eta).(1-d).\boldsymbol{\alpha}_1 + K_p(\eta).d.\left(\boldsymbol{\alpha}_1 - \boldsymbol{\alpha}_1^{\pi}\right)$	−
IDEFIX 2[d,f]	$\mathbf{f}_{\text{int}} = K_p(\eta).(1-d).\boldsymbol{\alpha}_1 + K_p(\eta).d.\left(\boldsymbol{\alpha}_1 - \boldsymbol{\alpha}_1^{\pi}\right)$	$p_1/p_2/\ldots/p_7/p_8$

[a] The proposed nonlinear elasticity model is defined by $\boldsymbol{\alpha}_1^{\pi} = a_f^{\pi}.\exp\left(b_f^{\pi}.\boldsymbol{\alpha}_1\right) \times \boldsymbol{\alpha}_1$. The model was proposed using Ragueneau, La Borderie, and Mazars (2000) works to take into consideration the thermodynamic adequacy: if $\varepsilon^{\pi} \geqslant 0$ then $0 \leqslant \varepsilon^{\pi} \leqslant 2\varepsilon$ and if $\varepsilon^{\pi} \leqslant 0$ then $0 \geqslant \varepsilon^{\pi} \geqslant 2\varepsilon$.

[b] When couplings are considered, two multiplied parameters p_{i1} and p_{i2} have, sometimes, to be identified (for example, that is the case with $d.a_f^{\pi}$ is considered). So, more constraints have to be defined to converge towards adequate parameters. Those additional constraints can be a maximal value on damage value, energy constraints, …

[c] η is the variable representing the unilateral effect or the closure of cracks. In an elastic part $(-F^e < F < F^e)$, $\eta = 1$. Then, between the elastic force F^e and the crack closure force F_c, η is evolving with F: $\eta = 1 - \frac{F}{F_c}$. And, beyond F_c, $\eta = 0$. The evolution is symmetrical in traction and compression.

[d] In IDEFIX model: $K_p(\eta) = k_1 \times (1-\eta)$, $\eta = d.\exp\left(-\left|\frac{\boldsymbol{\alpha}_1}{U_c}\right|\right)$, $d = d_{\infty}.\left(1 - \left(\frac{Y_0}{Y^d}\right)^q\right)$.

[e] IDEFIX parameters considered are constant and correspond to calibrated values.

[f] IDEFIX parameters are parameters to identify. The most influential parameters can be considered for the identification, and the other ones are kept constants to limit computational time.

Table 3.8: Proposed damping models - $\mathbf{f}_{\text{d}}$

Name	Expression	Parameters to identify
Viscous damping - **vD**	$\mathbf{f}_{\text{d}} = c_v \times \dot{\boldsymbol{\alpha}}_1$	c_v
Viscous damping (Rayleigh type) - **vRD**	$\mathbf{f}_{\text{d}} = (a_0.m_1 + a_1.k_1) \times \dot{\boldsymbol{\alpha}}_1$	a_0 and a_1
Viscous damping (mass proportional type) - **vMPD**	$\mathbf{f}_{\text{d}} = (a_0.m_1) \times \dot{\boldsymbol{\alpha}}_1$	a_0
Viscous damping (stiffness proportional type) - **vKPD**	$\mathbf{f}_{\text{d}} = (a_1.k_1) \times \dot{\boldsymbol{\alpha}}_1$	a_1

around 11%, figure 3.29a shows a very well matching between experimental and identified displacements. Then, the proposed nonlinear elasticity model (**NLel**) is the one also given minor errors demonstrating one more time the necessity to best characterise that phenomenon. On the contrary, using a coupling of damage and the proposed nonlinear elasticity model increases the number of parameters to identify, which could explain the difficulty to reproduce best the experimental function (fig. 3.29b). Finally, the IDEFIX model seems adequate to characterise the experimental responses provided that the model parameters are accurately calibrated.

3.5.2   Advanced damping models

Let us now focus on viscous damping models. The IDEFIX model has been accurately calibrated, and it can be used to study new formulations of viscous damping models. The internal variables taken into

Table 3.9: Errors of proposed model identifications

		Damping models			
		vD	**vRD**	**vMPD**	**vKPD**
	linC	30.3%	31.3%	30.5%	62.6%
	linNC	10.4%	10.8%	10.5%	10.6%
	dam	30.3%	19.7%	30.0%	19.0%
	NLel	11.7%	11.7%	11.7%	11.7%
	dam_NLel	30.3%	11.0%	16.5%	10.8%
	dam_NLel $(d_{max} = 0.8)^*$	30.3%	11.0%	16.5%	10.8%
	dam_NLel_uni	30.3%	31.3%	30.5%	30.6%
	dam_NLel_uni $(d_{max} = 0.8)^*$	30.3%	31.3%	30.5%	30.6%
	IDEFIX 1	29.6%	50.2%	29.7%	64.7%
	IDEFIX 2	14.4%	16.6%	15.3%	15.0%

(Row label rotated left: **Constitutive models**)

[*] A maximal damage value of 0.8 is chosen as an additional constraint for the identification.

(a) linNC / vD

(b) dam_NLel / vcD
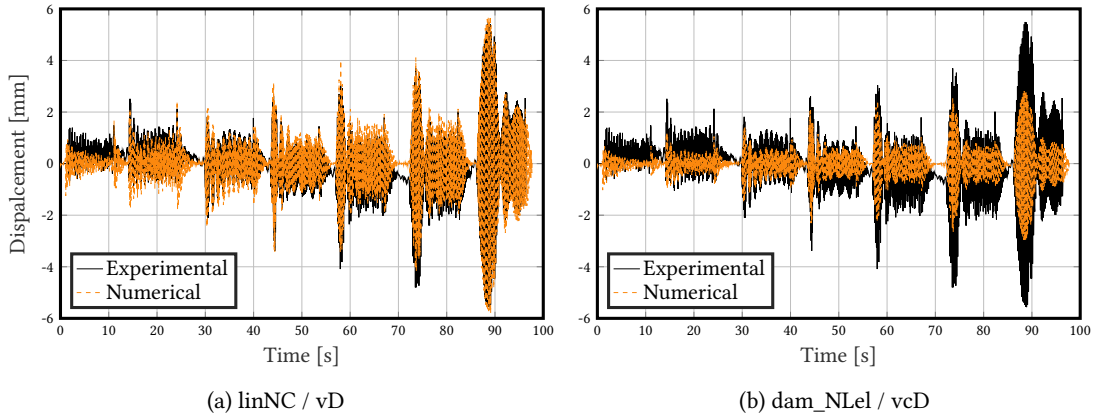
Figure 3.29: Displacement identifications

consideration in the IDEFIX model are the damage variable d, the sliding displacement u^π and the variable η characterising the pinching effect.

3.5.2.1 Model presentations

(a) Damage variable The equation (3.48) is inspired by Heitz, Giry, et al. (2019) for equivalent viscous damping model (eq. 3.38):

$$c_{v,\text{inv}}(d) = \frac{\alpha_{d,\text{inv}} \times d}{d^2 + \beta_{d,\text{inv}}.d + \gamma_{d,\text{inv}}} + \delta_{d,\text{inv}} \tag{3.48}$$

where $\alpha_{d,\text{inv}}$, $\beta_{d,\text{inv}}$, $\gamma_{d,\text{inv}}$ and $\delta_{d,\text{inv}}$ are the parameters to identify.[3]

(b)   Friction variable   The sliding displacement oscillates between positive and negative values following the input signal. When the absolute value of u^π increases, the experimental response amplitude follows the same tendency, as observed with the peaks at the block beginnings. So the function has to decrease with the sliding displacement absolute value increase. That is why the two functions in equations (3.49) and (3.50) are chosen:

$$c_{v,\text{lin}}\left(u^\pi\right) = -\alpha_{u^\pi,\text{lin}} \times \left|u^\pi\right| + \beta_{u^\pi,\text{lin}} \tag{3.49}$$

$$c_{v,\text{inv}}\left(u^\pi\right) = \frac{\alpha_{u^\pi,\text{inv}}}{\beta_{u^\pi,\text{inv}} + \left|u^\pi\right|} \tag{3.50}$$

where $\alpha_{u^\pi,\text{lin}}$, $\beta_{u^\pi,\text{lin}}$, $\alpha_{u^\pi,\text{inv}}$ and $\beta_{u^\pi,\text{inv}}$ are the parameters to identify.[4]

(c)   Pinching effect variable η follows a similar tendency to d, except for a few notable variations in the frequency imposed blocks. That is why the objective is to obtain an increasing function with a strong variation around the maximal value of η. It explains the two chosen functions in equations (3.51) and (3.52):

$$c_{v,\text{exp}}\left(\eta\right) = \alpha_{\eta,\text{exp}} \times \exp\left(\beta_{\eta,\text{exp}} \times \eta\right) \tag{3.51}$$

$$c_{v,\text{inv}}\left(\eta\right) = \frac{\alpha_{\eta,\text{inv}} \times \eta}{\beta_{\eta,\text{inv}} - \eta} \tag{3.52}$$

where $\alpha_{\eta,\text{exp}}$, $\beta_{\eta,\text{exp}}$, $\alpha_{\eta,\text{inv}}$ and $\beta_{\eta,\text{inv}}$ are the parameters to identify. Those models allow representing dissipations around null displacements.[5]

(d)   Input force amplitude consideration   Crambuer (2013) and Heitz, Giry, et al. (2019) (γ variable) recommended taking into consideration the input signal intensity to update damping models. This idea is also studied here by multiplying the proposed models by $\dfrac{F_{\text{input}}}{F_{\text{input,max}}}$ for each time step. For example, equation (3.48) becomes equation (3.53):

$$c_{v,\text{inv},f}\left(d\right) = \frac{F_{\text{input}}}{F_{\text{input,max}}}\left[\frac{\alpha_{d,\text{inv},f} \times d}{d^2 + \beta_{d,\text{inv},f}.d + \gamma_{d,\text{inv},f}} + \delta_{d,\text{inv},f}\right] \tag{3.53}$$

where $\alpha_{d,\text{inv},f}$, $\beta_{d,\text{inv},f}$, $\gamma_{d,\text{inv},f}$ and $\delta_{d,\text{inv},f}$ are the parameters to identify. For the two other variables, the adaptations are similar.[6]

3.5.2.2   Model calibrations

The parameters are calibrated using the identification method with the DSS2 test based on experimental data. First, initial parameters are defined by considering the maximal and minimal viscous damping coefficients deduced from the Rayleigh damping formulation. Then, the identification method gives parameters for each window, and the mean of all values is considered. Identified parameters are thus

---

[3]The index d is considered for the parameters of models depending on the damage variable, and inv is for an inverse evolution function (ratio of polynomials).

[4]The index u^π is considered for the parameters of models depending on the friction variable, lin is for a linear evolution function, and inv is for an inverse evolution function (ratio of polynomials).

[5]The index η is considered for the parameters of models depending on the pinching effect variable, exp is for an exponential evolution function, and inv is for an inverse evolution function (ratio of polynomials).

[6]The index f is considered for the parameters of models depending on the input for amplitude in addition to another variable.

presented in tables 3.10 to 3.12 respectively for d, u^π and η variables, with and without the input signal consideration.

Table 3.10: Parameters of equation (3.48) for d variable

Without F_{input} consideration		With F_{input} consideration	
Parameter	Identified value	Parameter	Identified value
$\alpha_{d,\text{inv}}$	3.00	$\alpha_{d,\text{inv},f}$	16.9
$\beta_{d,\text{inv}}$	4.94×10^{-4}	$\beta_{d,\text{inv},f}$	5.30×10^{-2}
$\gamma_{d,\text{inv}}$	4.25	$\gamma_{d,\text{inv},f}$	6.27
$\delta_{d,\text{inv}}$	3.83	$\delta_{d,\text{inv},f}$	15.1

Table 3.11: Parameters of equations (3.49) and (3.50) for u^π variable

Without F_{input} consideration		With F_{input} consideration	
Parameter	Identified value	Parameter	Identified value
$\alpha_{u^\pi,\text{lin}}$	3.33×10^3	$\alpha_{u^\pi,\text{lin},f}$	3.33×10^3
$\beta_{u^\pi,\text{lin}}$	4.97	$\beta_{u^\pi,\text{lin},f}$	17.5
$\alpha_{u^\pi,\text{inv}}$	2.94	$\alpha_{u^\pi,\text{inv},f}$	3.16
$\beta_{u^\pi,\text{inv}}$	0.693	$\beta_{u^\pi,\text{inv},f}$	0.196

Table 3.12: Parameters of equations (3.51) and (3.52) for η variable

Without F_{input} consideration		With F_{input} consideration	
Parameter	Identified value	Parameter	Identified value
$\alpha_{\eta,\text{exp}}$	8.76×10^{-2}	$\alpha_{\eta,\text{exp},f}$	0.366
$\beta_{\eta,\text{exp}}$	4.96	$\beta_{\eta,\text{exp},f}$	4.92
$\alpha_{\eta,\text{inv}}$	9.93	$\alpha_{\eta,\text{inv},f}$	10.1
$\beta_{\eta,\text{inv}}$	2.58	$\beta_{\eta,\text{inv},f}$	1.25

3.5.3   Evaluation of proposed model performances

Proposed models are now used to solve the nonlinear dynamic problem. Their performances are evaluated compared to the Rayleigh damping ($c_v = a_0.m_i + a_1.k_i$). Global response errors and energy descriptions are thus evaluated.

3.5.3.1 Result analyses

First, table 3.13 indicates the global response errors (computed as presented in section 2.4.1.2) obtained with a constant Rayleigh damping coefficient all along with computation and with IDEFIX constitutive model. Experimental responses are the reference ones. The system is solved numerically with $c_v = a_0.m_1 + a_1.k_1$ where a_0 and a_1 are constant coefficients evaluated with different viscous damping ratios as presented in table 3.13. They are computed with the same ξ for modes 1 and 2. Table 3.13 shows that the smallest errors are obtained with $\xi = 5\%$, so this value will be considered to evaluate the proposed damping model performances.

Table 3.13: Errors for a constant Rayleigh damping model

Errors	Damping ratios		
	$\xi = 0\%$	$\xi = 2\%$	$\xi = 5\%$
Displacement	76.91%	64.84%	62.38%
Velocity	61.94%	48.79%	46.84%
Acceleration	46.02%	40.64%	42.67%
Force	105.90%	67.44%	56.01%
Global	72.70%	55.43%	51.98%

Tables 3.14 and 3.15 present the global response errors respectively without and with the input signal amplitude consideration for proposed damping models. The general conclusion is that all proposed models are given similar global responses compared to the Rayleigh damping coefficient. If the responses are not improved and generally unconservative (fig. 3.30), the dissipations are modelled using physical phenomena without increasing the computational time significantly because all models are explicit. Very few differences are observed between considered variables except for the damage variable. Indeed, by focusing on nonlinear parameters, figures 3.31b and 3.31e show very similar damage variable evolutions. On the contrary, for the friction evolution (fig. 3.31c and 3.31f), more significant variations are observed: if u^π and η variables lead to similar friction forces and displacements than the constant Rayleigh damping, more energy is dissipated with the damping update depending on the damage variable rather than the other variables. Finally, in terms of viscous damping coefficients (fig. 3.31a and 3.31d), non-negligible variations are observed. Notably, low values are obtained with the update

Table 3.14: Errors for proposed damping models - without $\dfrac{F_{\text{input}}}{F_{\text{input,max}}}$

Errors[*]	d variable	u^π variable		η variable	
	Inverse function (eq. 3.48)	Linear function (eq. 3.49)	Inverse function (eq. 3.50)	Exponential function (eq. 3.51)	Inverse function (eq. 3.52)
Displacement	71.48%[(+9.10%)]	62.04%[(−0.34%)]	62.37%[(−0.01%)]	62.34%[(−0.04%)]	62.35%[(−0.03%)]
Velocity	55.93%[(+9.10%)]	46.54%[(−0.30%)]	46.73%[(−0.11%)]	46.70%[(−0.14%)]	46.75%[(−0.09%)]
Acceleration	43.13%[(+0.47%)]	42.24%[(−0.43%)]	42.29%[(−0.38%)]	42.25%[(−0.42%)]	42.38%[(−0.30%)]
Force	88.99%[(+32.98%)]	56.98%[(+0.96%)]	56.43%[(+0.42%)]	56.40%[(+0.38%)]	56.29%[(+0.27%)]
Global	64.89%[(+12.91%)]	51.95%[(−0.03%)]	51.96%[(−0.02%)]	51.92%[(−0.05%)]	51.94%[(−0.03%)]

[*] The subscripts correspond to the error differences with the classical Rayleigh damping coefficient computed with a viscous damping ratio $\xi = 5\%$, the value currently used in building codes (tab. 3.13).

Table 3.15: Errors for proposed damping models - with $\dfrac{F_{\text{input}}}{F_{\text{input,max}}}$

Errors[*]	d variable	u^π variable		η variable	
	Inverse function (eq. 3.53)	Linear function ($\sim$eq. 3.49 + 3.53)[**]	Inverse function ($\sim$eq. 3.50 + 3.53)[**]	Exponential function ($\sim$eq. 3.51 + 3.53)[**]	Inverse function ($\sim$eq. 3.52 + 3.53)[**]
Displacement	71.67%[(+9.29%)]	62.55%[(+0.17%)]	62.64%[(+0.26%)]	62.63%[(+0.25%)]	62.67%[(+0.28%)]
Velocity	56.02%[(+9.18%)]	46.45%[(−0.39%)]	46.48%[(−0.36%)]	46.51%[(−0.33%)]	46.49%[(−0.35%)]
Acceleration	43.26%[(+0.59%)]	42.74%[(+0.06%)]	42.46%[(−0.20%)]	42.73%[(+0.06%)]	42.62%[(−0.05%)]
Force	88.54%[(+32.53%)]	55.48%[(−0.54%)]	55.82%[(−0.19%)]	55.32%[(−0.69%)]	55.44%[(−0.57%)]
Global	64.87%[(+12.90%)]	51.80%[(−0.17%)]	51.85%[(−0.12%)]	51.80%[(−0.18%)]	51.80%[(−0.17%)]

[*] The subscripts correspond to the error differences with the classical Rayleigh damping coefficient computed with a viscous damping coefficient ratio $\xi = 5\%$, the value currently used in building codes (tab. 3.13).
[**] Combinations of the two indicated equations as discussed in paragraph 3.5.2.1(d).
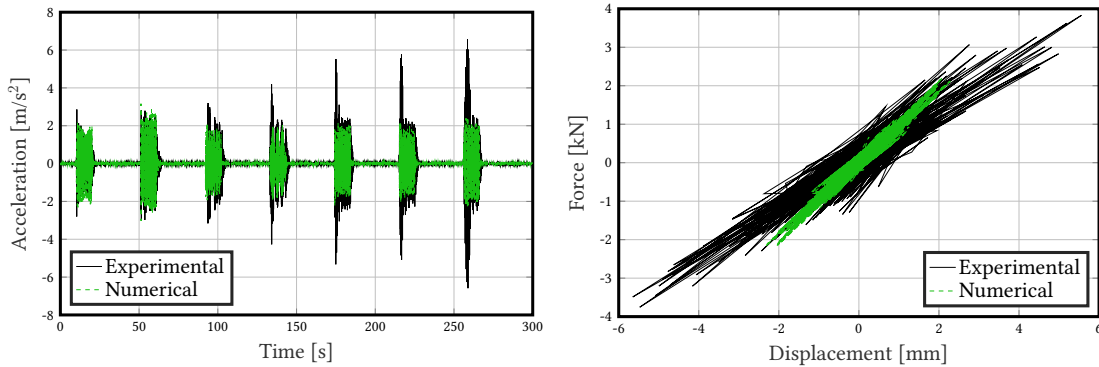
(a) Acceleration response - without $F_{\text{input}}/F_{\text{input,max}}$

(b) Constitutive law - without $F_{\text{input}}/F_{\text{input,max}}$

Figure 3.30: DSS2 test with IDEFIX constitutive model - Global responses with $c_{v,\text{inv}}\left(u^\pi\right)$ damping model

based on the damage variable, which explains the more considerable amount of energy dissipated through friction and the more significant differences in computation errors of tables 3.14 and 3.15. For the two other variables, if $F_{\text{input}}/F_{\text{input,max}}$ is not considered, the viscous damping coefficient is almost constant and close to the one obtained with Rayleigh damping, explaining the minor differences in table 3.14. Then, by considering $F_{\text{input}}/F_{\text{input,max}}$, substantial variations of damping ratios are observed in figure 3.31d when updates are considered. Remarkably, the most significant values are obtained during the harmonic parts of the signal. Rayleigh damping coefficient appears to be a mean of variations obtained with u^π and η variables. Table 3.15 shows very close responses in comparison with table 3.14. It demonstrates that considering the input signal does not improve the response. However, it also shows that viscous damping is not required all along with computation depending on the input signal amplitudes. Indeed, the acceleration response is accurately represented in white-noise signal parts even if the viscous damping coefficient is almost null.

Now, figures 3.32 to 3.34 present the energy content of computations with updated damping coefficients. First, figure 3.32 shows that all energy balances are validated since total and imparted energies are similar, which validates the use of updated damping coefficients to perform nonlinear dynamic computations. Again, the damage variable exhibits a different behaviour with respect to the other formulations since the largest maximum displacements are reached, so the final energies are the lowest.

(a) Viscous damping coefficient without $F_{\text{input}}/F_{\text{input,max}}$

(b) Damage variable without $F_{\text{input}}/F_{\text{input,max}}$

(c) Friction law without $F_{\text{input}}/F_{\text{input,max}}$

(d) Viscous damping coefficient with $F_{\text{input}}/F_{\text{input,max}}$

(e) Damage variable with $F_{\text{input}}/F_{\text{input,max}}$

(f) Friction law with $F_{\text{input}}/F_{\text{input,max}}$
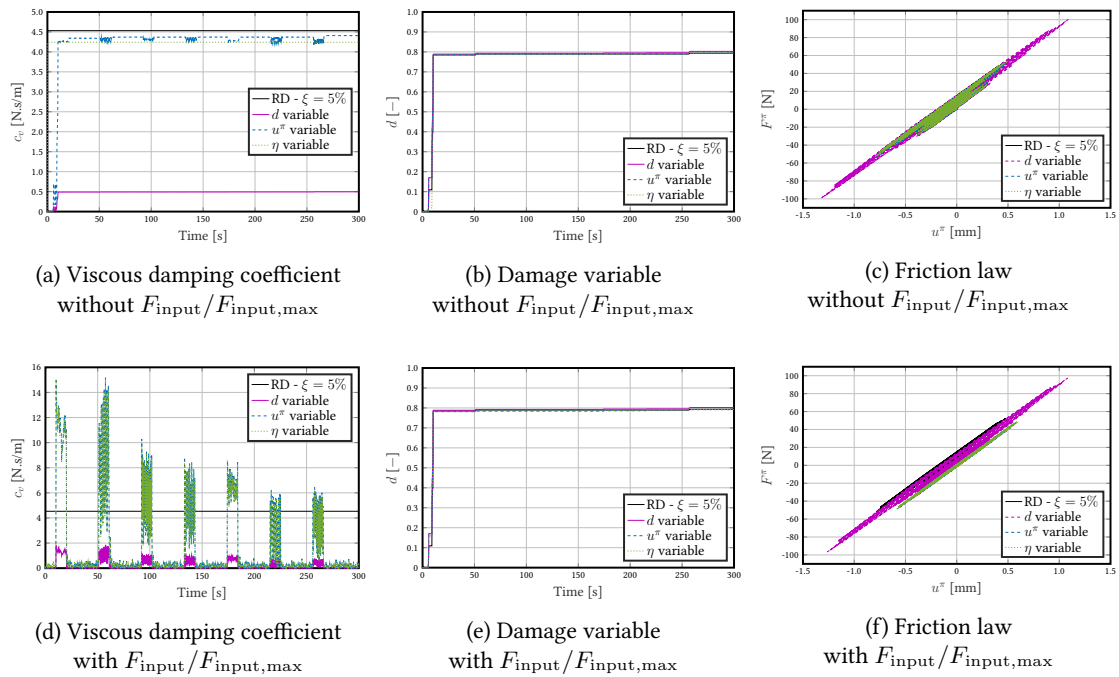
Figure 3.31: DSS2 test with IDEFIX constitutive model - Nonlinear parameters with proposed damping models depending on internal variables
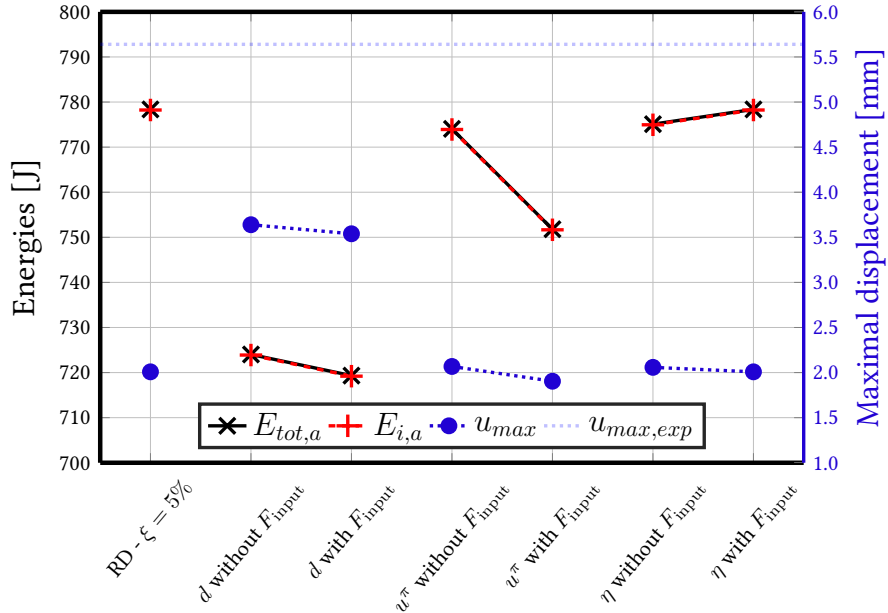
Figure 3.32: DSS2 test with IDEFIX model - Imparted and total energies (absolute energy balance) in parallel to the maximal displacement - proposed damping models depending on internal variables

(a) Rayleigh damping - $\xi = 5\%$

(b) Damping coefficient function of d variable

(c) Damping coefficient function of u^π variable

(d) Damping coefficient function of η variable
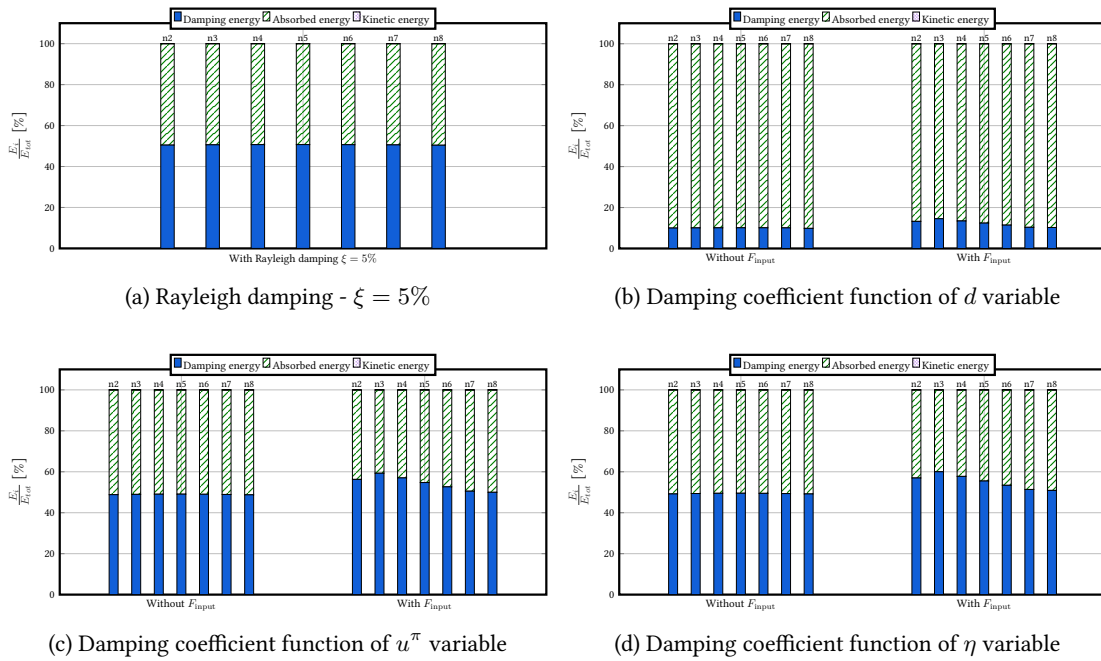
Figure 3.33: DSS2 test with IDEFIX model - Distribution of dissipative energies at the structural level along computation - proposed damping models depending on internal variables

Experimentally, a maximal displacement of 5.6 mm is obtained, so the damage variable seems to lead to a more accurate response if the extreme global responses are of interest. Then, taking into consideration $F_{\text{input}}/F_{\text{input,max}}$ seems to reduce the maximum displacements slightly. However, it does not strongly influence the energy content, as also observed in figure 3.33 for the three updating variables. In this figure, it also appears that the absorbed and damping energies are almost equally distributed except for the damage variable, where more dissipations occur at the material level.

Finally, figure 3.34 focuses on dissipative phenomena evolution, particularly the most dissipative ones: damage and friction. The grey curves for the three damping models show negligible damage because the friction phenomenon represents 100% of hysteretic energies from computation beginning. As expected, the friction energy evolves by steps.

(a) Rayleigh damping $\xi = 5\%$

(b) Damping coefficient function of u^π variable without F_{input}

(c) Damping coefficient function of u^π variable with F_{input}
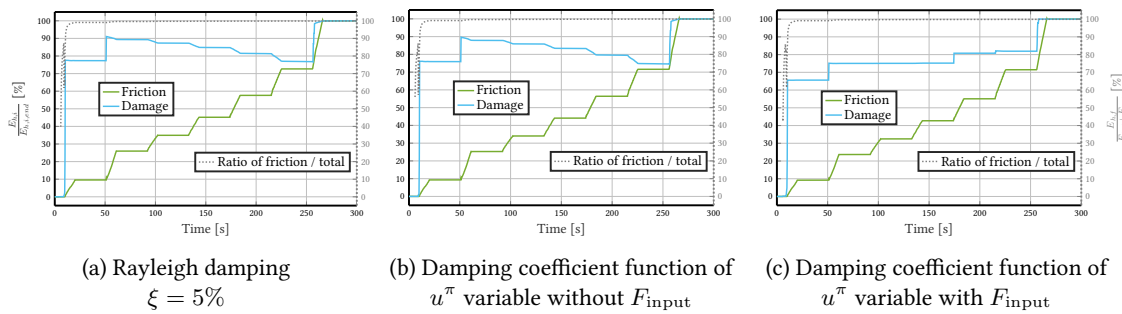
Figure 3.34: DSS2 test with IDEFIX model - Dissipation proportions at the material level - proposed damping models depending on internal variables

3.5.3.2   Conclusions

Viscous damping coefficient models depending on internal variables are proposed in this section. They demonstrate similar behaviours in comparison with a constant Rayleigh damping. Particularly the damage variable leads to more significant global response errors. However, it seems to induce a more accurate response if only the extreme global responses are of interest, demonstrating the strong influence of the variable of interest selection for evaluating damping formulations. In addition, it gives a more physical representation of energy dissipations because the absorbed energy (i.e. the hysteretic internal dissipation) represents almost 90% of the total energy. In addition, the input signal amplitude influence is studied. It is necessary to integrate this influence mainly for the most significant signal amplitudes when the nonlinear constitutive models are not dissipating enough energy.

3.6   A new damping matrix formulation - multi-fibre model

The previous section demonstrated that damping updates based on internal variables (mainly the damage d and friction u^π variables) could characterise the nonlinear dynamic responses of RC elements. Now, the objective is to adapt these results in the multi-fibre model presented in chapter 2. To achieve that goal, an elementary updated damping matrix formulation is developed in section 3.6.1. Then, applications are performed on experimental tests in section 3.6.2. Finally, a synthesis (section 3.6.3) finalises the analysis by comparing the proposed damping matrix performances with the classical damping formulations studied in chapter 2.

3.6.1   Formulation

In order to model the evolution of dissipation not taken into by the local model, an evolution of the damping with respect to material damage is proposed. The global damping matrix is assembled from elemental evolving damping matrices, leading to a local scale damping model. Two types of formulations are studied to evaluate the influence of the off-diagonal terms: a diagonal matrix and a matrix with modal coupling.

3.6.1.1   Generalities on off-diagonal terms in damping matrices

(a)   Problem description   Undamped MDOF linear systems excited by a seismic acceleration can be decoupled on the modal basis. Nevertheless, in the case of damped systems, the equations of motion are coupled because of the generally non-proportional damping considered (Thomson, Calkins, and Caravani, 1974). For example, Clough and Mojtahedi (1976) defined non-proportional damping as "a form of linear viscous damping which introduces coupling between the undamped modal coordinate equations of motion". As the Rayleigh formulation, using classical damping is a mathematical tool to overcome this difficulty. However, if a non-classical damping matrix is used, the system decoupling in the modal basis is no more possible. Between the 1960s and 1980s, many papers were interested in proposing or studying methodologies to approximate non-proportionally damped systems. The aim was to reduce the computational time and required memories to perform MDOF damped systems with the available computational facilities.

First, T. K. Caughey and O'Kelly (1965a) proposed necessary and sufficient conditions for linear damped systems to possess normal classical modes. For discrete problems, the condition is that the matrices $\mathbb{M}^{-1}\mathbb{C}$ and $\mathbb{M}^{-1}\mathbb{K}$ commute, that is, $\mathbb{C}\mathbb{M}^{-1}\mathbb{K} = \mathbb{K}\mathbb{M}^{-1}\mathbb{C}$. Similarly, for continuous systems,

damping and stiffness operators have to commute with conditions on boundary conditions. When T. K. Caughey and O'Kelly (1965b) conditions are not validated, in engineering especially, approximations are performed to obtain diagonal damping matrices leading to uncoupled equations. It is thus expected that the errors induced by the approximations are low enough (Thomson, Calkins, and Caravani, 1974).

(b)   Methods to approximate the damping matrix   Different methods to approximate the non-diagonal damping matrices are proposed in the literature. Thomson, Calkins, and Caravani (1974) focused on three methodologies (leading to similar responses) to determine a diagonal damping matrix. (i) The first method consisted in computing the modal damping matrix and neglecting its off-diagonal terms. It was defined as the "decoupling approximation" by Morzfeld, Ma, and Ajavakom (2008). (ii) In the second method, an optimization algorithm was used to compute the diagonal matrix minimizing the mean square error of the frequency response. (iii) For the third method, the objective was to match the peaks of coupled and uncoupled system responses to normalised differential equations. Lázaro (2016) explained that the first method was the most used. That is why many papers were interested in mathematical tools to diagonalise the damping matrix (Meirovitch, 1967; Pipes, 1963; Frazer, Duncan, and Collar, 1938; Veletsos and Ventura, 1986). Later, Goel (2001) proposed to use such a methodology with a damping matrix considering supplemental dampers for asymmetric structures, and Lázaro (2016) used the complex eigenvalue problem to characterise the damping matrix. Papers also proposed to compare different proposed formulations and system resolution procedures (Beredugo, 1976; Clough and Mojtahedi, 1976; S. Lee et al., 2011).

(c)   Induced errors and criterion definitions   To go further and characterise the reliability of proposed procedures, some papers finally focused on developing error formulations and performance criteria to use the approximation procedures. Hasselman (1976) showed that a problem is dynamically decoupled if the mode frequencies are sufficiently apart (eq. 3.54), even for a non-diagonal damping matrix.

$$\frac{\left|C_{ji}^{mod}\right|}{\sqrt[4]{4(\omega_j - \omega_i)^2 + \left(C_{ii}^{mod}\right)^2}}\frac{1}{\sqrt{C_{jj}^{mod}}} = \mathcal{O}(\varepsilon) \tag{3.54}$$

Then, Warburton and Soni (1977) proposed a criterion (eq. 3.55) leading to an acceptable error for a dynamic problem solved by neglecting the damping matrix diagonal terms. The criteria must be verified for modes with a significant influence on responses. In equation (3.55), the parameter $\varepsilon_{\text{coupling}}$ must be small: for example, for $\varepsilon_{\text{coupling}} = 0.05$, the error stays inferior to 10%.

$$\xi_i^{mod} < \varepsilon_{\text{coupling}} \left| \frac{C_{ii}^{mod}}{2C_{ij}^{mod}} \left(\frac{\omega_j^2}{\omega_i^2} - 1 \right) \right|_{\min j} \tag{3.55}$$

where ξ_i^{mod} is the modal damping ratio associated with mode i. Finally, Xu and Igusa (1991) proposed two criteria to discuss the influence of damping matrix off-diagonal terms on modal properties (eq. 3.56) and structural responses (eq. 3.57).

$$\frac{\left|C_{ji}^{mod}\right|}{\sqrt{(\omega_j - \omega_i)^2 + \left(C_{jj}^{mod} - C_{ii}^{mod}\right)^2}} = \mathcal{O}(\varepsilon) \tag{3.56}$$

$$\left(\frac{C_{jj}^{mod} + C_{ii}^{mod}}{2\sqrt{C_{jj}^{mod}C_{ii}^{mod}}} \right) \frac{\left|C_{ji}^{mod}\right|}{\sqrt{(\omega_j - \omega_k)^2 + \frac{1}{4}\left(C_{jj}^{mod} + C_{ii}^{mod}\right)^2}} = \mathcal{O}(\varepsilon) \tag{3.57}$$

For the four presented models, the terms C_{ii}^{mod} and C_{ij}^{mod} where $\{i,j\} \in [\![1, N]\!]^2$ are respectively the diagonal and off-diagonal terms of the modal damping matrix associated with modes i and j. In addition, the terms ω_i and ω_j are the eigenfrequencies also associated with these modes.

After damaging states, all criteria have been applied to the classical damping matrices of chapter 2. They are all verified with the MPD formulation because it is already a diagonal matrix, validating the criterion computations. Then, the criteria for RD, KPD, MD, and WPD are verified for almost the 30 first modes. It demonstrates that the studied problem can be solved by neglecting the off-diagonal terms of damping matrices. It is in adequacy with section 3.1, where it was demonstrated that the modes presented very low couplings. However, Hasselman (1976) criterion is more discriminating because it says that the studied problem can not be considered wholly decoupled. However, it is still possible to approximate it with diagonal matrices. So, the formulations of diagonal and non-diagonal elemental matrices can be proposed.

3.6.1.2   Algorithm to update damping matrix computations

The general algorithm of the proposed updated damping matrix computations is presented in figure 3.35. At the beginning of the dynamic computation, an internal variable and the damping coefficient function must be selected, and the function must be calibrated depending on the required damping level. Then, at each time step, the damping matrix is updated. The computation is performed at the elemental level before assembling the total matrix. The damping coefficient function is applied on the internal variable values at the Gauss points of section elements for each element. Then, the values are integrated into sections to determine the damping coefficients at fibre-element sections (fig. 3.36), and the elemental damping matrix can be computed depending on the chosen damping matrix form (diagonal or not).

(a)   Diagonal elemental damping matrix   To reduce the complexity linked with the coupling, only bending DOFs are considered. Two operators in Cast3M can be used: MANU RIGI operator (application of a punctual stiffness), applied on an element field corresponding to all considered DOFs, given a complete diagonal matrix, or MASS operator (application of a punctual mass) for all nodal elements, given a sparse diagonal matrix. Equation (3.58) defined the elemental matrix at beam element e for the complete form. The sparse one is identical except that the zero values are not stocked, representing a gain in memory.

$$\mathbb{C}_{\text{elem}}^{(e)} = \begin{bmatrix} c_v^{(e,u_{y,1})} & 0 & 0 & 0 \\ 0 & c_v^{(e,\theta_{z,1})} & 0 & 0 \\ 0 & 0 & c_v^{(e,u_{y,2})} & 0 \\ 0 & 0 & 0 & c_v^{(e,\theta_{z,2})} \end{bmatrix} \quad (3.58)$$

Initialization

Choice of the internal variable "V_{int}"

Choice of the damping coefficient function $c_{v,\text{fct}}$ (eq. 1.63 to 1.65)

For each element (e)

Determination of internal variable on the section element $V_{\text{int}}^{(e)}$

Application of the damping coefficient function $c_v^{(e)} = c_{v,\text{fct}}\left(V_{\text{int}}^{(e)}\right)$

Computation of the elemental damping matrix $\mathbb{C}_{\text{elem}}^{(n,\text{compo})}$

Updated damping matrix

Assembly of the damping matrix $\mathbb{C}_{\text{updated}}$

Figure 3.35: Algorithm of updated damping matrix computations
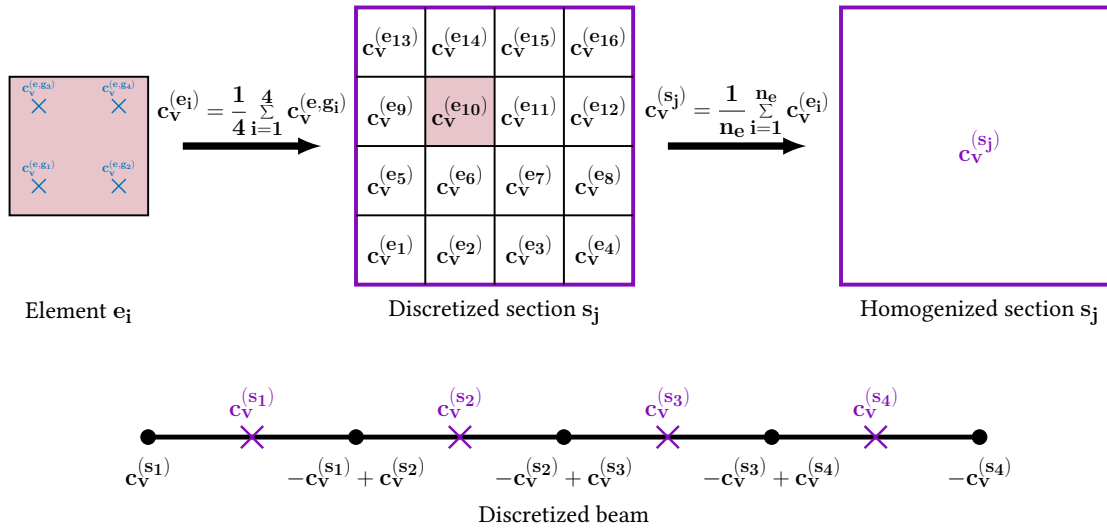
Figure 3.36: c_v from Gauss point to beam nodes

where $u_{y,1}$ and $\theta_{z,1}$ are associated with the element first node and $u_{y,2}$ and $\theta_{z,2}$ are associated with the second node.

(b)   Non-diagonal elemental damping matrix   The non-diagonal damping matrix is built as $\alpha \cdot \mathbb{K}^{(e)}$ with $\mathbb{K}^{(e)}$ the stiffness of the Timoshenko beam as implemented in Cast3M (Pegon, 1994). Reducing the matrix to the bending part, the elemental matrix writes like equation (3.59) where E is the Young's modulus, $G = \dfrac{E}{2(1+\nu)}$ the shear modulus, l_e the element length, S_e the element section, $S_y = \dfrac{S_e}{\alpha_{s_y}}$ the shear section in $\vec{y}$-direction, $S_z = \dfrac{S_e}{\alpha_{s_z}}$ the shear section in $\vec{z}$-direction and I_z the inertia moment around z-axis. In addition, index 1 refers to the element first node and index 2 to the second node. With Cast3M, to compute such a matrix, the `RIGI` operator (eq. 3.59) is used by considering a fictitious constitutive model. So, to consider only the coupling terms $\dfrac{EI_z}{l_e}$, the strategy is to build a fictitious model with an infinite Poisson's ratio (so that G converges to 0) and Young's modulus equal to $E_{\text{fictitious}} = \dfrac{c_v^{(e,n)} \times l_e}{I_z}$ because the values l_e and I_z are only geometrical and known.

$$
\begin{pmatrix} F_{y,1} \\ M_{z,1} \\ F_{y,2} \\ M_{z,2} \end{pmatrix} = \begin{bmatrix} \dfrac{GS_y}{l_e} & \dfrac{GS_y}{2} & -\dfrac{GS_y}{l_e} & \dfrac{GS_y}{2} \\ \dfrac{GS_y}{2} & \dfrac{EI_z}{l_e} + \dfrac{l_e GS_y}{4} & -\dfrac{GS_y}{2} & -\dfrac{EI_z}{l_e} + \dfrac{l_e GS_y}{4} \\ -\dfrac{GS_y}{l_e} & -\dfrac{GS_y}{2} & \dfrac{GS_y}{l_e} & -\dfrac{GS_y}{2} \\ \dfrac{GS_y}{2} & -\dfrac{EI_z}{l_e} + \dfrac{l_e GS_y}{4} & -\dfrac{GS_y}{2} & \dfrac{EI_z}{l_e} + \dfrac{l_e GS_y}{4} \end{bmatrix} \begin{pmatrix} u_{y,1} \\ \theta_{z,1} \\ u_{y,2} \\ \theta_{z,2} \end{pmatrix} \tag{3.59}
$$

3.6.1.3   Method parameters and calibration

The updated damping matrices proposed are based on some internal variables "V_{int}" and damping co-efficient functions, which must be selected and calibrated.

(a)   Internal variables   Two strategies are proposed for the selection of internal variables. The first one considers the constitutive model internal variables defined at the Gauss points of concrete fibres for each beam section. d and ε^π are considered as representative variables of nonlinear phenomena.[7] Furthermore, a function depending on the steel rebar stress σ_s is considered. Indeed, the steel stress can represent the crack opening in concrete.

The second strategy consists in computing a damage index for each beam element. The proposed damage indices d_{E_T} and d_{E_S} for element e are defined in equation (3.60) respectively by taking into consideration the tangent and secant Young's modulus.

$$d_{E_T}^{(e)} = 1 - \left[\frac{\mathbb{K}_0^{(e)} : \mathbb{K}_T^{(e)}}{\mathbb{K}_0^{(e)} : \mathbb{K}_0^{(e)}} \right] \quad \text{and} \quad d_{E_S}^{(e)} = 1 - \left[\frac{\mathbb{K}_0^{(e)} : \mathbb{K}_S^{(e)}}{\mathbb{K}_0^{(e)} : \mathbb{K}_0^{(e)}} \right] \tag{3.60}$$

where $\mathbb{K}_0^{(e)}$ is the initial elemental stiffness matrix of element (e) and $\mathbb{K}_T^{(e)}$ and $\mathbb{K}_S^{(e)}$ are the tangent and secant elemental stiffness matrices. The initial stiffness matrices for all elements are computed at the computation beginning. Then, at each time step, the tangent or secant modulus of the nonlinear model is evaluated, and a fictitious "damaged" constitutive model is built to compute the elemental tangent or secant stiffness matrix with RIGI operator (eq. 3.59). Then, the matrix products are performed with $\mathbb{A}_1 : \mathbb{A}_2 = \text{Tr}\left(\mathbb{A}_1^T.\mathbb{A}_2\right)$. Because stiffness matrices are considered, $\mathbb{A}_1^T = \mathbb{A}_1$ and the matrix products are performed with KOPS CMCT operator ($\mathbb{A}_1 = \mathbb{K}_0^{(e)}.\mathbb{K}_T^{(e)}$) of Cast3M, followed by EXTR DIAG to extract the product diagonal matrix ($\mathbb{A}_2 = $ diag $(\mathbb{A}_1)$), EXTR VALE to extract the values of the diagonal matrix $\mathbb{A}_2$ in a vector $\underline{V}_3$ and SOMM to sum the terms of $\underline{V}_3$.

(b)   Damping coefficient functions   Again, based on the study in section 3.5, the damping coefficient functions in equations (3.61) and (3.62) are chosen according to the evolution of damage and friction variables. Finally, for the steel stress (linked between steel plasticity and friction), an evolution similar to the friction phenomena is considered (eq. 3.63) because of the similar variations of these two values when nonlinearities develop. Indeed, the local degradation of concrete induces a stress recovery in rebars (fig. 3.37).

Figure 3.37: Steel/Concrete interface (Jehel, 2009)

$$\begin{cases} c_{v,\text{lin}}\left(d\right) & = & \alpha_{d,\text{lin}} \times d + \beta_{d,\text{lin}} \\ c_{v,\text{inv}}\left(d\right) & = & \dfrac{\alpha_{d,\text{inv}} \times d}{d^2 + \beta_{d,\text{inv}}.d + \gamma_{d,\text{inv}}} + \delta_{d,\text{inv}} \end{cases} \tag{3.61}$$

---

[7]The variable η associated to the unilateral effect is not studied here because it gave similar results than the friction variable for the SDOF system, and because the unilateral effect does not represent a significant dissipative phenomenon. In addition, the consideration of input signal amplitudes is not studied here because it was demonstrated, with the SDOF system study, that it does not improve the results and makes the function calibrations more complicated.

where $\alpha_{d,\text{lin}}$, $\beta_{d,\text{lin}}$, $\alpha_{d,\text{inv}}$, $\beta_{d,\text{inv}}$, $\gamma_{d,\text{inv}}$ and $\delta_{d,\text{inv}}$ are the parameters to calibrate,

$$
\begin{cases}
c_{v,\text{lin}}\left(\varepsilon^{\pi}\right) & = & -\alpha_{\varepsilon^{\pi},\text{lin}} \times \left|\varepsilon^{\pi}\right| + \beta_{\varepsilon^{\pi},\text{lin}} \\[2mm]
c_{v,\text{inv}}\left(\varepsilon^{\pi}\right) & = & \dfrac{\alpha_{\varepsilon^{\pi},\text{inv}}}{\beta_{\varepsilon^{\pi},\text{inv}} + \left|\varepsilon^{\pi}\right|}
\end{cases}
\tag{3.62}
$$

where $\alpha_{\varepsilon^{\pi},\text{lin}}$, $\beta_{\varepsilon^{\pi},\text{lin}}$, $\alpha_{\varepsilon^{\pi},\text{inv}}$ and $\beta_{\varepsilon^{\pi},\text{inv}}$ are the parameters to calibrate,

$$
\begin{cases}
c_{v,\text{lin}}\left(\sigma_s\right) & = & -\alpha_{\sigma_s,\text{lin}} \times \left|\sigma_s\right| + \beta_{\sigma_s,\text{lin}} \\[2mm]
c_{v,\text{inv}}\left(\sigma_s\right) & = & \dfrac{\alpha_{\sigma_s,\text{inv}}}{\beta_{\sigma_s,\text{inv}} + \left|\sigma_s\right|}
\end{cases}
\tag{3.63}
$$

where $\alpha_{\sigma_s,\text{lin}}$, $\beta_{\sigma_s,\text{lin}}$, $\alpha_{\sigma_s,\text{inv}}$ and $\beta_{\sigma_s,\text{inv}}$ are the parameters to calibrate.

A first evaluation of these parameters is done by considering the maximal and minimal values of Rayleigh damping matrix with a viscous damping ratio of 2%, as well as the extreme values of considered variables. The considered signal is the DSS2 test inducing nonlinearities. So, the parameters evaluated are presented in table 3.16 with $c_{v,RD,2\%,\text{max}} = 1.65 \times 10^7$ N.s/m and $c_{v,RD,2\%,\text{min}} = 1.72 \times 10^4$ N.s/m.

Table 3.16: Evaluated parameters of evolution functions based on maximal and minimal values of Rayleigh damping matrix

Internal variable V_{int}	Evolution function fct	Extreme values		Parameters			
		Minimal	Maximal	$\mathscr{P}_{1,0}{}^*$ $\alpha_{V_{\text{int}},\text{fct}}$	$\mathscr{P}_{2,0}{}^*$ $\beta_{V_{\text{int}},\text{fct}}$	$\mathscr{P}_{3,0}{}^*$ $\gamma_{V_{\text{int}},\text{fct}}$	$\mathscr{P}_{4,0}{}^*$ $\delta_{V_{\text{int}},\text{fct}}$
d-d_{E_S}- d_{E_T}	Linear (lin)	0	1	1.65×10^7	1.72×10^4	–	–
	Inverse (inv)			2.90×10^6	-0.132	0.0317	1.72×10^4
ε^{π}	Linear (lin)	-1.44×10^{-4}	1.44×10^{-4}	8.96×10^{10}	1.30×10^7	–	–
	Inverse (inv)			2.48	1.92×10^{-7}	–	–
σ_s	Linear (lin)	-2.31×10^7	2.31×10^7	0.561	1.30×10^7	–	–
	Inverse (inv)			3.97×10^{11}	3.06×10^4	–	–

* The notation $\mathscr{P}_i$ is used in the following parts to study the influence of the evolution function parameters. $\mathscr{P}_{i,0}$ is the identified value of parameter $\mathscr{P}_i$ as presented in this table.

3.6.2   Application of proposed damping matrices

The proposed damping model is applied on thr DSS2 test (input signal in figure 1.23b) to evaluate its performance to represent the RC beam global responses and characterise the energy distributions. First, a parametric study is performed on function parameters of table 3.16 (sec. 3.6.2.1), and then the proposed damping matrix evolutions in parallel of local dissipations are presented (sec. 3.6.2.2).

3.6.2.1   Parametric analysis

(a) d_{E_S} and d_{E_T} instabilities   For the variables d_{E_S} and d_{E_T}, the first dynamic computations exhibited strong instabilities in white-noise signal parts. So, a parametric study has been performed to evaluate the influence of using a limit on the tangent or secant modulus variation, ΔE_{lim}, under which

the updated damping matrix is not computed. As expected, increasing the limit induces a decrease in computational time because the higher is the limit, the fewer updates are computed during computations. The evaluation of global errors with the different studied limits is presented in figure 3.38. Again, the strong error values are due to the oscillations around null values, but what is more interesting is the comparison between the computed errors. For the displacement and force errors (fig. 3.38b and 3.38c), it appears that under $\Delta E_{\lim} = 5.0 \times 10^7$ Pa, the responses are not really influenced. For the acceleration (fig. 3.38a), a more substantial influence is observed for the different computations. However, until $\Delta E_{\lim} = 5.0 \times 10^7$ Pa, the global tendency is a decrease of errors with the limit increase because fewer instabilities are thus observed on dynamic responses. In addition, the energy analyses demonstrate first that the distribution of dissipated energies is not influenced, and then that the energy balances are validated until $\Delta E_{\lim} = 1.0 \times 10^7$ Pa. Finally, updating the damping matrix only if the secant or tangent Young's modulus is evolving of more than $\Delta E_{\lim} = 1.0 \times 10^7$ Pa allows improving the dynamic results by reducing the computational time.

(a) Acceleration errors   (b) Displacement errors   (c) Support force errors
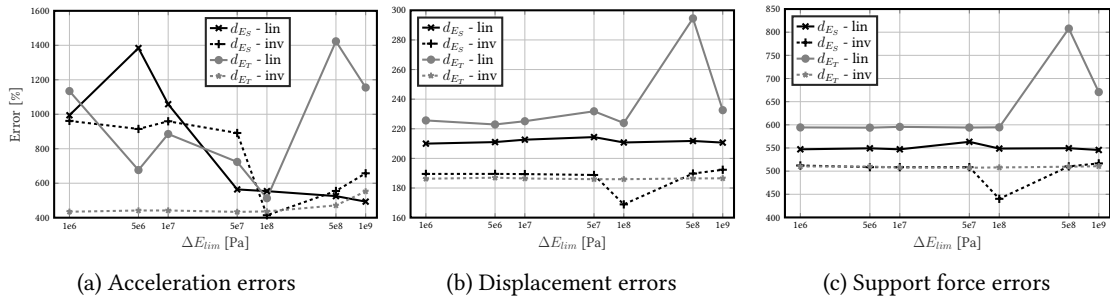
Figure 3.38: Parametric study for the update limit with d_{E_S} and d_{E_T} variables - non-diagonal damping matrix formulation

(b)   Function parameter analyses   The non-diagonal damping matrix formulation is studied here. The diagonal one, whose results are presented in appendix G.2, gives similar conclusions. In addition, only the linear functions are studied. Indeed, for σ_s variable, they are very close to the inverse ones. For d variable, it is the most straightforward function given also accurate results. So, two function parameters ($\alpha_{\mathrm{V_{int},fct}}$ and $\beta_{\mathrm{V_{int},fct}}$) are interesting. From identified values presented in table 3.16, and considered as the initial parameters $\mathscr{P}_{1,0}$ and $\mathscr{P}_{2,0}$, variations between $0.01 \times \mathscr{P}_{i,0}$ and $100 \times \mathscr{P}_{i,0}$ are studied. Figures 3.39 to 3.41 present the $\mathscr{P}_1 = \alpha_{\mathrm{V_{int},fct}}$ parameter analysis because it appears to be the most influential. The analysis of $\mathscr{P}_2 = \beta_{\mathrm{V_{int},fct}}$ is nevertheless presented in appendix G.1. Finally, four updating variables are studied: d_{E_S} (from eq. 3.60), d (from the nonlinear model), ε^π and σ_s.

First, if $\mathscr{P}_1$ is too small, the computations diverge. This parameter represents the function slope. So, with low $\mathscr{P}_1$ values, the damping is almost constant, whatever the nonlinearity amplitudes. The proposed updating formulation has no more interest. In addition, with a constant Rayleigh damping matrix, the computations were converging. So, it demonstrates that the evaluation of the proposed damping matrix formulation is working for a proper function calibration and so a proper consideration of dissipations through dissipative phenomena.

Figure 3.39 presents the global response errors in figures 3.39a to 3.39c and the errors in maximal values in figures 3.39d to 3.39f. For errors of maximal accelerations, displacements and forces, the positive values correspond to numerical values more significant than the experimental ones given conservative results if used for engineering design, and vice versa for negative values. Accelerations, displacements and forces are exhibiting similar evolutions. For d and d_{E_S} variables, the global response errors exhibit a general decrease with the increase of $\mathscr{P}_1$ parameter. It means that the viscous damping must be more prominent for the maximal values of damage. The influence is reverse for σ_s variable. The viscous

(a) Acceleration global errors

(b) Displacement global errors

(c) Support force global errors

(d) Error on the maximal
acceleration

(e) Error on the maximal
displacement

(f) Error on the maximal support
force
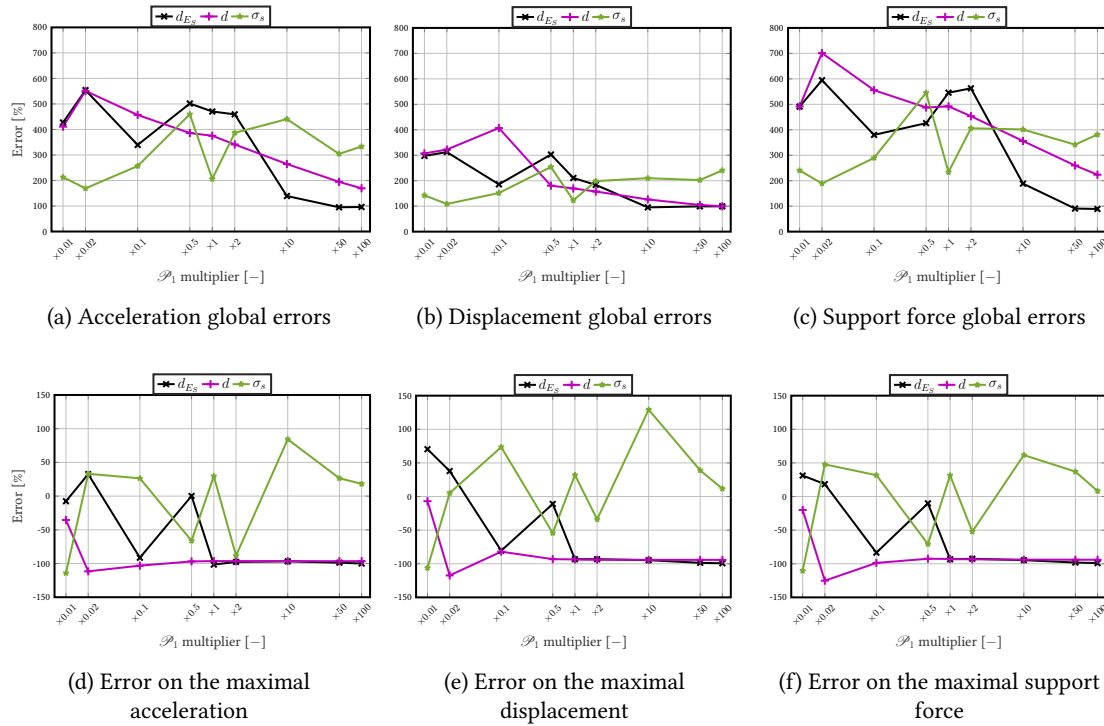
Figure 3.39: Parametric study of function parameters - non-diagonal damping matrix formulation - $\mathscr{P}_1$ evolution - global responses

damping must dissipate enough energy for large nonlinearities because the constitutive model does not do it sufficiently. Mainly, with d and d_{E_S} variables, the errors go from positive values to negative ones. So, even if the global error is minor for even more significant parameters, it is better to select a parameter given the most accurate maximal values in the conservative part in engineering design. With the σ_s variable, the errors oscillate around zero with all parameter variations.

Then, in figure 3.40, normalised maximal and minimal values of d and ε^π internal variables as well as σ_s values are plotted. The normalisation is performed with respect to $\mathscr{P}_{1,0}$ values. For d and d_{E_S}, increasing $\mathscr{P}_1$ leads to the low development of nonlinearities because too much energy is dissipated through viscous damping, which is not representative of the physical behaviour.

Finally, figure 3.41 focuses on the evolution of the energies. For d and d_{E_S}, similar evolutions are obtained. Energy balances are verified respectively from $0.5 \times \mathscr{P}_{1,0}$ and $1 \times \mathscr{P}_{1,0}$ (fig. 3.41b and 3.41a). From figures 3.41e and 3.41d, it can be concluded that with a too-small $\mathscr{P}_1$ parameter, too much energy is dissipated at the local scale leading to total energy being more considerable than the imparted one. With σ_s, again, oscillatory results are obtained depending on parameters. However, the best energy balances are obtained when the absorbed energy represents less than 40% of all dissipations as with $1 \times \mathscr{P}_{1,0}$ for example.

3.6.2.2 Local dissipations and updated damping matrices

In the parametric analysis, global responses and energy balances were presented and compared depending on variables used for updating the damping matrix and evolution function parameters. Let us focus on the damping matrix evolution (fig. 3.42) by considering local dissipations. One computation with a

(a) Damage (cracking)   (b) Friction strain   (c) Steel stress
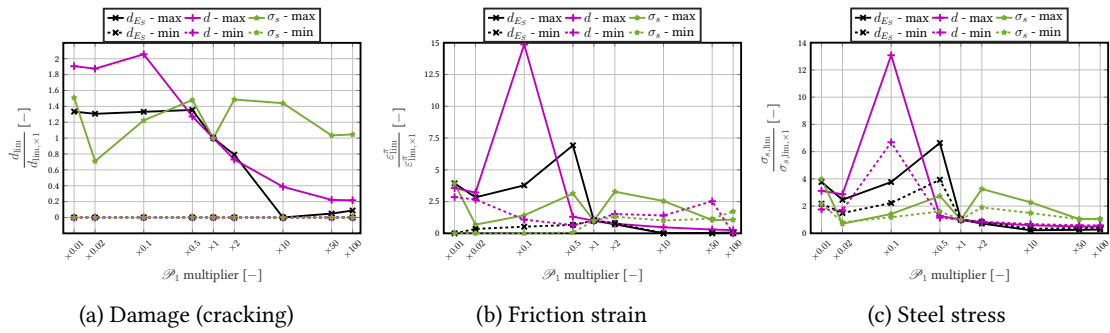
Figure 3.40: Parametric study of function parameters - non-diagonal damping matrix formulation - $\mathscr{P}_1$ evolution - normalised maximal and minimal values of some variables

(a) E_i vs E_{tot} and u_{max} (b) E_i vs E_{tot} and u_{max} (c) E_i vs E_{tot} and u_{max}
d_{E_S} variable d variable σ_s variable

(d) Dissipated energies   (e) Dissipated energies   (f) Dissipated energies
d_{E_S} variable d variable σ_s variable
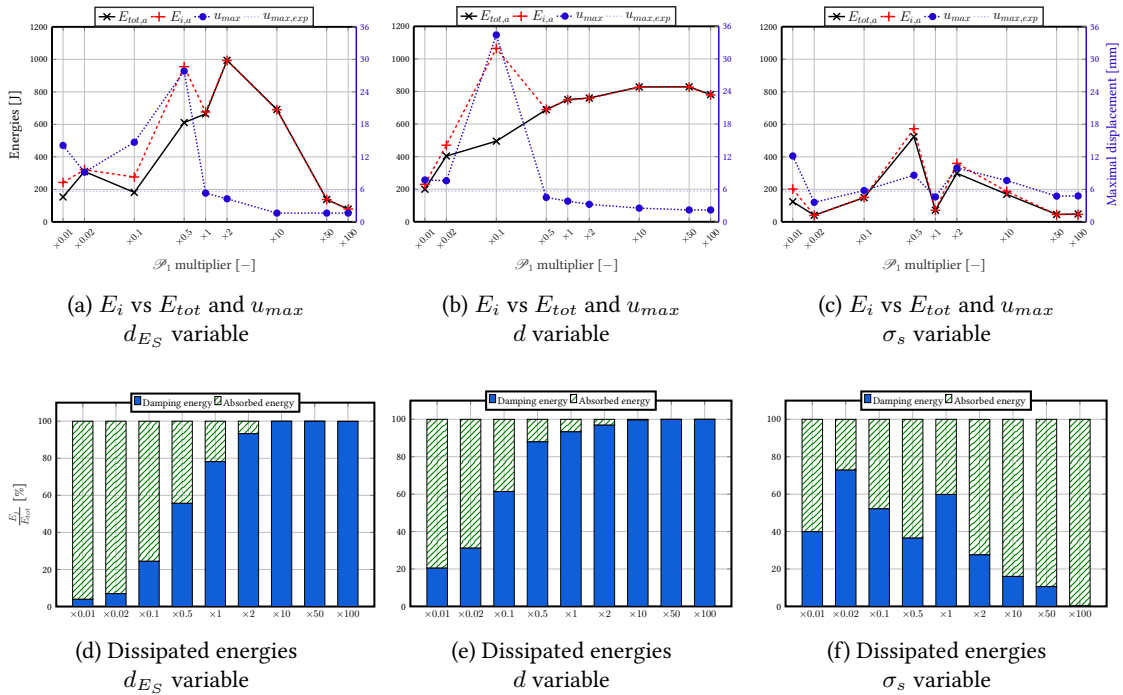
Figure 3.41: Parametric study of function parameters - non-diagonal damping matrix formulation - $\mathscr{P}_1$ evolution - energy analyses

diagonal damping matrix and d variable is considered and compared to the response of a non-diagonal damping matrix with d_{E_S} variable.

Figure 3.42 shows the two damping matrix types for the undamaged beam and after two damage levels. Only half of the beam elements are plotted. The diagonal and non-diagonal forms are well observable, but the coefficient order of magnitudes are highly different. The initial matrix (fig. 3.42a and 3.42d) presents small amplitudes for both types. So, the development of nonlinearities induces an increase in the damping matrix terms. Figures 3.42b, 3.42c, 3.42e and 3.42f demonstrate that only the damaged terms at the beam centre lead to more significant damping coefficients. For the non-diagonal

(a) Non-diagonal matrix
d_{E_S} variable - undamaged

(b) Non-diagonal matrix
d_{E_S} variable - low damage level

(c) Non-diagonal matrix
d_{E_S} variable - high damage level

(d) Diagonal matrix
d variable - undamaged

(e) Diagonal matrix
d variable - low damage level

(f) Diagonal matrix
d variable - high damage level
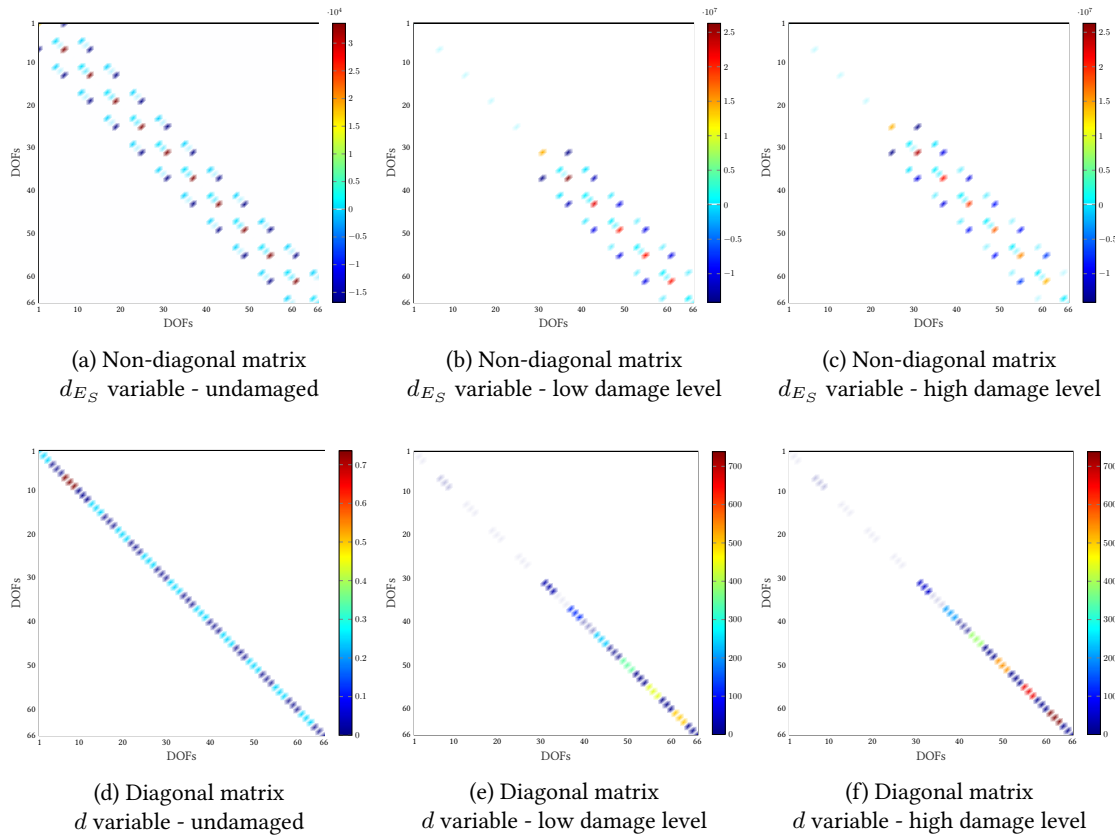
Figure 3.42: Updated damping matrices at different damage levels

damping matrix, it can even be observed that between both studied damage levels, more elements have suffered nonlinearities. Thus, the proposed damping matrix formulations are well evolving as expected.

The internal variable evolutions, as well as the steel stress one, are plotted in figure 3.43. Nonlinearities are well developed for both damping formulations. However, lower values are obtained with the diagonal damping matrix, meaning that the beam response drops too much. In parallel, by studying the global response errors, values two times larger are obtained with this matrix. So, the function parameters are not accurately calibrated, or the diagonal matrix form is not adapted. Besides, the friction hysteretic energy evolution in figure 3.44b presents instantaneous variations as the damage energy, contrary to figure 3.44a with the non-diagonal matrix. It can, thus, also be concluded that as soon as the damage variable increases, a strong damping matrix is computed, almost stopping the beam movement and avoiding the development of friction between crack surfaces. It is not corresponding to the expectation, so the non-diagonal damping matrix should be preferred.

3.6.3   Evaluation of matrix performances

3.6.3.1   Comparisons with classical damping formulations

Because computed results are in agreement with the experimental data, a comparison can now be performed with more classical damping formulations studied in chapter 2. The acceleration response is

(a) d evolution   (b) ε^π evolution   (c) η evolution   (d) σ_s evolution
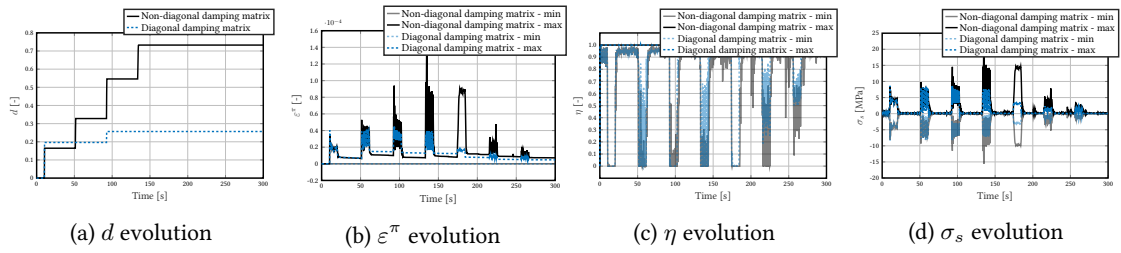
Figure 3.43: Updated damping matrix - Evolution of nonlinear variables and steel stresses - comparison of updated damping matrix formulations

(a) Non-diagonal matrix
d_{E_S} variable

(b) Diagonal matrix
d variable
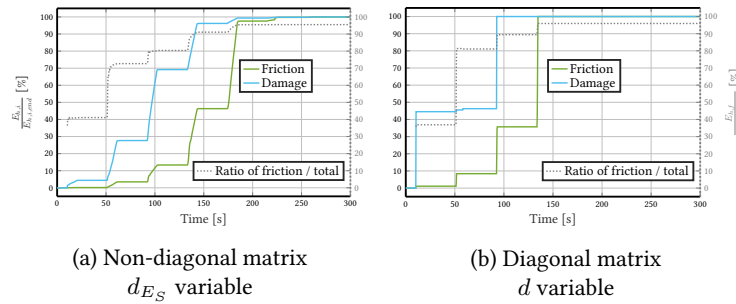
Figure 3.44: Updated damping matrix - Dissipation proportions at the material level - comparisons of updated damping matrix formulations

considered herein as the variable of interest, and parameters in table 3.16 are chosen for the damping coefficient functions of proposed damping formulations. Figure 3.45 proposes to compare all studied damping formulations in a plan of two numerical acceleration errors compared to experimental data: (i) the global error all along with computation, and (ii) the maximal acceleration error. Figures 3.45c and 3.45d are respectively the same as 3.45a and 3.45b with the most discussed formulations. Each colour represents a damping formulation. The marks characterise the viscous damping ratios for the classical damping formulations and the variable used for the updates in the case of proposed damping formulations. Some examples are indicated in the figures. Figure 3.45b is a zoom on the best formulations of figure 3.45a. First, as already discussed, the effect of viscous damping ratio choice is well observable for the classical formulations. The best one does not appear to be the same for all formulations. Now, figure 3.45a shows that the locally updated formulations are pretty well placed because they are staying in the left bottom angle as a considerable majority of classical formulations. By looking at figure 3.45b, it appears that the diagonal damping matrix with d_{E_S} variable, as well as the non-diagonal one with the friction variable ε^π, are the ones given the lowest global acceleration errors. Nevertheless, because the maximal acceleration error is negative, they should not be used for structural design. Conversely, the non-diagonal damping matrix with the damage variable d gives a more significant global error. However, it is best to characterise the maximum acceleration conservatively undergone by the structure. It is, in addition, positioned close to the Rayleigh-type damping formulations evaluated as the ones to prefer in chapter 2.

3.6.3.2   Conclusions

To conclude, an updated damping matrix based on local variables has been proposed in this section. The damping matrix is computed at the elemental scale before being assembled to compute structural non-

(a) All formulations

(b) Zoom on best formulations

(c) All formulations (main formulations)

(d) Zoom on best formulations (main formulations)
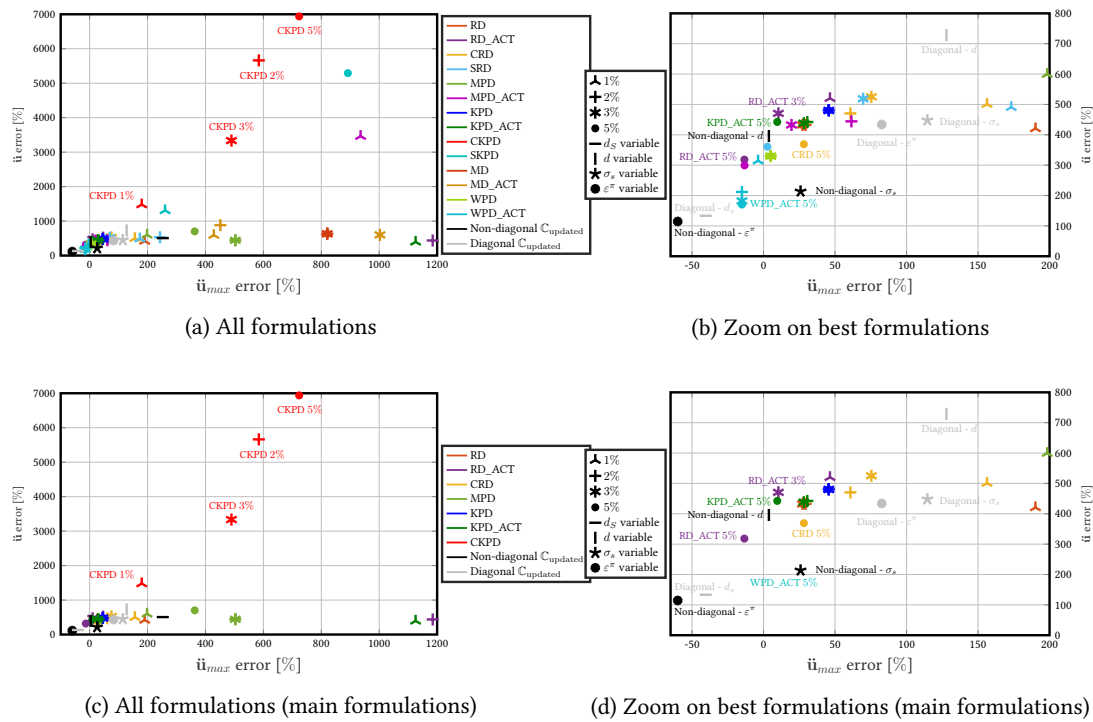
Figure 3.45: Comparison of classical and locally updated damping matrix performances to characterise the experimental accelerations

linear dynamic computations. Different internal variables have been studied, and functions to compute the damping coefficients from the identified variables on section elements have been discussed. The dynamic responses are strongly depending on these two properties of the method.

A comparison with the classical damping formulations studied in chapter 2 shows that the proposed damping matrices similarly match the experimental data than the classical ones. The method is thus validated. Notably, its advantage is that it is based on physical dissipative phenomena. The results can therefore be expected to be more predictive. The best results are obtained when the damage (cracking) and friction phenomena are considered. However, improvements are still required. The evolution function parameters have to be carefully calibrated. It is a limitation of the proposed method because, currently, the calibrations are performed with experimental data, so experiments are required. In terms of variable choice, d and d_{E_S} (or d_{E_T}) demonstrated similar behaviours meaning that the proposed damage index (eq. 3.60) accurately characterises the damage computed by the RICBET constitutive model. For these variables, the linear damping coefficient function has been extensively studied. But, if the damping matrix is too important for the large damage values, no nonlinearity develops, and the experimental behaviour is no more numerically represented. So, an inverse function should be interesting to improve the results. The function parameters less influence the friction variable. The difference may be that the friction variable constantly evolves during the computation inducing lots of damping matrix variations, while the damage variable increases by step, with crack initiation and propagation, so the damping matrix is only becoming larger and larger. Finally, the steel stress data may need improvements because the link between the steel stresses and concrete nonlinearities is poorly modelled. However, a focus could also be performed on that variable because it is a stable variable linked with the crack opening and dissipations at the concrete level.

3.7   Synthesis

3.7.1   Performed analyses and conclusions

Different analyses around the damping modelling in structural nonlinear dynamic computations have been proposed in this section. First, section 3.1 focused on the damping matrix projection on the modal basis to evaluate the development of couplings between modes when the tangent stiffness matrix is considered in damping matrix computation. Because the modes appeared to stay decoupled even when nonlinearities developed, the resolution on the modal basis was demonstrated as accurate even with the tangent stiffness matrix consideration. Then, based on the works developed by Heitz (2017), a viscous damping identification method was proposed with a SDOF system equivalent to the studied RC beam in section 3.3. Then, section 3.2 was interested in proposing an evaluation of the analytical eigenbasis associated with the complete system of interest to derive the equivalent SDOF model. Finally, the viscous damping identification method algorithm and all the method parameters were discussed in section 3.3.

The viscous damping identification method was then applied on experimental results and numerical data to characterise the viscous damping ratio evolution depending on a damage index representing the stiffness loss, in section 3.4. Experimentally, an exponential evolution of ξ was obtained with respect to the damage index. However, below $d = 0.6$, considering a constant viscous damping ratio of 4% was accurate. Above that limit, this parameter must be updated with the development of nonlinearities. Numerically, the determined evolutions appeared to depend on modelling properties, particularly on viscous damping matrix formulations. In addition, significant differences were observed with the experimental data, demonstrating a lack of accuracy in dissipation descriptions. That is why a nonlinear constitutive model characterising the RC behaviour was then used to identify the viscous damping ratio. The general conclusion already discussed in the literature and deduced from the identification method application is that viscous damping varies with the development of nonlinearities. So, the objective of section 3.5 was to analyse the performances of damping models as functions of constitutive model internal variables to achieve nonlinear dynamic computations well. In addition to giving a more physical representation of structural dissipations, using the proposed locally updated damping models allowed better to characterise the extreme global responses of the beam. Nevertheless, the global errors along time were in the same order of magnitude as the classical damping formulations, like Rayleigh damping.

Finally, the proposed updating damping models were applied to the multi-fibre model with the algorithm developed in section 3.6. Two strategies of damping matrices were proposed: one diagonal and one non-diagonal. The difficulty of developed damping models is due mainly to damping coefficient function calibrations. However, the first parametric analyses have demonstrated that it is possible to find function parameters leading to performative updating models. The global errors compared to experimental data were in the same order of magnitude as the Rayleigh damping matrix. However, improvements are still required to enhance the nonlinear dynamic computations.

The best results obtained with the locally updated damping models for the SDOF analyses and the multi-fibre computations are the ones considering the damage (cracking) variables if the extreme dynamic responses are of interest and the friction variable if the global dynamic responses are of interest. The damping coefficient functions can be calibrated with the experimental data. Nevertheless, if no experiment is available, a few time steps can be computed with a Rayleigh damping matrix to determine the maximal and minimal damping values and the variable variations.

Table 3.17 synthesizes the best damping formulations to choose for the different studied beam models and the use of classical or locally updated damping matrices. For the equivalent SDOF system, only Rayleigh damping was studied for the classical damping formulations. The selection of the viscous damping ratio depends on the variable of interest and the choice of the variable used for the updates in the proposed locally updated damping case. Similar conclusions are observed for the multi-fibre model:

Table 3.17: Synthesis of the best damping formulations for the studied analysis

Beam model	Constitutive model	Damping formulation	Variable of interest	Best damping model
Equivalent SDOF	**IDEFIX (nonlinear)**	**Classical**	Mean of all global dynamic responses	RD 5%
			Global acceleration	RD 2%
		Updated	Maximal displacement and largest dissipations at the local scale	d variable with the inverse function
			Global dynamic responses	u^π or η variables with linear or inverse functions
Multi-fiber (Cast3M)	**RICBET (nonlinear)**	**Classical**	Dynamic responses + energies	RD_ACT 2%
			Global acceleration	WPD_ACT 5%
			Maximal accelerations	SRD 5% / SKPD 1%
		Updated	Maximal conservative acceleration	Non-diagonal damping matrix with d variable and the linear function
			Global acceleration	Non-diagonal damping matrix with ε^π variable and the linear function

the best formulations and damping ratios depend on the variable of interest with the classical damping formulations. For the locally updated matrices, the non-diagonal formulation is the best with different variables again depending on the variable of interest.

3.7.2   Potential improvements

The objective of developing a new damping matrix formulation was to consider the local behaviour to describe the dissipations occurring during seismic excitations more physically. Three variables have mainly been studied: (i) the damage variable characterising the stiffness loss d, (ii) the friction variable characterising the dissipations between crack surfaces ε^π, and (iii) the steel stress σ_s because it could represent a stable equivalence of nonlinearities. Each variable was studied independently, but combinations, particularly of damage and friction variables, could be interesting because they characterise coupled dissipative phenomena. However, the major challenge would be the function calibrations. The more variables are considered, the more damping coefficient function parameters must be calibrated, leading to more complex parametric analyses. That is why strategies have to be developed to carry out these calibrations. The idea in progress is to couple the identification method developed in Matlab® software with the multi-fibre computations in Cast3M to identify the damping coefficient function parameters in an example test.

Finally, it is clear that the RC structure responses are also influenced by their environment. So, it is impossible to model all dissipations with local parameters. However, the computations performed with classical damping models in chapter 2 demonstrated a substantial lack of dissipations by hysteresis even with RICBET constitutive model characterising influential dissipative phenomena. That is why the idea could be to use a tiny part of viscous Rayleigh damping, for example, and to add increments of the proposed updated damping matrices. Thus, even if the nonlinear constitutive model is not dissipating enough energy through hysteresis, the updated damping matrices would add an equivalent hysteretic energy dissipation. By calibrating these dissipations to be equivalent to the lack between ex-

perimental and numerical hysteresis loops, the constant viscous damping would only characterise the environmental effects. So, the physical representation of dissipations would be improved.

Conclusions

Civil engineering structures uniqueness and size require the development of efficient numerical models to characterise structure safety under seismic excitations. The linear dynamic behaviour of structures depends on structural properties like its mass, stiffness and damping. The mass is easily described using the knowledge of the structure geometry and the materials composing the structure. For the stiffness, the description is a bit more complicated. However, the notion of damping is far more complex to define. Suppose proposed definitions agree on the idea that "damping is produced by processes that dissipate the energy stored in the oscillation" (Wikipedia, 2021). In that case, no consensus can be found in the literature to characterise this property physically. Many sources are dissipating energy in the case of structures submitted to earthquake excitations, whether they are phenomena inside the structure or interactions with its external environment. It was in the 1960s that Jacobsen (1960) first proposed an efficient tool to model the structural damping by an equivalent damping ratio determined with experimental tests. The idea of such equivalent damping is to consider a linear material behaviour and to displace the dissipations at the global level through damping models. It has mainly been studied in the literature with papers treating different structural elements. With the development of Finite Element (FE) numerical models and the improvement of computation facilities, more sophisticated models of structures under seismic excitations began to appear. However, the idea of equivalent damping remains widely used today because engineering software is generally considering linear material behaviour coupled to viscous damping formulations. Globally, accurate numerical responses are obtained with such formulations, and, above all, the computational times are adequate for engineers. However, to characterise more local phenomena, like crack opening and sliding in reinforced concrete structures, using efficient mathematical tools instead of physical and realistic models becomes insufficient.

Reinforced concrete structures, which are of interest in this PhD work, exhibit complex behaviours, mainly when submitted to seismic excitations. For critical structures like nuclear power plants, sophisticated simulations of their behaviour under seismic excitations are required to ensure their viability. Not only the structures must remain standing in case of an earthquake event, but the operating equipment must not be damaged. So, the numerical models must accurately characterise the maximal accelerations at different structural points to transfer the spectral acceleration to the equipment of interest. In addition, in the case of nuclear structures, airtightness must be maintained. So, the numerical models must permit precise assessment of cracking damage and its development relative to the structural displacement response. To reach those expected performances: (i) advanced numerical models are required, and (ii) the dissipations must be precisely characterised: global modelling of the dissipations is no more sufficient. That is why nonlinear computational models must be further developed, and the links between hysteretic dissipations and structural damping must be investigated and understood. Thus, recommendations could be formulated to assist the engineers in performing nonlinear dynamic computations.

Synthesis

Full-scale tests are beneficial for understanding reinforced concrete structures behaviour under earthquakes. However, they are costly, so strategies are required to develop models based on tests carried out on structural elements. In this objective, Heitz (2017) developed an exhaustive experimental campaign, during his PhD, on reinforced concrete beams (6 m × 20 cm × 40 cm). The campaign aimed to perform dynamic and quasi-static tests to propose data for evaluating seismic energy dissipations depending on structural, material and input excitation characteristics. The considerable amount of data provided has been the primary resource for the works developed in this thesis and can still be used afterwards. Table 3.18 synthesises the relevant information about the experimental campaign to understand carried out studies. Table 3.19 indicates the constitutive models chosen in Cast3M to characterise the experimental data and key input parameters.

Table 3.18: Experimental properties of the reinforced concrete structural elements studied

Beam HA16-C1A geometry	Length	6 m
	Concrete section	$0.4 \times 0.2 \text{ m}^2$
	Steel rebars	8 HA of diameter 8 mm (2.01%)
	Supports	Positioned at 0.05 m and 5.95 m
	Additional masses	310 kg
		Positioned at 1.52 m and 4.48 m
		On air cushion devices
Concrete properties C25/30 (6 months)	Young's modulus	26.2 GPa
	Compressive strength	36.9 MPa
	Tensile strength	2.09 MPa
	Concrete fracture energy	84.9 J/m^2
Steel properties[*]	Young's modulus	217 GPa
	Elastic limit	568 MPa
Eigenfrequencies	Mode 1	7.24 Hz
	Mode 2	23.5 Hz
	Mode 3	58.8 Hz
Tests / Excitations	Hammer shock	characterisation of the three first modes at different damage level
	Quasi-static	On strong floor with two actuators Four-point bending
		• QSC1 → mode 1
		• QSC2 → mode 2
	Dynamic[*]	On shake table
		• WN = white-noise
		• SC = band-passed white noise
		• DSS = decreasing sinus sweep
		• SS1 = natural seismic signal

[*] The steel remains in the elastic range for all applied excitations

Table 3.19: Characteristics of Cats3M constitutive models

Boundary conditions	Translational elastic supports	$K_T = 1.10 \times 10^7$ N/m
		Positioned at 0.05 m and 5.95 m
	Rotational elastic supports	$K_R = 1.00 \times 10^4$ N.m/rad
		Positioned at 0.05 m and 5.95 m
	Additional masses	Punctual
		Positioned at 1.52 m and 4.48 m
		No friction with the table
Concrete	Models	BARFRA and RICBET
	Behaviour	Nonlinear (hysteretic dissipations)
	Young's modulus	22 GPa
Steel	Model	ACIER_UNI
	Behaviour	Linear
	Young's modulus	208 GPa
Steel / concrete bound	Model	Perfect (no sliding)
Eigenfrequencies	Mode 1	7.11 Hz
	Mode 2	23.1 Hz
	Mode 3	58.2 Hz
Maximal excitations	Quasi-static[1]	$u_{a,\max} = 80$ mm
	Dynamic[2]	WN1 $\rightarrow \ddot{u}_{s,\max} = 0.65$ m/s^2
		DSS2 $\rightarrow \ddot{u}_{s,\max} = 1.33$ m/s^2
		DSS3 $\rightarrow \ddot{u}_{s,\max} = 1.84$ m/s^2

[1] Maximal actuator displacement   [2] Maximal shake table acceleration

The experimental campaign is used all along that thesis to answer three research questions defined using a critical review of the literature performed in the first chapter (1):

> **In the framework of nonlinear dynamic computations, which local and global viscous damping formulations best represent the experimental structural responses?**

> **How are local and global damping energy dissipation mechanisms evolving during nonlinear dynamic computations?**

> **How could we improve the damping modelling at the local scale, on a physical basis, to reduce the requirement of arbitrary equivalent viscous damping at the global scale?**

The research problems are discussed with five original contributions developed in chapters 2 and 3:

✓ Correlations between measured and computed data,
✓ Comparison of damping models based on energy balance studies in nonlinear dynamic analyses,

✓ Development of a methodology to identify the transient evolution of damping with respect to the structural element damage,

✓ Evaluation of an approximate analytical eigenbasis of a complex system,

✓ Development of a new local model of damping based on nonlinear internal variables of the concrete constitutive models (d, ε^π, …).

In chapter 2, a multi-fibre model of the reinforced concrete beams is developed using Cast3M software. The model calibration is performed based on hammer shock and quasi-static tests. Then, exhaustive numerical analyses are developed to compare **sixteen damping formulations** currently used in engineering (classification in table 2.11) with **different viscous damping ratios** varying from 0.5% to 5% and **with or without stiffness matrix or modal parameter updates**. The experimental data are considered to validate the formulation performances and propose recommendations, particularly in terms of acceleration, displacement, force responses, and the development of damage through the eigenfrequency evolutions. In all cases, the steel rebars remain in their elastic range along with computations, as expected experimentally. The computations are performed with **two nonlinear constitutive models** for concrete proposed in Cast3M: BARFRA and RICBET. The objective is to characterise the influence of dissipative phenomena modelling because only a "classical" damage model is considered in BARFRA. At the same time, the friction during crack opening and closing is added in dynamic computations with RICBET. Energy balance computations are also implemented with both models. At the structural level, information is deduced about the proportion of energy dissipated through viscous damping, that is to say, through unknown and/or un-modelled dissipative phenomena. Then, using the thermodynamic framework of the nonlinear constitutive models, energy dissipations through nonlinear dissipative phenomena are analysed depending on the viscous damping models. The numerical computation represents approximately 300 computations for more than $3,000$ hours of computational time on a supercomputer.[8]

Chapter 3 focuses on damping. The projection of the damping matrix on the modal basis is first studied to evaluate the development of mode coupling with nonlinearities. Then, an equivalent viscous damping identification method is proposed to evaluate the transient evolution of damping compared to concrete damage evolution. The method is based on an equivalent SDOF system, and the projection on the modal basis is used to obtain the equivalent problem. Because the studied system does not exhibit a theoretical modal basis, strategies to approximate the system modal properties are proposed and validated using experimental data and a multi-fibre model. The identification method considers a decomposition of the signal with windows. On each window, the first hypothesis is that the behaviour of the equivalent SDOF system is "linear" on the window, allowing the identifications of a viscous damping ratio and an eigenfrequency. A damage index is computed from the evolution of the eigenfrequency, and the viscous damping ratio is plotted as a function of the damage index. Then, a nonlinear constitutive model is used to improve the energy dissipation description. It was initially developed by Heitz, Giry, et al. (2019). It is representative of reinforced concrete behaviour. The observed dependency of viscous damping as a function of nonlinear variables (d, ε^π, η, …), finally, leads to the proposition of a damping model updated at the local scale. First, the model is developed for the equivalent SDOF system. Then, an adaptation is proposed for the multi-fibre model in Cast3M. A parametric analysis is thus performed to evaluate the best model parameters to match the experimental data and characterise the physical dissipations. Comparisons are mainly performed with the commonly used viscous damping formulations studied in chapter 2.

---

[8]This work was performed using HPC resources from the "Mésocentre" computing centre of CentraleSupélec and École Normale Supérieure Paris-Saclay supported by CNRS and Région Île-de-France (http://mesocentre.centralesupelec.fr/).

Conclusions

Major conclusions have been drawn at the end of each chapter. In the above synthesis, carried out works have been reported and the associated conclusions are again discussed and refined here. **They must be carefully considered because they are deduced from tests on a particular isolated reinforced concrete beam submitted to low amplitude dynamic signals.**

First, the critical review of the literature leads to the following critical conclusions discussed in chapter 1:
✓ **Damping models at the structural level**
  ► They are commonly linked with the velocity leading to "viscous damping" models.
  ► They are classified between classical and modal damping models. The computation of classical models is performed from mass and stiffness matrices. Modal analyses are performed for the modal damping models, and the eigenmodes are used for the damping matrix computation.
  ► Classical and modal damping models are generally used for their simplicity, mainly because they can dissipate energy without modelling dissipative phenomena. In addition, they represent an efficient mathematical tool because they are decoupled using the undamped modal basis.
  ► The Rayleigh damping formulation remains the most used. However, many difficulties are shared by the scientific community about the use of this type of matrix in dynamic analyses. That is why research focuses on improving this model. The most currently used adaptations are:
    * removing the mass proportional part to eliminate the spurious forces,
    * updating the stiffness matrix part to consider the structure degradation,
    * updating the two proportionality parameters.
  ► Many papers focus on comparing classical and modal damping formulations on particular examples. Using the tangent stiffness matrix is generally recommended because it is a way to reduce the damping forces and obtain more conservative results. However, the recommendations must be carefully considered because they are strongly dependent on studied structural elements and are seldom based on comparisons with experimental data. Remarkably, the choice of viscous damping ratio appears to play a significant role in the magnitude of the dynamic response.
  ► A significant difficulty with the classical and modal damping models is their lack of physical basis. Very few physically-based energetic analyses are proposed in the literature to describe the energy dissipations during dynamic computations.
  ► The literature proposes more complex damping models (than Rayleigh and modal damping). However, they are few used in engineering due to their implementation complexity, high computational time and because they are not significantly increasing the representativeness of physical behaviours.
✓ **Damping models at the local scale**
  ► To better characterise dissipative phenomena, papers focus on hysteretic damping at the material level.
  ► For reinforced concrete, complex models are proposed. However, due to the number and lack of knowledge of dissipative phenomena, it is impossible to model all of them precisely. So, hysteretic damping models are seldom used in engineering. They are accompanied by a small amount of viscous damping at the global scale when they are considered.
  ► Another strategy is to adapt the structural model at the local scale to consider the development of nonlinearities. The difficulty here is due to the lack of experimental evidence validating that strategy.[9]

---

[9]This aspect is at the heart of this thesis.

✓ **Damping identification**

    ► The objectives concerning damping modelling are multiple:

        ∗ identifying damping values to apply in numerical models,

        ∗ identifying damping evolution models as functions of damage index to update the damping model in numerical computations,

        ∗ using damping as a damage index for existing structure evaluations.

    ► The majority of analyses presented in literature lead to equivalent viscous damping ratios between 1% and 6%, according to the 5% generally considered in linear dynamic computations to assess the nonlinear demand in modern code for ductile elements. However, for cracked structural reinforced concrete elements, values of 20% can be reached. It demonstrates that a constant viscous damping ratio in nonlinear computations is inaccurate. The identified values must be carefully considered because of the identification method bias and the considerable dependency of the values with the studied structural elements.

    ► In the case of damage identification, no consensus exists in the literature to use damping as an indicator. Notably, even if it indicates the damaged state, it does not localise it. In addition, it is generally required to use free or forced harmonic vibrations, which is challenging to apply in existing structures. So, research still focuses on developing efficient methodologies to identify the damping based on free ambient vibrations.

In chapters 2 and 3, two hysteretic damping models dissipating energy at the local scale are studied compared to classical and modal damping models at the structural level. Then, a viscous damping identification method is proposed to evaluate the damping evolution with different input signals and in parallel to damage indices. Finally, a global damping matrix is proposed with local updates based on identified evolution of damping with respect to nonlinear variables.

Then, from chapter 2, it can be concluded that:

✓ **Multi-fibre model**

    ► Using a multi-fibre model is an appropriate choice to perform the nonlinear dynamic computation of the reinforced concrete beam because:

        ∗ the number of DOFs (22 beam elements, 16 concrete and 32 steel fibres for each section, 4 Gauss points for each fibre) is reduced, as well as the required memory and the computational time, compared to a 3D FE solid model,

        ∗ the material heterogeneity can be considered by applying one constitutive model for concrete elements and another for steel,

        ∗ the results are accessible because they are similar to beam models.

    ► It has been possible to accurately calibrate the numerical model natural frequencies using the numerous experimental data: the supports elastic stiffnesses have been calibrated using the undamaged beam eigenfrequencies and the concrete model parameters using the quasi-static responses.

✓ **Dynamic responses**

    ► First, in terms of constitutive models, it is observed that RICBET provides a better correlation with the experimental responses than BARFRA because it describes more physical dissipative phenomena. So, to improve the nonlinear dynamic computations, a better representation of physical dissipative phenomena is required.

    ► Between the classical Rayleigh and modal damping formulations, it is concluded that the matrices proportional to the stiffness matrix and the Rayleigh-type matrices give the best correlation between experimental and numerical dynamic responses. The numerical responses are improved by using the tangent stiffness matrix or updating the proportionality parameters. It is in adequacy with findings in the literature.

    ► A value of 0.5% is required for the viscous damping ratio when the beam concrete material stays

in its elastic range. It has to be increased until 2% when low nonlinearities (cracking, friction) developed and a little more for more substantial nonlinearities. The choice of this parameter is therefore strongly dependent on the input signal. Nevertheless, these values demonstrate that using nonlinear constitutive models, that is, models locally dissipating energy, allows reducing the influence of arbitrary viscous damping. Indeed, if a linear model is considered, a viscous damping ratio of 5% is generally recommended in the literature for seismic analysis.

✓ **Energy analyses**

▶ At the structural level, using the RICBET model, the significant-conclusion regarding energy analysis is that the viscous damping energy is generally dissipating more than 50% of all energy. In contrast, the other 50% are dissipated by hysteretic behaviours. It demonstrates the strong influence of the viscous damping even when locally nonlinear constitutive models are used to obtain a good correlation between measured and computed response parameters. The stiffness proportional damping formulations have the lowest influence on viscous damping. So, they should be preferred with the aim of a better characterisation of energies.

▶ The most dissipative local phenomenon appears to be the friction between crack surfaces at the local scale. For cycles with constant amplitudes, the friction (and not the damage) between the crack lips induces dissipations.

Table 3.20 synthesises the best damping formulations for different variables of interest. It demonstrates that, for nonlinear dynamic computations, compromises are required to choose the adequate viscous damping model. In addition, using nonlinear constitutive models is a way to model the dissipative phenomena physically. However, the development of nonlinearities (cracking, friction, unilateral contact, …) is influenced by choice of the viscous damping model. So it is not easy to evaluate the accuracy of the models. A better understanding of dissipations is required to reduce the influence of arbitrary viscous damping in nonlinear dynamic computations.

Table 3.20: Synthesis of the best damping formulations for the studied analysis (3.7)

Beam model	Constitutive model	Damping formulation	Variable of interest	Best damping model
Equivalent SDOF	**IDEFIX (nonlinear)**	**Classical**	Mean of all global dynamic responses	RD 5%
			Global acceleration	RD 2%
		Updated[*]	Maximal displacement and largest dissipations at the local scale	d variable with the inverse function
			Global dynamic responses	u^π or η variables with linear or inverse functions
Multi-fibre (Cast3M)	**RICBET (nonlinear)**	**Classical**	Dynamic responses + energies	RD_ACT 2%
			Global acceleration	WPD_ACT 5%
			Maximal accelerations	SRD 5% / SKPD 1%
		Updated[*]	Maximal acceleration (safety range)	Non-diagonal damping matrix with d variable and the linear function
			Global acceleration	Non-diagonal damping matrix with ε^π variable and the linear function

[*] New models proposed in this research.

Finally, chapter 3 focuses on the modelling of damping. The transient evolution of the viscous damping ratio $\xi(t)$ is analysed, and a damage-dependent evolution is found $\xi(t, d)$. Then, it led to the proposition of an updated damping matrix $\mathbb{C}_{\mathrm{updated}}$. The significant conclusions of chapter 3 are:

✓ **Projection of damping on the modal basis**

► The projection of the updated damping matrices when nonlinearities occur shows no accentuation of couplings between the modes. The system projection on the modal basis all along nonlinear computations is accurate.

► The analytical eigenbasis of the complex studied system can be evaluated using the eigenproperties of subsystems and strategies to combine these data.

✓ **Viscous damping identification**

► The proposed identification method has been calibrated using a three DOFs linear system whose analytical response is known. Parameters, like the choice of window length, parameters to be identified, their initial values, … must be chosen carefully at the beginning. In addition, constraints can be added if they help for the convergence and can be physically justified. For example, this is the case when the variation of parameters to be identified is limited from one window to another.

► The identification application on experimental data demonstrates that the viscous damping ratio follows an exponential function of the damage index d. Particularly under the value of $d = 0.6$, a constant viscous damping ratio of 4% is adequate. Nevertheless, the viscous damping ratio must evolve with the damage above that threshold.

► Adding a nonlinear constitutive model in the identification method allows a better characterisation of energy dissipations. Indeed, identified viscous damping ratios are lower than the linear model, representing only the un-modelled phenomena. This type of analysis could, so, be used to evaluate the performances of more complex nonlinear constitutive models and the significant influence or not of each modelled dissipative phenomenon.

✓ **Locally updated damping model**

► The new proposed damping model presents the advantage of updating the damping depending on the development of nonlinearities and considering the damage state of the structural element.

► When applied to the SDOF system, global dynamic errors of the same order of magnitude as with a constant Rayleigh damping coefficient are obtained, validating the ability of the proposed model to perform nonlinear dynamic analyses. Using the friction variable is better when the global response is studied compared to experimental data because it evolves along with computation. On the contrary, if only the maximal displacement or accelerations are of interest, the damage variable seems more efficient because it leads to damping evolutions only when more significant input forces are applied. The damage variable influences the extreme responses and leads to a lower number of required updating reducing the computation time.

► Two damping matrices have been studied for the multi-fibre model: with or without couplings. As for the SDOF system, the damage and friction variables have been studied, in addition to the steel stress that could be a stable indicator of nonlinearities. Again, the global errors are like those obtained with a matrix of the Rayleigh type. The proposed matrices can be considered in nonlinear dynamic computations. Again, the damage variable is better for studying extreme dynamic responses. At the same time, the friction one must be chosen to obtain the numerical response matching the best the experimental one along with computation. Work is in progress to combine damping and friction.

► The difficulty with the proposed damping models is the calibration of evolution functions. If experimental data are not existing, a computation with a Rayleigh damping matrix can be performed to get a referenced solution. However, the consideration of experimental data improves the calibration and consequently the dynamic response.

As a global conclusion, table 3.20, already presented in chapter 3 conclusion (3.7.1), synthesises the best damping models for the SDOF and multi-fibre models of the studied reinforced concrete beam depending on the variable of interest. It demonstrates that the modelling of damping in reinforced concrete nonlinear analyses must be done carefully.

Perspectives

Work performed during this thesis and conclusions previously developed present new research challenges, so few perspectives are outlined. First, some developments about the elemental updated damping matrices are already in progress. In particular, the significant difficulty with the proposed updating methodology is the calibration of evolution functions because an objective is that the models stay explicit to avoid requiring iterative computations. A coupling of the identification method developed in Matlab with the structural computations in Cast3M has been developed to improve the function parameter identification. Then, the friction and damage variables are the most influential ones, but very different results are obtained with these two variables. So, improvements could be obtained by combining these two variables. In addition, the input signal amplitude was considered in SDOF analyses, so it could also be used to improve the multi-fibre models. However, increasing the number of variables for the damping matrix update increases the number of parameters to calibrate. That is why a performative methodology to identify these parameters is first necessary. Finally, few analyses were performed with the steel stress variable. These analyses should be enhanced because the steel stress in the linear range could be a stable indicator of the nonlinear state in concrete. Indeed, few models are proposed in the literature to link the steel stresses with the crack opening in reinforced concrete elements (Cheng, 1996; Ziari and Reza Kianoush, 2009; Walraven and Bigaj-van Vliet, 2010a; Walraven and Bigaj-van Vliet, 2010b).

Works could be developed on rebars to further study energy dissipation in reinforced concrete elements. During the experimental campaign, steel rebars stay linear, so that other experiments would be required to perform experimental validations. But, first numerically, a description of energies could be possible with nonlinear steel constitutive models and strong earthquake input signals. The steel/concrete interface could also be of interest. Papers proposed interface models for multi-fibre numerical modelling (F. Wang et al., 2007; Combescure and F. Wang, 2007; Richard, 2010). These models are nonlinear, and energy is dissipated at the interface. So, the decomposition of energy dissipations between rebars, concrete and steel/concrete interface could increase the understanding about dissipations in reinforced concrete elements under seismic excitations.

Finally, the amount of experimental data could be used for different works. First, other beams could be studied with classical damping formulations to characterise the dissipations depending on structural parameters like the concrete strength or the steel rebar compositions. Especially, the beam HA16-C1A was considered in all dynamic analyses presented in the thesis works, but two other beams had been calibrated with the quasi-static data. They could also validate the proposed method of the updated damping matrices. Finally, to improve the comparison between proposed updated damping matrices and the classical and modal ones, other parameters could be studied for the classical damping formulations (choice of modes with imposed frequencies, choice of viscous damping ratios, …) and modal formulations (damping evolution functions, internal variables used for updating, …). Indeed, not all damping model parameters have been studied in the numerical Benchmark, as discussed in chapter 2 conclusions (section 2.6.1).

Bibliography

A/S, S. V. S. (1999). *ARTeMIS Modal Software for Operational Modal Analysis*. NOVI Science Park.

Abbasi, M. and M. A. Moustafa (2019). "Effect of Damping Modelling and Characteristics on Seismic Vulnerability Assessment of Multi-Frame Bridges". In: *Journal of Earthquake Engineering* 25.8, pp. 1–28. ISSN: 1363-2469, 1559-808X. DOI: 10.1080/13632469.2019.1592791.

Adelaide, L., B. Richard, and C. Cremona (2011). "Un modèle efficace pour la prédiction du comportement d'éléments de structure en béton armé corrodés : application aux poutres de Rance". In: *GC' 2011, Innovation dans le génie civil au service de la réhabilitation*. Paris.

Adhikari, S. (2006). "Damping Modelling Using Generalized Proportional Damping". In: *Journal of Sound and Vibration* 293.1-2, pp. 156–170. ISSN: 0022460X. DOI: 10.1016/j.jsv.2005.09.034.

Adhikari, S. and J. Woodhouse (2001a). "Identification of Damping: Part 1, Viscous Damping". In: *Journal of Sound and Vibration* 243.1, pp. 43–61. ISSN: 0022460X. DOI: 10.1006/jsvi.2000.3391.

Adhikari, S. and J. Woodhouse (2001b). "Identification of Damping: Part 2, Non-Viscous Damping". In: *Journal of Sound and Vibration* 243.1, pp. 63–88. ISSN: 0022460X. DOI: 10.1006/jsvi.2000.3392.

Adhikari, S. and J. Woodhouse (2000). "Towards Identification of a General Model of Damping". In: *Proceedings of SPIE-The International Society for Optical Engineering* 4062, pp. 377–383.

Adhikari, S. (2000). "Damping Models for Structural Vibration". PhD thesis. Trinity College, Cambridge: University of Cambridge.

Advanced Structural Concepts, I. (2004). *Nonlin*. Blacksburg, Virginia, United-States.

Alarcon, A. (2015). *Code_Aster : Algorithmes d'intégration Temporelle de l'opérateur DYNA_TRAN_MODAL*. Manuel de Référence R5.06.04.

Amara, K. B. (1996). "Griffith Energy Balance Model for Crack-Growth Prediction in Reinforced Concrete". In: *Journal of Engineering Mechanics* 122.7, pp. 683–689. ISSN: 0733-9399, 1943-7889. DOI: 10.1061/(ASCE)0733-9399(1996)122:7(683).

Anajafi, H., R. A. Medina, and E. Santini-Bell (2019). "Effects of the Improper Modelling of Viscous Damping on the First-Mode and Higher-Mode Dominated Responses of Base-Isolated Buildings". In: *Earthquake Engineering & Structural Dynamics* 49.1, pp. 51–73. ISSN: 1096-9845. DOI: 10.1002/eqe.3223.

Arnold, C. (1985). *Pounding Damage at Hotel De Carlo*.

Baba-Hamed, F. Z. and L. Davenne (2020). "Effect of the Viscous Damping on the Seismic Response of Low-rise RC Frame Building". In: *Revista Facultad de Ingeniería Universidad de Antioquia* 96, pp. 32–43. ISSN: 2422-2844, 0120-6230. DOI: 10.17533/udea.redin.20191045.

Basista, M. and D. Gross (1998). "The Sliding Crack Model of Brittle Deformation: An Internal Variable Approach". In: *International Journal of Solids and Structures* 35.5-6, pp. 487–509. ISSN: 00207683. DOI: 10.1016/S0020-7683(97)00031-0.

Beredugo, Y. O. (1976). "Modal Analysis of Coupled Motion of Horizontally Excited Embedded Footings". In: *Earthquake Engineering & Structural Dynamics* 4.4, pp. 403–410. ISSN: 1096-9845. DOI: 10.1002/eqe.4290040407.

Bernal, D. (1994). "Viscous Damping in Inelastic Structural Response". In: *Journal of Structural Engineering* 120.4, pp. 1240–1254.

Bhattacharjee, S. S. and F. Ghrib (1995). "Effects of Viscous Damping Models in Earthquake Stress Analysis of Concrete Dams". In: *7th Canadian Conf. Earthquake Eng.* Montreal, Canada, pp. 341–348.

Bhattacharjee, S. S. and P. Léger (1993). "Seismic Cracking and Energy Dissipation in Concrete Gravity Dams". In: *Earthquake Engineering & Structural Dynamics* 22.11, pp. 991–1007. ISSN: 00988847, 10969845. DOI: 10.1002/eqe.4290221106.

Boyere, E. (2011). *Code_Aster: Modélisation de l'amortissement en dynamique linéaire.* Tech. rep. Fascicule r5.05, p. 13.

BRGM (2019). *Zonage Sismique de La France - Le Plan Séisme.* http://www.planseisme.fr/Zonage-sismique-de-la-France.html.

Caillerie, D., P. Kotronis, and R. Cybulski (2015). "A Timoshenko Finite Element Straight Beam with Internal Degrees of Freedom: A Timoshenko Finite Element Straight Beam with Internal Degrees of Freedom". In: *International Journal for Numerical and Analytical Methods in Geomechanics* 39.16, pp. 1753–1773. ISSN: 03639061. DOI: 10.1002/nag.2367.

Cao, M. S. et al. (2017). "Structural Damage Identification Using Damping: A Compendium of Uses and Features". In: *Smart Materials and Structures* 26.4, p. 043001. ISSN: 0964-1726, 1361-665X. DOI: 10.1088/1361-665X/aa550a.

Cao, Z. et al. (2020). "Evaluation Method of Damping Ratio Using Earthquake Records and Its Application in Dam Engineering". In: *17th WCorld Conference on Earthquake Engineering.* Vol. 2f-0007. Sendai, Japan.

Capdevielle, S. (2017). *Comportement Des Grands Ouvrages de Génie Civil - Modélisation Par Éléments Poutres Multifibres.* Giens, France.

Capdevielle, S. et al. (2016). "A Multifiber Beam Model Coupling Torsional Warping and Damage for Reinforced Concrete Structures". In: *European Journal of Environmental and Civil Engineering* 20.8, pp. 914–935. ISSN: 1964-8189. DOI: 10.1080/19648189.2015.1084384.

Carneiro, J. et al. (2006). "The Use of Pseudo-Dynamic Method in the Evaluation of Damping Characteristics in Reinforced Concrete Beams Having Variable Bending Stiffness". In: *Mechanics Research Communications* 33.5, pp. 601–613. ISSN: 00936413. DOI: 10.1016/j.mechrescom.2005.05.010.

Carr, A. J. et al. (2017). "Damping Models for Inelastic Time History Analysis: A Proposed Modelling Approach". In: *16th World Conference on Earthquake, 16WCEE 2017.* Santiago, Chile.

Casas, J. R. and A. C. Aparicio (1994). "Structural Damage Identification from Dynamic-test Data". In: *Journal of Structural Engineering* 120.8, pp. 2437–2450. DOI: 10.1061/(ASCE)0733-9445(1994)120:8(2437).

Caughey, T. K. (1960). "Classical Normal Modes in Damped Linear Dynamic Systems". In: *Journal of Applied Mechanics* 27.2, pp. 269–271. ISSN: 0021-8936, 1528-9036. DOI: 10.1115/1.3643949.

Caughey, T. K. and M. E. J. O'Kelly (1965a). "Classical Normal Modes in Damped Linear Dynamic Systems". In: *Journal of Applied Mechanics* 32.3, pp. 583–588. ISSN: 0021-8936, 1528-9036. DOI: 10.1115/1.3627262.

Caughey, T. K. and M. E. J. O'Kelly (1965b). "Classical Normal Modes in Damped Linear Dynamic Systems". In: *Journal of Applied Mechanics* 32.3, pp. 583–588. ISSN: 0021-8936, 1528-9036. DOI: 10.1115/1.3627262.

Caughey, T. and A. Vijayaraghavan (1970). "Free and Forced Oscillations of a Dynamic System with "Linear Hysteretic Damping" (Non-Linear Theory)". In: *International Journal of Non-Linear Mechanics* 5.3, pp. 533–555. ISSN: 00207462. DOI: 10.1016/0020-7462(70)90015-6.

Celebi, M. et al. (2020). "Response of the Tallest California Building during the Mw7.1 July 5, 2019 Ridgecrest, California Earthquake". In: *17th World Conference on Earthquake Engineering.* Vol. 2c-0020. Sendai, Japan.

Chambreuil, C. et al. (2021). "Seismic Energy Dissipation in Reinforced Concrete Beam: Investigating Damping Formulations". In: *European Journal of Environmental and Civil Engineering*, pp. 1–27. ISSN: 1964-8189, 2116-7214. DOI: 10.1080/19648189.2021.2009380.

Charney, F. A. (2005). "Consequences of Using Rayleigh Damping in Inelastic Response History Analysis". In: *Congreso Chileno de Sismología e Ingeniería Antisísmica IX Jornadas*. Vol. A10-17. Concepción, Chile.

Charney, F. A. (2008). "Unintended Consequences of Modelling Damping in Structures". In: *Journal of Structural Engineering* 134.4, pp. 581–592. ISSN: 0733-9445, 1943-541X. DOI: 10.1061/(ASCE) 0733-9445(2008)134:4(581).

Charney, F. et al. (2017). "Modeling Inherent Damping in Nonlinear Dynamic Analysis". In: *16th World Conference on Earthquake Engineering*. Santiago, Chile.

Cheng, R. (1996). *Design of Concrete Structures for Retaining Aqueous Liquids - Design Tables to BS 8007*. Tech. rep. FIStructE.

Chopra, A. K. (1995). *Dynamics of Structures: Theory and Applications to Earthquake Engineering*. Prentice Hall. ISBN: 0-13-855231-2.

Chopra, A. K. and F. McKenna (2017). "Modeling Viscous Damping in Nonlinear Response History Analysis of Buildings". In: *16th World Conference on Earthquake Engineering*. Santiago, Chile.

Chopra, A. K. and F. McKenna (2016). "Modeling Viscous Damping in Nonlinear Response History Analysis of Buildings for Earthquake Excitation: Modal Damping". In: *Earthquake Engineering & Structural Dynamics* 45.2, pp. 193–211. ISSN: 00988847. DOI: 10.1002/eqe.2622.

Chowdhury, S. H., Y. C. Loo, and S. Fragomeni (2000). "Damping Formulae for Reinforced and Partially Prestressed Concrete Beams". In: *Advances in Structural Engineering* 3.4, pp. 327–335. ISSN: 1369-4332, 2048-4011. DOI: 10.1260/1369433001502256.

Chrisp, D. J. (1980). *Damping Models for Inelastic Structures*. Master Thesis. University of Canterbury.

Clough, R. W. and S. Mojtahedi (1976). "Earthquake Response Analysis Considering Non-Proportional Damping". In: *Earthquake Engineering & Structural Dynamics* 4.5, pp. 489–496. ISSN: 00988847, 10969845. DOI: 10.1002/eqe.4290040506.

Combescure, D. and F. Wang (2007). *Assessment of Existing RC Structures under Severe Dynamic Loading Using Non Linear Modelling*. CONSEC 07, Tours, France.

Correia, A. A., J. P. Almeida, and R. Pinho (2013). "Seismic Energy Dissipation in Inelastic Frames: Understanding State-of-the-Practice Damping Models". In: *Structural Engineering International* 23.2, pp. 148–158. ISSN: 1016-8664, 1683-0350. DOI: 10.2749/101686613X13439149157001.

Crambuer, R., B. Richard, et al. (2012). "Experimental Characterization and Modeling of Energy Dissipation in Reinforced Concrete Beams Subjected to Cyclic Loading". In: *15th World Conference on Earthquake Engineering*. Lisboa, Portugal.

Crambuer, R., B. Richard, et al. (2013). "Experimental Characterization and Modeling of Energy Dissipation in Reinforced Concrete Beams Subjected to Cyclic Loading". In: *Engineering Structures* 56, pp. 919–934. ISSN: 01410296. DOI: 10.1016/j.engstruct.2013.06.024.

Crambuer, R. (2013). "Contribution à l'identification de l'amortissement : approches expérimentales et numériques". PhD thesis. Cachan, France: École normale supérieure.

Crandall, S. H. (1991). "The Hysteretic Damping Model in Vibration Theory". In: *Proceedings of the Institution of Mechanical Engineers, Part C: Mechanical Engineering Science* 205.1, pp. 23–28. ISSN: 0263-7154, 2058-3397. DOI: 10.1243/PIME_PROC_1991_205_086_02.

Crandall, S. (1970). "The Role of Damping in Vibration Theory". In: *Journal of Sound and Vibration* 11.1, pp. 3–18. ISSN: 0022460X. DOI: 10.1016/S0022-460X(70)80105-5.

Crouse, C. B. and J. McGuire (2001). "Energy Dissipation in Soil-Structure Interaction". In: *Earthquake Spectra* 17.2, pp. 235–259. ISSN: 8755-2930. DOI: 10.1193/1.1586174.

Cruz, C. and E. Miranda (2019). "Reliability of Damping Ratios Inferred from the Seismic Response of Buildings". In: *Engineering Structures* 184, pp. 355–368. ISSN: 01410296. DOI: `10.1016/j.engstruct.2019.01.056`.

CSI (2011). *User Guide PERFORM-3D - Nonlinear Analysis and Performance Assessment for 3D Structures*. User Guide ISO PER053111M1. Berkeley, California, USA: Computers & Structures inc.

Daneshjoo, F. and A. Gharighoran (2008). "Experimental and Theoretical Dynamic System Identification of Damaged RC Beams". In: *Electronic Journal of Structural Engineering* 8, pp. 29–39.

Daneshjoo, F. and A. Gharighoran (2006). "Experimental Investigation of Damping in Cracked Concrete Beams Usable in Bridges (Beam-Slab)". In: *International Conference on Bridge Engineering*. Hong Kong, China. DOI: `10.13140/RG.2.1.2997.2567`.

Dao, N. D. and K. L. Ryan (2014). "Computational Simulation of a Full-Scale, Fixed-Base, and Isolated-Base Steel Moment Frame Building Tested at E-Defense". In: *Journal of Structural Engineering* 140.8. ISSN: 0733-9445, 1943-541X. DOI: `10.1061/(ASCE)ST.1943-541X.0000922`.

Demarie, G. V. and D. Sabia (2011). "Non-Linear Damping and Frequency Identification in a Progressively Damaged R.C. Element". In: *Experimental Mechanics* 51.2, pp. 229–245. ISSN: 0014-4851, 1741-2765. DOI: `10.1007/s11340-010-9360-4`.

Desmorat, R., F. Ragueneau, and H. Pham (2007). "Continuum Damage Mechanics for Hysteresis and Fatigue of Quasi-Brittle Materials and Structures". In: *International Journal for Numerical and Analytical Methods in Geomechanics* 31.2, pp. 307–329. ISSN: 03639061, 10969853. DOI: `10.1002/nag.532`.

Dhakal, R. P. and K. Maekawa (2001). "Post-Peak Cyclic Response Analysis and Energy Dissipation Capacity of RC Columns." In: *Doboku Gakkai Ronbunshu* 2001.676, pp. 117–133. ISSN: 1882-7187, 0289-7806. DOI: `10.2208/jscej.2001.676_117`.

Dolev, S. and (2008). *The Tuned Mass Damper in Taipei 101*.

Dragon, A., D. Halm, and T. Désoyer (1998). "Anisotropic Damage in Quasi-Brittle Solids: Modelling, Computational Issues and Applications". In: *Computer Methods in Applied Mechanics and Engineering* 183.2000, pp. 331–352.

Dubé, J.-F. (1994). "Modélisation simplifiée et comportement visco-endommageable des structures en béton : applications aux séismes et aux choc des ouvrages en béton armé". PhD thesis. Cachan, France: École normale supérieure.

Dubé, J.-F., G. Pijaudier-Cabot, and C. L. Borderie (1996). "Rate Dependent Damage Model for Concrete in Dynamics". In: *Journal of Engineering Mechanics* 122.10, pp. 939–947. ISSN: 0733-9399, 1943-7889. DOI: `10.1061/(ASCE)0733-9399(1996)122:10(939)`.

Dufour, F. (1998). *Modélisation Du Comportement Dynamique d'une Structure à Murs Porteurs En Béton Armé Renforcée à l'aide de Tissus à Fibres de Carbones*. Master of Science. CEA Saclay, ENS Cachan.

Dunkerley, S. (1893). "On the Whirling and Vibration of Shafts." In: *Proceedings of the Royal Society of London* 54, pp. 365–370. ISSN: 0370-1662.

Dutta, S. C. and R. Roy (2002). "A Critical Review on Idealization and Modelling for Interaction among Soil–Foundation–Structure System". In: *Computers & Structures* 80.20-21, pp. 1579–1594. ISSN: 00457949. DOI: `10.1016/S0045-7949(02)00115-3`.

Dwairi, H. M., M. J. Kowalsky, and J. M. Nau (2007). "Equivalent Damping in Support of Direct Displacement-Based Design". In: *Journal of Earthquake Engineering* 11.4, pp. 512–530. ISSN: 1363-2469, 1559-808X. DOI: `10.1080/13632460601033884`.

Ele, C. (2017). *Tremblement de Terre : L'impact Des Interactions Sol-Structure Sur Les Habitations et Ouvrages d'art*.

Eligehausen, R., E. P. Popov, and V. V. Bertero (1982). "Local Bond Stress-Slip Relationships of Deformed Bars under Generalized Excitations". In: *7th European Conference on Earthquake Engineering*. Vol. 4. Athens, Greece. DOI: `http://dx.doi.org/10.18419/opus-415`.

Elmenshawi, A. and T. Brown (2010). "Hysteretic Energy and Damping Capacity of Flexural Elements Constructed with Different Concrete Strengths". In: *Engineering Structures* 32.1, pp. 297–305. ISSN: 01410296. DOI: 10.1016/j.engstruct.2009.09.016.

Elmenshawi, A., M. Sorour, et al. (2010). "Damping Mechanisms and Damping Ratios in Vibrating Unreinforced Stone Masonry". In: *Engineering Structures* 32.10, pp. 3269–3278. ISSN: 01410296. DOI: 10.1016/j.engstruct.2010.06.016.

Enerzine.com (2011). *France : 5 centrales nucléaires en zones sismiques 3.*

Feng, M. Q. (2007). "Recent Advances in Structural Health Monitoring". In: *Journal of the Korean Society for Nondestructive Testing* 27.6, pp. 483–500. ISSN: 1225-7842.

Franchetti, P., C. Modena, and M. Feng (2009). "Nonlinear Damping Identification in Precast Prestressed Reinforced Concrete Beams". In: *Computer-Aided Civil and Infrastructure Engineering* 24.8, pp. 577–592. ISSN: 10939687, 14678667. DOI: 10.1111/j.1467-8667.2009.00612.x.

Frazer, R. A., W. J. Duncan, and A. R. Collar (1938). *Elementary Matrices and Some Applications to Dynamics and Differential Equations.* Cambridge, England: Cambridge University Press.

Frizzarin, M. et al. (2008). "Damage Detection Based on Damping Analysis of Ambient Vibration Data". In: *Structural Control and Health Monitoring* 17.4, pp. 368–385. ISSN: 15452255, 15452263. DOI: 10.1002/stc.296.

Ghavamian, S. (1998). "Méthode simplifiée pour la simulation du comportement sismique des structures en béton armé : traitement des effets de l'élancement et estimateur d'erreurs". PhD thesis. Cachan, France: École normale supérieure.

Goel, R. K. (2001). "Simplified Analysis of Asymmetric Structures with Supplemental Damping". In: *Earthquake Engineering & Structural Dynamics* 30.9, pp. 1399–1416. ISSN: 0098-8847, 1096-9845. DOI: 10.1002/eqe.77.

Grammatikou, S., M. N. Fardis, and D. Biskinis (2019). "Energy Dissipation Models for RC Members and Structures". In: *Earthquake Engineering & Structural Dynamics* 48.3, pp. 287–305. ISSN: 0098-8847, 1096-9845. DOI: 10.1002/eqe.3136.

Grange, S., J. Mazars, and P. Kotronis (2007). "Analyse sismique du comportement d'une structure de 7 étages à échelle 1 en béton armé : benchmark international NEES". In: *Congrès français de mécanique.* Courbevoie, France.

Guedes, J., P. Pegon, and A. Pinto (1994). *A Fibre/Timoshenko Beam Element in Castem 2000.* Rapport Technique Nr. I.94.31. I-21020 ISPRA (VA) Italy: Applied Mechanics Unit, Institute for Safety Technology, Joint Research Centre, Commission of the European Communities, p. 55.

Gulkan, P. and M. A. Sozen (1974). "Inelastic Responses of Reinforced Concrete Structure to Earthquake Motions". In: *Journal Proceedings* 71.12, pp. 604–610. ISSN: 0002-8061. DOI: 10.14359/7110.

Gutierrez Soto, M. and H. Adeli (2013). "Tuned Mass Dampers". In: *Archives of Computational Methods in Engineering* 20.4, pp. 419–431. ISSN: 1886-1784. DOI: 10.1007/s11831-013-9091-7.

Hall, J. F. (1988). "The Dynamic and Earthquake Behaviour of Concrete Dams: Review of Experimental Behaviour and Observational Evidence". In: *Soil Dynamics and Earthquake Engineering* 7.2, pp. 58–121. ISSN: 02677261. DOI: 10.1016/S0267-7261(88)80001-0.

Hall, J. F. (2006). "Problems Encountered from the Use (or Misuse) of Rayleigh Damping". In: *Earthquake Engineering & Structural Dynamics* 35.5, pp. 525–545. ISSN: 0098-8847, 1096-9845. DOI: 10.1002/eqe.541.

Hall, J. F. (2018). "Performance of Viscous Damping in Inelastic Seismic Analysis of Moment-Frame Buildings". In: *Earthquake Engineering & Structural Dynamics* 47.14, pp. 2756–2776. ISSN: 00988847. DOI: 10.1002/eqe.3104.

Halm, D. and A. Dragon (1998). "An Anisotropic Model of Damage and Frictional Sliding for Brittle Materials". In: *European Journal of Mechanics - A/Solids* 17.3, pp. 439–460. ISSN: 09977538. DOI: 10.1016/S0997-7538(98)80054-5.

Haquet, C. (2011). *Cinq centrales nucléaires françaises sont dans des zones à risque.* https://lexpansion.lexpress.fr/actualite-economique/cinq-centrales-nucleaires-francaises-sont-dans-des-zones-a-risque_1432975.html.

Hasselman, T. K. (1976). "Modal Coupling in Lightly Damped Structures". In: *AIAA Journal* 14.11, pp. 1627–1628. ISSN: 0001-1452, 1533-385X. DOI: 10.2514/3.7259.

Heitz, T., C. Giry, et al. (2019). "Identification of an Equivalent Viscous Damping Function Depending on Engineering Demand Parameters". In: *Engineering Structures* 188, pp. 637–649. ISSN: 01410296. DOI: 10.1016/j.engstruct.2019.03.058.

Heitz, T., A. Le Maoult, et al. (2018). "Dissipations in Reinforced Concrete Components: Static and Dynamic Experimental Identification Strategy". In: *Engineering Structures* 163, pp. 436–451. ISSN: 01410296. DOI: 10.1016/j.engstruct.2018.02.065.

Heitz, T. (2017). "Nonlinear Local Behaviours and Numerical Modelling of Damping in Civil Engineering Structures in Dynamic". PhD thesis. Cachan, France: Université Paris-Saclay, École Normale Supérieure de Cachan.

Heitz, T., C. Giry, et al. (2017). "How Are the Equivalent Damping Ratios Modified by Nonlinear Engineering Demand Parameters?" In: *6th ECCOMAS Thematic Conference on Computational Methods in Structural Dynamics and Earthquake Engineering (COMPDYN)*. Rhodes, Greece, pp. 15–17.

Heitz, T., B. Richard, et al. (2017). "Damping Identification and Quantification: Experimental Evidences and First Numerical Results". In: *16th World Conference on Earthquake Engineering*. Santiago, Chile.

Hillerborg, A., M. Modéer, and P.-E. Petersson (1976). "Analysis of Crack Formation and Crack Growth in Concrete by Means of Fracture Mechanics and Finite Elements". In: *Cement and Concrete Research* 6.6, pp. 773–781. ISSN: 00088846. DOI: 10.1016/0008-8846(76)90007-7.

Institut-Seism (2021). *Interaction Sol-Structure et Effets de Site.* https://www.institut-seism.fr/recherche/interaction-sol-structure-et-effets-de-site/. Intranet.

Iwan, W. D. and N. C. Gates (1979). "The Effective Period and Damping of a Class of Hysteretic Structures". In: *Earthquake Engineering & Structural Dynamics* 7.3, pp. 199–211. ISSN: 00988847, 10969845. DOI: 10.1002/eqe.4290070302.

Jacobsen, L. S. (1960). "Damping in Composite Structures". In: *II WCEE, Tokyo, 1960*.

Jehel, P. (2009). "Modélisation numérique des phénomènes d'amortissement par dissipation d'énergie matérielle dans les structures de type portique en béton armé sous séisme". PhD thesis. Cachan, France: École Normale Supérieure de Cachan.

Jehel, P., P. Léger, and A. Ibrahimbegovic (2014). "Initial versus Tangent Stiffness-Based Rayleigh Damping in Inelastic Time History Seismic Analyses". In: *Earthquake Engineering & Structural Dynamics* 43.3, pp. 467–484. ISSN: 1096-9845. DOI: 10.1002/eqe.2357.

Jones, R. and G. B. Welch (1967). *The Damping Properties of Plain Concrete: Effect of Composition and Relations with Elasticity and Strength.* Tech. rep. 00212829. London, UK: Ministry of Transport.

Karaton, M., Ö. F. Osmanlı, and M. E. Gülşan (2021a). "Investigation of Uncertainties in Nonlinear Seismic Analysis of the Reinforced Concrete Shear Walls". In: *International Journal of Civil Engineering* 19.3, pp. 301–318. ISSN: 1735-0522, 2383-3874. DOI: 10.1007/s40999-020-00567-8.

Karaton, M., Ö. F. Osmanlı, and M. E. Gülşan (2021b). "Numerical Simulation of Reinforced Concrete Shear Walls Using Force-Based Fiber Element Method: Effect of Damping Type and Damping Ratio". In: *Bulletin of Earthquake Engineering* 19.14, pp. 6129–6156. ISSN: 1570-761X, 1573-1456. DOI: 10.1007/s10518-021-01221-x.

Kareem, A. and K. Gurley (1996). "Damping in Structures: Its Evaluation and Treatment of Uncertainty". In: *Journal of wind engineering and industrial aerodynamics* 59.2, pp. 131–157.

Kareem, A., T. Kijewski, and Y. Tamura (1999). "Mitigation of Motions of Tall Buildings with Specific Examples of Recent Applications". In: *Wind and structures* 2.3, pp. 201–251.

Karnovsky, I. A. and O. I. Lebed (2000). *Formulas for Structural Dynamics: Tables, Graphs, and Solutions.* McGraw Hill Professional. McGraw Hill Professional.

Kelly, J. M., R. I. Skinner, and A. J. Heine (1972). "Mechanisms of Energy Absorption in Special Devices for Use in Earthquake Resistant Structures". In: *Society for Earthquake Engineering* 5.3, pp. 63–88.

Kimball, A. L. and D. E. Lovell (1927). "Internal Friction in Solids". In: *Physical Review* 30.6, pp. 948–959. ISSN: 0031-899X. DOI: 10.1103/PhysRev.30.948.

Kotronis, P. (2000). "Cisaillement dynamique de murs en béton armé. Modèles simplifiés 2D et 3D". PhD thesis. Cachan, France: École Normale Supérieure de Cachan.

Kotronis, P. (2008). "Stratégies de modélisation de structures en béton soumises à des chargements sévères". PhD thesis. Grenoble, France: Université Joseph-Fourier, Grenoble I.

Kotronis, P., L. Davenne, and J. Mazars (2004). "Poutre 3D multifibre Timoshenko pour la modélisation des structures en béton armé soumises à des chargements sévères". In: *Revue française de génie civil* 8.2/3, pp. 329–343.

Kowalsky, M. J., M. J. N. Priestley, and G. A. MacRae (1995). "Displacement-Based Design of RC Bridge Columns in Seismic Regions". In: *Earthquake Engineering & Structural Dynamics* 24.12, pp. 1623–1643. ISSN: 00988847, 10969845. DOI: 10.1002/eqe.4290241206.

Kumar, M. and A. S. Whittaker (2019). "Numerical Issues in Developing In-Structure Response Spectra for Seismically Isolated Nuclear Structures". In: *25th Conference on Structural Mechanics in Reactor Technology*. Charlotte, NC, USA, p. 13.

Kumar, S. and M. Kumar (2021). "Damping Implementation Issues for In-structure Response Estimation of Seismically Isolated Nuclear Structures". In: *Earthquake Engineering & Structural Dynamics*, eqe.3436. ISSN: 0098-8847, 1096-9845. DOI: 10.1002/eqe.3436.

La Borderie, C. (1991). "Phénomènes unilatéraux dans un matériau endommageable : Modélisation et application à l'analyse de structures en béton." PhD thesis. Paris, France: Université Paris 6.

Langlade, T. et al. (2021). "Modelling of Earthquake-Induced Pounding between Adjacent Structures with a Non-Smooth Contact Dynamics Method". In: *Engineering Structures* 241, p. 112426. ISSN: 01410296. DOI: 10.1016/j.engstruct.2021.112426.

Lanzi, A. and J. E. Luco (2018). "Elastic Velocity Damping Model for Inelastic Structures". In: *Journal of Structural Engineering* 144.6, p. 04018065. ISSN: 0733-9445, 1943-541X. DOI: 10.1061/(ASCE)ST.1943-541X.0002050.

Lázaro, M. (2016). "Eigensolutions of Non-Proportionally Damped Systems Based on Continuous Damping Sensitivity". In: *Journal of Sound and Vibration* 363, pp. 532–544. ISSN: 0022460X. DOI: 10.1016/j.jsv.2015.10.014.

Le Corvec, V. (2012). "Nonlinear 3D Frame Element with Multi-Axial Coupling under Consideration of Local Effects". PhD thesis. Berkeley, California, United States: University of California, Berkeley.

Lee, C.-L. (2019). "A Novel Damping Model for Earthquake Induced Structural Response Simulation". In: *2019 Pacific Conference on Earthquake Engineering*. Auckland/Wellington, New Zealand.

Lee, C.-L. (2020). "Proportional Viscous Damping Model for Matching Damping Ratios". In: *Engineering Structures* 207, p. 110178. ISSN: 01410296. DOI: 10.1016/j.engstruct.2020.110178.

Lee, C.-L. (2022). "Type 4 Bell-Shaped Proportional Damping Model and Energy Dissipation for Structures with Inelastic and Softening Response". In: *Computers & Structures* 258, p. 106663. ISSN: 00457949. DOI: 10.1016/j.compstruc.2021.106663.

Lee, S. et al. (2011). "Equivalent Modal Damping of Short-Span Bridges Subjected to Strong Motion". In: *Journal of Bridge Engineering* 16.2, pp. 316–323. ISSN: 1084-0702, 1943-5592. DOI: 10.1061/(ASCE)BE.1943-5592.0000149.

Léger, P. and S. Bhattacharjee (1994). "Energy Concepts in Seismic Fracture Analysis of Concrete Gravity Dams". In: *International Workshop on Dam Fracture*. Chambery, France, pp. 231–240.

Léger, P. and S. Dussault (1992). "Seismic-energy Dissipation in MDOF Structures". In: *Journal of Structural Engineering* 118.5, pp. 1251–1269. ISSN: 0733-9445, 1943-541X. DOI: 10.1061/(ASCE)0733-9445(1992)118:5(1251).

Levy, C. (1991). "An Iterative Technique Based on the Dunkerley Method for Determining the Natural Frequencies of Vibrating Systems". In: *Journal of Sound and Vibration* 150.1, pp. 111–118. ISSN: 0022460X. DOI: 10.1016/0022-460X(91)90405-9.

Livaoğlu, R. and A. Doğangün (2006). "Simplified Seismic Analysis Procedures for Elevated Tanks Considering Fluid–Structure–Soil Interaction". In: *Journal of Fluids and Structures* 22.3, pp. 421–439. ISSN: 08899746. DOI: 10.1016/j.jfluidstructs.2005.12.004.

Lou, M. et al. (2011). "Structure–Soil–Structure Interaction: Literature Review". In: *Soil Dynamics and Earthquake Engineering* 31.12, pp. 1724–1731. ISSN: 02677261. DOI: 10.1016/j.soildyn.2011.07.008.

Low, K. (2000). "A Modified Dunkerley Formula for Eigenfrequencies of Beams Carrying Concentrated Masses". In: *International Journal of Mechanical Sciences* 42.7, pp. 1287–1305. ISSN: 00207403. DOI: 10.1016/S0020-7403(99)00049-1.

Luco, J. E. (2008). "A Note on Classical Damping Matrices". In: *Earthquake Engineering & Structural Dynamics* 37.4, pp. 615–626. ISSN: 00988847, 10969845. DOI: 10.1002/eqe.776.

Luco, J. E. and A. Lanzi (2017). "A New Inherent Damping Model for Inelastic Time-History Analyses". In: *Earthquake Engineering & Structural Dynamics* 46.12, pp. 1919–1939. ISSN: 00988847. DOI: 10.1002/eqe.2886.

Luco, J. E. and A. Lanzi (2019). "Numerical Artifacts Associated with Rayleigh and Modal Damping Models of Inelastic Structures with Massless Coordinates". In: *Earthquake Engineering & Structural Dynamics* 48.13, pp. 1491–1507. ISSN: 0098-8847, 1096-9845. DOI: 10.1002/eqe.3210.

Luu, H. Q. et al. (2011). "Structural Dynamics of Slender Ductile Reinforced Concrete Shear Walls". In: *8th International Conference on Structural Dynamics, EURODYN*. Leuven, Belgium, p. 8.

Luu, H. et al. (2013). "Numerical Modelling of Slender Reinforced Concrete Shear Wall Shaking Table Tests under High-Frequency Ground Motions". In: *Journal of Earthquake Engineering* 17.4, pp. 517–542. ISSN: 1363-2469, 1559-808X. DOI: 10.1080/13632469.2013.767759.

Mander, J. B., M. J. N. Priestley, and R. Park (1988). "Theoretical Stress-strain Model for Confined Concrete". In: *Journal of Structural Engineering* 114.8, pp. 1804–1826. ISSN: 0733-9445, 1943-541X. DOI: 10.1061/(ASCE)0733-9445(1988)114:8(1804).

Martinez, D. R. and M. J. Kowalsky (2020). "Impact of Viscous Damping Model Assumptions on the Nonlinear Analysis of Multi-Span Bridges". In: *17th World Conference on Earthquake Engineering*. Vol. 2d-0029. Sendai, Japan.

MathWorks (2021). *Constrained Nonlinear Optimization Algorithms*.

Mazars, J., P. Kotronis, et al. (2006). "Using Multifiber Beams to Account for Shear and Torsion". In: *Computer Methods in Applied Mechanics and Engineering* 195.52, pp. 7264–7281. ISSN: 00457825. DOI: 10.1016/j.cma.2005.05.053.

Mazars, J., X. H. Nguyen, et al. (2005). *Étude Sur Le Fonctionnement Sismique de Structures à Murs à Cellules Contreventées*. Research Report Contrat N° 04 MGC 5 07, Org. Rapport final (Novembre) - Contrat DRAST/ Mission Génie Civil, 2005. 3S-R.

Meirovitch, L. (1967). *Analytical Methods in Vibrations*. New York, United States: Macmillan.

Miranda, E. and C. Cruz (2020). "Towards Improved Modeling of Damping for Seismic Analysis of Buildings". In: *17th World Conference on Earthquake Engineering*. Vol. 2b-0148. Sendai, Japan.

Morzfeld, M., F. Ma, and N. Ajavakom (2008). "On the Decoupling Approximation in Damped Linear Systems". In: *Journal of Vibration and Control* 14.12, pp. 1869–1884. ISSN: 1077-5463, 1741-2986. DOI: 10.1177/1077546308091212.

Moulin, S. (2010). *Code_Aster : Élément de Poutre Multifibre (Droite)*. Manuel de Référence R3.08.08.

Muravskii, G. (2004). "On Frequency Independent Damping". In: *Journal of Sound and Vibration* 274.3-5, pp. 653–668. ISSN: 0022460X. DOI: 10.1016/j.jsv.2003.05.012.

Nakamura, N. (2017). "Time History Response Analysis Using Extended Rayleigh Damping Model". In: *Procedia Engineering* 199, pp. 1472–1477. ISSN: 18777058. DOI: 10.1016/j.proeng.2017.09.408.

Nakamura, N. (2019). "Application of Causal Hysteretic Damping Model to Nonlinear Seismic Response Analysis of Super High-Rise Building: Substitution for Viscous Damping Including Tangent Stiffness Proportional Damping". In: *Journal of Structural and Construction Engineering (Transactions of AIJ)* 84.759, pp. 597–607. ISSN: 1340-4202, 1881-8153. DOI: 10.3130/aijs.84.597.

NF EN 1992-1-1 (2005). *Eurocode 2 - Calcul des structures en béton - Partie 1.1 : Règles générales et règles pour les bâtiments.* Norme européenne - Norme française NF EN 1992-1-1. AFNOR, p. 211.

NF EN 1998-1 (2005). *Eurocode 8 - Calcul des structures pour leur résistance aux séismes - Partie 1 : Règles générales, actions sismiques et règles pour les bâtiments.* Norme européenne - Norme française NF EN 1998-1. AFNOR, p. 186.

Ni, Y. et al. (2019). "Development of Practical Method for Incorporation of Elemental Damping in Inelastic Dynamic Time History Analysis". In: *2019 Pacific Conference on Earthquake Engineering.* Auckland/Wellington, New Zealand.

Nmai, C. K. and D. Darwin (1984). *Cyclic Behavior of Lightly Reinforced Concrete Beams.* Research Report SM Report No.12. University of Kansas, Lawrence, Kansas: The National Science Foundation.

Ohno, T. and T. Nishioka (1984). "An Experimental Study on Energy Absorption Capacity of Columns in Reinforced Concrete Structures." In: *Doboku Gakkai Ronbunshu* 350, pp. 23–33. ISSN: 1882-7187, 0289-7806. DOI: 10.2208/jscej.1984.350_23.

Olmos, B. A. and J. M. Roesset (2009). "Analytical Evaluation of the Accuracy of the Half-Power Bandwidth Method to Estimate Damping Ratios in a Structure". In: *4th International Conference on Structural Health Monitoring of Intelligent Infrastructure.* Zurich, Switzerland.

Orak, S. (2000). "Investigation of Vibration Damping on Polymer Concrete with Polyester Resin". In: *Cement and Concrete Research* 30.2, pp. 171–174. ISSN: 00088846. DOI: 10.1016/S0008-8846(99)00225-2.

Ozdemir, Z., M. Souli, and Y. Fahjan (2010). "Application of Nonlinear Fluid–Structure Interaction Methods to Seismic Analysis of Anchored and Unanchored Tanks". In: *Engineering Structures* 32.2, pp. 409–423. ISSN: 01410296. DOI: 10.1016/j.engstruct.2009.10.004.

Pant, D. R., A. C. Wijeyewickrema, and M. A. ElGawady (2013). "Appropriate Viscous Damping for Nonlinear Time-History Analysis of Base-Isolated Reinforced Concrete Buildings: Viscous Damping for Time-History Analysis of Base-Isolated Buildings". In: *Earthquake Engineering & Structural Dynamics* 42.15, pp. 2321–2339. ISSN: 00988847. DOI: 10.1002/eqe.2328.

Papagiannopoulos, G. A. and D. E. Beskos (2009). "On a Modal Damping Identification Model for Non-Classically Damped Linear Building Structures Subjected to Earthquakes". In: *Soil Dynamics and Earthquake Engineering* 29.3, pp. 583–589. ISSN: 02677261. DOI: 10.1016/j.soildyn.2008.10.005.

Papagiannopoulos, G. A. and G. D. Hatzigeorgiou (2011). "On the Use of the Half-Power Bandwidth Method to Estimate Damping in Building Structures". In: *Soil Dynamics and Earthquake Engineering* 31.7, pp. 1075–1079. ISSN: 02677261. DOI: 10.1016/j.soildyn.2011.02.007.

Pegon, P. (1994). *A Timoshenko Simple Beam Element in Castem 2000.* Rapport Technique. I-21020 ISPRA (VA) Italy: Applied Mechanics Unit, Institute for Safety Technology, Joint Research Centre, Commission of the European Communities, p. 19.

Penzien, J. (1964). "Damping Characteristics of Prestressed Concrete". In: *Journal Proceedings* 61.9, pp. 1125–1148. ISSN: 0002-8061. DOI: 10.14359/7824.

Petrini, L. et al. (2008). "Experimental Verification of Viscous Damping Modelling for Inelastic Time History Analyzes". In: *Journal of Earthquake Engineering* 12.1, pp. 125–145. ISSN: 1363-2469, 1559-808X. DOI: 10.1080/13632460801925822.

Pipes, L. A. (1963). *Matrix Methods for Engineering*. Englewood Cliffs, New Jersey, United States: Prentice-Hall.

Polycarpou, P. C. and P. Komodromos (2012). "A Methodology for an Efficient Three-Dimensional (3D) Numerical Simulation of Earthquake-Induced Pounding of Buildings". In: *15th World Conference on Earthquake Engineering*. Lisboa, Portugal.

Priestley, M. J. N., G. M. Calvi, and M. J. Kowalsky (2007). "Direct Displacement-Based Seismic Design of Structures". In: *2007 New-Zealand Society for Earthquake Engineering Conference*. Palmerston North, New Zealand.

Priestley, M. J. N. and D. N. Grant (2005). "Viscous Damping in Seismic Design and Analysis". In: *Journal of Earthquake Engineering* 09.2, pp. 229–255. ISSN: 1363-2469. DOI: 10.1142/S1363246905002365.

Puthanpurayil, A. M., A. J. Carr, and R. P. Dhakal (2018). "Application of Nonlocal Elasticity Continuum Damping Models in Nonlinear Dynamic Analysis". In: *Bulletin of Earthquake Engineering* 16.12, pp. 6269–6297. ISSN: 1570-761X, 1573-1456. DOI: 10.1007/s10518-018-0412-y.

Puthanpurayil, A. M., O. Lavan, et al. (2016). "Elemental Damping Formulation: An Alternative Modelling of Inherent Damping in Nonlinear Dynamic Analysis". In: *Bulletin of Earthquake Engineering* 14.8, pp. 2405–2434. ISSN: 1570-761X, 1573-1456. DOI: 10.1007/s10518-016-9904-9.

Qian, X., A. K. Chopra, and F. McKenna (2020a). "Adequacy of Linear Viscous Damping Models for Nonlinear Response History Analysis". In: *17th World Conference on Earthquake Engineering*. Vol. 2c-0035. Sendai, Japan.

Qian, X., A. K. Chopra, and F. McKenna (2020b). "Modelling Viscous Damping in Nonlinear Response History Analysis of Steel Moment-frame Buildings: Design-plus Ground Motions". In: *Earthquake Engineering & Structural Dynamics*. ISSN: 0098-8847, 1096-9845. DOI: 10.1002/eqe.3358.

Ragueneau, F., C. La Borderie, and J. Mazars (2000). "Damage Model for Concrete-like Materials Coupling Cracking and Friction, Contribution towards Structural Damping: First Uniaxial Applications". In: *Mechanics of Cohesive-frictional Materials* 5.8, pp. 607–625. ISSN: 1082-5010, 1099-1484. DOI: 10.1002/1099-1484(200011)5:8<607::AID-CFM108>3.0.CO;2-K.

Ragueneau, F., Q. T. Nguyen, and Y. Berthaud (2006). "Multifiber Analysis of Reinforced Concrete Beams Affected by Corrosion". In: *Journal de Physique IV (Proceedings)* 136, pp. 159–166. ISSN: 1155-4339, 1764-7177. DOI: 10.1051/jp4:2006136017.

Rayleigh, J. W. S. B. (1877). *The Theory of Sound - Volume I*. Vol. 1. New York, United States: Macmillan.

Rayleigh, J. W. S. B. (1896). *The Theory of Sound - Volume II*. Vol. 2. New York, United States: Macmillan.

Reid, T. J. (1956). "Free Vibration and Hysteretic Damping". In: *The Journal of the Royal Aeronautical Society* 60.544, pp. 283–283. ISSN: 0368-3931, 2398-4600. DOI: 10.1017/S0368393100135242.

Richard, B. (2010). "Comportement des éléments de structures en béton armé dégradés par corrosion - La problématique de la modélisation de l'interface acier/béton en présence de corrosion". PhD thesis. Paris, France: Université Paris-Est.

Richard, B. and F. Ragueneau (2013). "Continuum Damage Mechanics Based Model for Quasi Brittle Materials Subjected to Cyclic Loadings: Formulation, Numerical Implementation and Applications". In: *Engineering Fracture Mechanics* 98, pp. 383–406. ISSN: 00137944. DOI: 10.1016/j.engfracmech.2012.11.013.

Richard, B., F. Ragueneau, et al. (2010). "Isotropic Continuum Damage Mechanics for Concrete under Cyclic Loading: Stiffness Recovery, Inelastic Strains and Frictional Sliding". In: *Engineering Fracture Mechanics* 77.8, pp. 1203–1223. ISSN: 00137944. DOI: 10.1016/j.engfracmech.2010.02.010.

Riggs, H. R. and G. H. Powell (1986). "Rough Crack Model for Analysis of Concrete". In: *Journal of Engineering Mechanics* 112.5, pp. 448–464. ISSN: 0733-9399, 1943-7889. DOI: 10.1061/(ASCE)0733-9399(1986)112:5(448).

Rodrigues, H. et al. (2012). "A Comparative Analysis of Energy Dissipation and Equivalent Viscous Damping of RC Columns Subjected to Uniaxial and Biaxial Loading". In: *Engineering Structures* 35, pp. 149–164. ISSN: 01410296. DOI: 10.1016/j.engstruct.2011.11.014.

Rosenblueth, E. and I. Herrera (1964). "On a Kind of Hysteretic Damping". In: *Journal of Engineering Mechanics Division ASCE* 90, pp. 37–48.

Roth, S.-N., P. Léger, and A. Soulaïmani (2015). "A Combined XFEM–Damage Mechanics Approach for Concrete Crack Propagation". In: *Computer Methods in Applied Mechanics and Engineering* 283, pp. 923–955. ISSN: 00457825. DOI: 10.1016/j.cma.2014.10.043.

Ryan, K. L. and J. Polanco (2008). "Problems with Rayleigh Damping in Base-Isolated Buildings". In: *Journal of Structural Engineering* 134.11, pp. 1780–1784. ISSN: 0733-9445, 1943-541X. DOI: 10.1061/(ASCE)0733-9445(2008)134:11(1780).

Sakamoto, T. et al. (2006). "Investigation into Crack Phenomena of Unreinforced Concrete Structures for Aseismic Evaluation of Concrete Dams". In: *Notes*. Vol. 38. US Department of Commerce, National Bureau of Standards, Gaithersburg, Maryland, United States, p. 211.

Salane, H. J. and J. W. Baldwin (1990). "Identification of Modal Properties of Bridges". In: *Journal of Structural Engineering* 116.7, pp. 2008–2021. DOI: 10.1061/(ASCE)0733-9445(1990)116:7(2008).

Salehi, M. and P. Sideris (2018). "An Enhanced Rayleigh Damping Model for Dynamic Analysis of Inelastic Structures". In: *2018 Structure Congress*. Fort-Worth, Texas, United States.

Salzmann, A. (2003). "Damping Characteristics of Reinforced and Prestressed Normal-and High-Strength Concrete Beams". PhD thesis. Queensland, Australia: Griffith University.

Samouh, H. and P. Kotronis (2011). "Modélisation simplifiée des portiques avec remplissage en maçonnerie soumis à l'action sismique". In: *AFPS 2011*. Marne-la-Valle, France: Unpublished. DOI: 10.13140/2.1.4756.1761.

Saouma, V. E. (2000). *Lecture Notes in : Fracture Mechanics*. Dept. of Civil Environmental and Architectural Engineering University of Colorado, Boulder, CO 80309-0428.

Segal, F. and D. V. Val (2006). "Energy Evaluation for Ramberg–Osgood Hysteretic Model". In: *Journal of Engineering Mechanics* 132.9, pp. 907–913. ISSN: 0733-9399, 1943-7889. DOI: 10.1061/(ASCE)0733-9399(2006)132:9(907).

Seghir, A., A. Tahakourt, and G. Bonnet (2009). "Coupling FEM and Symmetric BEM for Dynamic Interaction of Dam–Reservoir Systems". In: *Engineering Analysis with Boundary Elements* 33.10, pp. 1201–1210. ISSN: 09557997. DOI: 10.1016/j.enganabound.2009.04.011.

Semblat, J. (1997). "Rheological Interpretation of Rayleigh Damping". In: *Journal of Sound and Vibration* 206.5, pp. 741–744. ISSN: 0022460X. DOI: 10.1006/jsvi.1997.1067.

Seybert, A. (1981). "Estimation of Damping from Response Spectra". In: *Journal of Sound and Vibration* 75.2, pp. 199–206. ISSN: 0022460X. DOI: 10.1016/0022-460X(81)90339-4.

Skinner, R. I. et al. (1980). "Hysteretic Dampers for the Protection of Structures from Earthquakes". In: *Bulletin of the New Zealand National Society for Earthquake Engineering* 13.1, pp. 22–36.

Smyrou, E., M. J. N. Priestley, and A. J. Carr (2011). "Modelling of Elastic Damping in Nonlinear Time-History Analyses of Cantilever RC Walls". In: *Bulletin of Earthquake Engineering* 9.5, pp. 1559–1578. ISSN: 1570-761X, 1573-1456. DOI: 10.1007/s10518-011-9286-y.

Song, Z. and C. Su (2017). "Computation of Rayleigh Damping Coefficients for the Seismic Analysis of a Hydro-Powerhouse". In: *Shock and Vibration* 2017, pp. 1–11. ISSN: 1070-9622, 1875-9203. DOI: 10.1155/2017/2046345.

Souid, A. et al. (2009). "Pseudodynamic Testing and Nonlinear Substructuring of Damaging Structures under Earthquake Loading". In: *Engineering Structures* 31.5, pp. 1102–1110. ISSN: 01410296. DOI: 10.1016/j.engstruct.2009.01.007.

Sousa, R. et al. (2020). "Shake Table Blind Prediction Tests: Contributions for Improved Fiber-Based Frame Modelling". In: *Journal of Earthquake Engineering* 24.9, pp. 1435–1476. ISSN: 1363-2469, 1559-808X. DOI: 10.1080/13632469.2018.1466743.

Spacone, E., F. C. Filippou, and F. F. Taucer (1996a). "Fibre Beam–Column Model for Non-linear Analysis of R/C Frames: Part I. Formulation". In: *Earthquake Engineering & Structural Dynamics* 25.7, pp. 711–725. ISSN: 0098-8847, 1096-9845. DOI: 10.1002/(SICI)1096-9845(199607)25:7<711::AID-EQE576>3.0.CO;2-9.

Spacone, E., F. C. Filippou, and F. F. Taucer (1996b). "Fibre Beam–Column Model for Non-linear Analysis of R/C Frames: Part II. Applications". In: *Earthquake Engineering & Structural Dynamics* 25.7, pp. 727–742. ISSN: 0098-8847, 1096-9845. DOI: 10.1002/(SICI)1096-9845(199607)25:7<727::AID-EQE577>3.0.CO;2-O.

Spacone, E. and S. El-Tawil (2004). "Nonlinear Analysis of Steel-Concrete Composite Structures: State of the Art". In: *Journal of Structural Engineering* 130.2, pp. 159–168. ISSN: 0733-9445, 1943-541X. DOI: 10.1061/(ASCE)0733-9445(2004)130:2(159).

Spencer, R. A. (1969). "Stiffness and Damping of Nine Cyclically Loaded Prestressed Concrete Members". In: *PCI Journal* 14.3, pp. 39–52. ISSN: 08879672. DOI: 10.15554/pcij.06011969.39.52.

Stevenson, J. (1980). "Structural Damping Values as a Function of Dynamic Response Stress and Deformation Levels". In: *Nuclear Engineering and Design* 60.2, pp. 211–237. ISSN: 00295493. DOI: 10.1016/0029-5493(80)90238-1.

Stojadinovic, B. and C. R. Thewalt (1996). "Energy Balanced Hysteresis Models". In: *11th World Conference on Earthquake Engineering*. Earthquake Engineering Research at Berkeley, College of Engineering, University of California at Berkeley, California, United States.

Su, L. et al. (2019). "Experimental Identification of Exponential Damping for Reinforced Concrete Cantilever Beams". In: *Engineering Structures* 186, pp. 161–169. ISSN: 01410296. DOI: 10.1016/j.engstruct.2019.02.015.

Tanaka, H. (1990). "Effect of Lateral Confining Reinforcement on the Ductile Behaviour of Reinforced Concrete Columns". PhD thesis. Christchurch, New Zealand: University of Canterbury.

Tassios, T. P. and E. N. Vintzēleou (1987). "Concrete-to-concrete Friction". In: *Journal of Structural Engineering* 113.4, pp. 832–849. ISSN: 0733-9445, 1943-541X. DOI: 10.1061/(ASCE)0733-9445(1987)113:4(832).

Taucer, F. F., E. Spacone, and F. C. Filippou (1991). *A Fiber Beam-Column Element for Seismic Response Analysis of Reinforced Concrete Structures*. Tech. rep. UCB/EERC-91/17. Earthquake Engineering Research Center - College of Engineering: University of California - Berkeley.

Thomson, W. T., T. Calkins, and P. Caravani (1974). "A Numerical Study of Damping". In: *Earthquake Engineering & Structural Dynamics* 3.1, pp. 97–103. ISSN: 00988847, 10969845. DOI: 10.1002/eqe.4290030108.

Tinawi, R. et al. (2000). "Seismic Safety of Gravity Dams: From Shake Table Experiments to Numerical Analyses". In: *Journal of Structural Engineering* 126.4, pp. 518–529. DOI: 10.1061/(ASCE)0733-9445(2000)126:4(518).

Torre-Casanova, A. (2012). "Prise en compte de la liaison acier-béton pour le calcul de structures industrielles". PhD thesis. Cachan, France: École Normale Supérieure de Cachan.

Turner, J. and A. Pretlove (1988). "A Study of the Spectrum of Traffic-Induced Bridge Vibration". In: *Journal of Sound and Vibration* 122.1, pp. 31–42. ISSN: 0022460X. DOI: 10.1016/S0022-460X(88)80004-X.

Uang, C.-M. and V. V. Bertero (1990). "Evaluation of Seismic Energy in Structures". In: *Earthquake Engineering & Structural Dynamics* 19.1, pp. 77–90. ISSN: 1096-9845. DOI: 10.1002/eqe.4290190108.

Val, D. V. and F. Segal (2005). "Effect of Damping Model on Pre-Yielding Earthquake Response of Structures". In: *Engineering Structures* 27.14, pp. 1968–1980. ISSN: 01410296. DOI: 10.1016/j.engstruct.2005.06.018.

Vassaux, M. et al. (2015). "Regularised Crack Behaviour Effects on Continuum Modelling of Quasi-Brittle Materials under Cyclic Loading". In: *Engineering Fracture Mechanics* 149, pp. 18–36. ISSN: 00137944. DOI: 10.1016/j.engfracmech.2015.09.040.

Veletsos, A. S. and C. E. Ventura (1986). "Modal Analysis of Non-Classically Damped Linear Systems". In: *Earthquake Engineering & Structural Dynamics* 14.2, pp. 217–243. ISSN: 00988847, 10969845. DOI: 10.1002/eqe.4290140205.

Vintzileou, E., T. Tassios, and M. Chronopoulos (2007). "Experimental Validation of Seismic Code Provisions for RC Columns". In: *Engineering Structures* 29.6, pp. 1153–1164. ISSN: 01410296. DOI: 10.1016/j.engstruct.2006.08.013.

Voldoire, F. (2019). "Modélisation de l'amortissement dans les structures en béton armé sous séisme". In: *10ème Colloque National AFPS 2019*. Strasbourg, France.

Walraven and Bigaj-van Vliet (2010a). *Model Code 2010 - Volume 1*. Technical Report Bulletin 55. Lausanne, Switzerland: International Federation for Structural Concrete (fib).

Walraven and Bigaj-van Vliet (2010b). *Model Code 2010 - Volume 2*. Technical Report Bulletin 56. Lausanne, Switzerland: International Federation for Structural Concrete (fib).

Wang, F. et al. (2007). "Simulation Analysis of Static and Shaking Table Tests on RC Columns with Insufficient Lap Splices". In: *19th International Conference on Structural Mechanics in Reactor Technology, SMiRT 19*. Toronto, Canada, p. 8.

Wang, I. (2011). "An Analysis of Higher Order Effects in the Half Power Method for Calculating Damping". In: *Journal of Applied Mechanics* 78.1. ISSN: 0021-8936, 1528-9036. DOI: 10.1115/1.4002208.

Wang, J.-T., F. Jin, and C.-H. Zhang (2012). "Estimation Error of the Half-Power Bandwidth Method in Identifying Damping for Multi-DOF Systems". In: *Soil Dynamics and Earthquake Engineering* 39, pp. 138–142. ISSN: 02677261. DOI: 10.1016/j.soildyn.2012.02.008.

Warburton, G. B. and S. R. Soni (1977). "Errors in Response Calculations for Non-Classically Damped Structures". In: *Earthquake Engineering & Structural Dynamics* 5.4, pp. 365–376. ISSN: 00988847, 10969845. DOI: 10.1002/eqe.4290050404.

Watson, S., F. A. Zahn, and R. Park (1994). "Confining Reinforcement for Concrete Columns". In: *Journal of Structural Engineering* 120.6, pp. 1798–1824. ISSN: 0733-9445, 1943-541X. DOI: 10.1061/(ASCE)0733-9445(1994)120:6(1798).

Wikipedia (2021). *Damping*. https://en.wikipedia.org/wiki/Damping.

Wilson, E. L. and J. Penzien (1972). "Evaluation of Orthogonal Damping Matrices". In: *International Journal for Numerical Methods in Engineering* 4.1, pp. 5–10. ISSN: 1097-0207. DOI: 10.1002/nme.1620040103.

Wu, B. (2015). "A Correction of the Half-Power Bandwidth Method for Estimating Damping". In: *Archive of Applied Mechanics* 85.2, pp. 315–320. ISSN: 0939-1533, 1432-0681. DOI: 10.1007/s00419-014-0908-0.

Xu, K. and T. Igusa (1991). "Dynamic Characteristics of Non-Classically Damped Structures". In: *Earthquake Engineering & Structural Dynamics* 20.12, pp. 1127–1144. ISSN: 00988847, 10969845. DOI: 10.1002/eqe.4290201204.

Zareian, F. and R. A. Medina (2010). "A Practical Method for Proper Modelling of Structural Damping in Inelastic Plane Structural Systems". In: *Computers & Structures* 88.1-2, pp. 45–53. ISSN: 00457949. DOI: 10.1016/j.compstruc.2009.08.001.

Zhu, Q., D. Kondo, and J. Shao (2008). "Micromechanical Analysis of Coupling between Anisotropic Damage and Friction in Quasi Brittle Materials: Role of the Homogenization Scheme". In: *International Journal of Solids and Structures* 45.5, pp. 1385–1405. ISSN: 00207683. DOI: 10.1016/j.ijsolstr.2007.09.026.

Ziari, A. and M. Reza Kianoush (2009). "Investigation of Flexural Cracking and Leakage in RC Liquid Containing Structures". In: *Engineering Structures* 31.5, pp. 1056–1067. ISSN: 01410296. DOI: 10.1016/j.engstruct.2008.12.019.

Appendices

Appendix A

DAMPING MODEL NOMENCLATURE

Nomenclature of the damping formulation acronyms used in the manuscript

Table A.1: Definition of the damping formulation acronyms (alphabetic order)

Acronym	Complete name
CKPD	Stiffness proportional damping with the commit stiffness matrix
CRD	Rayleigh damping with the commit stiffness matrix
CWPD	Wilson-Penzien damping with the commit stiffness matrix
IKPD	Stiffness proportional damping with the initial stiffness matrix
KPD	Stiffness proportional damping
KPD_ACT	Stiffness proportional damping with updated a_0 and a_1 parameters
MD	Modal damping
MD_ACT	Modal damping with updated parameters
MPD	Mass proportional damping
MPD_ACT	Mass proportional damping with updated a_0 and a_1 parameters
RD	Rayleigh damping
RD_ACT	Rayleigh damping with updated a_0 and a_1 parameters
SKPD	Stiffness proportional damping with the secant stiffness matrix
SRD	Rayleigh damping with the secant stiffness matrix
SWPD	Wilson-Penzien damping with the secant stiffness matrix
TKPD	Stiffness proportional damping with the tangent stiffness matrix
TRD	Rayleigh damping with the tangent stiffness matrix
TWPD	Wilson-Penzien damping with the tangent stiffness matrix
WPD	Wilson-Penzien damping
WPD_ACT	Wilson-Penzien damping with updated parameters

A.1   Rayleigh damping and derivatives

RD Rayleigh damping (page 19)

$$\mathbb{C} = a_0 \cdot \mathbb{M} + a_1 \cdot \mathbb{K}_0 \tag{A.1}$$

MPD Mass proportional damping (page 20)

$$\mathbb{C} = a_0 \cdot \mathbb{M} \tag{A.2}$$

IKPD Initial stiffness proportional damping (page 20)

$$\mathbb{C} = a_1 \cdot \mathbb{K}_0 \tag{A.3}$$

TKPD Tangent stiffness proportional damping (page 20)

$$\mathbb{C} = a_1 \cdot \mathbb{K}_T \tag{A.4}$$

CKPD Commit stiffness proportional damping

$$\mathbb{C} = a_1 \cdot \mathbb{K}_C \tag{A.5}$$

TRD Tangent Rayleigh damping (Rayleigh damping with tangent stiffness matrix)

$$\mathbb{C} = a_0 \cdot \mathbb{M} + a_1 \cdot \mathbb{K}_T \tag{A.6}$$

CRD Commit Rayleigh damping (Rayleigh damping with commit stiffness matrix)

$$\mathbb{C} = a_0 \cdot \mathbb{M} + a_1 \cdot \mathbb{K}_C \tag{A.7}$$

RDtdK Rayleigh damping with a time-dependent coefficient applied to the stiffness matrix

$$\mathbb{C} = a_0 \cdot \mathbb{M} + a_1(t) \cdot \mathbb{K}_0 \tag{A.8}$$

RDtd Rayleigh damping with time-dependent coefficients

$$\mathbb{C} = a_0(t) \cdot \mathbb{M} + a_1(t) \cdot \mathbb{K}_0 \tag{A.9}$$

TRDtdK Tangent Rayleigh damping with a time-dependent coefficient applied to the stiffness matrix

$$\mathbb{C} = a_0 \cdot \mathbb{M} + a_1(t) \cdot \mathbb{K}_T \tag{A.10}$$

TRDtd Tangent Rayleigh damping with time-dependent coefficients

$$\mathbb{C} = a_0(t) \cdot \mathbb{M} + a_1(t) \cdot \mathbb{K}_T \tag{A.11}$$

RDTKPDtdK Tangent Rayleigh damping + a tangent-stiffness proportional part with a time-dependent coefficient

$$\mathbb{C} = a_0 \cdot \mathbb{M} + a_1 \cdot \mathbb{K}_0 + a_1(t) \cdot \mathbb{K}_T \tag{A.12}$$

QBD Quasi-brittle damping (page 30)

$$\mathbb{C} = a_1 \cdot \mathbb{K}_{el} \tag{A.13}$$

IKPDL Initial stiffness proportional damping with a limit on the stiffness matrix (page 20)

$$\mathbb{C} = a_1 \cdot \overline{\mathbb{K}}_0 \leqslant \mathbb{C}_{lim} \tag{A.14}$$

A.2   Classical damping formulations

CD Caughey damping (page 21)

$$\mathbb{C} = \mathbb{M} \sum_i a_i \left[\mathbb{M}^{-1} \cdot \mathbb{K} \right]^i \tag{A.15}$$

BD Bernal damping (page 21)

$$\mathbb{C} = \mathbb{M} \cdot \sum_i a_i \left[\mathbb{M}^{-1} \cdot \mathbb{K} \right]^i, \quad \forall i \leqslant 0 \tag{A.16}$$

A.3   Modal damping

MD Modal damping (page 22)

$$\mathbb{C} = \sum_{i=1}^{N} \frac{4\pi}{T_i} \xi_i \frac{\left(\mathbb{M}\underline{\phi}_i \right) \left(\mathbb{M}\underline{\phi}_i \right)^T}{\underline{\phi}_i^T \mathbb{M}\underline{\phi}_i} \tag{A.17}$$

WPD Wilson and Penzien damping (page 22)

$$\mathbb{C} = \mathbb{M} \cdot \left[\sum_{i=1}^{N-1} \frac{2\xi_i \omega_i}{m_i} \underline{\phi}_i \underline{\phi}_i^T \right] \cdot \mathbb{M} \tag{A.18}$$

NLMD Nonlinear modal damping: the modal damping matrix is updated for each time step using eigenvalues analysis with the tangent stiffness matrix

A.4   Other damping formulations

NLVD Nonlinear viscous damping: bounded dampers are added to the model

ElVD Elastic velocity damping: inelastic damping forces are proportional only to elastic elements velocities

Appendix B

MATERIAL MODEL PARAMETERS

B.1 Concrete models

B.1.1 BARFRA model

- YOUN = Young's modulus
- NU = Poisson's coefficient
- RHO = density
- FC = compressive strength
- FC_R = residual compressive strength
- STRC = strain controlling softening in compression
- FT = tensile strength
- FT_R = residual tensile strength
- STRT = strain controlling softening in traction

B.1.2 RICBET model

- YOUN = Young's modulus
- NU = Poisson's coefficient
- RHO = density
- FT = tensile equivalent strength
- ALDI = brittleness in uni-axial traction
- GAM1 = kinematic work hardening modulus 1
- A1 = kinematic work hardening modulus 2
- SIGF = cracks closure stress
- FC = compressive strength
- AF = plasticity surface modulus
- AG = plasticity potential modulus
- AC = plasticity work hardening 1
- BC = plasticity work hardening 2
- SIGU = asymptotic compressive stress
- HYST = indicator to choose the cracks closure criterion: cracks closure to zero stress (HYST = 1) and cracks closure to zero strain (HYST = 2)

B.2   Steel model - ACIER_UNI

- YOUN = Young's modulus
- NU = Poisson's coefficient
- RHO = density
- STSY = plasticity stress
- EPSU = ultimate strain
- STSU = ultimate stress
- EPSH = strain at the beginning of work hardening
- BFAC = Ratio between the work hardening stiffness and the elastic stiffness
- R0FA = R0 coefficient (first coefficient governing Bauschinger effect)
- A1FA = A1 coefficient (second coefficient governing Bauschinger effect)
- A2FA = A2 coefficient (third coefficient governing Bauschinger effect)
- FALD = Ratio between the length between two shear rebars and the bending rebars diameter (to deal with rebars buckling)
- AFAC = A coefficient (to deal with rebars buckling)
- CFAC = C coefficient (to deal with rebars buckling)
- A6FA = A6 coefficient (to deal with rebars buckling)

DISSIPATIVE PHENOMENA (CLASSICAL DAMPING MODELS)

C.1   Damping formulation comparisons

(a) RD   (b) RD_ACT   (c) CRD   (d) SRD

(e) KPD   (f) KPD_ACT   (g) CKPD   (h) SKPD

(i) MPD   (j) MPD_ACT   (k) MD   (l) MD_ACT

(m) WPD   (n) WPD_ACT   (o) CWPD   (p) SWPD
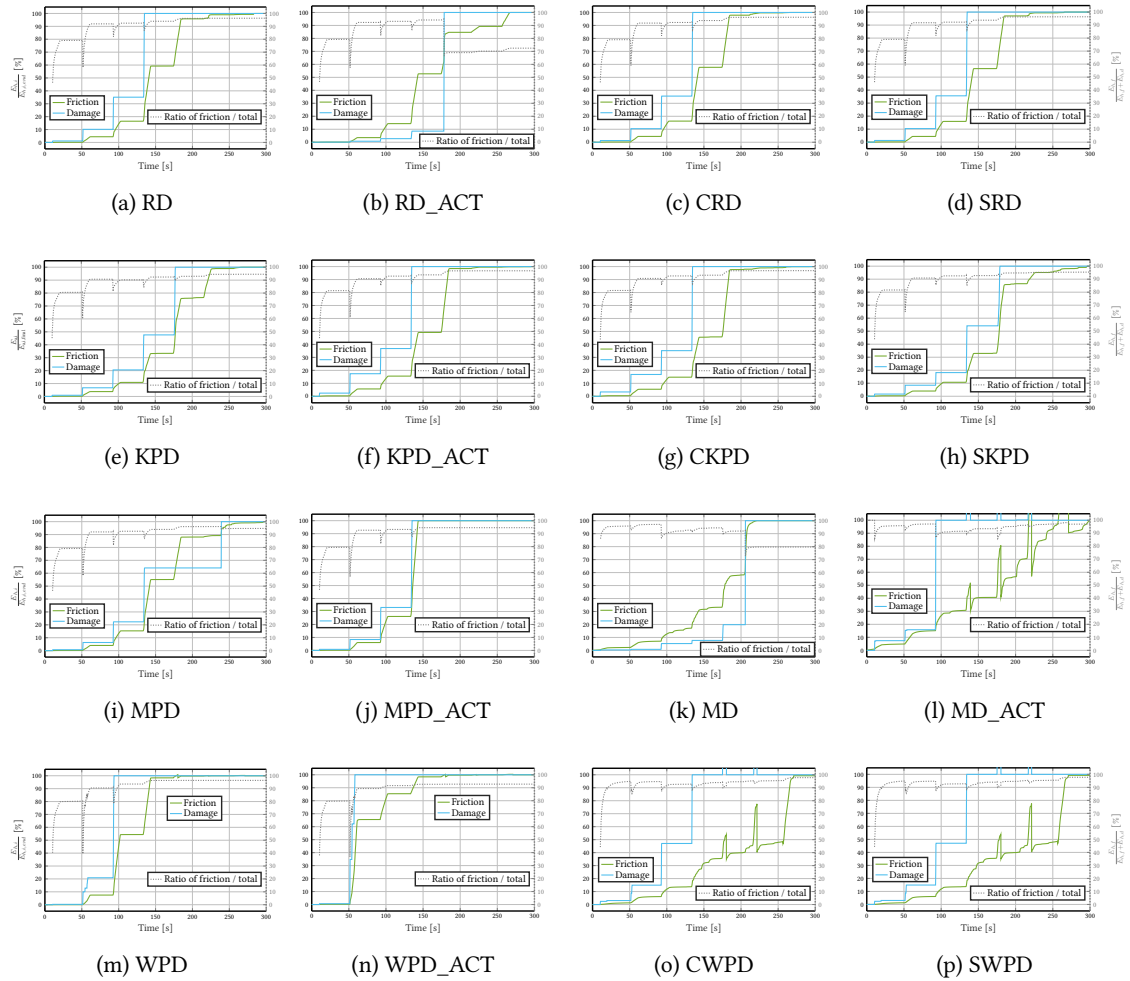
Figure C.1: DSS2 test - Dissipation proportions at material level - RICBET 2% - damping formulation influence

C.2   Damping ratio comparisons

(a) RD - 1%   (b) RD - 2%   (c) RD - 3%   (d) RD - 5%

(e) CRD - 1%   (f) CRD - 2%   (g) CRD - 3%   (h) CRD - 5%

(i) CKPD - 1%   (j) CKPD - 2%   (k) CKPD - 3%   (l) CKPD - 5%

(m) WPD - 1%   (n) WPD - 2%   (o) WPD - 3%   (p) WPD - 5%
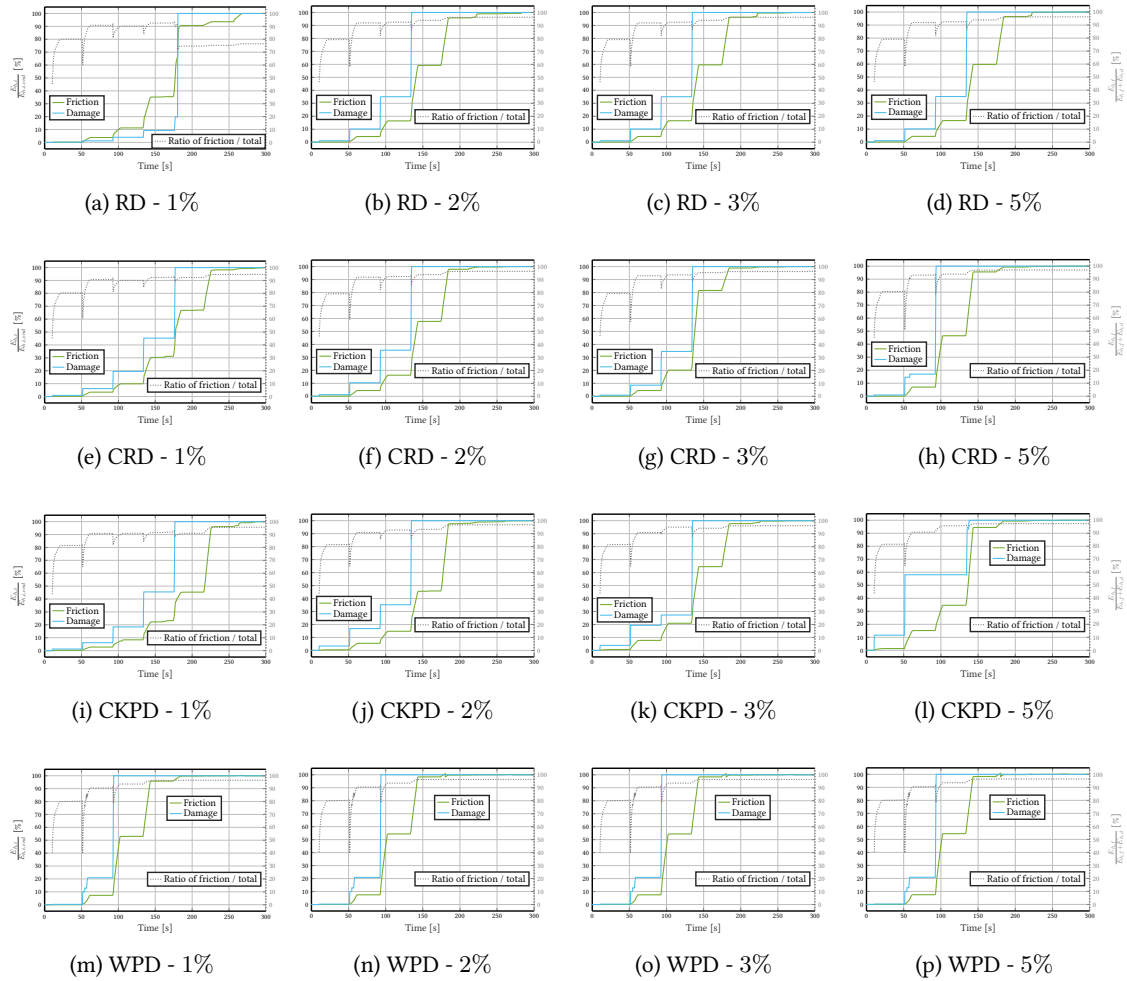
Figure C.2: DSS2 test - Dissipation proportions at material level - RICBET - damping ratio influence

3D REPRESENTATION OF NUMERICAL RESULTS

D.1   Beam displacement

(a) Time step 120

(b) Time step 121

(c) Time step 122

(d) Time step 123

(e) Time step 124

(f) Time step 125

(g) Time step 126

(h) Time step 127

(i) Time step 128

(j) Time step 129

(k) Time step 130
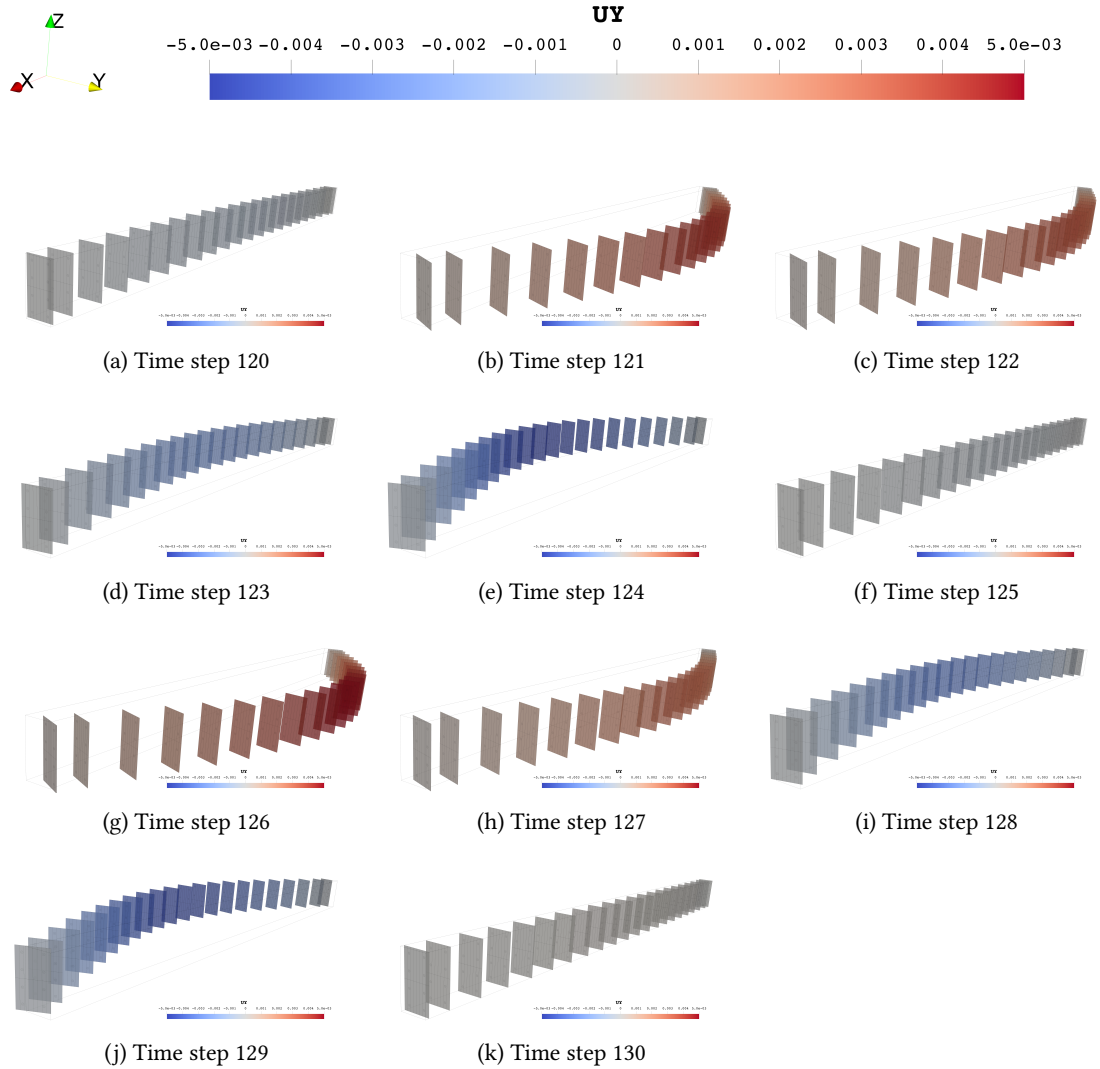
Figure D.1: DSS2 test - increment 4 - Beam displacement $[m]$ - RICBET - RD 2%

(a) RD - Time step 124

(b) RD - Time step 125

(c) RD - Time step 126

(d) CRD - Time step 124

(e) CRD - Time step 125

(f) CRD - Time step 126

(g) KPD - Time step 124

(h) KPD - Time step 125

(i) KPD - Time step 126

(j) CKPD - Time step 124

(k) CKPD - Time step 125

(l) CKPD - Time step 126

(m) MPD - Time step 124

(n) MPD - Time step 125

(o) MPD - Time step 126
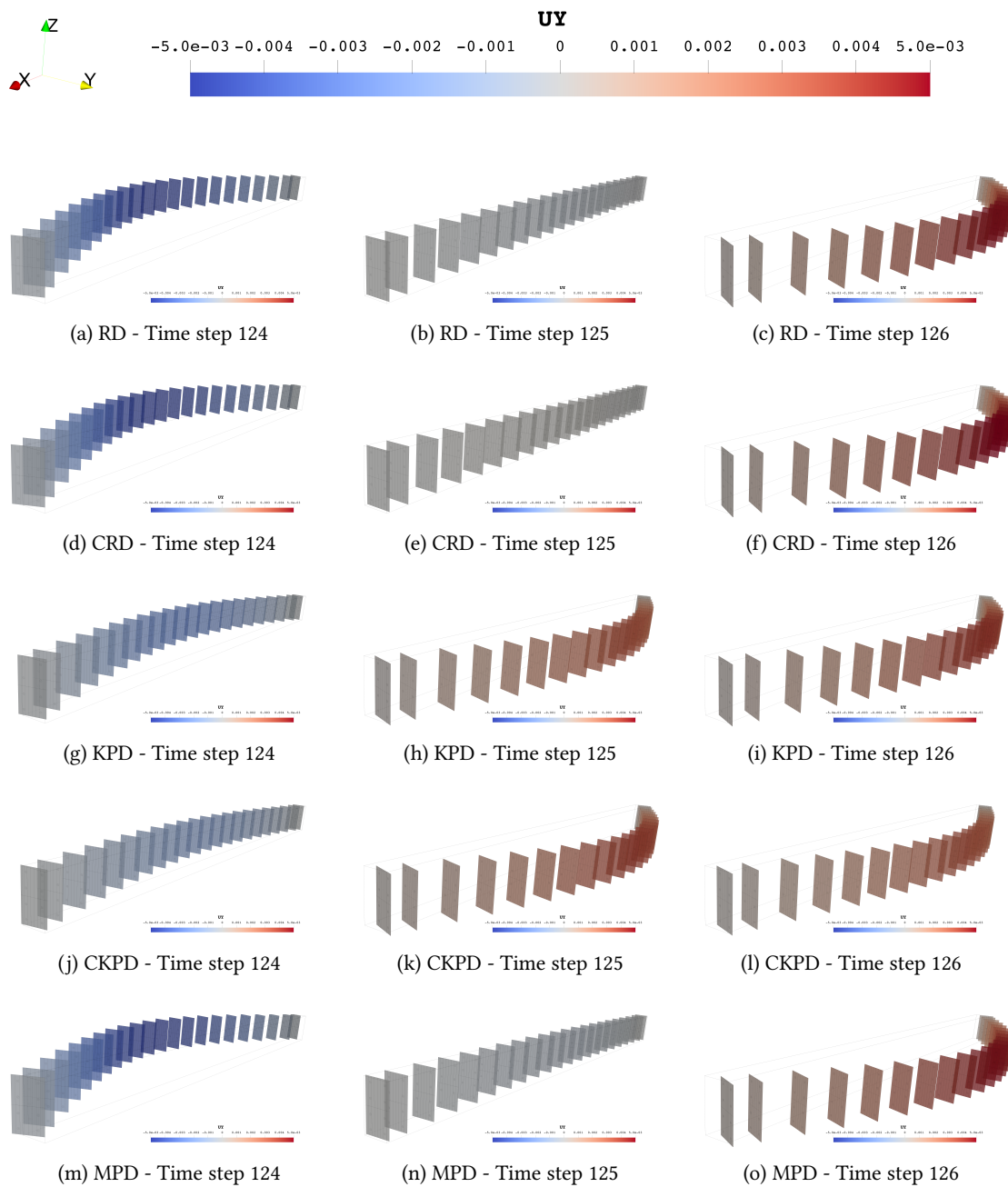
Figure D.2: DSS2 test - increment 4 - Beam displacement $[m]$ - damping formulation comparisons - RICBET 2%

D.2   Dissipative phenomena

D.2.1   Damage

(a) Increment 1   (b) Increment 2   (c) Increment 3

(d) Increment 4   (e) Increment 5   (f) Increment 6
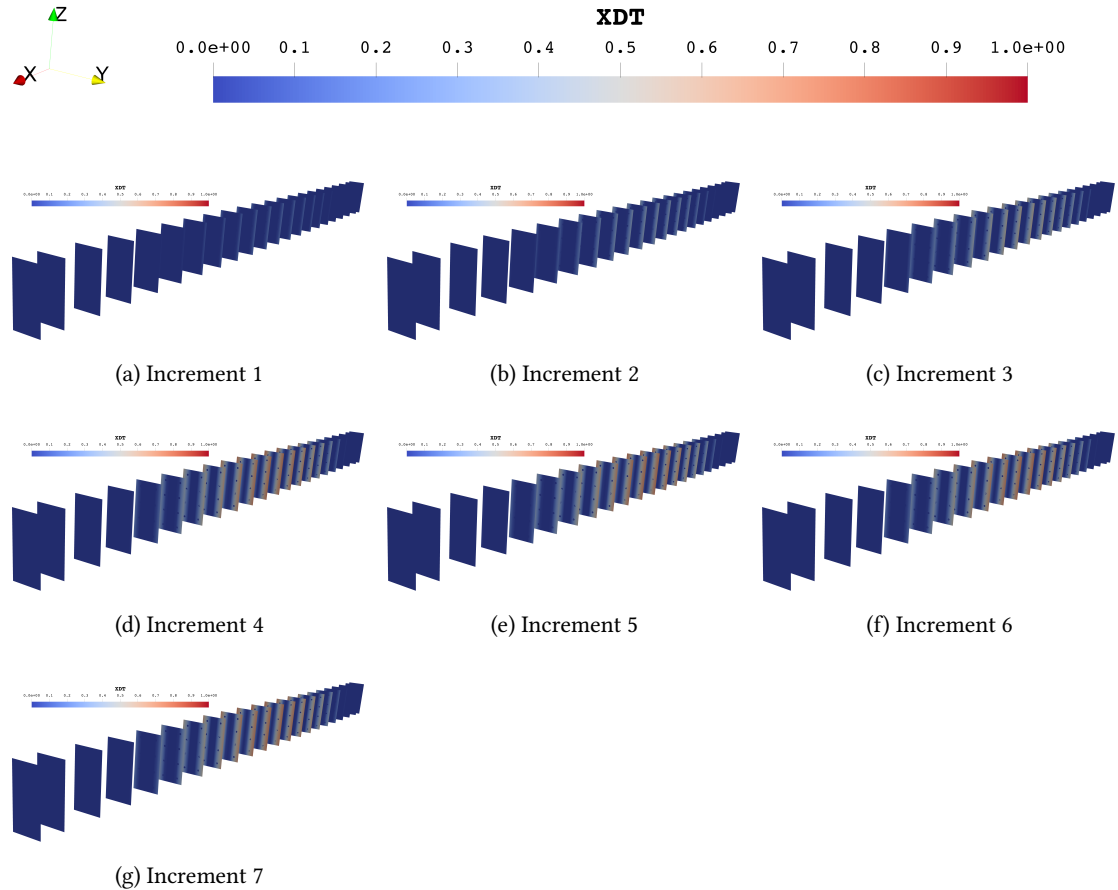
(g) Increment 7

Figure D.3: DSS2 test - Damage variable evolution along the beam - RICBET - RD 2%

Remark: The seventh increment for the MPD formulation does not exist because of the computation divergence.

(a) RD - increment 1

(b) RD - increment 4

(c) RD - increment 7

(d) CRD - increment 1

(e) CRD - increment 4

(f) CRD - increment 7

(g) KPD - increment 1

(h) KPD - increment 4

(i) KPD - increment 7

(j) CKPD - increment 1

(k) CKPD - increment 4

(l) CKPD - increment 7

(m) MPD - increment 1

(n) MPD - increment 4
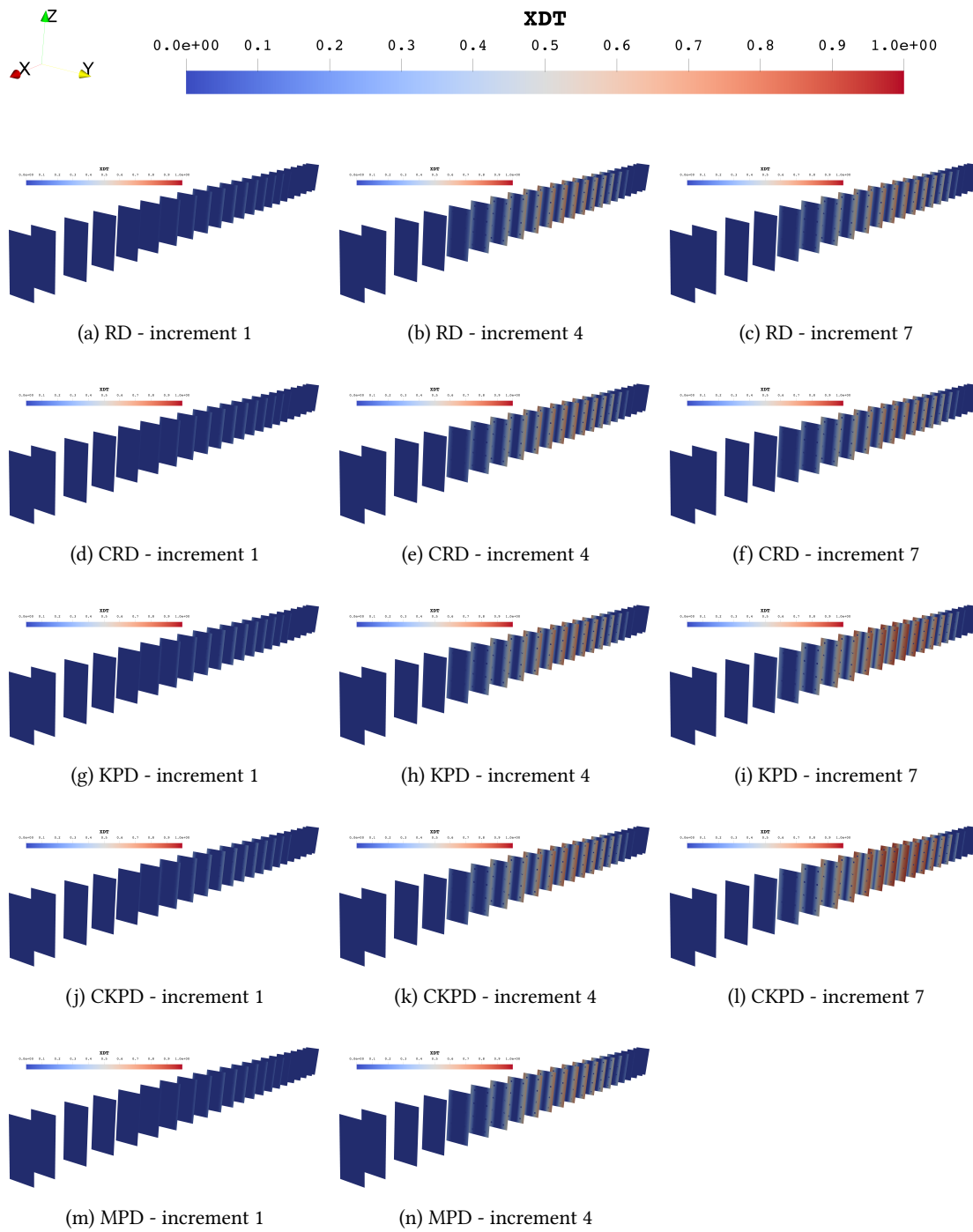
Figure D.4: DSS2 test - Damage variable evolution along the beam - damping formulation comparisons - RICBET 2%

D.2.2   Friction

(a) Increment 1

(b) Increment 2

(c) Increment 3

(d) Increment 4

(e) Increment 5

(f) Increment 6
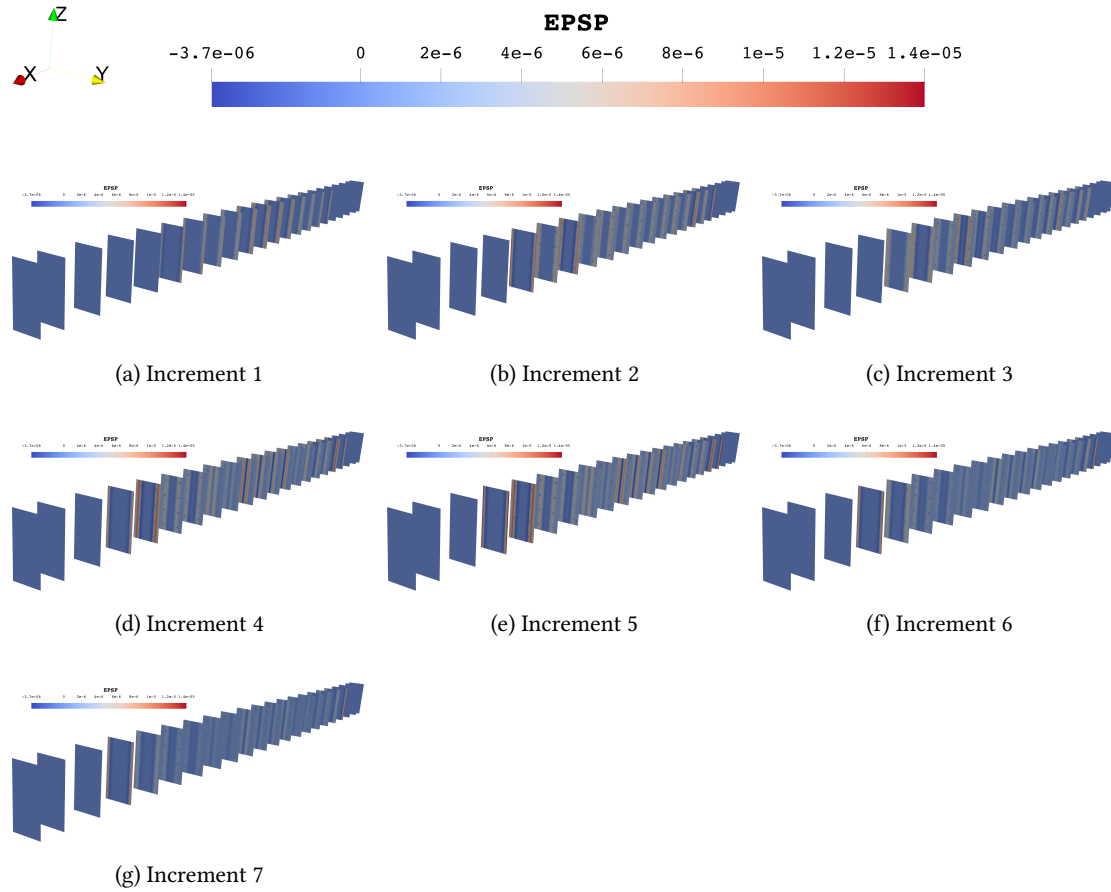
(g) Increment 7

Figure D.5: DSS2 test - Friction deformation variable evolution along the beam - RICBET - RD 2%

Remark: The seventh increment for the MPD formulation does not exist because of the computation divergence.
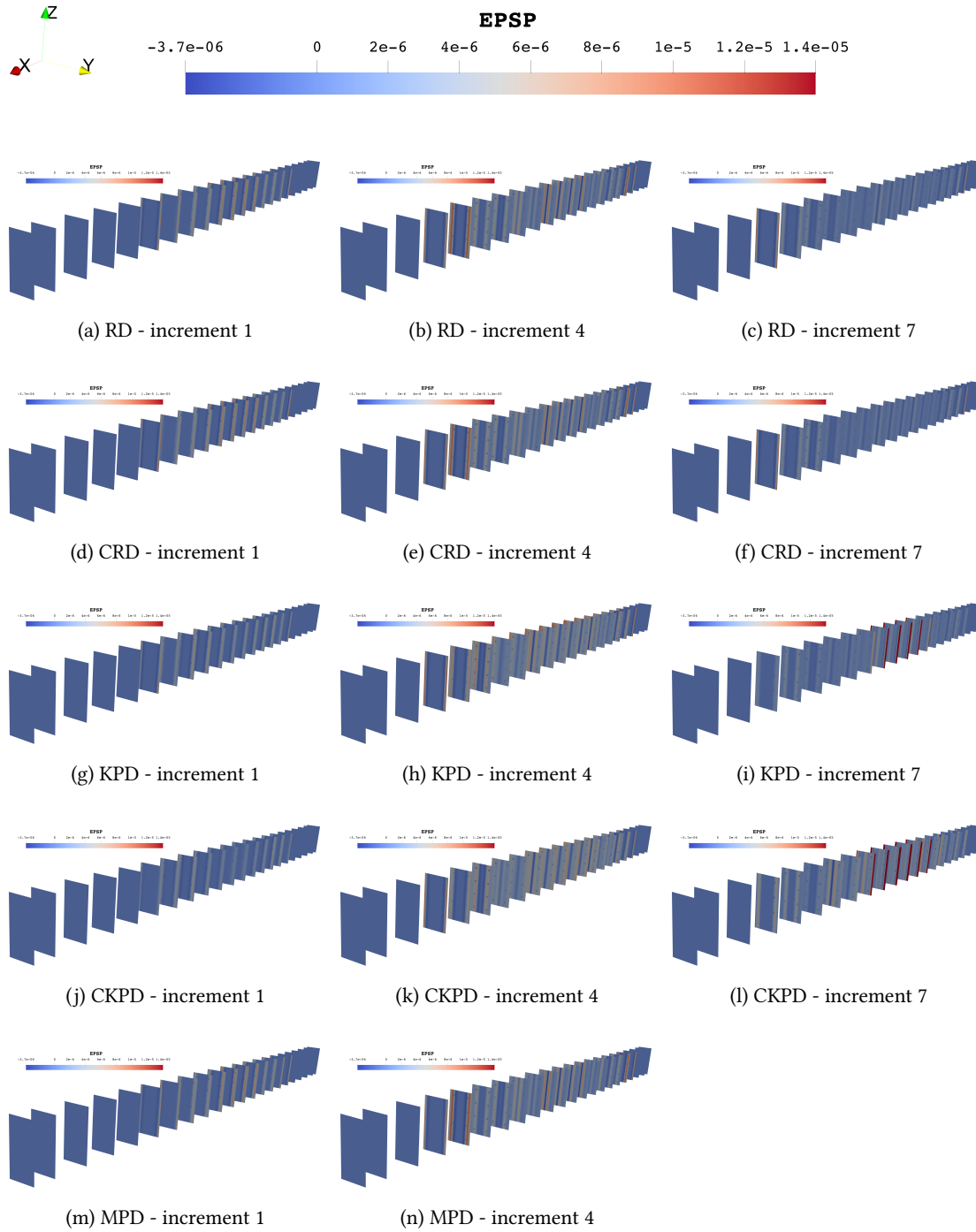
Figure D.6: DSS2 test - Friction deformation variable evolution along the beam - damping formulation comparisons - RICBET 2%

Appendix E

DEMONSTRATION OF THE ANALYTICAL MODAL BASIS OF DIFFERENT SYSTEMS

This appendix demonstrates the equations discussed in section 3.2 and particularly the analytical solutions of different subsystems proposed by Karnovsky and Lebed (2000).

E.1 Simply supported beam

The scheme of a simply supported beam is presented in figure 3.4. Let us consider a section of length dx of the beam (fig. E.1).
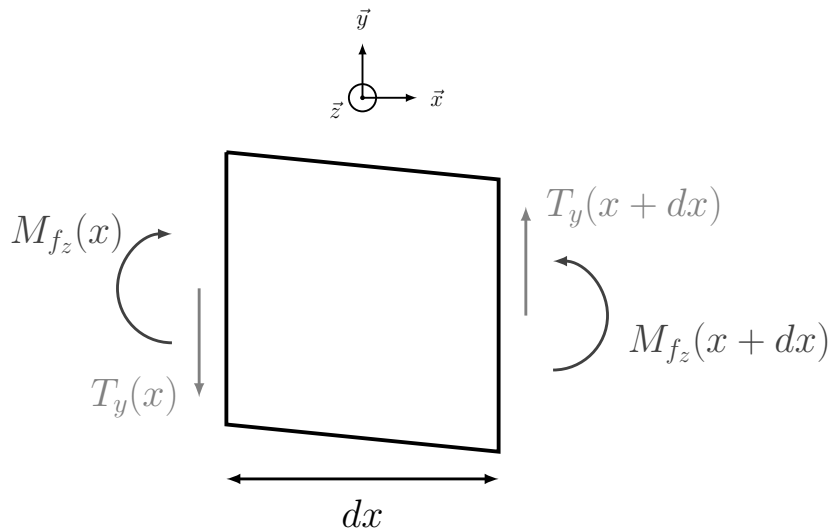
Figure E.1: Equilibrium of a beam section

E.1.1   Wave equation

The application of the fundamental principle of dynamics gives the following equations (eq. E.1):

$$\begin{cases} T_y(x+dx) - T_y(x) = \rho_c.S_h.dx.\dfrac{\partial^2 u_y}{\partial t^2} \\ -M_{f_z}(x) + T_y(x).dx + M_{f_z}(x+dx) = 0 \end{cases} \tag{E.1}$$

where $T_y = V$ is the shear force and $M_{f_z} = M$ the inertial momentum. Then, the system is rewritten is equation (E.2):

$$\begin{cases} \dfrac{dT_y}{dx} = \rho_c.S_h.\dfrac{\partial^2 u_y}{\partial t^2} \\ T_y(x) = -\dfrac{dM_{f_z}}{dx} \end{cases} \tag{E.2}$$

given equation (E.3):

$$-\frac{d^2 M_{f_z}}{dx^2} = \rho_c.S_h.\frac{\partial^2 u_y}{\partial t^2} \tag{E.3}$$

Finally, by applying the behaviour law in equation (E.4), the wave equation of the beam is deduced (eq. E.5).

$$M_{f_z}(x) = E_c.I_h\frac{\partial^2 u_y}{\partial x^2} \tag{E.4}$$

$$E_c.I_h\frac{\partial^4 u_y}{\partial x^4}(x,t) + \rho_c.S_h\frac{\partial^2 u_y}{\partial t^2}(x,t) = 0 \tag{E.5}$$

The equation can be solved by applying the separation of variables. The displacement is written in equation (E.6):

$$u_y(x,t) = X(x).T(t) \tag{E.6}$$

So, equation (E.5) becomes equation (E.7):

$$E_c.I_h.\frac{d^4 X(x)}{dx^4}.T(t) + \rho_c.S_h.X(x)\frac{d^2 T(t)}{dt^2} = 0 \tag{E.7}$$

$X(x).T(t)$ is different from 0 for all x and t since, otherwise, the beam would not vibrate. So, it is possible to divide the equation (E.7) by $X(x).T(t)$ given equations (E.8) or (E.9):

$$E_c.I_h.\frac{d^4 X(x)}{dx^4}.\frac{1}{X(x)} + \rho_c.S_h.\frac{1}{T(t)}\frac{d^2 T(t)}{dt^2} = 0 \tag{E.8}$$

$$\frac{1}{T(t)}\frac{d^2 T(t)}{dt^2} = -\frac{E_c.I_h}{\rho_c.S_h}.\frac{1}{X(x)}\frac{d^4 X(x)}{dx^4} = -\omega^2 \tag{E.9}$$

with ω^2 a constant because $\frac{1}{T(t)}\frac{d^2 T(t)}{dt^2}$ only depends on t and $-\frac{E_c.I_h}{\rho_c.S_h}.\frac{1}{X(x)}\frac{d^4 X(x)}{dx^4}$ only depends on x. Finally, the system in equation (E.10) is deduced:

$$\begin{cases} \dfrac{d^2 T(t)}{dt^2} + \omega^2.T(t) = 0 \\ \dfrac{d^4 X(x)}{dx^4} - \lambda^4.X(x) = 0 \end{cases} \tag{E.10}$$

with $\lambda^4 = \dfrac{\rho_c . S_h}{E_c . I_h} \omega^2$. The general form of the time equation is given in equation (E.11), while the space equation gives the solution in equation (E.12):

$$T(t) = A_t \cos(\omega t) + B_t \sin(\omega t) \tag{E.11}$$

$$X(x) = A_x \cos(\lambda x) + B_x \sin(\lambda x) + C_x \cosh(\lambda x) + D_x \sinh(\lambda x) \tag{E.12}$$

Finally, the wave equation solution is written in equation (E.13):

$$u_y(x,t) = [\cos(\omega t) + \sin(\omega t)] \times [A \cos(\lambda x) + B \sin(\lambda x) + C \cosh(\lambda x) + D \sinh(\lambda x)] \tag{E.13}$$

E.1.2 Modal properties

The boundary conditions of the simply supported beam are null displacements and momenta at beam ends (eq. E.14):

$$\begin{cases} u_y(0,t) = u_y(L,t) = 0 \\ \\ M_{f_z}(0,t) = M_{f_z}(L,t) = 0 \implies \dfrac{\partial^2 u_y}{\partial x^2}(0,t) = \dfrac{\partial^2 u_y}{\partial x^2}(L,t) = 0 \end{cases} \tag{E.14}$$

So, the system of four unknowns and four equations is expressed in equation (E.15):

$$\begin{cases} A + C = 0 \\ A \cos(\lambda . L) + B \sin(\lambda . L) + C \cosh(\lambda . L) + D \sinh(\lambda . L) = 0 \\ -A + C = 0 \\ -A \cos(\lambda . L) - B \sin(\lambda . L) + C \cosh(\lambda . L) + D \sinh(\lambda . L) = 0 \end{cases} \tag{E.15}$$

From the first and third equations, it can be deduced that $A = C = 0$, so:

$$\begin{cases} B \sin(\lambda . L) + D \sinh(\lambda . L) = 0 \\ -B \sin(\lambda . L) + D \sinh(\lambda . L) = 0 \end{cases} \tag{E.16}$$

Finally, the subtraction of both equations gives $2B . \sin(\lambda . L) = 0$. If $B = 0$, then $D = 0$ and the beam does not vibrate. So, $B \neq 0$ and $\sin(\lambda . L) = 0$, given $\lambda_i = \dfrac{i.\pi}{L}$ for all $i \in \mathbb{N}$. The system can thus define the displacement space function in equation (E.17):

$$\begin{cases} \varphi_i(x) &=& \sin\left(\dfrac{i\pi x}{L}\right) \\ \\ \lambda_i &=& \dfrac{i\pi}{L} \\ \\ \omega_i &=& \left(\dfrac{i\pi}{L}\right)^2 \sqrt{\dfrac{E_c . I_h}{\rho_c . S_h}} \end{cases} \qquad , \qquad \forall\, i \in \mathbb{N} \tag{E.17}$$

where $\{\varphi_i(x)\}_{i\in\mathbb{N}}$ and $\{\omega_i\}_{i\in\mathbb{N}}$ are respectively the mode shapes and eigenfrequencies.

E.2   Beam on translational and rotational elastic supports

To solve the problem of the beam on translational and rotational elastic supports (fig. 3.5), only the boundary conditions differ from the simply supported beam. The translational support stiffnesses induce non-null displacement, so the shear forces are linked to the displacements (eq. E.18). In addition, the rotations are limited by the rotational support stiffnesses, so the momenta are linked to the rotations at beam ends (eq. E.19). The boundary conditions correspond to table 3.1.

$$\begin{cases} T_y(0,t) & = & -K_{T,1} \times u_y(0,t) \\ T_y(L,t) & = & K_{T,2} \times u_y(L,t) \end{cases} \tag{E.18}$$

$$\begin{cases} M_{f_z}(0,t) & = & K_{R,1} \times \theta_z(0,t) \\ M_{f_z}(L,t) & = & -K_{R,2} \times \theta_z(L,t) \end{cases} \tag{E.19}$$

Based on the relations from section E.1.1, both systems can be rewritten in equations (E.20) and (E.21):

$$\begin{cases} -E_c.I_h.\dfrac{\partial^3 u_y}{\partial x^3}(0,t) & = & -K_{T,1} \times u_y(0,t) \\ -E_c.I_h.\dfrac{\partial^3 u_y}{\partial x^3}(L,t) & = & K_{T,2} \times u_y(L,t) \end{cases} \tag{E.20}$$

$$\begin{cases} E_c.I_h.\dfrac{\partial^2 u_y}{\partial x^2}(0,t) & = & K_{R,1} \times \dfrac{\partial u_y}{\partial x}(0,t) \\ E_c.I_h.\dfrac{\partial^2 u_y}{\partial x^2}(L,t) & = & -K_{R,2} \times \dfrac{\partial u_y}{\partial x}(L,t) \end{cases} \tag{E.21}$$

By considering the form of the displacement in equation (E.13), the four equations in systems E.20 and E.21 gives the relations in equation (E.22):

$$\begin{cases} K_{T,1}^*.A + \bar{\lambda}^3.B + K_{T,1}^*.C - \bar{\lambda}^3.D = 0 \\ A.\left[\bar{\lambda}^3 \sin\left(\bar{\lambda}\right) + K_{T,2}^* \cos\left(\bar{\lambda}\right)\right] - B.\left[-\bar{\lambda}^3 \cos\left(\bar{\lambda}\right) + K_{T,2}^* \sin\left(\bar{\lambda}\right)\right] + \\ \quad\quad C.\left[\bar{\lambda}^3 \sinh\left(\bar{\lambda}\right) + K_{T,2}^* \cosh\left(\bar{\lambda}\right)\right] + D.\left[\bar{\lambda}^3 \cosh\left(\bar{\lambda}\right) + K_{T,2}^* \sinh\left(\bar{\lambda}\right)\right] = 0 \\ \bar{\lambda}.A + K_{R,1}^*.B - \bar{\lambda}.C + K_{R,1}^*.D = 0 \\ A.\left[-\bar{\lambda} \cos\left(\bar{\lambda}\right) - K_{R,2}^* \sin\left(\bar{\lambda}\right)\right] + B.\left[-\bar{\lambda} \sin\left(\bar{\lambda}\right) + K_{R,2}^* \cos\left(\bar{\lambda}\right)\right] + \\ \quad\quad C.\left[\bar{\lambda} \cosh\left(\bar{\lambda}\right) + K_{R,2}^* \sinh\left(\bar{\lambda}\right)\right] + D.\left[\bar{\lambda} \sinh\left(\bar{\lambda}\right) + K_{R,2}^* \cosh\left(\bar{\lambda}\right)\right] = 0 \end{cases} \tag{E.22}$$

with $\bar{\lambda} = L.\lambda$, $K_{T,i}^* = \dfrac{K_{T,i}.L^3}{E_c.I_h}$ and $K_{R,i}^* = \dfrac{K_{R,i}.L}{E_c.I_h}$. In the case of the studied beam, $K_{T,1} = K_{T,2} = K_T$ and $K_{R,1} = K_{R,2} = K_R$, so $K_{T,1}^* = K_{T,2}^* = K_T^*$ and $K_{R,1}^* = K_{R,2}^* = K_R^*$. To solve the system E.22, the determinant in equation (E.23) has to be null:

$$\begin{vmatrix} K_T^* & \bar{\lambda}^3 & K_T^* & -\bar{\lambda}^3 \\ \bar{\lambda} & K_R^* & -\bar{\lambda} & K_R^* \\ \bar{\lambda}^3 \sin\left(\bar{\lambda}\right) + K_T^* \cos\left(\bar{\lambda}\right) & -\bar{\lambda}^3 \cos\left(\bar{\lambda}\right) + K_T^* \sin\left(\bar{\lambda}\right) & \bar{\lambda}^3 \sinh\left(\bar{\lambda}\right) + K_T^* \cosh\left(\bar{\lambda}\right) & \bar{\lambda}^3 \cosh\left(\bar{\lambda}\right) + K_T^* \sinh\left(\bar{\lambda}\right) \\ -\bar{\lambda} \cos\left(\bar{\lambda}\right) - K_R^* \sin\left(\bar{\lambda}\right) & -\bar{\lambda} \sin\left(\bar{\lambda}\right) + K_R^* \cos\left(\bar{\lambda}\right) & \bar{\lambda} \cosh\left(\bar{\lambda}\right) + K_R^* \sinh\left(\bar{\lambda}\right) & \bar{\lambda} \sinh\left(\bar{\lambda}\right) + K_R^* \cosh\left(\bar{\lambda}\right) \end{vmatrix}$$
$$\tag{E.23}$$

E.3 Beam on translational elastic supports

If only translational elastic supports are considered, the system in equation (E.19) becomes equation (E.24):

$$\begin{cases} M_{f_z}(0, t) &=& 0 \\ M_{f_z}(L, t) &=& 0 \end{cases} \tag{E.24}$$

E.3.1 Eigenfrequencies equation

The first equation of system E.24 leads to $A = C$, and the determinant to be annulled is given in equation (E.25):

$$\begin{vmatrix} \bar{\lambda}^3 \left[\sin\left(\bar{\lambda}\right) + \sinh\left(\bar{\lambda}\right)\right] + K_T^* \left[\cos\left(\bar{\lambda}\right) + \left[\cosh\left(\bar{\lambda}\right)\right]\right] \\ - \cos\left(\bar{\lambda}\right) + \cosh\left(\bar{\lambda}\right) & \begin{matrix} -\bar{\lambda}^3 \cos\left(\bar{\lambda}\right) + K_T^* \sin\left(\bar{\lambda}\right) \\ - \sin\left(\bar{\lambda}\right) \end{matrix} & \begin{matrix} \bar{\lambda}^3 \cosh\left(\bar{\lambda}\right) + K_T^* \sinh\left(\bar{\lambda}\right) \\ \sinh\left(\bar{\lambda}\right) \end{matrix} \end{vmatrix} \tag{E.25}$$

$$- \left[\bar{\lambda}^3 \left[\sin\left(\bar{\lambda}\right) + \sinh\left(\bar{\lambda}\right)\right] + K_T^* \left[\cos\left(\bar{\lambda}\right) + \left[\cosh\left(\bar{\lambda}\right)\right]\right]\right] \times \begin{vmatrix} \bar{\lambda}^3 & -\bar{\lambda}^3 \\ - \sin\left(\bar{\lambda}\right) & \sinh\left(\bar{\lambda}\right) \end{vmatrix}$$

$$+ \left[-\bar{\lambda}^3 \cos\left(\bar{\lambda}\right) + K_T^* \sin\left(\bar{\lambda}\right)\right] \times \begin{vmatrix} 2.K_T^* & -\bar{\lambda}^3 \\ - \cos\left(\bar{\lambda}\right) + \cosh\left(\bar{\lambda}\right) & \sinh\left(\bar{\lambda}\right) \end{vmatrix}$$

$$- \left[\bar{\lambda}^3 \cosh\left(\bar{\lambda}\right) + K_T^* \sinh\left(\bar{\lambda}\right)\right] \times \begin{vmatrix} 2.K_T^* & \bar{\lambda}^3 \\ - \cos\left(\bar{\lambda}\right) + \cosh\left(\bar{\lambda}\right) & - \sin\left(\bar{\lambda}\right) \end{vmatrix} = 0 \tag{E.26}$$

$$\bar{\lambda}^6 \times \left[2 - 2\cos\left(\bar{\lambda}\right)\cosh\left(\bar{\lambda}\right)\right] + K_T^{*\,2} \times \left[4\sin\left(\bar{\lambda}\right)\sinh\left(\bar{\lambda}\right)\right]$$
$$+ K_T^* \times \bar{\lambda}^3 \times \left[-4\cos\left(\bar{\lambda}\right)\sinh\left(\bar{\lambda}\right) + 4\sin\left(\bar{\lambda}\right)\cosh\left(\bar{\lambda}\right)\right] \tag{E.27}$$

Finally, the eigenfrequencies of this problem can be deduced from equation (E.28):

$$K_T^{*\,2} + K_T^* \times \frac{2\bar{\lambda}^3 \left[\sin\left(\bar{\lambda}\right)\cosh\left(\bar{\lambda}\right) - \cos\left(\bar{\lambda}\right)\sinh\left(\bar{\lambda}\right)\right]}{2\sin\left(\bar{\lambda}\right)\sinh\left(\bar{\lambda}\right)} + \frac{\bar{\lambda}^6 \times \left[1 - \cos\left(\bar{\lambda}\right)\cosh\left(\bar{\lambda}\right)\right]}{2\sin\left(\bar{\lambda}\right)\sinh\left(\bar{\lambda}\right)} = 0 \tag{E.28}$$

E.3.2 Eigenmode shapes

As in equation (E.12), the mode shapes can be defined by equation (E.29):

$$X_T(\bar{x}) = A\cos\left(\bar{\lambda}\bar{x}\right) + B\sin\left(\bar{\lambda}\bar{x}\right) + C\cosh\left(\bar{\lambda}\bar{x}\right) + D\sinh\left(\bar{\lambda}\bar{x}\right) \tag{E.29}$$

with $\bar{x} = {}^x/_L$. Let us consider $B = 1$. Because the momentum is null at beam ends, it can be deduced that $A = C$ from the equation in $\bar{x} = 0$. Then, from the equation in $\bar{x} = 1$, D can be defined as a function of A (eq. E.30):

$$D = \frac{\sin\left(\bar{\lambda}\right) + A\left[\cos\left(\bar{\lambda}\right) - \cosh\left(\bar{\lambda}\right)\right]}{\sinh\left(\bar{\lambda}\right)} \tag{E.30}$$

Finally, the boundary condition for $\bar{x} = 0$ in shear force leads to equation (E.31):

$$2A \times K_T^* = \bar{\lambda}^3 \left[-1 + D\right] \tag{E.31}$$

Then, by combining the equations (E.30) and (E.31), the expression of A can be deduced (eq. E.32):

$$A = \frac{\sinh\left(\bar{\lambda}\right) - \sin\left(\bar{\lambda}\right)}{2\dfrac{K_T^*}{\bar{\lambda}^3}\sinh\left(\bar{\lambda}\right) + \cos\left(\bar{\lambda}\right) - \cosh\left(\bar{\lambda}\right)} = \gamma_T \tag{E.32}$$

$$C = A = \gamma_T \tag{E.33}$$

$$D = \frac{\sin\left(\bar{\lambda}\right)}{\sinh\left(\bar{\lambda}\right)} + \gamma_T \times \frac{\cos\left(\bar{\lambda}\right) - \cosh\left(\bar{\lambda}\right)}{\sinh\left(\bar{\lambda}\right)} = \frac{\sin\left(\bar{\lambda}\right)}{\sinh\left(\bar{\lambda}\right)} + \gamma_T \gamma_{T1} \tag{E.34}$$

with $\gamma_{T1} = \dfrac{\cos\left(\bar{\lambda}\right) - \cosh\left(\bar{\lambda}\right)}{\sinh\left(\bar{\lambda}\right)}$. Finally, the eigenmodes are defined in equation (E.35):

$$X_T(\bar{x}) = \sin\left(\bar{\lambda}\bar{x}\right) + \frac{\sin\left(\bar{\lambda}\right)}{\sinh\left(\bar{\lambda}\right)} \sinh\left(\bar{\lambda}\bar{x}\right) + \gamma_T \times \left[\cos\left(\bar{\lambda}\bar{x}\right) + \cosh\left(\bar{\lambda}\bar{x}\right) + \gamma_{T1} \sinh\left(\bar{\lambda}\bar{x}\right)\right] \tag{E.35}$$

E.4   Beam on rotational elastic supports

If only rotational elastic supports are considered, the system in equation (E.18) becomes equation (E.36):

$$\begin{cases} u_y(0,t) &=& 0 \\ u_y(L,t) &=& 0 \end{cases} \tag{E.36}$$

E.4.1   Eigenfrequencies equation

The first equation of system E.36 leads to $A = -C$, and the determinant to be annulled is given in equation (E.37):

$$\begin{vmatrix} 2\bar{\lambda} & K_R^* & K_R^* \\ \cos\left(\bar{\lambda}\right) - \cosh\left(\bar{\lambda}\right) & \sin\left(\bar{\lambda}\right) & \sinh\left(\bar{\lambda}\right) \\ -\bar{\lambda}\left[\cos\left(\bar{\lambda}\right) + \cosh\left(\bar{\lambda}\right)\right] - K_R^*\left[\sin\left(\bar{\lambda}\right) + \sinh\left(\bar{\lambda}\right)\right] & -\bar{\lambda}\sin\left(\bar{\lambda}\right) + K_R^*\cos\left(\bar{\lambda}\right) & \bar{\lambda}\sinh\left(\bar{\lambda}\right) + K_R^*\cosh\left(\bar{\lambda}\right) \end{vmatrix} \tag{E.37}$$

$$\left[-\bar{\lambda}\left[\cos\left(\bar{\lambda}\right) + \cosh\left(\bar{\lambda}\right)\right] - K_R^*\left[\sin\left(\bar{\lambda}\right) + \sinh\left(\bar{\lambda}\right)\right]\right] \times \begin{vmatrix} K_R^* & K_R^* \\ \sin\left(\bar{\lambda}\right) & \sinh\left(\bar{\lambda}\right) \end{vmatrix}$$

$$- \left[-\bar{\lambda}\sin\left(\bar{\lambda}\right) + K_R^*\cos\left(\bar{\lambda}\right)\right] \times \begin{vmatrix} 2\bar{\lambda} & K_R^* \\ \cos\left(\bar{\lambda}\right) - \cosh\left(\bar{\lambda}\right) & \sinh\left(\bar{\lambda}\right) \end{vmatrix}$$

$$+ \left[\bar{\lambda}\sinh\left(\bar{\lambda}\right) + K_R^*\cosh\left(\bar{\lambda}\right)\right] \times \begin{vmatrix} 2\bar{\lambda} & K_R^* \\ \cos\left(\bar{\lambda}\right) - \cosh\left(\bar{\lambda}\right) & \sin\left(\bar{\lambda}\right) \end{vmatrix} = 0 \tag{E.38}$$

$$\bar{\lambda}^2 \times \left[4\sin\left(\bar{\lambda}\right)\sinh\left(\bar{\lambda}\right)\right] + K_R^{*\,2} \times \left[2 - 2\cos\left(\bar{\lambda}\right)\cosh\left(\bar{\lambda}\right)\right]$$
$$+ K_R^* \times \bar{\lambda} \times \left[-4\cos\left(\bar{\lambda}\right)\sinh\left(\bar{\lambda}\right) + 4\cosh\left(\bar{\lambda}\right)\sin\left(\bar{\lambda}\right)\right] = 0 \tag{E.39}$$

Finally, the eigenfrequencies of this problem can be deduced from equation (E.40):

$$K_R^{*\,2} \quad + \quad K_R^* \quad \times \quad \frac{2\bar{\lambda}\left[\cosh\left(\bar{\lambda}\right)\sin\left(\bar{\lambda}\right) - \cos\left(\bar{\lambda}\right)\sinh\left(\bar{\lambda}\right)\right]}{1 - \cos\left(\bar{\lambda}\right)\cosh\left(\bar{\lambda}\right)} \quad + \quad \frac{2\bar{\lambda}^2 \times \left[\sin\left(\bar{\lambda}\right)\sinh\left(\bar{\lambda}\right)\right]}{1 - \cos\left(\bar{\lambda}\right)\cosh\left(\bar{\lambda}\right)} \quad = \quad 0 \tag{E.40}$$

E.4.2   Eigenmode shapes

As in equation (E.12), the mode shapes can be defined by equation (E.41):

$$X_R(\bar{x}) = A\cos\left(\bar{\lambda}\bar{x}\right) + B\sin\left(\bar{\lambda}\bar{x}\right) + C\cosh\left(\bar{\lambda}\bar{x}\right) + D\sinh\left(\bar{\lambda}\bar{x}\right) \tag{E.41}$$

with $\bar{x} = {}^x\!/_L$. Let us consider $B = 1$. Because the displacement is null at beam ends, it can be deduced that $A = -C$ from the equation in $\bar{x} = 0$. Then, from the equation in $\bar{x} = 1$, D can be defined as a function of A (eq. E.42):

$$D = -\frac{\sin\left(\bar{\lambda}\right)}{\sinh\left(\bar{\lambda}\right)} + A\frac{\cosh\left(\bar{\lambda}\right) - \cos\left(\bar{\lambda}\right)}{\sinh\left(\bar{\lambda}\right)} \tag{E.42}$$

Finally, the boundary condition for $\bar{x} = 0$ in momentum leads to equation (E.43):

$$\bar{\lambda}\left[-A + C\right] = K_R^* \times \left[1 + D\right] \tag{E.43}$$

Then, by combining the equations (E.42) and (E.43), the expression of A can be deduced (eq. E.44):

$$A = \frac{\sinh\left(\bar{\lambda}\right) - \sin\left(\bar{\lambda}\right)}{\cos\left(\bar{\lambda}\right) - \cosh\left(\bar{\lambda}\right) - 2\dfrac{\bar{\lambda}}{K_R^*}\sinh\left(\bar{\lambda}\right)} = \gamma_R \tag{E.44}$$

$$C = -A = -\gamma_R \tag{E.45}$$

$$D = -1 - \frac{2\bar{\lambda}}{K_R^*} \times \gamma_R \tag{E.46}$$

Finally, the eigenmodes are defined in equation (E.47):

$$X_R(\bar{x}) = \sin\left(\bar{\lambda}\bar{x}\right) - \sinh\left(\bar{\lambda}\bar{x}\right) + \gamma_R \times \left[\cos\left(\bar{\lambda}\bar{x}\right) - \cosh\left(\bar{\lambda}\bar{x}\right) - \frac{2\bar{\lambda}}{K_R^*}\sinh\left(\bar{\lambda}\bar{x}\right)\right] \tag{E.47}$$

E.5 Simply supported beam with one additional mass

Let us consider the system in figure 3.6 with one additional mass.

The general form of the mode shapes when an additional mass is added on the beam is the same as for the systems previously studied (eq. E.12, E.29 or E.41). However, the basis in equation (E.48) can be considered to evaluate the problem response:

$$\begin{cases} X_1(kx) &=& \frac{1}{2}\left[\cosh(kx) + \cos(kx)\right] \\ X_2(kx) &=& \frac{1}{2}\left[\sinh(kx) + \sin(kx)\right] \\ X_3(kx) &=& \frac{1}{2}\left[\cosh(kx) - \cos(kx)\right] \\ X_4(kx) &=& \frac{1}{2}\left[\sinh(kx) - \sin(kx)\right] \end{cases} \tag{E.48}$$

So, the displacement can be written in equation (E.49) and the momentum in equation (E.50):

$$X_M(x) = \phi_0 \frac{X_2(kx)}{k} + Q_0 \frac{X_4(kx)}{k^3.E_c.I_h} + \frac{1}{k^2.E_c.I_h}\frac{\omega^2}{k}M_{add}X_M(x_{m_{add}}) \times X_4\left(k(x - x_{m_{add}})\right) \tag{E.49}$$

$$M_{f_z}(x) = \phi_0 X_4(kx).E_c.I_h.k + Q_0\frac{X_2(kx)}{k} + \frac{\omega^2}{k}M_{add}X_M(x_{m_{add}}) \times X_2\left(k(x - x_{m_{add}})\right) \tag{E.50}$$

Then, the boundary conditions are given in equation (E.51):

$$\begin{cases} X_M(L) &=& 0 \\ M_{f_z}(L) &=& 0 \\ X_M(x_{m_{add}}) &=& \phi_0\dfrac{X_2(k.x_{m_{add}})}{k} + Q_0\dfrac{X_4(k.x_{m_{add}})}{k^3.E_c.I_h} \end{cases} \tag{E.51}$$

With $\lambda = k.L$, $n = \frac{\omega^2.M_{add}}{k^4.E_c.I_h.L}$ and $b = L - x_{m_{add}}$, the matrix system in equation (E.52) is obtained.

$$\begin{bmatrix} \frac{X_2(\lambda)}{k} + n\lambda X_4(k.b)\frac{X_2(k.x_{m_{add}})}{k} & \frac{X_4(\lambda)}{k^3.E_c.I_h} + n\lambda X_4(k.b)\frac{X_4(k.x_{m_{add}})}{k^3.E_c.I_h} \\ X_4(\lambda).E_c.I_h.k + \frac{\omega^2 M_{add}}{k^2}X_2(k.x_{m_{add}})X_2(k.b) & \frac{X_2(\lambda)}{k} + \frac{n\lambda}{k}X_4(k.x_{m_{add}})X_2(k.b) \end{bmatrix}\begin{Bmatrix} \phi_O \\ Q_0 \end{Bmatrix} = \begin{Bmatrix} 0 \\ 0 \end{Bmatrix} \tag{E.52}$$

By cancelling the determinant, equation (E.53) is deduced, determining the problem eigenfrequencies.

$$2\sinh\left(\lambda\right)\sin\left(\lambda\right) + n\lambda\left[\sin\left(\lambda\right)\sinh\left(\xi_1\lambda\right)\sinh\left(\xi_2\lambda\right) - \sinh\left(\lambda\right)\sin\left(\xi_1\lambda\right)\sin\left(\xi_2\lambda\right)\right] = 0 \tag{E.53}$$

ALGORITHMS USED IN THE IDENTIFICATION METHOD

F.1 Newmark's algorithm for a linear system

Knowing the displacement, velocity and acceleration at the time step $t-1$, algorithm 3 gives the dynamic values at the next time step (t).

Algorithm 3: Newmark's algorithm

---

input : $\mathbf{U}(t-1)$, $\dot{\mathbf{U}}(t-1)$, $\ddot{\mathbf{U}}(t-1)$, $\ddot{\mathbf{U}}_s(t)$, Δt , γ , β , m_1 , c_1 , k_1 , κ_1

output: $\mathbf{U}(t)$, $\dot{\mathbf{U}}(t)$, $\ddot{\mathbf{U}}(t)$

begin

$$A = \frac{m_1}{\beta.\Delta_t^2} + c_1.\frac{\gamma}{\beta.\Delta t} + k_1$$

$$B = -m_1 \times \kappa_1 \times \ddot{\mathbf{U}}_s(t) + \left[\frac{m_1}{\beta.\Delta t^2} + c_1.\frac{\gamma}{\beta.\Delta t}\right] \times \mathbf{U}(t-1) + \left[\frac{m_1}{\beta.\Delta t} - c_1.\left(1 - \frac{\gamma}{\beta}\right)\right] \times \dot{\mathbf{U}}(t-1) + \left[m_1.\frac{^{1/2}-\beta}{\beta} - c_1.\Delta t.\left(1 - \gamma.\left(1 + \frac{^{1/2}-\beta}{\beta}\right)\right)\right] \times \ddot{\mathbf{U}}(t-1)$$

$$\mathbf{U}(t) = \frac{B}{A}$$

$$\dot{\mathbf{U}}(t) = \left(\frac{\gamma}{\beta.\Delta t}\right) \times [\mathbf{U}(t) - \mathbf{U}(t-1)] + \left(1 - \frac{\gamma}{\beta}\right) \times \dot{\mathbf{U}}w(t-1) + \Delta t.\left[1 - \gamma.\left(1 + \frac{^{1/2}-\beta}{\beta}\right)\right] \times \ddot{\mathbf{U}}(t-1)$$

$$\ddot{\mathbf{U}}(t) = \left(\frac{1}{\beta.\Delta t^2}\right) \times [\mathbf{U}(t) - \mathbf{U}(t-1)] + \left(\frac{1}{\beta.\Delta t}\right) \times \dot{\mathbf{U}}(t-1) + \left(\frac{^{1/2}-\beta}{\beta}\right) \times \ddot{\mathbf{U}}(t-1)$$

end

F.2   The "interior-point methods" for nonlinear optimization

The objective of the "interior-point method" implemented into Matlab® is to solve the problem in equation (F.1) using a sequence of approximate minimization problems (eq. F.2) (MathWorks, 2021).

$$\min_x f(x), \quad \text{subjected to} \quad h(x) = 0 \quad \text{and} \quad g(x) \leq 0 \tag{F.1}$$

$$\min_{x,s} f_\mu(x,s) = \min_{x,s} f(x) - \mu \sum_i \ln(s_i), \quad \text{subjected to} \quad s \leq 0, \quad h(x) = 0, \quad g(x) + s = 0 \tag{F.2}$$

The approximate problems in equation (F.2) are more accessible to solve than the initial problem because they are equally constrained problems. The algorithm first applied a direct step corresponding to the Newton step for each iteration. Moreover, a conjugate gradient step is used if the direct step can not be used.[1]

---

[1]More information about the algorithm is presented in MathWorks (2021) paper.

Appendix G

PARAMETRIC ANALYSIS OF UPDATED DAMPING MATRICES

G.1 Non-diagonal damping matrix formulation

G.1.1 p_2 evolution

(a) Acceleration global errors

(b) Displacement global errors

(c) Support force global errors

(d) Error on the maximal acceleration

(e) Error on the maximal displacement

(f) Error on the maximal support force
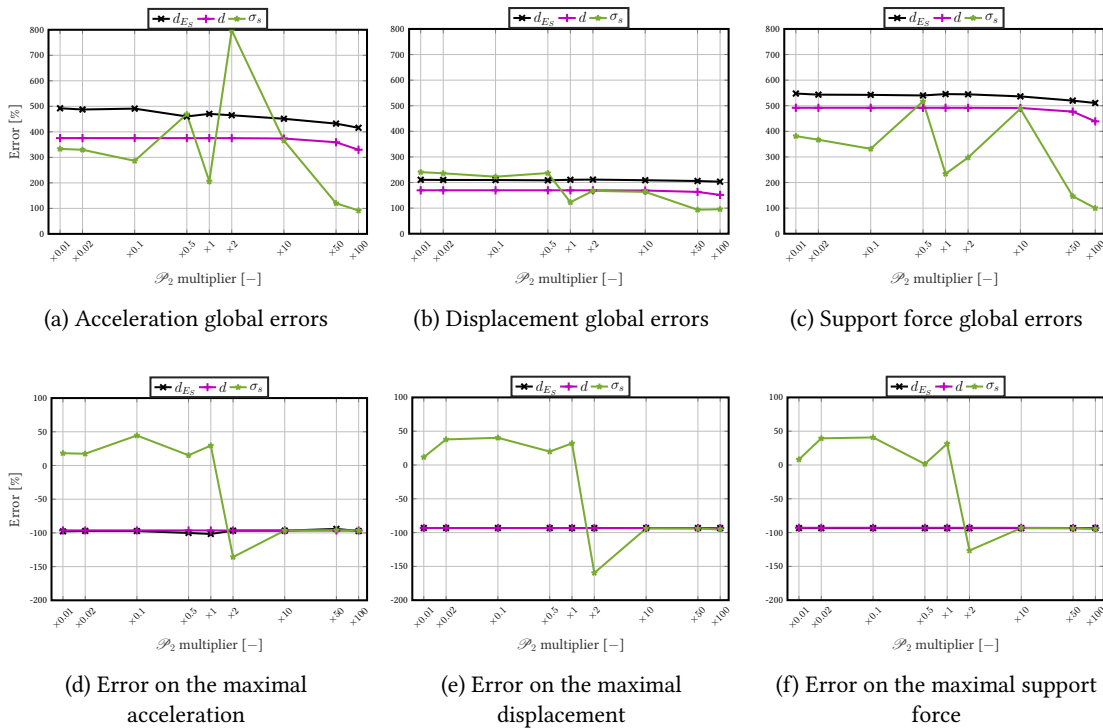
Figure G.1: Parametric study of function parameters - non-diagonal damping matrix formulation - $\mathscr{P}_2$ evolution - global responses

(a) Damage (cracking)   (b) Friction strain   (c) Steel stress
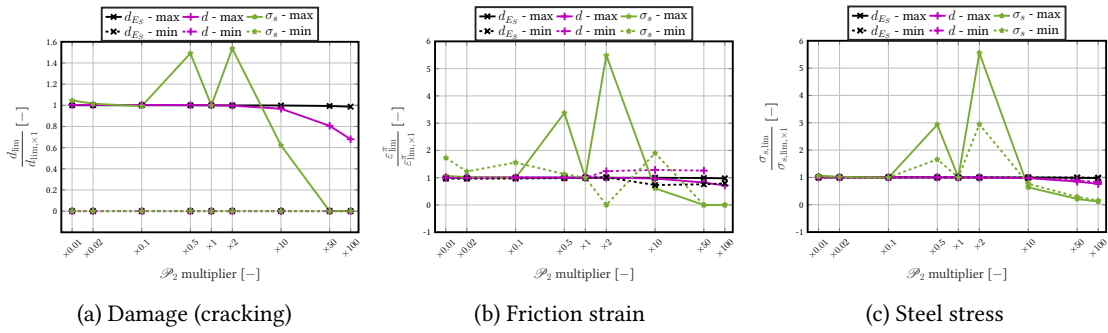
Figure G.2: Parametric study of function parameters - non-diagonal damping matrix formulation - $\mathscr{P}_2$ evolution - normalized maximal and minimal values of some variables

(a) E_i vs E_{tot} and u_{max} d_{E_S} variable

(b) E_i vs E_{tot} and u_{max} d variable

(c) E_i vs E_{tot} and u_{max} σ_s variable

(d) Dissipated energies d_{E_S} variable

(e) Dissipated energies d variable

(f) Dissipated energies σ_s variable
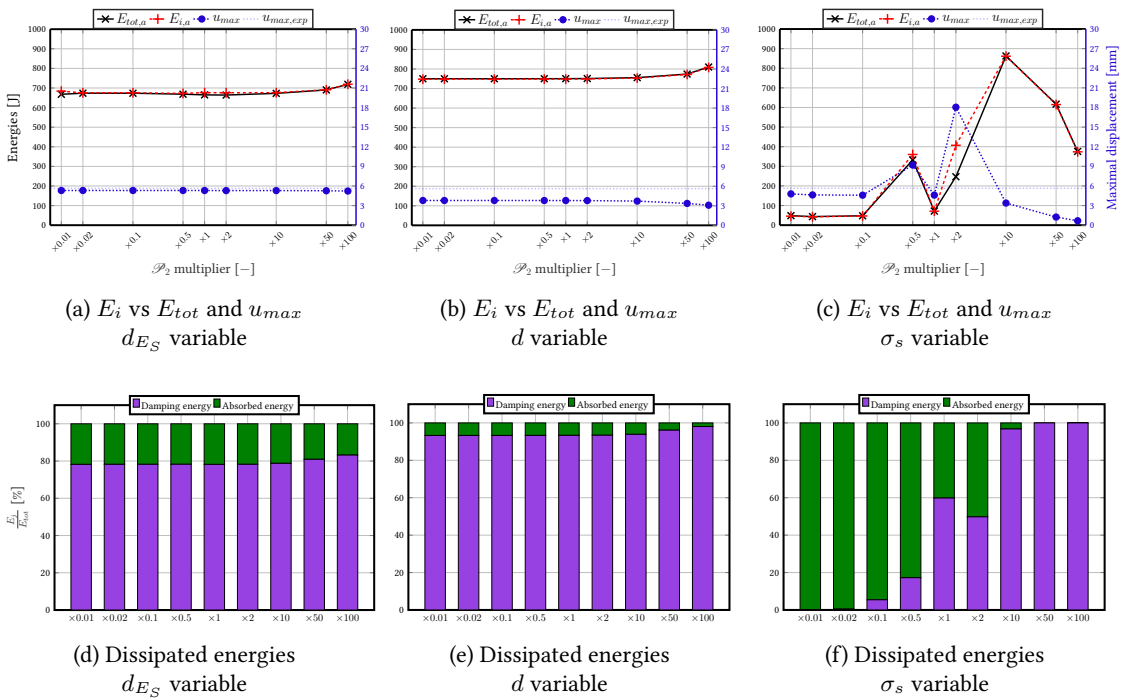
Figure G.3: Parametric study of function parameters - non-diagonal damping matrix formulation - $\mathscr{P}_2$ evolution - energy analyses

G.2   Diagonal damping matrix formulation

G.2.1 p_1 evolution

(a) Acceleration global errors

(b) Displacement global errors

(c) Support force global errors

(d) Error on the maximal acceleration

(e) Error on the maximal displacement

(f) Error on the maximal support force
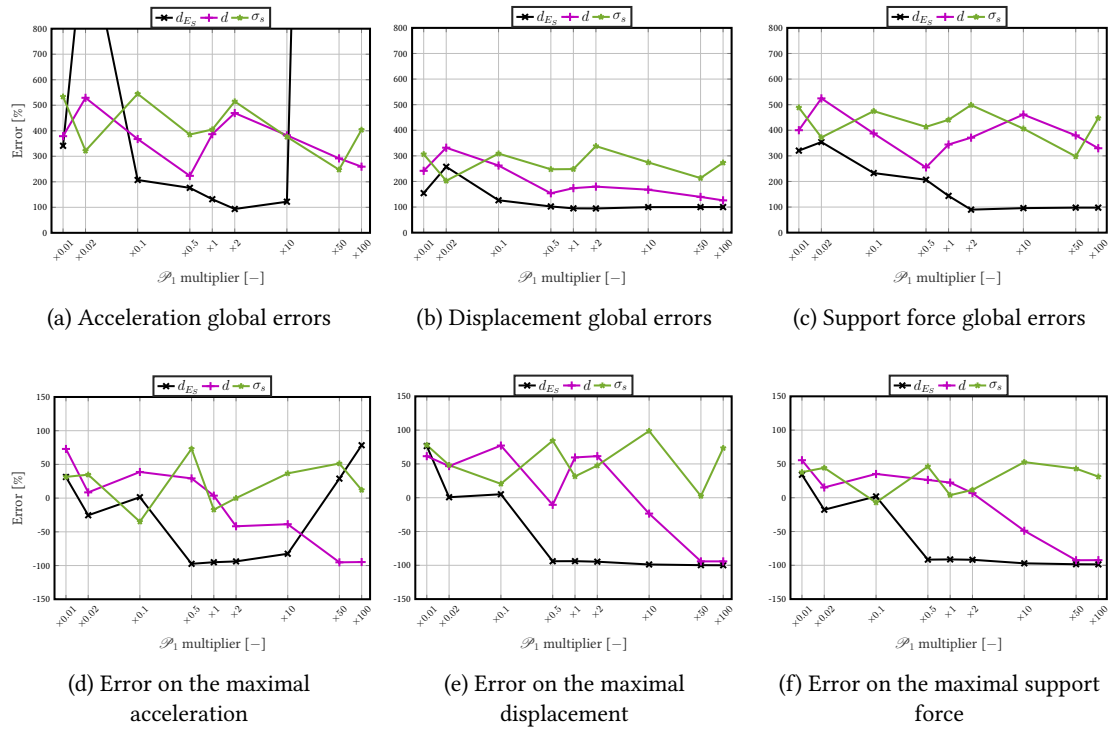
Figure G.4: Parametric study of function parameters - diagonal damping matrix formulation - $\mathscr{P}_1$ evolution - global responses

(a) Damage (cracking)

(b) Friction strain

(c) Steel stress
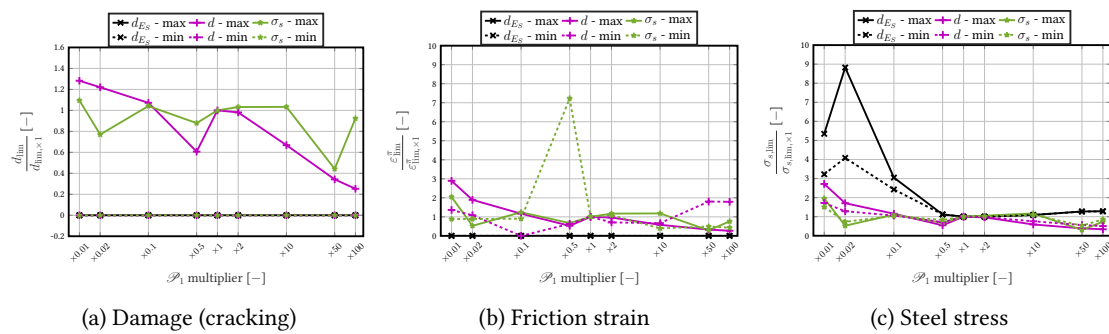
Figure G.5: Parametric study of function parameters - diagonal damping matrix formulation - $\mathscr{P}_1$ evolution - normalized maximal and minimal values of some variables

(a) E_i vs E_{tot} and u_{max}
d_{E_S} variable

(b) E_i vs E_{tot} and u_{max}
d variable

(c) E_i vs E_{tot} and u_{max}
σ_s variable

(d) Dissipated energies
d_{E_S} variable

(e) Dissipated energies
d variable

(f) Dissipated energies
σ_s variable
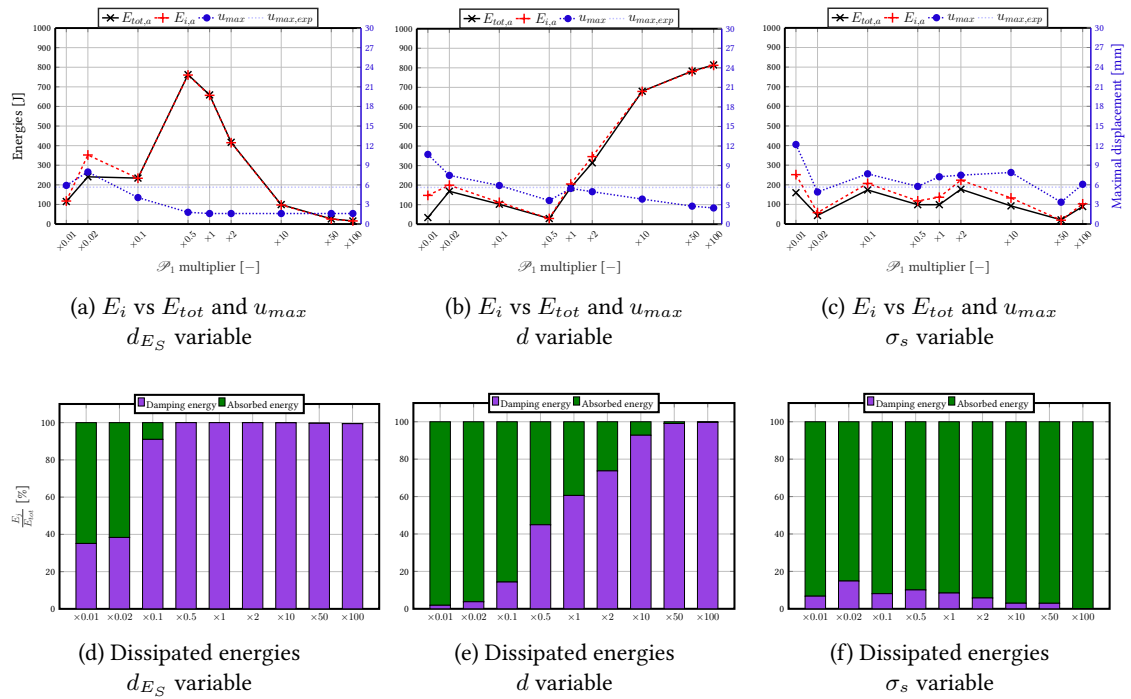
Figure G.6: Parametric study of function parameters - diagonal damping matrix formulation - $\mathscr{P}_1$
evolution - energy analyses

G.2.2 p_2 evolution

(a) Acceleration global errors   (b) Displacement global errors   (c) Support force global errors

(d) Error on the maximal acceleration   (e) Error on the maximal displacement   (f) Error on the maximal support force
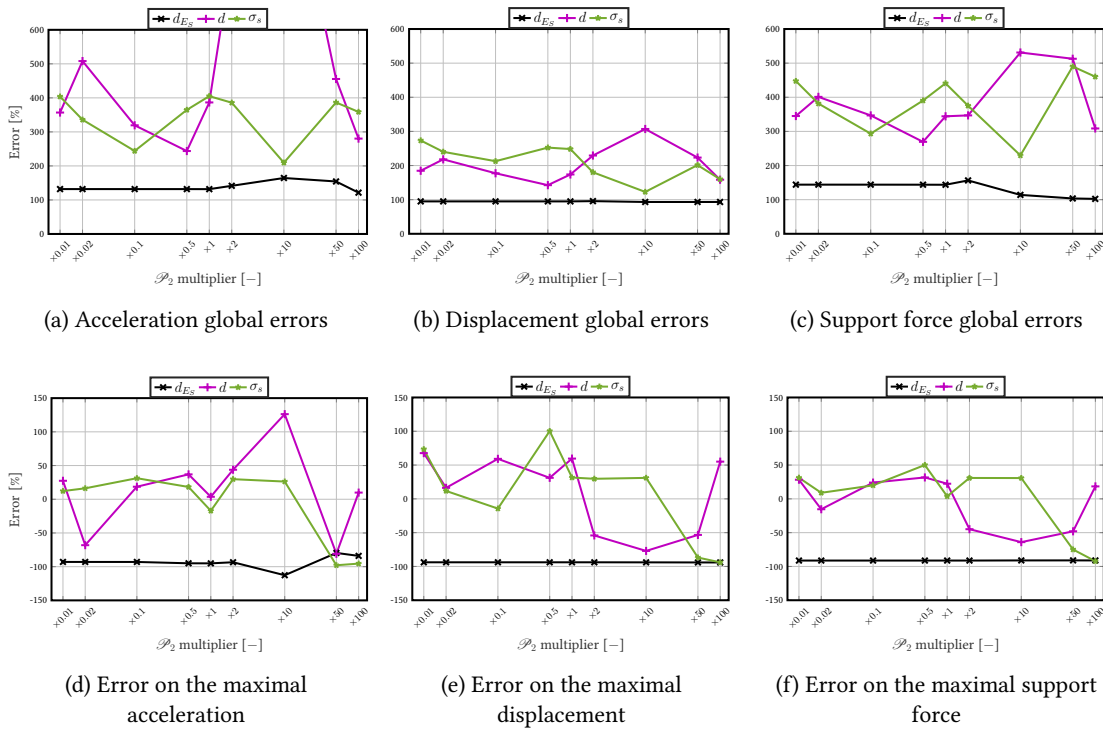
Figure G.7: Parametric study of function parameters - diagonal damping matrix formulation - $\mathscr{P}_2$ evolution - global responses

(a) Damage (cracking)   (b) Friction strain   (c) Steel stress
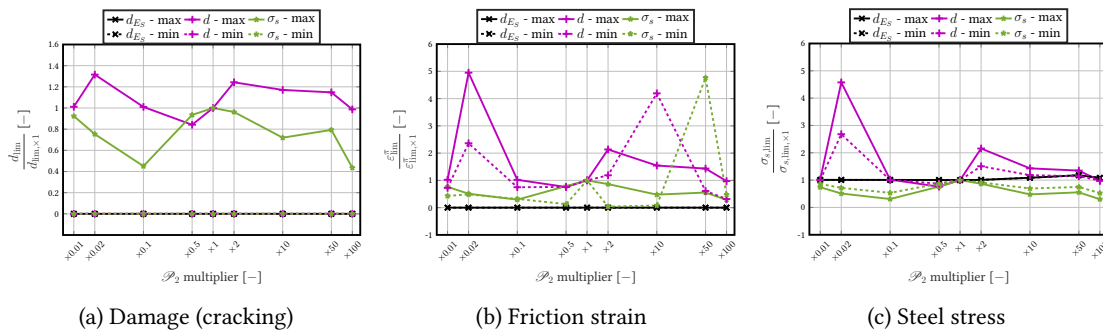
Figure G.8: Parametric study of function parameters - diagonal damping matrix formulation - $\mathscr{P}_2$ evolution - normalized maximal and minimal values of some variables

(a) E_i vs E_{tot} and u_{max}
d_{E_S} variable

(b) E_i vs E_{tot} and u_{max}
d variable

(c) E_i vs E_{tot} and u_{max}
σ_s variable

(d) Dissipated energies
d_{E_S} variable

(e) Dissipated energies
d variable

(f) Dissipated energies
σ_s variable
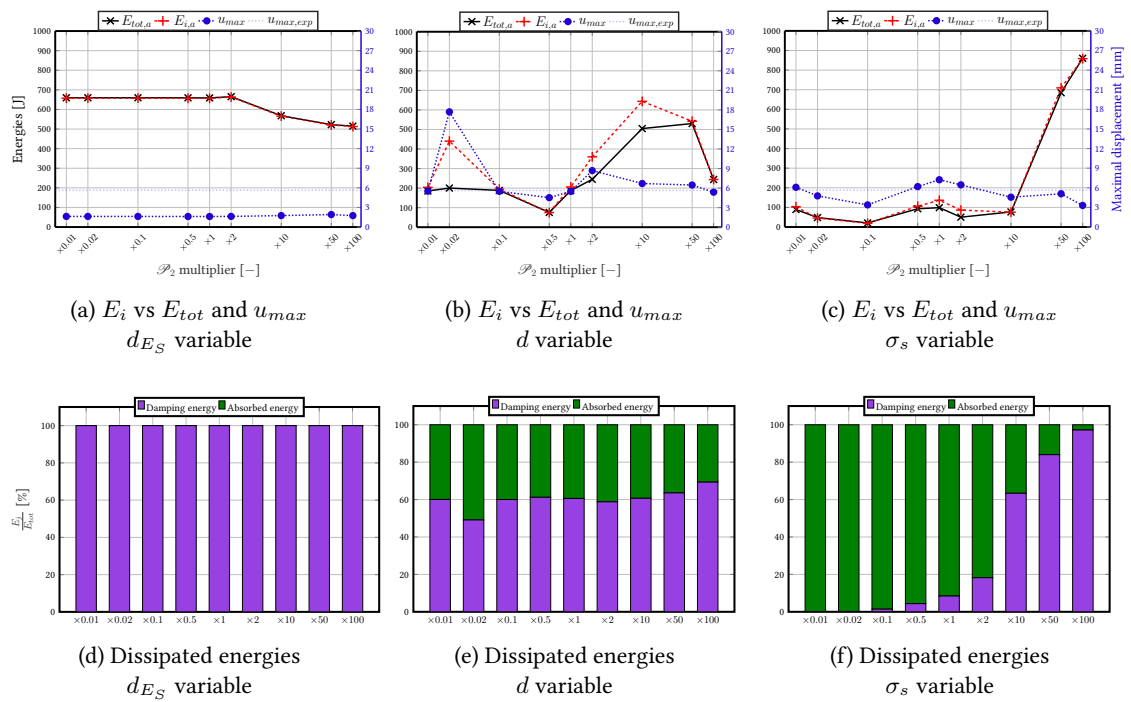
Figure G.9: Parametric study of function parameters - diagonal damping matrix formulation - $\mathscr{P}_2$ evolution - energy analyses

Titre : Modélisation de l'amortissement dans les analyses dynamiques non-linéaires de structures en béton armé : modèles matériaux et identification expérimentale

Mots clés : Amortissement, Béton armé, Dynamique, Modèle non-linéaire, Bilan énergétique, Identification et actualisation de l'amortissement

Résumé : En plus de la nouvelle réglementation sismique mise en place en 2011 sur le territoire français, l'accident nucléaire de Fukushima la même année a poussé le gouvernement français à investir pour la sécurité des bâtiments nucléaires. Pour assurer la viabilité de telles structures, des modèles performants sont nécessaires et doivent intégrer une description fine des phénomènes physiques. Dans le cas de structures en béton armé, la plus grande difficulté vient du manque de connaissances sur l'évolution de l'endommagement et la capacité du béton à dissiper de l'énergie. Les dissipations peuvent être modélisées à deux échelles : à l'échelle globale pour caractériser les interactions de la structure avec son environnement et à l'échelle locale pour modéliser les dissipations dans les matériaux. Grâce à des données expérimentales, un modèle numérique non-linéaire de poutre en béton armé a été développé pour évaluer la capacité de modèles classiques d'amortissement à représenter les phénomènes physiques. Ensuite, une méthode d'identification de l'amortissement est proposée pour déterminer l'évolution de l'amortissement en fonction de l'endommagement du béton. Enfin, en se basant sur l'étude des phénomènes dissipatifs les plus influents dans le béton, un modèle d'actualisation de l'amortissement à l'échelle locale est proposé.

Title : Modelling of damping in nonlinear dynamic analyses of reinforced concrete structures : constitutive formulations and experimental identification

Keywords : Damping, Reinforced Concrete, Dynamic, Nonlinear Model, Energy Balances, Damping Identification and updating

Abstract : In addition to the new seismic zoning of the French territory in 2011, the Fukushima nuclear accident the same year prompted the French government to focus on the safety of nuclear buildings. To ensure the viability of such structures, performative models are required, so they have to integrate fine physical phenomena descriptions. In the case of reinforced concrete structures, the significant difficulty comes from the lack of knowledge about the damage evolution and the ability of concrete to dissipate energy. Dissipations can be described at two scales : at the global scale to characterize the structure interaction with its environment and at the local scale to model material dissipations. Based on experimental data, a reinforced concrete beam numerical nonlinear model is developed to evaluate the ability of classical global scale damping models to characterize physical phenomena. Then, a damping identification method is proposed to determine the transient evolution of damping through concrete damage. Finally, a local scale damping update model is proposed based on the study of the most dissipative phenomena in concrete.